



HAL
open science

Studies of fibrous carbons for high-temperature thermal energy storage

Blagoj Karakashov

► **To cite this version:**

Blagoj Karakashov. Studies of fibrous carbons for high-temperature thermal energy storage. Chemical Sciences. Université de Lorraine, 2019. English. NNT : 2019LORR0224 . tel-02551704

HAL Id: tel-02551704

<https://hal.univ-lorraine.fr/tel-02551704>

Submitted on 15 Dec 2020

HAL is a multi-disciplinary open access archive for the deposit and dissemination of scientific research documents, whether they are published or not. The documents may come from teaching and research institutions in France or abroad, or from public or private research centers.

L'archive ouverte pluridisciplinaire **HAL**, est destinée au dépôt et à la diffusion de documents scientifiques de niveau recherche, publiés ou non, émanant des établissements d'enseignement et de recherche français ou étrangers, des laboratoires publics ou privés.



AVERTISSEMENT

Ce document est le fruit d'un long travail approuvé par le jury de soutenance et mis à disposition de l'ensemble de la communauté universitaire élargie.

Il est soumis à la propriété intellectuelle de l'auteur. Ceci implique une obligation de citation et de référencement lors de l'utilisation de ce document.

D'autre part, toute contrefaçon, plagiat, reproduction illicite encourt une poursuite pénale.

Contact : ddoc-theses-contact@univ-lorraine.fr

LIENS

Code de la Propriété Intellectuelle. articles L 122. 4

Code de la Propriété Intellectuelle. articles L 335.2- L 335.10

http://www.cfcopies.com/V2/leg/leg_droi.php

<http://www.culture.gouv.fr/culture/infos-pratiques/droits/protection.htm>

THÈSE

Pour l'obtention du titre de:

DOCTEUR de L'UNIVERSITÉ DE LORRAINE

Spécialité: Chimie

Présentée par:

BLAGOJ KARAKASHOV

Etudes de carbones fibreux pour le stockage compact d'énergie à haute température

Thèse soutenue publiquement le 13 décembre 2019 à Epinal devant le jury composé de:

Mme Sylvie BONNAMY	Directrice de Recherches au CNRS, ICMN (Interfaces, Confinement, Matériaux et Nano- structures), Université d'Orléans	Rapporteur
M. Cuong PHAM-HUU	Directeur de Recherches au CNRS, ICPEES (Institut de chimie et procédés pour l'énergie, l'envi- ronnement et la santé), Université de Strasbourg	Rapporteur
M. Philippe POULIN	Directeur de Recherches au CNRS, CRPP (Centre de Recherche Paul Pascal), Université de Bordeaux	Examineur
M. Alain CELZARD	Professeur, IJL (Institut Jean Lamour), Université de Lorraine	Directeur de thèse
Mme Vanessa FIERRO	Directrice de Recherches au CNRS, IJL (Institut Jean Lamour)	Co-directrice de thèse

*Institut Jean Lamour – UMR 7198- Département N2EV – Equipe 402
ENSTIB - BP 21042 - 88051 Épinal Cedex 9
Université de Lorraine – Pôle M4 - Collegium Sciences et Technologie*

Remerciements

Je tiens tout d'abord à remercier les membres du jury de ma soutenance de thèse, les rapporteurs Mme Sylvie Bonnamy, Directrice de Recherches au CNRS à l'Interfaces, Confinement, Matériaux et Nanostructures, et M. Cuong Pham-Huu, Directeur de Recherches au CNRS à l'Institut de chimie et procédés pour l'énergie, l'environnement et la santé, qui ont passés beaucoup de temps à lire soigneusement cette mémoire. Merci de m'avoir fait l'honneur d'accepter d'évaluer et finalement de discuter ce travail de thèse avec moi le jour de la soutenance. Merci à M. Philippe POULIN, Directeur de Recherches au CNRS à le Centre de Recherche Paul Pascal, de m'avoir fait l'honneur de présider mon jury de défense et d'apporter son expertise pour enrichir les discussions.

Je remercie tout particulièrement mon directeur de thèse M. Alain Celzard, Professeur à l'Université de Lorraine, qui m'a donné l'opportunité de travailler sur ce projet et de faire partie de son équipe de recherche. Je tiens à vous remercier pour la confiance que vous m'avez accordé au cours de ces trois années de thèse, pour vos conseils et votre expérience infinie. J'exprime aussi tous mes remerciements à ma co-directrice de thèse Mme Vanessa Fierro, Directrice de Recherches au CNRS à Institut Jean Lamour, qui a également partagé ses précieux savoir scientifiques. C'est un honneur de travailler avec des scientifiques et des professionnels comme vous deux.

J'aimerais exprimer ma gratitude à toutes les personnes des instituts et de la plateforme de recherche participant au projet Pc2TES pour la discussion fructueuse qui a eu lieu lors de la réunion du projet et pour m'avoir accepté pour effectuer une partie de mes travaux dans leurs laboratoires. Je remercié l'Agence Nationale de la Recherche du soutien financier de la Pc2TES ainsi que de mon travail de thèse.

Remercier à toutes et à tous les doctorant(e)s, étudiant(e)s et les personel de l'ENSTIB avec lesquels j'ai partagé tous ces grand moments pendant ces trois dernières années. C'est très agréable de remercier mes chers amis et collégiens, Angela, Séb, Pamela, Fran, Balázs, José, Víctor, Judith, Amalia, Imane, Clément, Xeudong, Alex, Caroline, Lara, Samantha et bien d'autre avec qui j'ai partagé d'innombrables moments exquis, au bureau, labo et tout autour. La liste est longue, mais croyez-moi, je suis heureux de vous avoir tous rencontrés. Je voudrais particulièrement remercier Philippe Gadonneix, notre gardien de laboratoire, d'avoir eu la

patience d'être toujours là pour m'aider dans le labo. I would like to say muchas gracias to Clara, a great friend and scientist, for introducing me and patiently sharing her valuable experience in the lab. Thanks to Zabour (Oussama) for sharing his positive energy and help whenever was needed. And here I would like to share my especially gratefulness for meeting, living, sharing most of my important and happy moments with you, my comrades: César (Hombre) and Jimena Castro - The Queen of Origin, always there to support me in all the challenging moments but also to nicely destroy each of my presentations; Zelig (Youri) – La future présidente de la république with a heart of a lion who never gave up on me, and Giuseppe di Napoli – The finest Italian with whom the moments together have special culinary/fashion/deep-discussion dimensions. Ви благодарам, моја интернационална фамилијо.

Фамилијата ми е се. Затоа од се срце, сакам најпрво да им се заблагодарам на моите прекрасни и херојски родители, Љубица и Љупчо, и брат - јунак, Јане, за неизмерната поддршка и љубов. И за крај, но сепак покрај мене од самиот почеток на ова животно патешествие, сакам да и се заблагодарам на мојата животна сопатничка, идна мајка на нашите деца, мојата Елена, на која од се срце и ја посветувам оваа докторска работа. Нашата љубов, поддршка и внимание беа, се и ќе бидат водечка енергија да продолжиме да чекорам по нашиот животен пат. Те љубам.

The road to success is neither paved nor straight, be prepared.

La route du succès n'est ni pavée ni droite, soyez prêt.

Путь до успеха не с ни у прав ни у па.нч, уогуубу сс.

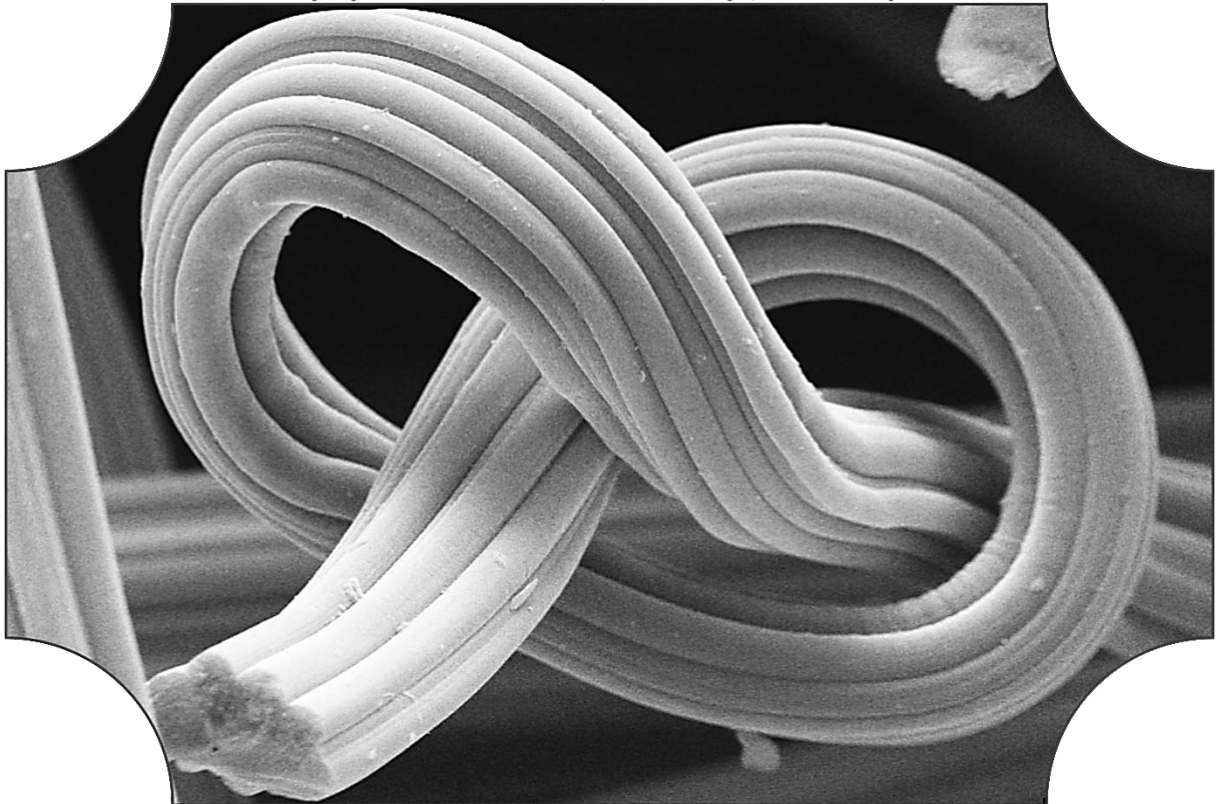


Table of contents

RÉSUMÉ DE LA THÈSE	13
INTRODUCTION GENERALE	33
CHAPTER I: STATE OF THE ART	37
I/1 General context	39
I/1.1 The value and potential of renewable energy for a sustainable future	39
I/1.2 Current status of Thermal Energy Storage (TES) systems	40
I/1.2.a Classification of TES systems	41
I/1.3 Phase-change materials (PCMs): a promising TES technology	42
I/1.3.a Peritectic compounds (PCs): a special category of PCMs	44
I/1.3.b Improvement of PC performances and properties	47
I/2 Generalities on carbon and porous materials	55
I/2.1 Basic carbon information	56
I/2.1.a Graphitic materials	57
I/2.2 Porous carbon, an ideal host material?	61
I/2.2.a Porous materials	61
I/3 Non-woven carbon fibre felts	67
I/3.1 CF structure and properties of importance for TES application	69
I/3.1.a Out-of-plane fluid permeability	69
I/3.1.b Mechanical properties	70
I/3.1.c Thermal conductivity	72
I/3.1.d CF chemical stability	74
I/4 Objectives of the thesis	76
I/5 Bibliography	78

CHAPTER II: CHARACTERISATION OF CARBON FELTS' MORPHOLOGY AND PHYSICAL PROPERTIES	87
II/1 Introduction	89
II/2 Experimental	90
II/2.1 De-sizing of as-received commercial CF	90
II/2.2 Sorting of commercial CF materials	91
II/2.3 Porosity and density	92
II/2.4 Textural analysis with mercury porosimetry	93
II/2.5 Imaging of CF structure	94
II/2.5.a Scanning Electron Microscopy (SEM)	95
II/2.5.b Tomography – 3D morphology studies	96
II/2.6 Wettability studies	97
II/2.7 Physical properties	98
II/2.7.a Out-of-plane air permeability	98
II/2.7.b Mechanical characterisation	100
II/2.7.c Thermal conductivity properties	103
II/3 Results and discussion	105
II/3.1 Morphological characterisations	105
II/3.1.a Porosity and density	105
II/3.1.b Textural analysis with mercury porosimetry	106
II/3.1.c Morphology investigated by SEM	108
II/3.1.d Tomography – CF morphology studies	117
II/3.2 Wettability studies	122
II/3.3 Physical properties	127
II/3.3.a Out-of-plane air permeability	127
II/3.3.b Mechanical properties	143
II/3.3.c Thermal conductivity	163
II/4 Conclusion	169
II/5 Bibliography	172

II/6 Annex	180
II/6.1 Available suppliers' specification information of the evaluated CFs	180
II/6.2 Morphological characteristics	181
II/6.3 Contact angle measurement results	184
II/6.4 Out-of-plane air permeability	185
II/6.4.a Sensitivity analysis showing the effect of percolation threshold and porosity on the value of the Archies' exponent	185
II/6.5 Mechanical properties	187
II/6.6 Thermal conductivity	191

CHAPTER III: CARBON FELTS' STRUCTURAL PROPERTIES AND CHEMICAL STABILITY IN MOLTEN SALTS

193

III/1 Introduction	195
III/2 Experimental	198
III/2.1 Materials and sample preparation	198
III/2.2 CF impregnation by molten inorganic salts of interest	201
III/2.3 Morphological and textural characterisations	202
III/2.3.a Carbon fibre morphology	202
III/2.3.b Textural properties of CF	202
III/2.4 Structural and elemental characterisation	204
III/2.4.a X-ray diffraction analysis	204
III/2.4.b Raman spectroscopy	205
III/2.4.c Elemental analysis	207
III/3 Results and discussion	208
III/3.1 Elemental composition of the investigated CF	208
III/3.2 Structural properties and carbon nanotexture of CF	212
III/3.3 CF complete impregnation in the investigated molten salts - process validation	224
III/3.4 Carbon chemical reactivity in molten LiOH	225
III/3.5 CF chemical stability with respect to their structural properties	228
III/3.6 CF chemical stability in LiBr or Li ₄ (OH) ₃ Br	248
III/3.7 Estimation of CF chemical stability at the application temperature	253
III/4 Conclusion	257

III/5	Bibliography	260
III/6	Annex	267
III/6.1	N ₂ adsorption isotherms	269
III/6.2	Additional SEM micrographs of chemically reactivated CFs in molten LiOH	271
CHAPTER IV: ADVANCED CARBON FELTS' MODIFICATIONS AND APPLICATION TESTS		273
IV/1	Introduction	275
IV/2	Experimental	277
IV/2.1	CF preform and CVD of C/C composites	277
IV/2.2	Morphological characterisation of prepared C/C composites	278
IV/2.2.a	Porosity and density	278
IV/2.2.b	Pyrocarbon microstructure and textural analysis	278
IV/2.2.c	Imaging of C/C composite microstructure	280
IV/2.3	Physical properties of C/C composites	280
IV/2.3.a	Mechanical characterisation	281
IV/2.4	Structural and elemental characterisation	282
IV/2.5	Chemical stability of C/C composites in molten lithium salts	282
IV/2.6	Preliminary analysis of stoichiometric Li-based PC, alone or in contact with CF host	283
IV/2.6.a	In-situ studies	283
IV/2.6.b	Structural properties analysis	284
IV/2.6.c	Thermal properties analysis	284
IV/3	Results and discussion	285
IV/3.1	Morphological characterisations of C/C composites	285
IV/3.1.a	Porosity and density	285
IV/3.1.b	Morphology investigated by SEM	286
IV/3.1.c	Textural analysis with polarised optical microscopy	290
IV/3.2	Physical properties of C/C composites	293
IV/3.2.a	Out-of-plane air permeability	293
IV/3.2.b	Mechanical properties	296
IV/3.2.c	Thermal conductivity	301
IV/3.3	Chemical stability of C/C composites in LiOH or Li ₄ (OH) ₃ Br	303

IV/3.4 Preliminary results of morphological, structural and thermal analysis of PC, alone or in CF-PC hybrid material	312
IV/4 Conclusion	319
IV/5 Bibliography	323
IV/6 Annex	327
IV/6.1 Results of C/C composite analysis	327
IV/6.2 Preliminary results of morphological, structural and thermal analysis of PC, alone or in CF-PC hybrid material	334
CONCLUSIONS ET PERSPECTIVES	335
LIST OF WORKS	343
ABSTRACT	346
RÉSUMÉ	346

Résumé de la thèse

L'augmentation de la population et le développement économique et industriel de nombreux pays du monde nécessitent de chercher des sources d'énergie constantes et stables. Plus important encore, les préoccupations globales liées au changement climatique ou à la pollution rendent absolument primordial le développement de nouvelles technologies et de matériaux durables qui améliorent les rendements, en particulier pour le stockage des énergies renouvelables sous ses diverses formes. Au cours des dernières décennies, d'importants travaux scientifiques ont été réalisés pour répondre à la demande pressante de technologies de remplacement pour la collecte et le stockage d'énergie verte et durable, telle que l'énergie solaire. Le stockage d'énergie thermique (en anglais Thermal Energy Storage, abrégé TES dans ce qui suit) est donc considéré comme une solution d'importance majeure pour répondre à ces attentes. Ce dispositif devrait jouer un rôle important dans le développement de technologies d'énergies propres, dans l'amélioration de la gestion globale de l'énergie et dans l'incorporation de l'énergie solaire ou d'autres sources d'énergies thermiques, dégageant un large excès d'énergie et pouvant se révéler être encore plus durable. En tant que tel, les systèmes TES sont définis par une capacité d'énergie constante et stable pouvant garantir une couverture continue des besoins en énergie.

Ce travail de thèse contribue au développement de matériaux pour le stockage d'énergie, à leur caractérisation en tant que tels mais aussi sous forme d'hybrides contenant un matériau à changement de phase en vue d'améliorer les capacités de stockage de différentes énergies renouvelables ou excédentaires sous forme d'énergie thermique. Cette thèse s'inscrit dans un projet ANR de plus grande ampleur, Pc2TES (« Composés péritectiques pour le stockage compact d'énergie thermique à haute température »), visant à développer un nouveau type de matériaux hybrides à fort potentiel pour la conception originale d'un système TES compact et innovant fonctionnant à « haute » température (300-400°C). En d'autres termes, le projet global ambitionne de parvenir à combiner les avantages de technologies couramment utilisées et étudiées tout en évitant leurs inconvénients respectifs.

Au vu des objectifs du projet et de leur rôle central dans cette thèse, des matériaux commerciaux à base de carbone fibreux ont été étudiés dans l'optique d'une utilisation bénéfique pour le stockage d'énergie à haute température. Il est en effet question de proposer des méthodes de caractérisation et d'optimisation de matériaux carbonés fibreux, d'origine

renouvelable ou synthétique, dans le but de fournir un hôte poreux à longue durée de vie, requis pour une efficacité accrue des composés péritectiques dans les systèmes TES.

Les objectifs principaux de la thèse étaient donc de mener des recherches approfondies sur une utilisation à long terme des carbones fibreux comme hôtes de matériaux à changement de phase dans un système TES. Cela constitue une première étape de l'utilisation de ce nouveau type de stockage depuis l'échelle du laboratoire jusqu'à une application commerciale. Il est donc nécessaire de poursuivre les études, au-delà de celles réalisées jusqu'à présent et en particulier en ce qui concerne les propriétés des matériaux, par des méthodes connues ou nouvelles de caractérisation et de modification avancée des matériaux. À cette fin, divers carbones fibreux et poreux du commerce ont été caractérisés en détail et modifiés.

Ce travail a été réalisé au sein de l'équipe 402 "Matériaux Biosourcés" de l'Institut Jean Lamour (IJL - UMR CNRS 7198), hébergée par l'Ecole Nationale des Techniques et Industries du Bois (ENSTIB), à l'Université de Lorraine. La réalisation de cette thèse dans le cadre du projet Pc2TES a été financée par l'ANR (ANR-16-CE06-0012-01). Plusieurs autres partenaires ont été impliqués dans les travaux du projet Pc2TES, tels que I2M (Institut de mécanique et d'ingénierie- UMR 5295), ICMCB (Institut de Chimie de la Matière Condensée de Bordeaux - UMR CNRS 5026), PLACAMAT (PLateforme Aquitaine de CARactérisation des MATériaux – UMS CNRS 3626), tous à Bordeaux, ainsi que, vers la fin, l'IS2M (Institut de Science des Matériaux de Mulhouse - UMR CNRS 7361). La description de chaque chapitre de thèse est maintenant présentée ci-dessous.

Chapitre I: Etat de l'art

Ce premier chapitre présente une revue actualisée des travaux menés pour le développement de méthodes et de matériaux utilisés dans le secteur du stockage d'énergie étudié, dans laquelle les objectifs de la thèse devraient fournir certaines des réponses manquantes. Les informations sur le TES sont détaillées, suivies d'une attention particulière portée aux matériaux à changement de phase et à leurs propriétés, ainsi qu'aux matériaux à base de carbone, supports potentiels pour un stockage d'énergie amélioré.

Dans les différents systèmes TES décrits, la chaleur latente et plus particulièrement les matériaux à changement de phase (MCP) jouent un rôle essentiel dans la mise en œuvre de ce type de stockage d'énergie. En tant que principal objectif du projet Pc2TES, le développement de composés péritectiques apparaît comme un nouveau type de MCP présentant un fort potentiel pour fournir des TES rentables économiquement. Ce principe est basé sur une idée

totalement nouvelle qui propose un stockage d'énergie par deux processus consécutifs: un processus de fusion / solidification et une réaction chimique liquide-solide. Néanmoins, des études antérieures montrent que les meilleures performances de tels MCP et l'amélioration de leur stabilité et de leur efficacité ne peuvent être obtenues que par l'utilisation de matériaux hôtes pour les y confiner. Ces derniers sont considérés comme le principal objectif du présent travail. Par conséquent, l'utilisation de matériaux poreux à base de carbone, tels que les feutres de carbone (FCs), a été choisie comme l'une des meilleures options en termes de coût, de disponibilité technologique et de propriétés pour atteindre les performances de stockage d'énergie les plus élevées. Puisque les FCs constituent le cœur de la discussion de cette thèse, les résultats d'études antérieures présentant les travaux effectués jusqu'à présent pour l'utilisation de tels matériaux comme hôtes de MCP dans les systèmes TES ont été rassemblés. En outre, ce chapitre bibliographique rassemble les principales caractéristiques bien connues des FCs étudiés, compilant des informations de base sur le carbone, en passant par les propriétés des matériaux carbonés poreux non tissés finaux.

En résumé, les fibres de carbone dérivées de précurseurs polymères synthétiques ou naturels sont des matériaux prêts à être commercialisés, moins chers que de nombreux autres matériaux poreux en carbone, métal ou céramique, et qui possèdent une structure non tissée tridimensionnelle unique conférant un grand volume et des propriétés physiques et thermochimiques particulières. Les fibres de carbone, constituants principaux des FCs, sont des matériaux du groupe des carbones graphitiques et sont composées de couches de carbone aromatiques plus ou moins alignées parallèlement à l'axe des fibres. La Figure 1 illustre schématiquement plusieurs caractéristiques des étapes de préparation préliminaires ou finales, telles que les matières premières utilisées en tant que précurseurs des fibres, les procédés de fabrication et/ou de synthèse et les post-traitements. Ces étapes ont des répercussions importantes sur les propriétés finales des FCs.

La connaissance des paramètres intrinsèques aux matériaux introduits est essentielle pour des prévisions précises de leurs performances dans le contexte de notre application finale. La structure des FCs doit présenter les avantages bien connus des matériaux carbonés, à savoir la légèreté mais aussi la stabilité dimensionnelle et chimique, ainsi que l'amélioration du transfert de chaleur dans l'hybride FC-MCP final. Pour cette raison, il est nécessaire de caractériser les FCs et de mieux comprendre leurs propriétés afin de déterminer leur potentiel d'application dans l'hybride FC-MCP. La caractérisation peut impliquer des grandeurs importantes telles que la densité, la porosité, la morphologie de la fibre/du feutre (taille,

tortuosité et anisotropie), les propriétés physiques et structurales, par exemple. Certaines d'entre elles peuvent influencer sur leur imprégnation par - et leur stabilité dans - le MCP fondu, telles que:

- les caractéristiques morphologiques de la fibre, du tissu et de sa structure ;
- le comportement vis-à-vis des fluides: perméabilité et mouillabilité ;
- les propriétés mécaniques: module de compression, résistance et rétablissement de la forme de départ ;
- les propriétés de transfert de chaleur: conductivité thermique ;
- le degré de graphitisation et les propriétés texturales/chimiques du carbone ;
- la stabilité chimique et la durabilité aux températures élevées.

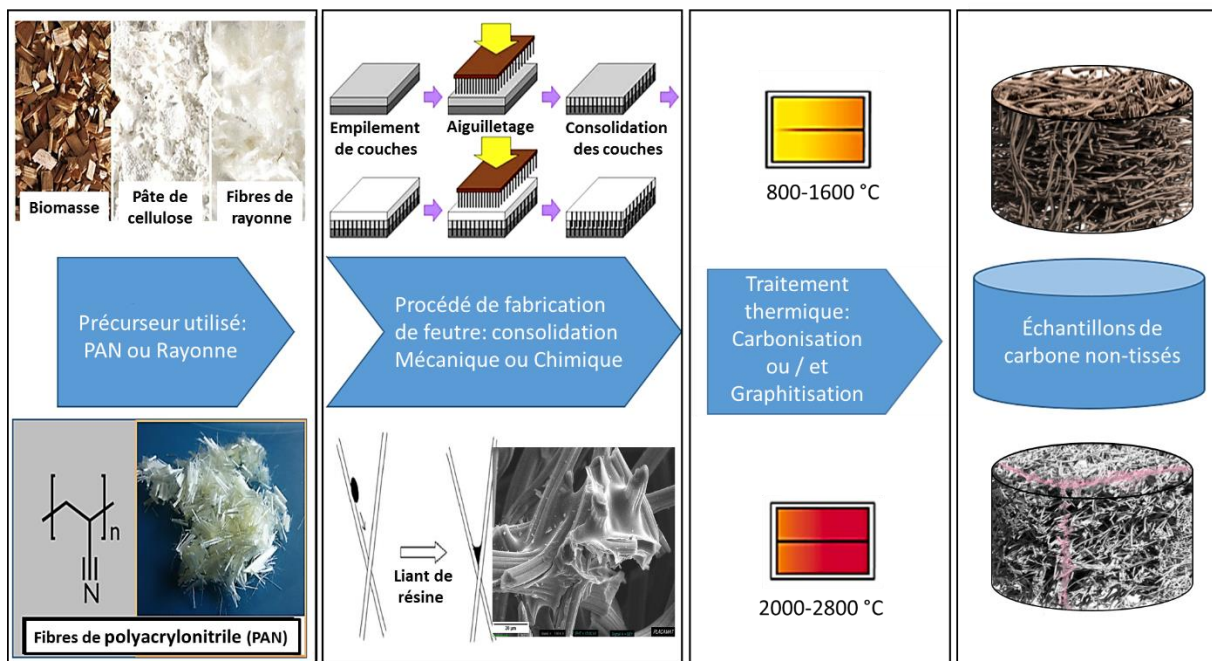


Figure 1 Présentation abrégée des caractéristiques de base des feutres de carbone.

Toutes les qualités des FCs abordées dans le chapitre I en font des candidats très prometteurs comme matériaux hôtes de MCP pour l'application TES. Cependant, ils ont aussi des faiblesses qui doivent être considérées avec beaucoup de prudence afin d'être compétitifs par rapport à d'autres candidats potentiels, carbonés ou non. Le but de cette thèse est également d'étudier ces faiblesses et les moyens de les surmonter grâce à des méthodes de modification appropriées et de montrer les améliorations apportées.

Chapitre II: Caractérisation de la morphologie des feutres de carbone et de leurs propriétés physiques

Le principal aspect à prendre en compte lors du choix d'une structure hôte appropriée est le niveau requis des propriétés des matériaux. Cette décision influencera et améliorera les performances de stockage du MCP choisi. Par conséquent, les défis initiaux de ce chapitre sont l'étude de matériaux avec des : structure poreuse, texture de feutre ou de fibre, et chimie de surface, définies. Les structures hôtes carbonées doivent être facilement et complètement imprégnées de MCP. Cela signifie qu'elles doivent présenter des structures poreuses ouvertes avec la plus grande porosité possible afin de maximiser la densité énergétique du matériau hybride final. La structure devrait aussi convenir au confinement du MCP et résister au processus d'infiltration sans modification. Théoriquement, toute modification de la matière première et des étapes de fabrication devrait mener à de subtiles différences dans les propriétés finales des matériaux commerciaux finaux examinés. Néanmoins, un choix simple du matériau de type FC le plus adapté à l'utilisation envisagée est impossible en raison du manque d'informations précises sur les propriétés de ces matériaux. Par conséquent, la nécessité de comprendre en détail les relations entre le processus de fabrication et les propriétés finales des FCs, et de combler le manque de données concernant les propriétés des matériaux, a pleinement justifié de les caractériser de manière aussi approfondie que possible.

À notre connaissance, aucune autre étude n'a mis en œuvre ce type d'analyse approfondie en examinant 18 échantillons commerciaux de FCs, reçus de 5 fournisseurs différents, en tant que structures hôtes carbonées pour systèmes TES. Ce chapitre porte ainsi sur la caractérisation expérimentale de la structure de FCs et examine l'influence de la structure tissu/fibre sur leur densité, leur porosité, leur morphologie globale, leur mouillabilité et leurs autres propriétés physiques : perméabilité, compressibilité et conductivité thermique. Des approches par modélisation ont également été envisagées pour prédire certaines des propriétés des matériaux qui ne sont pas directement déduites des résultats expérimentaux, telles que la tortuosité des matériaux et le module d'élasticité en compression. Parmi les études présentées, d'importantes propriétés des FCs pouvant influencer sur la préparation et l'utilisation finale des hybrides FC-MCP sont mises en évidence, considérées comme des facteurs clés du succès du développement et de la montée en gamme de ces matériaux.

Différents fournisseurs ont gracieusement envoyé différents types de FCs, formant un large éventail de matériaux allant des FCs souples aux panneaux rigides, en passant par les FCs rigidifiés. Ils couvrent une grande diversité de densités apparentes et de densités squelettiques.

Une large gamme de porosités totales résultantes est donc attendue et bien observée expérimentalement. Ainsi, les échantillons de FCs dérivés de PAN et de Rayonne présentent des valeurs de densité apparente comprises entre 0,073 et 0,227 g cm⁻³, des densités squelettiques autour de 1,514-1,908 g cm⁻³, et des porosités entre 87,5 et 95,7%, respectivement, quels que soient le diamètre des fibres, la rigidité et la technique de formation des feutres. Les résultats indiquent clairement que la porosité de ces matériaux légers est plus influencée par la densité apparente que par celle du squelette. Une étude par imagerie, au moyen de techniques telles que la microscopie électronique à balayage (MEB) et la tomographie à rayons X, a montré que tous les FCs étaient anisotropes et constitués de couches de fibres posées au hasard les unes sur les autres. Les FCs étaient consolidées, soit mécaniquement (par aiguilletage, assisté ou non par une consolidation chimique supplémentaire), soit chimiquement avec une résine carbonisée ultérieurement (tel que schématisé en Fig. 1). Il a été constaté que les FCs étaient fabriqués à partir de fibres ex-Rayon ou ex-PAN de diamètres différents et de sections transversales circulaires ou non (voir Fig. 2). En conséquence, un ensemble complet de matériaux avec des structures poreuses assez différentes et donc des propriétés physiques différentes, indépendamment de leur porosité, a été étudié.

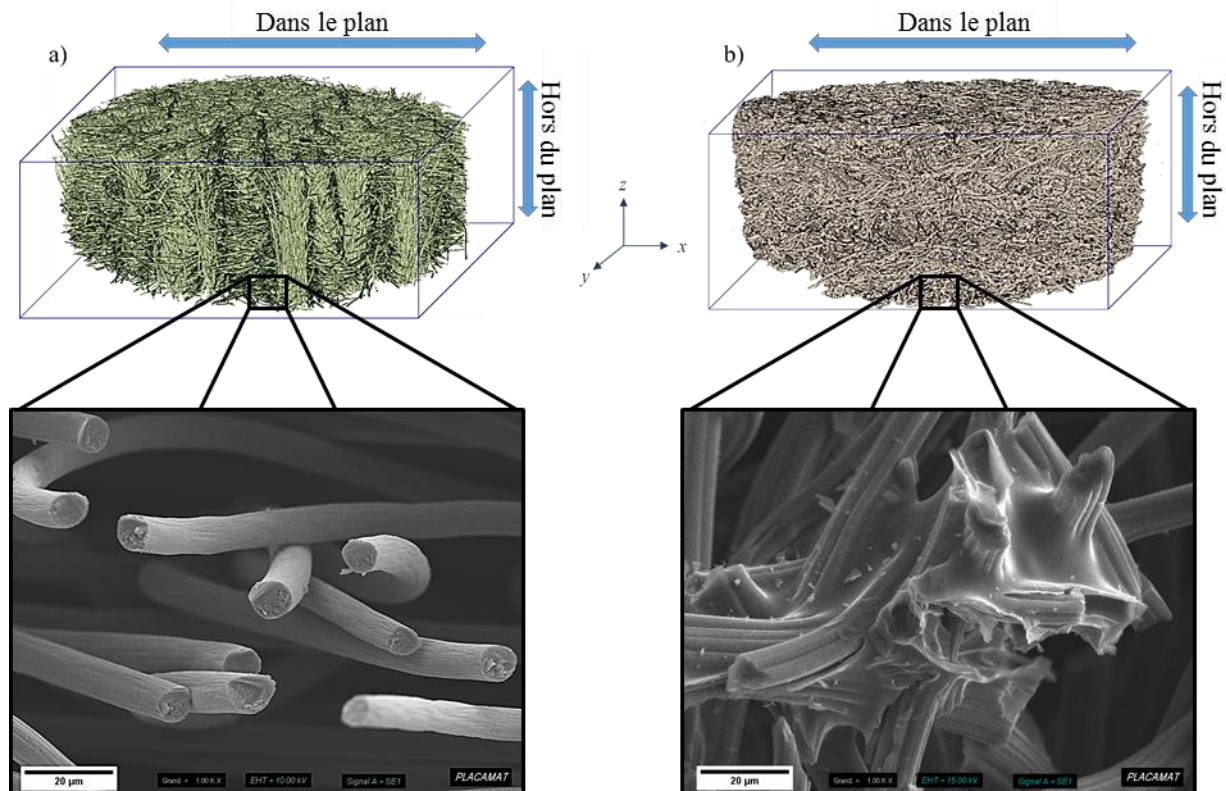


Figure 2 Représentation réaliste en 3D: (a) FC souple, et (b) échantillons de panneaux rigides de FC, pour les directions x , y , z . Le détail met en avant la morphologie de fibres de carbone a) ex-PAN et b) ex-Rayonne, en présence de liant dans ce dernier cas.

Les tentatives effectuées pour trier les matériaux par groupes et sous-groupes d'échantillons étroitement liés ont révélé des comportements cohérents dans des plages de structures ou de porosités limitées, mais n'ont généralement pas pu prendre en compte toutes les observations relatives aux propriétés des différents matériaux. L'énorme dispersion des résultats d'une famille de matériaux à une autre s'explique par la multiplicité des structures, de sorte qu'aucune méthode analytique ne peut représenter intégralement l'ensemble des échantillons de FCs étudiés.

La mouillabilité des FCs dépend de la structure du feutre, de la rugosité de la surface des fibres et de l'hétérogénéité chimique, dans une certaine mesure. Les FCs souples à base de Rayonne présentent ainsi des angles de contact avec l'eau légèrement inférieurs à ceux des matériaux à base de PAN, plus hydrophobes. Les valeurs d'angle de contact mesurées placent les échantillons dans la gamme des matériaux hydrophobes à super-hydrophobes. Cependant, la meilleure mouillabilité de ces structures carbonées hautement poreuses et perméables en présence de liquides moins polaires rend difficile, voire empêche, la mesure directe des angles de contact correspondants. L'énergie de surface des FCs étudiés devra donc être mesurée à l'avenir avec des techniques plus appropriées.

L'étude du comportement du transport de fluide dans les FCs devient impérative dès lors que leur infiltration est considérée pour la production des hybrides FC-MCP prévus. En effet, la porosité ou le diamètre de la fibre sont considérés comme les principaux paramètres affectant l'écoulement du fluide à travers un milieu poreux fibreux. Comme prévu, une perméabilité dépendant du diamètre de la fibre et de la porosité (hors du plan) a pu être observée au sein de familles individuelles et de sous-groupes de matériaux. Cependant, des différences évidentes par rapport à ce comportement logique sont expliquées par différentes propriétés morphologiques lors de la fabrication des matériaux commerciaux. Puisque les matériaux d'intérêt sont généralement extrêmement complexes et difficiles à caractériser, nous avons tenté de modéliser ce comportement et de trouver une relation universelle englobant toutes les valeurs mesurées. Dans la plage de porosité étudiée, l'utilisation des modèles empiriques et analytiques existants s'est avérée inefficace dans l'estimation de la perméabilité réduite des matériaux considérés. Toutefois, l'application des équations de perméabilité pertinentes aux FCs étudiés a permis de calculer le coefficient d'Archie et le facteur de tortuosité visqueuse à partir des valeurs mesurées de porosité, du diamètre des fibres et de la perméabilité. Par conséquent, la Figure 3 présente une courbe universelle reliant la tortuosité globale à l'exposant d'Archie. Une équation adéquate a donc été proposée pour ajuster tous les FCs sur une large gamme de porosités et de structures.

Enfin, les FCs étudiés peuvent être classés en fonction de leur coefficient d'Archie, grâce à la relation ainsi mise en évidence. Elle conduit ainsi à la détermination d'un paramètre remarquable pour la prédiction des propriétés morphologiques et de la perméabilité.

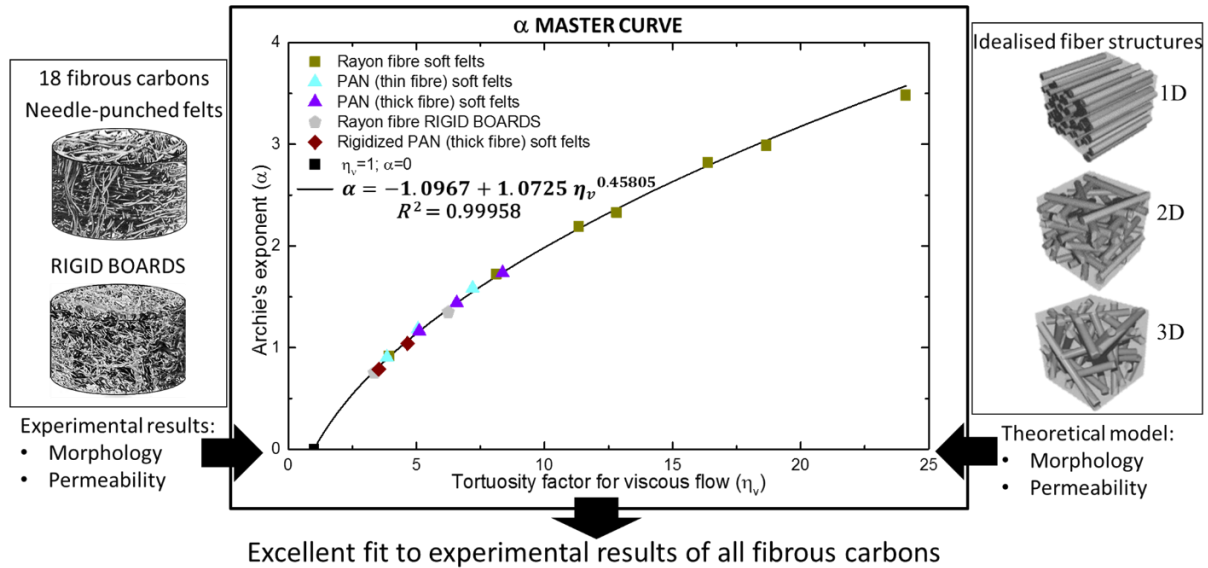


Figure 3 Relation entre le coefficient d'Archie des FCs étudiés et leur facteur de tortuosité visqueuse.

Le chapitre s'intéresse également à la détermination des caractéristiques mécaniques des matériaux. En effet, un certain degré de compression (déformation) du FC est attendu en cas d'imprégnation sous pression par le MCP fondu. Les propriétés mécaniques des FCs lors de leur compression longitudinale uniaxiale (hors du plan) sont manifestement complexes et fortement dépendantes de leurs caractéristiques microstructurales, telles que la morphologie et les propriétés des fibres, et des caractéristiques morphologiques des feutres. En conséquence, les divers FCs présentent d'importantes différences de comportement mécanique en fonction de leurs techniques de fabrication (voir Fig. 4). Si la structure est renforcée par l'adhésion de fibres par liaison chimique, la courbe de contrainte-déformation présente une déformation permanente élasto-plastique typique des FCs rigidifiés ou sous forme de panneaux rigides. Au contraire, si la structure est flexible comme dans le cas des FCs souples aiguilletés, une courbe de déformation viscoélastique non linéaire est observée. Une approche différente est donc proposée pour estimer le comportement élastique des multiples familles et sous-groupes de matériaux de type FC. En outre, les résultats de contrainte-déformation de compression de certains FCs souples ne permettent pas le calcul du module d'élasticité simplement par application de la loi de Hooke couramment utilisée, et nécessitent de modéliser leur comportement élastique. Ainsi, l'emploi du modèle ajusté de Mooney – Rivlin mène à la détermination du module élastique des FCs souples

à partir de ses paramètres constitutifs définis en fonction de la déformation. Les valeurs des paramètres mécaniques intrinsèques des FCs ont alors été obtenues, permettant une prévision plus précise de leurs performances, utiles lors de la préparation de composites.

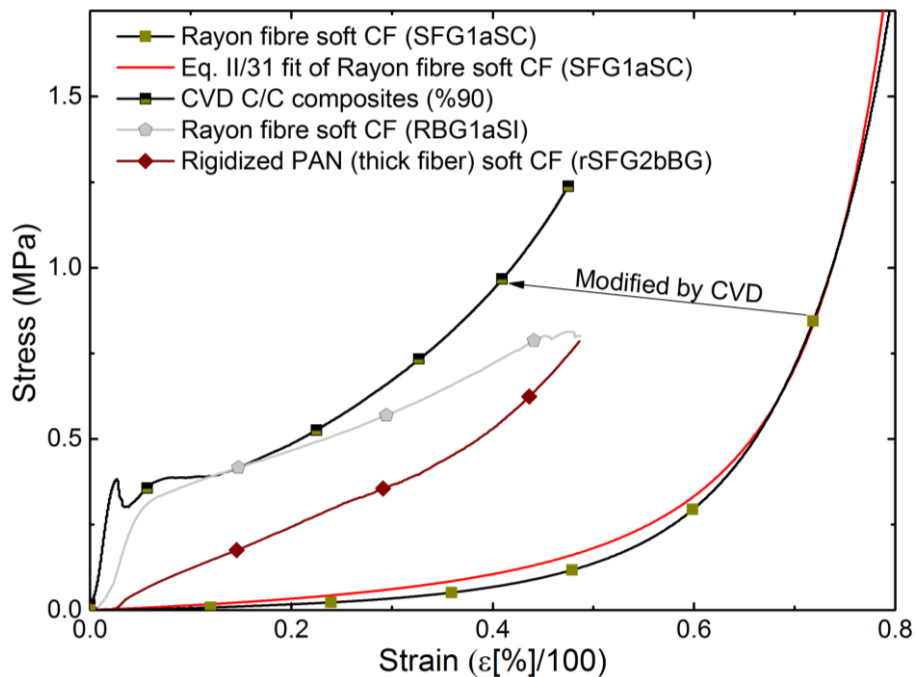


Figure 4 Caractéristiques contrainte-déformation de divers panneaux souples, flexibles rigidifiés, et rigides à base de FCs, et des composites C/C (carbone/carbone) produits à partir de FCs souples. La ligne rouge présente l'ajustement des FCs souples par le modèle de Mooney-Rivlin utilisé pour les calculs du module élastique.

Un autre objectif de cette partie est d'étudier les propriétés mécaniques des FCs souples par deux méthodes de caractérisation différentes: une dynamique et destructive, introduite ci-dessus, et une quasi-statique et non destructive, puis de comparer les mesures collectées par ces deux protocoles. La nouveauté réside dans la production d'informations importantes sur la précision et/ou la dispersion des propriétés viscoélastiques des FCs souples, quantifiées par les deux procédés. D'une manière générale, les mesures suggèrent des résultats identiques ou très proches entre les deux techniques. Des écarts sont uniquement observés pour les matériaux reçus d'un même fournisseur et fabriqués selon un protocole suffisamment différent par rapport à celui des matériaux des autres fournisseurs. Après avoir effectué les analyses selon les deux méthodes, la compression mécanique dynamique (destructive) s'est avérée plus appropriée pour la détermination d'un module d'élasticité global, alors que la méthode QMA (quasi-static mechanical analysis, non destructive) ne convient que pour l'estimation du module d'élasticité de FCs souples, pour une charge de pré-compression définie. Cette dernière technique a également été utilisée pour calculer le facteur de perte, qui n'avait encore jamais été évalué

pour les FCs. Cela peut se révéler très intéressant en cas d'autres applications telles que l'isolation acoustique. En conclusion, la manière de caractériser les propriétés mécaniques des FCs souples hautement compressibles consiste à utiliser la méthode en corrélation avec l'utilisation finale du matériau examiné.

Dans ce chapitre, l'effet sur l'efficacité du transfert de chaleur des hybrides FC-MCP a également été évalué en étudiant la conductivité thermique de structures hôtes en FC. De manière générale, la conductivité thermique des fibres de carbone considérées individuellement est fortement anisotrope, tout comme celle du FC final. Ainsi, on constate que la conductivité thermique des fibres de carbone augmente principalement avec la hausse de la température du traitement thermique final lors de la fabrication. Outre l'influence des propriétés des précurseurs et de l'histoire thermique de fabrication, la disposition des fibres de carbone dans la structure anisotrope du feutre explique également la dispersion des valeurs de conductivité thermique. Les résultats expérimentaux de la conductivité thermique effective sont beaucoup plus élevés dans le plan (IP : in-plane) que hors du plan (OP : out-of-plane), en raison de l'orientation préférentielle de la fibre dans le plan des FCs. Il a donc été mis en exergue que la conductivité thermique dans la direction OP est plus affectée par les modifications de la tortuosité du feutre et de la réorientation des fibres que dans la direction IP. Ainsi, elle dépend principalement de la résistance thermique entre les points de contact entre les fibres.

Chapitre III: Propriétés structurales des feutres de carbone et stabilité chimique dans des sels de lithium fondus

Le MCP envisagé peut devenir extrêmement corrosif dans certaines circonstances, en fonction notamment de l'augmentation de la température d'utilisation, de la présence d'impuretés (humidité, oxygène), et de l'apparition de réactions chimiques avec les matériaux hôtes. D'autre part, la stabilité chimique des FCs candidats aux hybrides FC-MCP pour des températures moyennes à élevées est inconnue, et requiert donc des études approfondies pour tester la stabilité chimique de ces matériaux. La recherche de critères de sélection de matériaux fibreux carbonés chimiquement stables est donc un autre objectif de cette thèse, ainsi que la recherche des raisons probables de l'apparition de réactions non désirées entre les constituants des hybrides FC-MCP.

Dans ce chapitre, la composition élémentaire et la texture des fibres de carbone ont été étudiées en analysant des FCs de différentes origines (voir Chapitre II), avant d'étudier leur stabilité chimique dans des sels de lithium fondus. Les recherches bibliographiques effectuées

ont permis de voir qu'il n'existe pas d'étude systématique similaire concernant l'effet des propriétés des fibres de carbone sur leur stabilité chimique au contact de LiOH, LiBr et $\text{Li}_4(\text{OH})_3\text{Br}$ fondus (ce dernier correspond au MCP d'intérêt pour notre application).

Dans les échantillons de FCs ex-PAN et ex-Rayonne, l'historique de fabrication et le changement des variables de production sont considérés comme extrêmement importants et influencent la transformation ultérieure du précurseur en fibres de carbone et donc leurs propriétés texturales finales. La Figure 5 résume les résultats d'analyse élémentaire, de diffraction des rayons X (DRX) et de spectroscopie Raman, qui démontrent que la pureté des fibres de carbone, la taille et l'ordre local des cristallites augmentent lorsqu'on passe de FCs carbonisés aux FCs graphitisés. De plus, les résultats de DRX et Raman révèlent la présence de FCs désordonnés ou partiellement graphitisables provenant de précurseurs Rayonne et PAN. En règle générale, l'absence de réflexions DRX et de bandes Raman liées à l'empilement tri-périodique permet de conclure au caractère turbostratique du carbone étudié.

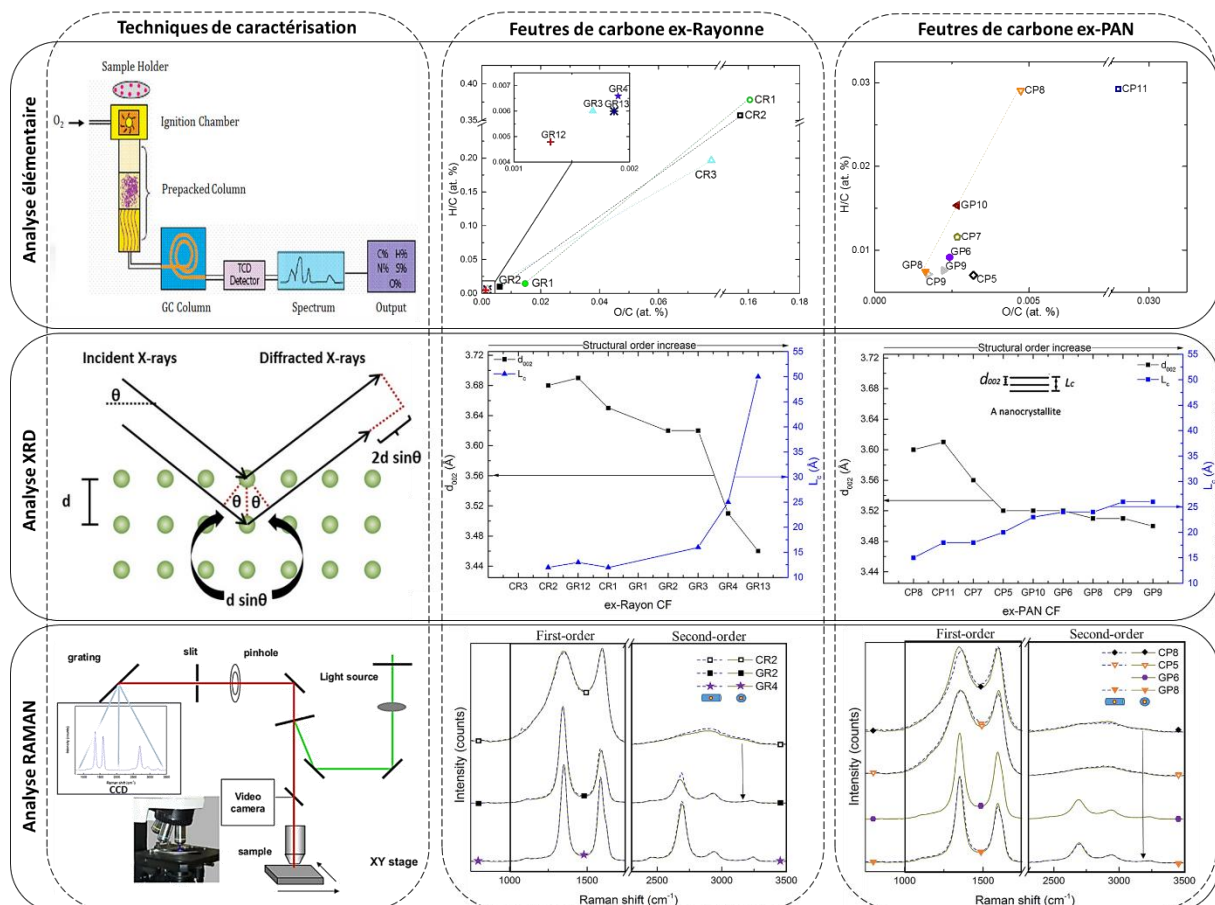


Figure 5 Analyse élémentaire, spectroscopies DRX et Raman utilisées pour obtenir des informations chimiques et texturales sur les FC, ex-Rayonne ou ex-PAN.

Des renseignements très importants sur la stabilité chimique du matériau carboné ont été obtenus, notamment lors des tests des FCs dans du LiOH fondu. En général, les résultats de la réactivité chimique ont révélé que la perte de masse de carbone augmente toujours avec la température, en raison de la hausse considérable de la vitesse de réaction. Les variables expérimentales liées à l'historique de fabrication des FCs ainsi que la température de l'essai influencent la réaction chimique entre le FC et le LiOH. Autant pour les matériaux ex-PAN que les ex-Rayonne, la réactivité du LiOH diminue à mesure que la pureté du carbone augmente et le FC devient très stable, même pour la température testée la plus élevée. Il a donc été démontré que même avec des propriétés texturales similaires, les différences de teneurs en hétéroatomes ont un effet très significatif sur la stabilité chimique des FCs. Néanmoins, une pureté en carbone élevée et une organisation graphitique améliorée doivent être préférées pour une plus grande stabilité chimique des FCs en contact avec du LiOH fondu et pour une gestion thermique améliorée dans l'hybride FC-MCP final.

Les résultats de l'analyse post-réaction de la nanotexture des FCs suivent une tendance similaire avec une réactivité chimique qui décroît depuis les FCs carbonisés jusqu'aux graphitisés, et une texture de surface qui est modifiée sévèrement à légèrement, respectivement. De plus, les analyses d'adsorption de gaz montrent que la réactivité chimique des FCs avec LiOH entraîne généralement une perte de carbone avec une faible surface spécifique et un faible développement de la microporosité, due à la réaction chimique intense et à l'absence d'intercalation du Li métallique dans les FCs examinés. Ceci est en bon accord avec les résultats similaires de stabilité chimique obtenus pour des FCs avec un ordre textural différent mais une pureté élevée en C. Une analyse MEB a été réalisée pour déterminer si la structure de la fibre de carbone était uniformément activée lors du contact superficiel avec LiOH ou selon un motif défini, en raison des caractéristiques variées des FCs. La Figure 6 illustre la morphologie gravement endommagée ou entièrement préservée de fibres de carbone pour des FCs carbonisés ou graphitisés, en bon accord avec les différences de résultats de burn-off.

L'étude de la stabilité chimique des FCs dans LiBr fondu a ensuite été effectuée, de la même manière que pour LiOH. Cela a révélé l'effet de chaque sel inorganique avant que des tests identiques ne soient effectués dans le MCP binaire fondu. LiBr seul n'a pas d'incidence sur la structure des matériaux carbonés et sa réactivité chimique avec le FC a été considérée comme négligeable. En effet, après des tests de réactivité chimique dans du composé péritectique fondu ($\text{Li}_4(\text{OH})_3\text{Br}$), qui est le MCP d'intérêt ici, les matériaux présentaient des valeurs de burn-off inférieures à 50%, très inférieures à celles obtenues avec du LiOH dans tous

les FCs testés. Enfin, les réactions chimiques des FCs dans le MCP étudié doivent être considérées comme similaires à celles de LiOH. Mais la présence physique de la phase LiBr, inerte, modère les réactions d'oxydo-réduction avec l'hydroxyde. La morphologie de surface et la nanotexture des FCs montrent également des modifications structurales moins importantes avec $\text{Li}_4(\text{OH})_3\text{Br}$ qu'avec LiOH (voir Fig. 6).

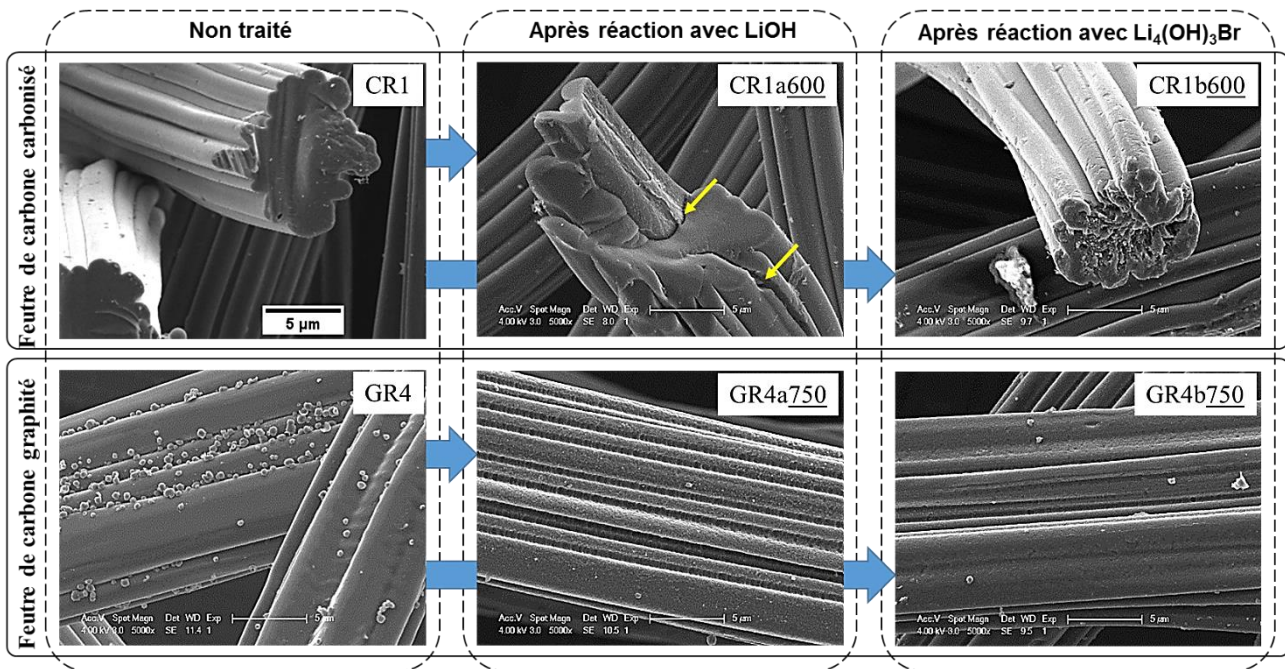


Figure 5 Micrographies MEB de FCs ex-Rayonne (carbonisé ou graphitisé) avant (à gauche) et après réaction avec LiOH (au milieu) ou $\text{Li}_4(\text{OH})_3\text{Br}$ (à droite) pour la température la plus haute testée (indiquée en °C et soulignée dans la notation de l'échantillon). Les flèches jaunes indiquent les endommagements de la fibre de carbone après réaction avec LiOH.

En fonction de la stabilité chimique du FC dans la phase LiOH présente dans le MCP, le rapport stœchiométrique (c'est-à-dire correspondant à $\text{Li}_4(\text{OH})_3\text{Br}$ non modifié) peut être modifié en cas de réaction, ce qui risque de faire baisser la densité d'énergie thermique à stocker. Par conséquent, le choix du FC le plus inerte devrait inhiber la réaction chimique dans le LiOH fondu à la température d'application, garantissant ainsi l'un des principaux avantages de l'utilisation de $\text{Li}_4(\text{OH})_3\text{Br}$ non modifié dans sa composition: son potentiel de stockage d'énergie élevé.

De plus, une étude détaillée a été réalisée pour estimer l'énergie d'activation des réactions apparaissant avec des FCs dans LiOH fondu. En outre, sur la base des recherches bibliographiques effectuées, aucune valeur d'énergie d'activation n'est signalée pour des matériaux carbonés similaires à ceux considérés dans les conditions de test actuelles et dans du

LiOH fondu. Cependant, l'idée principale de cette partie est d'obtenir plus d'informations sur les résultats de burn-off et de les estimer à la température d'application (entre 300 et 400°C). Les résultats expérimentaux des tests de stabilité chimique sont en excellent accord avec les valeurs estimées par application de la loi d'Arrhenius, distinguant encore une fois les FCs graphitisés, à la pureté et à la structure améliorées, en tant que candidats potentiels aux matériaux hybrides FC-MCP.

Chapitre IV: Modifications avancées des feutres de carbone et tests d'application

Les FCs disponibles dans le commerce ont été caractérisés de manière détaillée dans les deux chapitres précédents en diversifiant une partie des matériaux examinés en tant que supports de carbone prometteurs pour les TES péritectiques innovants. En outre, l'identification des paramètres clés des matériaux a fourni un guide utile pour une amélioration supplémentaire des FCs, dépassant certaines des lacunes observées et favorisant une performance accrue dans l'utilisation finale prévue. Les FCs souples aiguilletés se sont révélés être des matériaux très poreux avec des fonctionnalités capables de résoudre bon nombre des interrogations relatives à l'application de stockage d'énergie thermique. Cependant, la nature flexible et l'absence de connexions solides entre les fibres des FCs souples conduisent à des performances de transfert mécanique et de transfert de chaleur inférieures à celles des fibres de carbone individuelles qui les composent ou des FCs rigides/rigidifiés étudiés.

Dans ce chapitre, une méthode isobare-isotherme de dépôt chimique en phase vapeur (chemical vapour deposition, abrégé CVD), présentée schématiquement sur la Figure 7, a été utilisée pour modifier un FC souple, afin d'améliorer les propriétés des matériaux. Les composites C/C résultants présentent des caractéristiques nouvelles qui ont été comparées à celles de la préforme FC pure et/ou d'autres matériaux carbonés similaires. La méthode de modification appliquée a tiré parti du squelette du FC, hautement poreux, sur lequel une couche de pyrocarbone a été déposée, modifiant ainsi la surface des fibres de carbone (présentée à la Fig. 7). Des informations importantes ont été obtenues par l'étude des morphologies C/C, de leurs performances physiques, ainsi que de leurs compositions et de leurs caractéristiques texturales, et enfin de leur stabilité chimique dans LiOH, LiBr et $\text{Li}_4(\text{OH})_3\text{Br}$ fondus. Par conséquent, l'objectif de cette partie est d'identifier les paramètres clés de conception et de performance, afin de fournir des indications utiles pour l'amélioration des matériaux hybrides FC-MCP et de leur utilisation finale.

Comme prévu, le dépôt de pyrocarbone sur les préformes de FC a entraîné une augmentation linéaire de la densité apparente des composites C/C produits avec le temps. Les FCs légers et hautement perméables permettent ainsi une réaction/dépôt chimique homogène du gaz précurseur pendant le processus de CVD, ce qui favorise un dépôt uniforme de pyrocarbone sans zone préférentielle dans la préforme.

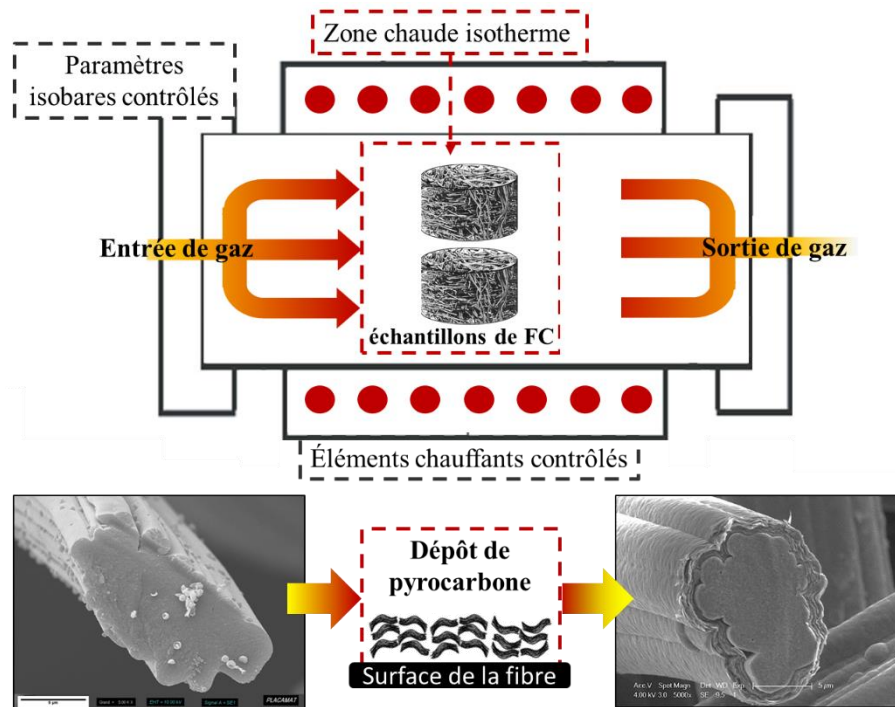


Figure 6 Présentation schématique du réacteur CVD, et dépôts de carbone pyrolytique sur la surface de fibres de carbone pour la préparation de composites C/C.

Après réalisation de la CVD, l'analyse MEB montre que la présence d'une couche de pyrocarbone dans la zone située entre les fibres génère des jonctions fixes dans les composites C/C produits. La taille et la surface des connexions rigides nouvellement formées augmentent avec le temps de dépôt. Plus important encore, les composites C/C produits ont toujours une porosité ouverte interconnectée, même après la plus longue durée de dépôt testée. La microscopie optique en lumière polarisée a permis de mettre en évidence la nature laminaire du pyrocarbone anisotrope présentant des couches de carbone déposées presque perpendiculairement à la section transversale de la fibre. La fibre de carbone, la matrice de pyrocarbone déposée et l'ensemble des composites C/C se révèlent tout à fait anisotropes à la fois en termes de nanotexture et de structure globale des matériaux, ce qui influence également les propriétés physiques et structurales examinées.

L'augmentation de la fraction de pyrocarbone déposé a entraîné une diminution linéaire de la perméabilité des composites C/C, dans la direction OP, en fonction à la fois de la baisse de la porosité et de l'augmentation du diamètre des fibres. Cependant, les composites C/C produits présentent une surface inférieure et un écoulement moins tortueux du fluide par rapport aux panneaux composites rigides FC et autres composites C/C mentionnés dans la littérature. La production de composites C/C a fourni des matrices aux propriétés physiques améliorées et contrôlées par rapport aux FCs souples initiaux. Par conséquent, les changements morphologiques et la formation de jonctions aux points de contact entre les fibres ont stimulé les propriétés thermiques et mécaniques, sans modifier radicalement la porosité globale du matériau. Le dépôt de la matrice de pyrocarbone a entraîné un comportement élastique linéaire et un transfert efficace d'une charge de compression beaucoup plus élevée, très différent de la déformation viscoélastique et non linéaire de la préforme de départ (revoir Fig. 4). Ainsi, les composites C/C préparés possèdent à la fois un module élastique plus important et une plus grande résistance à la compression, transformant la préforme FC flexible hyperélastique en un matériau élastique-plastique ou fragile. Les jonctions en pyrocarbone formées présentent également des chemins conducteurs pour les phonons, réduisant la résistance de contact thermique et améliorant la conductivité thermique des composites C/C, principalement dans la direction IP et en bonne corrélation avec l'anisotropie globale du composite C/C. Enfin, un équilibre raisonnable doit toujours être identifié car les propriétés physiques mesurées sont antagonistes, et une augmentation de la densité entraînera toujours une perméabilité plus faible tandis que les propriétés mécaniques et de transfert de chaleur seront meilleures.

Enfin, la couche de pyrocarbone déposée donne une stabilité chimique améliorée aux composites C/C dans l'environnement oxydant testé. Tous les résultats de burn-off ont montré une perte de masse réduite de plus de 50% par rapport au FC souple de départ qui avait été choisi parce que le plus stable chimiquement parmi les autres. Ainsi, l'objectif principal est d'étudier comment les composites C/C produits résistent ou subissent l'oxydation lorsqu'ils sont exposés aux sels de lithium fondus, en comparant les caractéristiques texturales pré/post-réaction.

L'analyse élémentaire réalisée a révélé une teneur plus élevée en carbone des composites C/C préparés par rapport au FC souple de départ. Cela est principalement dû au procédé de dépôt chimique en phase vapeur appliqué et de l'augmentation du poids de carbone. L'excellente superposition des spectres Raman suggère une grande homogénéité texturale de la surface extérieure des dépôts de pyrocarbone, dans les différentes zones testées. En outre, les

informations de déconvolution ont confirmé la présence d'une microstructure de pyrocarbone laminaire rugueuse, en bon accord avec l'analyse par microscopie optique en lumière polarisée. De plus, la stabilité chimique améliorée du composite C/C peut être démontrée par l'augmentation de la teneur en carbone et le niveau réduit en hétéroatome, ce qui est compatible avec la présence d'une surface de pyrocarbone laminaire régénéré rugueuse chimiquement stable.

L'étude de la morphologie des matériaux et de la nanotexture a permis de mieux comprendre les mécanismes d'oxydation des composites C/C dans les sels de lithium fondus. La Figure 7 montre la surface externe non modifiée de pyrocarbone, conservant sa morphologie d'origine, même après une réaction chimique avec le LiOH hautement réactif à la température testée la plus élevée. Cependant, la présence de micro-cavités sur le dépôt de pyrocarbone, due à la différence de coefficients de dilatation thermique entre les dépôts de pyrocarbone fragiles et les fibres de carbone ex-Rayonne, a entraîné de multiples points d'accès pour les sels de lithium fondus à l'interface du composite. Par conséquent, la réaction a pu avoir lieu à l'interface entre la fibre de carbone et la couche de pyrocarbone et a progressé vers l'intérieur de la structure de la fibre, en raison d'une quantité plus élevée de groupes oxygénés attribués à son origine ex-Rayonne. Les micrographies de la Figure 7 révèlent une fois de plus que la nature fortement oxydante du LiOH testé et sa présence réduite dans le MCP avec LiBr, correspondent aux résultats de burn-off. Les analyses d'adsorption de gaz effectuées mettent en évidence une très faible surface spécifique, diminuée de plus de 50% par rapport à celle obtenue pour le FC souple de départ, à cause de la nanotexture non poreuse du pyrocarbone. Les résultats ont indiqué que la présence de porosité de surface est uniquement due à l'existence de fissures et de micro-cavités dans le pyrocarbone, permettant l'adsorption de gaz à l'interface fibre de carbone/pyrocarbone et dans la nanoporosité de la fibre. Par conséquent, on constate que la baisse de la surface totale est proportionnelle à la diminution des sites actifs, entraînant ainsi une diminution du burn-off. De plus, les valeurs de burn-off du composite C/C ont conduit à l'estimation d'une énergie d'activation similaire à celle de la préforme en FC d'origine. La similarité de l'énergie d'activation est principalement attribuable à la diminution du burn-off mesuré, qui est proportionnelle à la diminution de la surface totale.

Même si une diminution de la porosité a été notée par rapport au FC de départ, on s'attend à une meilleure performance du composite hybride FC/CC-MCP final à partir des améliorations apportées au feutre modifié. Ainsi, de futurs tests devraient étudier la production de dépôt de pyrocarbone dépourvus de micro-vides et moins enclin aux fissures. Enfin, des

analyses additionnelles doivent démontrer si les modifications apportées et l'amélioration observée des performances de la structure carbonée hôte sont raisonnables et rentables par rapport à la diminution de la porosité et de la densité énergétique finale du composite hybride FC/CC-MCP.

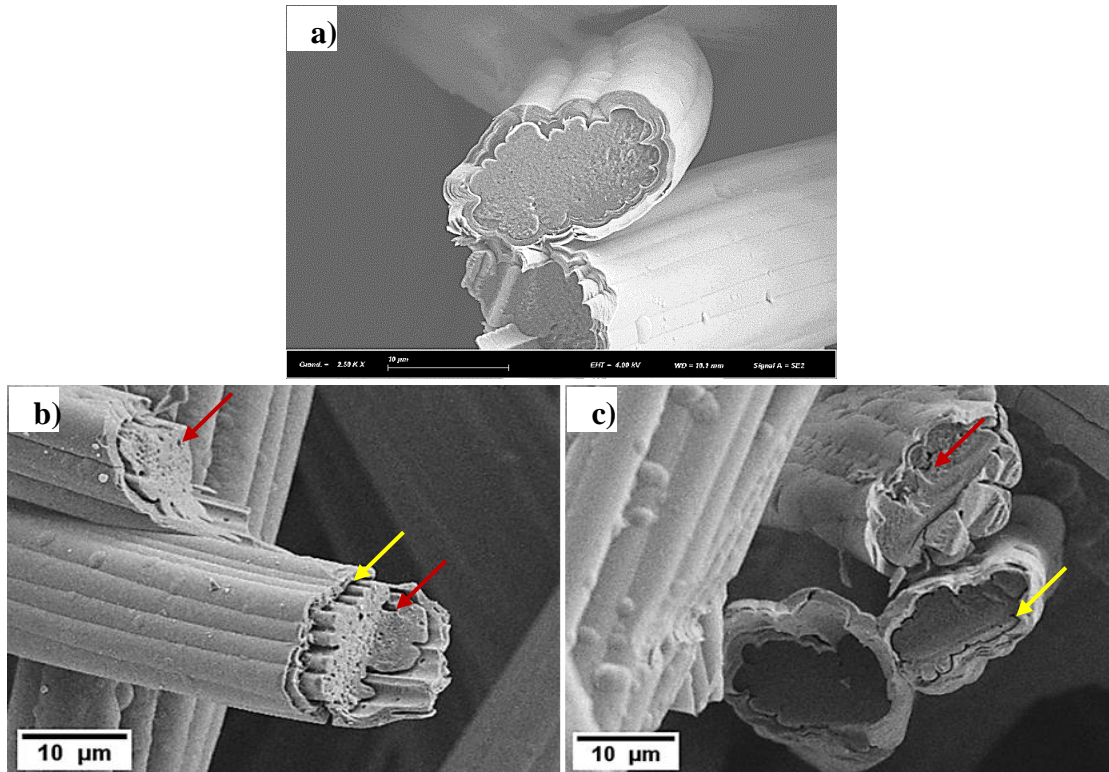


Figure 7 Images MEB des microstructures du composite C/C: a) avant réaction chimique, b) après essais dans le LiOH fondu, et c) après imprégnation avec $\text{Li}_4(\text{OH})_3\text{Br}$ fondu, pour la température testée la plus élevée (750°C). Les flèches jaunes indiquent la décohésion de l'interface pyrocarbone/fibre, et les flèches rouges mettent en évidence la formation de cavités à la surface de la fibre de carbone.

La dernière partie de ce chapitre présente également l'analyse préliminaire des propriétés et des performances en stockage thermique du MCP, seul ou sous forme de composite avec l'un des FCs souples étudiés. Les analyses MEB in-situ montrent une bonne mouillabilité du FC par le MCP fondu et confirment la possibilité de l'utiliser comme matériau hôte. Cette observation est renforcée par la stabilité chimique constatée vis-à-vis du MCP. En effet, les résultats de l'analyse morphologique et structurale ne montrent aucune influence négative du FC sur la recristallisation du MCP (voir Fig. 8) et sur ses propriétés structurales après infiltration dans la matrice carbonée. En fin, les résultats préliminaires de DSC soulignent

également la nécessité d'améliorer les synthèses du MCP et les méthodes d'analyse de l'effet du FC dans l'hybride FC/MCP.

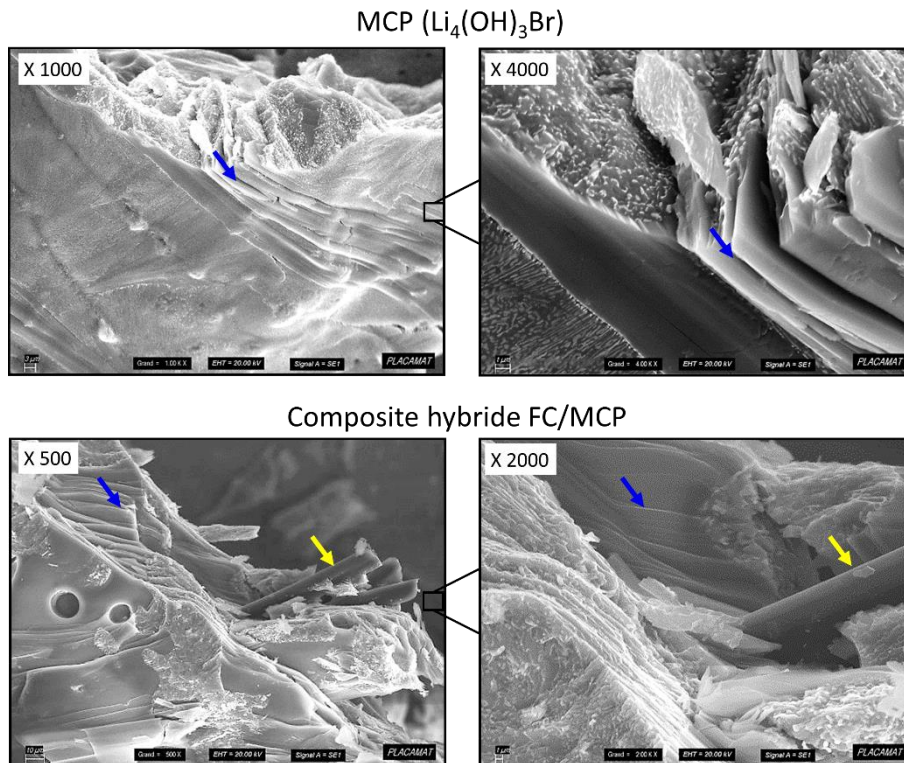


Figure 8 SEM visualisation of the MCP, alone (top row) or the hybrid FC/MCP composite (bottom row), at different magnifications. The blue or yellow pointers show the existence of lamellar crystal morphology of the MCP or carbon fibres in the hybrid FC/MCP.

Les principales conclusions et perspectives sont résumées à la fin de ce manuscrit. Nous pensons que les recherches menées dans le cadre de cette thèse apporteront des avancées dans la recherche sur les feutres de carbone, vers de nouvelles applications, telles que le stockage d'énergie thermique et notamment avec des matériaux à changement de phase infiltrés dans leur structure fibreuse. Les essais préliminaires des performances du système TES à base d'hybrides FC/MCP ont malheureusement été réalisés très tardivement en raison de nombreux problèmes techniques liés à l'appareil de calorimétrie à balayage différentiel spécialement acquis par l'I2M pour le projet. Par conséquent, après les résultats préliminaires, les caractéristiques thermodynamiques détaillées des hybrides FC/MCP, ainsi que celles du MCP non confiné, doivent encore être effectuées, en particulier après un cyclage suffisamment long, afin de fournir les réponses aux principales interrogations ayant motivé ce travail de thèse. Néanmoins, la présente étude des propriétés des FCs constitue le début d'un nouveau chapitre de leur utilisation future dans le cadre des systèmes TES visant à développer des solutions d'énergie propre et renouvelable.

Introduction générale

Les feutres de carbone (FCs) sont des matériaux hautement poreux qui ont fait l'objet de nombreuses études en raison de leur applicabilité à de multiples domaines. La diversité de leurs structures alliant fibres longues ou courtes dans des arrangements plus ou moins denses et anisotropes, de leurs propriétés allant de souple et flexible à rigide et offrant un bon compromis entre légèreté et performances, et de leur origine synthétique ou naturelle, est en effet remarquable. Ainsi, ces matériaux couvrent un large éventail d'utilisations et sont notamment connus dans les secteurs de l'énergie, de la construction aéronautique et automobile, et particulièrement dans le développement de produits et de technologies nouvelles. Les FCs peuvent en outre être optimisés en fonction du domaine d'application considéré, par exemple pour obtenir un bon transfert de charge ou de chaleur, voire une stabilité améliorée vis-à-vis de l'oxydation. Des applications avancées peuvent donc être imaginées dans le stockage de l'énergie thermique sur la base de feutres de carbone.

Des études antérieures ont démontré que le stockage de l'énergie thermique (TES) dans les centrales solaires thermique à concentration est rentable. Les systèmes TES et leurs performances modifient en effet l'utilisation de l'énergie solaire à différents niveaux, en décalant la distribution de l'énergie lorsque le soleil ne brille pas ou en maximisant la production d'énergie lors des pics de demande. Plus concrètement, l'utilisation du stockage d'énergie thermique est considérée comme l'une des solutions principales pour le stockage des excédents d'énergie renouvelable et leur utilisation contrôlée dans les systèmes d'alimentation.

Alors que seuls les coûts et l'efficacité des matériaux stockant l'énergie thermique ont été évalués jusqu'ici, l'utilisation et l'évaluation de nouveaux matériaux de support et de renforcement pour l'amélioration des performances du précédent constituent actuellement une tendance croissante dans ce secteur de l'énergie. Ce travail prend part à la révolution énergétique en cours en étudiant différents FCs commerciaux en tant que structures carbonées hôtes pour de nouvelles solutions TES. Dans ce manuscrit, les différentes sections établissent des corrélations entre la morphologie, les propriétés physiques ou structurales des FCs et leurs performances lors de l'utilisation finale. De plus, il a également été démontré que les carbones fibreux étudiés pouvaient être facilement optimisés en fonction du domaine d'application visé. Par conséquent, l'objectif principal de cette thèse est l'étude de matériaux carbonés commerciaux fibreux présentant des caractéristiques appropriées pour servir à la fois comme

structures hôtes et comme milieux de dispersion pour des matériaux à changement de phase dans les applications de stockage d'énergie thermique.

Les travaux de cette thèse ont été réalisés dans le cadre du projet Pc2TES (« Composés péritectiques pour le stockage compact d'énergie thermique à haute température »), financé par l'Agence Nationale de la Recherche sous le numéro ANR-16-CE06-0012-01. Les partenaires de ce projet sont des institutions scientifiques françaises pour, d'une part, l'étude et la caractérisation des matériaux de stockage de l'énergie avec I2M (Institut de mécanique et d'ingénierie- UMR 5295), ICMCB (Institut de Chimie de la Matière Condensée de Bordeaux - UMR CNRS 5026) et PLACAMAT (PLateforme Aquitaine de CARactérisation des MATériaux – UMS CNRS 3626), et d'autre part, l'étude et le développement de matériaux hôtes carbonés avec l'Institut Jean Lamour (IJL - UMR CNRS 7198) et en partie en collaboration avec l'IS2M (Institut des sciences des matériaux de Mulhouse - UMR CNRS 7361). L'objectif du projet Pc2TES était de fabriquer et d'étudier l'utilisation d'un nouveau matériau composite TES qui stockera l'énergie par deux processus consécutifs : un processus de fusion/solidification et une réaction chimique liquide-solide, tous deux améliorés par l'utilisation de matrices hôtes carbonées. Les matériaux hybrides correspondants seront donc préparés en utilisant des composés péritectiques comme nouveau type de matériaux à changement de phase (MCP) avec une densité d'énergie élevée, et des matériaux à base de carbone fibreux pour l'amélioration de la stabilité et des performances du MCP.

Afin d'atteindre les objectifs de la thèse et du projet général, il était nécessaire d'étudier les FCs du point de vue de la préparation des matériaux hybrides FC-MCP et de leurs performances finales, tout en comprenant et en examinant les problèmes pouvant être rencontrés. La thèse est alors structurée en quatre chapitres. Le premier est un état de l'art qui rappelle le contexte actuel des systèmes TES et l'utilisation de matériaux à base de carbone comme matrices pour ce type d'application. Il résume également les informations générales utiles sur le carbone et les matériaux non tissés ainsi que sur les différentes formes qu'ils peuvent prendre. Le deuxième chapitre décrit les travaux expérimentaux et analytiques menés pour étudier la morphologie et les propriétés physiques des FCs commerciaux, et l'effet possible de ces propriétés sur la préparation et les performances des hybrides FC-MCP. Le troisième chapitre traite de la caractérisation structurale des mêmes matériaux en FC par analyse élémentaire, diffraction des rayons X et spectroscopie Raman. En outre, l'évaluation des caractéristiques structurales des FCs nous a permis d'identifier les principaux avantages de ces structures hôtes carbonées, stables chimiquement au contact du MCP fondu comme démontré

ici. Enfin, une méthode de modification a été utilisée dans le quatrième chapitre pour surmonter certains des inconvénients identifiés précédemment, et pour pouvoir améliorer les performances du FC dans l'hybride FC-MCP final. Ainsi, les propriétés des matériaux résultants ont été évaluées et comparées à celles initialement mesurées. La dernière partie de ce chapitre présente également l'analyse préliminaire des propriétés et des performances en stockage thermique du MCP, seul ou sous forme de composite avec l'un des FCs souples étudiés. Finalement, après la conclusion générale, une liste des publications, parues et en préparation, et des communications, orales ou par affiches, est fournie.

CHAPTER I: STATE OF THE ART

I/1 General context

I/1.1 The value and potential of renewable energy for a sustainable future

More and more obviously, the use of fossil fuels energy brings serious and life-threatening to our planet, which issue has attracted worldwide researchers' interest in developing renewable energy and other advanced technological solutions. In a period of several decades, significant scientific work has been made to provide alternative technologies for harvesting and obtaining clean and sustainable energy such as solar energy, wind power, biofuels, and hydrogen (Dincer and Acar 2018; Gielen et al. 2019). These technologies are already considered crucial for multiple economic and environmental objectives within the new worldwide renewable energy policies ("Global Market Outlook for Solar Power 2018-2022" 2018). Yet the rapid increase of global life and technology standards imposes a rate of energy consumption which has been dramatically and continuously increased (Nejat et al. 2015). As a response to these new global scenarios, new technologies and energy systems are under development in order to support the maximal use of renewable energy whenever and wherever demanded.

The direct harvesting of solar energy is believed by many as one of the leading and most effective solutions for a clean and cheap global energy source. Further on, the collection of this energy through concentrated solar power (CSP) plants has numerous advantages, such as low or zero greenhouse gases emissions, simultaneously possessing huge energy reserves that can contribute to solving the worldwide energy supply problems (Sioshansi and Denholm 2010). Whereas renewable, still the solar radiation is intermittent, only producing during clear daylight and noticeably mismatching the electrical energy demand peaks during a 24 hours period (described by Fig. I/1-1). This is the reason why, nowadays, several different energy storage systems are investigated for connecting production and supply, further improving the CSP plants' efficiency and large-scale production (Kuravi et al. 2013). In general, multiple renewable energy storage systems are lately seen as a key component of clean and reliable electricity and other energy supply, smoothing the fluctuations and limiting the weaknesses of the future and globally visualised renewable energy resource (Keck et al. 2019).

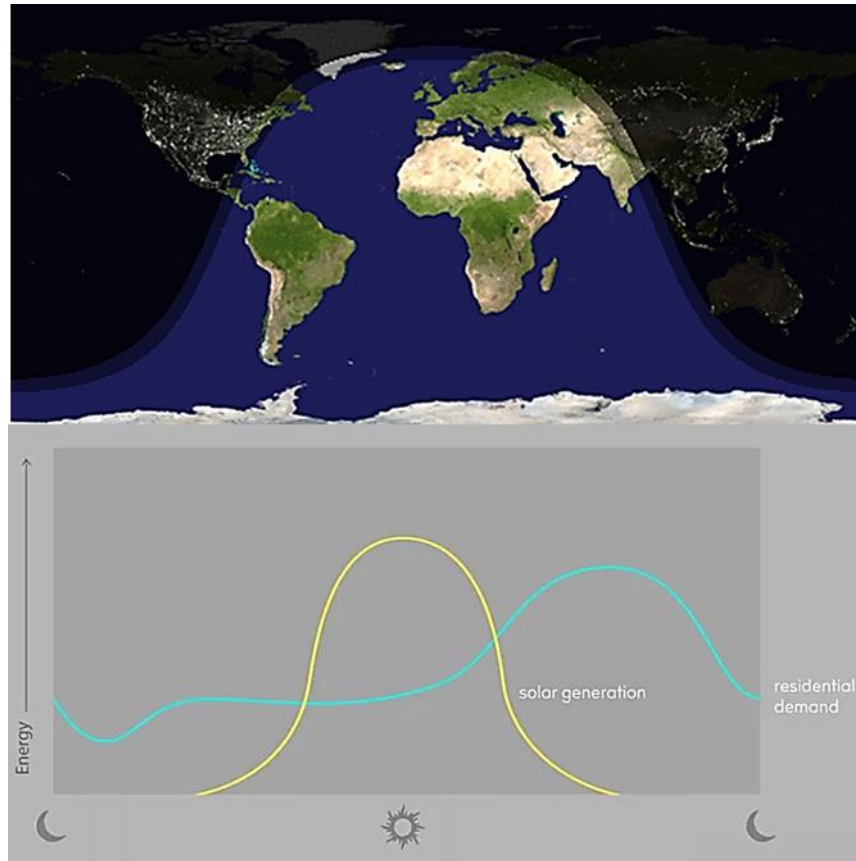


Figure I/1-1 Continuous mismatch between accessible solar energy supply and electrical energy demand (source: upper figure: <https://imgur.com/gallery/qaart8Y>, update: 17/01/2019).

I/1.2 Current status of Thermal Energy Storage (TES) systems

Thermal Energy Storage (TES), seen as one amongst others of the main actors and part of the clean energy technologies, can improve the total thermal management and achievement of a CSP plant, thus secure a day-and-night optimal energy cover of the electricity demand (Wei et al. 2018). Cost-effective TES solutions can also be adapted to many different heat energy sources emitting excess amount of energy that can be of further sustainable use. As an outcome, TES has been gaining great attention and has experienced a quick scientific expansion in the last two decades (shown in Fig. I/1-2) (Liu, Saman, and Bruno 2012; Calderón et al. 2019). Nowadays, TES is considered as a firm and stable power capacity opposite to the conservative “supplementary” output to the conventional fossil fuel energy support systems. Another asset they show is the potential of the aforementioned combined system not only to extend but also to shift their electricity production from periods of low to high electrical energy cost, thus further increasing its economic viability (Santana 2017).

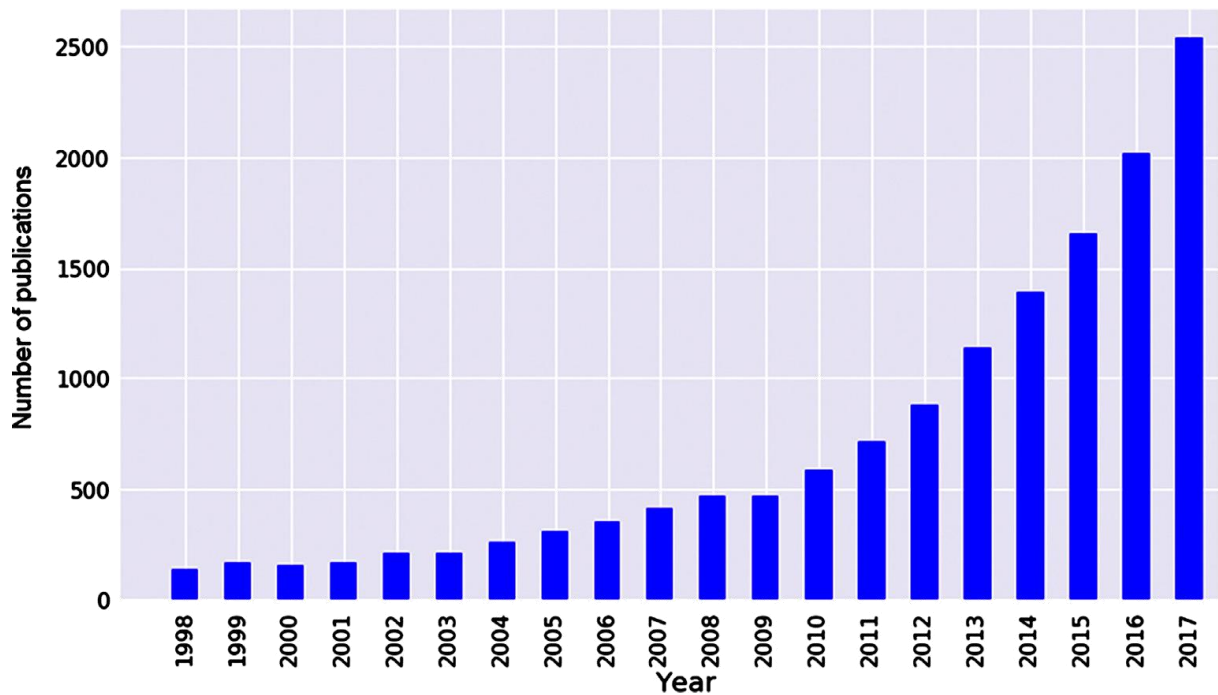


Figure I/1-2 TES scientific expansion seen as a number of concerned publications in the period of the last two decades (after Calderón et al. 2019).

I/1.2.a Classification of TES systems

To date, there are three types of TES systems, classified as sensible heat storage systems, latent heat storage systems, and thermal chemical storage systems or a combination of these (scheme presented in Fig. I/1-5) (Ibrahim et al. 2017).

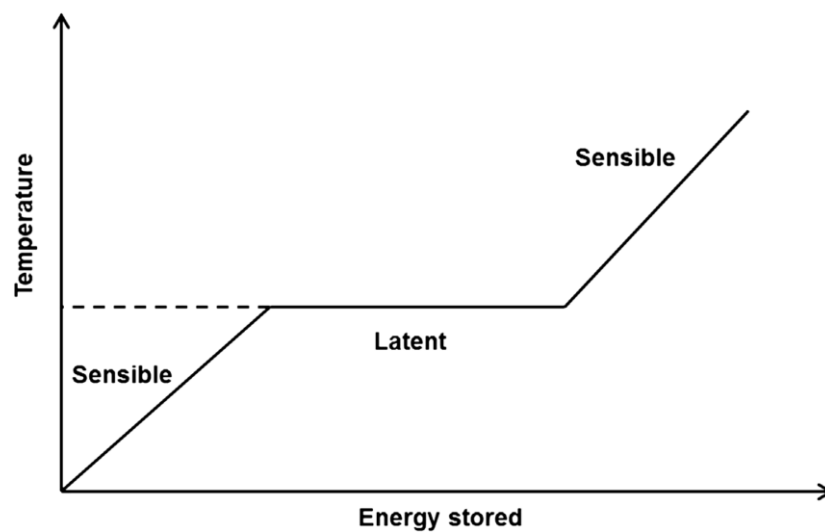


Figure I/1-3 Solid-liquid phase change medium for sensible/latent TES heat storage.

Out of all systems, sensible TES storage is the most mature, which stores and releases energy only through temperature variation and simply depends on the storage medium specific heat capacity (seen in Fig. I/1-3) (Palomba and Frazzica 2018). The latent heat storage takes advantage of the isothermal endothermic and exothermic phase-change processes (e.g., solid to liquid and vice-versa) of a phase-change material (PCM) medium, exploiting enhanced energy densities compared to the sensible storage systems (seen in Fig. I/1-3) (Liu et al. 2016). Finally, regarding thermal chemical storage, energy accumulation is achieved through completely reversible chemical reactions of the medium (combination or decomposition), along with endothermic and exothermic processes (Fig. I/1-4) (Pelay et al. 2017).

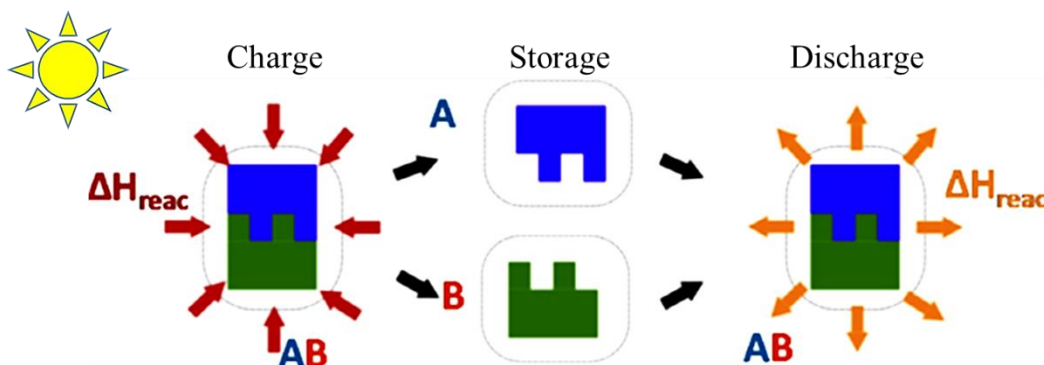


Figure I/1-4 Thermochemical storage process (after Palomba and Frazzica 2018).

I/1.3 Phase-change materials (PCMs): a promising TES technology

Among the different described TES systems, latent heat and more particularly PCMs play a vital role in the development of this kind of energy storage. Presently, PCMs are hot scientific and industrial topics and offer promising TES technology owing large heat capacity during their phase-change process, at which thermal energy can be stored at almost constant temperature (Lin et al. 2018). Lately, PCM-based systems have become more attractive not only as a result of their high energy densities but also due to the possibility of using them at medium- and high-temperature (120-1000 °C), making them good candidates for the temperature requirements of CSP (Achchaq et al. 2018). These technology advantages make PCMs highly interesting and effective for big-scale energy storage, with a small environmental footprint and a competitive price compared to other solutions (Zhou and Wu 2018).

To our knowledge, PCM uses in medium- and high-temperature TES systems are recently promoted for fast-forwarding development, with few installed and operational pilot plants. Worldwide researchers have reported new studies on further selection, characterisation and development of PCMs for medium- and high-temperature TES systems (Gil et al. 2010; Kenisarin 2010; Liu, Saman, and Bruno 2012; Cárdenas and León 2013; Xu, Li, and Chan 2015; Liu et al. 2016; Mohamed et al. 2017; Pelay et al. 2017; Pandey et al. 2018; Wei et al. 2018; Zhou and Wu 2018). The fact that more than 160 000 potential PCM candidates have been suggested explains the huge number of researchers working on this topic. Simultaneously to the discovery, classification and characterisation of the PCM storage materials need to be based on several evaluation factors such as thermal and physical properties, chemical stability, economic viability and so on (Wei et al. 2018).

In general, PCMs are classified into either organic, inorganic or eutectic category, depending on their simple organic/inorganic or complex blend nature, respectively (scheme presented in Fig. I/1-5). Pandey et al. (2018) gave detailed classification and characterisation of each of the PCM categories and their sub-categories, with a focus on materials performing at medium- and high-temperature.

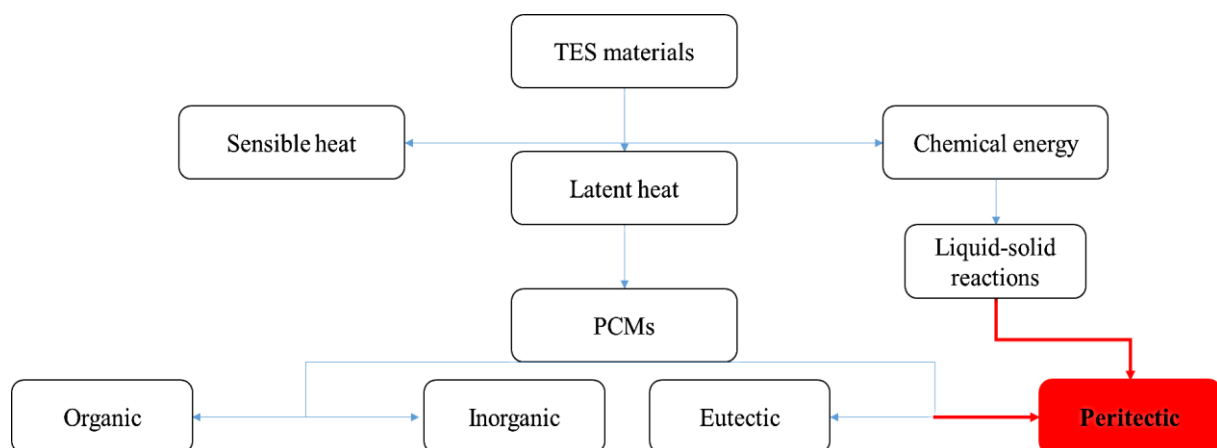


Figure I/1-5 TES materials with detailed PCM characterisation and indicating the peritectic group of materials, combining melting/solidification and liquid/solid chemical energy storage processes.

I/1.3.a Peritectic compounds (PCs): a special category of PCMs

Up to date, a special category of peritectic PCMs had been erroneously recognised as eutectics, as they also store energy not only by melting/solidification but additionally through liquid/solid chemical reaction (seen in Fig. I/1-5) (Pandey et al. 2018). Due to their supplementary chemical energy accumulation, the provided effective volumetric energy densities outdo most of the currently used PCMs and can be compared to or even be higher than the solid-gas reaction of the thermal chemical TES. The breakthrough of these promising peritectic (PC) materials opens a new route for the development of novel ultra-compact TES systems with a broader temperature range (300 – 700 °C) (described in Table I/1.1) (Achchaq and Barrio 2017).

Table I/1-1 Several peritectic binary systems with their corresponding values of peritectic temperature T_P , enthalpy change ΔH and energy density E_p , followed by the corresponding temperature range of peritectic reaction $\Delta T_{L \rightarrow P}$ and total energy density between the solid and liquid points $E_{L \rightarrow P}$ (after Achchaq and Barrio 2017).

Binary system A/B	T_P (°C)	ΔH ($J \cdot g^{-1}$)	E_p ($kWh \cdot m^{-3}$)	$\Delta T_{L \rightarrow P}$ (°C)	$E_{L \rightarrow P}$ ($kWh \cdot m^{-3}$)
LiBr/LiOH	303.9	803	434	76	591
KOH/LiOH	314.82	535	238	24	283
Li/LiOH	334.93	308	182	34	253
CsOH/LiOH	373.63	354	214	55	388
Cr/Zn	483.12	118	234	483	679
Mg/Ag	491.94	332	286	6	304
Li/Zn	510.02	304	372	5	565
Mn/Ni	587.35	297	637	493	1642
Ce/Mg	625.22	368	235	4	239
Ca/Zn	642.05	201	224	5	232
Sr/Zn	649.97	167	206	83	349
Li/Si	690.57	1136	377	20	467
CaCl ₂ /CaF ₂	734.94	438	290	98	402

This family of heat storage materials with combined processes of melting/solidification and liquid/solid reactions has several advantages over all the other TES materials, but especially over gas-solid thermal chemical reaction storage materials (having the highest energy densities out of all present TES technologies). In the PC materials, the separation and recombination of the solid and liquid phases is only driven by temperature, thus performed at atmospheric

pressure in both charge and discharge cycles. Unlike gas-solid thermal chemical reaction storage systems with phases separated in high-pressure tanks, here a one-pot storage concept can be developed, holding the PC composite and the embedded heat exchangers. Another notable and outstanding asset of the PC TES system is the advantageous properties offered by the joint use of sensible, latent and thermo-chemical reactions (described in Table I/1.2). The PC, with these assets, can be seen as a compact, simple and cost-effective TES system.

Table I/1-2 The different known TES technologies and related properties. Bolded and darker background table cells correspond to the novel ultra-compact peritectic (PC) heat storage system properties (Source: kick-off project presentation: Pc2TES ANR -16-CE06-0012-01).

TES technology	Sensible heat	Latent heat	Thermo-chemical reactions
Effective energy density (kWh·m ⁻³)	Low 30-70	Medium 80-200	High 200-500
Energy recovery	Variable temperature	Constant temperature	Variable temperature
Technology simplicity	Simple	Simple	Complex
Investment cost (€·kWh ⁻¹)	15 - 60	100 -250	Too high

Ideally, the PC phase forms/melts and the reversible chemical reaction occurs in a defined temperature range (Achchaq and Barrio 2017). Figure I/1-6 presents one of the possible cases for the energy storage/delivery upon heating/cooling a binary system, operational at the stoichiometric composition. The PC compound is formed by a reversible chemical reaction on cooling, where a liquid phase (L) initially reacts with a primary solid (α) to produce a new stoichiometric compound (β). Only a defined ratio of a given binary system allows the formation reaction and facile management of the stoichiometric PC compound (β), with increased energy potential with respect to other PCMs. Achchaq and Barrio (2017) presented a more detailed description and different step developments of the PC compound formation.

From all the presented PC binary systems (seen in Table I/1.1), inorganic anhydrous salts are considered as the most attractive storage candidates mainly due to their low cost, lightweight, effectiveness, and higher chemical stability compared to metals and alloys. Concerning the inorganic anhydrous salts, the cations are mainly alkali (e.g. Li, Na, K) and alkali earth metals (e.g. Ca, Mg), whereas nitrates, nitrites, hydroxides, bromides, carbonates, chlorides, sulphates, and fluorides can be chosen as anions (Achchaq et al. 2015)

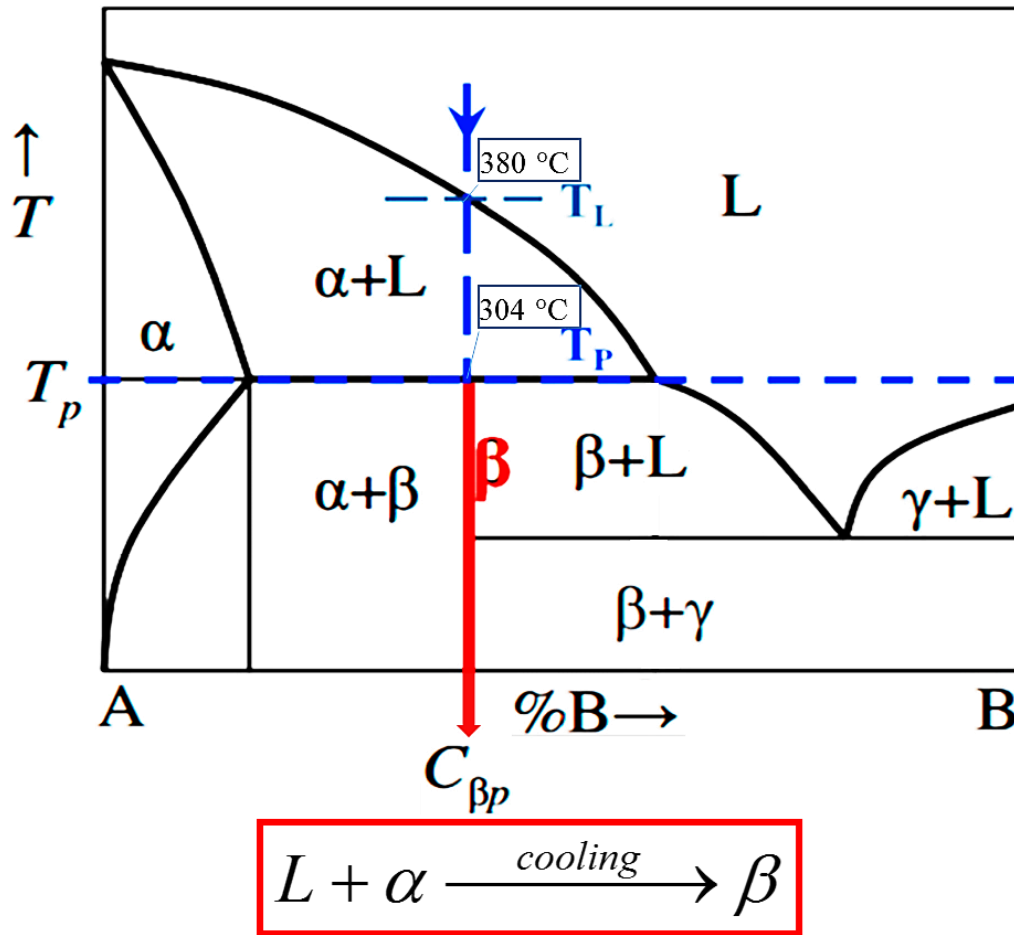


Figure I/1-6 Theoretical phase diagram of a PC binary system, with the corresponding temperature range (T_L to T_P) of peritectic reaction of the particular LiBr/LiOH system given as example. The stoichiometric $C_{\beta p}$ composition at which the compound β is formed during the peritectic transition is presented in the red rectangle (after Achchaq and Barrio 2017).

Yet not all of the suggested inorganic anhydrous salts or other PC binary systems can be easily used in practical applications. The choice of the presented PCs or other PCMs need to follow several prerequisites, such as: phase transition temperature within the application operational range, high latent heat storage capacity, high thermal conductivity, small volume change, no or slight supercooling, stable thermo-chemical properties, low environmental impact and, last but most important, low cost and easy availability (Lin et al. 2018). Wei et al. (2018) summarise and present a refined grouping of these and other principles for the selection of PCMs based on their thermal, physical, dynamic, chemical, economic and technical performances for a given TES application.

An ideal TES storage system based on low-cost materials and performing long-term energy stability within a low volume storage unit is a quite challenging goal to achieve. Explicitly, the initial search of PCMs, especially PCs (inorganic salts) with significantly higher energy density can be seen as the first step towards compact storage systems, thus reducing the investment costs (Palomo del Barrio et al. 2012).

Herein, a unique inorganic anhydrous LiOH/LiBr PC binary system, within the stoichiometric $C_{\beta p}$ composition at which a compound β is formed during the peritectic transition, was considered as a promising PCM intermediate for storing the heat derived from CSP or other energy sources. The corresponding isothermal enthalpy change of $803 \text{ kJ}\cdot\text{kg}^{-1}$ and the energy storage temperature range (304-380 °C) were the main system characteristics for its selection out of other candidates (Achchaq et al. 2019).

Regardless of the high demand for the PCMs practical application and their promising energy storage potential, the technological readiness level (TRL) is still low and needs to be increased. Concerning the chosen LiOH/LiBr PC, and similar to all other PCM systems, there is no single system incorporating all desired and previously mentioned material properties for an ideal TES. This is the reason why one needs to find solutions for using the PCM (in our case a PC) of interest and improve the physical properties of the material that might be too low, thus leading to a satisfactory low-cost storage system.

I/1.3.b Improvement of PC performances and properties

The relevant PC candidates must be such that their storage (latent and peritectic reaction temperature) conditions are within the operating temperature range of their envisaged application. Then, the PC with the highest expected volumetric energy density can be identified, provided that it is compatible with the other materials of the TES. The selected PC material must also allow realising a low-cost system, which can be further developed/upgraded for its future commercialisation.

Next, different technical modifications and materials performance improvement shall be possible to overcome the remaining weaknesses of the selected PC. For example, improvement of the non-congruent (sluggish transition phase) and heat transfer enhancement are considered as important challenges to be overcome for achieving long-lasting TES materials with improved stability and efficiency.

The potentially high energy density of the PC transition is viable only if maintained for many charge/discharge cycles. In other words, excellent reversibility is necessary. But degradation of the performances may occur due to liquid/solid separation during the pro-peritectic (α) phase formation and the subsequent slow peritectic transformation process (seen in Fig. I/1-7). The phase separation and the slow long-range atom diffusion transformation can prevent the complete disappearance of the solid pro-peritectic (α) phase. As a result, an unbalanced PC system is obtained, with lower energy efficiency than the theoretical one (Achchaq and Barrio 2017).

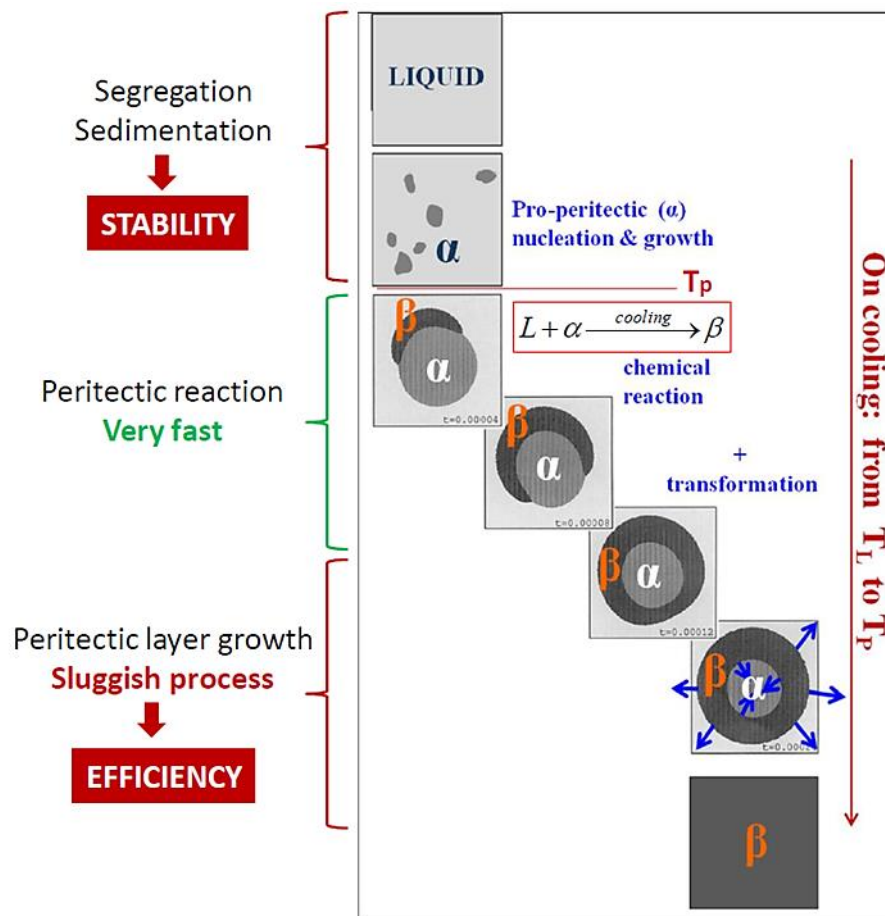


Figure I/1-7 Peritectic transition steps with presented problems on cooling from the liquid (L) to the solid peritectic (β) phase (Source: kick-off project presentation: Pc2TES ANR -16-CE06-0012-01).

Several other authors have also presented similar issues of materials' non-congruent melting, in different inorganic PCM studies (Frusteri et al. 2005; Amaral et al. 2017; Alva, Lin, and Fang 2018; Zhou and Wu 2018). The use of different types of thickening and nucleation agents were recognised as potential solutions for limiting the phase separation and increasing their mutual specific surface area. As for PCs, suitable porous structures and solid fillers have

been seen as solutions for introducing heterogeneous nucleation sites of the concerned initial pro-peritectic (α) and corresponding peritectic (β) phases. Such porous structures can be simultaneously considered as host materials for preventing phase separation and as heat transfer boosters for improving the low thermal conductivity of the PC (Achchaq et al. 2015).

Aside from the phase transition issues seen in the PC materials, advanced research has been made to improve heat transfer and thermal conductivity of PCMs through the development of hybrid materials, here referred to as phase-change composites (PCC). Different heat transfer enhancement methods for the poorly investigated medium- and high-temperature PCMs have been summarised in a few recent reviews (Ibrahim et al. 2017; Mohamed et al. 2017; Lin et al. 2018; Wei et al. 2018). Inorganic PCMs have much higher thermal conductivity (up to or above $1 \text{ W} \cdot \text{m}^{-1} \cdot \text{K}^{-1}$) compared to organic PCMs. Yet, their thermal conductivity is still considered as too low and hence is a drawback in many medium- to high-temperature TES systems. Therefore, different strategies have been proposed for the improvement of PCM heat transfer performances, such as introducing materials of high surface area or particles of high conductivity, embedding the PCM in porous matrices, or encapsulating it. The PCC fabrication is usually performed by components mixing, impregnation or compression. In all the aforementioned cases, filler percolation network formation is crucial for achieving thermal conductivity improvement (Zhang, Xiao, and Ma 2016). Materials used for PCM systems improvement are carbon-, metallic- or ceramic-based, depending on the compatibility and the final working conditions of the developed composite.

I/1.3.b1 Fibrous carbon materials for PCC preparation

The use of carbon materials for PCC preparation is among the most explored methods for PCM heat transfer enhancement. Many carbon material properties are indeed favorable for their use in PCC, such as high thermal conductivity and stability, low density (usually less than $2.26 \text{ g} \cdot \text{cm}^{-3}$, which is only a fraction of metals' density) and lower cost compared to metals and ceramics. In many cases, a small carbon volume fraction is needed for achieving the required heat transfer. Different structural types of carbon have been studied for their use in PCC, in the form of carbon fibres, carbon nanotubes, expanded graphite, graphene, alone or mixed together or in combination with other materials (Nomura et al. 2015).

Many studies have presented carbon fibres and materials based on them as relevant PCC candidates and heat transfer promoters (Table I/1-3) (Fukai et al. 2000, 2002, 2003; Hamada et al. 2005; Frusteri et al. 2005; Frusteri, Leonardi, and Maggio 2006; Karaipekli, Sarı, and

Kaygusuz 2007; Nakaso et al. 2008; Wang et al. 2011; Babapoor, Azizi, and Karimi 2015; Nomura et al. 2015; Tian et al. 2016; Samimi et al. 2016; Huang et al. 2017; Zhang et al. 2017; Jiang et al. 2018). The authors related the advantageous use of carbon fibres in PCC application to:

- high aspect ratio (fibre diameter as low as 6-20 μm and length ranging from less than 1 mm to several millimeters);
- notable and highly anisotropic thermal conductivity (from around $10 \text{ W} \cdot \text{m}^{-1} \cdot \text{K}^{-1}$ and up to $900 \text{ W} \cdot \text{m}^{-1} \cdot \text{K}^{-1}$ perpendicular and parallel to the fibre axis, respectively, and highly dependent on fibre density and on other carbon fibre properties and/or manufacturing processes);
- high chemical stability at elevated temperatures (again dependent on carbon fibre properties and manufacturing processes);
- commercial availability at moderate cost, set up as random carbon fibres or as carbon fibre preforms broadly used in many different applications (well-known and market-ready materials, cheaper than most of other suggested carbon/metal/ceramic PCM boosters);
- up-to-date modification methods for carbon fibre/fibrous structures adjustments, compatibility and enhancement effect improvement with/over PCMs, respectively;
- ease of molten PCM impregnation (under pressure or simple gravity-driven processes).

Table I/1-3 Studies on PCC thermal conductivity enhancement by carbon fibres/carbon fibrous structures.

Cf ¹ Precursor / Manufacturer:	PCC fabrication method:	Cf ¹ thermal conductivity: (W·m ⁻¹ ·K ⁻¹):	Cf ¹ density: (g·cm ⁻³):	Cf ¹ dimensions: diameter (μm) / length(mm):	PCM nature/ Melting point (° C) / Thermal conductivity (W·m ⁻¹ ·K ⁻¹):	Other additives/modifications used/performed:	Nature of study:	TES technology (° C):	PCC carbon loading (wt% or vol%):	Reference:
- / -	Melt-dispersion or cf ¹ brush formation	220	2.17	10 / 5-200-	Paraffin wax / 41-43 / 0.26 in solid	-	E ²	< 100 (l.t. ⁴)	up to 2 vol%	(Fukai et al. 2000)
- / -	Cf ¹ brush formation	190	-	10 / -	n-octadecane/ 28.1 / 0.34 in solid	-	E ² and N ³	< 100 (l.t. ⁴)	up to 1 vol%	(Fukai et al. 2002)
- / -	Cf ¹ brush formation	190	2.12	10 / -	Paraffin wax / 40-53 / 0.21 in solid	-	E ² and N ³	< 100(l.t. ⁴)	up to 1 vol%	(Fukai et al. 2003)
- / -	Cf ¹ brush formation	190	2.12	10 / 60	n-octadecane / 28.1 / 0.34 in solid	-	E ²	< 100 (l.t. ⁴)	up to 1 vol%	(Hamada et al. 2005)
- / -	Melt-dispersion	175–200	1.80	6 / 0.2-6	Inorganic PCM44 (Mg(NO ₃) ₂ ·6H ₂ O–MgCl ₂ ·6H ₂ O–NH ₄ NO ₃) / 44 / 0.47	-	E*	< 100 (l.t. ⁴)	up to 10 wt%	(Frusteri et al. 2005)
- / -	Melt-dispersion	175–200	1.80	6 / 0.2	Inorganic PCM44 (Mg(NO ₃) ₂ ·6H ₂ O–MgCl ₂ ·6H ₂ O–NH ₄ NO ₃) / 44 / 0.47	-	N ³	< 100 (l.t. ⁴)	up to 7 wt. %	(Frusteri, Leonardi, and Maggio 2006)
- / -	Melt-dispersion	190	1.80	6 / 5	Stearic acid / 67–70 / 0.29 in solid	-	E ²	< 100 (l.t. ⁴)	up to 10 wt%	(Karaipekli, Sari, and Kaygusuz 2007)
- / -	Stretched cf ¹ cloth or cf ¹ brush formation	190	2.12	10 / -	Paraffin wax / 49 / 0.21 in solid	-	E ² and N ³	< 100 (l.t. ⁴)	up to 0.4 vol.% cloth; up to 0.75 vol.% brushes	(Nakaso et al. 2008)
- / -	Powdered (ball-milled) cf ¹ melt dispersion	-	-	0.2-0.5 / 0.005-0.05	Palmitic acid / 62.5 / 0.29 in solid	KOH modified cf ¹	E ²	< 100 (l.t. ⁴)	up to 5 wt. %	(Wang et al. 2011)

Table I/1-3 (Continued).

Cf ^I Precursor / Manufacturer:	PCC fabrication method:	Cf ^I thermal conductivity: ($W \cdot m^{-1} \cdot K^{-1}$):	Cf ^I density: ($g \cdot cm^{-3}$):	Cf ^I dimensions: diameter (μm) / length (mm):	PCM nature/ Melting point ($^{\circ}C$) / Thermal conductivity ($W \cdot m^{-1} \cdot K^{-1}$):	Other additives/modifications used/performed:	Nature of study:	TES technology ($^{\circ}C$):	PCC carbon loading (wt% or vol%):	Reference:
Pitch based (XN-100) / Nippon Graphite Fibre Co., Ltd	Melt-dispersion and hot-press	900 (// axis); 10 (\perp axis)	2.22	10 / 0.0066	Erythritol / 118 / 0.73	–	E ²	< 120 (l.t. ⁴)	up to 25 vol%	(Nomura et al. 2015)
– / Zoltek Co.	Melt-dispersion	–	–	10/ 2-8	Paraffin wax / 42-49 / 0.21 in solid	–	E ²	< 100 (l.t. ⁴)	up to 0.69 wt.%	(Babapoor, Azizi, and Karimi 2015)
– / Fluka Company	Melt-dispersion	–	–	- / -	Ethylene-vinyl acetate-paraffin form-stable / 45.63 / -	Expanded graphite	E ²	< 100 (l.t. ⁴)	up to 3.32 wt.%	(Tian et al. 2016)
– / Zoltek Co.	Melt-dispersion	50	2.00	- / -	Paraffin wax / 42-49 / 0.21 in solid	–	E ² and N ³	< 100 (l.t. ⁴)	up to 0.69 wt.%	(Samimi et al. 2016)
Pitch based (XN-100) /Nippon Graphite Fibre Co.,Ltd	Melt-dispersion and hot-press	900 (// axis); 10 (\perp axis)	2.22	10 / 0.0066	Erythritol / 118 / 0.73	Indium particles (thermal conductivity: $82.8 W \cdot m^{-1} \cdot K^{-1}$)	E ²	< 120 (l.t. ⁴)	20-21 vol%	(Nomura et al. 2016)
– / XFNANO Corporation	Melt-dispersion	–	–	0.2-0.6 / 0.005-0.05	C ₁₆ H ₃₄ O, 1-hexadecanol (CPCM _{s5}) / 47–50 / 0.2125	–	E ²	< 100 (l.t. ⁴)	up to 0.5 wt.%	(Xiang Huang et al. 2017)
- / -	Melt-dispersion	900	–	9 / 0.0045-0.0225	Erythritol / 116 / 0.77	–	E ²	< 120 (l.t. ⁴)	up to 10 wt%	(Zhang et al. 2017)
Pitch based (XN-100) / Nippon Graphite Fibre Co.,Ltd; CBCF ₆	CBCF ₅ vacuum impregnation	900	2.22	10 / 3	Paraffin wax / 58-60 / 0.24 in solid	CBCF ₅ ; use of carbonised phenolic resin (PF-4292, Changchun Plastics Co., Ltd)	E ²	< 100 (l.t. ⁴)	5-20.3 vol% (Cf ^I + carbonised phenolic resin)	(Jiang et al. 2018)

Cf^I– Carbon fibres
E²- Experimental
N₃ - Numerical

l.t.4 – low temperature

CPCM_{s5} - composite phase-change materials (high-density polyethylene-organic cetyl alcohol phase-change material)

CBCF₆ - carbon bonded carbon fibres (mesophase pitch + carbonised phenolic resin PF-4292, Changchun Plastics Co., Ltd);

I/1.3.b2 Observed limitations of the carbon fibre PCC application

While a considerable amount of research has been conducted on carbon fibres use and proficiency as PCM promoters, their applications have been rather limited. Carbon fibre-based PCCs are prepared by carbon fibre brush formation or carbon cloth stretch method (presented in Fig. I/1-8 a) and b), respectively) (Fukai et al. 2000, 2002, 2003; Nakaso et al. 2008), or from random melt dispersed systems (presented in Fig. I/1-8 c)) (Fukai et al. 2000; Frusteri et al. 2005; Frusteri, Leonardi, and Maggio 2006; Karaipekli, Sarı, and Kaygusuz 2007; Wang et al. 2011; Babapoor, Azizi, and Karimi 2015; Tian et al. 2016; Samimi et al. 2016; Huang et al. 2017; Zhang et al. 2017) plus additional hot press method (presented in Fig. I/1-8 d)) (Nomura et al. 2015, 2016), or lately by vacuum impregnation method of lab-synthesised carbon network preforms (Jiang et al. 2018).

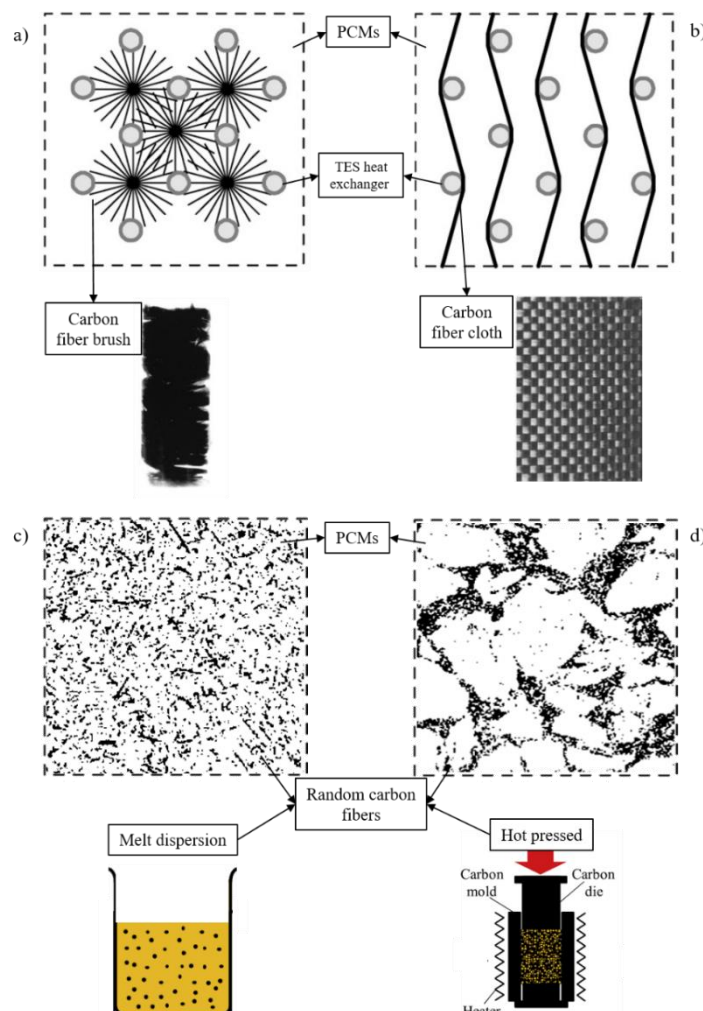


Figure I/1-8 Carbon fibre PCC prepared by: a) carbon fibre brush formation, b) carbon cloth stretch method, c) random melt dispersed system, and d) hot press method.

As previously studied, carbon fibre use for PCC application raises many challenges, demanding further investigation. One of the most significant is composite inhomogeneity, identified when using the simple melt-dispersion method for composite preparation. This PCC constituent separation results in composite instability and thermal conductivity decrease, which intensifies upon cycling tests. Further improvement steps were made by changing from melt-dispersion to direct hot press preparation using solid PCM. Upgraded heat exchange was observed through the formation of an enhanced percolation network, even at a low carbon fibre volume. Yet, the stability of the hot-press prepared PCC was still beyond acceptable application limits and the non-improved carbon fibre contacts once more caused a high thermal resistance (at the studied operation temperature). Stability and thermal conductivity improvement attempts were also performed by adhesion of low-temperature melting metal (e.g. In), giving “metal connections” between carbon fibres. However, the adhesion of heavier and expensive metal PCM promoters may endanger the advantageous low density and cost of carbon fibres. An additional problem, for long-term use of metal PCM promoters and especially in the case of inorganic salt usage, can be the possible pollution and congruity issues between the constituting composite materials. In the case of carbon fibre brushes or stretched carbon fibre cloths, improved fibre connection and thermal conductivity have been achieved in-between the heat exchangers of the storage system. However, the use of these kinds of fibrous carbons cannot play the major stabilisation role of a multiphase system, by providing heterogeneous nucleation sites for the phase-change transitions of PC heat storage materials. Additionally, the fabrication of carbon fibre brushes and carbon cloths can dramatically affect the low-cost and simplicity of PCC systems, while partly solving the observed issues. Other PCC alternatives suggest the use of high volume or weight carbon loadings, which can dramatically reduce the theoretical PC latent heat storage and jeopardise their most important application concept.

Manifold thermal conductivity improvement is evidenced in all of the above-stated studies, yet their objective is focused on heat transfer enhancement of low-temperature TES systems. Working with inorganic anhydrous salts in medium- to high-temperature systems demands additional limitations to overcome. However, when compared to organic or other low-temperature PCMs, inorganic anhydrous salts possess much higher thermal conductivity. Gheribi, Torres, and Chartrand (2014) presented thermal conductivity values of many molten salts at their melting points, wherein the values for LiBr and LiOH (as PC candidates of interest) are 0.475 and $1.273 \text{ W} \cdot \text{m}^{-1} \cdot \text{K}^{-1}$, respectively. From all predicted and experimental data, it appears that lithium salts (halides, carbonates, nitrates, nitrites, sulphates, and hydroxides)

always exhibit the highest thermal conductivity compared to other alkali and some alkaline earth (divalent) salts. These results additionally confirm the reasonable choice of LiBr /LiOH PC as an advantageous system compared to other organic and inorganic salts as PCMs. Yet, carbon fibre PCC development is still foreseen as necessary for achieving a sufficient heat transfer with respect to the application.

Moreover, most of the previously demonstrated fabrication methods and additives for carbon fibre PCC cannot be used for medium- to high-temperature PCM. This is hypothesised from the lack of information concerning composite compatibility and stability at medium- to high-temperature working conditions. Ten out of sixteen reviewed carbon fibre PCC studies explicitly defined the carbon fibres as proved to be resistant to corrosion attack and chemically stable composite candidates. Yet, none of these studies focused on the carbon stability characterisation for the envisaged long-term application. The carbon fibre chemical stability might be taken as an ascertained fact only for use in low-temperature PCC. When carbon fibre materials are considered for composite formation with inorganic salts, for final application at elevated temperatures (in the range from 300 °C to 400 °C), in-depth composites studies should be carried out for testing their thermo-chemical stability. Chemical inertness between the carbon host and the storage material is a critical issue for the long-term operation of PC system. This is vital for binary PC composite systems with a defined ratio of molten salt. The inertness between the carbon host and the energy storage material should be maintained for obtaining complete and reversible peritectic reactions, by which increased energy density can be achieved compared to other latent heat and thermal chemical reaction TES systems.

I/2 Generalities on carbon and porous materials

In search of the most suitable carbon material, the following pages describe carbon and porous materials. Broadening our fundamental knowledge in the field of carbon and porous materials is essential to understand the advanced application of carbon fibres in hybrid PCM composites. Below, the presentation of carbon fibrous materials with different porous structures is provided with details of their properties. Herein, it must be noticed that the final properties of the carbon fibrous materials are influenced by several early or final preparation stage factors, such as raw materials used as fibre precursors, manufacturing and/or synthesis processes, and post-treatments, further presented and discussed.

I/2.1 Basic carbon information

Carbon is one of the most abundant elements on Earth and plays a crucial role in bio- and eco-systems. Carbon has millennium-long importance for humanity. Since their early industrial usage, many versatile carbon-based materials have been developed and many more are still to be developed. Their use is widespread, from home to industry, in almost every sphere of today's and tomorrow's human progress, as carbon has been always a hot scientific topic for many sectors (seen in Fig. I/2-1).

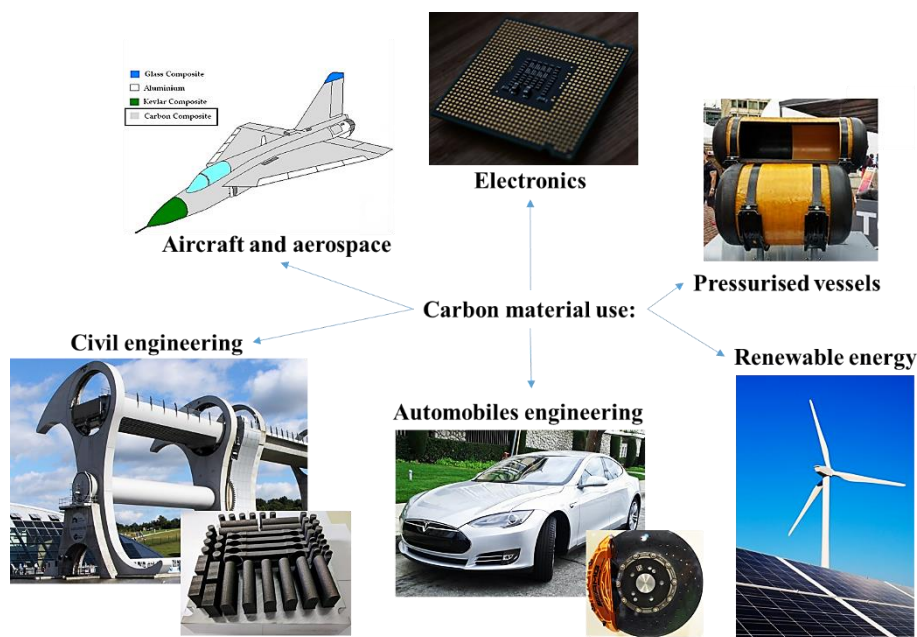


Figure I/2-1 Incorporation of carbon materials in different humankind uses.

Carbon is an incomparable element in the number and the diversity of its possible allotropes. Carbon allotropes are essentially built of carbon atoms, but they have broadly variable structures and properties (Delhaès et al., 2006). For illustration, diamond is by far the hardest known material, whereas graphite, based on the same atoms but arranged in a different structure, is one of the softest. While the diamond is transparent to visible light and an electrical insulator, graphite is opaque and highly conducting. Those paradoxical opposite properties explain why the use of carbon is one of the top choices in many novel materials.

In order to understand the formation of carbon allotropes from different precursors, and to observe the reasons of their versatile performances and properties, it is crucial to have a clear view of the atomic configuration of the carbon atoms and the various ways by which they can bond to each other (Pierson 1993).

The versatility of carbon has been used for classifying the corresponding materials, for example, based on the chemical nature of their carbon-carbon bonds (structures), on the differences in their production ways, on the changes of structure at high temperatures, on the nanotexture, and on the appearance period (Inagaki et al. 2014). Figure I/2-2 represents the classification of carbon materials depending on the nature of the atomic bonds. Here, carbon materials are divided into diamond-like structures with C-C bonds based on sp^3 orbitals, graphite (graphite, graphitic and amorphous carbon), nanotubes and fullerenes in sp^2 hybridisation, and carbynes in sp hybridisation.

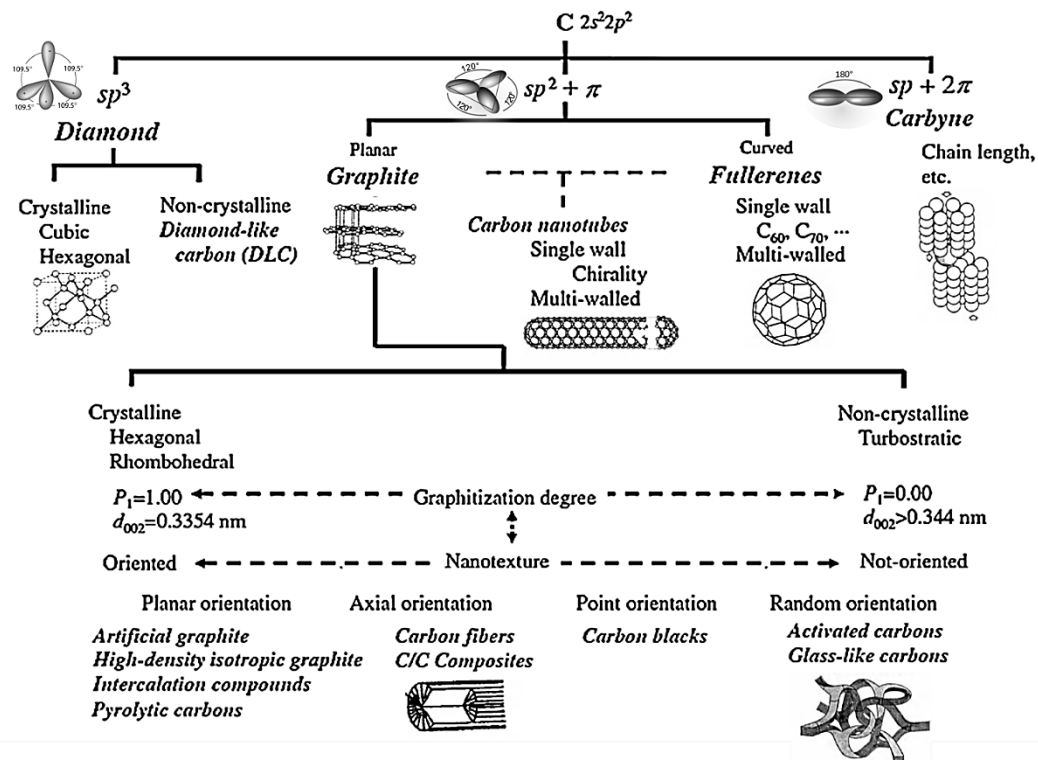


Figure I/2-2 Carbon materials classification tree, with details in the graphitic materials group (after Inagaki et al. 2014).

I/2.1.a Graphitic materials

Regarding the required properties of the PC host material, the carbon allotrope of our interest will be searched in the family of graphitic materials. The basic architecture in this family is based on a hexagonal packing of aromatic units. Each of the parallel planes of those basic structural units is made-up of a sp^2 -hybridised carbon atom combined with three neighboring sp^2 -hybridised atoms to form a hexagonal pattern (seen in Fig. I/2-3). The free delocalised electron (the fourth valence), oriented perpendicular to the atomic sheets, is non-symmetrical (unlike the sigma (σ) orbital) and is called by convention a π orbital. These hexagonal carbon layers present a highly anisotropic nature due to strong covalent bonding

because of the sp^2 orbitals in the same layers, but weak bonding of van der Waals type between the π electron clouds of stacked piles.

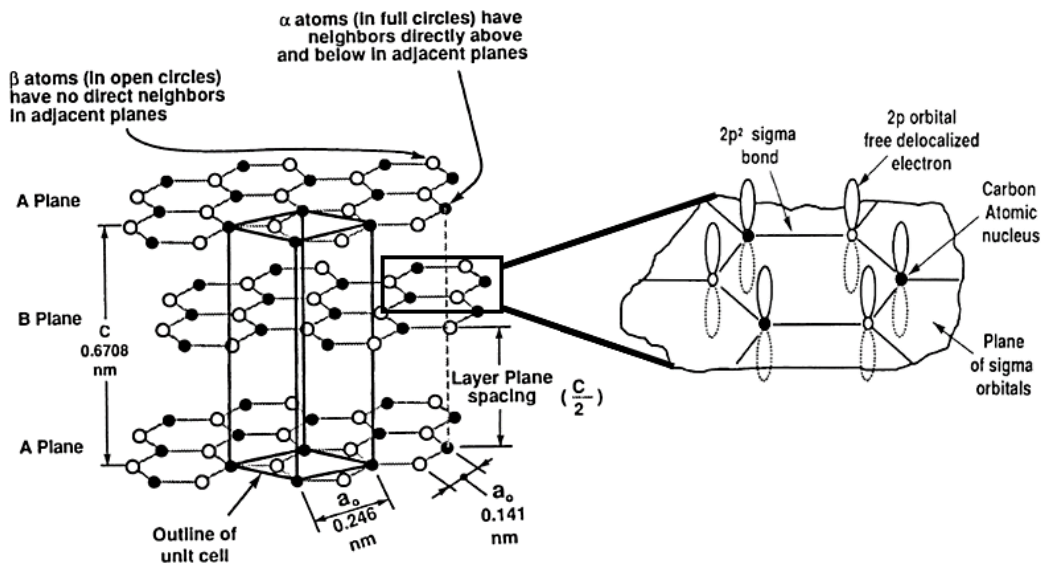


Figure I/2-3 3-D representation of the graphite hexagonal stacking ABAB (left) with a zoom on the sp^2 hybridised structure showing the σ bond and the π electrons (after Pierson 1993).

Regular close-packing of such carbon layers give graphite crystals, which most commonly are hexagonal graphite with ABAB stacking (seen in Fig. I/2-3) and possibly a minor proportion of rhombohedral graphite with ABCABC stacking (Inagaki and Kang 2014).

The term "graphite" by itself describes an ideal regular packing of graphite crystals. The perfect hexagonal graphite structure defined above is composed of theoretically infinite carbon planes with perfect hexagonal ABAB stacking and without defects. This ideal graphite structure is theoretical, thus never found, either in natural or synthetic form. Yet, the term is frequently misused to describe graphitic materials. These materials may be described as "graphitic carbons", consisting of carbon with the graphite structure, but possessing structural lattice defects (seen in Fig. I/2-4). On the other hand, they can be "turbostratic" or even "non-crystalline", which are materials consisting of carbon atoms with the identical planar hexagonal planes of the graphite structure, however with much more structural defects, thus missing the crystallographic order in the L_c direction (seen in Fig. I/2-4) at long range (Boehm, Setton, and Stumpp 2009).

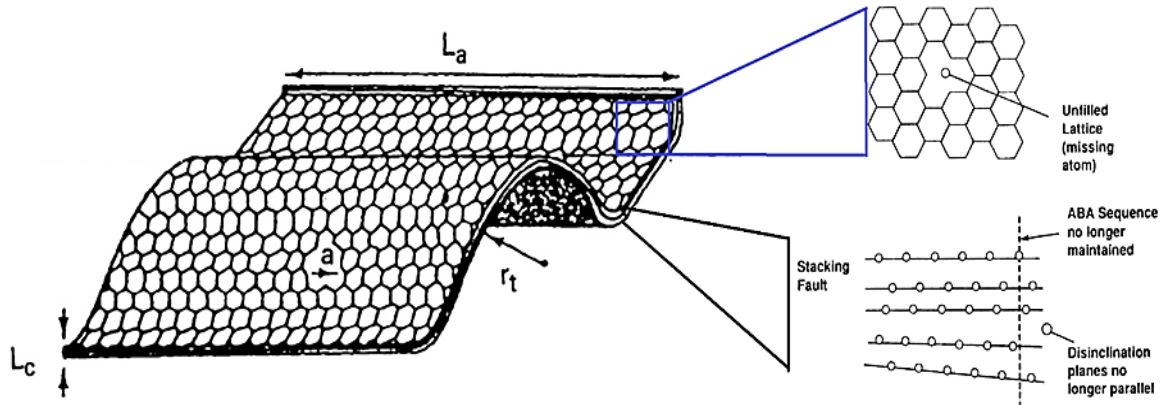


Figure I/2-4 Scheme of crystallite imperfections in graphite showing unfilled lattice, stacking fault, and disinclination (after Pierson 1993).

Under ordinary environment, i.e., at room temperature and atmospheric pressure, turbostratic stacking and non-crystalline structures are metastable. Therefore, they are assumed to be stabilised by the presence of hydrogen and other external atoms, which bond to carbon atoms located at the edges of the layers, and by hanging bonds. The space between two layers of turbostratic stacking is higher than that of graphitic stacking. The interlayer spacing in graphite crystals has been accurately determined to be 0.3354 nm (seen in Fig. I/2-3) (Franklin 1951). The interlayer spacing of turbostratic stacking is reported to be 0.344 nm, but nowadays it is understood that a unique value cannot be established, because of the presence of foreign atoms at the edges of layers and the occurrence of carbon atoms under sp^3 hybridisation in some of the materials.

Different “graphitic carbons” are obtained by carbonisation of various precursors, defined as organic materials with fossil or renewable origin, relatively poorly cross-linked and prone of structural reorganisation. Initial carbonisation occurs at temperatures as low as 700–1300 °C in an inert atmosphere or under vacuum in specific cases. The carbonisation process is usually accompanied by the elimination of different heteroatoms found in the originating material, such as hydrogen, oxygen, nitrogen, sulphur, phosphor, and halogens (Edwards 1989). A turbostratic structure is usually observed once the carbonisation of many carbon precursors is performed. By further heat treatment at higher temperatures (up to 3000 °C), graphite layers grow in both directions, parallel to the layers (increase of crystallite size L_a) and perpendicular to the layers (increase in the thickness of parallel stacking, which is measured as crystallite size L_c) (seen in Fig. I/2-4). The values of L_a and L_c critically depend on the temperature of carbonisation and on the nature of the precursors (Franklin 1951). Depending on the possibility of some carbon materials to perform further growth of the graphite layers, or not, by treatment

at higher temperatures, they can be classified into graphitisable, partially- or non-graphitisable (presented in Fig. I/2-5) (Russell, Gibbins, and Williamson 1999). Thus, in different graphitic materials, the shape, size, and degree of imperfection of the elementary crystallites, their general orientation, as well as bulk characteristics such as porosity and level of impurities, may differ significantly from one carbon material to another. As a result, the properties of these various materials may show considerable differences.

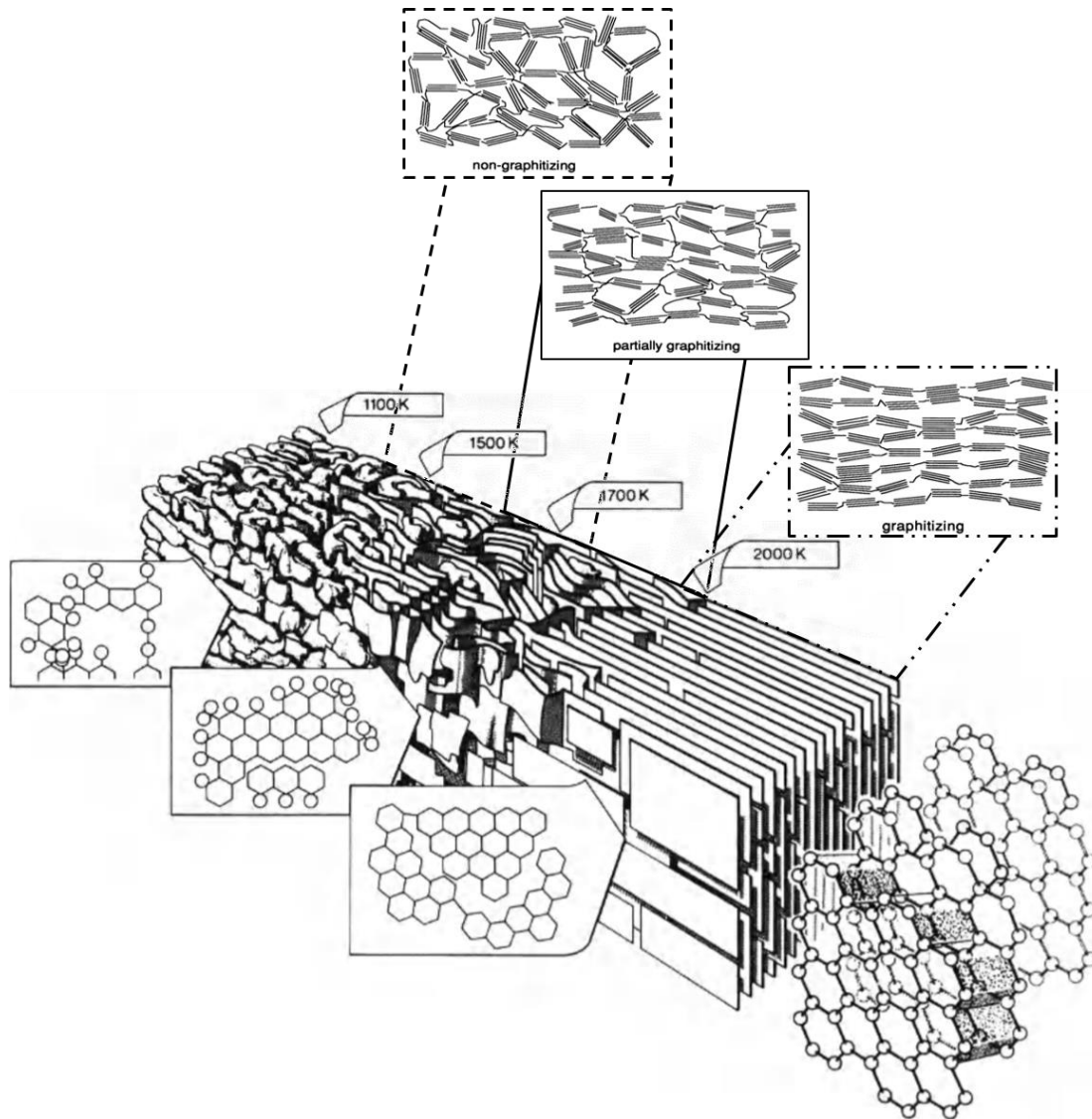


Figure I/2-5 Heat-induced structural improvement of non-, partially- or graphitising carbonaceous materials leading to different "graphitic carbons" (after Edwards 1989).

The aforementioned classification into graphitising, partially- and non-graphitising leads to carbon materials with a variety of nanotextures that show very different behaviours under high-temperature treatment. The anisotropic structure of carbon layers is well known to favour orientation in most carbon materials. From the point of view of nanotexture, and based

on the preferential orientation of carbon layers, carbon materials are classified into two groups, random (or non-oriented) and oriented, and the latter into three subgroups: planar, axial, and point orientations (Inagaki and Kang 2014). The classification is presented in Figure I/2-6, along with some examples of carbon materials for each nanotexture. As far as the present application of carbon materials is concerned, carbon fibre axial orientation can now be further considered.

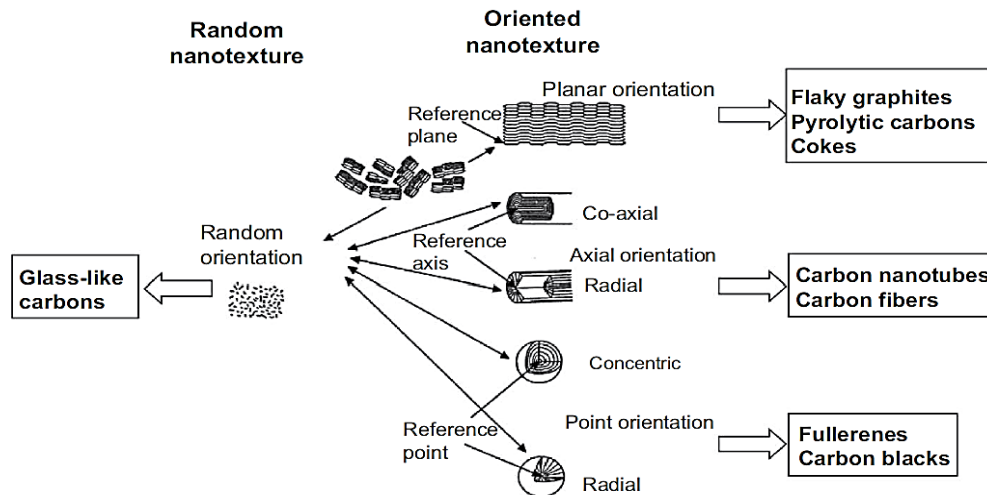


Figure I/2-6 Classification of “graphitic carbons” by means of their nanotexture (after Inagaki et al. 2014).

I/2.2 Porous carbon, an ideal host material?

Different porous materials may match the application considered herein, as they combine the properties to perform all or most requested features improving PC performances in TES. Thus, studying low-cost carbon fibre porous structures with suitable features for their use as PC host and dispersion media is of main interest in the present thesis.

I/2.2.a Porous materials

Generally speaking, porous materials are multiphase, with at least one phase being non-solid, named pores or voids (Bear 1972). Pores can be divided into closed and open pores, the latter category itself divided into throughout pores and dead-end pores (de Boer 2000). Undoubtedly, there are many intermediate situations (relatively incomplete open cells with holed walls), but the two former ones are the most frequently encountered since they correspond to two distinct types of porous materials, possessing dissimilar properties and applications. In a true porous medium, all or substantial part of the void space should be interconnected and

possesses a so-called “intrinsic permeability to fluid flow” (Dullien 2012). Intrinsic permeability has a dimension of m^2 and only relies on the solid’s geometry, not on the properties of the fluid which flows through it (Szymkiewicz 2013). Due to the thesis objective of characterisation porous carbon materials for hybrid PC composite preparation, these specifications and definitions disqualify all solid materials containing individual holes and parts of void space that are not interconnected. These definitions of porous media are also given based on fluid flow aspects since part of this thesis deals with permeability and infiltration properties of porous fibrous carbon materials.

Many porous materials different in natures and applications, from fibrous woven or non-woven materials to granular materials and to a multitude of cellular materials correspond to the definitions given above. While some of the results further presented can be applied to a broader range of materials, non-woven carbon fibre felts are those of interest in this thesis and will, therefore, be further examined. A brief introduction to fibrous carbons, their precursors and their manufacturing/synthesis processes is given below.

I/2.2.a1 Non-woven porous fabrics

Textile fabrics can be woven or knitted, braided, or formed as layers of non-woven materials normally made of fibres derived from (natural or synthetic) polymers, i.e., from macromolecules presenting covalently bonded, repeating units (McCarthy 2013). Fibrous materials are soft, porous and voluminous, and rather quite resistant to mechanical deformation with respect to their low density. They require a low amount of material to form a stable porous structure (Kellie 2016).

These characteristics have enabled fibrous materials to be used in a wide range of industrial applications and to provide solutions to a wide range of social challenges. Fabrics are thus essential in a broad range of industrial sectors by offering durable, flexible, lightweight and cost-effective materials (Horrocks and Anand 2015). It is hard to imagine a world without materials made of fibres, being presented in our daily life in a wide spectrum of applications such as textiles, furniture, insulating materials, packaging, transportation or medicine, for example (McCarthy 2013). Many other highly specialised applications also take advantage of a number of different types of fibrous materials and their particular properties.

As materials of major interest in the present thesis, non-woven fabrics represent one of the biggest branches of textile and other industries. Eliminating conventional textile operations, such as drawing, roving, spinning, weaving, or knitting, non-woven fabrics are typically

manufactured directly from single fibres. The straightforwardness of non-woven formation, coupled with high output, permits non-wovens to compete favourably with many rival materials. Non-wovens are relevant in terms of performances and price seen as simple low-cost substitutes of more expensive traditional materials in high-performance special demand applications (Wang and Gong 2006; Shahani et al. 2014). Today, tuned high-performance fibres are incorporated in different kinds of non-wovens such as ballistic protection, insulation, fireproof layers, reinforcement, energy storage, among many other ordinary or specific applications (Kellie 2016). Additionally, novel non-woven materials set up on the concept of structural analogy with other materials have emerged recently, and are slowly but surely overtaking important positions in many industries.

A non-woven can be defined as "a manufactured sheet, web or batt of directionally or randomly orientated fibres, bonded by friction, and/or cohesion and/or adhesion, excluding paper and products which are woven, knitted, tufted, stitch-bonded incorporating binding yarns or filaments, or felted by wet-milling, whether or not additionally needed" (cited from Russell 2007). Non-woven structures can differ from other textile structures because:

- they principally consist of single fibres or layers of fibrous webs rather than yarns;
- their anisotropy is equally reflected in terms of organisation and in terms of properties due to both fibre alignment (fibre orientation distribution) and arrangement, and/or type of structure-formatting bonds;
- they occasionally slightly deviate in fabric weight and/or fabric thickness;
- they are highly porous and permeable structures.

Non-wovens' structure and properties are determined by fibre properties, type of bonding elements and method, bonding interfaces between the fibres and binder elements (if existing), and fabric structural architecture. The important dimensional and structural parameters influencing the properties of non-wovens are fibre dimensions and morphology, fibre orientation distribution, fabric dimensions and morphology, structural properties of bond points, and porous structural parameters. The important properties of non-wovens can be modified according to their end-use, but the most important parameters are the mechanical properties, fluid treatment and heat handling properties, as well as other physical and chemical properties required by the application (Russell 2006).

The non-woven fabrics pass through few manufacturing stages that influence the properties of the final materials (seen in Fig. I/2-7). Because only the most important information about properties and characteristics of interest here are discussed below, the reader needing additional information on non-woven production, fibre type and other processes of finalising the fabrics can refer to Tanchis (2008).

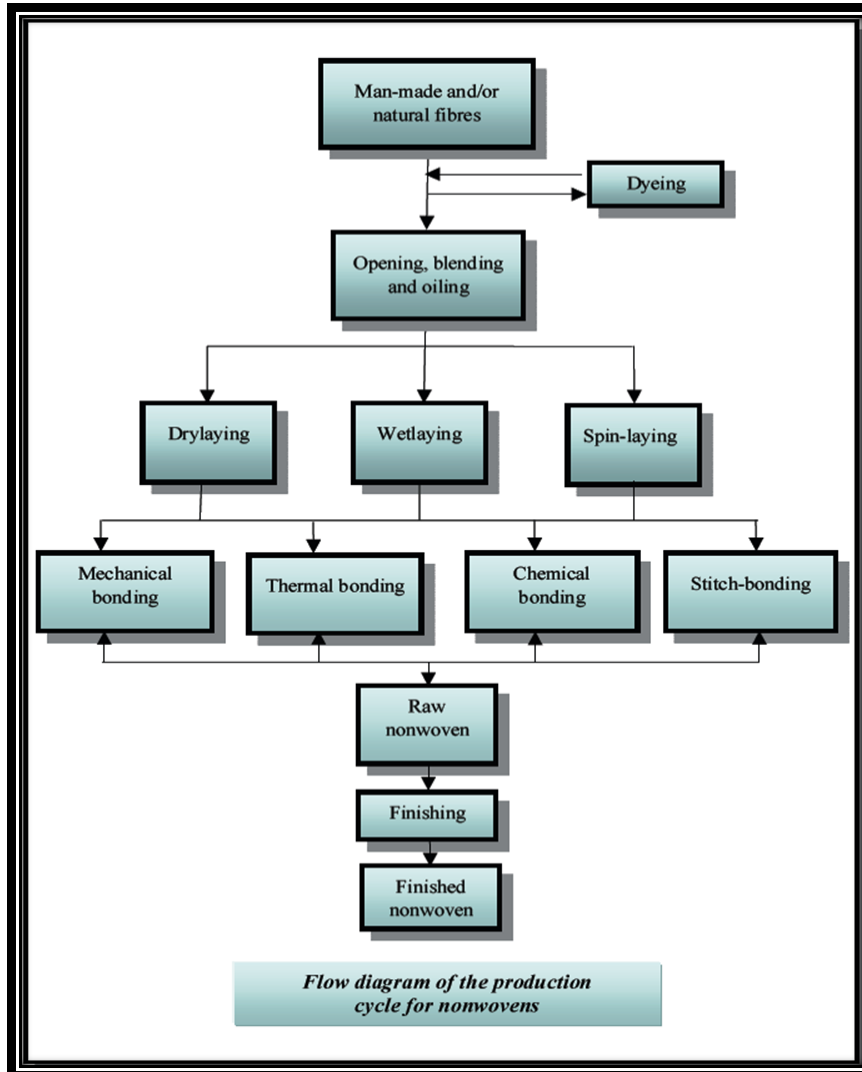


Figure I/2-7 Production stages of non-woven fabrics (after Tanchis 2008).

As already proved and introduced above, non-woven fabrics are formed by different bond structures, whose type, shape, rigidity, size, and density influence fabrics' properties. Therefore, it is of high importance that they are characterised in-depth. The reason why the bonding part of the manufacturing process is broadened in this thesis is due to the use of more than one type of non-wovens, thus one of their differences comes from the bonding production step.

The choice of bond structure in the fabric mainly depends on the selection of both the manufacturing process and the application of these materials. One way of manufacturing mechanically bonded non-wovens is interlocking either individual fibres or loose fibrous strands. These kinds of connections are flexible and the constituent fibres are able to slide or move within the bonding joints. In contrast, chemically bonded fabrics are formed by adhesion or cohesion between polymer surfaces, in which a minor part of the fibrous network is rigid and the freedom of movements within the bond points and the fibres is strongly reduced (Prabha Karan 2016). Thus, needle-punch mechanical bonding and chemical bonding processes are of high interest and are thus explained further.

Typically, periodic needle-punched fabrics have their unique structural architecture because of the interaction of fibres with the needle barbs. By reorientation and migration of fibre segments from the surface of the web in the direction of the interior of the fabric, new pillars of fibre segments are rearranged roughly perpendicular to the fabrics' plane (seen in Fig I/2-8). Non-wovens' layers are thus reinforced by the formation of such rearranged fibrous pillars, and hence the layers are compacted and interlocked with each other (Lee 2002). Fabric production parameters that influence the bond points are: dimension/number of needle barbs (on the needles) in relation to the fibre diameter, punch density, and needle penetration.

Since this bonding process rearranges fibre segments, it induces and/or increases structural anisotropy, compared to the original web. As a result, the structure of needle-punched fabrics has some fibre parts aligned in the transverse direction (through-plane), though the main fibre population remains aligned in-plane (Lee, Yun, and Park 2005). This brings the hypothesis that, due to the specificity of the manufacturing process, needle-punched fabrics lead to higher porosity and a larger number of curved, inter-connected, pore channels than in other non-woven and woven fabrics. These hypotheses are further supported by results on the differences in physical material properties between the different types of non-woven porous structures.

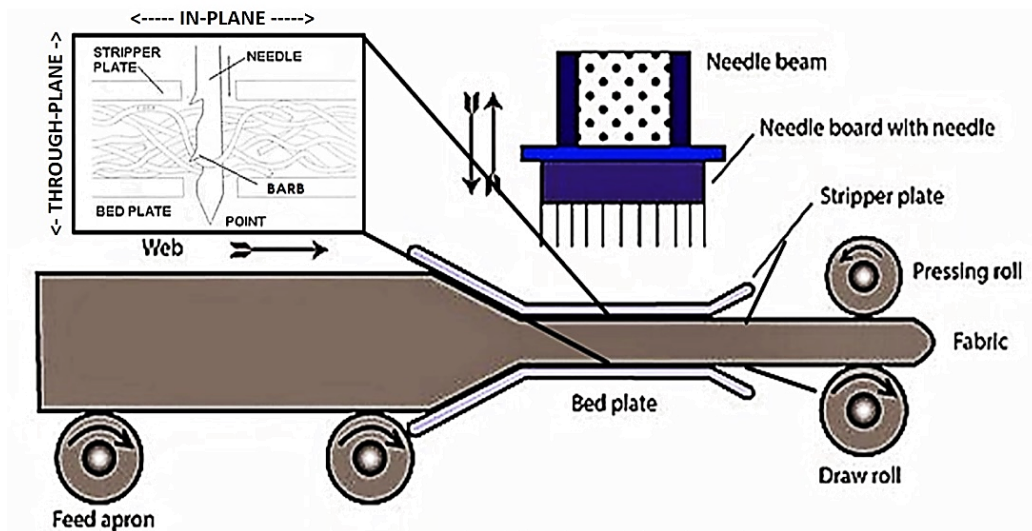


Figure I/2-8 Basic view of the needle-punching process.

Some of the resultant needle-punched non-wovens can be next surface-coated or infiltrated with solutions of phenolic resin at various concentrations (Shi et al. 2015), thereby giving them an additional chemical consolidation. Rigidised felts are thus obtained, which have a modified morphology with respect to the initial soft materials, and therefore modified material structures and properties have been investigated in this thesis.

In contrast, chemically bonded fabrics are formed by adhesion or cohesion between polymer surfaces. A minor part of the fibrous network thus becomes rigid as the freedom of movements within the bond points and the fibres is strongly reduced (seen in Fig. I/2-9) (Cheng et al. 2015; Prabha Karan 2016; Zhang et al. 2017)

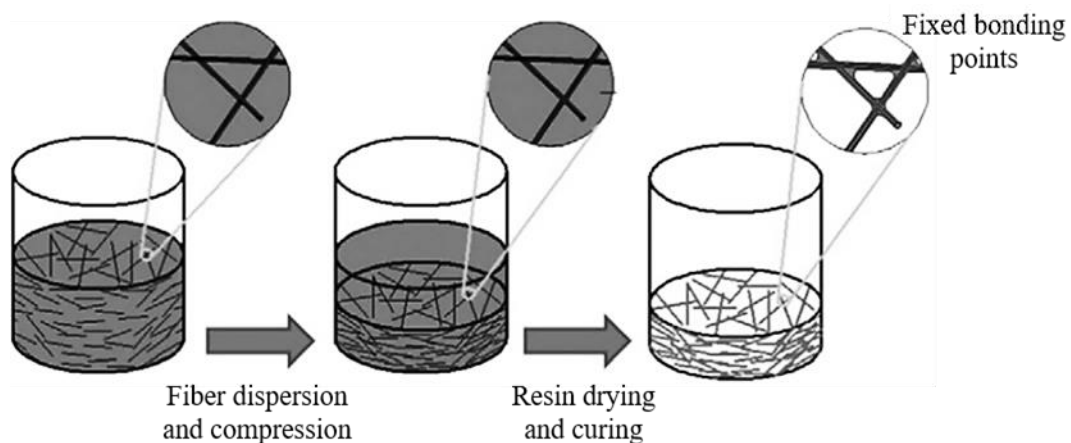


Figure I/2-9 Simple production method of chemically bonded non-woven fabrics (after Cheng et al. 2015).

The delivery of the resin in the material is largely ruled by the way it is introduced into the web and how it flows in-between the fibres, but 5 wt. % of binder is often enough to bond them at their surfaces and interconnections (Russell 2006). The resultant physical properties thus depend on fibres, bonds and the interaction between them, and on their relative spatial arrangement, surface and bulk properties (Kellie 2016). Since a large number of fibres may be entangled and welded by a coating of binder connecting fibre crossover points and/or interfibrous porosity, this results in solid bond points, making these materials quite different from their needle-punched counterparts. The main purposes of using this felt manufacturing process are to obtain materials with improved mechanical and heat transfer properties and minimised further textural modification, and thus to reduce the possibility of fibre separation (Davies and Rawlings 1994).

I/3 Non-woven carbon fibre felts

What was presented above on carbon and porous non-woven materials is the base onto which the materials of interest, carbon fibre-based non-wovens (further referred to carbon felts), can be now described further. Carbon felts (CFs) have been extensively studied due to their various applications. CFs derived from synthetic or natural polymeric precursors possess unique three-dimensional non-woven structure and high volume, physical and thermo-chemical properties. These material features allow them to be the core component of energy supply, aircraft, and automobile construction sectors, with a huge focus on the development of new technologies and products (Castañeda et al. 2017).

Carbon fibres, being the main constituents of CFs, are materials from the graphitic group introduced above, and consist of aromatic carbon layers more or less aligned parallel to the fibre axis. As it is usually the case (Das et al. 2016; Huong Le, Bechelany, and Cretin 2017; Minke, Kunz, and Turek 2017), two types of precursors are mainly used for producing carbon fibres: polyacrylonitrile (PAN) (~ 96% of the carbon fibre market, due to economic and fibre quality details) and regenerated cellulose (Rayon) (driven by the sustainable change towards renewable materials) (seen in Fig. I/3-1). During the different heat-treatment steps, the carbon content within the precursor fibre increases up to > 99 wt. %. For each precursor, the temperature treatment, the degree of molecular alignment and the degree of conversion from polymer to carbon, also influence the properties of the final carbon fibre (Newcomb 2016).

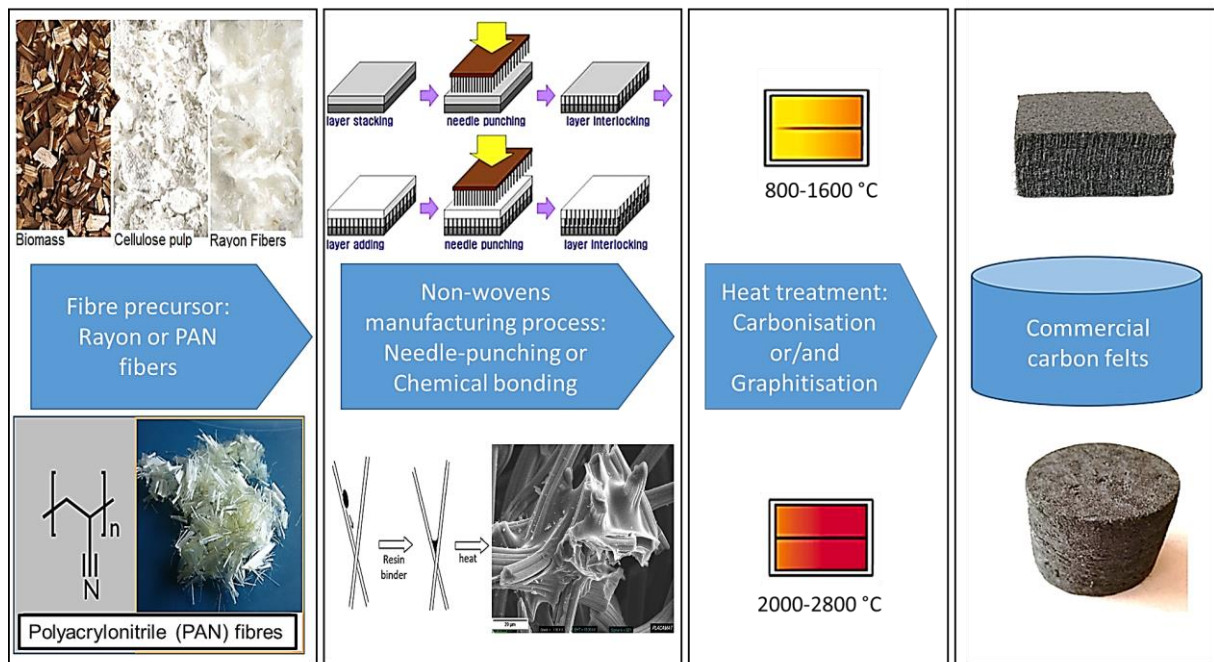


Figure I/3-1 Shortcut presentation of the basic characteristics of the CFs.

After the non-woven formation process, the prepared precursor materials are thermally treated at temperatures typically in the ranges 800–1600 °C for carbonisation, or 2000–2800 °C for graphitisation and further improvement of the graphitic crystalline structure of carbon fibres (Fig. I/3-1) (Rahaman, Ismail, and Mustafa 2007; Xiaosong Huang 2009). Moreover, the choice of precursors and heat processing parameters used in their manufacture can affect the graphitisation stage of the carbon fibres, thus it can lead to a change of properties between carbonised and graphitised felts. Despite various precursors and other manufacturing parameters, carbonised and graphitised non-wovens present exactly the same aspect (Fig. I/3-2).



Figure I/3-2 Needle-punched carbon felt samples (carbonised to graphitised, from left to right).

I/3.1 CF structure and properties of importance for TES application

Studies of the properties of different kinds of porous CFs are of immense significance in the mission of defining an appropriate candidate for the present TES application. The awareness of the introduced intrinsic materials parameters is critical for accurate predictions of their performances in the present context. The CF host has to demonstrate the well-known carbon material advantages of being lightweight but at the same time has to offer dimensional stability and heat transfer enhancement to the final CF-PC hybrid composite.

CFs present a wide range of characteristics, depending on the production way and the precursors used in their preparation. For that reason, it is necessary to characterise the CFs and better understand their properties in order to determine their application in the CF-PC hybrid composite. The characterisation can involve important quantities such as density, porosity, surface area, fibre/felt structure (size, tortuosity, and anisotropy), elemental composition, and graphitic structure, for instance. Important CF properties may influence their impregnation and inertness with molten PC, such as:

- morphological characteristics of fibre, fabric, and fabric bond structure;
- fluid handling properties: permeability and wettability;
- mechanical properties: compression modulus, strength, and recovery;
- heat transfer properties: thermal conductivity;
- chemical stability and durability at medium to high temperatures.

I/3.1.a Out-of-plane fluid permeability

Many research works have been devoted to this topic in the past decades, combining experimental characterisation, simulation of porous media and modelling, as reported in several monographs (Scheidegger 1958; Dullien 1992; Chen and Ewing 2002; Sahimi 2011). However, as far as CFs are concerned, published studies are quite limited, despite the significance of the topic, especially in the field of electrochemistry in general, and of gas diffusion layers for fuel cells in particular. Only a few studies focused on the changes of permeability of CFs either as a function of porosity, which was modified by axial compression (Gostick et al. 2006; Itonen, Mikkola, and Lindbergh 2004), or as a function of thickness (Dohle et al. 2003; Chun et al. 2011). Other papers just reported values of permeability of composite materials made of CF coated with a microporous layer (Williams et al. 2004; Hung et al. 2013), or such that various amounts of PTFE was used to achieve chemically-bonded CF (Prasanna et al. 2004; El-kharouf et al. 2012; Mangal et al. 2015; Fadzillah et al. 2017).

One of the most fundamental requirements of CF is the ability to be fully infiltrated by molten PC. In an ideal scenario, this should be realised rapidly and at atmospheric pressure, further related to CF intrinsic permeability and defining the ease at which the hybrid material can be prepared. As for CF non-wovens, this property is directly related to their fibre- and felt-architecture (Soltani et al. 2017).

The fibre architecture and surface chemistry, hosts' permeability and tortuosity, infiltration liquid viscosity, and the temperature are quantities known to influence the process of infiltration of non-wovens (Park 2015). A careful infiltration process design and well-controlled parameters are required to reproduce a homogeneous CF-PC hybrid composite. Therefore, CF porous structure characterisation is considered as one of the main thesis challenges. In addition, the different permeability properties of the investigated CFs are important information to be analysed for their influence on PC stabilisation and improvement of the thermal energy storage capacity. The structure of the materials of interest is generally extremely complex and difficult to characterise. This is additionally complicated by differences in the manufacturing techniques and initial materials used to produce the commercial CF.

The work to characterise accurately the essential permeability parameters of CF materials is made to correlate material properties to performances and/or apply an advanced material modification. Nevertheless, measuring, discussing, and comparing fluid flow properties in various CFs can be quite challenging, thus research of general materials' trends will be performed based on empirical and analytical studies.

I/3.1.b Mechanical properties

The compression response of non-wovens to transverse compressive forces plays an important role in almost all applications involving liquid loading/infiltration processes for composites preparation (P. A. Kelly, Umer, and Bickerton 2006).

Earlier research studies investigated the influence of fibre type differences (Dunlop 1983; Parikh et al. 2004), different fibre properties (Schoppee 1998; Beil and Roberts 2002; Debnath and Madhusoothanan 2009; Das and Pourdeyhimi 2010), and manufacturing technology (Debnath and Madhusoothanan 2012, 2013; Ventura et al. 2014) on the compression behaviour of non-wovens. Non-wovens' mechanical properties are strongly dependent on their microstructural features, like fibre morphology and properties (fibre precursor, fibre cross-section, fibre diameter, crimp shapes of different fineness, elastic modulus, and fibre denier),

and felt morphology characteristics (fibre volume fraction, fibre orientation distribution, bonding technique).

Non-woven felts also demonstrate various macroscopic mechanical responses depending on their manufacturing techniques, which might influence the anisotropic distribution of the constituent fibres with preferential alignment/orientations, and inter-fibre junctions/bonds/entanglements. In the case of different types of non-wovens, various mechanical behaviours can be observed (Adolphe and Dolez 2018). If the structure is bound by fibres (as in chemically bonded nonwovens), the stress-strain curve exhibits a permanent deformation typical of brittle materials; on the contrary, if the structure is flexible (Jirsak, Burian and Sasková 2003) (as in the needle-punched non-wovens), a non-linear elastic deformation curve is observed (Zhang et al. 2017) (both stress-strain curves displayed in Fig. I/3-3). The stress-strain curve shape dissimilarity is linked to the difference in structural compression behaviour. While after the initial elastic part, a full structural destruction occurs in the brittle CF materials, continuous elastic reorganisation of semi-free or mobile fibres/filaments takes place upon compression loading of the flexible needle-punched structure.

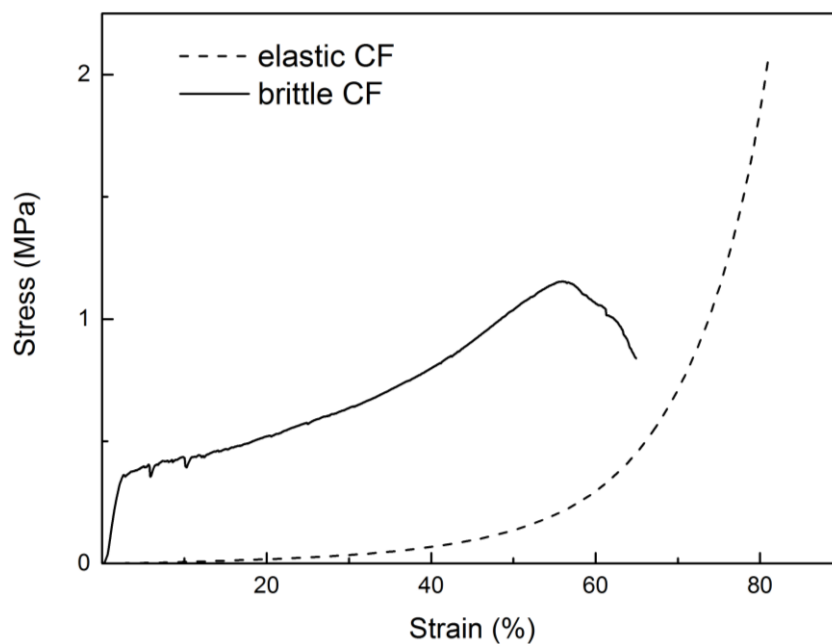


Figure I/3-3 Compression stress strain curve for brittle CF (solid line) and elastic CF (dashed line).

Studying the mechanical properties of the CFs of interest is important due to their submission to some degree of compression during the preparation of CF-PC hybrid composites. Material's compression should be expected herein, due to the possible involvement of pressure-assisted infiltration of the CFs with the molten PC. This is the reason why superior compression resistance and recovery capability are desired to maintain the initial morphology of the CF.

The experimental stress-strain data were fitted with analytical hyperelasticity models, and additional information were obtained for mechanical properties, not directly measurable due to the special behaviour of the elastic CFs.

I/3.1.c Thermal conductivity

From the studies previously performed by Danes and Bardon (1997), the anisotropic bulk thermal properties of carbon fibre non-wovens are due to the different anisotropic graphite crystallites, fibres and felts contributions (seen in Fig. I/3-4). As observed by Kelly (1981), the thermal conductivity of graphite is highly anisotropic, which influences the anisotropic thermal conductivity both perpendicular and parallel to the fibre direction. The thermal conductivity of carbon fibres is directly linked to the graphitic plane structure defects, consisting of porosity, non-carbon atoms, and structural disorder and orientation of the crystalline structures (presented in Fig. I/2-4 and Fig. I/2-5). With the increase of the temperature of the CF production process, the concentration of fibre structure defects is reduced and the graphitic order is improved, thereby resulting in enhanced thermal conductivity. Recent reviews on commercially available PAN-based carbon fibres have shown that at room temperature and conditions, the fibres' thermal conductivity, along the fiber axis, is in the range from ≈ 5 up to $\approx 156 \text{ W} \cdot \text{m}^{-1} \cdot \text{K}^{-1}$ (Newcomb 2016). The thermal conductivity values for the Rayon-based carbon fibres, again along the fibre axis, were found in the range between 5 and $15 \text{ W} \cdot \text{m}^{-1} \cdot \text{K}^{-1}$ (Panerai et al. 2017).

CFs are flexible/rigid porous materials, made of carbon fibres with/without additional bonding material in the intersections, with the fibres being arranged mostly in the in-plane felt direction. Measurements of the thermal conductivity can also be used as a tool to characterise CFs prepared from various precursors under different manufacturing conditions. The morphology parameters that can have high influence over the overall carbon non-wovens' thermal conductivity are fibre aspect ratio (fibre diameter to length), mean fibre diameter, fibre-to-fibre contacts, bonding technique, felt porosity and density and fibre orientation (felt anisotropy) in the materials.

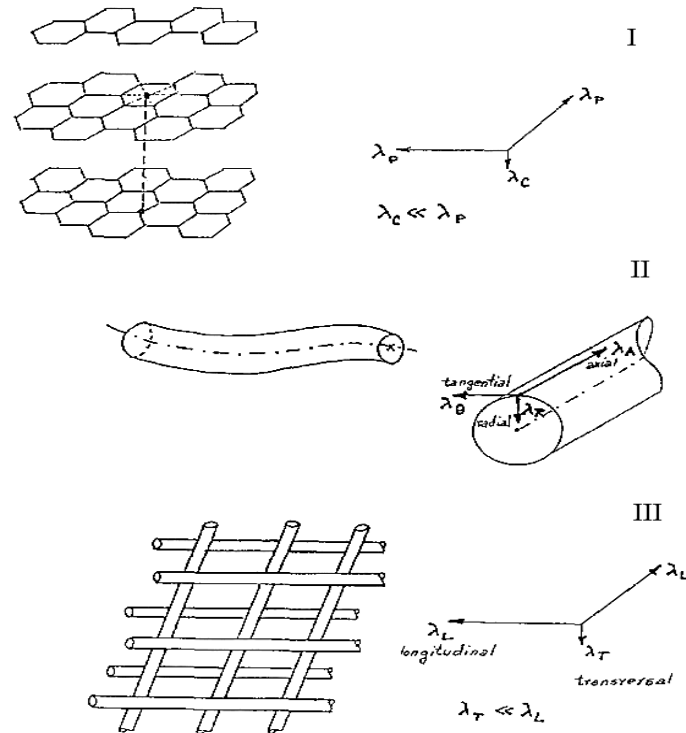


Figure I/3-4 Three levels of anisotropic thermal conductivity observed in carbon non-wovens (after Danes and Bardon 1997).

The CF application in hybrid PC composite should also be addressed by studying their heat transport direct and/or indirect influence on the energy storage performances and stability. Complete CF infiltration by molten PC can be achieved at higher heat transfer rates, advantageous for rapid and atmospheric pressure process, thereby making it time- and cost-effective. The observed insufficiency of PC thermal conductivity, as for the foreseen application, also can be overcome by their infiltration in CF materials, as previously presented by other studies for low-temperature PCM (Jiang et al. 2018). With the introduction of conductive carbon fibres in the hybrid materials, efficient and permanent heat transfer pathways can be established and an increase of PC thermal conductivity is expected. Effective and stable heat transfer also should support the peritectic phase formation and boost the slow peritectic transformation process, balancing the energy storage system for achieving the PC theoretical energy efficiency.

I/3.1.d CF chemical stability

Chemical reactivity may occur naturally between different materials, depending on their nature, and may lead to undesirable and even dramatic degradation of the system involving them. Because of obvious efficiency and economic consequences, mutual reactivity should be prevented or at least significantly reduced. Unlike highly investigated organic PCMs, inorganic PCMs are potentially corrosive compounds. Nowadays, the chemical compatibility of TES containers and heat exchangers with molten inorganic PCs is extensively studied and the results reported technical challenges for developing TES systems (Vasu et al. 2017). Different TES candidates such as fluorides, carbonates, sulphates, chlorides, hydroxides, and other inorganic salts, their eutectic or peritectic mixtures, defy the corrosion resistance of various containment materials. The TES operational performances and stability are tested upon long-term cycling of medium- to high-temperature systems (Liu et al. 2016). Thus, the chemical reactivity of some storage materials can make them become extremely corrosive under given circumstances, governed by, but not restricted to, increased operational temperature, impurity traces or moisture/oxygen presence, dynamic conditions, and chemical reactions with the containment/composite materials (Zhou and Wu 2018). Furthermore, the chemical stability of CF candidates for medium- to high-temperature CF-PC hybrid composites is completely omitted, thus solely corrosion studies with different metallic-based materials are provided (Vasu et al. 2017; Palomba and Frazzica 2018; Ruiz-Cabañas et al. 2018; Zhou and Wu 2018). As there is a high discovery interest of non-corrosive, economically viable and easily available metal-based material, similar research is hereunder reproduced for the foreseen CF-PC hybrid composite application.

The lack of research on carbon materials used for CF-PC hybrid composites requires in-depth studies of these materials for their chemical stability performances. As introduced, several of the former works about carbon fibres, regarding CF-PCM hybrid composites, solely inform about materials' excellent corrosion resistance and chemical attack stability but miss experimental evidences. Finding the selection criteria of chemically stable carbon fibrous materials is, therefore, another purpose of this thesis, as well as investigating the probable reasons for the occurrence of undesired destabilisation reactions between the composites' elements. Such chemically stable CF host materials also have to answer the two simultaneous challenges of establishing high composite stability and of performing thermal conductivity enhancement.

Carbon science usually takes advantage of the chemical reactivity of inorganic salts at high temperature, with the aim of achieving controlled reactions. A famous example of this is the production of activated carbons for various applications. In general, chemical activation is performed to develop and to open the porosity of carbon materials, with applications in liquid- and gas-phase treatments and in electrochemical storage and conversion. Usually, the chemical activation process involves the use of carbon or carbon precursors mixed with a chemical activating agent, followed by reaction at medium to high temperature (typically in the range 500 – 750 °C), either in air, in self-generated atmosphere or under inert gas. Finally, the excess chemical agent and inorganic reaction products are washed away from the resultant activated carbons. Many studies have been carried out to finely tune the preparation and characterisation processes of chemically activated carbons (Linares-Solano et al. 2007). In most studies, the emphasis is given on the parameters affecting the activation process, such as carbon precursors' nature, activation agent/carbon ratio, and reaction temperature and time. Linares-Solano et al. (2007) reported a number of inorganic salts used and compared as chemical activating agents for the preparation of activated carbons, like zinc chloride, alkaline carbonates and more notably alkaline hydroxides (mainly KOH and NaOH, but also LiOH).

The purpose of developing activated carbons with tailored micro- and mesoporosity has also motivated additional researches toward the use of advanced activating agents, such as eutectics and other mixtures of inorganic salts, as unique “salt-templating” method (Fechler, Fellingner, and Antonietti 2013). This method led to carbon materials with fine-tuned pore structure only as a result of the chemical activation with multiphase inorganic salts (Pampel, Denton, and Fellingner 2016). Eutectic salts, with one non-porogen inorganic salt, almost chemically nonreactive, and the other one acting as a carbon porogen (activating agent) have been generally used (Silvestre-Albero et al. 2015). The carbon porogen interacts with the carbon or precursor material through oxidation and dehydration reactions (Liu and Antonietti 2014).

From a practical point of view, several conclusions derived from the chemical activation studies of carbon materials can be useful to investigate the chemical stability of commercial CF with respect to inorganic PC molten salts. In-depth knowledge of the occurring chemical reactions throughout long-life usage of CF-PC hybrid composite requires adequate consideration of the most important influencing/initiating variables. Acknowledging the variables' significance will also allow us understanding the reasons why some CF candidates might be better PC hosts than others are. This study should minimise the possibility of carbon/PC chemical reactivity and boost the lifetime of the hybrid composite. The chemical

nature of the commercial CF candidates and the inorganic PC of interest are taken as the two crucial variables affecting the composite chemical stability. Other experimental parameters can also independently influence the overall study process, such as CF/PC ratio, heating rate, final temperature, time duration, and presence of gas flow.

Studies on chemical reactions between inorganic molten salts and CF should be considered as a mutual hub for carbon as an active material or host in a hybrid CF-PC composite. Yet the desired chemical reactivity in the former case should be strictly prohibited in the latter case and for their final applications, respectively. Nonetheless, influencing variables, experimental factors and reaction mechanisms should be taken as similar due to the resemblance of the investigation conditions.

I/4 Objectives of the thesis

The study of thermal energy storage systems is eagerly awaited (Liu, Saman, and Bruno 2012; Pandey et al. 2018), but the use of carbon non-wovens (carbon felts – CF) as energy storage materials' support is yet to be addressed.

The use of the CF hosts for improving thermal energy storage and delivery of CF-PC hybrid composite lacks knowledge about essential materials' properties of importance in such application. In order to choose the most suitable CF candidate and to show its perspective points, dedicated research work is needed to collect information about different CF parameters.

To our knowledge, there is no similar scientific work with a comparable number of analysed samples from different commercial carbonaceous non-wovens. There are characterisation works available in the literature, aimed at determining properties of specific non-wovens for different applications, but most of them involve the use of lab-made materials or only focus on specific carbon felt characteristics. Thus, in the present thesis, 18 commercial samples, received from 5 different suppliers, most of them having properties unknown to us, were considered as potential application candidates.

Improved stability and efficiency of the final composites are expected as results of the experimental and analytical studies of the CFs, including a detailed investigation of materials' effect on composite formation and performances. The identification of the crucial design parameters should provide a useful guide for further material improvement and use in this specific application.

Some of the main objectives addressed in this thesis are, therefore, to study several CF properties for understanding, and if possible, improving them for their final application, such as:

- characterisation of CF morphology and physical properties for the ease of their infiltration with molten PC and effect on the final CF-PC hybrid composite – Chapter II
- carbon structure and chemical stability of the CF host, properties of the materials influencing the interactions in contact with the molten PC or its constituent inorganic salts – Chapter III
- performing application tests and advanced morphological modifications of the CFs to improve their properties with respect to the original materials, all with the aim of obtaining the most efficient CF-PC final hybrid material – Chapter IV

I/5 Bibliography

- Achchaq, F., Risueño E., Mahroug I., Legros P., Karakashov B., Palomo del Barrio E., Celzard A., Fierro V., and Toutain J.. 2018. "Development of a Carbon Felt/Salt-Based Hybrid Material for Thermal Energy Storage Applications." <https://doi.org/10.17265/1934-8975/2018.07.004>.
- Achchaq F., and Palomo Del Barrio E.. 2017. "A Proposition of Peritectic Structures as Candidates for Thermal Energy Storage." *Energy Procedia, Materials & Energy I* (2015), 139 (December): 346–51. <https://doi.org/10.1016/j.egypro.2017.11.219>.
- Achchaq, F., Palomo del Barrio., Lebraud E., Péchev S., and Toutain J.. 2019. "Development of a New LiBr/LiOH-Based Alloy for Thermal Energy Storage." *Journal of Physics and Chemistry of Solids* 131 (August): 173–79. <https://doi.org/10.1016/j.jpics.2019.04.001>.
- Achchaq F., Palomo del Barrio E., Renaud A., and Ben-Khemis S.. 2015. "Characterization of Li₂K(OH)₃ as Material for Thermal Energy Storage at High Temperature."
- Adolphe, D. C., and P. I. Dolez. 2018. "2 - Advanced Strength Testing of Textiles." In *Advanced Characterization and Testing of Textiles*, 25–57. The Textile Institute Book Series. Woodhead Publishing. <https://doi.org/10.1016/B978-0-08-100453-1.00003-9>.
- Alva, Guruprasad, Yaxue Lin, and Guiyin Fang. 2018. "An Overview of Thermal Energy Storage Systems." *Energy* 144 (February): 341–78. <https://doi.org/10.1016/j.energy.2017.12.037>.
- Amaral, C., R. Vicente, P. A. A. P. Marques, and A. Barros-Timmons. 2017. "Phase Change Materials and Carbon Nanostructures for Thermal Energy Storage: A Literature Review." *Renewable and Sustainable Energy Reviews* 79 (November): 1212–28. <https://doi.org/10.1016/j.rser.2017.05.093>.
- Babapoor, A., M. Azizi, and G. Karimi. 2015. "Thermal Management of a Li-Ion Battery Using Carbon Fibre-PCM Composites." *Applied Thermal Engineering* 82 (May): 281–90. <https://doi.org/10.1016/j.applthermaleng.2015.02.068>.
- Barrio, Elena Palomo Del, Sabri Ben Khemis, David Mourand, Frederic Noel, Vanessa Ho-Kon-Tiat, Jean-Luc Dauverge, Yannick Anguy, Cristina Prieto Rios, and Aleix Jove Llovera. 2012. Composite material for storing heat energy at high temperatures. United States US20120138849A1, filed June 15, 2010, and issued June 7, 2012.
- Bear, J. 1972. "Flow of Immiscible Fluids." *Dynamics of Fluids in Porous Media. J. Bear (Ed.). Dover Publications, New York*, 441–446.
- Beil, Norman B., and William W. Roberts. 2002. "Modeling and Computer Simulation of the Compressional Behavior of Fibre Assemblies: Part I: Comparison to van Wyk's Theory." *Textile Research Journal* 72 (4): 341–51. <https://doi.org/10.1177/004051750207200411>.
- Boehm, H. P., R. Setton, and E. Stumpp. 2009. "Nomenclature and Terminology of Graphite Intercalation Compounds (IUPAC Recommendations 1994)." *Pure and Applied Chemistry* 66 (9): 1893–1901. <https://doi.org/10.1351/pac199466091893>.
- Boer, Reint de. 2000. *Theory of Porous Media*.
- Calderón, Alejandro, Camila Barreneche, Karla Hernández-Valle, Esther Galindo, Mercè Segarra, and A. Inés Fernández. 2019. "Where Is Thermal Energy Storage (TES) Research Going? – A Bibliometric Analysis." *Solar Energy*, January. <https://doi.org/10.1016/j.solener.2019.01.050>.
- Cárdenas, Bruno, and Noel León. 2013. "High Temperature Latent Heat Thermal Energy Storage: Phase Change Materials, Design Considerations and Performance Enhancement Techniques." *Renewable and Sustainable Energy Reviews* 27 (November): 724–37. <https://doi.org/10.1016/j.rser.2013.07.028>.

- Castañeda, Locksley F., Frank C. Walsh, José L. Nava, and Carlos Ponce de León. 2017. “Graphite Felt as a Versatile Electrode Material: Properties, Reaction Environment, Performance and Applications.” *Electrochimica Acta* 258 (December): 1115–39. <https://doi.org/10.1016/j.electacta.2017.11.165>.
- Chen, Zhangxin, and Richard E. Ewing. 2002. *Fluid Flow and Transport in Porous Media: Mathematical and Numerical Treatment*. Vol. 295. Contemporary Mathematics. American Mathematical Society. <http://dx.doi.org/10.1090/conm/295>.
- Cheng, Haiming, Changqing Hong, Xinghong Zhang, and Huafei Xue. 2015. “Lightweight Carbon-Bonded Carbon Fibre Composites with Quasi-Layered and Network Structure.” *Materials & Design* 86 (December): 156–59. <https://doi.org/10.1016/j.matdes.2015.07.091>.
- Chun, Jeong Hwan, Ki Tae Park, Dong Hyun Jo, Sang Gon Kim, and Sung Hyun Kim. 2011. “Numerical Modeling and Experimental Study of the Influence of GDL Properties on Performance in a PEMFC.” *International Journal of Hydrogen Energy* 36 (2): 1837–45. <https://doi.org/10.1016/j.ijhydene.2010.01.036>.
- Danes, Florin, and Jean-Pierre Bardon. 1997. “Conductivité Thermique Des Feutres de Carbone, Isolants À Forte Anisotropie: Modèle de Conduction Par La Phase Solide.” *Revue Générale de Thermique* 36 (4): 302–11. [https://doi.org/10.1016/S0035-3159\(97\)80690-3](https://doi.org/10.1016/S0035-3159(97)80690-3).
- Delhaès, P., Issi, J.P., Bonnamy, S., Launois, P., 2006. Polymorphism and Structure of Carbons, in: Loiseau, A., Launois, Pascale, Petit, P., Roche, S., Salvétat, J.-P. (Eds.), Understanding Carbon Nanotubes: From Basics to Applications, Lecture Notes in Physics. Springer Berlin Heidelberg, Berlin, Heidelberg, pp. 1–47. https://doi.org/10.1007/3-540-37586-4_1
- Das, Dipayan, and Behnam Pourdeyhimi. 2010. “Compressional and Recovery Behaviour of Highloft Nonwovens,” December. <http://nopr.niscair.res.in/handle/123456789/10745>.
- Das, Sujit, Josh Warren, Devin West, and Susan M. Schexnayder. 2016. “Global Carbon Fibre Composites Supply Chain Competitiveness Analysis.” ORNL/SR-2016/100 | NREL/TP-6A50-66071. Oak Ridge National Laboratory; The University of Tennessee, Knoxville. <https://doi.org/10.2172/1333049>.
- Davies, I. J., and R. D. Rawlings. 1994. “Mechanical Properties in Flexure and Tension of Low Density Carbon-Carbon Composites.” *Carbon* 32 (8): 1449–56. [https://doi.org/10.1016/0008-6223\(94\)90139-2](https://doi.org/10.1016/0008-6223(94)90139-2).
- Debnath, Sanjoy, and M Madhusoothanan. 2009. “Compression Properties of Polyester Needle-punched Fabric.” *Journal of Engineered Fibres and Fabrics* Volume 4, Issue 4.
- Debnath, Sanjoy, and M Madhusoothanan. 2009. 2012. “Studies on Compression Properties of Polyester Needle-Punched Nonwoven Fabrics under Dry and Wet Conditions.” *Journal of Industrial Textiles* 41 (4): 292–308. <https://doi.org/10.1177/1528083711416394>.
- Debnath, Sanjoy, and M. Madhusoothanan. 2013. “Studies on Compression Behaviour of Polypropylene Needle Punched Nonwoven Fabrics under Wet Condition.” *Fibres and Polymers* 14 (5): 854–59. <https://doi.org/10.1007/s12221-013-0854-4>.
- Dincer, Ibrahim, and Canan Acar. 2018. “Chapter 1.1 - Potential Energy Solutions for Better Sustainability.” In *Exergetic, Energetic and Environmental Dimensions*, edited by Ibrahim Dincer, C. Ozgur Colpan, and Onder Kizilkan, 3–37. Academic Press. <https://doi.org/10.1016/B978-0-12-813734-5.00001-9>.
- Dohle, H, R Jung, N Kimiaie, J Mergel, and M Müller. 2003. “Interaction between the Diffusion Layer and the Flow Field of Polymer Electrolyte Fuel Cells—experiments and Simulation Studies.” *Journal of Power Sources* 124 (2): 371–84. [https://doi.org/10.1016/S0378-7753\(03\)00800-0](https://doi.org/10.1016/S0378-7753(03)00800-0).

- Dullien, F. A. L. 1992. *Porous Media: Fluid Transport and Pore Structure*. 2nd ed. San Diego, CA: Academic Press.
- Dullien, F. A.L. 2012. *Porous Media*.
- Dunlop, J. I. 1983. "On the Compression Characteristics of Fibre Masses." *The Journal of The Textile Institute* 74 (2): 92–97. <https://doi.org/10.1080/00405008308631770>.
- Edwards, I. A. S. 1989. "Chapter 1 - Structure in Carbons and Carbon Forms." In *Introduction to Carbon Science*, edited by Harry Marsh, Ian A. S. Edwards, Rosa Menendez, Brian Rand, Sebastian West, Andrew J. Hosty, Khim Kuo, et al., 1–36. Butterworth-Heinemann. <https://doi.org/10.1016/B978-0-408-03837-9.50006-3>.
- El-kharouf, Ahmad, Thomas J. Mason, Dan J. L. Brett, and Bruno G. Pollet. 2012. "Ex-Situ Characterisation of Gas Diffusion Layers for Proton Exchange Membrane Fuel Cells." *Journal of Power Sources* 218 (November): 393–404. <https://doi.org/10.1016/j.jpowsour.2012.06.099>.
- Fadzillah, D. M., M. I. Rosli, M. Z. M. Talib, S. K. Kamarudin, and W. R. W. Daud. 2017. "Review on Microstructure Modelling of a Gas Diffusion Layer for Proton Exchange Membrane Fuel Cells." *Renewable and Sustainable Energy Reviews* 77 (September): 1001–9. <https://doi.org/10.1016/j.rser.2016.11.235>.
- Fechler, Nina, Tim-Patrick Fellingner, and Markus Antonietti. 2013. "'Salt Templating': A Simple and Sustainable Pathway toward Highly Porous Functional Carbons from Ionic Liquids." *Advanced Materials* 25 (1): 75–79. <https://doi.org/10.1002/adma.201203422>.
- Franklin, R. E. 1951. "The Structure of Graphitic Carbons." *Acta Crystallographica* 4 (3): 253–61. <https://doi.org/10.1107/S0365110X51000842>.
- Frusteri, F., V. Leonardi, and G. Maggio. 2006. "Numerical Approach to Describe the Phase Change of an Inorganic PCM Containing Carbon Fibres." *Applied Thermal Engineering* 26 (16): 1883–92. <https://doi.org/10.1016/j.applthermaleng.2006.01.018>.
- Frusteri, F., V. Leonardi, S. Vasta, and G. Restuccia. 2005a. "Thermal Conductivity Measurement of a PCM Based Storage System Containing Carbon Fibres." *Applied Thermal Engineering* 25 (11): 1623–33. <https://doi.org/10.1016/j.applthermaleng.2004.10.007>.
- Frusteri, F., V. Leonardi, S. Vasta, and G. Restuccia. 2005b. "Thermal Conductivity Measurement of a PCM Based Storage System Containing Carbon Fibres." *Applied Thermal Engineering* 25 (11): 1623–33. <https://doi.org/10.1016/j.applthermaleng.2004.10.007>.
- Fukai, Jun, Yuichi Hamada, Yoshio Morozumi, and Osamu Miyatake. 2002. "Effect of Carbon-Fibre Brushes on Conductive Heat Transfer in Phase Change Materials." *International Journal of Heat and Mass Transfer* 45 (24): 4781–92. [https://doi.org/10.1016/S0017-9310\(02\)00179-5](https://doi.org/10.1016/S0017-9310(02)00179-5).
- Fukai, Jun, Yuichi Hamada, Yoshio Morozumi, and Osamu Miyatake. 2003. "Improvement of Thermal Characteristics of Latent Heat Thermal Energy Storage Units Using Carbon-Fibre Brushes: Experiments and Modeling." *International Journal of Heat and Mass Transfer* 46 (23): 4513–25. [https://doi.org/10.1016/S0017-9310\(03\)00290-4](https://doi.org/10.1016/S0017-9310(03)00290-4).
- Fukai, Jun, Makoto Kanou, Yoshikazu Kodama, and Osamu Miyatake. 2000. "Thermal Conductivity Enhancement of Energy Storage Media Using Carbon Fibres." *Energy Conversion and Management* 41 (14): 1543–56. [https://doi.org/10.1016/S0196-8904\(99\)00166-1](https://doi.org/10.1016/S0196-8904(99)00166-1).
- Gheribi, Aïmen E., Jesus A. Torres, and Patrice Chartrand. 2014. "Recommended Values for the Thermal Conductivity of Molten Salts between the Melting and Boiling Points." *Solar Energy Materials and Solar Cells* 126 (July): 11–25. <https://doi.org/10.1016/j.solmat.2014.03.028>.

- Gielen, Dolf, Francisco Boshell, Deger Saygin, Morgan D. Bazilian, Nicholas Wagner, and Ricardo Gorini. 2019. "The Role of Renewable Energy in the Global Energy Transformation." *Energy Strategy Reviews* 24 (April): 38–50. <https://doi.org/10.1016/j.esr.2019.01.006>.
- Gil, Antoni, Marc Medrano, Ingrid Martorell, Ana Lázaro, Pablo Dolado, Belén Zalba, and Luisa F. Cabeza. 2010. "State of the Art on High Temperature Thermal Energy Storage for Power Generation. Part 1—Concepts, Materials and Modellization." *Renewable and Sustainable Energy Reviews* 14 (1): 31–55. <https://doi.org/10.1016/j.rser.2009.07.035>.
- "Global Market Outlook for Solar Power 2018-2022." 2018. <http://www.solarpowereurope.org/global-market-outlook-2018-2022/>.
- Gostick, Jeff T., Michael W. Fowler, Mark D. Pritzker, Marios A. Ioannidis, and Leya M. Behra. 2006. "In-Plane and through-Plane Gas Permeability of Carbon Fibre Electrode Backing Layers." *Journal of Power Sources* 162 (1): 228–38. <https://doi.org/10.1016/j.jpowsour.2006.06.096>.
- Hamada, Yuichi, Wataru Otsu, Jun Fukai, Yoshio Morozumi, and Osamu Miyatake. 2005. "Anisotropic Heat Transfer in Composites Based on High-Thermal Conductive Carbon Fibres." *Energy, 3rd International Symposium on Advanced Energy Conversion Systems and Related Technologies*, 30 (2): 221–33. <https://doi.org/10.1016/j.energy.2004.04.024>.
- Horrocks, A. Richard, and Subhash C. Anand. 2015. *Handbook of Technical Textiles: Technical Textile Processes*. Woodhead Publishing.
- Huang, Xiang, Guruprasad Alva, Lingkun Liu, and Guiyin Fang. 2017. "Microstructure and Thermal Properties of Cetyl Alcohol/High Density Polyethylene Composite Phase Change Materials with Carbon Fibre as Shape-Stabilized Thermal Storage Materials." *Applied Energy* 200 (August): 19–27. <https://doi.org/10.1016/j.apenergy.2017.05.074>.
- Huang, Xiaosong. 2009. "Fabrication and Properties of Carbon Fibres." *Materials* 2 (4): 2369–2403. <https://doi.org/10.3390/ma2042369>.
- Hung, Chih Jung, Ching Han Liu, Tse Hao Ko, Wei Hung Chen, Shu Hui Cheng, Wan Shu Chen, Alan Yu, and A. M. Kannan. 2013. "Effect of Diffusion Layers Fabricated with Different Fibre Diameters on the Performance of Low Temperature Proton Exchange Membrane Fuel Cells." *Journal of Power Sources* 221 (January): 134–40. <https://doi.org/10.1016/j.jpowsour.2012.08.030>.
- Huong Le, Thi Xuan, Mikhael Bechelany, and Marc Cretin. 2017. "Carbon Felt Based-Electrodes for Energy and Environmental Applications: A Review." *Carbon* 122 (October): 564–91. <https://doi.org/10.1016/j.carbon.2017.06.078>.
- Ibrahim, Nasiru I., Fahad A. Al-Sulaiman, Saidur Rahman, Bekir S. Yilbas, and Ahmet Z. Sahin. 2017. "Heat Transfer Enhancement of Phase Change Materials for Thermal Energy Storage Applications: A Critical Review." *Renewable and Sustainable Energy Reviews* 74 (July): 26–50. <https://doi.org/10.1016/j.rser.2017.01.169>.
- Ihonen, Jari, Mikko Mikkola, and Göran Lindbergh. 2004. "Flooding of Gas Diffusion Backing in PEFCs Physical and Electrochemical Characterization." *Journal of The Electrochemical Society* 151 (8): A1152–61. <https://doi.org/10.1149/1.1763138>.
- Inagaki, Michio, and Feiyu Kang. 2014. *Materials Science and Engineering of Carbon: Fundamentals - 2nd Edition*.
- Inagaki, Michio, Feiyu Kang, Masahiro Toyoda, and Hidetaka Konno. 2014. *Advanced Materials Science and Engineering of Carbon - 1st Edition*. <https://doi.org/10.1016/B978-0-12-407789-8.00001-6>.
- Jiang, Zhao, Ting Ouyang, Yang Yang, Lei Chen, Xiaohua Fan, Yunbo Chen, Weiwei Li, and Youqing Fei. 2018. "Thermal Conductivity Enhancement of Phase Change Materials

- with Form-Stable Carbon Bonded Carbon Fibre Network.” *Materials & Design* 143 (April): 177–84. <https://doi.org/10.1016/j.matdes.2018.01.052>.
- Jirsak, Oldrich, Tomas Burian, and Pavlina Sasková. 2003. “Improvements in Compressional Properties of Highlofts.” 2003.
- Karaipekli, Ali, Ahmet Sarı, and Kamil Kaygusuz. 2007a. “Thermal Conductivity Improvement of Stearic Acid Using Expanded Graphite and Carbon Fibre for Energy Storage Applications.” *Renewable Energy* 32 (13): 2201–10. <https://doi.org/10.1016/j.renene.2006.11.011>.
- Keck, Felix, Manfred Lenzen, Anthony Vassallo, and Mengyu Li. 2019. “The Impact of Battery Energy Storage for Renewable Energy Power Grids in Australia.” *Energy*, February. <https://doi.org/10.1016/j.energy.2019.02.053>.
- Kellie, George. 2016. *Advances in Technical Nonwovens – PaperC*.
- Kelly, B. T. 1981. “Physics of Graphite.”
- Kelly, P. A., R. Umer, and S. Bickerton. 2006. “Viscoelastic Response of Dry and Wet Fibrous Materials during Infusion Processes.” *Composites Part A: Applied Science and Manufacturing*, Selected Contributions from the 7th International Conference on Flow Processes in Composite Materials held at University of Delaware, USA, 37 (6): 868–73. <https://doi.org/10.1016/j.compositesa.2005.02.008>.
- Kenisarin, Murat M. 2010. “High-Temperature Phase Change Materials for Thermal Energy Storage.” *Renewable and Sustainable Energy Reviews* 14 (3): 955–70. <https://doi.org/10.1016/j.rser.2009.11.011>.
- Kuravi, Sarada, Jamie Trahan, D. Yogi Goswami, Muhammad M. Rahman, and Elias K. Stefanakos. 2013. “Thermal Energy Storage Technologies and Systems for Concentrating Solar Power Plants.” *Progress in Energy and Combustion Science* 39 (4): 285–319. <https://doi.org/10.1016/j.pecs.2013.02.001>.
- Lee, J., L. Yun, and J. Park. 2005. “Anisotropic Properties of Needle Punched Carbon/Carbon Composites.”
- Lee, S. 2002. “Effect of Punching Density on the Mechanical and Thermal Properties of Needle-Punched Nonwoven Carbon/Phenolic Composites.” 2002.
- Lin, Yaxue, Yuting Jia, Guruprasad Alva, and Guiyin Fang. 2018. “Review on Thermal Conductivity Enhancement, Thermal Properties and Applications of Phase Change Materials in Thermal Energy Storage.” *Renewable and Sustainable Energy Reviews* 82 (February): 2730–42. <https://doi.org/10.1016/j.rser.2017.10.002>.
- Linares-Solano, A., D. Lozano-Castello, M. Lillo-Rodenas, and D. Cazorla-Amoros. 2007. “Carbon Activation by Alkaline Hydroxides.” In *Chemistry & Physics of Carbon. Series: Chemistry and Physics of Carbon, ISBN: 978-1-4200-4298-6. CRC Press, Edited by Ljubisa Radovic, Pp. 1-62, 1–62*. <https://doi.org/10.1201/9781420042993.ch1>.
- Liu, Ming, Wasim Saman, and Frank Bruno. 2012. “Review on Storage Materials and Thermal Performance Enhancement Techniques for High Temperature Phase Change Thermal Storage Systems.” *Renewable and Sustainable Energy Reviews* 16 (4): 2118–32. <https://doi.org/10.1016/j.rser.2012.01.020>.
- Liu, Ming, N. H. Steven Tay, Stuart Bell, Martin Belusko, Rhys Jacob, Geoffrey Will, Wasim Saman, and Frank Bruno. 2016. “Review on Concentrating Solar Power Plants and New Developments in High Temperature Thermal Energy Storage Technologies.” *Renewable and Sustainable Energy Reviews* 53 (January): 1411–32. <https://doi.org/10.1016/j.rser.2015.09.026>.
- Liu, Xiaofeng, and Markus Antonietti. 2014. “Molten Salt Activation for Synthesis of Porous Carbon Nanostructures and Carbon Sheets.” *Carbon* 69 (April): 460–66. <https://doi.org/10.1016/j.carbon.2013.12.049>.

- Mangal, Prafful, Lalit M. Pant, Nicholas Carrigy, Mark Dumontier, Valentin Zingan, Sushanta Mitra, and Marc Secanell. 2015. "Experimental Study of Mass Transport in PEMFCs: Through Plane Permeability and Molecular Diffusivity in GDLs." *Electrochimica Acta* 167 (June): 160–71. <https://doi.org/10.1016/j.electacta.2015.03.100>.
- McCarthy, Brian J. 2013. *Polymeric Protective Technical Textiles*.
- Minke, Christine, Ulrich Kunz, and Thomas Turek. 2017. "Carbon Felt and Carbon Fibre - A Techno-Economic Assessment of Felt Electrodes for Redox Flow Battery Applications." *Journal of Power Sources* 342 (February): 116–24. <https://doi.org/10.1016/j.jpowsour.2016.12.039>.
- Mohamed, Shamseldin A., Fahad A. Al-Sulaiman, Nasiru I. Ibrahim, Md. Hasan Zahir, Amir Al-Ahmed, R. Saidur, B. S. Yılbaş, and A. Z. Sahin. 2017. "A Review on Current Status and Challenges of Inorganic Phase Change Materials for Thermal Energy Storage Systems." *Renewable and Sustainable Energy Reviews* 70 (April): 1072–89. <https://doi.org/10.1016/j.rser.2016.12.012>.
- Nakaso, Koichi, Hirofumi Teshima, Akito Yoshimura, Seiichi Nogami, Yuichi Hamada, and Jun Fukai. 2008. "Extension of Heat Transfer Area Using Carbon Fibre Cloths in Latent Heat Thermal Energy Storage Tanks." *Chemical Engineering and Processing: Process Intensification* 47 (5): 879–85. <https://doi.org/10.1016/j.cep.2007.02.001>.
- Nejat, Payam, Fatemeh Jomehzadeh, Mohammad Mahdi Taheri, Mohammad Gohari, and Muhd Zaimi Abd. Majid. 2015. "A Global Review of Energy Consumption, CO₂ Emissions and Policy in the Residential Sector (with an Overview of the Top Ten CO₂ Emitting Countries)." *Renewable and Sustainable Energy Reviews* 43 (March): 843–62. <https://doi.org/10.1016/j.rser.2014.11.066>.
- Newcomb, Bradley A. 2016. "Processing, Structure, and Properties of Carbon Fibres." *Composites Part A: Applied Science and Manufacturing* 91 (December): 262–82. <https://doi.org/10.1016/j.compositesa.2016.10.018>.
- Nomura, Takahiro, Kazuki Tabuchi, Chunyu Zhu, Nan Sheng, Shuangfeng Wang, and Tomohiro Akiyama. 2015. "High Thermal Conductivity Phase Change Composite with Percolating Carbon Fibre Network." *Applied Energy* 154 (September): 678–85. <https://doi.org/10.1016/j.apenergy.2015.05.042>.
- Nomura, Takahiro, Chunyu Zhu, Sheng Nan, Kazuki Tabuchi, Shuangfeng Wang, and Tomohiro Akiyama. 2016. "High Thermal Conductivity Phase Change Composite with a Metal-Stabilized Carbon-Fibre Network." *Applied Energy* 179 (October): 1–6. <https://doi.org/10.1016/j.apenergy.2016.04.070>.
- Palomba, Valeria, and Andrea Frazzica. 2018. "Recent Advancements in Sorption Technology for Solar Thermal Energy Storage Applications." *Solar Energy*, June. <https://doi.org/10.1016/j.solener.2018.06.102>.
- Pampel, Jonas, Caleb Denton, and Tim-Patrick Fellingner. 2016. "Glucose Derived Ionothermal Carbons with Tailor-Made Porosity." *Carbon* 107 (October): 288–96. <https://doi.org/10.1016/j.carbon.2016.06.009>.
- Pandey, A. K., M. S. Hossain, V. V. Tyagi, Nasrudin Abd Rahim, Jeyraj A. /L. Selvaraj, and Ahmet Sari. 2018. "Novel Approaches and Recent Developments on Potential Applications of Phase Change Materials in Solar Energy." *Renewable and Sustainable Energy Reviews* 82 (February): 281–323. <https://doi.org/10.1016/j.rser.2017.09.043>.
- Panerai, Francesco, Joseph C. Ferguson, Jean Lachaud, Alexandre Martin, Matthew J. Gasch, and Nagi N. Mansour. 2017. "Micro-Tomography Based Analysis of Thermal Conductivity, Diffusivity and Oxidation Behavior of Rigid and Flexible Fibrous Insulators." *International Journal of Heat and Mass Transfer* 108 (May): 801–11. <https://doi.org/10.1016/j.ijheatmasstransfer.2016.12.048>.

- Parikh, D.V., T.A. Calamari, W.R. Goynes, Y. Chen, and O. Jirsak. 2004. "Compressibility of Cotton Blend Perpendicular-Laid Nonwovens." *Textile Research Journal* 74 (1): 7–12. <https://doi.org/10.1177/004051750407400102>.
- Pelay, Ugo, Lingai Luo, Yilin Fan, Driss Stitou, and Mark Rood. 2017. "Thermal Energy Storage Systems for Concentrated Solar Power Plants." *Renewable and Sustainable Energy Reviews* 79 (November): 82–100. <https://doi.org/10.1016/j.rser.2017.03.139>.
- Pierson, Hugh O., ed. 1993. "Handbook of Carbon, Graphite, Diamonds and Fullerenes." In *Handbook of Carbon, Graphite, Diamonds and Fullerenes*, v–vi. Oxford: William Andrew Publishing. <https://doi.org/10.1016/B978-0-8155-1339-1.50003-7>.
- Prabha Karan, C. 2016. *Nonwovens: Process, Structure, Properties and Applications*. Woodhead Publishing India PVT. Limited.
- Prasanna, M., H. Y. Ha, E. A. Cho, S. -A. Hong, and I. -H. Oh. 2004. "Influence of Cathode Gas Diffusion Media on the Performance of the PEMFCs." *Journal of Power Sources*, Selected papers presented at the Eighth Grove Fuel Cell Symposium, 131 (1): 147–54. <https://doi.org/10.1016/j.jpowsour.2004.01.030>.
- Rahaman, M. S. A., A. F. Ismail, and A. Mustafa. 2007. "A Review of Heat Treatment on Polyacrylonitrile Fibre." *Polymer Degradation and Stability* 92 (8): 1421–32. <https://doi.org/10.1016/j.polymdegradstab.2007.03.023>.
- Ruiz-Cabañas, F. Javier, Cristina Prieto, Aleix Jové, Virginia Madina, A. Inés Fernández, and Luisa F. Cabeza. 2018. "Steam-PCM Heat Exchanger Design and Materials Optimization by Using Cr-Mo Alloys." *Solar Energy Materials and Solar Cells* 178 (May): 249–58. <https://doi.org/10.1016/j.solmat.2018.01.038>.
- Russell, Nigel V, Jon R Gibbins, and Jim Williamson. 1999. "Structural Ordering in High Temperature Coal Chars and the Effect on Reactivity." *Fuel* 78 (7): 803–7. [https://doi.org/10.1016/S0016-2361\(98\)00210-5](https://doi.org/10.1016/S0016-2361(98)00210-5).
- Russell, S. 2006. *Handbook of Nonwovens - 1st Edition*.
- Sahimi, Muhammad. 2011. *Flow and Transport in Porous Media and Fractured Rock: From Classical Methods to Modern Approaches*. Hoboken, NJ: John Wiley & Sons.
- Samimi, Fereshteh, Aziz Babapoor, Mohammadmehdi Azizi, and Gholamreza Karimi. 2016. "Thermal Management Analysis of a Li-Ion Battery Cell Using Phase Change Material Loaded with Carbon Fibres." *Energy* 96 (February): 355–71. <https://doi.org/10.1016/j.energy.2015.12.064>.
- Santana, Carlos Alberto Polanco. 2017. "Renewable Power Generation Costs in 2017." https://www.academia.edu/36350084/Renewable_Power_Generation_Costs_in_2017.
- Scheidegger, A. E. 1958. "The Physics of Flow Through Porous Media." *Soil Science* 86 (6): 355.
- Schoppee, Meredith M. 1998. "A Poisson Model of Nonwoven Fibre Assemblies in Compression at High Stress." *Textile Research Journal* 68 (5): 371–84. <https://doi.org/10.1177/004051759806800507>.
- Shahani, Fereshteh, Soltani, Parham, Zarrebini, and Mohammad. 2014. "The Analysis of Acoustic Characteristics and Sound Absorption Coefficient of Needle Punched Nonwoven Fabrics." 2014.
- Shi, Wei, Jia Yan Li, Qi Fan You, Tong Lu, and Yi Tan. 2015. "Preparation and Properties of Rigid Carbon Felt Thermal Insulation." *Materials Science Forum* 833: 48–51. <https://doi.org/10.4028/www.scientific.net/MSF.833.48>.
- Silvestre-Albero, A., J. Silvestre-Albero, M. Martinez-Escandell, M. Molina-Sabio, A. Kovacs, and F. Rodriguez-Reinoso. 2015. "Novel Synthesis of a Micro-Mesoporous Nitrogen-Doped Nanostructured Carbon from Polyaniline." *Microporous and Mesoporous Materials* 218 (December): 199–205. <https://doi.org/10.1016/j.micromeso.2015.07.023>.

- Sioshansi, R., and P. Denholm. 2010. "The Value of Concentrating Solar Power and Thermal Energy Storage." *IEEE Transactions on Sustainable Energy* 1 (3): 173–83. <https://doi.org/10.1109/TSTE.2010.2052078>.
- Soltani, Parham, Mohammad Zarrebini, Reyhaneh Laghaei, and Ali Hassanpour. 2017. "Prediction of Permeability of Realistic and Virtual Layered Nonwovens Using Combined Application of X-Ray μ CT and Computer Simulation." *Chemical Engineering Research and Design* 124 (Supplement C): 299–312. <https://doi.org/10.1016/j.cherd.2017.06.035>.
- Szymkiewicz, Adam. 2013. "Mathematical Models of Flow in Porous Media." In *Modelling Water Flow in Unsaturated Porous Media*, 9–47. GeoPlanet: Earth and Planetary Sciences. Springer, Berlin, Heidelberg. https://doi.org/10.1007/978-3-642-23559-7_2.
- Tian, Benqiang, Wenbin Yang, Lijuan Luo, Jing Wang, Kai Zhang, Jinghui Fan, Juying Wu, and Tao Xing. 2016. "Synergistic Enhancement of Thermal Conductivity for Expanded Graphite and Carbon Fibre in Paraffin/EVA Form-Stable Phase Change Materials." *Solar Energy* 127 (April): 48–55. <https://doi.org/10.1016/j.solener.2016.01.011>.
- Vasu, Anusuah, Ftwi Y. Hagos, M. M. Noor, R. Mamat, W. H. Azmi, Abdul A. Abdullah, and Thamir K. Ibrahim. 2017. "Corrosion Effect of Phase Change Materials in Solar Thermal Energy Storage Application." *Renewable and Sustainable Energy Reviews* 76 (September): 19–33. <https://doi.org/10.1016/j.rser.2017.03.018>.
- Ventura, Heura, Mònica Ardanuy, Xavier Capdevila, Francesc Cano, and José Antonio Tornero. 2014. "Effects of Needling Parameters on Some Structural and Physico-Mechanical Properties of Needle-Punched Nonwovens." *The Journal of The Textile Institute* 105 (10): 1065–75. <https://doi.org/10.1080/00405000.2013.874628>.
- Wang, Jifen, Huaqing Xie, Zhong Xin, Yang Li, and Chou Yin. 2011. "Investigation on Thermal Properties of Heat Storage Composites Containing Carbon Fibres." *Journal of Applied Physics* 110 (9): 094302. <https://doi.org/10.1063/1.3656991>.
- Wang, X. Y., and R. H. Gong. 2006. "Thermally Bonded Nonwoven Filters Composed of Bicomponent Polypropylene/Polyester Fibre. I. Statistical Approach for Minimizing the Pore Size." *Journal of Applied Polymer Science* 101 (4): 2689–99. <https://doi.org/10.1002/app.23915>.
- Wei, Gaosheng, Gang Wang, Chao Xu, Xing Ju, Lijing Xing, Xiaoze Du, and Yongping Yang. 2018. "Selection Principles and Thermophysical Properties of High Temperature Phase Change Materials for Thermal Energy Storage: A Review." *Renewable and Sustainable Energy Reviews* 81 (January): 1771–86. <https://doi.org/10.1016/j.rser.2017.05.271>.
- Williams, Minkmas V., Eric Begg, Leonard Bonville, H. Russell Kunz, and James M. Fenton. 2004. "Characterization of Gas Diffusion Layers for PEMFC." *Journal of The Electrochemical Society* 151 (8): A1173–80. <https://doi.org/10.1149/1.1764779>.
- Xu, Ben, Peiwen Li, and Cholik Chan. 2015. "Application of Phase Change Materials for Thermal Energy Storage in Concentrated Solar Thermal Power Plants: A Review to Recent Developments." *Applied Energy* 160 (December): 286–307. <https://doi.org/10.1016/j.apenergy.2015.09.016>.
- Zhang, P., X. Xiao, and Z. W. Ma. 2016. "A Review of the Composite Phase Change Materials: Fabrication, Characterization, Mathematical Modeling and Application to Performance Enhancement." *Applied Energy* 165 (March): 472–510. <https://doi.org/10.1016/j.apenergy.2015.12.043>.
- Zhang, Qiang, Zhiling Luo, Qilin Guo, and Gaohui Wu. 2017. "Preparation and Thermal Properties of Short Carbon Fibres/Erythritol Phase Change Materials." *Energy Conversion and Management* 136 (March): 220–28. <https://doi.org/10.1016/j.enconman.2017.01.023>.

- Zhang, Yao, Zixing Lu, Zhenyu Yang, Dahai Zhang, Jianjun Shi, Zeshuai Yuan, and Qiang Liu. 2017. "Compression Behaviors of Carbon-Bonded Carbon Fibre Composites: Experimental and Numerical Investigations." *Carbon* 116 (May): 398–408. <https://doi.org/10.1016/j.carbon.2017.02.012>.
- Zhou, Cheng, and Sike Wu. 2018. "Medium- and High-Temperature Latent Heat Thermal Energy Storage: Material Database, System Review, and Corrosivity Assessment." *International Journal of Energy Research* 0 (0). <https://doi.org/10.1002/er.4216>.

CHAPTER II:
CHARACTERISATION OF
CARBON FELTS'
MORPHOLOGY AND PHYSICAL
PROPERTIES

II/1 Introduction

The high competitiveness of CF materials in many industrial applications is due to their unique characteristics, a combination of structural and physical properties, especially lightness, and the manufacturing process at high productivity and low cost. Therefore, it is very appropriate that these materials and their associated properties become involved in applications such as enhancement supports for TES. The disadvantages of the PC storage materials, such as phase separation and precipitation (discussed in subchapter I/1.3), which can significantly reduce their efficiency, are among the reasons why they should be infiltrated into a host structure.

The main aspect that must be taken into account when choosing a suitable host structure is the required level of material properties, which will influence and improve the storage performances of the chosen PC. Therefore, the initial challenges in this chapter are the study of materials with a defined porous structure, felt/fibre texture, and surface chemistry. The carbon hosts should be easily and fully impregnated with PC, i.e., should present open porous structures with the highest possible porosity to maximise the energy density of the final material. At the same time, the structure should be highly tortuous and suitable for PC hosting and to withstand the infiltration process without being modified. And lately, the carbon host should also improve/stabilise the systems' thermal characteristics, and present long-life performance under varying temperatures (300-400°C).

The main descriptions of porous carbon materials, provided in Subchapter I/2, deliver the basis for further explanations of their properties. Theoretically, changing any of the raw material and the manufacturing steps should give subtle differences in the final commercial materials. Considering that the CF suppliers specified only a narrow range of bulk physical properties, such as weight per unit area, averaged thermal conductivity, felt thickness, and carbon content (seen in Annex Table II/6-1), any straightforward choice of the most suitable CF material for their envisaged use was impossible. The need to deeply understanding the relationships between the manufacturing process and final CF properties and filling the gap of missing data for the material properties, therefore, gave us a reason to fully characterise and explore the properties of this kind of materials.

To the best of our knowledge, no other studies have been applied to this kind of in-depth analysis by examining various commercial CFs as carbon hosts for TES systems. The present chapter focuses on the experimental characterisation of the CF structure and considers the

influence of fabric/fibre structure on their density, porosity, overall morphology, wettability and physical properties (permeability, compressibility, and thermal conductivity properties). A model approach is also investigated to predict some of the material properties not directly deduced from the experimental results. From the following studies, we highlight important CF properties that can influence the preparation and the final use of the CF-PC hybrid composites, considered a key factor in successful composite development and upscaling.

The work carried out hereafter is organised as follows. First, the used CF materials and the performed de-sizing treatment are described and the experimental part presents a detailed description of the different techniques employed. Then, the results of applied experimental and analytical studies are presented and discussed, and the final conclusions are derived.

II/2 Experimental

II/2.1 De-sizing of as-received commercial CF

Different surface treatments of carbon fibres, called sizing, are frequently carried out after the CFs come out of the carbonisation process. Most commercial methods include a coating of the carbon fibres with organic materials (Zhang 2012). The surface treatments do not change the chemical structure of the fibre surface itself, but only introduces additional species at the fibre surface (Zhang 2014). The process usually consists of forming an extremely thin polymer layer, either applied from a solution or an emulsion of polymers and/or additives (Dai et al. 2011). The fibre type and the final application derived from the manufacturer govern the selection of sizing materials.

Since one of the targets of the project is to infiltrate porous host materials by hot and sometimes corrosive liquids, carbon was selected for its chemical stability. But such valuable property was threatened by possible unknown additives at the carbon fibre surface.

To increase and ensure the purity of the present carbon materials, an additional heat-treatment was performed prior to further investigation, as previously presented by Naito et al. (2010). The samples were subjected to slow pyrolysis in a tubular horizontal furnace (Carbolite), with a heating rate of $3^{\circ}\text{C min}^{-1}$ and under a continuous flow of pure nitrogen. After reaching 900°C , the dwell time was fixed at 2h before slow cooling in nitrogen atmosphere down to room temperature. The setpoint of 900°C was chosen since the CF were already industrially heat-treated at higher temperatures ($1000\text{-}2400^{\circ}\text{C}$, see Table II/6-1), and was considered high enough for carbonising any kind of polymer coating.

II/2.2 Sorting of commercial CF materials

18 commercial samples were received from 5 different suppliers, further sorted into various groups and sub-groups for easier presenting and discussing the characterisation data, see Table II/2-1. The samples were labelled as either soft felt, rigidized soft felt or rigid board (SF, rSF, and RB, respectively), followed by a letter related to the final heat-treatment temperature (C for carbonisation or G for graphitisation), plus a number referring to the precursor (1 for Rayon or 2 for PAN) and a small letter corresponding to the fibre diameter (a for thin fibres or b for thick fibres). The last, one or two, capital letters consider the samples' supplier origin. For instance, SFC1aC refers to a soft felt, carbonised at 1200°C, originating from a Rayon preform made of thin fibres (diameter 9-12 µm), kindly provided from one of the commercial suppliers (assigned as "C" for "CeraMaterials"). Table II/2-1 gives also reference to the commercial supplier codes of the investigated materials.

Table II/2-1 Sorting of 18 commercial CFs investigated here into groups and sub-groups, depending on their characteristics.

Final production heat mode:	Precursor	Fibre diameter	Commercial name:	Used sample code:
Needle-punched non-woven Soft CFs				
Carbonised	Rayon	9-12 µm	Carbon (Rayon) felt CeraMaterials	SFC1aC
Graphitised			Graphite (Rayon) felt CeraMaterials	SFG1aC
Carbonised			RSF1 Beijing Great Wall Co.	SFC1aBG
Graphitised			RSF2 Beijing Great Wall Co.	SFG1aBG
Carbonised			SIGRATHERM® KFA5	SFC1aSI
Graphitised			SIGRATHERM® GFA10	SFG1aSI
Graphitised			GF2 Schunk	SFG1aSC
Carbonised	PAN	9-10 µm	PX 35 ZOLTEK™	SFC2aZF
Graphitised			GFE-1 CeraMaterials	SFG2aC
Carbonised			BESF Beijing Great Wall Co.	SFC2aBG
Carbonised		17-20 µm	Carbon (PAN) felt CeraMaterials	SFC2bC
Graphitised			Graphite (PAN) felt CeraMaterials	SFG2bC
Carbonised			PSF1 Beijing Great Wall Co.	SFC2bBG
Graphitised			PSF2 Beijing Great Wall Co.	SFG2bBG
Chemically rigidized needle-punched non-woven Soft CFs				
Graphitised	PAN	17-20 µm	PRF3 Beijing Great Wall Co.	rSFG2bBG
Carbonised			Carbon Board CeraMaterials	rSFC2bC
Chemically bonded Rigid Board CFs				
Carbonised	Rayon	9-12 µm	SIGRATHERM® MFA	RBG1aSI
Graphitised			Graphite Board CeraMaterials	RBG1aC

II/2.3 Porosity and density

The porosity ε (dimensionless) of all CF samples was calculated from equation (II/1), where ρ_b (g cm^{-3}) and ρ_s (g cm^{-3}) are bulk and skeletal densities, respectively:

$$\varepsilon = 1 - \frac{\rho_b}{\rho_s} \quad (\text{II/1})$$

ρ_s was measured by helium pycnometry with an AccuPyc II 1340 (Micromeritics, USA) automatic apparatus (seen in Fig. II/2-1). In the case of all CFs, the helium pycnometry measurements were carried out done solely after grinding the materials, thus directly leading to the skeletal density of the carbon. The powdered samples were dried overnight at 105°C to avoid the presence and influence of humidity on the achieved results. A standard 1 cm^3 chamber was utilised and flushed 10 times with helium to reassure the gas purity in the chamber, followed by 30 analytical runs.



Figure II/2-1 Helium pycnometer AccuPyc II 1340 (Micromeritics, USA) automatic apparatus.

ρ_b was determined by weighing 10 cylindrical samples and measuring their dimensions (thickness and diameter of CF or boards), then averaging the obtained results. The mass of the samples was measured with an analytical balance with an accuracy of 0.001 g, and the diameter (predefined by the use of cutting tools with defined diameter) was confirmed with an electronic calliper with an accuracy of 0.01 mm. The thickness measurement of rigid board CF was also measured by using the same calliper.

The thickness measurement of the soft CF is more problematic since soft CF are highly compressible, and using a calliper can lead to erroneous results (Kok and Gostick 2015). The

thickness of non-woven materials, defined as the distance between the upper and lower surfaces of the material measured under a specified pressure (Mao 2016), is normally measured as the gap between a flat solid surface and a presser foot or other measuring instrument used to apply a known, moderate pressure.

Herein, the thickness of soft CFs was measured by using an Instron 5944 universal testing machine equipped with a 2 kN load cell (seen in Fig. II/2-2) and applying a modified ASTM D5729-97(2004)e1₁ standard. The samples were placed between two parallel solid surfaces: a fixed lower one, and a vertically adjustable one. The thickness of each soft CF was defined at a pressure described by the aforementioned standard and then averaged by measuring 10 different samples of each material.



Figure II/2-2 Measurement of carbon non-woven material's thickness by use of an Instron 5944 universal testing machine.

II/2.4 Textural analysis with mercury porosimetry

Pore diameter, total pore volume, and pore size distribution are key information about the materials' porous structure which can be obtained from mercury intrusion porosimetry (MIP). MIP involves the intrusion of mercury into the material at different pressures by the use of a porosimeter. Mercury does not wet most substances, thus does not spontaneously penetrate

¹ ASTM D5729-97(2004)e1: Standard Test Method for Thickness of Nonwoven Fabrics | Engineering360

pores by capillarity. In the MIP technique, mercury must be forced into the pores by applying different pressures, which allows us to evaluate the pore radii from equation II/2, also known as the Washburn equation (Giesche 2006):

$$P = -\frac{2\gamma \cos \theta}{r_{pore}} \quad (\text{II/2})$$

where γ (mN m^{-1}) is the surface tension of mercury; θ is the contact angle between the material surface and the mercury; P (MPa) is the applied pressure; r_{pore} (nm) is the material pore radius filled at pressure P .

A Micromeritics AutoPore IV 9500 (Micromeritics) mercury porosimeter (seen in Fig. II/2-3), operating from 0.001 to 414 MPa, was used in this study. The analyses were performed in two stages: primarily, the low-pressure chamber was used for the pressure range 0.001–0.24 MPa; then the sample holder filled with sample and mercury was relocated to the high-pressure chamber where the pressure was increased from 0.24 to 414 MPa. By applying pressures up to 414 MPa, the mercury intrusion porosimeter is capable of measuring pore diameters as small as 3.6 nm (Webb 2001).

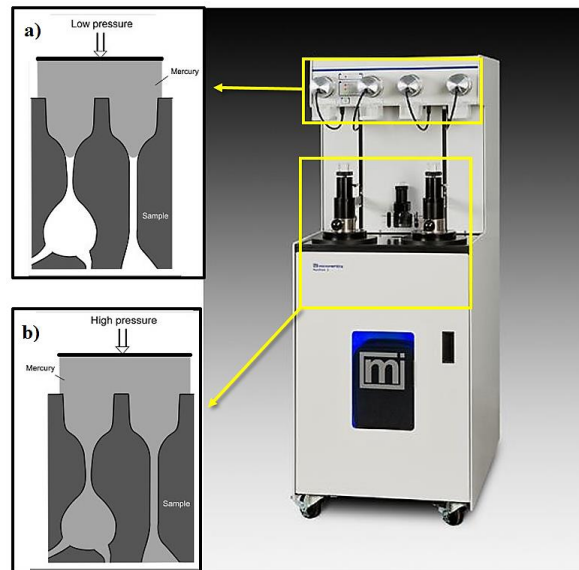


Figure II/2-3 Micromeritics AutoPore IV 9500 (Micromeritics) mercury porosimeter; a) low pressure chamber; b) high pressure chamber.

II/2.5 Imaging of CF structure

The CF structures can be investigated, at the micro- and/or macro-scale, by means of advanced techniques such as scanning electron microscopy (SEM) and X-ray tomography, respectively. Contrary to the 2-D observations by SEM, the X-ray tomography technique allows

virtual 3D reconstruction and investigation of the fibre networks (Soltani, Johari, and Zarrebini 2015).

II/2.5.a Scanning Electron Microscopy (SEM)

The most widely used of all electron beam instruments undoubtedly is the scanning electron microscope (SEM). It can produce images of the sample surface with a wide range of magnifications. In the SEM technique, a beam of high-energy electrons is concentrated towards a sample to generate different signals at the surface. Due to sample-electrons interactions, signals are generated which contain valuable information about the surface structure of the sample. Figure II/2-4 shows a scheme of a scanning electron microscope.

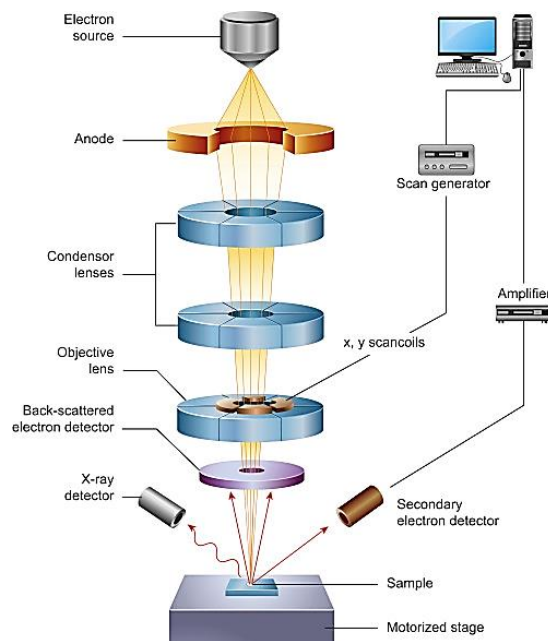


Figure II/2-4 Scheme of an electron-scanning microscope (SEM).

All the CFs have been thoroughly investigated by SEM observations, using a secondary electron detector. The secondary electron detector allows observing the overall felt morphology and texture formed during the manufacturing process. An ultra-thin nano-layer of silver was primarily deposited on the samples' surface by vacuum sputtering for insuring an electrical contact with the sample holder surface and resulting in the evacuation of the electric charges. The fibre structure and average dimensions of their cross-section were determined by Scanning Electron Microscopy (SEM) (using an EVO 50 instrument, equipped with Everhart-Thornley secondary electron detector and operating at maximum 30 kV or Philips XL30 SFEG, equipped with field-enhanced thermionic emission gun, performing at 4 kV). Cross-sections and fibre diameters of at least 20 different fibres were measured from each sample for determining the

average fibre diameter. Such count was carried out by using ImageJ software, and the average fibre diameter was automatically calculated from the software on a number of SEM images of each CF sample.

II/2.5.b Tomography – 3D morphology studies

X-ray tomography (XT) is a non-destructive imaging method which permits the characterisation of the microstructure of porous media (Rocha and Cruz 2010). The 3D quantification of the internal architecture of an object can be performed by using XT and related image analysis. As the specimen rotates through 180°, it gets fully irradiated with X-rays. At each degree increment, a radiograph projection is taken, and then the series of radiograph projections are used to construct 2D slices. The X-ray beam is attenuated by the presence of solid material and such changes of intensity emerging from the sample under study is captured by the detector array. The attenuation is linked to material density, typically represented by grey-scale 2D pixels. Figure II/2-5 represents the schematic diagram of an XT scanning device.

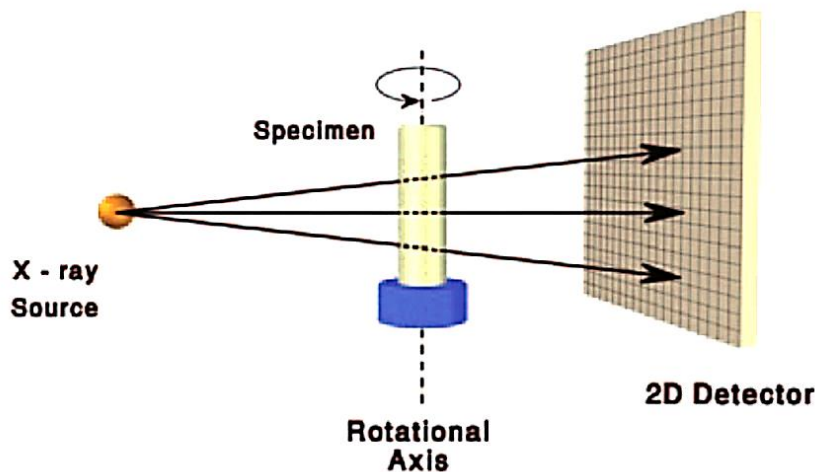


Figure II/2-5 Schematic representation of X-ray tomography apparatus.

From the acquired 2D grey images and their additional image processing, a reconstruction of the original 3D microstructure can be provided. A 3D material model obtained from X-ray tomography can be used to present the geometric properties of the fibrous material at the microscopic scale (Nouri et al. 2016).

For the validation of the data obtained from SEM and as precise as possible quantification of the morphologies of the commercial CFs, X-ray micro-computed tomography (μ -CT) studies were performed. μ -CT scanner was employed to generate the 3D images of five different CF matrices, derived from different subgroups. The X-rays were generated at 60 kV to form a beam current of 150 μ A. Samples for μ -CT had diameters from 4 to 6 mm and heights

(thicknesses) deduced from the manufacturing process. At last, a set of reconstructed 3D cross-section images were acquired by using VGStudio software. The pixels (voxels in 3D) of the reconstructed cross-section images in x,y-plane (in-plane) stacked in the z-plane (out-of-plane) made up a cylindrical matrix. The voxel size (of 4 μm per voxel) was recorded so that the physical size could be identified. Before performing the CT scans, efforts were made to minimise the effect of cutting the sample over its initial state, as well as to properly align the prepared sample with respect to the reference x,y and z-axis and the one from the tomography scanning stage.

Based on the obtained 3D reconstruction of the samples, precise morphology quantifications and finite volume method were performed, from which further predictions of the fluid flow properties can be theoretically achieved.

II/2.6 Wettability studies

Wettability studies usually and primarily involve the measurement of contact angles, which specify the degree of interaction between a solid with a given liquid. There are some important parameters involved in the wettability of a surface. Roughness, surface chemistry, and surface energy of the material are the most important ones determining the contact angle of a liquid onto a surface. Even though there is no specific number that defines the limit between hydrophobicity and hydrophilicity, small contact angles ($< 90^\circ$) of water on the surface correspond to high wettability (hydrophilic materials), while large contact angles ($> 90^\circ$) correspond to low wettability (hydrophobic materials) (Yuan and Lee 2013).

For studying the wettability of a material, a straightforward technique is initially performed. This technique consists of measuring the angle formed at the contact with a liquid droplet. A simple technique is the sessile drop method, where a drop of liquid is placed on the surface of the material of interest and the angle between the liquid and surface gives the contact angle (seen in Fig. II/2-6)).

In our case of CFs, for which high hydrophobicity is expected (Meng and Park 2014), the sessile drop method was performed by using a drop-shape analyser (DSA100, Krüss, Germany). With the use of an automatic drop deposition system, droplets of distilled H_2O of 2 μL were placed on the sample surface. The contact angles were measured by extrapolation with the Krüss software from the droplet images captured with a digital camera (seen in Fig. II/2-6 b)). The measurements were repeated on clean the dry surfaces and always performed at 20°C and 50% relative humidity. The average contact angle was obtained by determining the angles

on the left- and right-hand sides of each droplet and taking the average of at least 10 droplets on different regions of the CFs.

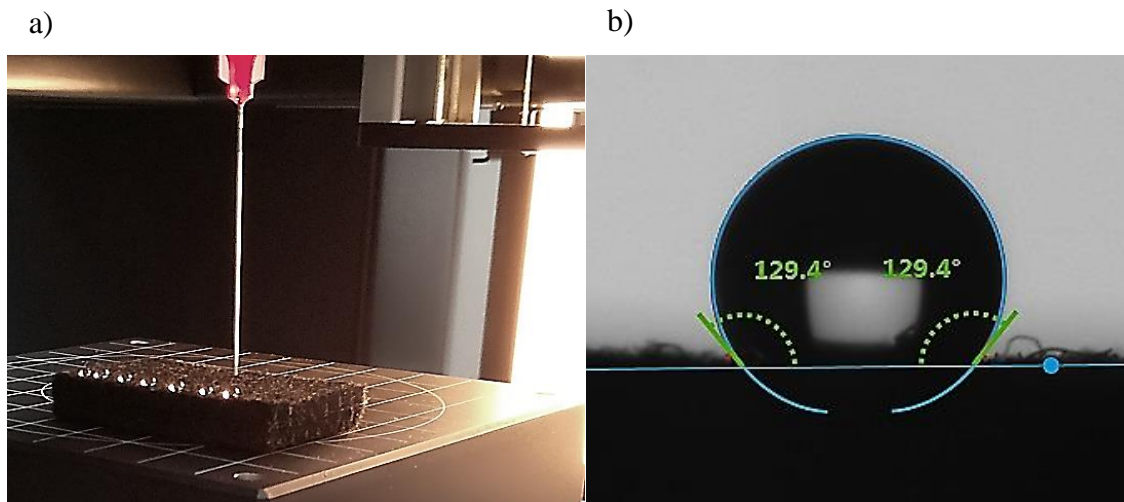


Figure II/2-6 Sessile drop method analysis by a drop-shape analyser (DSA100, Krüss, Germany).

II/2.7 Physical properties

II/2.7.a Out-of-plane air permeability

The fluid flow through a porous media such as non-woven fabrics follows Darcy's law, described by equation (II/3):

$$\sigma = \frac{\Delta P \cdot A}{Q \cdot L} = \frac{R_f}{L} \quad (\text{II/3})$$

where the airflow resistivity (σ , Pa·s m⁻²) is calculated from the pressure drop (ΔP , Pa) across a known section (A , m²) with an air flow rate (Q , m³ s⁻¹) over a given thickness (L , m). Darcy's law is broadly utilised in several engineering areas where the fluid under concern is Newtonian with small Reynolds' number ($Re < 10$). The inertial effects are thus not critical so that the viscous interaction between the fluid and the porous solid is the main source of pressure drop (Soltani, Johari, and Zarrebini 2013).

The airflow resistance R_f , being the product $\sigma \times L$ according to equation (II/3), was directly measured with a Sigma airflow resistance meter (Mecanum, Canada). This apparatus (Fig. II/2-5) is specially designed to measure the airflow resistance of materials within the range $10 - 10^6$ Pa·s m⁻¹, and complies with two international standards: ISO 9053:1991² and ASTM

² ISO 9053:1991 : Acoustics - Materials for Acoustical Applications -- Determination of Airflow Resistance

C522-03(2016)³. The pressure regulator maintained the steady-state flow of air throughout the specimen, and a differential pressure transducer was used to quantify the static pressure difference between the free faces of the specimen with respect to the atmosphere. Valid measurements were only made in the region of laminar airflow where, apart from random measurement errors, the airflow resistance (thus the airflow permeability) was strictly constant. Then, the airflow permeability k (m^2) of all samples was calculated by the software SIGMA-X of the device, by application of equation (II/4):

$$k = \frac{\nu L}{R_f} \quad (\text{II/4})$$

where $\nu = 1.84 \times 10^{-5}$ Pa s is the dynamic viscosity of air at room temperature.

Cylindrical specimens of diameter 44.44 mm and height predefined by the thickness of the materials were cut and fitted tightly into the specimen holder (seen in Fig. II/2-7). The CFs were only characterised along their out-of-plane direction, i.e., perpendicular to the bedding plane of the fibres (as seen in Fig. II/2-8). The measurement was done at five different air flow velocities and the average result was calculated. All airflow velocities were below 5 mm s^{-1} . A series of 3 measurements per CF at airflows below the turbulent level were performed and the results are gathered in the results section, II/2-7.



Figure II/2-7 Left - prepared sample and sample holder for airflow resistance measurement; right - top view of sample holder with installed sample.

³ ASTM C522-03(2016): Standard Test Method for Airflow Resistance of Acoustical Materials | Engineering360

II/2.7.b Mechanical characterisation

Having the possibility of analysing samples' mechanical properties by two different methods, all soft CF materials were investigated by one dynamic and destructive method on the one hand, and by one quasi-static and non-destructive method on the other hand.

The conventional method for studying the mechanical properties of materials is mechanical compression. Through this method, the complete stress-strain characteristics of the materials are determined by applying continuously increasing loads and measuring the resultant deformation. Regardless of its destructive character, this technique is still the most frequently used for both flexible and rigid fibrous materials (Mahboobeh 2013).

Herein, the samples were investigated by compression using an Instron 5944 universal testing machine equipped with a 2 kN head (already seen in Fig. II/2-2), at a load rate of $0.5 \text{ mm} \cdot \text{min}^{-1}$. During the compression test, stress and deformation were constantly recorded. Based on obtained stress vs. strain curves, elastic modulus and yield strength can be correctly estimated. When clearly observed, the linear elastic part of the curves defined the elastic modulus, E (MPa), within the "proportional limits" of Hookes' law application (Fung 1967):

$$E = \frac{\sigma}{\epsilon} \quad (\text{II/5})$$

where $\sigma = \frac{F}{S_0}$, expressed in MPa, presents the uniaxial non-zero stress (being the compression force, F (N), applied at defined cross-section area, S_0 (m^2) and ϵ (dimensionless) is the strain, or relative deformation (change in thickness, ΔL , divided by the original thickness, L (mm)). The yield strength (MPa) – also called elastic limit – was defined as the highest height of the elastic region, and corresponds to the end of the elastic behaviour and the beginning of plastic behaviour.

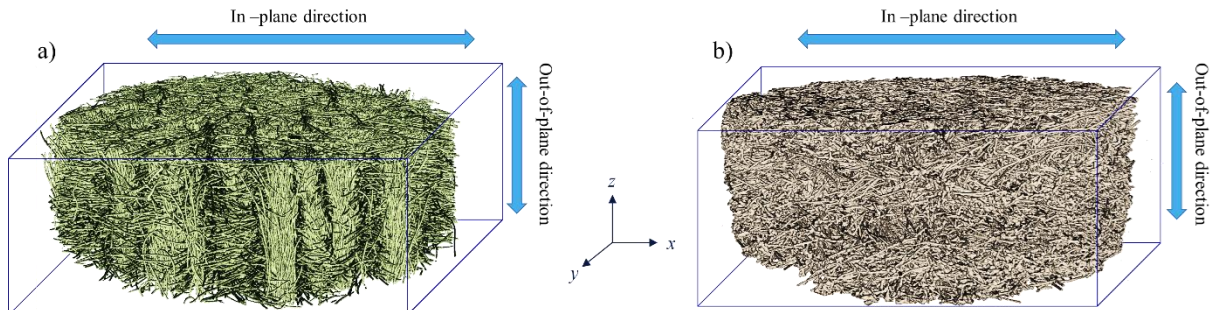


Figure II/2-8 3D realistic representation of tomography data: (a) soft felt, and (b) rigid board samples, with x -, y -, z -directions.

Three cylindrical samples of diameter approximately 44.4 mm and thickness deduced by the use of an Instron 5944 (as explained in subchapter II/2.3), were tested in the out-of-plane (OP) direction (seen in Fig. II/2-8) for each kind of CFs.

A novel and non-destructive technique, based on quasi-static mechanical vibration, was also examined in the case of soft CFs. These materials present mechanical properties that may differ from purely hyperelastic⁴ to incompletely elastic, depending on their properties deduced from the fabrication process. Thus performing proper characterisation using one single method may not be enough.

The quasi-static mechanical analysis (QMA) is a quite recent and uncommon method for the identification of the elastic modulus of porous materials. The process for measuring the properties of poroelastic materials is explained in detail elsewhere (Delgado Sánchez 2017). Briefly, it is based on polynomial relations among compression stiffness, elastic modulus, Poissons' ratios⁵, and shape factor. The estimation of the latter parameters can be obtained from high-order axisymmetric finite element simulations, using a disc-shaped sample under static compression. The shape factor is defined as half the radius to thickness ratio of the sample. The established relations work in the low-frequency range (below any resonances) and also account for the fact that the disc sample might swell sideways when compressed between two rigid plates to which it is bonded.

For the tests performed herein, a zero Poisson ratio was assumed for all soft CFs. Zero Poisson ratio is indeed observed due to the inability of such highly porous and layered materials to produce significant lateral deformation in the (stiffer) IP direction when the material is compressed or extended in the OP direction (seen in Fig. II/2-9). This behaviour was also confirmed under dynamic conditions by strobing the vibrating test sample over a range of amplitudes (Rice and Göransson 1999). With a given Poisson ratio, the solution of the system yields the real elastic modulus of the evaluated soft CFs.

⁴ Hyperelastic materials are an exceptional class of materials because of their mechanical properties. This kind of materials tends to react elastically when subjected to very large strains, under different deformation conditions, exhibiting a non-linear material behaviour as well as significant change of shape. The generally used linear elastic models do not accurately describe the elastic behaviour of hyperelastic materials, whose stress-strain relationship is described by parameters that are scalar functions of the deformation (Ogden 1997).

One of the most common examples of hyperelastic material is rubber, exhibiting a non-linear stress-strain relationship. In addition, the elastic behaviour of some porous fibrous non-wovens is often very close to that of hyperelastic materials. Hyperelasticity thus offers a means of modelling the stress-strain behaviour of such materials.

⁵ Poisson's ratio is the ratio of materials' transversal (lateral) expansion to longitudinal compression strain in the direction of compression force. The Poisson's ratio of a linear elastic material must be in the range from -1.0 and 0.5, because of the concepts of stability and requirement for the elastic parameters to have positive values.

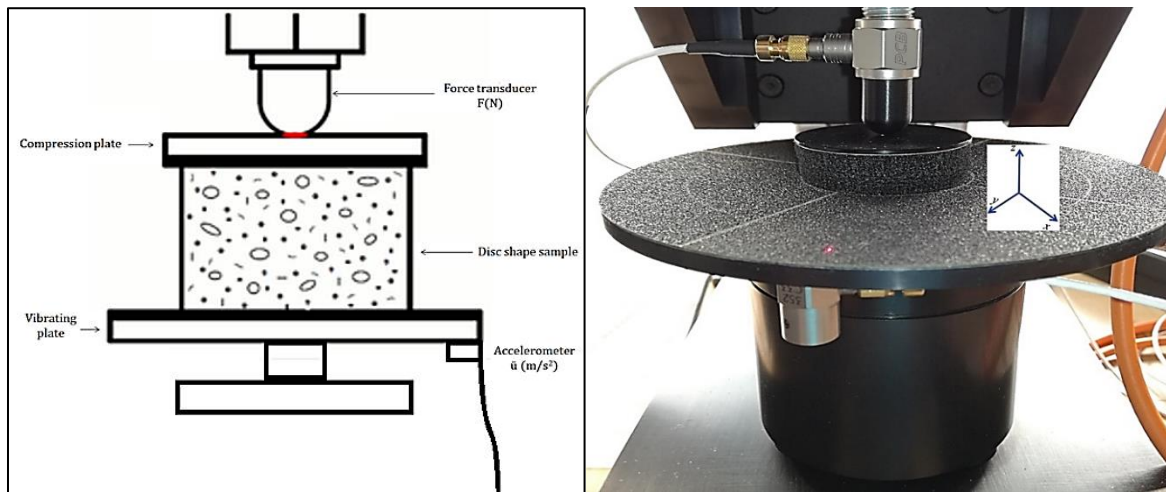


Figure II/2-9 Scheme (left) and real representation (right) of quasi-static mechanical analyser (QMA) with installed sample.

The procedure consists in placing (sandwiching) the disc-shaped sample between two rigid plates. The inferior plate is axially excited by an electrodynamic shaker whereas the superior plate is fixed. The plates' surfaces are coated with sandpaper to avoid sliding of the sample against them (seen in Fig. II/2-9 right). A shaker with a pseudo-random noise in an unchanged frequency of 20 Hz is used to excite the bottom plate, which is also connected to an accelerometer. On the other top side, a force transducer is connected to the superior plate. The accelerometer measures the acceleration of the bottom plate, whereas the force transducer measures the reaction force, supplied through the sample, on the top plate.

Moreover, to ensure linearity in the porous materials' behaviour, an ideal compression rate needs to be determined. By testing materials of unknown rigidity, it is hard to predict the ideal strain. In general, the stiffness vs. strain measurements are performed to help identifying the proper strain to use and ensure that the elastic properties do not depend on the experimental conditions. For the same purpose, soft CFs are tested within a strain range from 0.5 to 9.5 %, as software predefined limits for protection of the test equipment. Figure II/2-10 shows the different ideal sections that should be found during testing, seen from the real part of the stiffness as a function of the compression rate (blue curve). When a plateau is observed, it is of good use to select a strain within this region.

The quasi-static compression test was performed on at least two samples of each material. CF specimens of different thicknesses (fabrication defined), ranging from 9 to 20 mm, and a unique diameter of 44.4 mm, were therefore analysed.

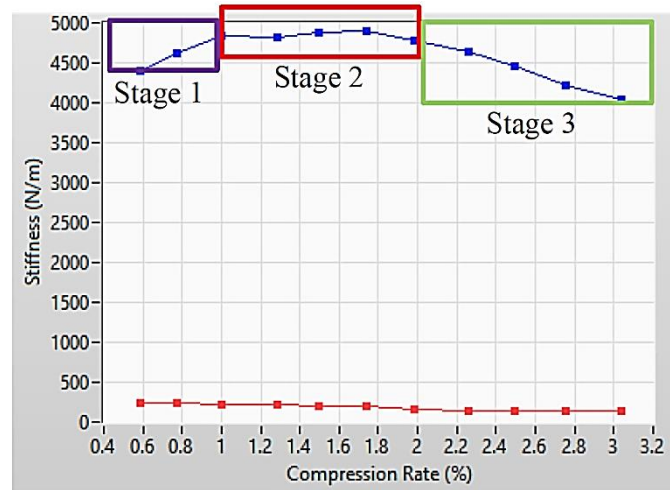


Figure II/2-10 Stiffness vs. strain measurement (blue line – real and red line – imaginary part of the stiffness as a function of the compression rate).

II/2.7.c Thermal conductivity properties

The hot-disc technique is a transient plane source method for the rapid thermal conductivity of solid materials. The basic theory behind the thermal conductivity measurement with the hot disc sensor is discussed elsewhere (Bohac et al. 2000). Briefly, this method is based on the transient heating of a flat double spiral inserted between two pieces of the studied material (seen in Fig. II/2-11). From the temperature increase of the heat source, and provided that the total time of measurement is chosen within a correct time window defined by the theory and the experimental situation, one can get both the thermal conductivity and the thermal diffusivity from one single experiment.

The thermal properties are strongly influenced by the anisotropy of the materials (at fibre and felt scale), making difficult to measure their conductivity using conventional instruments (hot-wire and hot-strip, flash method, guarded hot plate, etc.), since most of these give an apparent overall conductivity of the material. On the other hand, based on the knowledge of the volume heat capacity of the carbon material, the transient plane source method can be applied to the case of anisotropic materials. In the case of non-woven CFs, thermal properties along two of the orthogonal and principal axes are considered to be the same (IP thermal conductivity - κ_{xy}), thus dissimilar from that along the third axis (OP thermal conductivity - κ_z) (Zhang, Li, and Tao 2017).

Nowadays, anisotropic materials are used in various ways, depending on the application, thus can be stacked either perpendicular or parallel to heat flow. In the case of CFs, with fibre and felt texture anisotropic morphology, their performances are largely affected by

the different foreseen applications, since the thermal conductivities in the directions of the plane κ_{xy} (parallel to the oriented fibres) and of the thickness κ_z , are quite different from each other.

The thermal conductivity was measured before and after the de-sizing step, explained in subchapter II/2.1. Additionally, the thermal conductivity was measured with isotropic and anisotropic modes of the measurement device, in order to compare the values and discuss the influence of the material anisotropy.

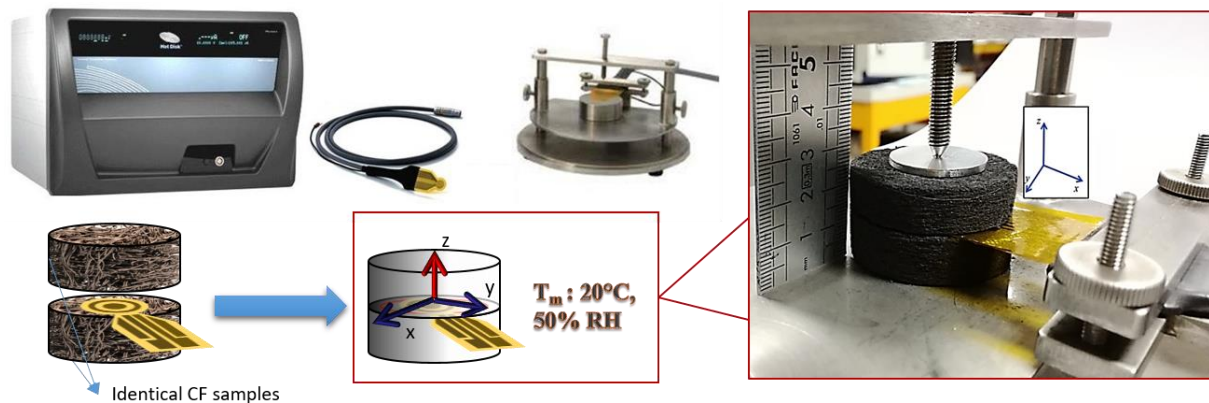


Figure II/2-11 HotDisk TPS 2500 device with details of the measurement probe and CF sample installation for testing (defined matrix orientations).

The thermal conductivity of all carbon materials of different porosities was measured with a Hot Disk TPS 2500 device under fixed conditions of temperature and moisture (20°C and 50% relative humidity). A flat double spiral of nickel covered by Kapton® (whose diameter was driven by experimental conditions), acting both as a heater and as a temperature sensor, was sandwiched between two identical samples whose surface was smoothed and with adequate dimensions for considering the samples as semi-infinite media (seen in Fig. II/2-11). By imposing a heat pulse at a controlled power to the materials, the temperature response was recorded as a function of time. As a general principle with such a system, highly porous and poorly conducting materials make the temperature increase significantly even at low heating powers. Due to this, the stabilisation time (time between measurements over the same sample) was always longer than 30 minutes. The thermal conductivity was calculated from the Hot Disk 7.2.8 software, upgraded with an additional lab-made code kindly supplied by I2M – Bordeaux for improving the accuracy of the measurements by taking into account the contact resistance between the sensor and the investigated material.

II/3 Results and discussion

II/3.1 Morphological characterisations

II/3.1.a Porosity and density

Since various CFs were received from different suppliers, various ranges of bulk and skeletal densities, and hence of resultant total porosity, were expected and were indeed observed, as presented in Fig. II/3-1 (a) and b), respectively) and Table II/6-2. The CF samples derived from ex-PAN and ex-Rayon precursors, regardless of fibre diameter, rigidity and felt formation technique, exhibited bulk density, skeletal density and porosity values in the range of 0.073-0.227 g cm⁻³, 1.514-1.908 g cm⁻³ and 87.5-95.7%, respectively. If we consider that one of the final targets is easy impregnation, the results clearly show that all evaluated samples may be relevant host materials for the PC, given their high porosity. Nevertheless, the differences in porosity can also be seen as non-negligible and therefore have an influence on the energy density of the final composite.

The ex-Rayon needle-punched non-woven soft CFs had clearly lower bulk density and higher porosity than rigidized soft and rigid board CFs, because of the chemical bonding process by which the latter materials were modified or formed, respectively. The addition of resin binder forms agglomeration and accumulations at the intersection where fibres touch or nearly touch each other, thus bridging the gap between the fibre surfaces. Consequently, the density of the materials slightly increased, thus making the total porosity decreased by 5% on average. The materials investigated here from the ex-Rayon rigid boards group had measured densities and porosities in the same ranges as observed elsewhere (Zhang et al. 2017), reported to be 0.1 – 0.5 g cm⁻³ and 70 – 90%, respectively.

A linear relationship was observed when plotting the porosity values against the bulk density of all examined CFs, not observed when doing the same with the skeletal density. The results clearly indicated that the porosity of these voluminous materials is more influenced by the bulk density than by the skeletal one (seen in Fig. II/3-1).

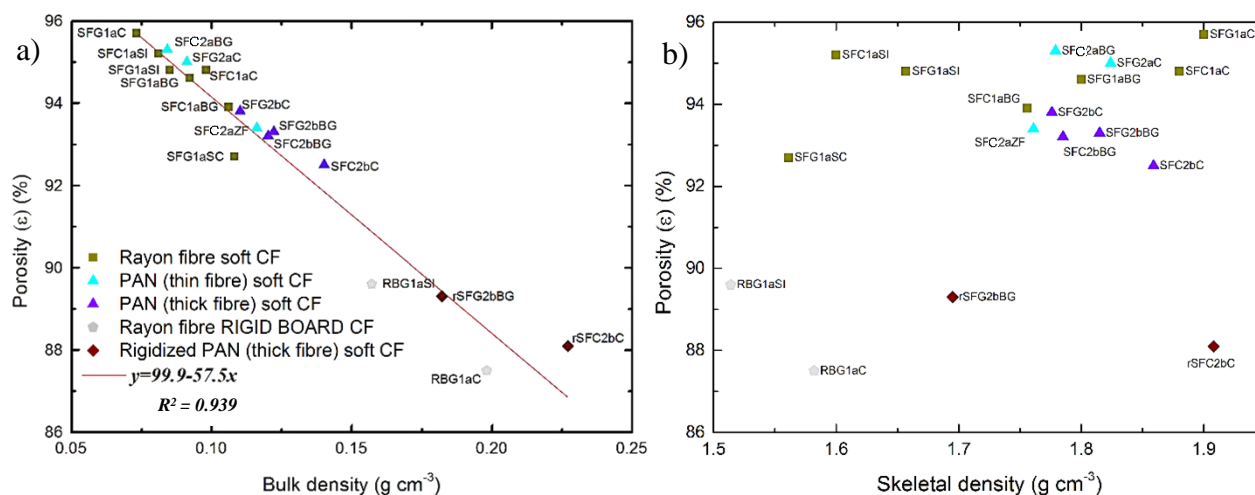


Figure II/3-1 a) Bulk density (g cm^{-3}) or b) skeletal density (g cm^{-3}) vs. porosity (%) of the examined commercial CFs; different symbols or colors represent different groups or subgroups respectively; the legend of a) is the same as for b).

The theoretical density of a graphite crystal is 2.26 g cm^{-3} (Pierson 1993). However, most carbon materials have different densities due to the presence of structural imperfections such as porosity, graphitic lattice vacancies and/or dislocations, plus lattice impurities consisting of foreign elements (due to the type of used precursor, heat treatments and other influencing factors). In general, all carbonised CFs showed lower skeletal density when compared to the corresponding graphitised CFs (seen from SFC1aSI \rightarrow SFG1aSI, SFC1aC \rightarrow SFG1aC, SFC1aBG \rightarrow SFG1aBG, and SFC2bBG \rightarrow SFG2bBG). The process of graphitisation is accompanied by further carbon fibre shrinkage, which is usually correlated to the appearance or growth/alignment of the graphitic structures and elimination of foreign elements, as reported by (Frank et al. 2014).

II/3.1.b Textural analysis with mercury porosimetry

Determining accurately pore size and pore volume distributions of non-woven materials such as soft CFs is more problematic than for rigid ones. Soft non-woven materials are less frequently described by mercury porosimetry, despite the importance of the provided parameters for transport models and material design. As reported before, the reasons for this are connected to the flexible fibrous CF structure, which is ill-defined compared to a set of discrete pores in a fixed rigid structure, in addition to the relative easiness with which deformation occurs in these materials (Rutledge, Lowery, and Pai 2009; Mathias et al. 2010).

Therefore, analyses of porosity by mercury intrusion were solely conducted with samples from the ex-Rayon rigid boards group, thus avoiding possible material deformation during the measurements. The same was not performed even with the rigidized PAN (thick fibre) CFs, due to the change in materials' rigidity at the sample size for analysis. The technique confirmed that most of the pore volume could be ascribed to very big pores and/or voids (seen in Table II/3-1). Comparing the results obtained from He pycnometry and mercury porosimetry, their porosity values did not evidence any big deviation (less than 5.8 % in both materials). This minor difference might be attributed to the fact that helium can penetrate much narrower pores, whereas the entrance of mercury is limited to pores wider than 3.6 nm.

Table II/3-1 Measured bulk density, He pycnometry (left) porosity and Hg porosimetry (right) density and porosity values, with additional material information obtained with the latter, for the materials of the ex-Rayon rigid boards group.

Code name	Bulk density (g cm ⁻³)	Overall Porosity by He pycnometry (%)	Bulk Density at (0.0036 MPa) (g cm ⁻³)	Porosity by Mercury Porosimetry (%)	Intrusion volume (cm ³ g ⁻¹)	Average Pore Diameter (4V/A) (µm)
RBG1aSI	0.157	89.60	0.15	85.57	5.67	53.28
RBG1aC	0.198	87.50	0.20	82.42	4.22	51.35

The intrusion curves presented in Figure II/3-2 a) show that mercury intrusion occurs abruptly in a narrow range of pressure, resulting in a narrow distribution of interconnection sizes. The corresponding pore size distributions presented in Figure II/3-2 b) are indeed unimodal, having their maximum at 59 and 94 µm for samples RBG1aSI and RBG1aC, respectively. Therefore, completely interconnected pore structures are expected to be straightforwardly infiltrated by the molten PC. Comparing the results of pore size distribution from both samples and their SEM micrographs, some correlation can be observed. Fibres and binder are distributed more homogeneously and more randomly in RBG1aSI than in RBG1aC, as observed from the lower difference between the calculated average pore diameter and the maximum of the corresponding pore size distribution. This can be due to a different manufacturing process, which results in the observed differences of macroporous structure properties and pore size distribution. However, the slight difference in void volume and pore size distribution should present different CF hosting capacity and stabilisation abilities of the molten PC and its different pre-peritectic stages, through the multiple charge/discharge cycles.

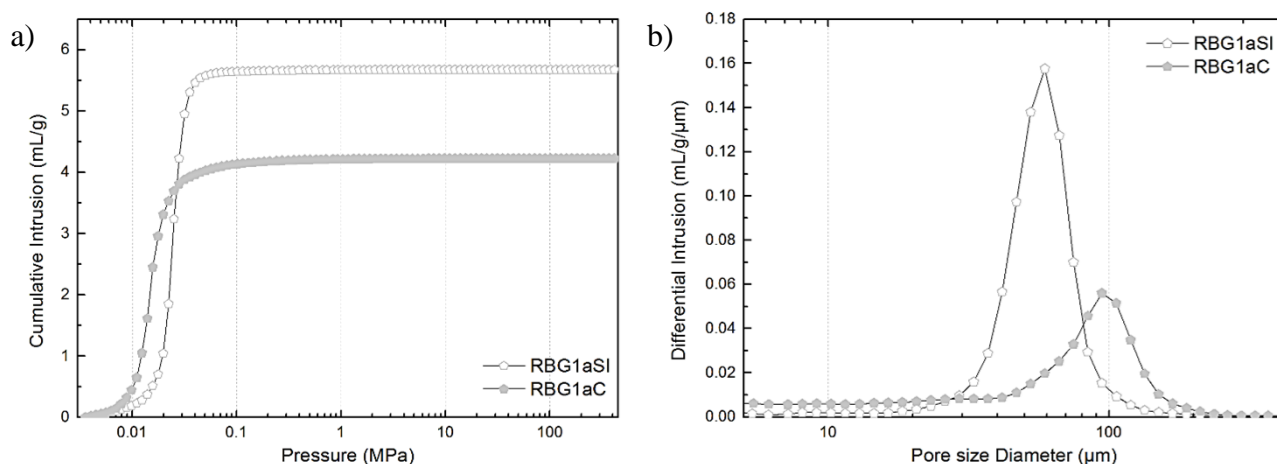


Figure II/3-2 a) raw Hg porosimetry intrusion curves and b) corresponding pore size distribution of ex-Rayon rigid boards.

II/3.1.c Morphology investigated by SEM

One of the most remarkable characteristics of needle-punched nonwovens is their high porosity and large pore size, as reported by González-García et al. (1999). Thus, the performed SEM studies confirmed similar CF features.

Evidence from SEM observations shows that all CFs were anisotropic and made of randomly laid/dispersed fibre layers, consolidated by needle-punching and/or chemical bonding. All samples were quite correctly described by the schematic representations of either soft or rigid board CFs shown from Fig. II/3-14 to Fig. II/3-16, respectively, in which x-, y- and z- directions are indicated. As already explained before, these directions originate from those of the machine with which the materials were prepared. The x- and y-directions are almost full equivalents and define the “in-plane” (IP) direction, i.e., the bedding plane of the fibres within which no preferential orientation exists. The orthogonal direction, z, is the “out-of-plane” (OP) direction of the materials.

All soft CFs appeared to be organised according to a rather repetitive architecture, in which the IP-oriented fibres followed a defined pseudo-weaving pattern because of the fibres laying manufacturing step, prior to the needle-punching process. Part of the fibres directly exposed to the impact of needles and their barbs were abruptly redirected along the OP-direction, reinforcing the overall felt structure. Other fibres were indirectly affected by the needle-punched redirected ones and occasionally deviated from their initial orientation. Needling marks resulting from punching movements were also observed in the x-y plane. The various commercial origins of the CFs and the differences in fibre types and assembly processes

resulted in soft CFs with different morphologies. The explained characteristics can be observed in the SEM micrographs from Figure II/3-3 to Figure II/3-5.

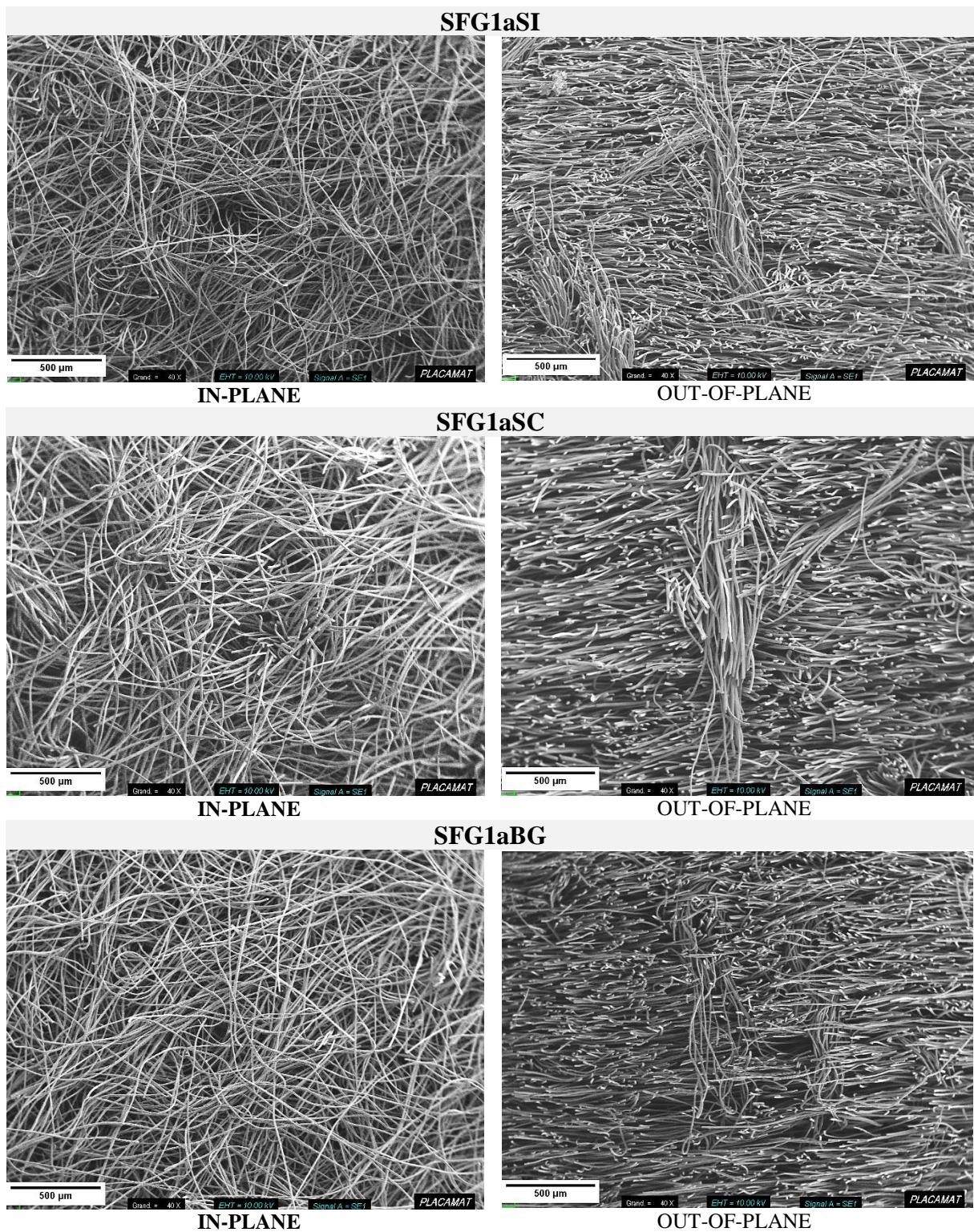
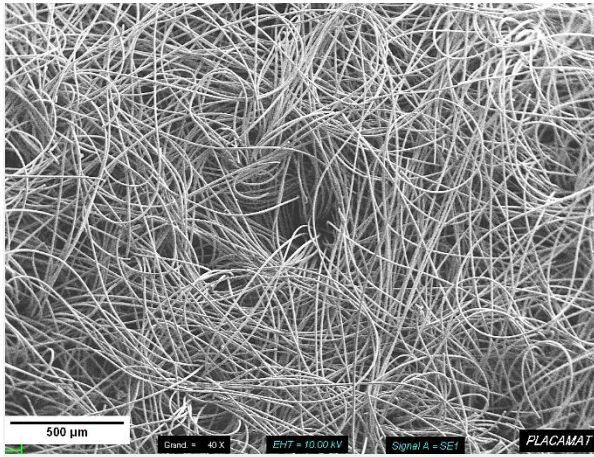
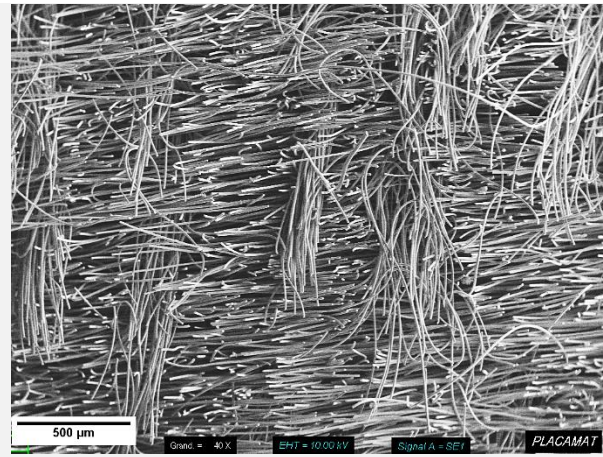


Figure II/3-3 Left side “in-plane” and right “out-of-plane” directional morphology observed from the SEM micrographs of Rayon-derived soft CFs.

SFC2aBG



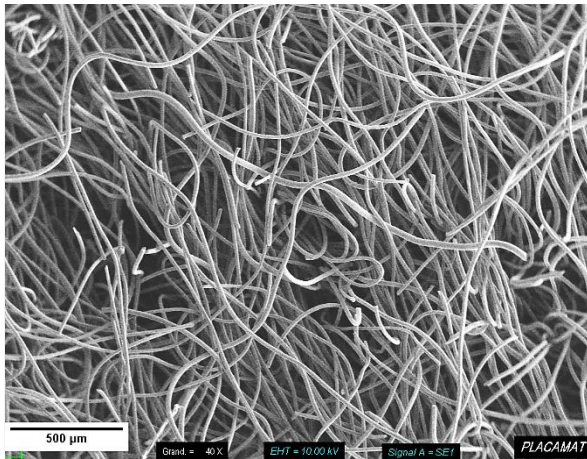
IN-PLANE



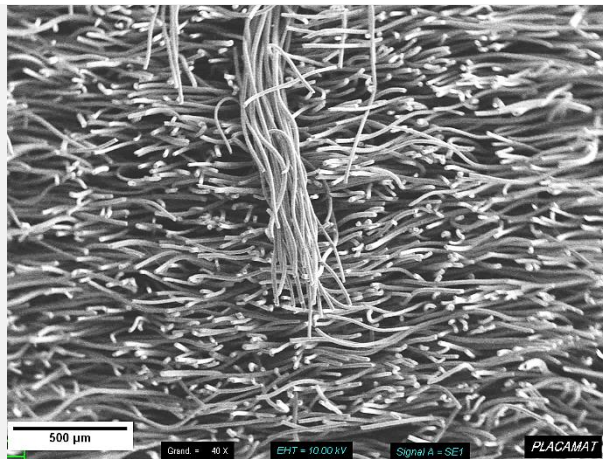
OUT-OF-PLANE

Figure II/3-4 Same as in Fig. II/3-3 but for PAN (thin fibre)-derived soft CFs

SFC2bBG

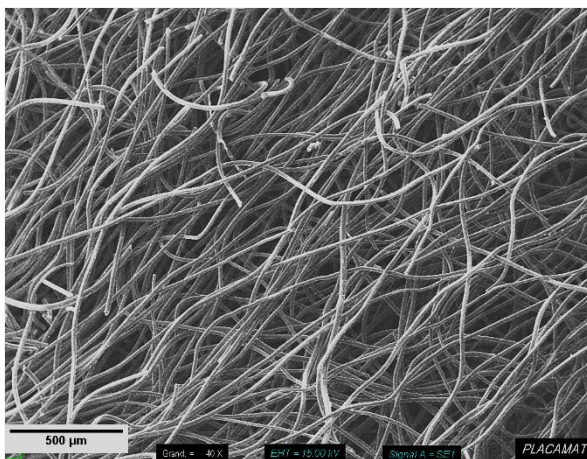


IN-PLANE

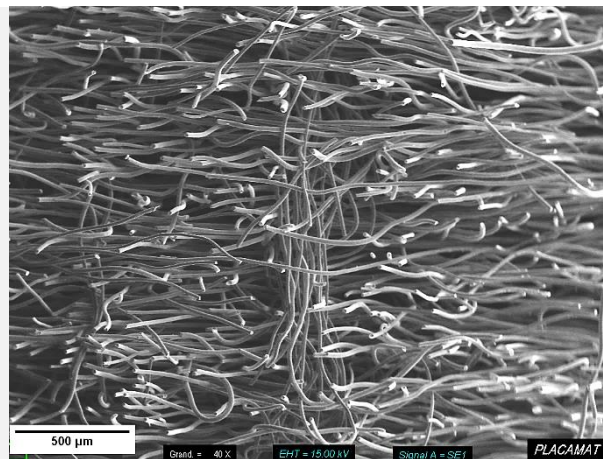


OUT-OF-PLANE

SFG2bC



IN-PLANE



OUT-OF-PLANE

Figure II/3-5 Same as in Fig. II/3-3 but for PAN (thick fibre)-derived soft CFs.

The group of thick-fibre, PAN-derived rigidized CFs had the same morphology as that of the aforementioned soft CFs, except at the surface in the IP direction, see Fig. II/3-6. The corresponding two samples were indeed additionally chemically bonded, thus discrete regions of rigidized fibre layers were formed. Such modification has two main motivations: (i) it is industrially used as an upscaling technique for obtaining thicker materials by joining two or more needle-punched soft felts on top of each other (along the OP direction); (ii) it improves the mechanical properties by decreasing the probability of fibres release and movement.

rSFC2bBG

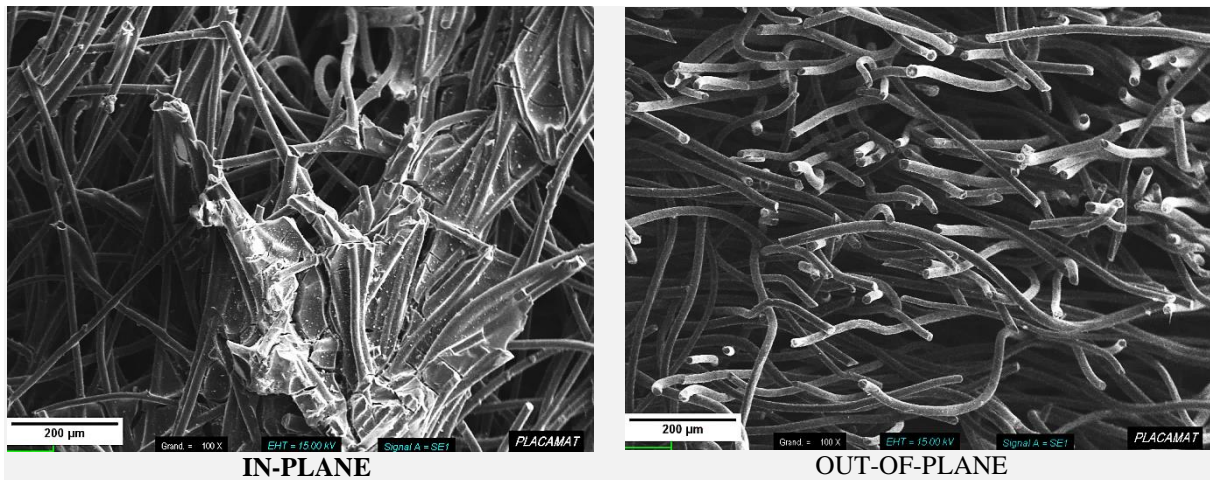
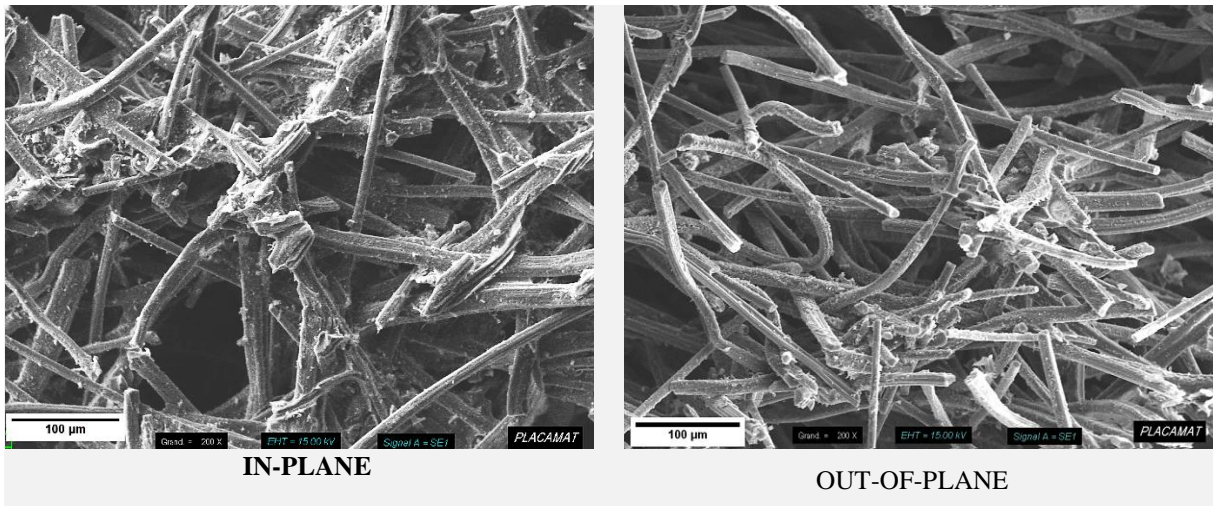


Figure II/3-6 Same as in Fig. II/3-3 but for rigidized PAN (thick fibre)-derived soft CFs.

On the other hand, the group of rigid board CFs presented completely different morphological characteristics: fibre intersections were bonded by more or less discrete regions made of glasslike carbon derived from phenolic resin. They consisted of many clusters and bundles of fibres, due to the different manufacturing and chemical bonding processes, much more frequent in the case of RBG1aC as seen from Fig. II/3-7. The evident higher presence of clusters and bundles of fibres and lower homogeneity in RBG1aC, compared to RBG1aSI, was previously confirmed and in good correlation with the results from the mercury porosimetry characterisations. No clear needling pattern could be seen, unlike what was observed in all other groups of soft and rigidized soft CFs. However, it was still obvious that the distributions of fibres in the IP direction (Fig. II/3-7; left) and OP direction (Fig. II/3-7; right) are different due to the fibres laying manufacturing step, prior to the thermo-chemical bonding process. In addition, the micrographs of both materials clearly show different fibre lengths, suggesting that they could be made from chopped or recycled ex-Rayon carbon fibres, as previously reported by Panerai et al. (2017). The potential use of CFs from recycled carbon fibres as a host in the foreseen storage system is expected to decrease the final cost of the composite, without

compromising its performances. In addition, the formation of CF from chopped fibre blend should significantly reduce the number of enlarged pores apparent in the needle-punched CF and, accordingly, present an even better environment for the stabilisation of the PC.

RBG1aC



RBG1aSI

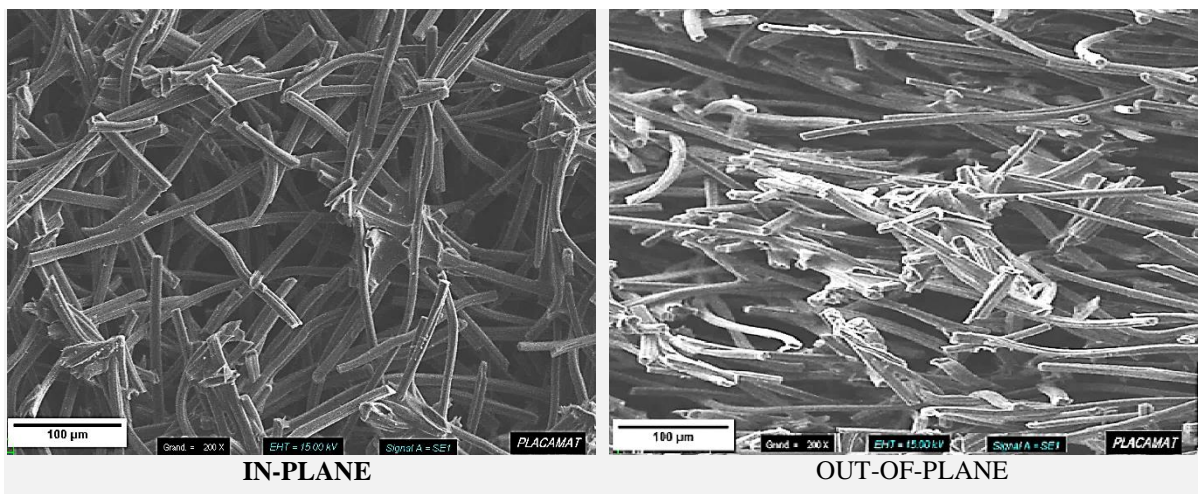


Figure II/3-7 Same as in Fig. II/3-3 but for Rayon-derived rigid board CFs.

The CFs are also described in terms of fibre morphology, nature of the fibres, and structural properties. The carbon fibre microstructure depends on precursors' properties and processing conditions, thus there are different proposed models to describe the cross-sectional fibre microstructures (Huang 2009; Newcomb 2016). Averaged fibre diameters of all investigated CFs were analysed from the SEM micrographs, as previously described, and averaged values are presented in Table II/6-2 and Figure II/3-8. Measurements must be performed with care since fibres often have non-circular cross-sections (Dresselhaus 1988). In general, there is a deviation from the average fibre diameter for all evaluated carbon fibres from different CFs (see Figure II/3-7). However, the deviations in the ex-Rayon carbon fibres were

observed mainly due to the non-circular cross-sections, whereas in the ex-PAN the same was observed due to the presence of carbon fibres with different diameters of generally circular cross-sections. From the obtained results, the fibres cross-section structure was found to be influenced solely by the nature of the precursor, regardless of the felt manufacturing technique. There is no clear thermal shrinkage of the investigated carbon fibres' diameters of corresponding carbonised/graphitised CFs (produced from the same precursor but manufactured at a different final temperature).

Further on, as described in subsection II/2.2, different groups of soft CFs were recognised, accounting on the fibre diameter measurements, with average fibre diameters 9 - 12 μm on the one hand, and 18 - 20 μm on the other hand (see Figure II/3-8).

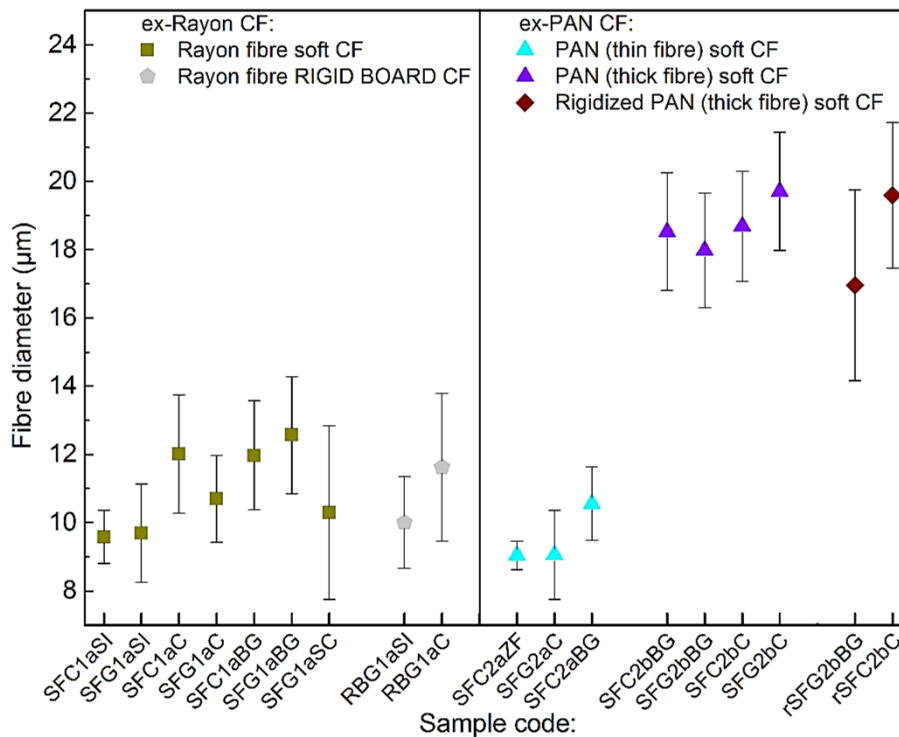


Figure II/3-8 Averaged fibre diameter values for each of the commercial CFs; different symbol or color represent different group or subgroup, respectively.

The magnified cross-section micrographs of the CF, exposed in Fig. II/3-10 and 11 and Fig. II/3-12 and 13, show the two typical and distinct types of carbon fibres, Rayon- and PAN-derived, respectively. The carbon fibres derived from renewable (Rayon) and synthetic (PAN) organic fibres mainly differ in their appearance. In the case of Rayon, the individual fibres appear as bundles of several elementary fibrils, melted together lengthways, while the structure derived from PAN is uniform and solid, as also noticed by Zhong et al. (1993). SEM micrographs of the examined soft CFs are additionally presented from Fig. II/6-1 to Fig. II/6-3, donating supplementary information on the various fibres' structures and cross-sections.

Rayon-derived carbon fibres present uneven and inhomogeneous surfaces, such as a hollow and/or a noncircular cross-section (lima bean or circular serrated, lobular and other forms presented in Fig. II/3-9). As a result, we observed higher deviations in the average fibre diameter of SFG1aSC compared to the other Rayon-derived CFs due to the uneven, lima bean, shape of the constituting carbon fibres. The fibre surfaces are typically finely ribbed, parallel to the fibre axis. Pits (inner holes) at different scales were also observed in each of the Rayon-derived carbon fibres.

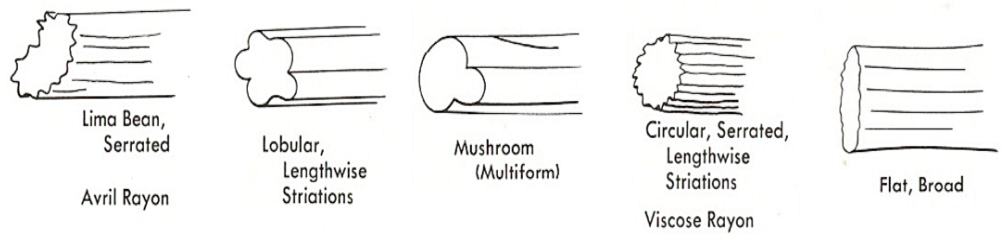


Figure II/3-9 Rayon-derived carbon fibres surface forms (modified after <https://www.pinterest.com/pin/524810162808656920/12.04.2018>).

Figures II/3-10 and 11 present fibres with several occasional particles of an additional material adhering to their surface. These impurities are probably related to the de-sizing of the felt, or presumably, they can be tarry coating residues, known as a typical side-products from graphitisation, reported by González et al. (2017) and Rabbow et al. (2015), respectively. Also, the freshly regenerated Rayon may contain different types of impurities (e.g. lignin and hemicellulose), which were not properly removed during the washing step in the fibre formation process (Park 2015).

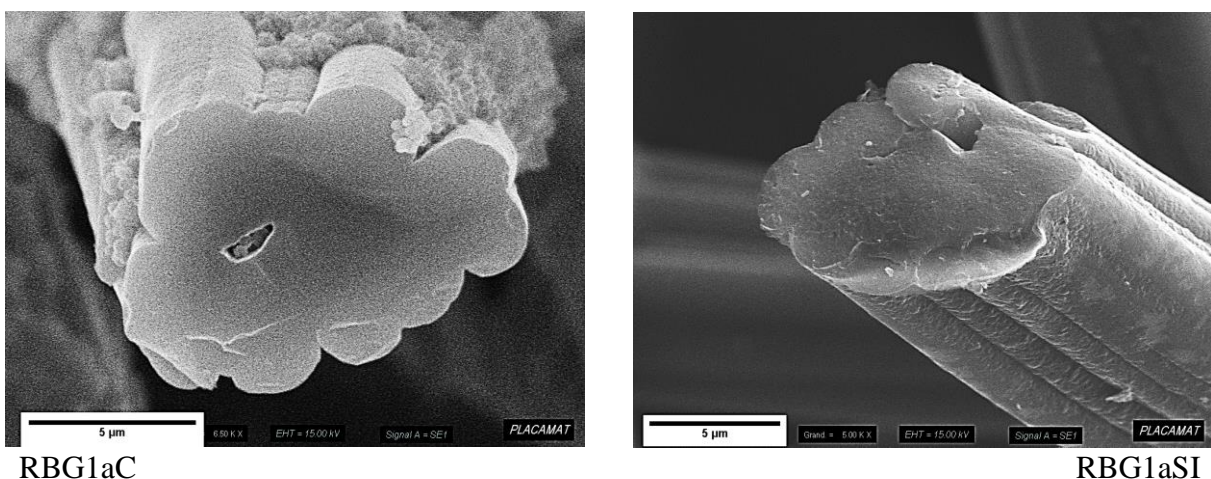
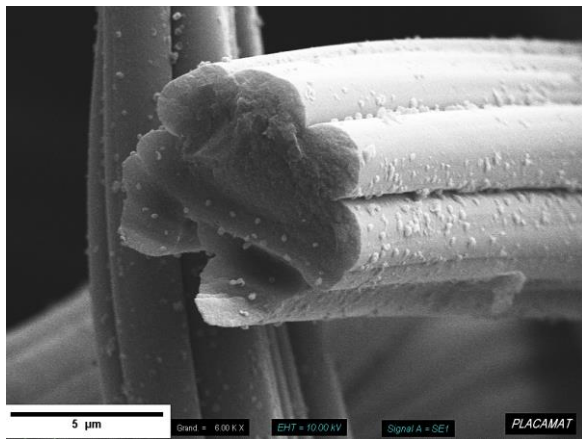
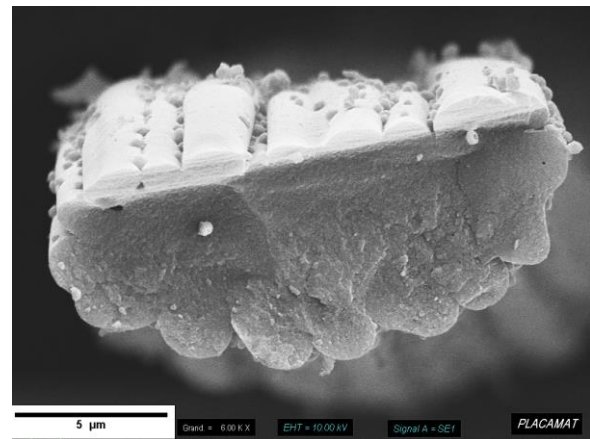


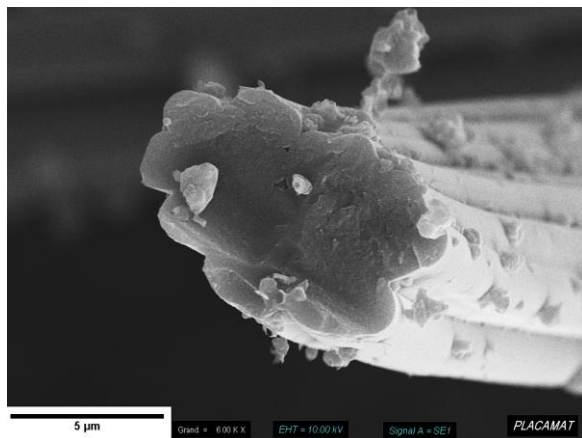
Figure II/3-10 Fibre cross-section of Rayon rigid board CFs.



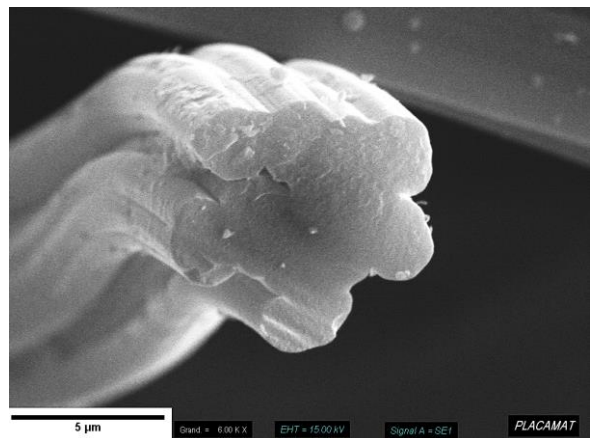
SFG1aSI



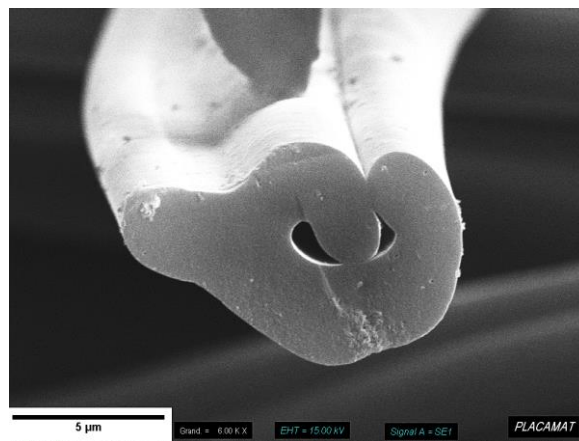
SFG1aSC



SFG1aBG



SFG1aC

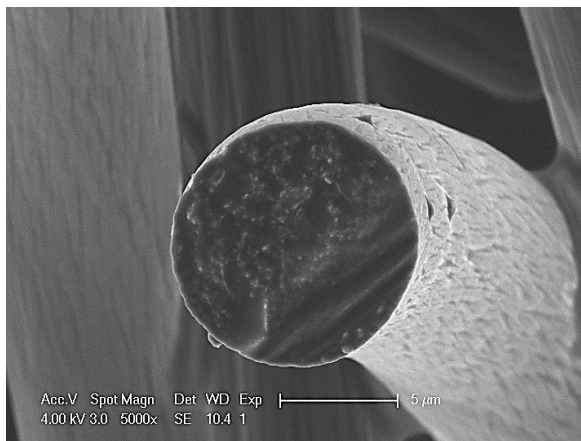


SFC1aSI

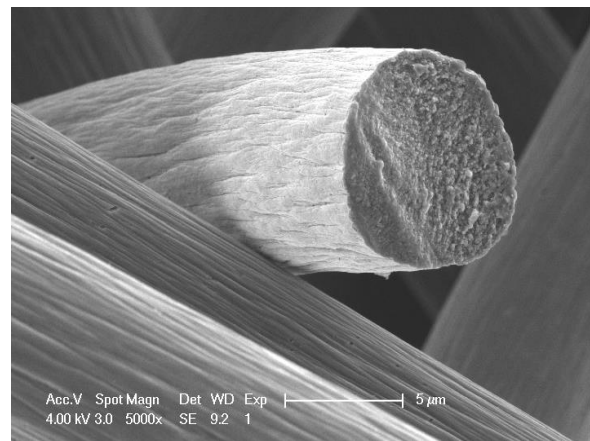
Figure II/3-11 Fibre structure and cross-section of Rayon soft CFs.

The observed PAN-derived fibres mostly have a cylindrical shape, with shallow grooves along the axis (seen in Fig. II/3-12 and 13 and in more details in Fig. II/6-2 and 3). As reported by Qian et al. (2016), the observed longitudinal grooves should be formed during the wet spinning process of the PAN precursor and the formation of the fibre. In addition, as described by Wu et al. (2016), the differences observed in the shape and the appearance of the grooves may result from the various oxidation treatments in the CF manufacturing process.

From the SEM micrographs, two different groups of soft CFs were recognised, with average fibre diameters of 9-10.5 μm on the one hand, and of 18-20 μm on the other hand (see Fig. II/3-12 and 13). The group of two rigidized PAN-derived CFs was formed from fibres with a similar diameter to that of the PAN-derived (thin fibre) soft CFs group, with average fibre diameters between 17 and 19.5 μm . Deviations of the average fibre diameters seen for the PAN-derived CFs are only observed due to the presence of carbon fibres of different diameters. Clear core-rim structure, as previously observed by Rabbow et al. (2015), or any other obvious inner fibre structure orientation was not recognisable for the obtained micrographs at the used magnifications. Further morphological and structural analysis of the investigated fibres are presented in Chapter III, through the assessment of the carbon nanostructure by use of Raman spectroscopy and XRD.

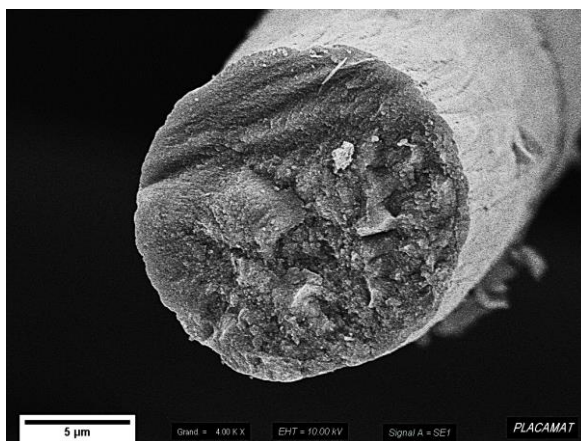


SFC2aZF

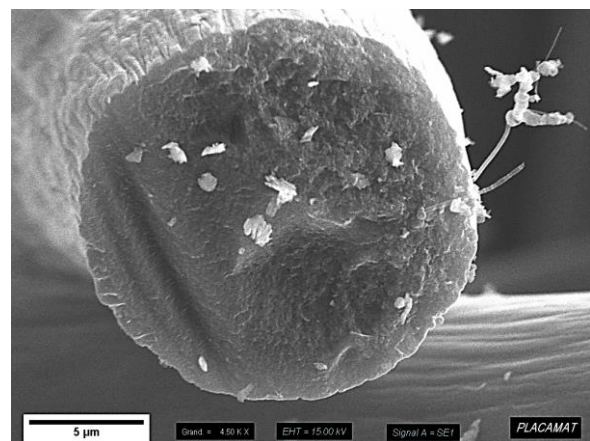


SFG2aC

Figure II/3-12 Fibre cross-section of PAN (thin fibre) soft CFs.



SFC2bBG



SFG2bBG

Figure II/3-13 Fibre cross-section of PAN (thick fibre) soft CFs.

II/3.1.d Tomography – CF morphology studies

An essential understanding of non-woven porous media morphology depends on in-depth knowledge of their micro-scale internal structure. In addition to SEM analysis, CFs were morphologically studied with X-ray micro-computed tomography (μ CT). As SEM analyses are restricted to the outer parts of the samples, μ CT proved that they can be good representatives of the entire bulk, suggesting that the commercial CFs are highly reproducible. Selected samples from the defined groups of CFs were submitted to μ CT analysis and realistic 3D images of their structure were obtained from the recovered 2D slices. Two Rayon-derived, two PAN-derived soft CFs and one rigid board CF, were imaged because of the previous analysis of morphological and porosity dissimilarities, resulting from the combination of different manufacturing treatments that are exclusive to each supplier and defined CF group. Although the obtained scans were performed at low resolution, still the technique was able to provide valuable information on the fibre volume and orientations in the CFs.

The imaging results can be found in Fig. II/3-14 to Fig. II/3-16 seen as photorealistic renderings of the IP/OP materials' profiles and 3D view of the CFs structure. Thus, for each material, an additional table is presented in the figures with details on the averaged fibre orientations in the x-,y- and z-axis. This average fiber orientation was estimated at the microstructural level using the fibre analysis software module (VGStudio MAX – Volume Graphics). For precise analysis results, a specific simulation mesh⁶ is directly imported into the software, allowing the calculation of averaged fiber orientation for each of the mesh cells.

Apart from the averaged fiber orientation, the above-explained analysis also provides information on the fibre volume fraction, derived from grey-scale analysis. Table II/3-2 shows the porosity of the CFs, calculated from equation (II/1) and the pore volume fraction (pore volume fraction = 100 – scanned fibre volume fraction) of a defined cylindrical volume in the field-of-view of the μ CT analysis. It is found that the computational estimations of the pore volume fraction, directly from the 2D slices (grey-scale analysis), is in good correlation with the calculated overall porosity, thus higher deviations were observed only for the SFG1aSC and SFG2bC. In both cases, the difference could be due to the cutting of cylindrical samples of very small diameter and lower number of heterogeneously distributed needle-punched connection

⁶ The mesh consists of discrete geometrical and topological cells (subdivisions) from continuous geometric spaces. Usually, mesh cells are discrete local approximations, simplifications, of a complex geometry under study, partitioning the geometric input domain. Meshes are created by the execution of computer algorithms. The final goal of these mesh cells is to accurately captures the geometry of the input domain, with the highest possible resolution and the smallest number of cells, to allow further processing of the calculations.

fibres, which had a slight impact on the increase of the volume of the sample. The computed value should also be handled with caution because the fibre volume fraction is calculated on grey values and the areas between neighbouring carbon fibres can be misinterpreted as fibre regions. Therefore, the overall pore volume fraction could be underestimated, as in the case of chemically bonded RBG1aC.

Table II/3-2 Comparison of porosities (%) calculated and from equation (II/1) and deduced from μ CT images analysis.

SAMPLE CODE:	Overall porosity fraction	Imaged porosity fraction
Rayon soft CF		
SFG1aBG	94.6	94.42
SFG1aSC	92.7	96.45
PAN (thin fibre) soft CFs		
SFC2aZF	93.4	93.53
PAN (thick fibre) soft CFs		
SFG2bC	93.8	96.98
Rayon rigid board CFs		
RBG1aC	87.5	86.04

All examined soft CFs showed a clear needling pattern, yet with different frequencies of needle-punch marks and in a good correlation with the SEM analysis. μ CT also gives quantitative information on the carbon fibre orientations. The fibres in the soft CFs are mainly randomly and homogeneously oriented in the x-y plane, with exception seen for SFG2bC. This difference might be observed due to the use of a highly directional layering technique during the pre-fabrication of this CF and prior to the needle-punching process. Further, the differences in the z-axis fibre orientations are the result of the needle-punching process, which creates different fractions of fibre entanglements in the OP direction. While Rayon-derived soft CFs and SFG2bC (PAN-derived (thick fibre) soft CF) present a lower fibre orientation in the OP direction, compared to the IP direction, the SFC2aZF (PAN-derived (thin fibre) soft CF) is much more influenced by the needle-punch barbed needles, as observed in Fig. II/3-15 b). The increase in the needle-punch density decreased the fibre orientation in the IP direction by reorienting more fibres in the OP direction, resulting in the identical distribution of fibres within each the CF x-,y- and z-axis.

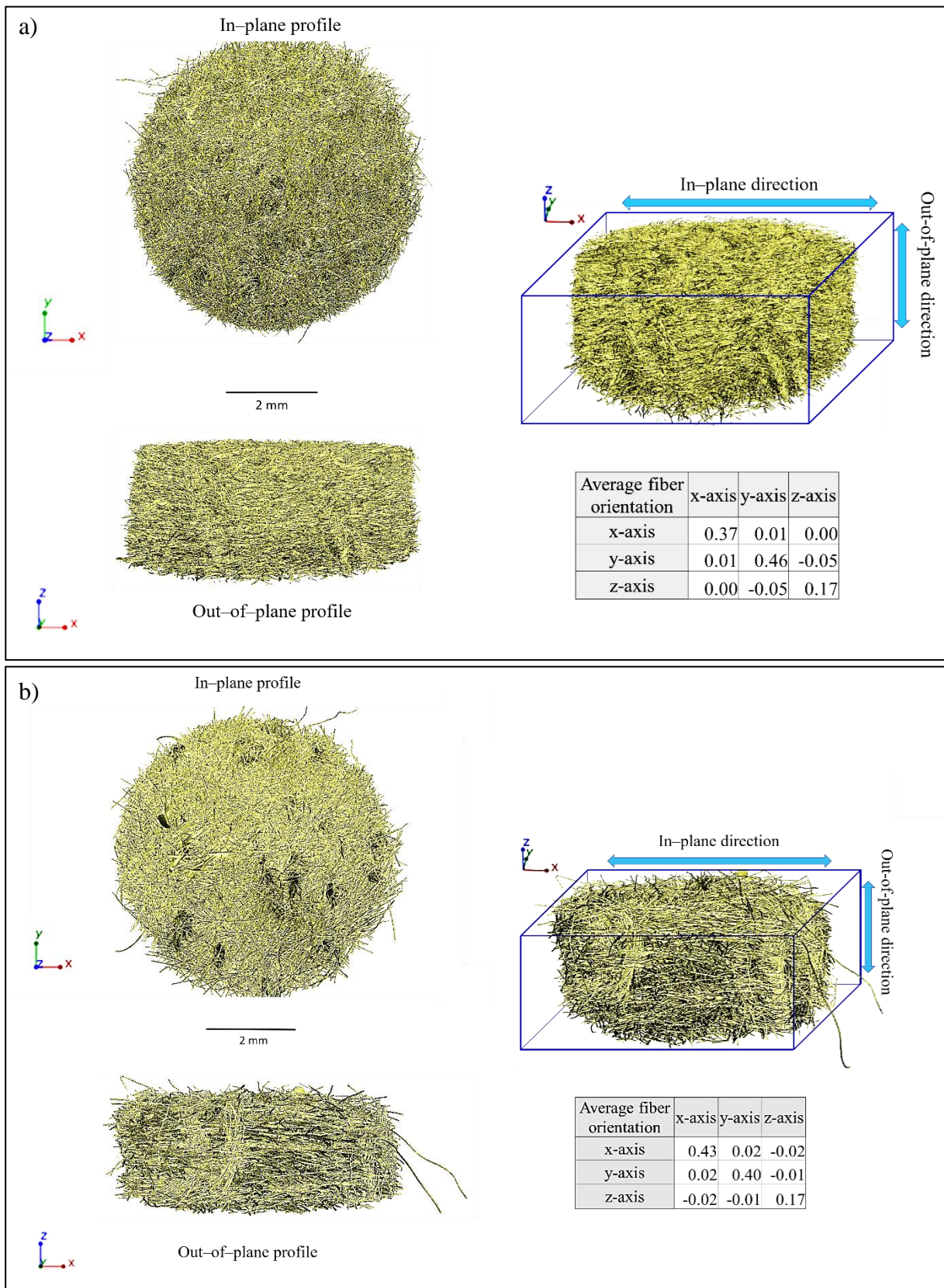


Figure II/3-14 3D rendering of the μ CT binarised data in IP profile (xy view), OP profile (xz view) and 3D reconstructions of Rayon soft CFs: a) SFG1aBG and b) SFG1aSC; additional tables present averaged fibre orientations in the scanned x,y and z axis, respectively.

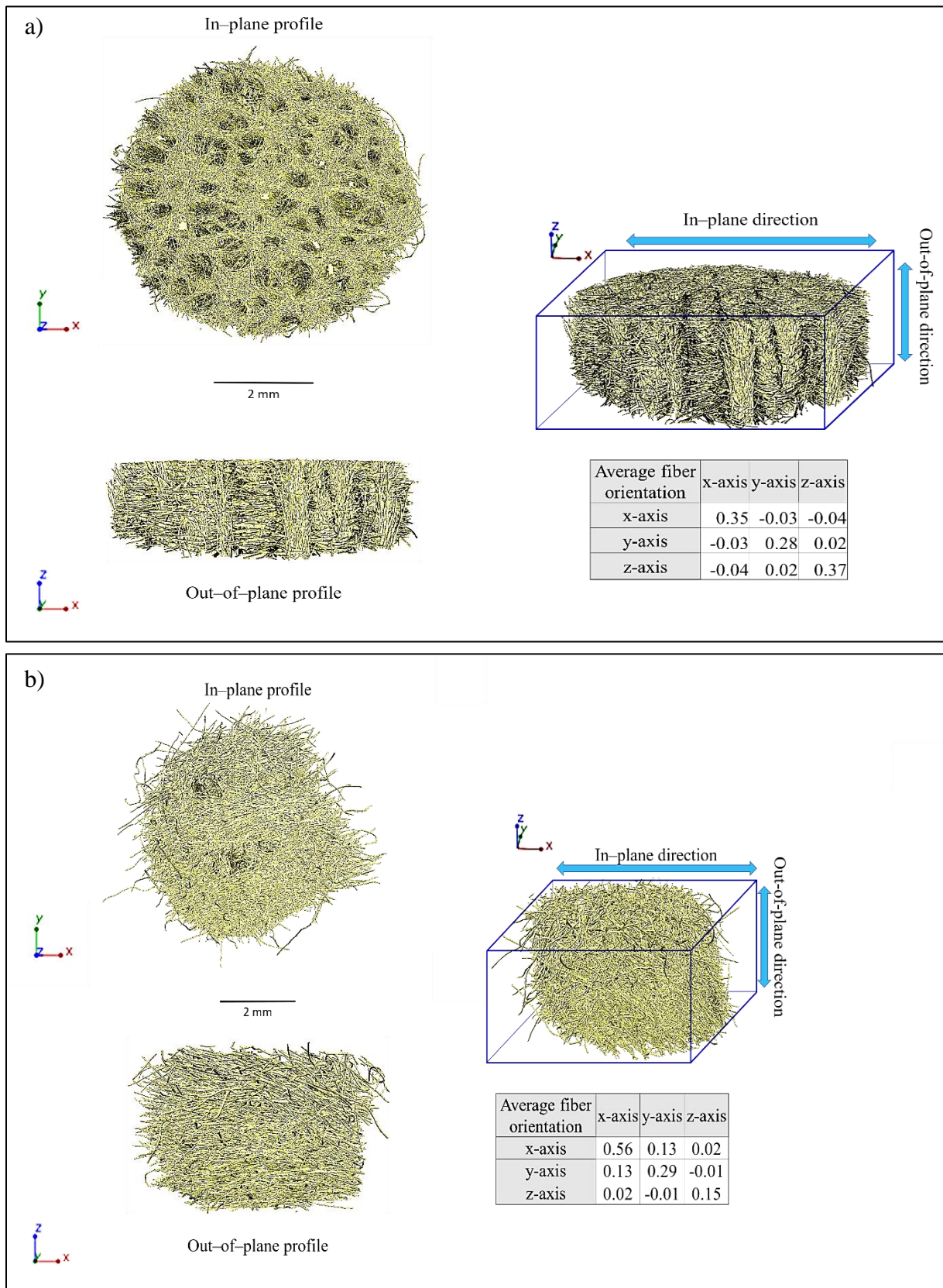


Figure II/3-15 Same as in Fig. II/3-14 but for PAN-derived soft CFs: a) SFC2aZF (thin fibre) and b) SFG2bC (thick fibre).

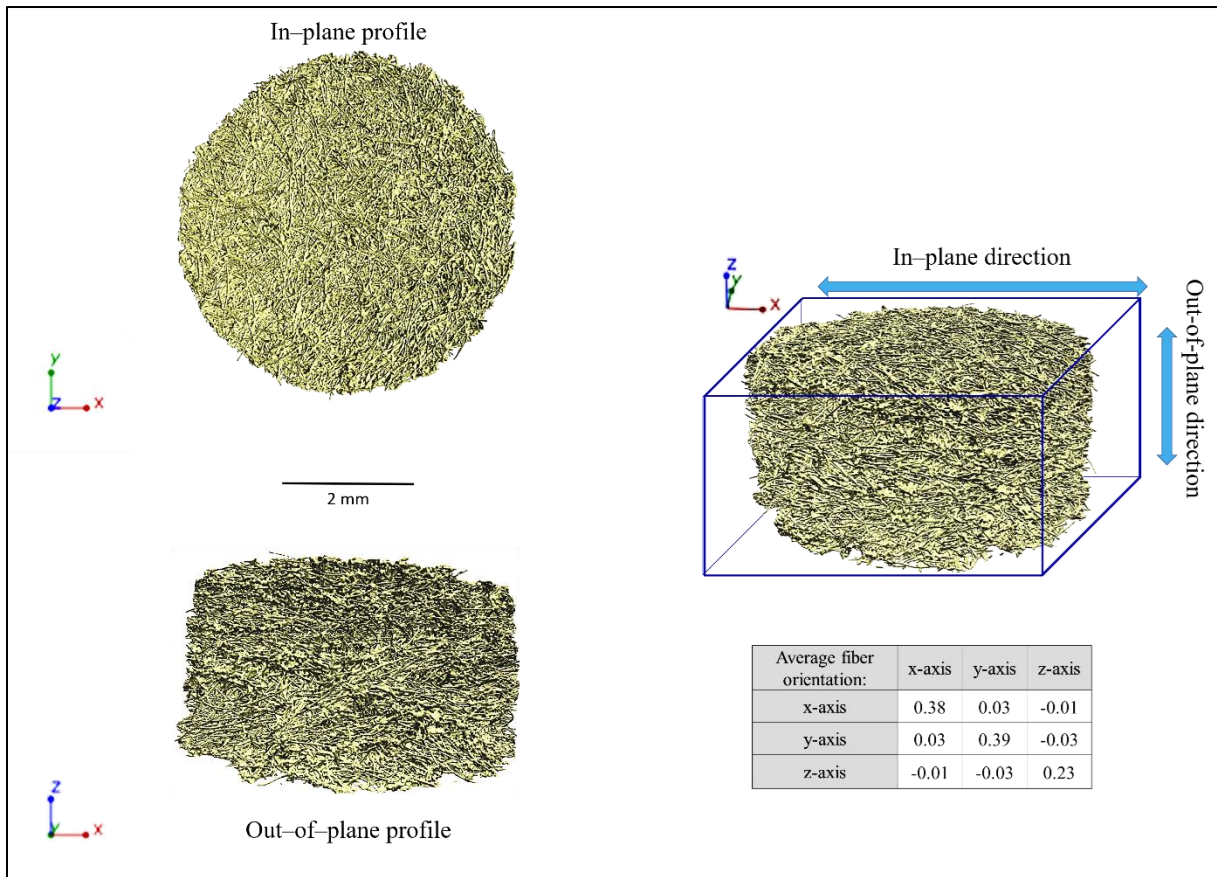


Figure II/3-16 Same as in Fig. II/3-14 but for Rayon rigid board CFs: RBG1aC.

The figures also highlight appreciable morphological differences between rigid board RBG1aC and the soft CFs. The manufacturing technique used in the production of rigid board RBG1aC again results in nearly transversely isotropic materials' morphology. However, the RBG1aC presents numerous clusters and bundles of fibres due to the chemical bonding manufacturing process, not present in the needle-punched CFs. Therefore, the RBG1aC is assumed to be fabricated by overspreading of carbon fibres along the IP direction. However, the use of organic binder and the observed variation of fibres length (seen as chopped or recycled carbon fibres of different lengths) finally yields a slightly modified CF morphology, and increased OP fibre orientation of the highly interconnected fibre network.

Different computer simulations were recently coupled with μ CT to study the effect of micro-structure on permeability, compressibility and thermal conductivity of fibrous media (Vignoles 2015; Jaganathan 2008; Panerai et al. 2017; Soltani, Johari, and Zarrebini 2015; Soltani et al. 2017). Seen as a promising strategy, similar studies should allow future integration of the CF into new areas of use, such as the TES, by comparing the computed data with the experimental data.

II/3.2 Wettability studies

The wettability of the CFs may depend to some extent on felt structure, fibre surface roughness, and chemical heterogeneity. Since the examined CFs are anisotropic materials, the impregnation of the CFs should also depend on the flow direction in the defined principal directions. Therefore, the wettability tests were performed on the IP surface or in the OP direction, and in agreement with the planned strategy for their future impregnation with molten PC. The performed contact angle measurements with water always showed similar values. However, Rayon-based soft CFs showed slightly lower contact angles with water than the more hydrophobic PAN-based materials. The measured contact angle values ranged from 121.5 to 150.7°, placing the samples in the range of hydrophobic to super-hydrophobic materials. Average contact angle values and contact angle deviations of the groups of CFs and for each separate sample are presented in Figure II/3-17 and Table II/6-3.

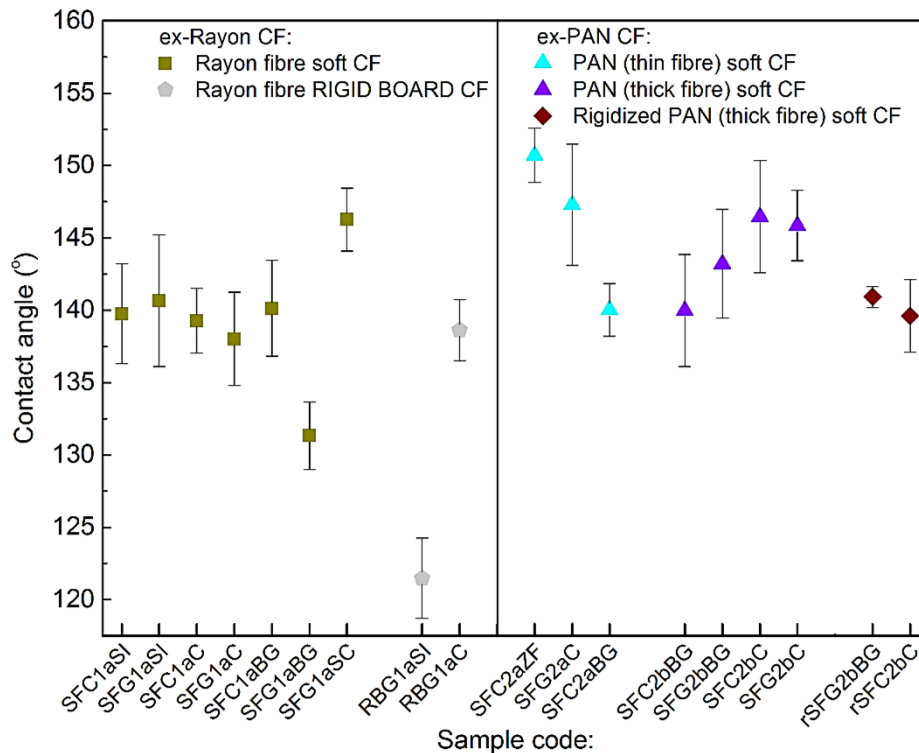


Figure II/3-17 Averaged contact angle values for each of the commercial CFs.

It was observed that there were no significant differences between the samples in each group, except separate cases such as SFG1aBG and RBG1aSI, where the difference in the CF IP surface and fibre morphology resulted in lower contact angle with water. In the case of RBG1aSI, the significant contact angle difference with respect to RBG1aC (from the same group) might also be due to the observed fibre agglomerations differences in the IP surface morphology (seen in Fig. II/3-7).

The high importance of the felt surface morphology can also be confirmed by the similar contact angle results for the corresponding CFs, such as SFC1aSI → SFG1aSI, SFC1aC → SFG1aC, and SFC2bC → SFG2bC. Although a clear difference was observed from their results of elemental analysis (presented in Chapter III/3.1), suggesting a different presence of functional groups, the results concerning the contact angle do not follow the same trends. The opposite was observed by Park and Kim (2005) and Zhang et al. (2016), who performed ozone treatment or surface etching of GF to increase oxygen-containing functional group presence, resulting in improved wettability with water. The comparison of their results with the present ones suggests that, although the corresponding CFs demonstrate different elemental composition, the foreign elements/groups (especially oxygen-containing groups) are more present in the carbon fibre core than on its surface. As reported by Shen, Li, and Liu (2008), heat treatment of carbons under inert atmospheres (such as nitrogen) flow should increase carbon hydrophobicity by removing hydrophilic surface functionalities, particularly various oxygen groups.

In all studied materials, the water droplet retained its spherical shape, as already observed for PAN-derived carbon felts (Rabbow et al. 2015). Figure II/3-18 shows photos of water droplets deposited on SFG1aSI (Rayon soft CF) and rSFG2bBG (rigidized PAN (thick fibre) soft CF), taken 60 seconds after the water drops were deposited on the felt surface.

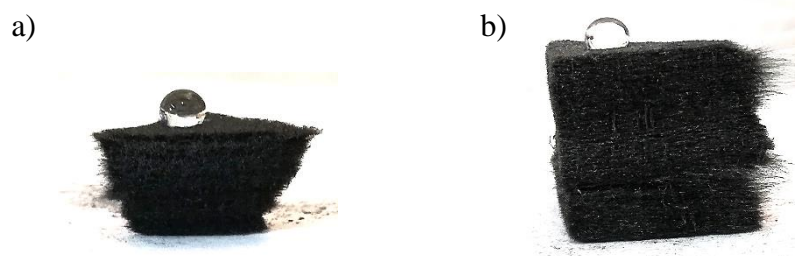


Figure II/3-18 Photos of water dripped on SFG1aSI (a) and rSFG2bBG (b); taken 60 seconds after deposition.

Moreover, measuring contact angles with water might not provide information about their behaviour with other liquids, such as molten PCs. This is a reason for additional studies on other liquids and on the surface energy of the evaluated CFs. Yet when performing the same experiments with other liquids, the liquid drop immediately sinks into the felts' interior, regardless of the examined CF. The improved wetting might occur due to the higher surface energy of the hydrophobic carbon fibres surface compared to that of the testing liquid, opposite to what was observed when the test was performed with water, as previously seen by Zhang

(2012). The improved wettability of the CFs with ethylene glycol and diiodomethane validated the need for applying other techniques for the measurement of the contact angle and the surface energy of the examined CFs.

Capillary wicking (spontaneous impregnation) tests were additionally performed with the use of a force tensiometer (see Fig. II/3-19) and different liquids following a protocol explained by (Pucci, Liotier, and Drapier 2015). The cited authors modified and extended the Washburn equation defining the spontaneous capillary rise in a single capillary tube, to describe the capillary wicking in a porous material, resembling a bundle of capillary tubes. The contact angles as previously shown are measured in static conditions (as explained in II/2.6), yet due to the envisaged dynamic impregnation of the CFs, it should be more correct to determine a dynamic advancing contact. To our knowledge, this method was not previously used to evaluate both morphological characteristics of porous media and apparent advancing contact angle of CFs. Therefore, wicking tests were carried out in the OP directions of one needle-punched soft CF sample (SFC2aZF). Different liquids should be selected with differences in their surface tension, especially in terms of polar and dispersive components. The use of *n*-hexane is compulsory due to its low surface tension and the absence of a polar component, resulting in a totally wetting liquid, necessary for calculating the geometrical parameters of the fibrous medium. Performing experimental tests with *n*-hexane, the square mass variation as a function of time (seen in Fig. II/3-20 a)) is obtained, and the Washburn equation is used to calculate the geometrical parameters of the evaluated CF. Afterward, additional tests are performed with other liquids and by the use of the same equation (with integrated geometrical parameter) the apparent advancing contact angle is calculated. However, the relation of the experiments with the Washburn model is valid only if, during capillary wicking, a linear trend is well verified from the curves recorded by the tensiometer.

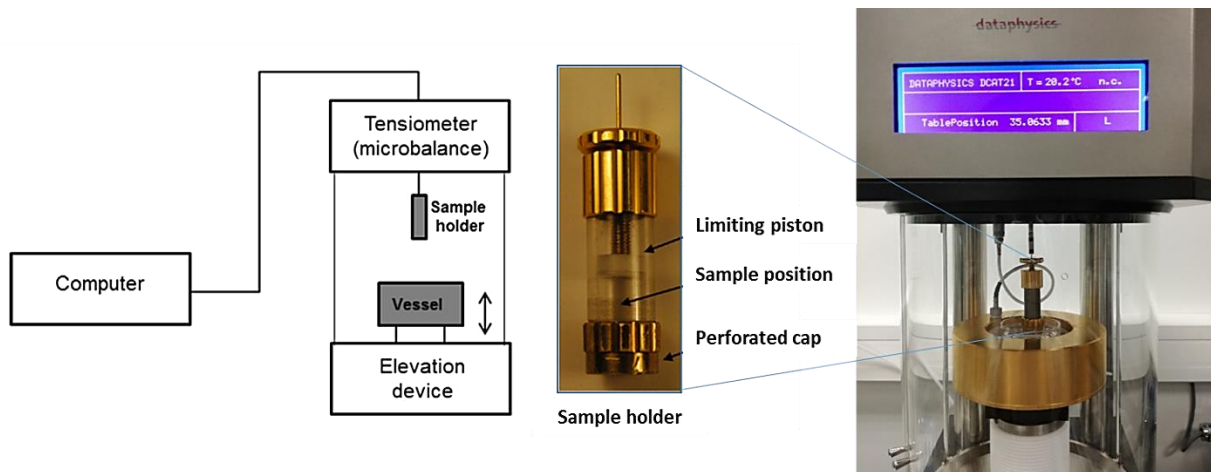


Figure II/3-19 Schematic (left) and real (right) representation of tensiometer (Dataphysics DCAT21) and cylindrical sample holder (right).

A constant value of the geometric porous medium factor was calculated from the linear fit of the initial linear part of the Washburn curves obtained with *n*-hexane (seen in Fig. II/3-20 a)). However, after the initial linear part, a change of slope was observed before reaching saturation of the CF by the test liquid and weight equilibrium. The change of slope was observed due to the stacking of two samples on top of each other to fill the required minimum sample size and ensure good contact with the limiting piston, thus making it possible to fix the position and the porosity of the CF during the measurement. To avoid this issue, samples with a thickness greater than the required minimum sample size should be used, avoiding additional intersections in the felt morphology, especially in the OP direction.

Nevertheless, further experimental tests did not yield accurate results since the initial linear part of the Washburn curves was sometimes not obtained, thus preventing the calculation of the dynamic contact angle. As a result, the estimation of advancing contact angles with different liquids, thus of the surface energy value of the evaluated CFs, could not be achieved. In both cases with water and ethylene glycol, with a high polar component, the capillary wicking was not achieved. A slight weight increase was observed due to the wetting of the thin filter paper (seen in Fig. II/3-20 b) and d)), added between the sample holder and the tested CF to ensure complete wetting of the samples' front and suppress additional uncertainties. The main reason for the lack of wetting in the capillary wicking experiment is the high hydrophobicity of the evaluated CFs. Therefore, the results suggest that there are few or no polar function groups on the carbon fibre surface, in good correlation with the performed static contact angle measurements. The tests performed with diiodomethane (see Fig. II/3-20 c)) showed a non-linear increase in weight as a function of time and absence of weight equilibrium

even after 400 seconds. Apart from the presence of a polar component of the test liquid, other reasons for this behaviour should come from the high porosity and permeability of the evaluated CF. According to Chwastiak (1973), in order to observe capillary wicking, the capillary effects should overcome the viscous flow effects, which is much more difficult to be achieved within materials with high porosity and thus high permeability.

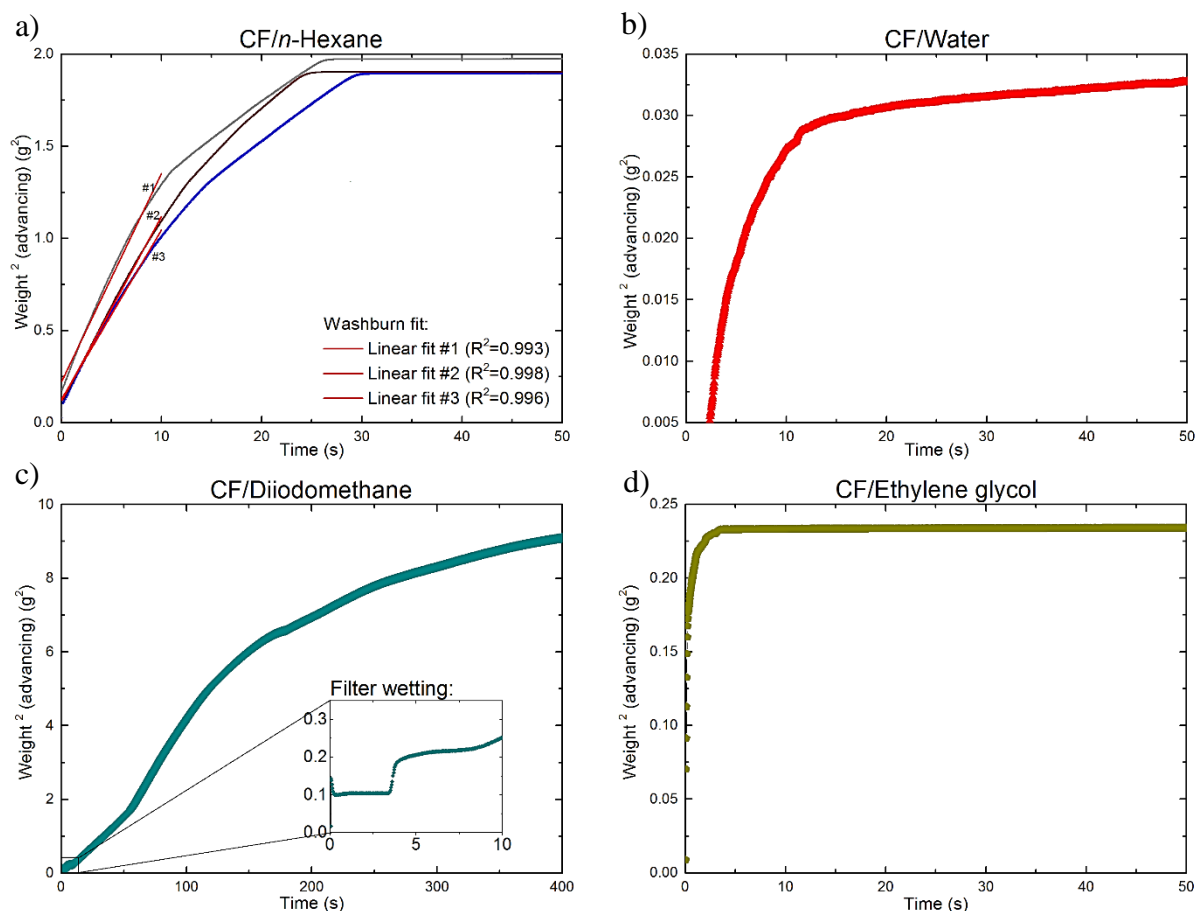


Figure II/3-20 Washburn curves performed to determine the CFs' geometric factor with (a) *n*-hexane and the apparent advancing contact with: b) water, c) diiodomethane, and d) ethylene glycol in the OP direction.

The calculation of the surface energy values should allow us predicting how well the solid will be wetted by other liquids, and also should give better estimations of the CF wetting with the molten PC. Therefore, a future study of the solid surface energy should also be addressed thanks to a novel gravimetric vapour sorption analysis with two other liquids to finally provide a general estimated surface energy value of the materials of interest.

II/3.3 Physical properties

II/3.3.a Out-of-plane air permeability

II/3.3.a1 CF out-of-plane permeability results

Studying the fluid transport behaviour in CFs becomes of considerable interest as soon as their infiltration is considered for producing the foreseen hybrid CF-PC composites. Fibre architecture and surface chemistry, permeability and tortuosity, liquid viscosity and temperature are quantities known to influence the infiltration process of non-woven materials (Park 2015). Therefore, any difference in fluid transport properties is important information to know before selecting one or the other fibrous material for making composites. The corresponding values of out-of-plane (OP) permeability are given in Table II/6-4 and are presented in Fig. II/3-21, as a function of either porosity a) or fibre diameter b), respectively.

Indeed, as previously observed elsewhere (Kok and Gostick 2015; Soltani, Johari, and Zarrebini 2014; Soltani et al. 2017), the porosity or fibre diameter are the main ones that affect fluid flow through fibrous porous media. The various structures of the present materials, however, did not allow observing any universal trend when all CFs were considered together. Nevertheless, and as expected, porosity-dependent permeability could be observed within individual families and subgroups of materials: see Fig. II/3-21 a). Thus, in most needle-punched soft CFs, the permeability increased with the overall porosity. However, clear deviations from this logical behaviour were also seen in the groups of Rayon-derived soft CFs and thick-fibre PAN-derived soft CFs, lower porosity sometimes leading to higher permeability. This might be explained by different manufacturing-induced morphological properties of the materials, especially in terms of the number of fibre webs and of needle-punching effect. The morphological differences induced by the CF' fabrication process can be clearly seen from the performed SEM micrographs (seen in Fig. II/3-3) and tomography realistic 3D images (seen in Fig. II/3-14). For example, the observed wider needle-punched marks in SFG1aSC, compared to SFG1aBG, should influence the higher permeability at lower porosity.

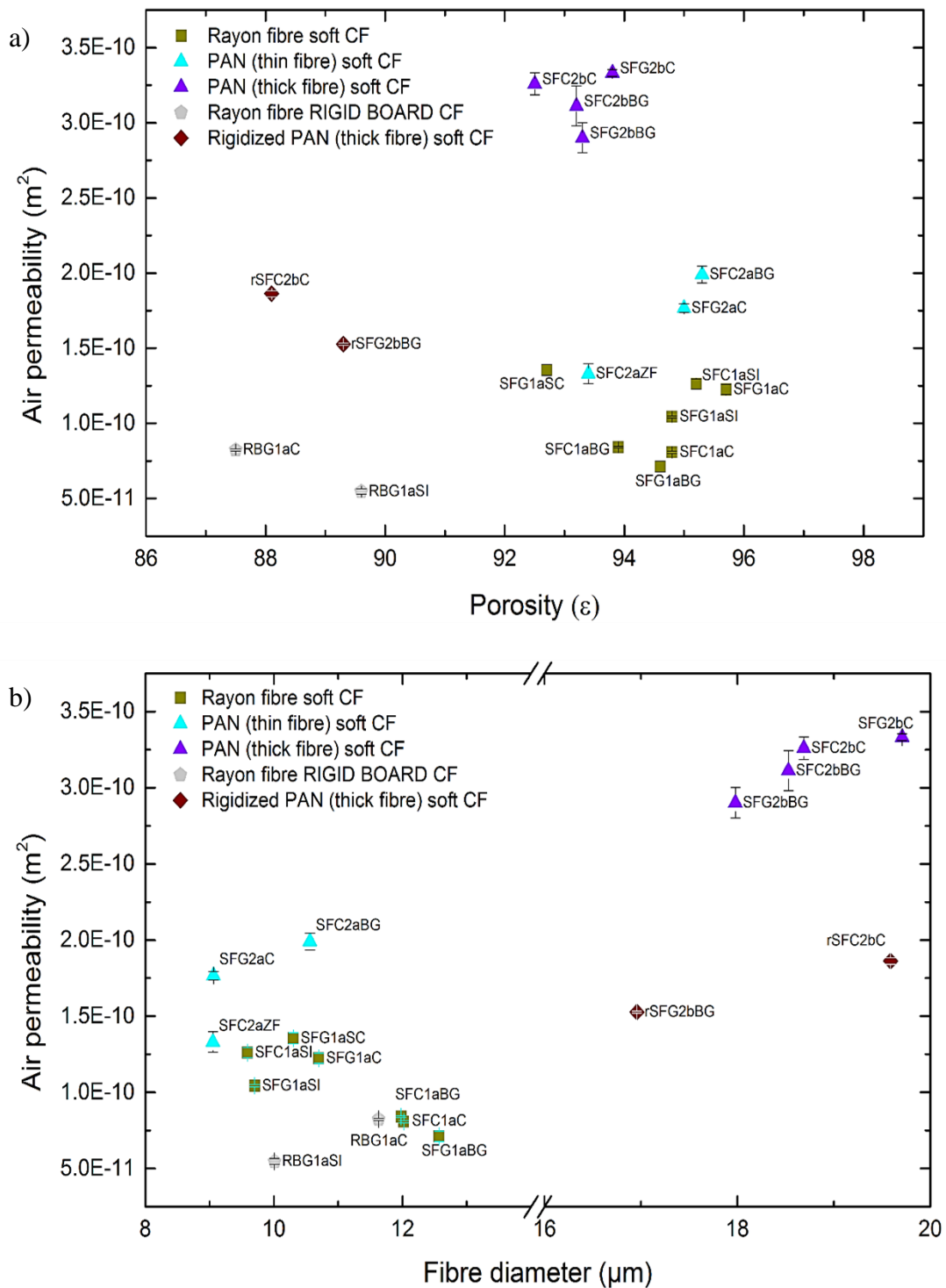


Figure II/3-21 Out-of-plane permeability of all materials, as a function of: a) overall porosity, and b) average fibre diameter. Each symbol represents a given CF group, and the same symbols with different colours represent materials from different sub-groups of the same group.

Due to their higher carbon fibre volume fraction, and to binder between fibres blocking and narrowing the pores, Rayon-derived rigid board CFs had lower permeability than most needle-punched soft felts, rigidized or not, as also observed elsewhere (El-kharouf et al. 2012; Park 2015). The same kind of conclusion applies to thick-fibre PAN-derived CFs, the rigidized ones being clearly less permeable than the soft ones, which were free of chemical bonding. Furthermore, no increase of permeability with porosity was observed in the groups of Rayon-derived rigid board CFs and thick-fibre PAN-derived rigidized soft CF. As observed from the mercury porosimetry results in Fig. II/3-2 and SEM micrographs in Fig. II/3-7, RBG1aC indeed differ in terms of pore size distribution and fibre interconnections compared to RBG1aSI, which results in higher permeability at lower porosity.

As for the effect of fibre diameter, shown in Fig. II/3-21 b), opposite effects were observed: the permeability of rigidized and non-rigidized thick-fibre PAN-derived soft CFs increased with fibre diameter, whereas that of Rayon-derived soft CFs decreased. It can also be seen that Rayon-derived materials presented lower permeability than their PAN-derived counterparts did in similar ranges of porosity and fibre diameter. In addition to the aforementioned effect of the morphology differences induced by the fabrication methods, the Rayon-derived fibres indeed present highly inhomogeneous surfaces and non-circular cross-sections compared to the smooth and almost cylindrical PAN-derived fibres (see Fig. II/3-11, 12 and 13). All other things being equal, this may cause a higher drag to the fluid flow in Rayon-derived materials, thus lowering their permeability.

Comparing Fig. II/3-21 a) and b) also evidenced that the airflow permeability of materials made of thicker fibres is slightly higher than those made of thinner ones, whereas their porosity is generally lower than that of non-wovens made of thin fibres. Indeed, and as reported by other authors (Hung et al. 2013; Fadzillah et al. 2017), decreasing the fibre diameter increases their contact area and reduces the average pore size, all other things being constant.

Plotting the ratio of permeability k to squared fibre radius r^2 thus appears to be a better option. Because it is dimensionless, k/r^2 is called reduced permeability, and it is the quantity most frequently used for characterising fluid flow through fibrous materials (Tomadakis and Robertson 2005). The corresponding graph is given in Fig. II/3-22 and the data indeed appeared less scattered than in Fig. II/3-21 a). However, given that several families of materials are considered together, still, one single trend could not be observed, but a general trend appeared, according to which k/r^2 increases with porosity (ϵ). Since the materials of interest are generally

extremely complex and difficult to characterise, attempts were made below to model such behaviour and to find a universal relationship embracing all measured values.

II/3.3.a2 Theoretical background of permeability

The permeability properties of fibrous non-woven materials have been many times investigated by the use of experimental, analytical and numerical manners. Having this in mind and with the aim of obtaining better correlations between the CFs' properties and permeability measurements, supplementary investigations are needed for their comparison with permeability models and experimental values found in the literature.

Generally speaking, three basic standard structures: granular, tubular and fibrous, have been considered from which permeability-porosity relationships have been suggested. The corresponding equations have been, and still are, improved by considering different approaches and refinements, among them the variational bounds theory, based on statistical correlation functions between pore structure and permeability (Soltani et al. 2017), the percolation theory, which considers the porous medium as a random medium without spatial correlation (Hunt and Ewing 2009), or the fractal theory, describing the porous structure with statistical geometrical self-similarities (Cai et al. 2015). The roughness and the complexity of the pore surface, quantified by the fractal dimension of the porous medium under consideration (Henderson, Brêttas, and Sacco 2010), indeed have a strong impact on the permeability.

In the former studies, obvious observations were noticed such as an increase of permeability with the open porosity of the medium, and then these trends were successfully accounted for by application of the Kozeny-Carman equation. The well-known Kozeny-Carman equation (Carman 1937) can take various forms such as:

$$k = \frac{\varepsilon (V_p/S_p)^2}{2 \eta_v} = \frac{\varepsilon r_h^2}{8 \eta_v} = \frac{\varepsilon r_h^2}{4 K_c} = \frac{\varepsilon^3}{K_c S_b^2} = \frac{\varepsilon^3}{K_c S_s^2 (1-\varepsilon)^2} \quad (\text{II/6})$$

where k and ε are again the permeability and the porosity, respectively. V_p and S_p are the volume and the surface of the pore space, respectively. η_v is the tortuosity factor for viscous flow, i.e., a ratio of the average fluid path through the porous material to material thickness, in viscous flow conditions. $r_h = 2V_p/S_p$ is the hydraulic radius. $K_c = 2\eta_v$ is called Kozeny constant ($K_c = 2$ for straight cylindrical tubes whereas $K_c \approx 5$ for many porous materials). $S_b = \varepsilon/(V_p/S_p)$ is the internal accessible surface area per unit volume of bulk material, and S_s is the same but expressed by unit volume of solid material so that $S_s = S_b/(1-\varepsilon)$. In the context of fractal

mathematics, the Kozeny-Carman equation may also be written in the following, more general form (Henderson, Br ettas, and Sacco 2010):

$$k = C \frac{\varepsilon^{\alpha+2}}{(1-\varepsilon)^n} \quad (\text{II/7})$$

where C is a coefficient including the geometrical parameters of the porous medium, α is called Archie's constant, and n is a real number corresponding to the fractal dimension of the medium. It should be mentioned here that $n = 1 + \alpha$ (Bayles, Klinzing, and Chiang 1989), and hence the fractal dimension has the same physical meaning as Archie's exponent. By definition, Archie's exponent is directly related to the formation factor (see below) that allows estimating the tortuosity factor, for example. For geologists, it plays the same role as the cementation index (Sen, Scala, and Cohen 1981) and, for mathematicians, the same as the fractal dimension.

Usually, the parameters C , α and n are determined by fitting equation (II/7) to experimental data corresponding to different materials or materials categories (Jackson and James 1986). However, calculations show that estimating the permeability with such equations is much more difficult for a fibrous structure than for any porous medium. Indeed, a deviation between experimental and calculation results from equation (II/6) is observed for porosities higher than 0.2 (Xiao and Yin 2016). This problem is related to the geometrical details of the porous medium such as shape, spatial distribution, orientation and volume fraction of fibres, having a significant impact on the tortuosity. Although tortuosity may have various definitions, depending on the considered phenomenon, this quantity is a way of describing the complexity of the structure of a porous material, i.e., how sinuous and interconnected it is (Letellier et al. 2014). Therefore, different fibrous geometries are still investigated today in order to get a deeper understanding and a better prediction of the structure-property relationships in materials models (Xiao and Yin 2016; Bargmann et al. 2018).

Nevertheless, some uncertainties and controversy have been reported. For example, Costa claimed that the value of Archie's exponent can vary from 1 to 4 in the case of the unified Kozeny-Carman equation applied to porous media, including fibrous ones (Costa 2006). Bayles et al. stipulated that the value of Archie's exponent can consistently be greater than unity, and that it is itself a function of both porosity and particle size distribution in the medium (Bayles, Klinzing, and Chiang 1989). Tomadakis and Sotirchos suggested a generalised Archie's law in order to estimate, explicitly, the bulk diffusion tortuosity η_b as a function of the porosity of the medium on the one hand, ε , and of the percolation threshold of the system on the other hand,

ε_p , i.e., the critical porosity below which the fluid flow vanishes. The bulk tortuosity differs from the viscous one by the fact that the former is derived from Brownian diffusion random-walk simulation results in a porous medium, and not from viscous flow throughout the same medium. In the case of randomly overlapping fibres, the bulk diffusion tortuosity reads (Tomadakis and Sotirchos 1993):

$$\eta_b = \left(\frac{1 - \varepsilon_p}{\varepsilon - \varepsilon_p} \right)^\alpha \quad (\text{II/8})$$

and this kind of structure also imposes that (Tomadakis and Sotirchos 1991):

$$r_h = -\frac{r}{\ln \varepsilon} \quad (\text{II/9})$$

where r is again the fibre radius.

Whereas the Kozeny-Carman model is based on a purely geometrical hydraulic radius, Johnson et al. developed a more accurate model based on a dynamical radius, Λ , which is an intrinsic measure of the dynamically interconnected pore size (Johnson, Koplik, and Dashen 1987). Therefore, it is a dynamical length scale directly related to transport, unlike the aforementioned hydraulic radius. In this context, the equation (II/6) becomes:

$$k = \frac{\Lambda^2}{8F} \text{ where } \Lambda = -r_h \left(\frac{d \ln F}{d \ln \varepsilon} \right)^{-1} \quad \text{and} \quad F = \eta_b / \varepsilon \quad (\text{II/10})$$

F is called formation factor and corresponds to the ratio of the bulk diffusivity of a chemical species in a fluid to the bulk diffusivity of this chemical species in a porous medium saturated with the same fluid. It thus represents a relative resistance to transport through a fluid with respect to a porous medium saturated with the same fluid.

Combining equations (II/8), (II/9) and (II/10), one finally gets the permeability-porosity relationship for porous structures made of randomly overlapping fibres of mean circular radius r (Tomadakis and Robertson 2005):

$$\frac{k}{r^2} = \frac{\varepsilon}{8 (\ln \varepsilon)^2} \left(\frac{\varepsilon - \varepsilon_p}{1 - \varepsilon_p} \right)^\alpha \left(\frac{\varepsilon - \varepsilon_p}{(1 + \alpha)\varepsilon - \varepsilon_p} \right)^2 \quad (\text{II/11})$$

Equation (II/11) behaves asymptotically like equation (II/7) when $\varepsilon_p \rightarrow 0$, $n = 2$ and $\varepsilon \rightarrow 1$. Tomadakis and Robertson recommended the values of α and ε_p reported in Table II/3-3, depending on the structure of the fibrous medium and on the main direction of the flow through it (Tomadakis and Robertson 2005). For instance, for a fluid flow parallel to perfectly

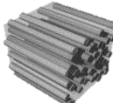
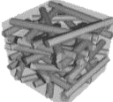
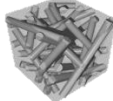
aligned fibres (i.e., the 1D // problem in Table II/3-3), $\alpha = \varepsilon_p = 0$; thus, the theoretical reduced permeability is the highest:

$$\frac{k_{1D//}}{r^2} = \frac{\varepsilon}{8 (\ln \varepsilon)^2} \quad (\text{II/12})$$

and the bulk tortuosity is obviously the lowest: $\eta_{b\ 1D//} = 1$. In the other cases, the tortuosity is always higher than 1, and for instance, the tortuosity factor for viscous flow reads:

$$\eta_v = \frac{k_{1D//}}{k} > 1 \quad (\text{II/13})$$

Table II/3-3 Archie's law parameters for the bulk diffusion tortuosity expressed by equation (II/13) (after Tomadakis and Robertson 2005).

Structure	Flow	ε_p	α
1D 	// to fibres	0	0
	⊥ to fibres	0.33	0.707
2D 	// to fibres layers	0.11	0.521
	⊥ to fibres layers	0.11	0.785
3D 	All directions	0.037	0.661

The Tomadakis - Robertson equation (II/11) is probably the most efficient one for fitting the permeability-porosity relationship of a number of fibrous media, as observed in many former studies (Gostick et al. 2006; Zamel and Li 2013; Soltani et al. 2017; Ke et al. 2018; Simaafrookhteh et al. 2018). For this reason, it will receive special attention in the next subsection. But former models should also be considered. For instance, the empirical model of Davies (1953), represented by equation (II/14), is supposed to fit the OP permeability data of highly porous fibrous materials whose porosity ε is higher than 70 %:

$$\frac{k}{r^2} = \left\{ 16(1 - \varepsilon)^2 [1 + 56(1 - \varepsilon)^3] \right\}^{-1} \quad (\text{II/14})$$

Tamayol and Bahrami (2011) investigated the OP permeability of several fibrous structures involving square, staggered, and hexagonal arrangements of unidirectional aligned fibres, along with simple 2D felts and simple cubic matrices. They proposed the following analytical equation:

$$\frac{k}{r^2} = 0.032\sqrt{\varepsilon} \left[\left(\frac{\pi}{4(1-\varepsilon)} \right)^2 - \left(\frac{\pi}{2(1-\varepsilon)} \right) + 1 \right] \quad (\text{II/15})$$

Van Doormaal and Pharoah (2009) used a Lattice Boltzmann approach for simulating fluid flow through idealised porous layers and a Monte Carlo method for generating their geometry. The resultant calculated permeability of random fibrous porous materials was fitted by the following equation:

$$\frac{k}{r^2} = 0.28 \frac{\varepsilon^{4.3}}{1-\varepsilon} \quad (\text{II/16})$$

Other fractal and mechanistic models have also been proposed by the group of Fan and Ding (Shou, Fan, and Ding 2011; Shou et al. 2013) and are not reported in detail here, although they have been tested as explained below.

II/3.3.a3 Application of the models to the experimental results

The values of reduced permeability measured by Gostick et al. (2006) on commercial fibrous carbon gas diffusion layers for fuel cells are introduced in Fig. II/3-22, in addition to the present results for the 18 CFs. As can be seen, no model was able to correctly fit a broad variety of materials, whose different structures explain why it happened that samples having higher porosities than others could have lower reduced permeabilities, and vice-versa. The model of Davies (equation II/14) underestimated the reduced permeability of all materials except the group of Rayon-derived soft CFs (see Fig. II/3-22 a)). The underestimation can be explained by the drag theory (Soltani et al. 2017), according to which the model does not take into account the lower drag performed from the fibres oriented along the fluid flow. The overestimation seen in the case of Rayon-derived soft CFs is explained by the preferential orientation of fibres perpendicular to the OP direction and the higher drag due to non-circular fibre cross-sections and rough fibre surfaces.

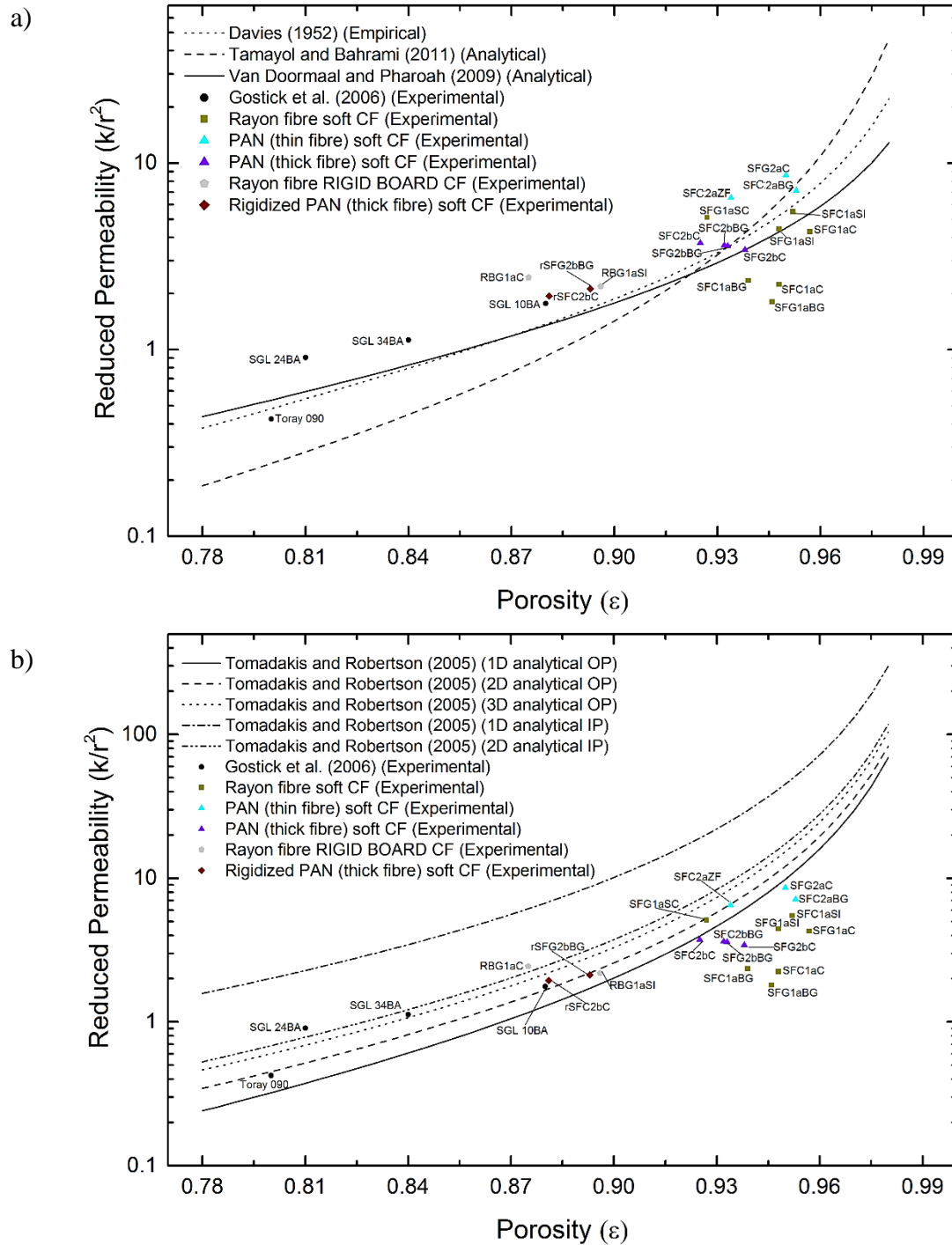


Figure II/3-22 Out-of-plane reduced permeability of all present materials as well as a few other ones from the literature, as a function of overall porosity. The symbols have the same meaning as in Fig. II/3-21. The curves correspond to the application of models of: (a) Davies (eq. II/14), Tamayol – Bahrami (eq. II/15), and Van Doormaal – Pharoah (eq. II/16); and (b) Tomadakis – Robertson (eq. II/11).

The same kind of conclusions also applies to the Tamayol – Bahrami model (equation II/15), for which the discrepancy between experimental and calculated values was found to be even higher (see again Fig. II/3-22 a)). These deviations are based on the differences between the model's assumption of perfectly layered structures, with fibres randomly oriented along the IP direction and layered orthogonally to the fluid flow, and the real non-woven materials structure, with random deflections in the fibre orientation. As previously shown in (Tamayol and Bahrami 2011; Cai et al. 2015; Soltani et al. 2017), and although most of the present materials have porosities outside the range formerly simulated in the original paper, the model of Van Doormaal – Pharoah (equation II/16) was worth testing as well because it refers to various porous transport layers including carbon fibre non-woven materials having a typical fibre diameter ranging from 7 to 12 μm . This model led to the curve having the lowest slope, thus passing closer to most groups of CFs, and hence producing the best compromise for the whole set of needle-punched soft felts (at a porosity ε higher than 92%). This can be explained by the very realistic approach of the simulation of porous layers made by Van Doormaal and Pharoah (2009). Moreover, these authors indicated that structures made of orthogonal neighbouring layers of randomly oriented fibres are a good approximation of random fibre structures, as proved by the statistical similarity of their OP permeability estimations.

Testing the models of Fan and Ding (Shou, Fan, and Ding 2011; Shou et al. 2013) produced exactly the same kind of curves as those shown in Fig. II/3-22. In other words, no improvement in the fits was obtained. The models preserved the shape of the evolution of the reduced permeability as a function of porosity in a manner similar to the other analytical models presented in the manuscript. However, we have observed that due to some morphological differences, samples with higher porosities than others may have reduced permeabilities, and vice-versa. Therefore, as we have seen above, the suggested models remain very dependent on fitting parameters, thus estimating correctly the permeability of the material only at lower or higher porosity.

Finally, and unlike most other research works dealing with one family of fibrous mats having different porosities, fitting equation (II/11) with the parameters of Table II/3-3 was again impossible for all materials together, as it clearly overestimated the reduced permeability in most cases, see Fig. II/3-22 b). The agreement between experimental and predicted values was only fair in the range of low to medium porosities investigated here, and especially in the case of thick-fibre PAN-derived rigidized soft CFs and Rayon-derived rigid board CFs, considering these materials as intermediates between 2D \perp and 3D random structures. The reduced

permeability of only two soft CFs, SFG1aSC and SFC2aZF, was even exactly the one predicted by the 3D Tomadakis – Robertson model. The feature shared by the last two materials is the wider size of needle marks and high needle-punching density, observed by tomography (see Fig. II/3-14 b) and Fig. II/3-15 a), respectively), compared to the other soft CFs. These results suggest that some needle-punched and/or chemically bonded samples can be well represented by equation (II/11), as previously observed by Soltani, Johari, and Zarrebini (2013). The rest of the investigated materials' reduced permeability values were definitely lower than what was predicted by any form of Eq. (II/11), including the one corresponding to the 1D \perp structure, which leads to the lowest possible values.

Nevertheless, it should be stressed that finding Tomadakis' model as the most suitable one is logical since the corresponding equation contains the largest number of free parameters such as ε and F , themselves containing implicitly Archie's exponent or fractal dimension (see again Subchapter II/3.3.a1). The other models are all derived from the unified Kozeny-Carman equation with α fixed by fitting and with only one free parameter, ε . Besides, Tomadakis' model also considers ε_p , which is not the case for the other models and this is the reason why it better fits the experimental values collected from the literature. However, in the case of most CFs, the calculated reduced permeability is still overestimated, as seen in Fig. II/3-22 b). When $\varepsilon \rightarrow 1$, Tomadakis' model converges towards its asymptotic value $C/(1-\varepsilon)^n$, where C is the same coefficient as in equation (II/7) and where $n = 2$. The discrepancy observed in Fig. II/3-22 b) at high porosity thus means that the values of C and n are not the right ones for our materials when $\varepsilon \rightarrow 1$, and hence the highly porous CFs are not correctly represented by the standard 1D, 2D and 3D "flow structures" shown in Table II/3-3.

Moreover, the multi-layered consolidated structure of the present fibrous CFs provides a much higher resistance to air flow. Such superior resistance should correspond to a significantly increased tortuosity factor, and indeed, the only way of shifting downwards the curves shown in Fig. II/3-22 b) is using values of α that are much higher than those given in Table II/3-3. The Archie's exponent was then calculated as follows. For randomly overlapping fibre structures the combination of equations (II/6) and (II/9) leads to:

$$\frac{k}{r^2} = \frac{\varepsilon}{8\eta_v (\ln \varepsilon)^2} \quad (\text{II/17})$$

and since the Kozeny constant K_c is equal to $2 \eta_v$, it reads:

$$K_c = \frac{\varepsilon r^2}{4k (\ln \varepsilon)^2} \quad (\text{II/18})$$

The corresponding data can be readily calculated, given that ε , k and r have been measured and were given in Table II/6-4. Now, the expression of the tortuosity factor can be found by identification of equations (II/11) and (II/17):

$$\eta_v = \left[\left(\frac{\varepsilon - \varepsilon_p}{1 - \varepsilon_p} \right)^\alpha \left(\frac{\varepsilon - \varepsilon_p}{(1 + \alpha)\varepsilon - \varepsilon_p} \right)^{-2} \right]^{-1} = \eta_b \left(1 + \frac{\alpha\varepsilon}{\varepsilon - \varepsilon_p} \right)^2 \quad (\text{II/19})$$

Given the very high porosity values of the present materials, already listed in Table II/6-4 and ranging from ~ 88 to $\sim 96\%$, the percolation threshold ε_p can be considered as negligible in equation (II/19). Such approximation was already successfully used for describing the physical properties of highly porous graphite materials (Celzard, Marêché, and Furdin 2003). Equation (II/19) thus simplifies into:

$$\eta_v = \frac{(1 + \alpha)^2}{\varepsilon^\alpha} \quad (\text{II/20})$$

so the Archie's exponent α is the solution of the final equation:

$$\frac{(1 + \alpha)^2}{\varepsilon^\alpha} = \frac{K_c}{2} = \frac{\varepsilon r^2}{8k (\ln \varepsilon)^2} \quad (\text{II/21})$$

The mathematical analysis revealed that the obtained solution is always unique within $[0; +\infty[$. Resolving equation (II/21) for each of our CFs led to the results given in Fig. II/3-23, where α has been plotted as a function of η_v .

It is usually accepted that the Archie's exponent, or cementation index, is close to 1.5 (Sen, Scala, and Cohen 1981). It is indeed the case most frequently encountered with many materials (Wong, Koplik, and Tomanic 1984; Celzard and Marêché 2002), and it is even exactly equal to 3/2 for a dilute assembly of spheres (Groupe Poreux 1987). In the present case, it can be seen that, whereas half of the tested materials presented Archie's exponent in the range 1 – 2, values as high as almost 3.5 were also found. The same kind of comment can be done for the Kozeny constant: whereas its value is close to 5 for most common materials, values in the range 7 – 14 were reported for more complex granular materials having fractal geometry (Bayles, Klinzing, and Chiang 1989). The present materials are definitely more complex than granular ones, thereby leading to lower permeabilities, since K_c ranged from roughly 7 to 50, i.e., varied by almost one order of magnitude. This finding agrees with former results for which the values of K_c were even found to span over two orders of magnitude (Tomadakis and Robertson 2005).

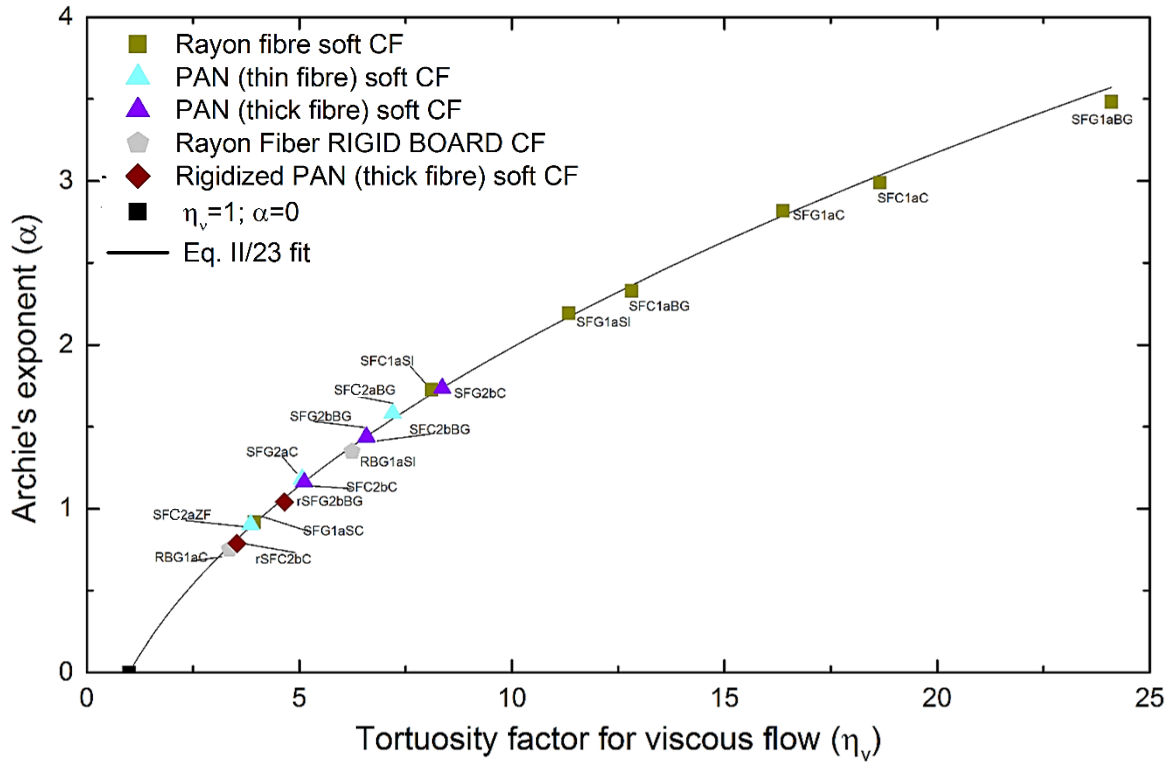


Figure II/3-23 Archie's coefficient, α , vs. viscous tortuosity factor, η_v , for all fibrous carbon materials investigated here, calculated from equation (II/21), i.e., assuming that the percolation threshold is zero. The solid line is a fit of equation (II/23) to the data points, plus one added at ($\eta_v = 1$; $\alpha = 0$). The symbols have the same meaning as in Fig. II/3-21, plus one added for ($\eta_v = 1$; $\alpha = 0$).

Fig. II/3-23 shows that despite so many different families of materials are gathered in one single plot, all data points fall on the same master curve. This finding strongly suggests that α is not a free parameter but may be considered as an intrinsic property of the fibrous medium. To the best of our knowledge, this is the first time that the master curve shown in Fig. II/3-23 is obtained. It could be fitted with very good accuracy in the range of investigated values (determination factor $R^2 = 0.99895$) by a second-order polynomial such that:

$$\alpha = 0.08435 + 0.2264 \eta_v - 0.00362 \eta_v^2 \quad (\text{II/22})$$

To further improve the quality of the prediction, one additional point was added at $\alpha = 0$, for which $\eta_v = \eta_b = 1$. With such additional data, for which no real material exists, the polynomial fit was slightly less perfect, whereas the following relationship was truly excellent instead (determination coefficient $R^2 = 0.99958$):

$$\alpha = -1.0967 + 1.0725 \eta_v^{0.45805} \quad (\text{II/23})$$

The same numerical treatment was also applied to the experimental data points presented by Jackson and James (1986) for fibrous materials having a range of porosities even broader than that of our CF samples, i.e., such that $0.346 \leq \varepsilon \leq 0.995$. The result is given in Fig. II/3-24, which clearly demonstrates that the aforementioned master curve can be extended to many other different fibrous materials. In contrast to other studies, the fibres average radius r , the porosity ε and the permeability k have been measured, from which K_c and hence η_v could be obtained from equation (II/21). Then, the solution of equation (II/20) led to the values of α . In other words, α is now *experimentally* determined and no more numerically fixed, as it was the case in former works. The main limitation of this analysis is the fact that if data are too noisy, then the scattering of α values may become very important. However, very good alignment of data can be seen in Fig. II/3-24, despite the extreme diversity of the samples, suggesting that materials should be classified according to their increasing value of α .

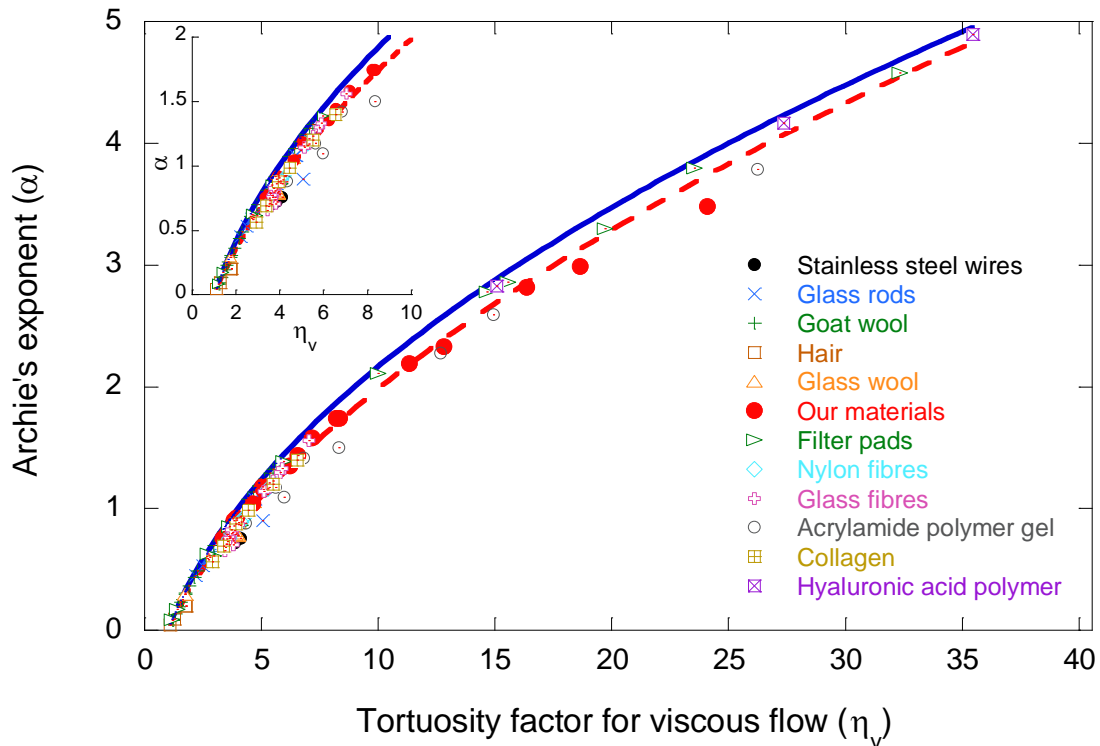


Figure II/3-24 Same as Fig. II/3-23, but with the addition of 106 other fibrous materials referenced on the plot, having porosity within the range 34.6 up to 99.5% and whose data were taken from (Jackson and James 1986). The red dashed line is the fit of equation (II/24) to the whole set of data, whereas the solid blue line corresponds to the boundary expressed by equation (II/25). The inset is a zoom on the lowest values of α and η_v .

A fit of the form of equation (II/23) was tried again on the whole set of data, thus encompassing all samples including our own ones, with a determination coefficient of 0.99669:

$$\alpha = -0.7405 + 0.73836 \eta_v^{0.56635} \quad (\text{II/24})$$

Broadening this way the ranges of both porosities and materials for applying the same kind of fit obviously led to a slight decrease in accuracy in the more restricted domain of CFs, but demonstrates that the clear correlation between Archie's coefficient and tortuosity still holds. Equation (II/23) should thus be preferred as long as usual CFs are concerned.

Of course, Equations (II/22) to (II/24) are expected to be valid only for tortuosity factors $\eta_v \geq 1$. It can be seen that equation (II/23) and (II/24) are close to the simple expression:

$$\alpha = -1 + \eta_v^{0.5} \quad (\text{II/25})$$

or, in other words, they suggest that:

$$\eta_v = (1 + \alpha)^2 \quad (\text{II/26})$$

which is indeed the lower boundary of the viscous tortuosity when $\varepsilon \rightarrow 1$ (see again equation (II/20)). In Fig. II/3-24, the data corresponding to such limit have been reported, and it can be clearly seen that all experimental data are either on or below this limiting curve.

The combination of equations (II/19) and (II/24) suggests that η_b should be always close to 1 in our series of materials. Calculating η_b from Archie's law, which is the simplest form of equation (II/8) when the percolation threshold ε_p is assumed to be zero, and which thus reads:

$$\eta_b = \varepsilon^{-\alpha} \quad (\text{II/27})$$

indeed led to values within the range 1.06 – 1.21 (see also Fig. II/3-26 below).

Thus, Archie's exponent is defined only by the tortuosity factor η_b , and hence allows the calculation of the formation factor $F = \eta_b/\varepsilon$. The corresponding results are shown in Fig. II/3-25.

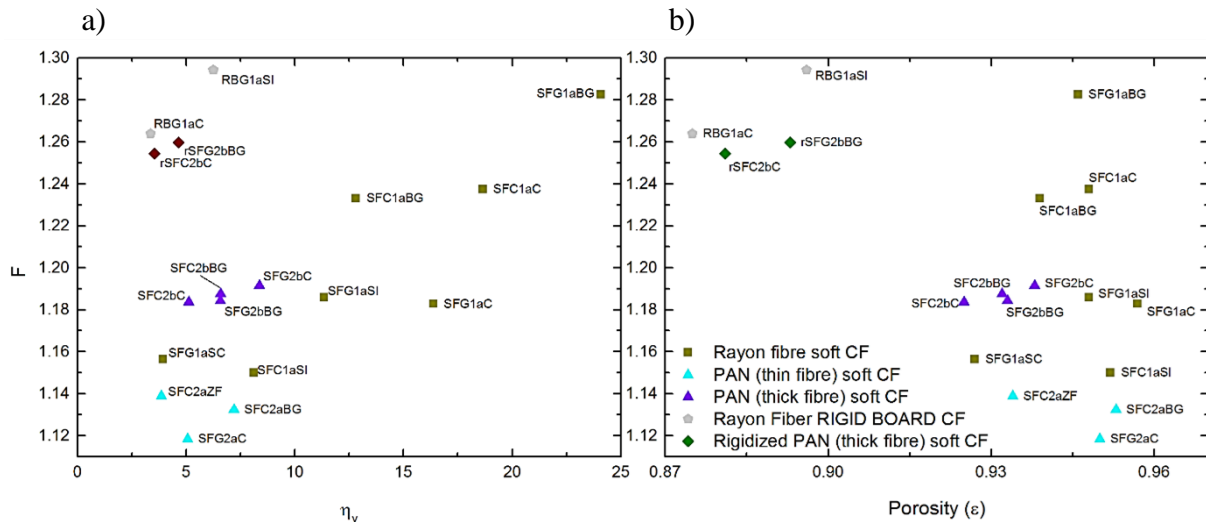


Figure II/3-25 Formation factor F calculated from the data of Fig. II/3-23 and from the known porosity of the materials (see again equation (II/10)), and plotted as a function of: a) tortuosity factor for viscous flow, η_v ; and b) porosity, ε . The symbols have the same meaning as in Fig. II/3-21.

Fig. II/3-25 illustrates the broad variety of CFs considered here since no trend could be observed. For instance, some materials were both highly porous and highly tortuous at the same time, such as all Rayon-derived soft felts except SFG1aSC, whereas others were both less porous and less tortuous, especially RBG1aC or rSFC2bC. Such radically opposite behaviours are explained by the structure, whose randomness can lead to high tortuosity despite the high porosity on the one hand, or whose high needle-punching density and/or numerous fibres clumps, clusters and bundles formations can lead to many straight canals throughout the material and hence to a lower tortuosity despite a lower porosity on the other hand. Of course, intermediate situations exist for which lower tortuosities correspond to higher porosities (e.g., SFG2aC, SFC2aBG and to a lower extent SFG1aSC and SFC2aZF). But for most materials, the tortuosity globally increased with the porosity, as seen in Fig. II/3-26.

The general trend that can be seen in Fig. II/3-26 for η_v is totally counterintuitive as long as materials of similar structure are considered. Moreover, the corresponding Kozeny's constants ($K_c = 2\eta_v$) are far higher than those predicted by Tomadakis and Roberson (2005) using the fixed parameters of Table II/3-3. But in the case of CFs, and as recalled above, the structure is controlled by the manufacturing process and the need of maintaining a mechanical integrity of these materials: those of higher porosity have a more deformable character so that a higher mechanical consolidation (hence a higher entanglement of fibres) is required, leading

to a much more complex and intricate structure. The same applies to thick materials, whatever their porosity, made by the consolidation of successive layers of fibrous mats.

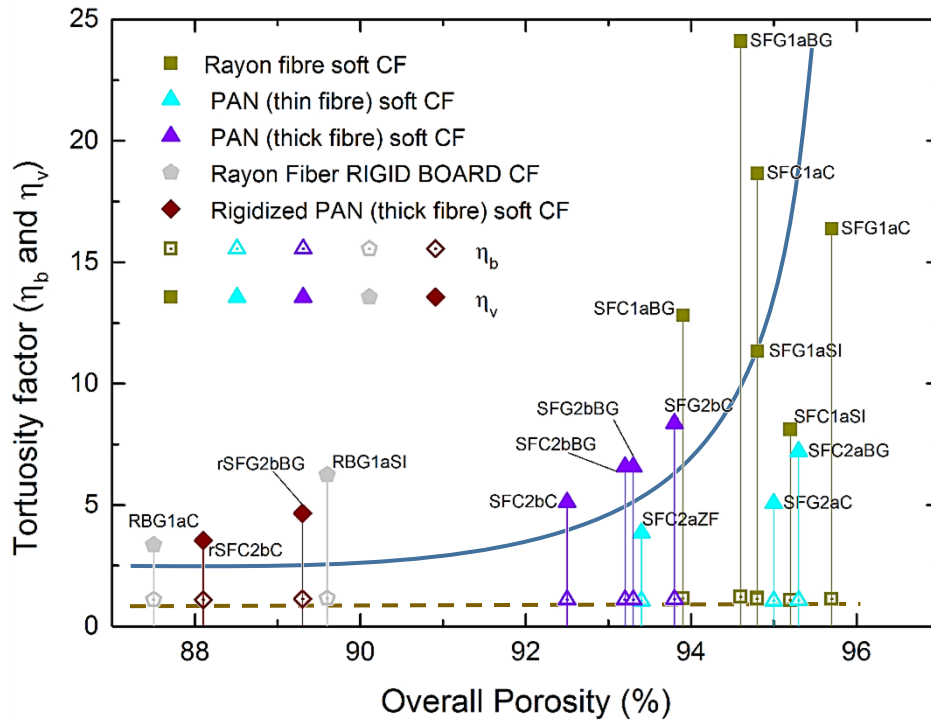


Figure II/3-26 Tortuosity factors of all samples, as a function of their overall porosity. The symbols have the same meaning as in Fig. II/3-21. Solid and empty symbols stand for η_v and η_b , respectively. The corresponding full and dashed lines, respectively, are just guides for the eye.

Given that, the results presented in Fig II/3-23 to Fig. II/3-25 were obtained from the assumption that the percolation threshold is negligible, a sensitivity analysis was also carried out and additionally presented in Fig. II/6.4.a.

II/3.3.b Mechanical properties

The objective of this part was to study the mechanical and viscoelastic properties of the CF porous structures as a function of their structural characteristics. The CF host materials might be subjected to some degree of compression (deformation) due to the possible involvement of pressure-assisted impregnation with the molten viscous PC. This is the reason why superior compression resistance and recovery capability are desired, for preserving the initial morphology of the host material and thus for assuring the high energy storage potential of the hybrid CF-PC composite. Thus, the ability of the CFs to withstand stresses applied in the OP direction has been evaluated by means of experimental and analytical investigation. An

additional objective of this chapter was to study the mechanical properties by two different methods of characterisation and to compare the recovered data.

II/3.3.b1 CF investigation by dynamic compression method

Samples' compression pressure vs. strain curves are presented in Figures II/3-27 for all the soft CFs. The deformation of most soft CFs (see Fig. II/3-27 a) and c)) is generally highly complex with almost continuous non-linear load-displacement response during the monotonic loading. The mechanical properties of these materials should be governed by viscoelastic mechanisms (fibre stretching and rotation) along with irreversible mechanisms (fibre slip, fibre breakage and felt bond breakage and/or disentanglements). Indeed, by performing uniaxial compression experiments, we found that the soft CFs did not return completely to their initial thickness, suggesting that the viscoelastic behaviour is influenced by permanent plastic deformations. Thus, this proposed mechanical response corresponds to networks of randomly cross-linked elastic "fibres" with limited irreversible extensibility and compressibility. As suggested by Jearanaisilawong (2008), this class of elastic fibrous materials encompasses the nonwoven fabrics as well as elastomers and biological materials with macromolecular components such as elastin, collagen, titin, and DNA.

The logarithmic presentation of the results of experimental stress vs. strain suggests that at least two compression regimes establish the deformation of the soft CFs. These consecutive deformation regimes are important characteristics addressed by several previous studies (Chen, Cheng, and Chou 2001; Kelly, Umer, and Bickerton 2006; Comas-Cardona et al. 2007). Primarily, a viscoelastic deformation (shown by the transparent blue zone in Fig. II/3-27 b) and d)) of the soft CFs is due to re-orientation, slippage, stretching and/or nesting of constituent fibres at lower strain values (until the porosity decreases under 50% or lower, depending on the evaluated soft CF). As observed from the SEM analysis (seen from Fig. II/3-3 to II/3-5) the IP oriented fibre layers, positioned one above the other, present only very few fibre-to-fibre contacts, leading to the high porosity of these materials. Under viscoelastic deformations, the IP fibre layers are compacted, which narrows the pores between the layers. Thus, minimal stress response was observed under the influence of external uniaxial loads. An increase in the stress response in this regime is observed only for the PAN-derived (thin) soft CFs, considered to be materials with increased needle-punch density, so the fibres in the OP direction exhibit higher compression resistance compared to the materials of the other groups of soft CFs. At higher strain, the interfibrous void space is almost completely occupied by carbon fibers, having a compact fibre structure that prevents further viscoelastic deformation of the fibres. Therefore,

the viscoelastic deformations stop almost completely and the constituent fibres are completely deformed by irreversible plastic mechanisms (transparent red zone in Fig. II/3-27 b) and d)). This compression regime includes a permanent evolution of the web structure, complete fibre-to-fibre contacts and plastic fibre deformation due to the accumulation of stresses resulting from friction between fibres and compaction between fibres, so that the strain becomes slowly constant. The two proposed regimes of deformation result in increased CFs stiffness under monotonic loads, due to the complex non-linear viscoelastic/plastic evolution of the evaluated soft CFs.

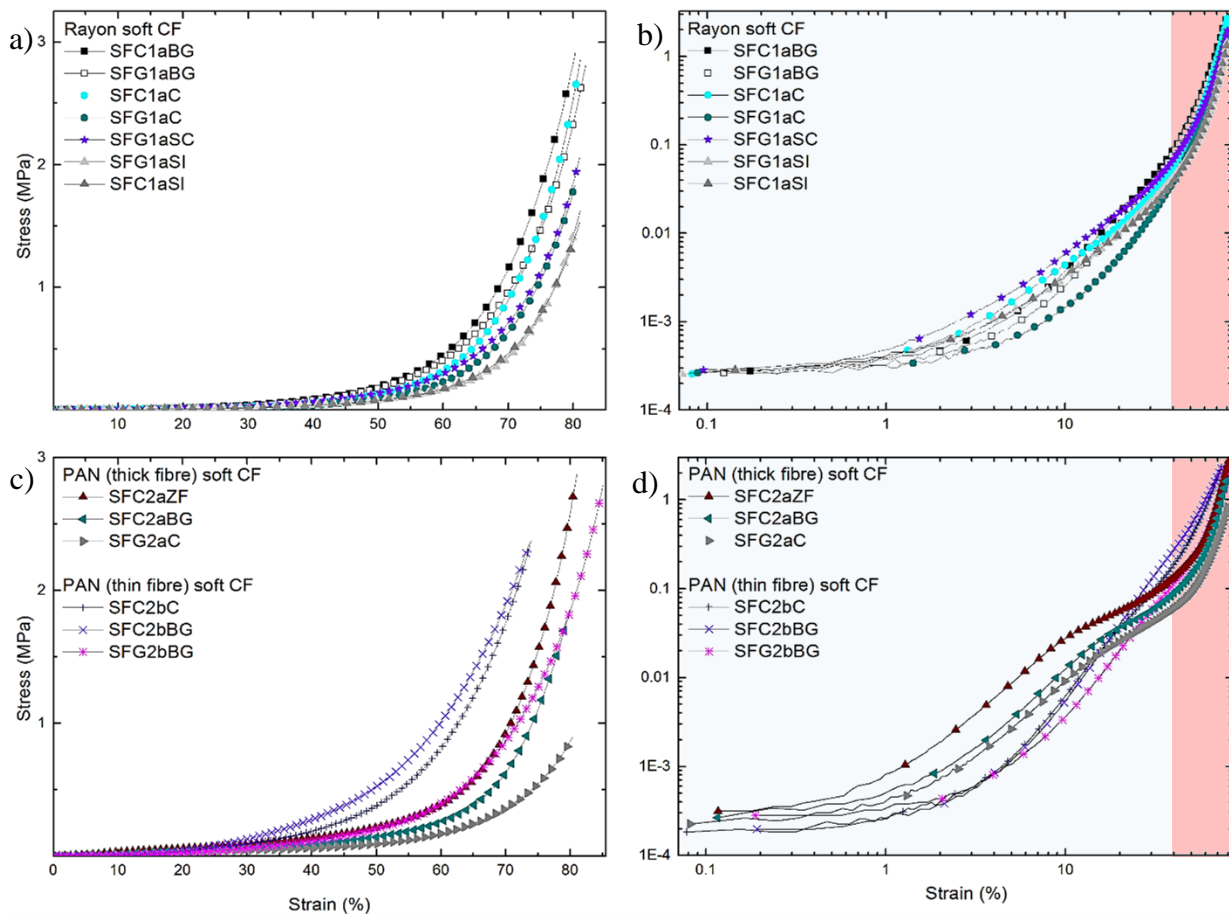


Figure II/3-27 Stress-strain characteristics of: a) Rayon-derived and c) PAN-derived (thin/thick) soft CFs; Logarithmic representation of a) and c) are given in b) and d), respectively, with indication of the compression zones influenced by different deformation regimes (“viscoelastic” – transparent blue and “solid” – transparent red zone).

During the uniaxial compression of all the soft CFs with the conventional method, here referred to the dynamic mechanical compression tests, we can observe different effects from the fibre and/or felt properties on the compression resistance of the investigated materials:

- Effect of fibre orientation on compression properties

Different fibre orientation distributions were observed from the evaluated commercial CFs, fabricated by different needle-punch processes (needle-punch density and penetration depth) and needle types, also reported in previous studies (Ghane et al. 2011; Mahboobeh 2013; Sun 2014). As discussed in subchapter II/3.1.c and II/3.1.d, fibre reorientation is induced during the needle-punch operation since barbed needles push fibres, randomly lying in the IP direction, into the OP direction.

The averaged fibre orientation values from the tomography analysis (seen in subchapter II/3.1.d) are found useful when discussing the effect of fibre orientation on the CF compression properties. Based on the μ CT analysis (seen in Fig. II/3-14 and Fig. II/3-15), higher punch density and penetration depth should have resulted in increased OP fibre orientation seen solely for the PAN-derived thin fibre CFs, when compared to the soft CFs of the other groups. Therefore, the increased fibre distribution in the OP direction, resulted in CFs (such as SFC2aZF, SFC2aBG, and SFC2aC) with a higher compression stress response even at a strain under 20%, not observed in the materials of the other soft CF groups, at similar bulk densities (see Fig. II/3-28). The compression resistance begins to be controlled only by the solid compression of the fibre-to-fibre contacts, at a higher strain of 30 or 50% and as the needle-punched fibre bundles (oriented in OP direction) slide and change orientation thereby neglecting the influence of the orientation of the uncompressed (initial) fibre. This confirms that the CF overall morphological differences have a greater effect on the material's compression properties for a low compression strain up to 30 %, beyond which densification and solid compression of the material play the main role in the bulk dynamic compression of these materials.

- Effect of fabric bulk density on compression properties

As shown in Fig. II/3-28, the resistance to compression of all the soft CFs generally increases with their bulk density. When considering the soft Rayon-derived CFs, we can observe that this tendency is the most evident and constant (taking into account the strain increase from 10 to 50 %). From the μ CT analysis, it is obvious that most of the soft Rayon-derived CFs have similar fibre orientation (seen in Fig. II/3-14). If we consider similar fibre

orientation distribution, most likely the differences in fibre morphology (fibre cross-section and/or crimp) and IP fibre layer repetitiveness influence the changes seen from the bulk density. Therefore, the increase in bulk density contributes to improved compression rigidity.

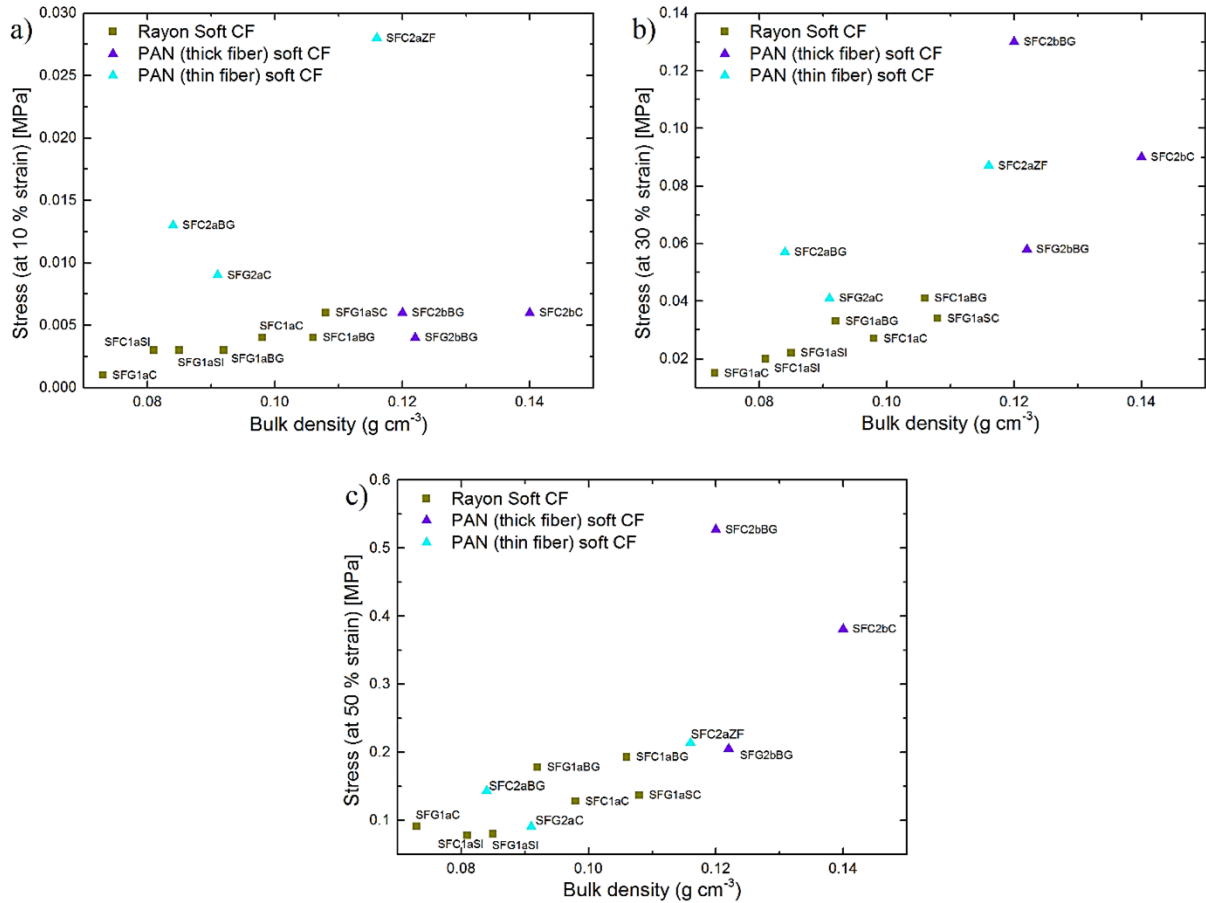


Figure II/3-28 Effect of bulk density on the stress applied to CFs for deforming them at: a) 10% strain, b) 30% strain, and c) 50% strain. The symbols have the same meaning as in Fig. II/3-21.

As a rule of thumb, one can expect a much higher contribution of these fibre/felt properties and felt density in the case when the CFs are made from the same material and manufacturing process, and changing only one known fibre parameter.

In the case of the rigidized PAN-derived soft CFs, higher compression resistance is observed at much lower strain, compared to the previous soft CF groups (values given in Table II/6-5). The manufacturing differences, as rigid bonds introduced on the top and bottom IP surfaces of the felts (seen in Fig. II/3-6) and between two or more needle-punched soft CF on top of each other (along the OP direction), prevented the viscoelastic deformation observed for the soft CFs. Thus, bonding the CFs' surface fibres with a rigid matrix should have a major contribution to the mechanical properties of the evaluated CFs by decreasing the probability of fibres free movement. Therefore, when uniaxially compressed, these materials present clear linear elastic stress vs. strain deformation parts before being non-linearly deformed and densified (see Fig. II/3-29). The observation of a linear stress vs. strain part allowed the calculation of simple elastic modulus, using equation (II/5) (see Table II/3-4). After the initial linear part, the fixed connections between the fibres and the binder should be continuously destroyed, releasing the fibres to rearrange until a complete fibre-to-fibre solid compression occurs. Thus, the materials are irreversibly deformed after the elastic deformation limit. The value of the yield strength (elastic limit) was considered as the stress up to which the materials can be deformed elastically and reversibly returned to its original dimensions. The strength of these materials increased with the increase of the fabric density, mainly due to the increase of binder concentration as seen by Shi et al. (2015).

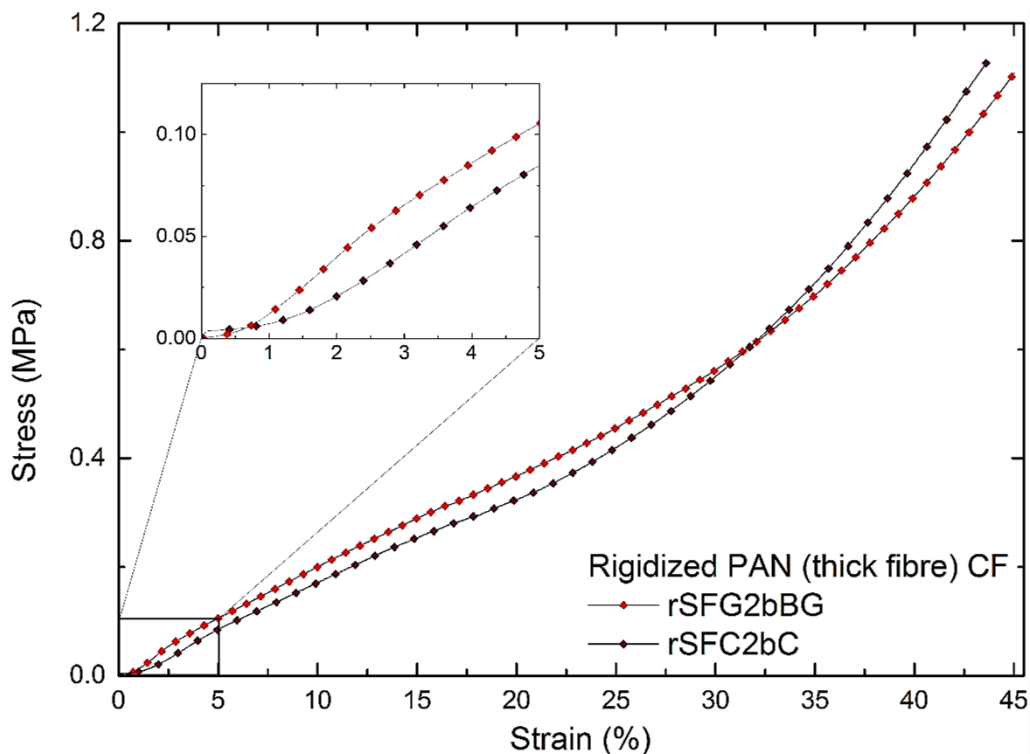


Figure II/3-29 Stress vs. strain characteristics of rigidized PAN-derived soft CFs. The inset is a zoom on the initial linear deformation.

Table II/3-4 Averaged elastic modulus and yield strength of rigidized PAN (thick fibre) and Rayon rigid board CFs; Structural characteristics are inserted for comparison.

Sample code:		Bulk density (g cm ⁻³)	Overall Porosity (%)	Elastic Modulus <i>E</i> [MPa]	Yield strength [MPa]
Rigidised PAN (thick fibre) CFs					
rSFG2bBG	Ave. (MPa)	0.182	89.3	2.26	0.045
	Stdv. (MPa)	0.010	-	0.28	0.001
rSFC2bC	Ave. (MPa)	0.227	88.1	1.81	0.102
	Stdv. (MPa)	0.014	-	0.46	0.041
Rayon rigid board CFs					
RBG1aSI	Ave. (MPa)	0.157	89.6	13.48	0.171
	Stdv. (MPa)	0.012	-	0.25	0.001
RBG1aC	Ave. (MPa)	0.198	87.5	20.30	0.360
	Stdv. (MPa)	0.000	-	0.76	0.002

Figure II/3-30 represents the OP direction compression stress-strain curves of the Rayon rigid board CF manufactured from chemically bonded chopped fibres and Table II/3- 4 presents the calculated elastic modulus, using equation (II/5), and yield strength values. These materials deformed linearly at a much lower strain, under 2%, and then the stress increased non-linearly with the strain, similar to the compression deformation of other chemically bonded chopped fibre structures, observed by Zhang et al. (2017). For both evaluated CFs, a constant non-linear deformation was observed after the yield strength. Beyond the elastic limit (yield strength), the material started deforming plastically, i.e., presented a permanent deformation from the collapse and disintegration of the bonded fibre layers in the OP direction. These observations clearly separate the rigid board CFs from the rest of the evaluated soft or rigidized soft CFs, for which the non-linear deformation is mainly due to fibre viscoelastic rearrangements.

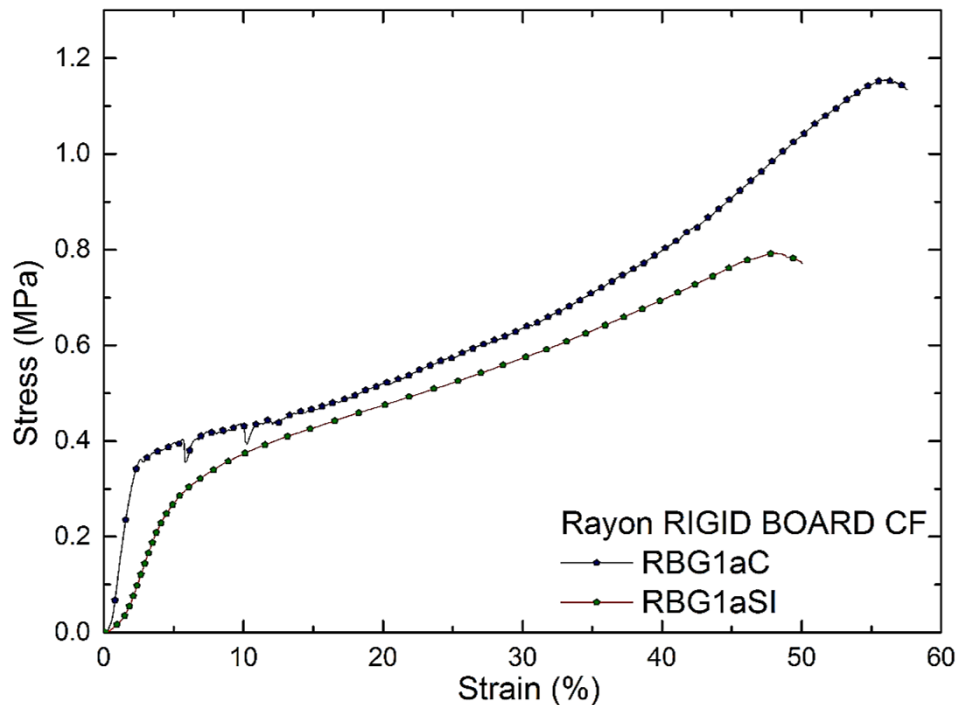


Figure II/3-30 Stress-strain characteristics of Rayon rigid board CFs.

Contrary to the soft CFs, for which the fibre orientation distribution has the main effect on their mechanical properties, the same properties for the rigidized soft CFs and rigid board CFs mainly depend on the interface bonding strength between the fibres and the carbon binder. The phenomenon of binder distribution and accumulation on the fibre intersections contributes, as expected, to the overall materials' mechanical properties. As previously reported by Shi et al. (2015), this is due to the increase of the effective load transfer between the fibres, when exposed to external compression or other mechanical forces. Therefore, the elastic modulus and strength values of the RBG1aC samples were higher than those of RBG1aSI, mainly due to the increased binder concentration (seen from the increase of the felt density) and enhanced interface bonding between the binder and carbon fibres. Considering the differences in the fabrication technique, we can also observe that the rigidized soft CF samples, with evident lower and peripheral binder concentration, have a much lower modulus and strength than the rigid board CF samples, with regularly distributed regions of fibre-matrix connections.

In the case of the rigidized soft CFs and rigid board CFs, we considered the evaluated materials as initially linear elastic or Hookean, i.e., for which the force necessary to compress them by a certain thickness is proportional to this thickness (Timoshenko 1983). However, the soft CF compression involves large strains by which the deformations are essentially non-linear and the related stresses depend on the elementary fibre/felt properties. With respect to the soft CFs, the free continuous and complex fibre deformation mechanism mostly results in

continuous non-linear deformation, reducing their compression resistance by delaying the beginning of the fibre-to-fibre solid compression. Therefore, the experimental stress-strain results suggest the hyperelastic nature of the soft CFs. Thus, the mechanical properties of these non-linear elastic materials cannot be directly represented by concepts of linear elasticity, but by constants defined from experimental functions of the non-linear deformation (Mihai and Goriely 2017).

Such compressional behaviour of fibrous nonwovens was first studied by Wyk (1946) considering the fibre bending and the number of fibre-to-fibre contacts as main parameters for modelling their mechanical behaviour. Then, Wyks' empirical solutions were followed and modified by many other scientists taking into account the felt morphology and the fibre-to-fibre viscoelastic/irreversible effects. However, the objective of this part was not the development of new analytical solutions for the non-linear behaviour of soft CFs, but to analyse this behaviour by the use of existing analytical, simple and efficient model and to compare the obtained results. For simple and practical application, and even if the estimation of the experimental data might not lead to the best fits, we investigated the use of a hyperelastic model containing not many terms and constant coefficients. This way, the obtained model solutions were easily altered or related directly to the linear elastic constitutive parameters of interest. Hence, for determining important information, not directly measurable, such as CFs' elastic modulus, and to further correlate the experimental stress vs. strain data, values derived from the measurements were fitted with an empirical hyperelasticity model.

Since the soft CFs were observed to be hyperelastic, when dealing with loading conditions such as uniaxial compression, they can be considered as rubber-like (non-linear elastic) materials. As previously described by Jearanaisilawong (2008), the fibre structure of nonwovens (such as the studied soft CFs) can be defined as randomly interconnected networks of fibres, resembling the microstructure of elastomers, presented by randomly crosslinked networks of polymer chains. Following the same concept allowed us to adopt a hyperelasticity material model, commonly used to model rubber elasticity, for the investigation of the soft CF' elastic modulus. Thus, the Mooney-Rivlin model (Mooney 1940; Rivlin and Keightley 1948) is broadly accepted as a good prototype model for investigating the elastic behaviour of rubber-like materials up to 200 % strain (in tension tests) (Ogden 1997; Nowak 2008).

As previously applied by Wood (1978), in practice the elastic modulus is estimated with the inverse characterisation method simply by fitting the Mooney-Rivlin model with the obtained experimental data. When investigating nonwoven fibrous materials with diameter

smaller than the diameter of the device plates, the deformation of the sample is mostly perpendicular to the direction of the plates and lateral material's expansion (along the IP direction) is prevented. Therefore, Tarnow (2005) and Jaganathan et al. (2009) concluded that the Poisson's ratio, being the ratio of the transverse to axial strain, is assumed to be close to zero. Hence, we considered the value of zero for this parameter by taking into account the information found in the literature and the performed QMA tests (presented in subchapter II/2.7.b).

The hyperelastic materials can be described under the hypothesis of the existence of strain energy potential (Nowak 2008). From the proposed Mooney-Rivlin model strain energy potential and the experimental compression stress-strain results of soft fibrous materials, one can consider the absence of lateral deformation (i.e., zero Poisson ratio), thus the dominant OP longitudinal $\frac{\Delta L}{L}$ deformation in the z-axis reads:

$$\lambda_z = 1 + \frac{\Delta L}{L} \quad (\text{II/29})$$

With a known potential of strain energy, it is possible to determine the dependence of the nominal stress as a function of strain. Therefore, with $\frac{\Delta L}{L} < 0$ and compression stress, $\frac{F}{S_0} < 0$, where F is the compression force on the initial CF sample cross-section area, S_0 , the modified Mooney-Rivlin equation reads:

$$\frac{F}{2S_0(\lambda_z - \frac{1}{\lambda_z^2})} = C_{10} + \frac{C_{01}}{\lambda_z} \quad (\text{II/30})$$

The left-hand side represents the resulting stress and the right-hand side of equation (II/30) is linear with respect to the variable $\frac{1}{\lambda_z}$, thus it enables determination of the Mooney-Rivlin constants C_{10} and C_{01} . Hence, a numerical function was created for simultaneous identification of the two Mooney-Rivlin constants, using equation (II/31):

$$\frac{F}{S_0} = 2 \left(1 - \frac{1}{1 - \lambda_z^2} \right) [(1 - \lambda_z)C_{10} + C_{01}] \quad (\text{II/31})$$

The fit of the model with the experimental stress-strain curves of the soft CFs (see Table. II/3-5 and Fig. II/6-5 and II/6-6) makes it possible to identify the two Mooney-Rivlin constants. As presented by Salençon (2001) and Mihai and Goriely (2017), the obtained Mooney-Rivlin constants can be further correlated with the Lamé constant, μ , which have the same meaning as the nonlinear shear modulus, through equation (II/32):

$$2(C_{10} + C_{01}) = \mu \quad (\text{II/32})$$

Finally, a single value of the elastic modulus, E^* , can be defined as twice the shear modulus by the relation:

$$E^* = 2\mu \quad (\text{II/33})$$

when considering only dominant OP deformation. The resultant values of the elastic modulus are presented in Table. II/3-5 for each of the evaluated soft CFs.

Table II/3-5 Identified Mooney-Rivlin constants from the experimental data fit with equation (II/31) and single values of the elastic modulus, E^* , obtained by successive use of equations (II/32) and (II/33).

Sample code:	Experimental data fit with Eq. (II/31)			Elastic modulus E^*
	C_{10}	C_{01}	R^2	(MPa)
RAYON fibre soft CFs				
SFG1aBG	0.0308	0.0048	0.9931	0.142
SFC1aBG	0.0263	0.0086	0.9923	0.140
SFG1aSC	0.0156	0.0051	0.9956	0.083
SFC1aC	0.0080	0.0104	0.9937	0.074
SFG1aC	0.0049	0.0086	0.9943	0.054
SFC1aSI	0.0045	0.0055	0.9966	0.040
SFG1aSI	-0.0088	0.0117	0.9995	0.012
PAN thin fibre soft CFs				
SFC2aZF	0.0196	0.0072	0.9977	0.107
SFC2aBG	0.0081	0.0069	0.9977	0.060
SFC2aC	0.0131	0.0012	0.9985	0.057
PAN thick fibre soft CFs				
SFC2bBG	0.0741	0.0060	0.9930	0.320
SFC2bC	0.0305	0.0170	0.9958	0.190
SFG2bBG	0.0488	-0.0020	0.9937	0.187

When the calculated single elastic modulus values are plotted as a function of the materials' bulk density, most soft CFs present similar trends compared to the plot of the stress (at different strains) vs. materials' bulk density (compare Fig II/3-28 and Fig. II/3-31 a)). Although the elastic modulus values followed similar trends, the differences observed between the PAN-derived (thin fibre) and the Rayon-derived soft CFs' compression resistance (seen in Fig II/3-28) disappeared and both groups presented comparable modulus at similar bulk density.

Calculated lower elastic modulus values, E^* , for PAN-derived (thin fibre) CFs are based on the difference between the model's assumption of purely non-linear material's deformation, with rubber-like properties, and real nonwoven materials, with modified fibrous viscoelastic deformations. Therefore, as presented in Fig. II/6-6 b, in the case of the PAN-derived (thin fibre) soft CFs, the model underestimated the experimental stress data until the beginning of the solid compression regions (above 50 % of porosity) lowering the values of the identified Mooney-Rivlin constants. The opposite is observed from the fitting of the Rayon-derived and PAN-derived (thick fibre) soft CFs (seen in II/6-5 and 6-6 a) experimental stress vs. strain curves. These model fit differences are observed due to differences in fibre layer formation and fibre orientation distribution, the PAN-derived (thin fibre) soft CFs having the highest fibre orientation distribution in the direction of compression (OP direction).

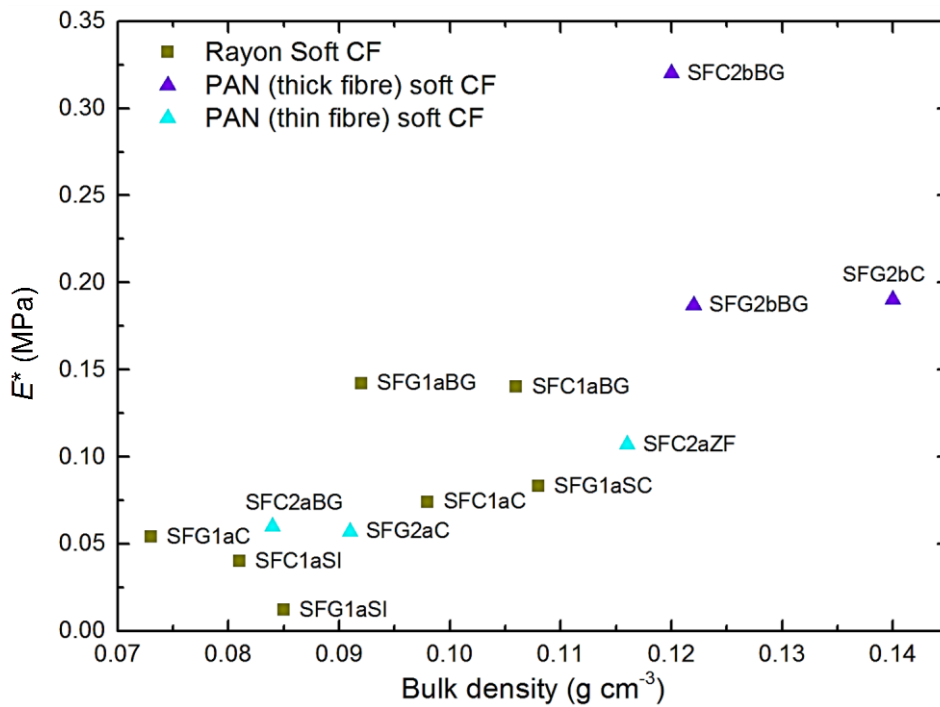


Figure II/3-31 Single elastic modulus values of soft CFs, calculated by eq. II/33, as a function of bulk density. The symbols have the same meaning as in Fig. II/3-21.

The single elastic moduli (presented as symbols) obtained by using eq. II/33 were further plotted together with the (many) values of elastic modulus (presented as lines) calculated as the slopes of the tangents to the experimental stress-strain increase curves, as a function of the strain increase (see Fig II/3-32). As previously observed by Biot (1963) for the uniaxial compression of rubber-like materials, the elastic modulus is nearly an exponential function of the strain in the examined stress range. Thus, the derived modulus variation is quite broad for all investigated soft CFs, from almost zero at low strain and increases exponentially with the

strain increase (with a determination coefficient above 0.9819) for the Rayon-derived soft CFs (seen in Fig II/3-32 a)). The same kind of results also applies to the PAN-derived thick fibre soft CFs, yet with a much lower determination coefficient, above 0.9241. Whereas in the case of the PAN-derived thin fibre CFs, the directly derived elastic modulus values do not increase exponentially with the strain (seen in Fig II/3-32 c)).

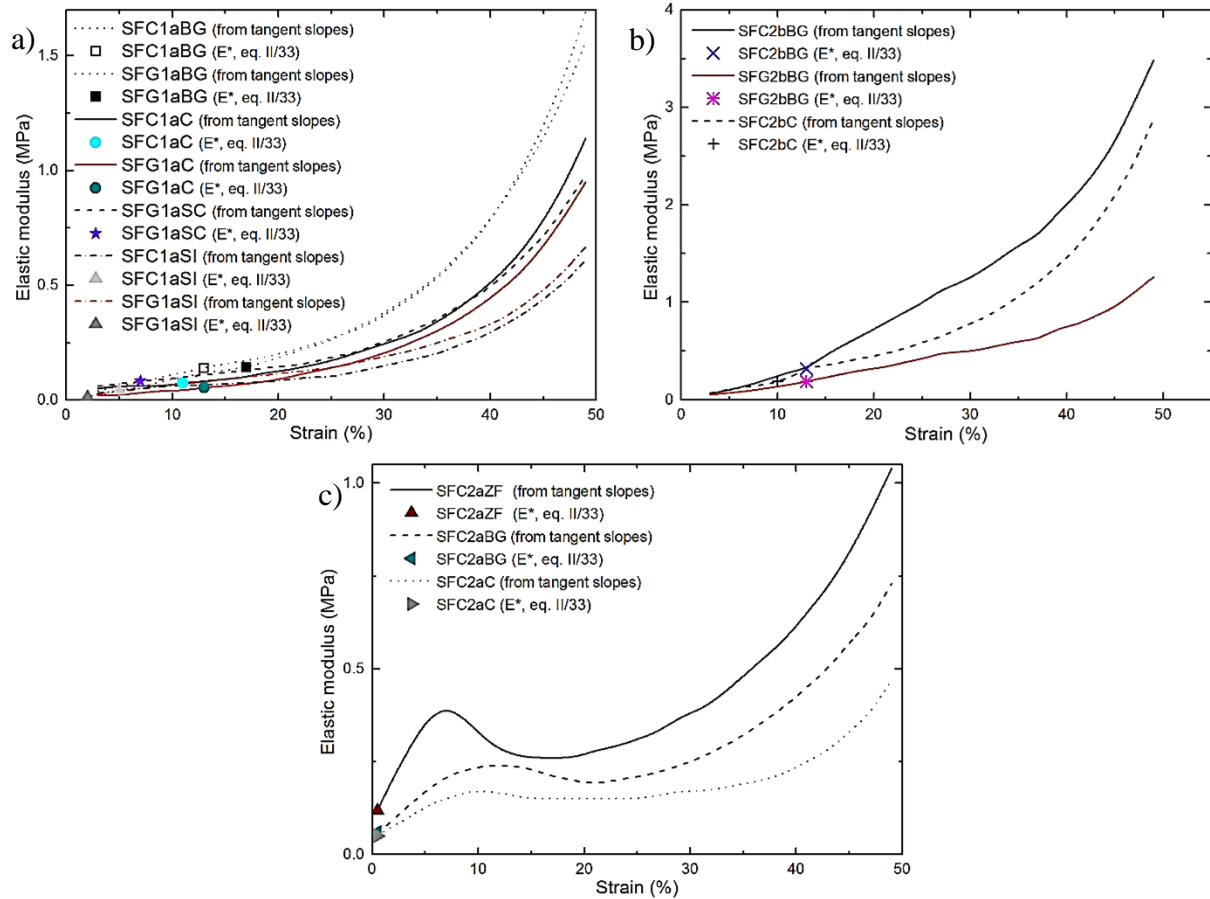


Figure II/3-32 Single elastic modulus values (E^*) (symbols), calculated by eq. II/33, and elastic moduli directly obtained from the slopes of the tangents (lines) to the experimental stress-strain curves for: a) Rayon-derived, b) PAN-derived (thick fibre) and c) PAN-derived (thin fibre) soft CFs.

The use of eq. II/33 provides unique elastic modulus values of the Rayon-derived and PAN-derived thick fibre soft CFs at a given strain (presented as symbols in Fig. II/3-32 a) and b)), whereas the same for the PAN-derived thin fibre CF are only defined at the beginning of the material deformation (seen in Fig. II/3-32 c)). The close correlation between the single modulus values of the corresponding CFs, such as SFC1aC↔SFG1aC, SFC1aBG↔SFG1aBG, and SFC1aSI↔SFG1aSI, should be also correlated with their morphological similarity expressed by the experimental stress-strain information. Therefore, the presented deviation of the continuous non-linear deformation behaviour of the PAN-derived thin fibre CFs, also seen

from the moduli estimated from the slopes of the tangents to the stress-strain curves (presented as lines in Fig. II/3-32 c)), should influence the estimation of the single elastic modulus with the use of Mooney-Rivlin constants. Therefore, the different compression behaviour of the PAN-derived thin fibre CFs is observed due to the high fibre orientation distribution in the OP direction (seen in Fig. II/3-15). Due to these morphological features of the PAN-derived (thin fibre) soft CFs, the viscoelastic compression of these materials is initially dominated by elastic (bending) deformation of the OP fibre bundles. The elastic deformation of the OP fibre bundles thus presents a higher compression resistance to the uniaxial OP load, not observed for the CF samples of the other two groups.

Table II/3-6 Calculated single value of the elastic modulus (eq. II/5), E , obtained from the linear elastic part of the stress vs. strain curves of PAN-derived thin fibre soft CFs.

Sample code:	Elastic Modulus E [MPa]	Yield strength [MPa]
PAN thin fibre soft CFs		
SFC2aZF	0.4	0.030
SFC2aBG	0.25	0.032
SFG2aC	0.17	0.019

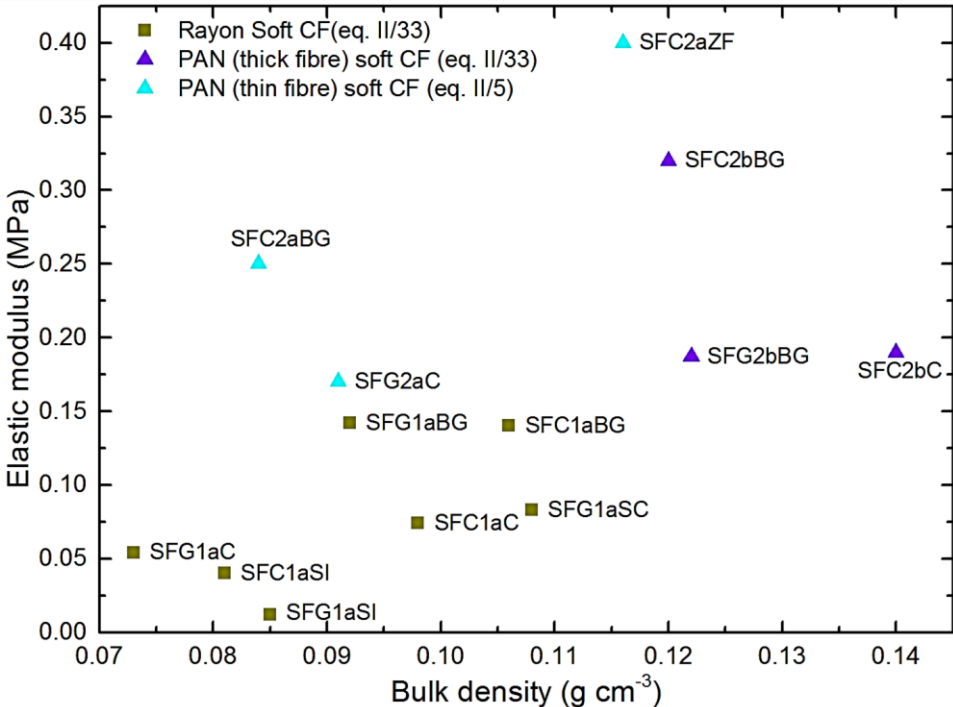


Figure II/3-33 Single values of elastic modulus, calculated either by eq. (II/5) for PAN-derived (thin fibre) or by eq. (II/33) for Rayon- and PAN-derived (thick fibre) soft CFs as a function of bulk density. The symbols have the same meaning as in Fig. II/3-21.

Further, single elastic modulus values for the PAN-derived (thin fibre) CFs were also defined from the slopes of the initial linear elastic parts of stress-strain curves with the use of equations (II/5) (presented in Table II/3-6). Thus, the calculated elastic modulus, by use of equations (II/5), was compared with the same for the Rayon-derived and PAN-derived (thick fibre) soft CFs, calculated with equation (II/31), as a function of the fabrics' bulk density. Fig. II/3-33 shows that, in spite of differences in the modulus estimation, the presented results are in good correlation with the viscoelastic properties of the evaluated soft CFs, compared to Fig. II/3-28. When studied under uniaxial compression, the result strongly suggests that a single elastic modulus of the evaluated soft CFs can be obtained by use of eq. (II/5), related to a linear behaviour, or by parameters that are explicit functions of the deformation, eq. (II/31), depending on the material morphological and deformation properties. Therefore, it can be accepted that for materials with continuous non-linear deformation, a single elastic modulus solutions can be found with the use of the hyperelasticity Mooney-Rivlin model, even if the fit slightly underestimate materials' viscoelastic deformation. Whereas in the case of the PAN-derived (thin fibre) soft CFs, the presence of initial regions of linear elastic deformation leads to lower modulus estimations with the hyperelasticity Mooney-Rivlin model, thus the use of the linear theory is more accurate. The latter experimental results and modulus calculations can be additionally supported by uniaxial compression studies of woven fabrics, where again the experimental stress vs. strain curves present an initial linear part prior to non-linear deformation of the evaluated fabrics (Matsudaira and Qin 1995; Saunders, Lekakou, and Bader 1999; Baoxing Chen, Lang, and Chou 2001). The comparison between the evaluated PAN-derived (thin fibre) soft CFs and woven fabrics is acceptable since in both cases the observed initial linear part of the compression curve should be the result of bending deformations of the fibres with increased compression resistance to the applied load.

II/3.3.b2 CF investigation by non-destructive compression method

Next, all soft CF materials were investigated not only with the aforementioned destructive method but also by the quasi-static, non-destructive method. Frequently, soft porous materials are characterised by quasi-static mechanical analysis (QMA) to initially identify the Poisson's ratio, which allows the calculation of the elastic modulus and damping loss factor⁷

⁷ The loss factor is a parameter that defines the ability of a material to convert part of the acoustic (vibration) energy into heat through sound attenuation, with a theoretical maximum value of 1. The loss factor is an important parameter in many scientific and industrial fields, such as medical ultrasonography, vibration and noise control (Jarzynski 1990).

(Delgado-Sánchez et al. 2018). However, in the present case of fibrous porous materials (with weak loose fiber connections), the lack of lateral materials' deformation (along the IP direction) during the characterisation process makes it possible to do measurements with an imposed zero value of the Poisson ratio. As already observed by Jaouen, Renault, and Deverge (2008) and, Bonfiglio et al. (2018), this fixed value of the Poisson ratio can be correctly used to directly calculate the true elastic modulus and loss factor of soft fibrous materials.

The choice of the proper measurement parameters, explained in part II/2.7.b (such as sample geometry, compression rate, and excitation frequency), is very important for correctly determining the vibro-acoustic performances of the tested soft CFs. The stiffness vs. strain measurements performed to help identifying a proper compression rate to be used are shown in Fig. II/3-34. The results show that no plateau (linear section) is identified, as presented in Fig. II/2-10 (Stage 2), from the real part of the stiffness plotted as a function of the compression rate. As previously observed from the dynamic compression tests, the results suggest a strong dependence of the elastic properties on the used compression rate. Therefore, the evaluated soft CFs become stiffer with the increment of the static preload. Given the constant increase in stiffness under a higher strain, the range of compression rate values used during the characterisation tests must be always provided when analysing porous and fibrous materials. Thus, in the case of the soft CFs, the tested materials were preloaded with a static pressure in the range of 1 to 3 % before elastic modulus and loss factor measurements were made. The compression rate range was compared and selected from the range of strain at which the materials' stiffness was similar from the two compression methods, as well as comparing the studied CF with other fibrous felts analysed in previous works (Bonfiglio et al. 2018). The excitation frequency was also fixed and identical in each measurement, as it had previously been observed that it had an effect on the elastic properties of fibrous materials, in addition to the effect of the pre-compression load.

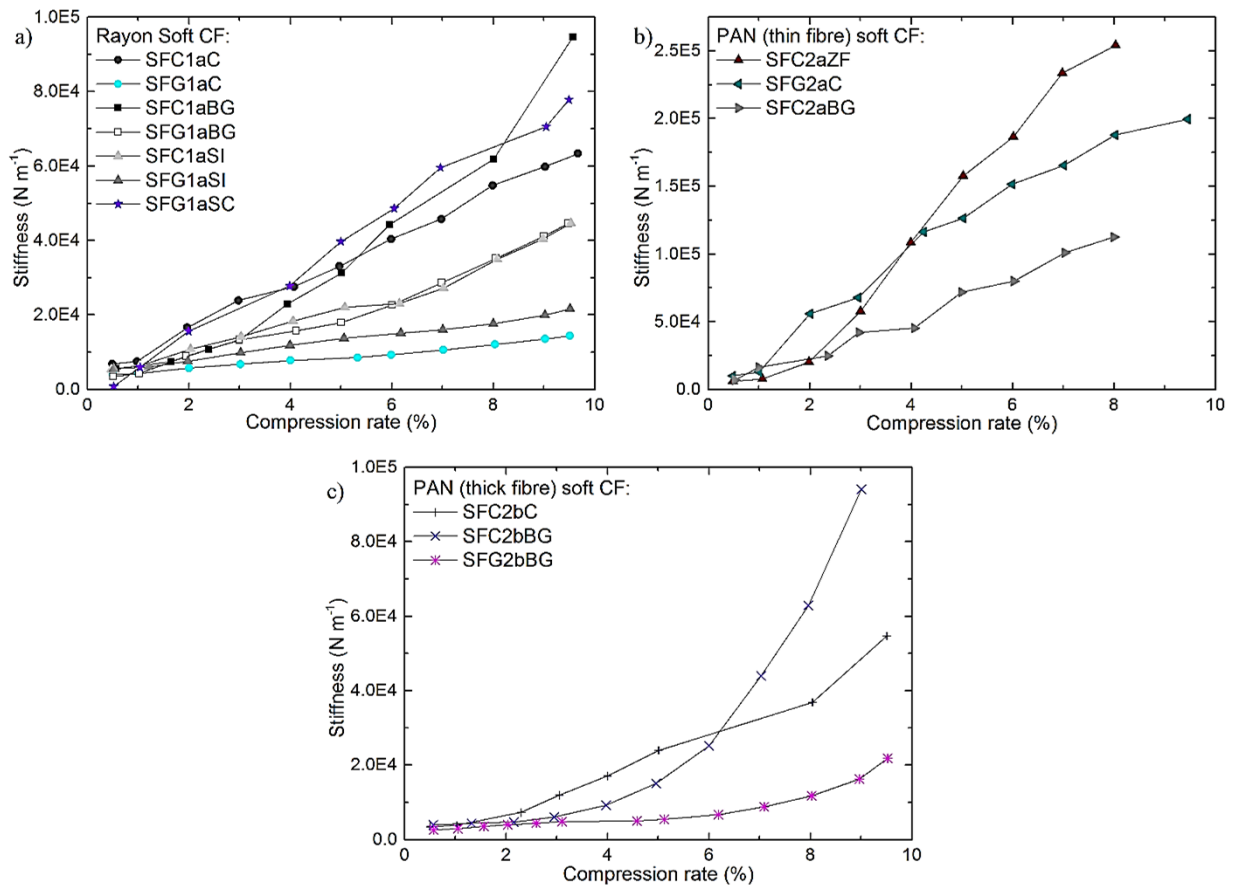


Figure II/3-34 Stiffness vs. strain measurements for the evaluated subgroups of soft CFs: a) Rayon-derived, b) PAN-derived (thin fibre) and c) PAN-derived (thick fibre) materials.

Table II/6-6 gathers all the measurements of elastic modulus and loss factor of the soft CFs obtained by the QMA method. By plotting elastic modulus results (seen in Fig. II/3-35) as a function of bulk density, we observed similar effect of the soft CFs' morphological characteristics on their elastic properties compared to the results from the dynamic compression method. Even though a general trend is difficult to observe, the elastic modulus globally increases with fabrics' density, concerning sub-/groups of different soft CFs. Again, PAN-derived (thin fibre) soft CFs give the highest elastic modulus compared to the samples from the Rayon-derived and PAN-derived (thick fibre) samples over the wide range of materials' densities. Changes in elastic modulus are again observed due to the higher frequency of fibres re-orientation induced by manufacturing from the IP to the OP direction, as evidenced by the SEM and tomography characterisation of the soft needle-punched CF. With regard to all PAN-derived soft CFs, we can consider that by decreasing the fibre diameter and by introducing more web-layers, in the IP direction, the value of the elastic modulus is also higher because of the improved fibre to fibre contacts in the studied range of static preload. Still, these observations

would be clearer by analysing series of CFs in which only one known manufacturing parameter or material property is modified, which has not been possible.

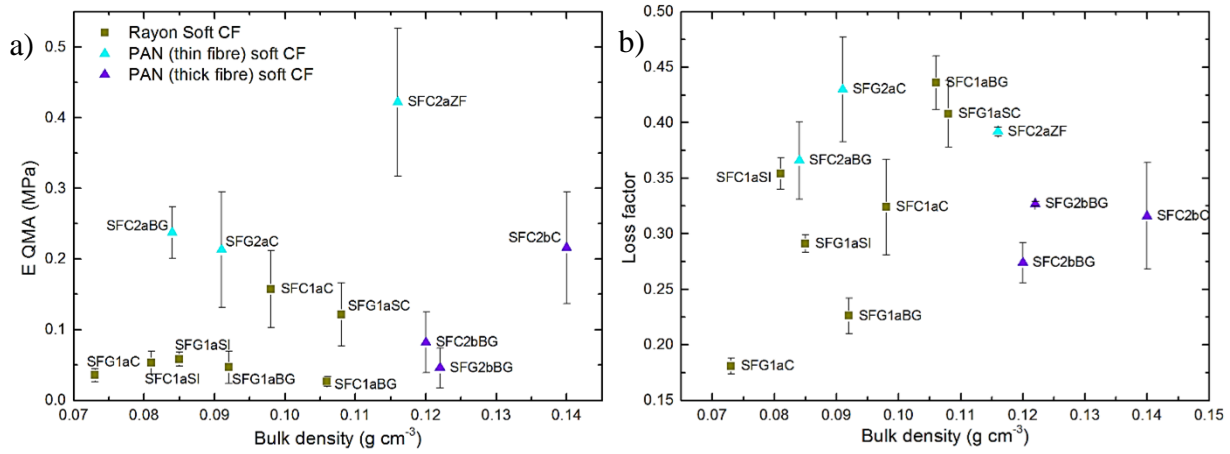


Figure II/3-35 Elastic and damping parameters obtained by QMA as a function of bulk density: a) Elastic modulus and b) loss factor. The symbols have the same meaning as in Fig. II/3-21.

The damping loss factor of the soft CFs was also obtained by QMA measurements (see Table II/6-6 and Fig. II/3-35). The loss factor of soft CFs was found in the range from 0.181 to 0.436, and show scattered increasing trend with the increase of the materials' bulk density. However, the loss factor is seen to be density-dependent, when observed within individual families and subgroups of soft CFs, evident from the results of the Rayon-derived materials. The damping (reduction in the amplitude of oscillation due to energy loss of the system to overcome some resistive force) in porous and fibrous fluid-filled media comes from two different mechanisms. One mechanism is due to the viscous drag at the interfaces between the surface of the fibrous material and the fluid in motion relative to the felt. The other one is associated with the deformation of the solid fibrous network. As previously observed by Rice and Göransson (1999), both mechanisms co-exist for materials investigated under atmospheric pressure. Therefore, the inhomogeneous cross-section of the Rayon-derived CFs may cause a higher viscous drag, thus presenting similar loss factor values similar to the other PAN-derived (thin) CFs (with circular cross-section) of identical or higher bulk density. In the case of the PAN-derived (thick fibre) CFs, the values of the loss factor were found to be low even at high bulk density due to the increased fibre diameter and IP interlayer voids as compared to the other soft CFs, made of thinner carbon fibres. By QMA measurements, we obtained the loss factor at a fixed frequency of 20 Hz. Normally, such a quantity is investigated for acoustic insulation applications of this kind of materials and is studied in a higher frequency range of 100-5000

Hz. Therefore, these results could be considered as initial information for future investigations of the evaluated soft CFs in many other applications.

II/3.3.b3 Comparison of destructive and non-destructive methods

Information on the intrinsic CFs' mechanical parameters is crucial for a more accurate prediction of their performances used here for composite preparation but also for vibro-acoustic applications and many others. Therefore, from the broad variety of soft CFs we did an attempt to compare directly the results of the two methods used to determine the elastic modulus. The novelty consists in providing important information on the accuracy and/or dispersion of the viscoelastic properties of soft CFs, measured with a dynamic and destructive method or a quasi-static and non-destructive method.

The elastic modulus results from the QMA method were plotted against the previously calculated results of the dynamic mechanical compression method, and presented in Fig. II/3-36. The symbols on or close to the diagonal straight line, added as a guide for the eye, correspond to identical elastic modulus results whereas the symbols placed beneath indicate a lower modulus estimated from the QMA method, in the chosen range of compression rate. Symbols above the line mean the same but for results from the dynamic compression method. In a general way, the results suggest identical or very close results from both methods, except for samples: SFC1aBG, SFG1aBG, SFC2bBG, and SFG2bBG. These deviations are observed only for the indicated materials, received from one supplier. In the case of the mentioned soft CFs, and even though derived from different precursors, the materials should have been manufactured according to similar protocols, displaying morphological and mechanical properties distinctly different from those of the rest of the examined materials. Given that the examined soft CFs have a constant offset of their stiffness under a different compression rate (see Fig. II/3-34), one can further consider calculating the elastic modulus outside the limits of this study. Thus, the measurement of the elastic modulus with the QMA method at a compression rate between 5 and 6 % (seen in Fig. II/6-7) improves the comparison with the results of elastic modulus derived from the dynamic mechanical compression method. This could be due to the different space re-arrangement of the constituent fibres under compression and the lower amount of additional fibre-to-fibre contacts occurring up to the same compression rate, as compared to the other soft CFs. Clearly, the choice of the compression rate at which the modulus is calculated needs to be adjusted according to the CFs characteristics and mainly with regard to the final application of the evaluated material. For this reason, the investigation of the soft CFs' elastic modulus by the QMA method must be supported by the information of the

static preload used, when comparing the observed elastic behaviour of the same material deduced from different techniques.

Although destructive, the dynamic mechanical compression is more suitable for determining a global elastic modulus, using equation (II/33) or equation (II/5), for hyperelastic materials or materials with an initial linear response under constant load increase, respectively. In contrast, QMA is only suitable for determining the elastic modulus of soft CFs at a defined pre-compression load, without giving the global materials' elastic modulus.

When working with highly compressible materials, it is very important to know the absolute force at which the initial thickness of the materials was measured, before the compression tests are performed. When performing measurements with the dynamic compression method, after the initial contact with a predefined force value, we are aware of the constant material deformation at the applied force, as explained in subchapter II/2.3 and the applied modified ASTM D5729-97(2004)e1 standard. On the contrary, when performing mechanical analysis with the QMA method, the "initial contact" is estimated using the value of the nominal force, but also the rate of its change to avoid any false negative motions. It is therefore difficult to deduce an absolute force value at which the initial contact was recorded. Thus, the comparison of the results obtained should be carried out with great vigilance, since the initial thickness of the soft CFs can be modified during different tests of the same method (as in the case of the QMA) or different mechanical compression methods.

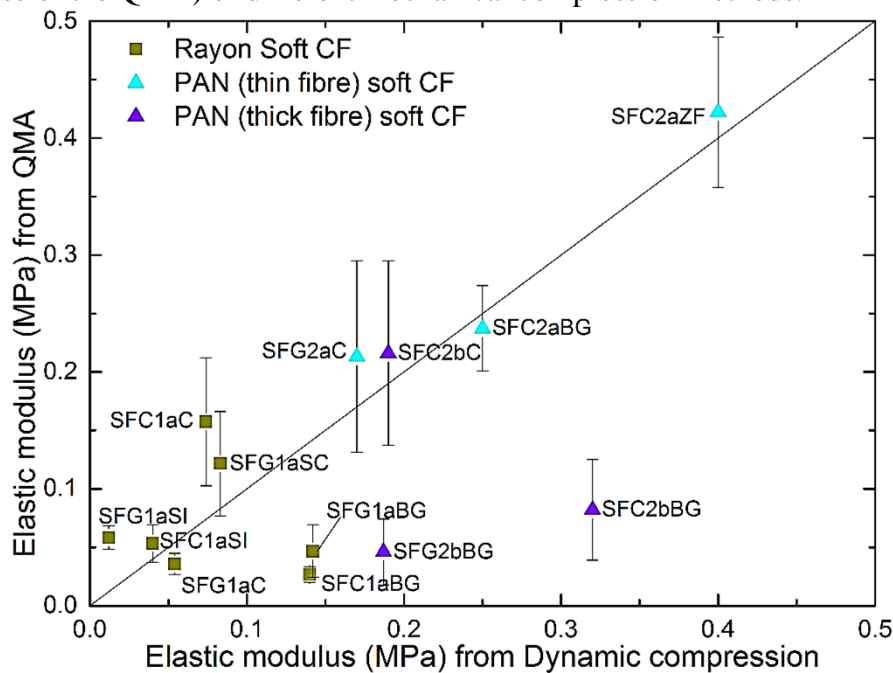


Figure II/3-36 Relationship between the elastic modulus from QMA and the elastic modulus from dynamic compression method. The symbols have the same meaning as in Fig. II/3-21.

The obtained results also indicate which of the two methods of characterisation is more appropriate for studying the elastic properties of the soft CFs if they are used for static purposes, where creep is expected under persistent mechanical load, or in a vibro-acoustic application. In this context, the characterisation method of use, such as the dynamic mechanical compression method or the quasi-static (QMA) one, should be carefully chosen depending on the materials' final application. In any case, the QMA method was previously observed to be only suitable for measuring the elastic modulus of viscoelastic materials in the absence of brittle mechanical deformation (Delgado Sánchez 2017).

II/3.3.c Thermal conductivity

Thermal conductivity measurements were carried out for all commercial CFs, and recovered data are detailed in Table II/6-7. By investigating their thermal conductivities, the CF candidates and their effect on the heat transfer efficiency of the foreseen CF-PC composites can be anticipated. The experimental, room-temperature, thermal conductivity of soft, rigidized soft and rigid board CFs was measured with the Hot Disk method in the conditions explained in subchapter II/2.7.c.

Before performing the de-sizing treatment (explained in subchapter II/2.1), the thermal conductivity of the as-received CFs was measured once to evaluate the possible modifying effect of this step. Figure II/6-8 presents the thermal conductivity values of CFs before and after de-sizing, obtained only by the use of the isotropic analysis mode, for comparison purposes. From the observed results, it is clear that most of the samples' thermal conductivity did not change after de-sizing and was found always in-between the deviation limits. Exceptions were observed in the case of the SFC1aSI, SFC1aC, SFG1aC, SFC1aBG, and SFG1aBG (Rayon-derived soft CFs), for which the increase of the overall thermal conductivity (after the de-sizing treatment) is correlated with the increase of carbons' elemental content and improved C-C covalent bonding (further discussed in subchapter III/3.1). In the case of commercially graphitised SFG2aC, the slight increase of thermal conductivity might be influenced by the carbonisation of a deposited organic sizing material, possibly present as a thin layer covering the fibre surface of the as-received CFs.

All the next thermal conductivity results were exclusively obtained after the additional de-sizing step. Generally speaking, the thermal conductivity of single carbon fibres and then of the final non-wovens is highly anisotropic. Thus, it is found that the thermal conductivity of carbon fibres mainly increases with the carbonisation and additional graphitisation temperature

in the final manufacturing heat treatment. It is also accepted that the polymer structure of the carbon fibre precursor can directly influence the final graphitic plane organisation, the existence of non-carbon atoms, and the disorientation of the graphitic structures (Lee et al. 2018). In addition to the precursor properties and the manufacturing thermal history of the CFs, their differences in the anisotropic felt morphology, are further reason for the dispersion of the thermal conductivity values.

From Fig. II/3-37, we observed the effect of the carbon fibre and CF's morphology properties on the strong deviation of the thermal conductivity values obtained by the isotropic analysis mode compared to the anisotropic mode. Initially, to confirm the validity of the thermal conductivity results in the anisotropic mode, we used equation II/34 and, simultaneously, observed a good fit between the calculated and the experimental isotropic thermal conductivity values. As explained by Dinges (2006) and Miller et al. (2006), the IP and OP thermal conductivity obtained with a single transient plane source test in the anisotropic mode can be correlated with the isotropic measurement using the following equation:

$$\kappa_{xyz} = \sqrt{\kappa_{xy}\kappa_z} \quad (\text{II/34})$$

where κ_{xyz} is the isotropic thermal conductivity calculated from the experimental measurements of the thermal conductivity in the IP-direction - κ_{xy} and the thermal conductivity in the OP direction - κ_z .

The validated measurements, obtained in the anisotropic analysis mode, can therefore be used to discuss the different heat transfer behaviour of the examined CFs. Generally speaking, all measured values are 1 to 3 orders of magnitude lower than the single carbon fibre axial conductivity, found in the literature. The morphology of the highly porous CFs and the presence of an insulating gas phase are therefore considered as the main reasons for the decrease in examined thermal conductivity compared to that of single carbon fibre. The experimental results of effective⁸ thermal conductivity are different in the OP direction from in the IP direction, parallel to the plane of the measurement, confirming the CFs' anisotropic nature. Indeed, the present CFs are generally much less conductive in the OP (κ_z) direction than in the IP (κ_{xy}) direction. The anisotropic thermal behaviour is due to the fibre orientation, mainly with a higher frequency in the IP than in the OP direction of the CF.

⁸ The effective thermal conductivity is defined as a property of heat transfer for porous materials, measured from the contribution of each phase (solid and gaseous) to the thermal conductivity of the material as a whole if it is isotropic, or along of its different plans if it is anisotropic.

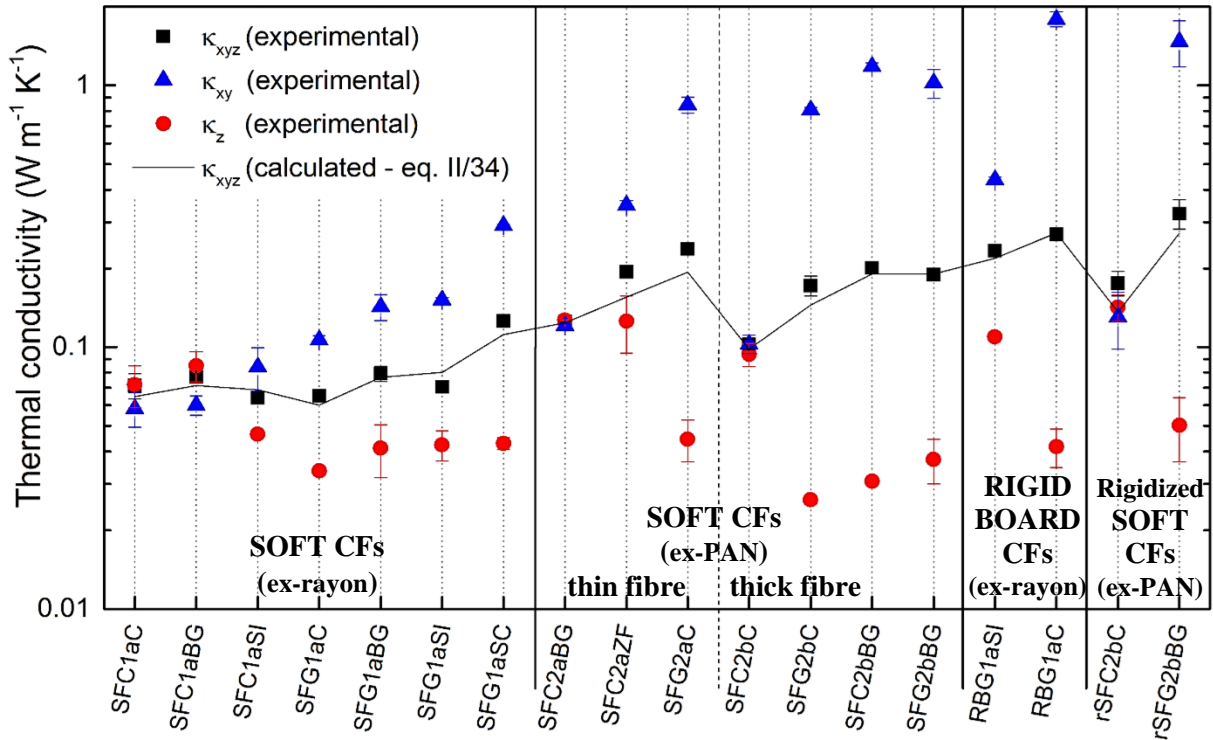


Figure II/3-37 Thermal conductivity values of all CFs measured by isotropic (black squares - κ_{xyz}) and anisotropic mode (blue triangles for the IP direction - κ_{xy} and red circles for the OP direction - κ_z thermal conductivity); the black solid line represents the calculated κ_{xyz} from the separate measurements of κ_{xy} and κ_z .

In the case of the IP thermal conductivity (κ_{xy}), the difference of the recovered results is mainly of fibres' conductive nature, yet if all other felt-forming parameters are considered similar. The influence of the fibres' conductivity is clearly observed from the corresponding CFs, such as SFC1aC \leftrightarrow SFG1aC, SFC1aBG \leftrightarrow SFG1aBG, SFC1aSI \leftrightarrow SFG1aSI, and SFC2bC \leftrightarrow SFG2bC. Manufactured only by increasing the final heat temperature, the corresponding graphitised CFs show increased thermal conductivity and differences between the values in the IP and OP directions. Exceptions, such as SFC2bBG, even though only carbonised at about 1200°C (information from the manufacturer) showed highly directional and anisotropic thermal conductivity similar to the corresponding graphitised SFG2bBG. These advantages are based on differences in precursors' properties used in the fabrication of SFC2bBG, with a high C purity and improved structural order, compared to the other evaluated carbonised CFs.

On the other hand, the thermal conductivity in the OP direction mainly depends on the thermal resistance between the flexible or rigid contacts and frequency of carbon fibres reoriented in the same plane by the needle-punching process. Similar observations were

evidenced by Ramousse et al. (2008), showing that the thermal conductivity in the OP direction (κ_z) is more affected by changes in felts' tortuosity and fibre re-orientation than in the IP direction (κ_{xy}).

In the case of practically all carbonised CF (Rayon- and PAN-derived), heat-treated at a lower temperature, we evidenced close thermal conductivity values in both IP and OP directions compared to the graphitised ones. This consistency is based on the lower conductive nature of the constituting carbon fibres when compared to the same from the graphitised materials, with an improved graphitic structure. It can also be seen that the difference between the thermal conductivity in the IP and OP directions is lower for highly needle-punched CFs, such as SFC2aZF, compared to other materials with higher fibre orientation in the IP direction. These results are in good correlation with the results obtained from the tomography analysis (presented in subchapter II/3.1.d). A similar effect was observed in previous studies (Lee and Kang 2005; Zhao, Liu, and Liang 2016), which confirmed the influence of needle-punching density on thermal conductivity by producing series of carbon fibre preforms with different needle punching densities. Therefore, the intertwined combination of conductive nature and orientation of the carbon fibres has a mutual effect on the anisotropic heat transfer behaviour of the evaluated CFs, and which is difficult to evaluate separately because of the varied manufacturing techniques.

The evaluated soft Rayon-derived CFs are usually much less conductive in the IP direction (κ_{xy}) than the soft PAN-derived CFs, when comparing CFs manufactured with similar final heat treatment. This may be due to the higher aspect ratio and circular cross-section of the PAN-derived carbon fibres, but mainly to the improved graphitic structure, which results in higher thermal conductivity in the fibres' axial plane compared to the Rayon-derived fibres. A similar comparison cannot be performed with the rigid board and rigidized soft CFs, due to the effect of the binder, possibly introduced in different amounts and by various manufacturing methods.

The investigated thermal conductivity of the rigid board CFs again emphasizes their anisotropic morphology, because of the preferred fibre orientation and inhomogeneous dispersion of the binder interconnection. Improved thermal conductivity in the IP direction is observed due to the formation of fibre connections, enhancing the CF conduction in the dominant fibre orientation. Hence, the observed results are in good correlation with former studies, suggesting the high influence of the fibre and binder continuity on the CFs' thermal

conductivity (Lee, Yun, and Park 2005; Panerai et al. 2017). The same kind of discussion can be applied to the thermal conductivity results of the rigidized soft CFs.

Fig. II/3-38 illustrates the increase in effective thermal conductivity with the bulk density. Given that the fibre orientation in most of the evaluated CFs is higher in IP than in the OP direction, it turns out that the IP effective thermal conductivity is less influenced by the density variation than the same in the OP direction. Higher bulk density should result in higher carbon fibres content per unit volume and smaller pores between fibres. Therefore, since the thermal conductivity of the carbon fibres is much higher than that of air (at least 200 times higher), its contribution to the effective thermal conductivity increases with the increase in the fabrics' density. The increase of the bulk density can also be correlated to the increase of the needle-punching density, with the felt becoming more compact with more fibres oriented in the OP direction, resulting in an additional increase in thermal conductivity. In the case of the rigid boards and the rigidized soft CFs, the thermal resistance of the carbon fibre contacts is reduced as the binder concentration increases, correlated to the increase in fabric density. Again, clearer observations were additionally prevented by significant differences in fibre/felt morphologies and differences in the final heat treatment.

Additionally, the effective thermal conductivity was inaccurately described by simple analytical models, with regard to the wide variety of investigated CFs, with variations in the carbon fibre and felt parameters. As observed by other authors (Stark and Fricke 1993; Ramousse et al. 2008; Radhakrishnan, Lu, and Kandlikar 2010), the need of constants, in-depth knowledge of the thermal properties of the complex solid matrix and the surrounding gas phase makes many volume-average and fractal model less acceptable than the available experimental determination methods. Nevertheless, the recovered CFs' morphology and properties information should make it possible to progress in the optimisation of an analytical modelling solution, which will facilitate the search for advanced material for the concerned or other applications.

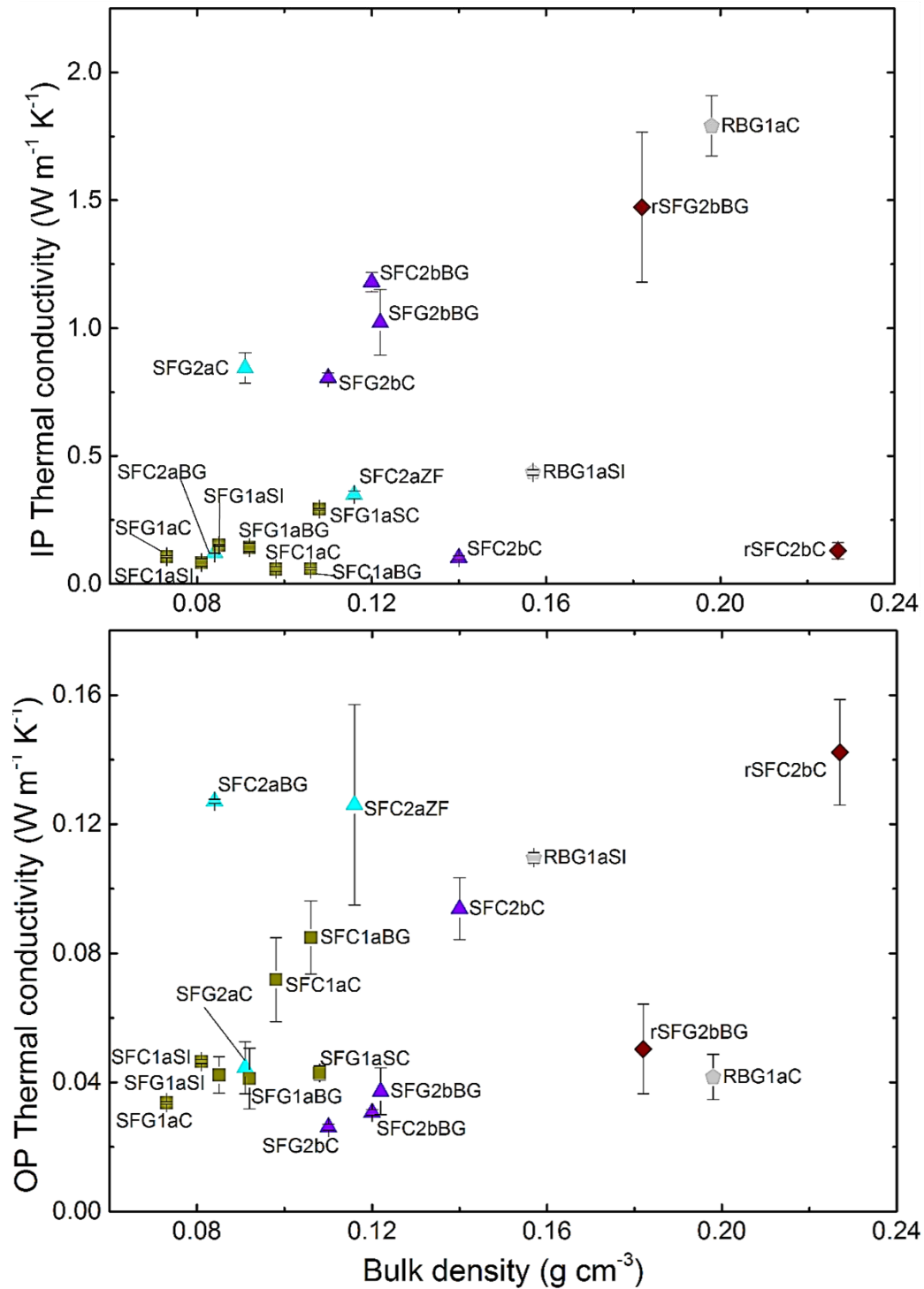


Figure II/3-38 Thermal conductivity of all materials in: a) IP direction, and b) OP direction, as a function of bulk density. The symbols have the same meaning as in Fig. II/3-21.

II/4 Conclusion

In this chapter, 18 commercial fibrous carbons ranging from soft CFs to rigid boards through rigidized CFs were thoroughly investigated in terms of general fibre/felt structure and physical material properties. These materials were derived from either PAN or Rayon fibres having different diameters, were graphitised or not, and consolidated with various techniques usually employed in the industry, i.e., either mechanically (through needle-punching, assisted or not with an additional chemical bonding) or chemically with a resin subsequently carbonised. As a result, a full set of materials with rather different porous structures and hence different physical properties, irrespective to their porosity, was investigated.

Attempts carried out for sorting the materials by groups and sub-groups of closely related samples revealed consistent behaviours within limited ranges of structures or porosities, but generally failed to account for all observations across the properties of the different materials. The huge scattering of the results from one family of materials to another was explained by the versatility of structures so that no single experimental or analytical method could represent the whole set of evaluated CF samples.

The evaluated CFs were found to be highly hydrophobic, which prohibited wettability tests with different methods and liquids and the calculation of solid surface energy, with the aim of predicting their wettability with other liquids and lastly with the molten PC. Therefore, future studies should be focused on CFs' surface energy analyses by gravimetric vapour sorption measurements, seen as a novel method without the problems associated with liquid wetting based methods.

In the case of the OP air permeability, the versatile CF structures were also investigated with analytical models that dramatically overestimated the reduced permeability in the porosity range of interest. This finding also applied to the very popular Tomadakis-Sotirchos equation, despite its higher number of free parameters. Nevertheless, by applying relevant permeability equations to the studied CFs, the Archie's coefficient and the viscous tortuosity factor were then calculated from measured values of porosity, fibre diameter, and permeability. Finally, a universal curve linking the bulk tortuosity to the so-called Archie's exponent was presented. A fitting equation was therefore proposed, encompassing all CFs in broad ranges of porosities and structures. Based on this new equation, evaluated CFs can be classified according to their Archie's coefficient, thus leading to an outstanding predicting character of their morphological and permeability properties.

Emphasis was then placed on the identification of materials' deformation behaviours governed by different mechanisms during the uniaxial longitudinal compression of different CFs studied here, which may occur during the preparation of the energy storage composite. The viscoelastic properties of most soft CFs are seen to be highly complex, with almost continuous non-linear stress evolution at constant strain rate deformation, unlike the linear, buckling and densification compression regions observed for the rigid boards and rigidized CFs. In other words, there are large differences in mechanical behaviour between the different CFs' groups or subgroups with variations of fibres and types of mechanical and/or chemical bonding. A different approach is therefore proposed, stemming from the experimentally justified need to model the elastic behaviour of some soft CFs and from the impossibility of determining a single elastic modulus value with the commonly used Hookean law. Thus, the mathematical simplicity of the used Mooney–Rivlin model allowed us to determine analytically soft CFs' elastic modulus from its constitutive parameters defined as functions of the deformation. This part also presented and discussed compression behaviour investigation by two different techniques, one dynamic and destructive, and a rather new quasi-static and non-destructive method. The possibility of implementing two different test methods made it possible to compare the elastic modulus results obtained under different test regimes, one concerning creep and the other vibro-acoustic deformations. A good correlation was found between the elastic modulus calculated from the stress-strain curves and the QMA values. Hence, the differences observed between the results highlight the inability of the QMA method to determine a global materials' elastic modulus and is only appropriate for determining the elastic modulus of soft CFs at a defined pre-compression load. Additionally, the damping loss factor was measured and presented for the first time for this kind of soft CFs.

With the aim of preparing hybrid composite material based on CFs, the thermal conductivity was also studied. The effective thermal conductivity of the investigated CFs was found to be much lower than that of single carbon fibre due to various fibre structural defects and arrangements in the felt, involving significant structural and thermal contact resistances. These results also show that the thermal conductivity of most CFs is highly anisotropic, with higher values in the IP direction compared to the same in the OP direction. Therefore, higher heat transfer in the CF-PC composite should be expected parallel to the CFs' IP direction and properly adjusted to the conditions of its final application use. Finally, it is observed that the increase in fabric density has a higher influence on the effective thermal conductivity in the OP than in the IP direction.

As demonstrated in this chapter, the examined CFs' morphological and physical properties have been identified and can be further tuned to develop optimal materials for the foreseen application. As the results from the performed characterisation show many properties of the evaluated CFs have been defined, but much remains to be done to develop appropriate characterisation methods and understand property-performance relationships. As a result, as supports for future energy storage materials, the CFs must be given increased attention to gain industrial and market value in the end-use under study.

II/5 Bibliography

- Bargmann, Swantje, Benjamin Klusemann, Jürgen Markmann, Jan Eike Schnabel, Konrad Schneider, Celal Soyarslan, and Jana Wilmers. 2018. "Generation of 3D Representative Volume Elements for Heterogeneous Materials: A Review." *Progress in Materials Science* 96 (July): 322–84. <https://doi.org/10.1016/j.pmatsci.2018.02.003>.
- Bayles, Gary A., George E. Klinzing, and Shiao-Hung Chiang. 1989. "Fractal Mathematics Applied to Flow in Porous Systems." *Particle & Particle Systems Characterization* 6 (1–4): 168–75. <https://doi.org/10.1002/ppsc.19890060128>.
- Biot, M. A. 1963. "Surface Instability of Rubber in Compression." *Applied Scientific Research, Section A* 12 (2): 168–82. <https://doi.org/10.1007/BF03184638>.
- Bohac, Vlastimil, Mattias K. Gustavsson, Ludovit Kubicar, and Silas E. Gustafsson. 2000. "Parameter Estimations for Measurements of Thermal Transport Properties with the Hot Disk Thermal Constants Analyzer." *Review of Scientific Instruments* 71 (6): 2452–55. <https://doi.org/10.1063/1.1150635>.
- Bonfiglio, Paolo, Francesco Pompoli, Kirill V. Horoshenkov, Mahmud Iskandar B. Seth A. Rahim, Luc Jaouen, Julia Rodenas, François-Xavier Bécot, et al. 2018. "How Reproducible Are Methods to Measure the Dynamic Viscoelastic Properties of Poroelastic Media?" *Journal of Sound and Vibration* 428 (August): 26–43. <https://doi.org/10.1016/j.jsv.2018.05.006>.
- Cai, Jianchao, Liang Luo, Ran Ye, Xiangfeng Zeng, and Xiangyun Hu. 2015. "Recent Advances on Fractal Modeling of Permeability for Fibrous Porous Media." *Fractals* 23 (01): 1–9. <https://doi.org/10.1142/S0218348X1540006X>.
- Carman, P. C. 1937. "Fluid Flow through Granular Beds." *Trans. Inst. Chem. Eng.* 15: 150–66.
- Celzard, A., and J. F. Marêché. 2002. "Fluid Flow in Highly Porous Anisotropic Graphites." *Journal of Physics: Condensed Matter* 14 (6): 1119–1129. <https://doi.org/10.1088/0953-8984/14/6/301>.
- Celzard, A., J. F. Marêché, and G. Furdin. 2003. "Describing the Properties of Compressed Expanded Graphite through Power Laws." *Journal of Physics: Condensed Matter* 15 (43): 7213–7226. <https://doi.org/10.1088/0953-8984/15/43/006>.
- Chen, B, A. H. -D Cheng, and T. -W Chou. 2001. "A Nonlinear Compaction Model for Fibrous Preforms." *Composites Part A: Applied Science and Manufacturing* 32 (5): 701–7. [https://doi.org/10.1016/S1359-835X\(00\)00148-2](https://doi.org/10.1016/S1359-835X(00)00148-2).
- Chen, Baoxing, Eric J. Lang, and Tsu-Wei Chou. 2001. "Experimental and Theoretical Studies of Fabric Compaction Behavior in Resin Transfer molding1Dedicated to Professor Ah S. Argon.1." *Materials Science and Engineering: A* 317 (1): 188–96. [https://doi.org/10.1016/S0921-5093\(01\)01175-3](https://doi.org/10.1016/S0921-5093(01)01175-3).
- Chwastiak, S. 1973. "A Wicking Method for Measuring Wetting Properties of Carbon Yarns." *Journal of Colloid and Interface Science* 42 (2): 298–309. [https://doi.org/10.1016/0021-9797\(73\)90293-2](https://doi.org/10.1016/0021-9797(73)90293-2).
- Comas-Cardona, S., P. Le Grogne, C. Binetruy, and P. Krawczak. 2007. "Unidirectional Compression of Fibre Reinforcements. Part 1: A Non-Linear Elastic-Plastic Behaviour." *Composites Science and Technology* 67 (3): 507–14. <https://doi.org/10.1016/j.compscitech.2006.08.017>.
- Costa, Antonio. 2006. "Permeability-Porosity Relationship: A Reexamination of the Kozeny-Carman Equation Based on a Fractal Pore-Space Geometry Assumption." *Geophysical Research Letters* 33 (2). <https://doi.org/10.1029/2005GL025134>.
- Dai, Zhishuang, Fenghui Shi, Baoyan Zhang, Min Li, and Zuoguang Zhang. 2011. "Effect of Sizing on Carbon Fiber Surface Properties and Fibers/Epoxy Interfacial Adhesion."

- Applied Surface Science* 257 (15): 6980–85.
<https://doi.org/10.1016/j.apsusc.2011.03.047>.
- Davies, C. N. 1953. “The Separation of Airborne Dust and Particles.” *Proceedings of the Institution of Mechanical Engineers, Part B: Management and Engineering Manufacture* 1 (1–12): 185–213. <https://doi.org/10.1177/095440545300100113>.
- Delgado Sánchez, Clara. 2017. “Nouvelles Méthodes D’optimisation et de Caractérisation de Mousses À Base de Tanins Pour L’isolation Thermique Du Bâtiment.” Thesis, Université de Lorraine.
- Delgado-Sánchez, C., F. J. Santiago-Medina, V. Fierro, A. Pizzi, and A. Celzard. 2018. “Destructive vs. Non-Destructive Methods for the Mechanical Characterisation of Tannin-Based Thermoset Foams.” *Polymer Testing* 69 (August): 332–39. <https://doi.org/10.1016/j.polymertesting.2018.05.046>.
- Dinges, Carl. 2006. “Thermal Properties – Anisotropic Thermal Conductivity and Thermal Diffusivity Determined Using the Hot Disk Thermal Constants Analyser (the TPS Technique).”
- Doormaal, Mark A. Van, and Jon G. Pharoah. 2009. “Determination of Permeability in Fibrous Porous Media Using the Lattice Boltzmann Method with Application to PEM Fuel Cells.” *International Journal for Numerical Methods in Fluids* 59 (1): 75–89. <https://doi.org/10.1002/flid.1811>.
- Dresselhaus, Mildred S. 1988. *Graphite fibers and filaments*. Berlin, Allemagne, France.
- El-kharouf, Ahmad, Thomas J. Mason, Dan J. L. Brett, and Bruno G. Pollet. 2012. “Ex-Situ Characterisation of Gas Diffusion Layers for Proton Exchange Membrane Fuel Cells.” *Journal of Power Sources* 218 (November): 393–404. <https://doi.org/10.1016/j.jpowsour.2012.06.099>.
- Fadzillah, D. M., M. I. Rosli, M. Z. M. Talib, S. K. Kamarudin, and W. R. W. Daud. 2017. “Review on Microstructure Modelling of a Gas Diffusion Layer for Proton Exchange Membrane Fuel Cells.” *Renewable and Sustainable Energy Reviews* 77 (September): 1001–9. <https://doi.org/10.1016/j.rser.2016.11.235>.
- Frank, Erik, Lisa M. Steudle, Denis Ingildeev, Johanna M. Spörl, and Michael R. Buchmeiser. 2014. “Carbon Fibers: Precursor Systems, Processing, Structure, and Properties.” *Angewandte Chemie International Edition* 53 (21): 5262–98. <https://doi.org/10.1002/anie.201306129>.
- Fung, Yc. 1967. “Elasticity of Soft Tissues in Simple Elongation.” *American Journal of Physiology-Legacy Content* 213 (6): 1532–44. <https://doi.org/10.1152/ajplegacy.1967.213.6.1532>.
- Ghane, M., R. Saghafi, M. Zarrebini, and D. Semnani. 2011. “Evaluation of Bending Modulus of Needle-Punched Fabrics Using Two Simply Supported Beam Method.” *Fibres & Textiles in Eastern Europe* Nr 4 (87).
- Giesche, Herbert. 2006. “Mercury Porosimetry: A General (Practical) Overview.” *Particle & Particle Systems Characterization* 23 (1): 9–19. <https://doi.org/10.1002/ppsc.200601009>.
- González, Zoraida, Cristina Flox, Clara Blanco, Marcos Granda, Juan R. Morante, Rosa Menéndez, and Ricardo Santamaría. 2017. “Outstanding Electrochemical Performance of a Graphene-Modified Graphite Felt for Vanadium Redox Flow Battery Application.” *Journal of Power Sources* 338 (January): 155–62. <https://doi.org/10.1016/j.jpowsour.2016.10.069>.
- González-García, J., P. Bonete, E. Expósito, V. Montiel, A. Aldaz, and R. Torregrosa-Maciá. 1999. “Characterization of a Carbon Felt Electrode: Structural and Physical Properties.” *Journal of Materials Chemistry* 9 (2): 419–26. <https://doi.org/10.1039/A805823G>.

- Gostick, Jeff T., Michael W. Fowler, Mark D. Pritzker, Marios A. Ioannidis, and Leya M. Behra. 2006. "In-Plane and through-Plane Gas Permeability of Carbon Fiber Electrode Backing Layers." *Journal of Power Sources* 162 (1): 228–38. <https://doi.org/10.1016/j.jpowsour.2006.06.096>.
- Groupe, Poreux P. C. 1987. "Transport in Heterogeneous Porous Media." *Physica Scripta* T19B (January): 524–530. <https://doi.org/10.1088/0031-8949/1987/T19B/033>.
- Henderson, Nélio, Juan C. Brêttas, and Wagner F. Sacco. 2010. "A Three-Parameter Kozeny–Carman Generalized Equation for Fractal Porous Media." *Chemical Engineering Science* 65 (15): 4432–42. <https://doi.org/10.1016/j.ces.2010.04.006>.
- Huang, Xiaosong. 2009. "Fabrication and Properties of Carbon Fibers." *Materials* 2 (4): 2369–2403. <https://doi.org/10.3390/ma2042369>.
- Hung, Chih Jung, Ching Han Liu, Tse Hao Ko, Wei Hung Chen, Shu Hui Cheng, Wan Shu Chen, Alan Yu, and A. M. Kannan. 2013. "Effect of Diffusion Layers Fabricated with Different Fiber Diameters on the Performance of Low Temperature Proton Exchange Membrane Fuel Cells." *Journal of Power Sources* 221 (January): 134–40. <https://doi.org/10.1016/j.jpowsour.2012.08.030>.
- Hunt, Allen, and Robert Ewing. 2009. *Percolation Theory for Flow in Porous Media*. 2nd ed. 2009 edition. Berlin: Springer.
- Jackson, Graham W., and David F. James. 1986. "The Permeability of Fibrous Porous Media." *The Canadian Journal of Chemical Engineering* 64 (3): 364–74. <https://doi.org/10.1002/cjce.5450640302>.
- Jaganathan, S., H. Vahedi Tafreshi, E. Shim, and B. Pourdeyhimi. 2009. "A Study on Compression-Induced Morphological Changes of Nonwoven Fibrous Materials." *Colloids and Surfaces A: Physicochemical and Engineering Aspects* 337 (1): 173–79. <https://doi.org/10.1016/j.colsurfa.2008.12.019>.
- Jaganathan, Sudhakar. 2008. *An Investigation on Fluid Flow in Fibrous Materials Via Image-Based Fluid Dynamics Simulations*.
- Jaouen, Luc, Amélie Renault, and Mickael Deverge. 2008. "Elastic and Damping Characterizations of Acoustical Porous Materials: Available Experimental Methods and Applications to a Melamine Foam." *Applied Acoustics* 69 (12): 1129–40. <https://doi.org/10.1016/j.apacoust.2007.11.008>.
- Jarzynski, Jacek. 1990. "Mechanisms of Sound Attenuation in Materials." In *Sound and Vibration Damping with Polymers*, 424:167–207. ACS Symposium Series 424. American Chemical Society. <https://doi.org/10.1021/bk-1990-0424.ch010>.
- Jearanaisilawong, Petch. 2008. "A Continuum Model for Needle-punched Nonwoven Fabrics." Thesis, Massachusetts Institute of Technology.
- Johnson, David Linton, Joel Koplik, and Roger Dashen. 1987. "Theory of Dynamic Permeability and Tortuosity in Fluid-Saturated Porous Media." *Journal of Fluid Mechanics* 176: 379–402. <https://doi.org/10.1017/S0022112087000727>.
- Ke, Xinyou, Joseph M. Prah, J. Iwan D. Alexander, and Robert F. Savinell. 2018. "Redox Flow Batteries with Serpentine Flow Fields: Distributions of Electrolyte Flow Reactant Penetration into the Porous Carbon Electrodes and Effects on Performance." *Journal of Power Sources* 384 (April): 295–302. <https://doi.org/10.1016/j.jpowsour.2018.03.001>.
- Kelly, P. A., R. Umer, and S. Bickerton. 2006. "Viscoelastic Response of Dry and Wet Fibrous Materials during Infusion Processes." *Composites Part A: Applied Science and Manufacturing*, Selected Contributions from the 7th International Conference on Flow Processes in Composite Materials held at University of Delaware, USA, 37 (6): 868–73. <https://doi.org/10.1016/j.compositesa.2005.02.008>.

- Kok, Matthew D. R., and Jeff T. Gostick. 2015. "Transport Properties of Electrospun Fibrous Membranes with Controlled Anisotropy." *Journal of Membrane Science* 473 (January): 237–44. <https://doi.org/10.1016/j.memsci.2014.09.017>.
- Lee, J., L. Yun, and J. Park. 2005. "Anisotropic Properties of Needle Punched Carbon/Carbon Composites."
- Lee, Jae Yeol, and Tae Jin Kang. 2005. "Thermal Conductivity of Needle Punched Preforms Made of Carbon and OxiPAN Fibres," January.
- Lee, Jin-woo, Soo-Jeong Park, Yun-hae Kim, and Riichi-Murakami. 2018. "Thermal Characteristics of Carbon Fiber Reinforced Epoxy Containing Multi-Walled Carbon Nanotubes." *Results in Physics* 9 (June): 1–5. <https://doi.org/10.1016/j.rinp.2017.11.016>.
- Letellier, M., V. Fierro, A. Pizzi, and A. Celzard. 2014. "Tortuosity Studies of Cellular Vitreous Carbon Foams." *Carbon* 80 (December): 193–202. <https://doi.org/10.1016/j.carbon.2014.08.056>.
- Mahboobeh, FAHIMIAN. 2013. *Processing- Structure- Property Relationship in Needle Punched Nonwoven Natural Fiber Mat Composites - ProQuest*.
- Mao, N. 2016. "6 - Methods for Characterisation of Nonwoven Structure, Property, and Performance." In *Advances in Technical Nonwovens*, edited by George Kellie, 155–211. Woodhead Publishing Series in Textiles. Woodhead Publishing. <https://doi.org/10.1016/B978-0-08-100575-0.00006-1>.
- Mathias M. F., Roth J., Fleming J., and Lehnert W. 2010. "Diffusion Media Materials and Characterisation." *Handbook of Fuel Cells*, Major Reference Works, , December. <https://doi.org/10.1002/9780470974001.f303046>.
- Matsudaira, M., and H. Qin. 1995. "Features and Mechanical Parameters of a Fabric's Compressional Property." *The Journal of The Textile Institute* 86 (3): 476–86. <https://doi.org/10.1080/00405009508658774>.
- Meng, Long-Yue, and Soo-Jin Park. 2014. "Superhydrophobic Carbon-Based Materials: A Review of Synthesis, Structure, and Applications." *Carbon Letters* 15 (2): 89–104.
- Mihai L., Angela, and Alain Goriely. 2017. "How to Characterize a Nonlinear Elastic Material? A Review on Nonlinear Constitutive Parameters in Isotropic Finite Elasticity." *Proceedings of the Royal Society A: Mathematical, Physical and Engineering Sciences* 473 (2207): 20170607. <https://doi.org/10.1098/rspa.2017.0607>.
- Miller, Michael G., Jason M. Keith, Julia A. King, Brian J. Edwards, Nils Klinkenberg, and David A. Schiraldi. 2006. "Measuring Thermal Conductivities of Anisotropic Synthetic Graphite–liquid Crystal Polymer Composites." *Polymer Composites* 27 (4): 388–94. <https://doi.org/10.1002/pc.20231>.
- Mooney, M. 1940. "A Theory of Large Elastic Deformation." *Journal of Applied Physics* 11 (9): 582–92. <https://doi.org/10.1063/1.1712836>.
- Naito, Kimiyoshi, Jenn-Ming Yang, Yibin Xu, and Yutaka Kagawa. 2010. "Enhancing the Thermal Conductivity of Polyacrylonitrile- and Pitch-Based Carbon Fibers by Grafting Carbon Nanotubes on Them." *Carbon* 6 (48): 1849–57. <https://doi.org/10.1016/j.carbon.2010.01.031>.
- Newcomb, Bradley A. 2016. "Processing, Structure, and Properties of Carbon Fibers." *Composites Part A: Applied Science and Manufacturing* 91 (December): 262–82. <https://doi.org/10.1016/j.compositesa.2016.10.018>.
- Nouri, Nima, Francesco Panerai, Kaveh A. Tagavi, Nagi N. Mansour, and Alexandre Martin. 2016. "Evaluation of the Anisotropic Radiative Conductivity of a Low-Density Carbon Fiber Material from Realistic Microscale Imaging." *International Journal of Heat and Mass Transfer* 95 (April): 535–39. <https://doi.org/10.1016/j.ijheatmasstransfer.2015.12.004>.

- Nowak, Z. 2008. "Constitutive Modelling and Parameter Identification for Rubber-like Materials." *Engineering Transactions*, no. Vol. 56, iss. 2: 117–57.
- Ogden, R. W. 1997. *Non-Linear Elastic Deformations*. Dover Civil and Mechanical Engineering. New York, NY: Dover Publications.
- Panerai, Francesco, Joseph C. Ferguson, Jean Lachaud, Alexandre Martin, Matthew J. Gasch, and Nagi N. Mansour. 2017. "Micro-Tomography Based Analysis of Thermal Conductivity, Diffusivity and Oxidation Behavior of Rigid and Flexible Fibrous Insulators." *International Journal of Heat and Mass Transfer* 108 (May): 801–11. <https://doi.org/10.1016/j.ijheatmasstransfer.2016.12.048>.
- Park, Soo-Jin. 2015. *Carbon Fibers*. Springer Series in Materials Science. Springer Netherlands.
- Park, Soo-Jin, and Byung-Joo Kim. 2005. "Roles of Acidic Functional Groups of Carbon Fiber Surfaces in Enhancing Interfacial Adhesion Behavior." *Materials Science and Engineering: A* 408 (1): 269–73. <https://doi.org/10.1016/j.msea.2005.08.129>.
- Pierson, Hugh O., ed. 1993. "Handbook of Carbon, Graphite, Diamonds and Fullerenes." In *Handbook of Carbon, Graphite, Diamonds and Fullerenes*, v–vi. Oxford: William Andrew Publishing. <https://doi.org/10.1016/B978-0-8155-1339-1.50003-7>.
- Pucci, Monica Francesca, Pierre-Jacques Liotier, and Sylvain Drapier. 2015. "Capillary Wicking in a Fibrous Reinforcement – Orthotropic Issues to Determine the Capillary Pressure Components." *Composites Part A: Applied Science and Manufacturing* 77 (October): 133–41. <https://doi.org/10.1016/j.compositesa.2015.05.031>.
- Qian, X., Y. G. Zhang, X. F. Wang, Y. J. Heng, and J. H. Zhi. 2016. "Effect of Carbon Fiber Surface Functionality on the Moisture Absorption Behavior of Carbon Fiber/Epoxy Resin Composites." *Surface and Interface Analysis* 48 (12): 1271–77. <https://doi.org/10.1002/sia.6031>.
- Rabbow, Thomas J., Markus Trampert, Peter Pokorny, Paul Binder, and Adam H. Whitehead. 2015. "Variability within a Single Type of Polyacrylonitrile-Based Graphite Felt after Thermal Treatment. Part I: Physical Properties." *Electrochimica Acta* 173 (August): 17–23. <https://doi.org/10.1016/j.electacta.2015.05.020>.
- Radhakrishnan, Arjun, Zijie Lu, and Satish G. Kandlikar. 2010. "Effective Thermal Conductivity of Gas Diffusion Layers Used in PEMFC: Measured with Guarded-Hot-Plate Method and Predicted by a Fractal Model." *ECS Transactions* 33 (1): 1163–76. <https://doi.org/10.1149/1.3484610>.
- Ramousse, Julien, Sophie Didierjean, Olivier Lottin, and Denis Maillet. 2008. "Estimation of the Effective Thermal Conductivity of Carbon Felts Used as PEMFC Gas Diffusion Layers." *International Journal of Thermal Sciences* 47 (1): 1–6. <https://doi.org/10.1016/j.ijthermalsci.2007.01.018>.
- Rice, H. J., and P. Göransson. 1999. "A Dynamical Model of Light Fibrous Materials." *International Journal of Mechanical Sciences* 41 (4): 561–79. [https://doi.org/10.1016/S0020-7403\(98\)00082-4](https://doi.org/10.1016/S0020-7403(98)00082-4).
- Rivlin, S. R., and Rideal Eric Keightley. 1948. "Large Elastic Deformations of Isotropic Materials IV. Further Developments of the General Theory." *Philosophical Transactions of the Royal Society of London. Series A, Mathematical and Physical Sciences* 241 (835): 379–97. <https://doi.org/10.1098/rsta.1948.0024>.
- Rocha, Rodrigo P. A., and Manuel E. Cruz. 2010. "Calculation of the Permeability and Apparent Permeability of Three-Dimensional Porous Media." *Transport in Porous Media* 83 (2): 349–73. <https://doi.org/10.1007/s11242-009-9445-7>.
- Rutledge, Gregory C., Joseph L. Lowery, and Chia-Ling Pai. 2009. "Characterization by Mercury Porosimetry of Nonwoven Fiber Media with Deformation." *Prof. Rutledge via Erja Kajosalu*, April.

- Salençon, Jean. 2001. "Thermoelasticity." In *Handbook of Continuum Mechanics: General Concepts Thermoelasticity*, edited by Jean Salençon, 295–359. Berlin, Heidelberg: Springer Berlin Heidelberg. https://doi.org/10.1007/978-3-642-56542-7_7.
- Saunders, R. A, C Lekakou, and M. G Bader. 1999. "Compression in the Processing of Polymer Composites 1. A Mechanical and Microstructural Study for Different Glass Fabrics and Resins." *Composites Science and Technology* 59 (7): 983–93. [https://doi.org/10.1016/S0266-3538\(98\)00137-7](https://doi.org/10.1016/S0266-3538(98)00137-7).
- Sen, P. N., C. Scala, and M. H. Cohen. 1981. "A Self-Similar Model for Sedimentary Rocks with Application to the Dielectric Constant of Fused Glass Beads." *Geophysics* 46 (5): 781–95. <https://doi.org/10.1190/1.1441215>.
- Shen, Wenzhong, Zhijie Li, and Yihong Liu. 2008. Surface Chemical Functional Groups Modification of Porous Carbon. *Recent Patents on Chemical Engineering* 1 (1): 27–40.
- Shi, Wei, Jia Yan Li, Qi Fan You, Tong Lu, and Yi Tan. 2015. "Preparation and Properties of Rigid Carbon Felt Thermal Insulation." *Materials Science Forum* 833: 48–51. <https://doi.org/10.4028/www.scientific.net/MSF.833.48>.
- Shou, Dahua, Jintu Fan, and Feng Ding. 2011. "Hydraulic Permeability of Fibrous Porous Media." *International Journal of Heat and Mass Transfer* 54 (17): 4009–18. <https://doi.org/10.1016/j.ijheatmasstransfer.2011.04.022>.
- Shou, Dahua, Youhong Tang, Lin Ye, Jintu Fan, and Feng Ding. 2013. "Effective Permeability of Gas Diffusion Layer in Proton Exchange Membrane Fuel Cells." *International Journal of Hydrogen Energy* 38 (25): 10519–26. <https://doi.org/10.1016/j.ijhydene.2013.06.043>.
- Simaafrookhteh, S., M. Shakeri, M. Baniassadi, and A. Alizadeh Sahraei. 2018. "Microstructure Reconstruction and Characterization of the Porous GDLs for PEMFC Based on Fibers Orientation Distribution." *Fuel Cells* 18 (2): 160–72. <https://doi.org/10.1002/fuce.201700239>.
- Soltani, Parham, Majid Safar Johari, and Mohammad Zarrebini. 2013. "Tomography-Based Determination of Transverse Permeability in Fibrous Porous Media." *Journal of Industrial Textiles* 44 (5): 738–56. <https://doi.org/10.1177/1528083713512357>.
- Soltani, Parham, Majid Safar Johari, and Mohammad Zarrebini. 2014. "Effect of 3D Fiber Orientation on Permeability of Realistic Fibrous Porous Networks." *Powder Technology* 254 (March): 44–56. <https://doi.org/10.1016/j.powtec.2014.01.001>.
- Soltani, Parham, Majid Safar Johari, and Mohammad Zarrebini. 2015. "Tomography-Based Determination of Transverse Permeability in Fibrous Porous Media." *Journal of Industrial Textiles* 44 (5): 738–56. <https://doi.org/10.1177/1528083713512357>.
- Soltani, Parham, Mohammad Zarrebini, Reyhaneh Laghaei, and Ali Hassanpour. 2017. "Prediction of Permeability of Realistic and Virtual Layered Nonwovens Using Combined Application of X-Ray μ CT and Computer Simulation." *Chemical Engineering Research and Design* 124 (Supplement C): 299–312. <https://doi.org/10.1016/j.cherd.2017.06.035>.
- Stark, C., and J. Fricke. 1993. "Improved Heat-Transfer Models for Fibrous Insulations." *International Journal of Heat and Mass Transfer* 36 (3): 617–25. [https://doi.org/10.1016/0017-9310\(93\)80037-U](https://doi.org/10.1016/0017-9310(93)80037-U).
- Sun, Ning. 2014. *Structures of Needle-punched Fabrics and Needling Mechanism*.
- Tamayol, Ali, and Majid Bahrami. 2011. "Transverse Permeability of Fibrous Porous Media." *Physical Review E* 83 (4): 046314:1-9. <https://doi.org/10.1103/PhysRevE.83.046314>.
- Tarnow, Viggo. 2005. "Dynamic Measurements of the Elastic Constants of Glass Wool." *The Journal of the Acoustical Society of America* 118 (6): 3672–78. <https://doi.org/10.1121/1.2118267>.

- Timoshenko, Stephen P. 1983. *History of Strength of Materials: With a Brief Account of the History of Theory of Elasticity and Theory of Structures*. New York, NY: Dover.
- Tomadakis, Manolis M., and Teri J. Robertson. 2005. "Viscous Permeability of Random Fiber Structures: Comparison of Electrical and Diffusional Estimates with Experimental and Analytical Results, Viscous Permeability of Random Fiber Structures: Comparison of Electrical and Diffusional Estimates with Experimental and Analytical Results." *Journal of Composite Materials* 39 (2): 163–88. <https://doi.org/10.1177/0021998305046438>.
- Tomadakis, Manolis M., and Stratis V. Sotirchos. 1991. "Effective Kundsens Diffusivities in Structures of Randomly Overlapping Fibers." *AIChE Journal* 37 (1): 74–86. <https://doi.org/10.1002/aic.690370107>.
- Tomadakis, Manolis M., and Stratis V. Sotirchos. 1993. "Ordinary and Transition Regime Diffusion in Random Fiber Structures." *AIChE Journal* 39 (3): 397–412. <https://doi.org/10.1002/aic.690390304>.
- Vignoles, G. L. 2015. "17 - Modeling of Chemical Vapor Infiltration Processes." In *Advances in Composites Manufacturing and Process Design*, edited by Philippe Boisse, 415–58. Woodhead Publishing. <https://doi.org/10.1016/B978-1-78242-307-2.00017-8>.
- Webb, Paul A. 2001. "An Introduction To The Physical Characterization of Materials by Mercury Intrusion Porosimetry with Emphasis On Reduction And Presentation of Experimental Data." 2001.
- Wong, Po-zen, Joel Koplik, and J. P. Tomanic. 1984. "Conductivity and Permeability of Rocks." *Physical Review B* 30 (11): 6606–14. <https://doi.org/10.1103/PhysRevB.30.6606>.
- Wood, Lawrence A. 1978. "Uniaxial Extension and Compression in Stress-Strain Relations of Rubber." *Rubber Chemistry and Technology* 51 (4): 840–51. <https://doi.org/10.5254/1.3535767>.
- Wu, Shuai, Yunqi Liu, Yicheng Ge, Liping Ran, Ke Peng, and Maozhong Yi. 2016. "Surface Structures of PAN-Based Carbon Fibers and Their Influences on the Interface Formation and Mechanical Properties of Carbon-Carbon Composites." *Composites Part A: Applied Science and Manufacturing* 90 (November): 480–88. <https://doi.org/10.1016/j.compositesa.2016.08.023>.
- Wyk, C. M. van. 1946. "20—Note on the Compressibility of Wool." *Journal of the Textile Institute Transactions* 37 (12): T285–92. <https://doi.org/10.1080/19447024608659279>.
- Xiao, Feng, and Xiaolong Yin. 2016. "Geometry Models of Porous Media Based on Voronoi Tessellations and Their Porosity–permeability Relations." *Computers & Mathematics with Applications*, The Proceedings of ICMMES 2014, 72 (2): 328–48. <https://doi.org/10.1016/j.camwa.2015.09.009>.
- Yuan, Yuehua, and T. Randall Lee. 2013. "Contact Angle and Wetting Properties." In *Surface Science Techniques*, 3–34. Springer Series in Surface Sciences. Springer, Berlin, Heidelberg. https://doi.org/10.1007/978-3-642-34243-1_1.
- Zamel, Nada, and Xianguo Li. 2013. "Effective Transport Properties for Polymer Electrolyte Membrane Fuel Cells – With a Focus on the Gas Diffusion Layer." *Progress in Energy and Combustion Science* 39 (1): 111–46. <https://doi.org/10.1016/j.pecs.2012.07.002>.
- Zhang, Hu, Yue-Ming Li, and Wen-Quan Tao. 2017. "Theoretical Accuracy of Anisotropic Thermal Conductivity Determined by Transient Plane Source Method." *International Journal of Heat and Mass Transfer* 108 (May): 1634–44. <https://doi.org/10.1016/j.ijheatmasstransfer.2017.01.025>.
- Zhang, Jing. 2012. "Different Surface Treatments of Carbon Fibers and Their Influence on the Interfacial Properties of Carbon Fiber/Epoxy Composites." Phdthesis, Ecole Centrale Paris.

- Zhang, Wenyong. 2014. *Modification of Carbon Fiber / Epoxy Matrix Interphase in a Composite Material : Design of a Self-Healing Interphase by Introducing Thermally Reversible Diels-Alder Adducts*. Lyon, INSA. <http://www.theses.fr/2014ISAL0127>.
- Zhang, Yao, Zixing Lu, Zhenyu Yang, Dahai Zhang, Jianjun Shi, Zeshuai Yuan, and Qiang Liu. 2017. "Compression Behaviors of Carbon-Bonded Carbon Fiber Composites: Experimental and Numerical Investigations." *Carbon* 116 (May): 398–408. <https://doi.org/10.1016/j.carbon.2017.02.012>.
- Zhang, Zhengyang, Jingyu Xi, Haipeng Zhou, and Xiping Qiu. 2016. "KOH Etched Graphite Felt with Improved Wettability and Activity for Vanadium Flow Batteries." *Electrochimica Acta* 218 (November): 15–23. <https://doi.org/10.1016/j.electacta.2016.09.099>.
- Zhao, Xiaoming, Yuanjun Liu, and Tenglong Liang. 2016. "Influence of the Needle Number on the Heat Insulation Performance of Pre-Oxidized Fibre Felts." *Fibres and Textiles in Eastern Europe* 24 (6(120)): 129–37. <https://doi.org/10.5604/01.3001.0011.7307>.
- Zhong, S., C. Padeste, M. Kazacos, and M. Skyllas-Kazacos. 1993. "Comparison of the Physical, Chemical and Electrochemical Properties of Rayon- and Polyacrylonitrile-Based Graphite Felt Electrodes." *Journal of Power Sources* 45 (1): 29–41. [https://doi.org/10.1016/0378-7753\(93\)80006-B](https://doi.org/10.1016/0378-7753(93)80006-B).

II/6 Annex

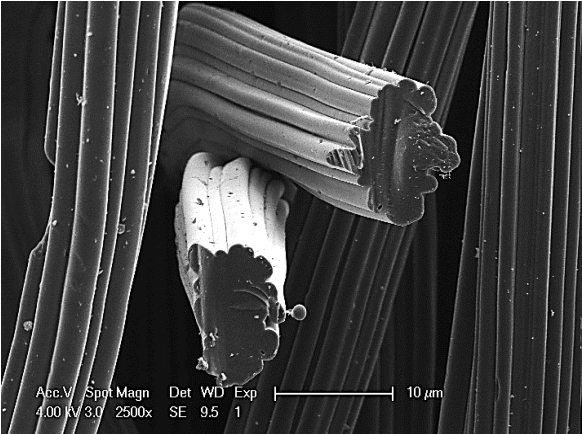
II/6.1 Available suppliers' specification information of the evaluated CFs
 Table II/6-1 Manufacturer available properties data for all received and used samples for the purposes of the project.

PROVIDER:	SGL Carbon Group			CeraMaterials							Schunk	Beijing Graphite Great Wall						ZOLTEK
USED CODE in Chapter II:	SFC1aSI	SFG1aSI	RBG1aSI	SFC2bC	SFC1aC	SFG1aC	SFG2bC	SFG2aC	rSFC2bC	RBG1aC	SFG1aSC	SFC1aBG	SFC2bBG	SFG1aBG	SFG2bBG	SFC2aBG	rSFG2bBG	SFC2aZF
USED CODE in Chapter III:	CR3	GR3	GR12	CP8	CR1	GR1	GP8	GP6	CP11	GR13	GR4	CR2	CP9	GR2	GP9	CP7	GP10	CP5
Carbon fibre precursor	/	Rayon	/	PAN	Rayon	Rayon	PAN	PAN	PAN	Rayon	Rayon	Rayon	PAN	Rayon	PAN	PAN	PAN	PAN
Heat treatment (°C) (inert atmosphere)	1000	2000	2000	1200	1200	2000	2000	/	/	2000	/	1200	1200	2200-2400	2200-2400	/	/	/
Thickness (cm)	0.65	1.15	/	0.635 - 5.08	0.635 - 5.09	0.635 - 5.11	0.635 - 5.10	0.1 - 1.5 (±0.35)	/	/	1	/	/	/	/	/	/	1.27
Fibre diameter (µm)	/	10 - 12	/	/	/	/	/	/	/	/	/	/	/	/	/	/	/	12.5
Carbon content (%)	/	/	/	≥ 97	≥ 97	≥ 99	≥ 99	99.8	/	/	/	/	/	/	/	/	/	95
Ash content (% ') or (ppm *)	1.7 '	≤ 400 *	1000*	≤1 '	≤1 '	≤0.5 '	≤0.5 '	/	/	/	≤ 300 *	/	/	/	/	/	/	/
Weight per unit area (g/m ²)	540	1000	/	/	/	/	/	/	/	/	/	/	/	/	/	/	/	1700
Bulk Density (g/cm ³)	/	/	0.2	0.12	0.15	0.085	0.12	0.09 - 0.15	/	/	/	/	/	/	/	/	/	0.102
Thermal conductivity (at 23°C)(W /m*K)	/	/	0.22	0.22	0.21	0.29	0.35	/	/	/	/	/	/	/	/	/	/	/

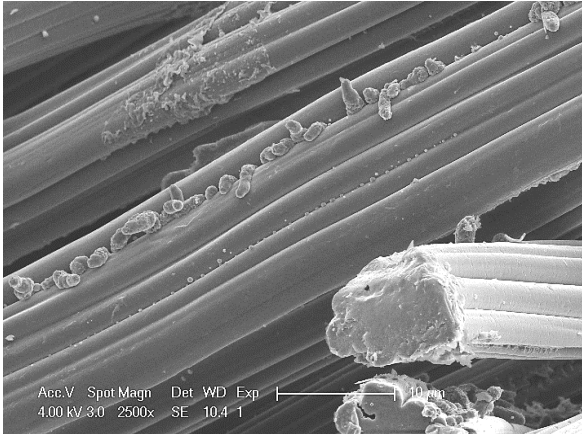
II/6.2 Morphological characteristics

Table II/6-2 Averaged density and porosity for the examined 18 CFs.

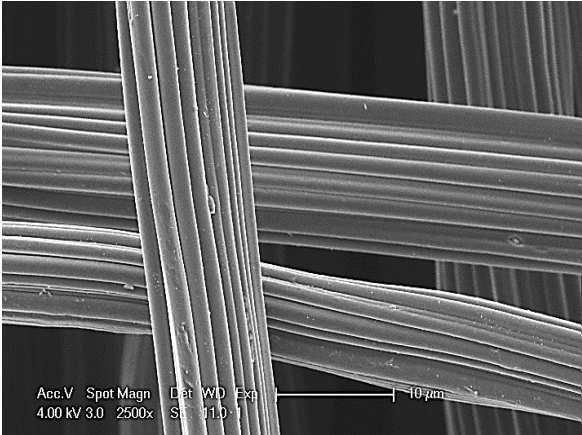
Sample code:	Bulk density (g cm ⁻³)	Skeletal density (g cm ⁻³)	Overall Porosity (%)	Fibre diameter	
				ave. (µm)	std. (µm)
Rayon soft CFs					
SFG1aC	0.073	1.900	95.7	10.70	1.28
SFC1aSI	0.081	1.600	95.2	9.59	0.78
SFG1aSI	0.085	1.657	94.8	9.70	1.44
SFG1aBG	0.092	1.800	94.6	12.57	1.71
SFC1aC	0.098	1.880	94.9	12.02	1.73
SFC1aBG	0.106	1.756	93.9	11.98	1.59
SFG1aSC	0.108	1.561	92.7	10.30	2.54
PAN (thin fibre) soft CFs					
SFC2aBG	0.084	1.779	95.3	10.56	1.07
SFG2aC	0.091	1.824	95.0	9.06	1.31
SFC2aZF	0.116	1.761	93.4	9.05	0.42
PAN (thick fibre) soft CFs					
SFG2bC	0.110	1.776	93.8	19.71	1.73
SFC2bBG	0.120	1.785	93.2	18.53	1.72
SFG2bBG	0.122	1.815	93.3	17.98	1.67
SFC2bC	0.140	1.859	92.5	18.69	1.60
Rayon RIGID BOARD CFs					
RBG1aSI	0.157	1.514	89.6	10.01	1.34
RBG1aC	0.198	1.582	87.5	11.63	2.17
Rigidized PAN (thick fibre) CFs					
rSFG2bBG	0.182	1.695	89.3	16.96	2.92
rSFC2bC	0.227	1.908	88.1	19.59	2.13



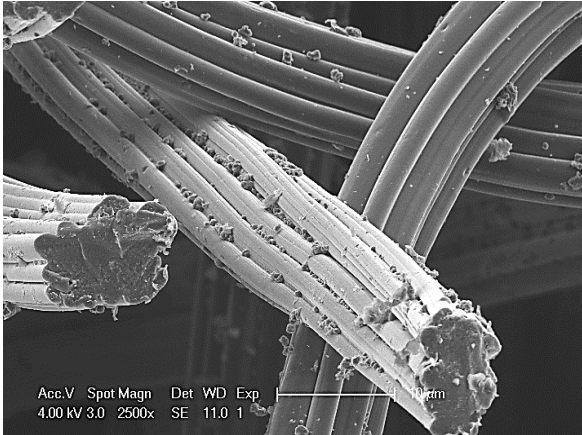
SFC1aC



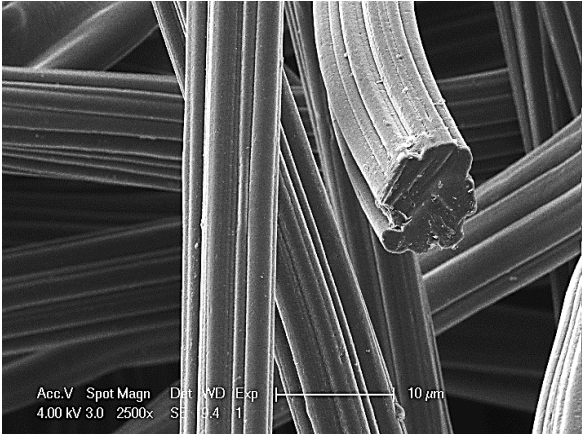
SFG1aC



SFC1aBG



SFG1aBG

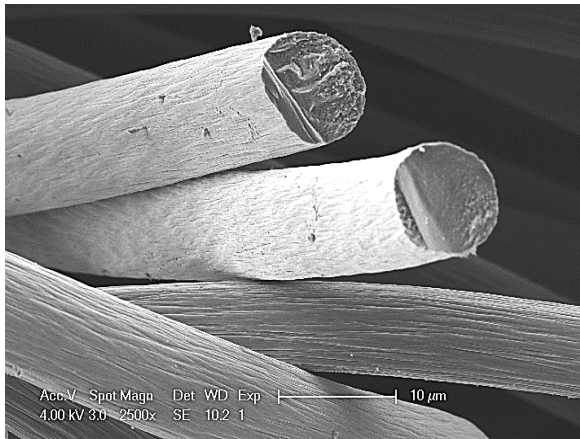


SFC1aSI

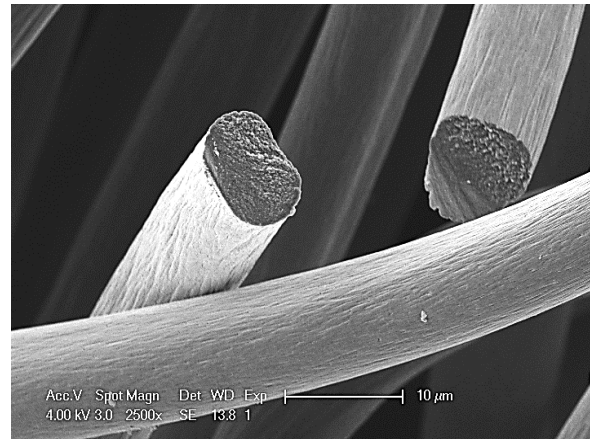


SFG1aSI

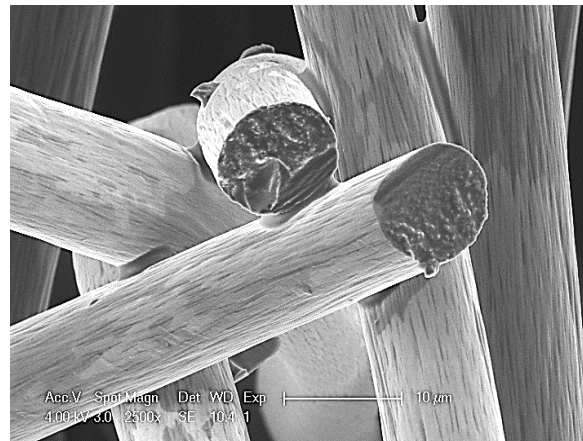
Figure II/6-1 Fibre structure and cross-section of Rayon Soft CFs.



SFC2aBG



SFG2aC



SFC2aZF

Figure II/6-2 Same as in Fig. II/6-1 but for PAN (thin fibre)-derived soft CFs.

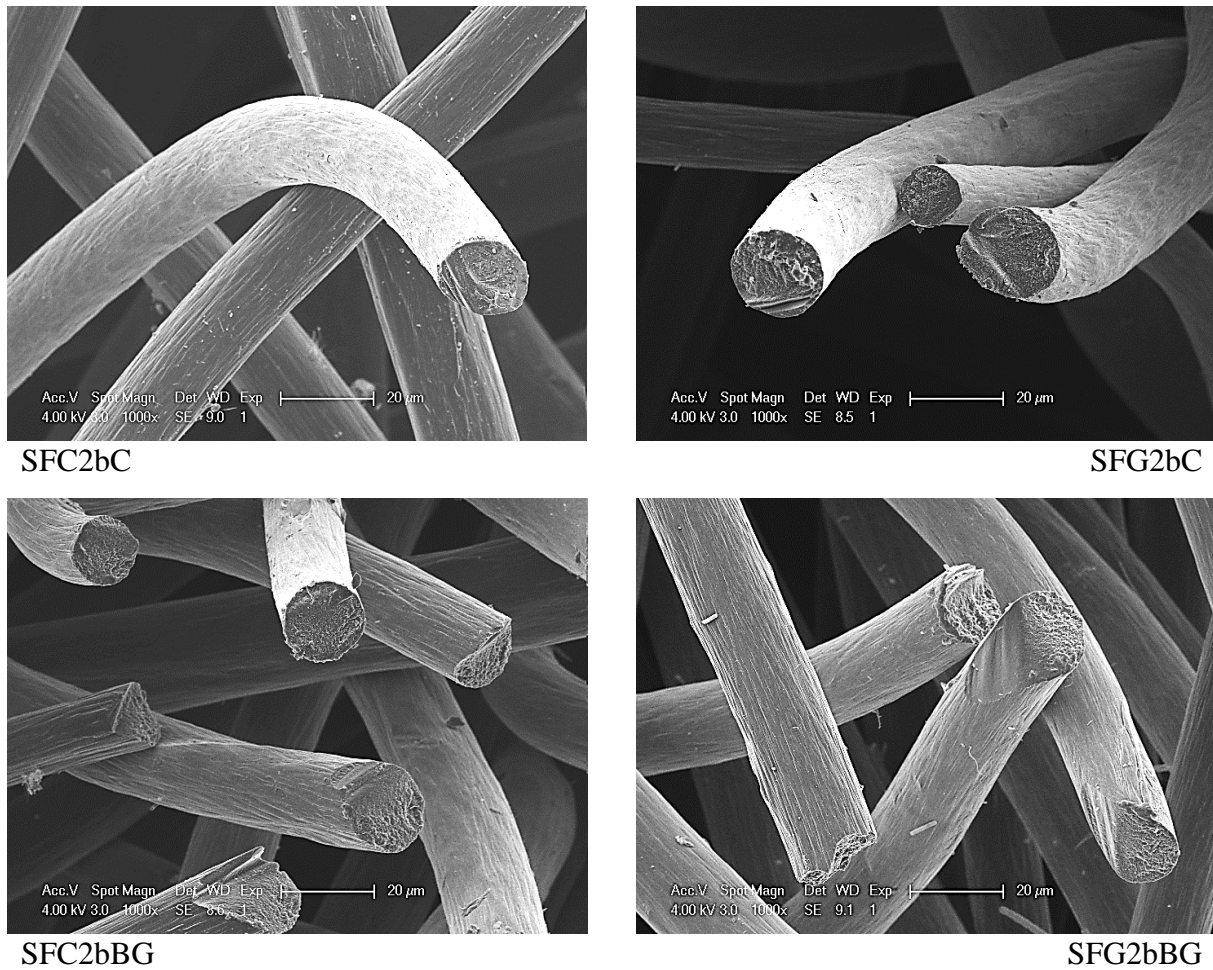


Figure II/6-3 Same as in Fig. II/6-1 but for PAN (thick fibre)-derived soft CFs.

II/6.3 Contact angle measurement results

Table II/6-3 Water contact angle on all CFs: averaged degree values (ave.) and standard deviation values (std.).

Sample code:	Contact angle		Sample code:	Contact angle	
	ave. [°]	std. [°]		ave. [°]	std. [°]
Rayon Soft CFs			PAN (thick fibre) soft CFs		
SFG1aBG	131.33	2.35	SFC2bBG	139.99	3.87
SFG1aC	138.03	3.22	SFG2bBG	143.22	3.76
SFC1aC	139.29	2.24	SFG2bC	145.86	2.44
SFC1aSI	139.75	3.45	SFC2bC	146.47	3.89
SFC1aBG	140.14	3.31			
SFG1aSI	140.66	4.55	Rayon RIGID BOARD CFs		
SFG1aSC	146.27	2.17	RBG1aSI	121.48	2.77
PAN (thin fibre) soft CFs			RBG1aC	138.63	2.11
SFC2aBG	140.03	1.81	Rigidised PAN (thick fibre) CFs		
SFG2aC	147.30	4.18	rSFC2bC	139.61	2.52
SFC2aZF	150.71	1.86	rSFG2bBG	140.93	0.72

II/6.4 Out-of-plane air permeability

Table II/6-4 Air permeability in the out-of-plane direction (with standard deviation) of all CFs investigated here; average fibre diameter and total porosity are included for comparison.

Sample code:	Fibre diameter	Overall Porosity	Air permeability (OP-direction)	
	ave.(μm)	(%)	(m^2)	Stdv.(m^2)
Rayon Needle-punched Soft CFs				
SFG1aSC	10.30	92.7	1.35E-10	3.68E-12
SFC1aBG	11.98	93.9	8.41E-11	6.58E-13
SFG1aBG	12.57	94.6	7.12E-11	3.49E-12
SFC1aC	12.02	94.8	8.07E-11	7.02E-13
SFG1aSI	9.70	94.8	1.04 E-10	7.51E-13
SFC1aSI	9.59	95.2	1.26 E-10	3.34E-12
SFG1aC	10.70	95.7	1.22 E-10	3.34E-12
PAN (thin fibre) Needle-punched Soft CFs				
SFC2bBG	18.53	93.2	3.11E-10	1.31E-11
SFG2bBG	17.98	93.3	2.90E-10	1.01E-11
SFG2bC	19.71	93.8	3.33E-10	2.23E-12
SFC2bC	18.69	92.5	3.26E-10	7.38E-12
PAN (thick fibre) Needle-punched Soft CFs				
SFC2aZF	9.05	93.4	1.33E-10	6.66E-12
SFG2aC	9.06	95.0	1.77E-10	2.81E-12
SFC2aBG	10.56	95.3	1.99E-10	5.62E-12
PAN (thick fibre) Rigidized Needle-punched Soft CFs				
rSFG2bBG	16.96	89.3	1.53E-10	7.09E-13
rSFC2bC	19.59	88.1	1.86E-10	2.13E-12
Rayon rigid board CFs				
RBG1aC	11.63	87.5	8.24E-11	6.86E-13
RBG1aSI	10.01	89.6	5.47E-11	1.90E-12

II/6.4.a Sensitivity analysis showing the effect of percolation threshold and porosity on the value of the Archies' exponent

Given that the results presented in Fig. II/3-23 and Fig. II/3-25 were obtained from the assumption that the percolation threshold is negligible, a sensitivity analysis was also carried out. First, a few nonzero values of ε_p were tested, and how the values of Archie's exponent changed with the viscous tortuosity factor was calculated, as shown in Fig. II/6-4 a). It can be seen that using $\varepsilon_p = 0.037$, i.e., the value expected for random 3D materials (see again Table II/3-3) very poorly affected the Archie's exponent, especially in the range of low to moderate tortuosity factors. Values as high as $\varepsilon_p = 0.11$, i.e., corresponding to purely 2D materials (which

is unrealistic in our case, as seen from SEM and tomography analysis) led to higher changes (up to one unit) but again at extreme values of tortuosities only. The impact of a nonzero percolation threshold should thus be considered as negligible, and especially for materials having porosities close to 1.

Finally, the same kind of sensitivity analysis was carried out as for the impact of the porosity, assuming again that $\varepsilon_p = 0$. It can be seen in Fig. II/6-4 b) that α was strongly affected by the value of ε . Nevertheless, the couples of values (α, η_v) strictly remained on the same master curve as the one presented in Fig. II/3-23, thus supporting its robustness and suggesting that α should be considered as an intrinsic property of the porous medium and not as constants, as formerly recommended by Tomadakis and Robertson (2005).

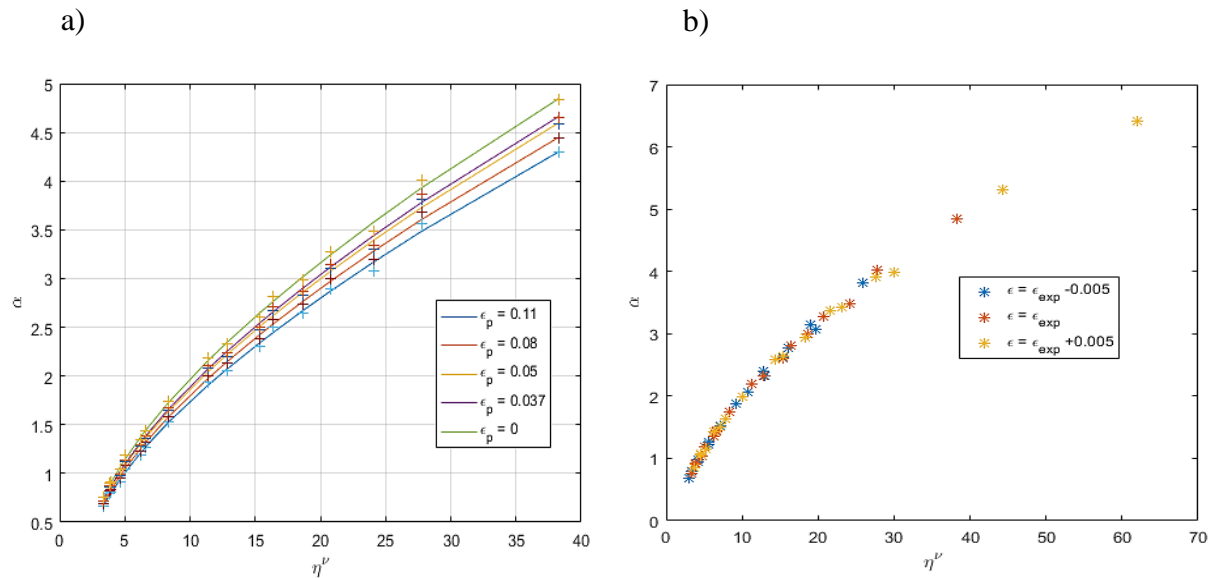


Figure II/6-4 Sensibility analysis showing the effect of: a) percolation threshold ε_p , and b) porosity ε , on the value of the Archie's exponent α .

II/6.5 Mechanical properties

Table II/6-5 Compression stresses at three different strains and morphological characteristics of the materials from the soft and the rigidized soft CFs.

Sample code:	Fibre diameter	Bulk density	Overall Porosity	Stress [MPa]		
	ave. (µm)	(g cm ⁻³)	(%)	Strain (at 10 %)	Strain (at 30 %)	Strain (at 50 %)
Rayon Soft CFs						
SFG1aSC	10.30	0.108	92.7	0.006	0.034	0.137
SFC1aBG	11.98	0.106	93.9	0.004	0.041	0.193
SFG1aBG	12.57	0.092	94.6	0.003	0.033	0.178
SFC1aC	12.02	0.098	94.8	0.004	0.027	0.128
SFG1aSI	9.70	0.085	94.8	0.003	0.022	0.080
SFC1aSI	9.59	0.081	95.2	0.003	0.020	0.078
SFG1aC	10.70	0.073	95.7	0.001	0.015	0.091
PAN (thick fibre) soft CFs						
SFC2bC	18.69	0.140	92.5	0.006	0.090	0.381
SFC2bBG	18.53	0.120	93.2	0.006	0.130	0.527
SFG2bBG	17.98	0.122	93.3	0.004	0.058	0.205
PAN (thin fibre) soft CFs						
SFC2aZF	9.05	0.116	93.4	0.028	0.087	0.214
SFC2aBG	10.56	0.084	95.3	0.013	0.057	0.143
SFG2aC	9.06	0.091	95.0	0.009	0.041	0.091
Rigidized PAN (thick fibre) CFs						
rSFC2bC	19.60	0.227	88.1	0.171	0.552	/
rSFG2bBG	17.00	0.182	89.3	0.200	0.565	/

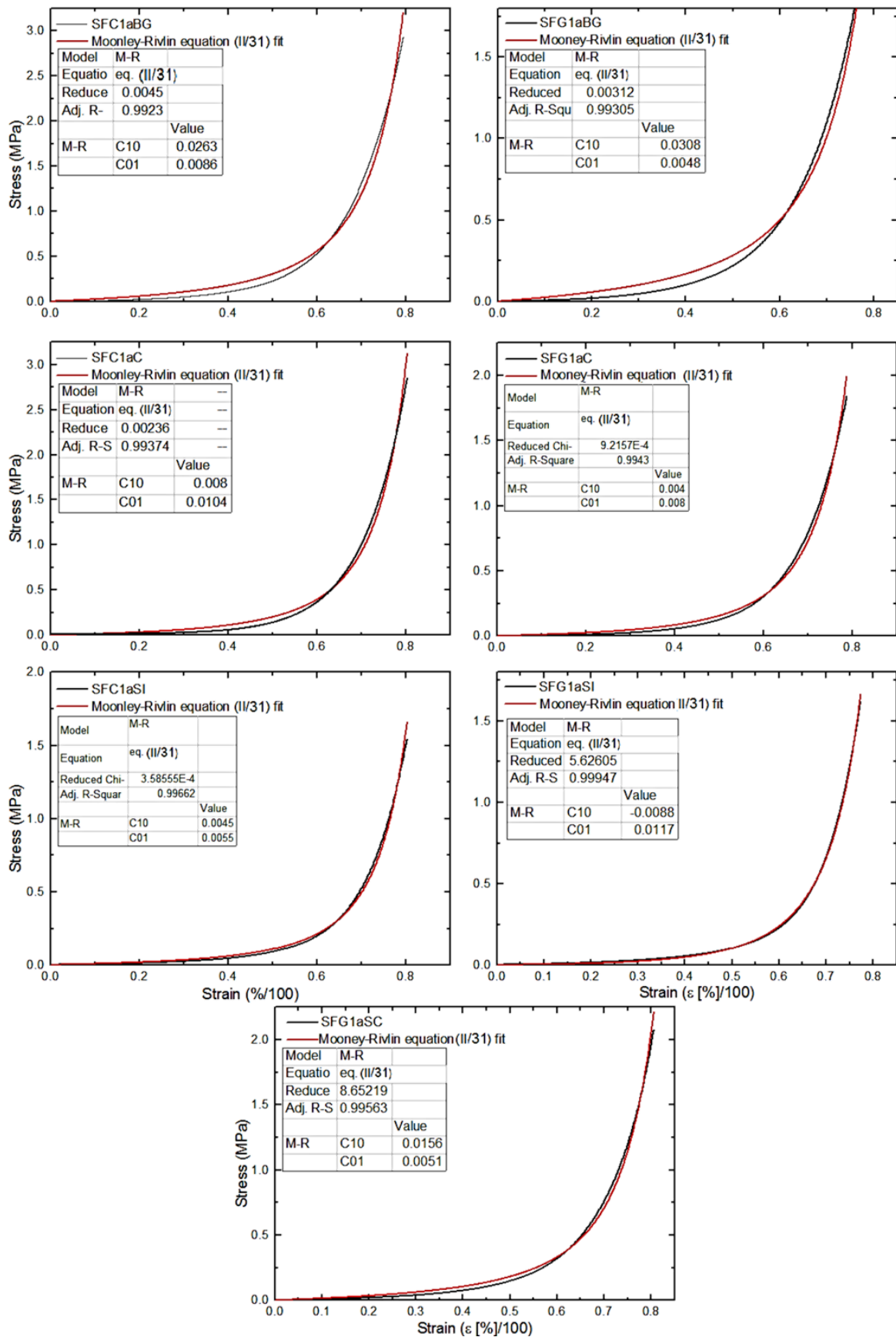


Figure II/6-5 Experimental stress vs. strain curves (black line) and M-R eq. (II/31) fit (red line) for Rayon-derived soft CFs in a uniaxial compression test.

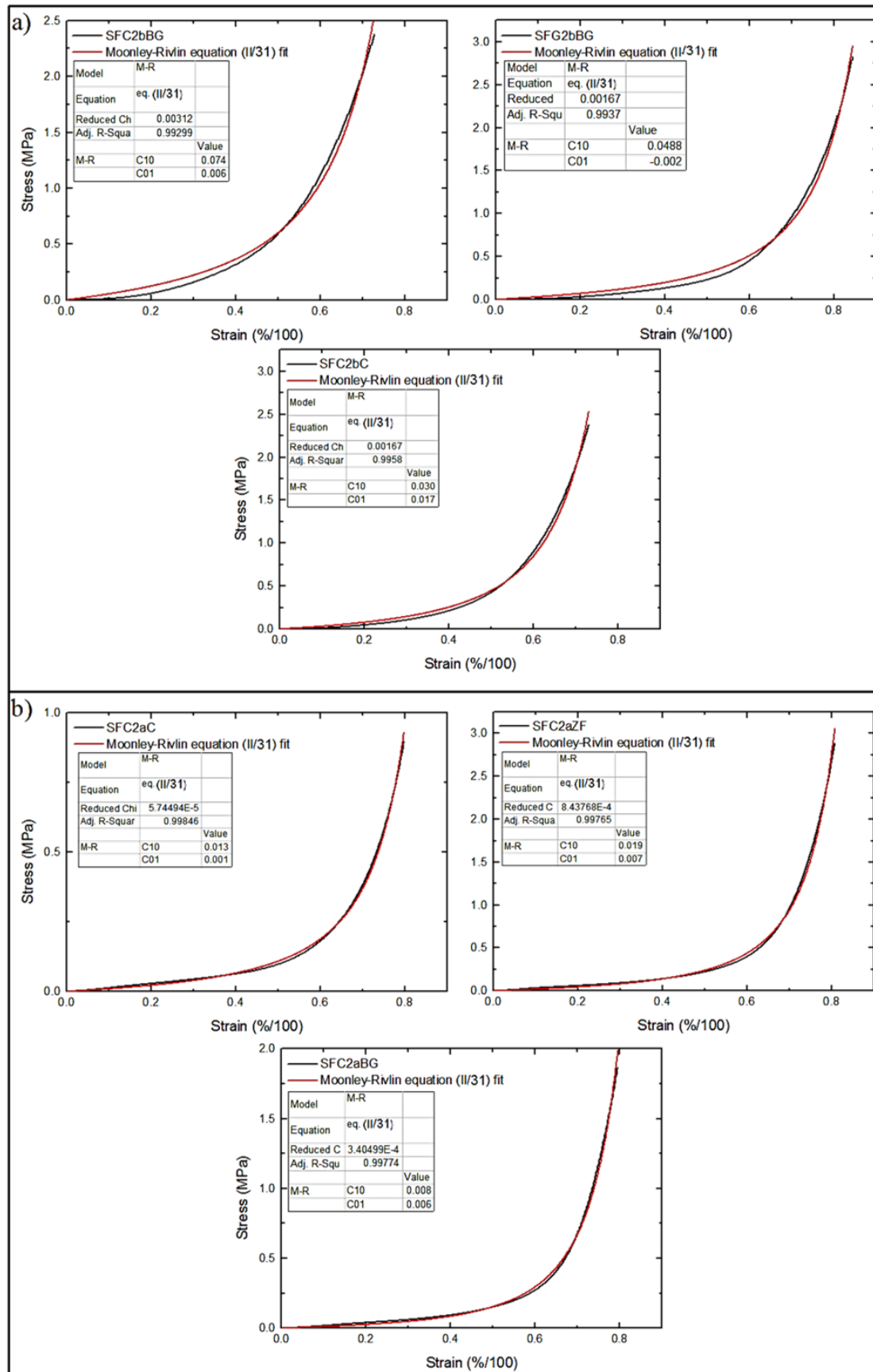


Figure II/6-6 Same as Fig. II/6-5 but for: a) PAN-derived (thick fibre) and b) PAN-derived (thin fibre) soft CFs.

Table II/6-6 Elastic modulus and damping loss factor of the soft CFs obtained by QMA measurements, with additional information of materials fibre diameter, bulk density, porosity and used compression rate.

Sample code:	Fibre diameter	Bulk density	Overall Porosity	Compression rate	Elastic Modulus (E)	Loss factor (η):		
	ave. (μm)	(g cm^{-3})	(%)	(%)	(MPa)	Stdv. (MPa)		Stdv.
Rayon Soft CFs								
SFG1aC	10.7	0.073	95.7	1-3	0.036	0.009	0.181	0.007
SFC1aSI	9.59	0.081	95.2	1-3	0.053	0.016	0.354	0.014
SFC1aC	12.02	0.098	94.8	1-3	0.157	0.055	0.324	0.043
SFG1aSI	9.7	0.085	94.8	1-3	0.058	0.010	0.291	0.008
SFG1aBG	12.57	0.092	94.6	1-3	0.047	0.022	0.226	0.016
SFC1aBG	11.98	0.106	93.9	1-3	0.027	0.007	0.436	0.024
SFG1aSC	10.3	0.108	92.7	1-3	0.122	0.045	0.408	0.030
PAN (thick fibre) soft CFs								
SFG2bBG	17.98	0.122	93.3	2-3	0.046	0.028	0.327	0.002
SFC2bBG	18.53	0.12	93.2	2-3	0.082	0.043	0.274	0.018
SFC2bC	18.69	0.14	92.5	2-3	0.216	0.079	0.316	0.048
PAN (thin fibre) soft CFs								
SFC2aBG	10.56	0.084	95.3	1-2	0.237	0.036	0.366	0.035
SFG2aC	9.06	0.091	95	1-2	0.213	0.082	0.430	0.047
SFC2aZF	9.05	0.116	93.4	1-2	0.422	0.105	0.392	0.004

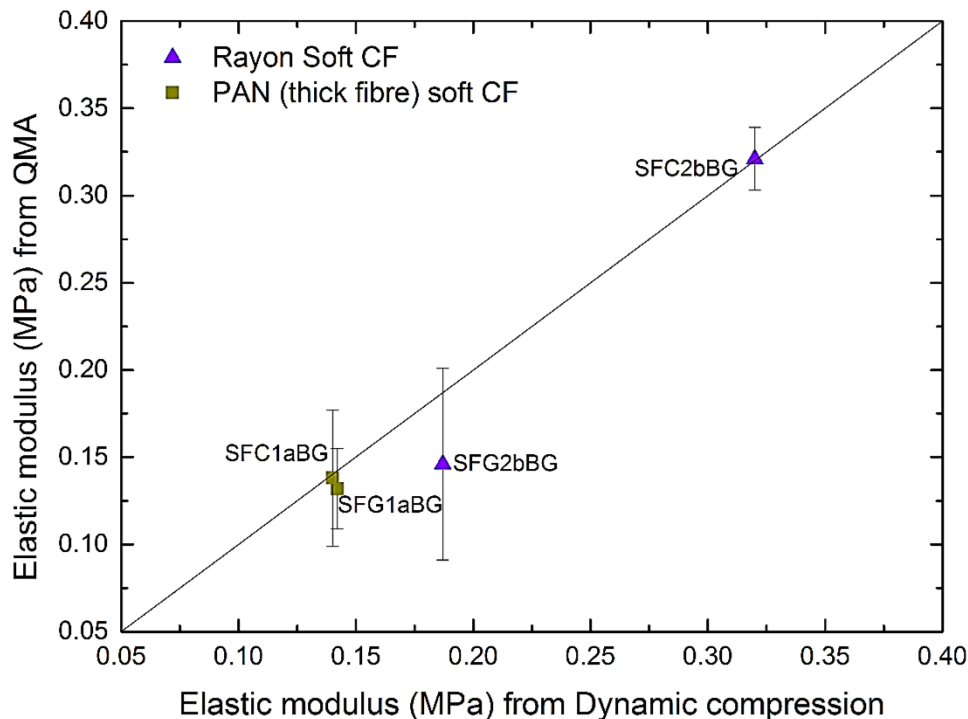


Figure II/6-7 Relationship between the elastic modulus from QMA (at compression rate range of 5-6%) versus the elastic modulus from dynamic mechanical compression method, for soft CFs provided from one supplier. The symbols have the same meaning as in Fig. II/3-21.

II/6.6 Thermal conductivity

Table II/6-7 Obtained values of thermal conductivity in isotropic and anisotropic analysis mode, with additional information of materials' fibre diameter, bulk density, and porosity.

Sample code:	Fibre diameter	Bulk density	Overall Porosity	Thermal conductivity (κ_{xyz})		Thermal conductivity (κ_z) (OP-direction)		Thermal conductivity (κ_{xy}) (IP-direction)	
	ave.(μm)	(g cm^{-3})	(%)	($\text{W m}^{-1} \text{K}^{-1}$)	Stdv.($\text{W m}^{-1} \text{K}^{-1}$)	($\text{W m}^{-1} \text{K}^{-1}$)	Stdv.($\text{W m}^{-1} \text{K}^{-1}$)	($\text{W m}^{-1} \text{K}^{-1}$)	Stdv.($\text{W m}^{-1} \text{K}^{-1}$)
Rayon Soft CFs									
SFG1aC	10.7	0.073	95.7	0.065	0.001	0.034	0.000	0.107	0.004
SFC1aSI	9.59	0.081	95.2	0.064	0.001	0.046	0.000	0.084	0.0156
SFC1aC	12.02	0.098	94.8	0.071	0.008	0.072	0.013	0.058	0.009
SFG1aSI	9.7	0.085	94.8	0.071	0.002	0.042	0.006	0.152	0.003
SFG1aBG	12.57	0.092	94.6	0.079	0.005	0.041	0.009	0.143	0.016
SFC1aBG	11.98	0.106	93.9	0.077	0.000	0.085	0.011	0.060	0.005
SFG1aSC	10.3	0.108	92.7	0.126	0.002	0.043	0.002	0.292	0.003
PAN (thick fibre) soft CFs									
SFG2bC	19.71	0.110	93.8	0.172	0.015	0.026	0.001	0.806	0.018
SFG2bBG	17.98	0.122	93.3	0.190	0.003	0.037	0.007	1.023	0.129
SFC2bBG	18.53	0.120	93.2	0.201	0.005	0.031	0.001	1.181	0.038
SFC2bC	18.69	0.140	92.5	0.103	0.005	0.094	0.009	0.103	0.008
PAN (thin fibre) soft CFs									
SFC2aBG	10.56	0.084	95.3	0.126	0.001	0.127	0.000	0.121	0.001
SFG2aC	9.06	0.091	95.0	0.238	0.006	0.038	0.005	0.810	0.154
SFC2aZF	9.05	0.116	93.4	0.194	0.005	0.126	0.031	0.349	0.015
Rayon RIGID BOARD CF									
RBG1aSI	10.01	0.160	89.6	0.234	0.008	0.110	0.002	0.436	0.011
RBG1aC	11.63	0.200	87.5	0.270	0.010	0.042	0.007	1.791	0.118
Rigidized PAN (thick fibre) soft CFs									
rSFG2bBG	16.96	0.180	89.3	0.324	0.041	0.050	0.014	1.473	0.293
rSFC2bC	19.59	0.230	88.1	0.176	0.019	0.142	0.016	0.130	0.032

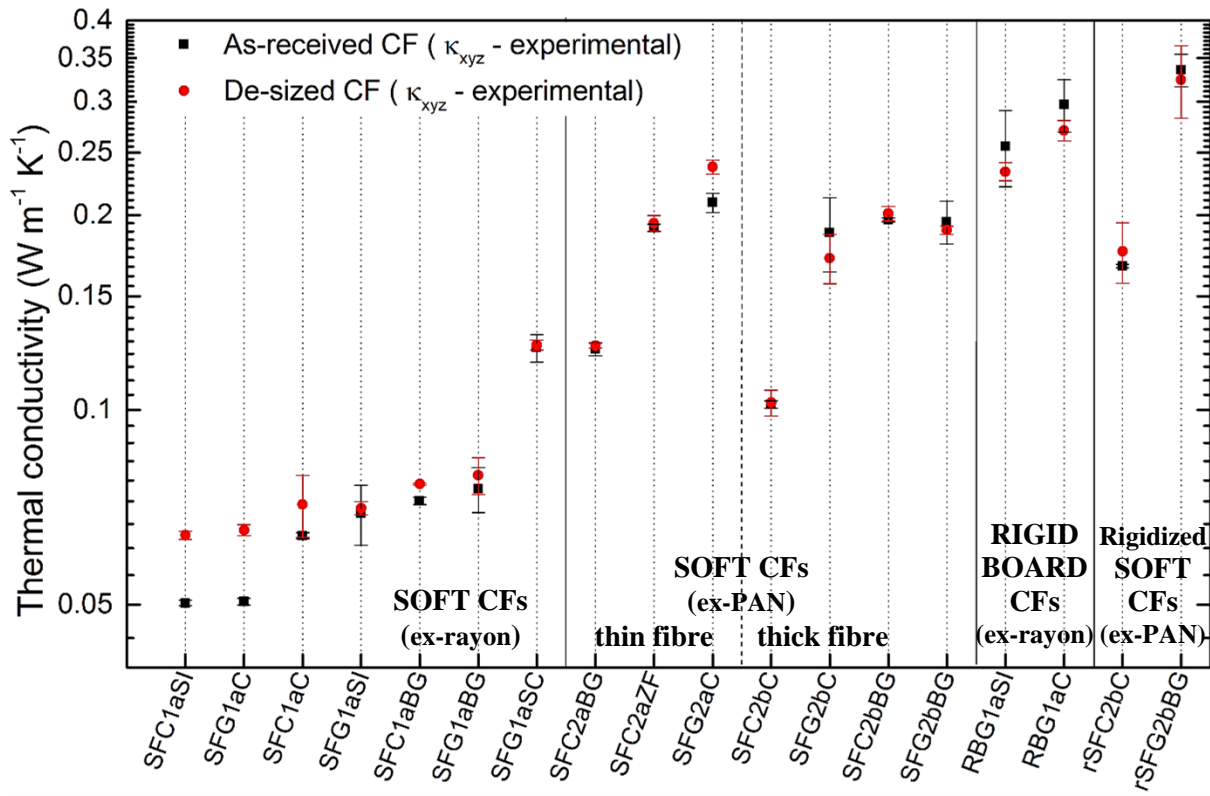


Figure II/6-8 Thermal conductivity values measured for all the investigated CFs, as received (black squares) and de-sized (red circles), obtained only by the use of the isotropic Hot Disk analysis mode.

CHAPTER III: CARBON
FELTS' STRUCTURAL
PROPERTIES AND CHEMICAL
STABILITY IN MOLTEN SALTS

III/1 Introduction

Many studies on carbon fibre have confirmed the influence on the final carbon structure of the used precursor, of its graphitisation degree, and of the manufacturing process (Zickler et al. 2006; Kong et al. 2012; H. Wang et al. 2014; Al Aiti et al. 2018). The effect of these key parameters is mainly ascribed to the initial presence, size, and orientation of the precursor crystals, and to the different manufacturing and conversion techniques of the initial precursor into the final carbon fibre, with maintained or improved structural properties.

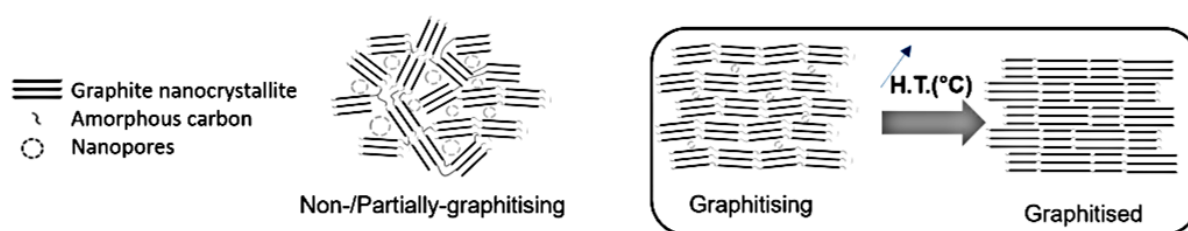


Figure III/1-1 Franklin's structural models of different carbon structures.

Even though several works presented initial information over the disordered and graphite layer structures, it was not until Franklins' studies that scientists had access to deeper explanation on the carbon structural properties and the different graphitisation stages (Harris 2001). From the performed pyrolysis and XRD analysis, one of Franklins' most valued scientific contributions is the clear differentiation between non- or partially-graphitising and graphitising carbon materials (as seen from Fig. III/1-1), obtained from different precursors. Even though high-temperature treatment was performed (as high as 3000°C), the investigated bio-sourced chars present a highly porous structure with small graphitic nanocrystallite domains, cross-linked by poorly aromatic amorphous carbon domains. The graphitic nanocrystallite domains are so randomly distributed and strongly connected that further improvement to a parallel stacking arrangement is limited and only observed for some small parts of the material (Oberlin et al., 2006). The opposite was concluded for chars of fossil origin, seen as graphitising at lower temperature (up to 2200°C) and even fully graphitised at higher temperature (Franklin Rosalind E. 1951). The observed almost parallel graphitic nanocrystallite domains, connected with assumed weak amorphous carbon domains are further aligned and covalently bonded in the latter graphitised material, with completely absent nanoporosity. These established carbon differences are very important for the further explanations of the

examined CF structural properties, coming from different precursors and manufactured through different protocols.

As a precursor of interest (used for the production of 9 out of 18 investigated materials), poly(acrylonitrile) (PAN) is predominantly used (since 1961) for the conventional production of carbon fibres through a controlled process based on several heat treatments and additional manufacturing steps (Huang 2009; Al Aiti et al. 2018). Due to its fossil origin, derived from crude oil and natural gas, its properties are easily modified during the manufacturing steps with respect to different final applications (Minke, Kunz, and Turek 2017). In any case, the manufacturing process variables are highly important and influence the subsequent transformation of PAN into carbon fibres and thus their final structural properties (Yusof and Ismail 2012). For example, carbon fibres' purity, graphitic crystallite size, and preferred orientation have been shown to highly depend, and increase with, heat treatment temperature and treatment time (Xiao et al. 2014).

In the context of global industrial adaptation to the use of greener starting materials and due to the polluting and cost-influencing production of ex-PAN carbon fibres (Kong et al. 2012), the search for suitable CF has been expanded by studying biosourced materials. Thus, the other half of the examined CF is derived from regenerated cellulose fibres (Rayon), recognized as a suitable and renewable precursor. As the cellulose polymer chains can be highly oriented and Rayon fibres well structured, this biosourced material is seen as an attractive rival to the extensive use of synthetic carbon fibre precursors (Kong et al. 2012). The Rayon structural properties have been deeply studied and a structural correspondence was observed between the cellulose crystallite size and the graphitic-order of the produced carbon fibres (Kim et al. 2001).

The carbon fibres' purity and structural order have been further studied, by testing carbon fibres of different origins, to investigate their influence when chemically reacted with various inorganic salts (mainly KOH and NaOH) (Maciá-Agulló et al. 2007). As far as the performed bibliographic research allowed to see, there is not a systematic study concerning the effect of the carbon fibres' structural properties on their chemical reactivity with LiOH, LiBr and $\text{Li}_4(\text{OH})_3\text{Br}$ (as PC of application interest). This lack is a result of the different focus of the works published so far, dealing with chemical activation of carbon fibres with the main motivation of producing high specific surface area materials, namely activated carbon fibres. These studies were performed from both PAN and Rayon precursor and each time focused on

the use of inorganic salts with improved performances (Suzuki 1994; Moon, Kim, and Lim 2006; Wang et al. 2011; Zhang et al. 2016).

Therefore, one of the main objectives of the present work was to provide information on the opposite, i.e., on the CF chemical stability, and on the effect of their structural properties when fully impregnated with molten inorganic salts or their mutual PC, such as of that for TES application. Due to their possible differences, such as carbon fibre precursors, manufacturing processes and/or final heat treatments, the reactivity of CF was expected to be different in the presence of a molten inorganic salt and in the presented experimental conditions.

Over the years, few different studies have evaluated the chemical activation of different carbon materials with LiOH (Mora et al. 2006; Sutcu and Dural 2006; Aweed 2008; Mikova, Chesnokov, and Kuznetsov 2009; Krstić et al. 2018), yet none concluded to consider the use of lithium salts as chemical activating agents.

Therefore, in addition to the effect of CF structural properties, a characterisation approach is proposed herein for evaluating their chemical stability in molten alkali hydroxide (LiOH), alkali halide (LiBr) or their PC ($\text{Li}_4(\text{OH})_3\text{Br}$). The separate tests were performed with LiOH and LiBr, considered as an important variable due to the different natures of these inorganic salts (Wietelmann and Bauer 2000). Doing this way, the individual effect can be clearly observed and some conclusions can be drawn for the final CF chemical stability in the molten PC. To the best of our knowledge, this is also the first time that commercially available CFs or any other carbon fibre material were tested for their chemical stability with LiOH, LiBr or the PC of interest.

By performing tests in more severe conditions, the main objective of this study was to evaluate and identify chemically stable CFs for their future use in CF-PC hybrid composite preparation and further use in the TES application. The thermo-chemical stability and reliability of the examined CF materials in the separate compounds or their stoichiometric PC composition should demonstrate different structural and morphology alterations. This was evaluated from the subsequent morphology and properties, as well as by comparing with the CF initial state.

The last part of the study deals with the chemical reaction kinetics, using Arrhenius law, thus considering the influence of the temperature on the chemical reaction rate. Fitting the results from CF chemical reactivity data in molten LiOH, the main purpose was to get information on the apparent activation energy of the governing chemical reaction, thereby estimating the carbon burn-off (B-O) in the temperature range of the application.

III/2 Experimental

III/2.1 Materials and sample preparation

The involvement of different carbon fibres' precursors and manufacturing factors influence the final properties of the different CFs for their application in the present study. Again, not less than 18 commercial carbonised or graphitised CF were analysed (presented in Table III/2-1), obtained from 5 different manufacturers with significant differences, most of which initially unknown to us.

Prior to the chemical reactivity tests, inorganic salts LiOH (anhydrous, $\geq 98\%$, Alfa Aesar, Kandel, Germany, melting temperature of 462°C) and LiBr (anhydrous, $\geq 99.8\%$, Alfa Aesar, Kandel, Germany, melting temperature of 552°C) were initially heated up to 120°C to eliminate any expected water content. They were further powdered prior to each experiment, always performed inside a glove bag (Glas-ColTM 108D X-27-27H, Terre Haute, IN, USA) under inert atmosphere because of the salts' hygroscopic behaviour.

For testing the CF chemical stability in molten PC, an additional synthesis step was performed by mixing the present LiOH and LiBr at their stoichiometric weight ratios (45 wt. % LiOH / 55 wt. % LiBr), and synthesising the PC ($\text{Li}_4(\text{OH})_3\text{Br}$). The use of nickel crucibles (50 mL, VWR), cleaned with acetone, deionised water and dried before each use, was demanded to avoid corrosion throughout the synthesis and thus to modify the PC composition. Again, a glove bag was used, filled with nitrogen, to avoid hydration of the initial inorganic salts or the mixtures. Further, a synthesis protocol, modified from (Achchaq et al. 2019), was chosen and performed in a horizontal stainless steel tube furnace (Carbolite Gero furnace, Neuhausen, Germany) from room temperature up to 450°C with a heating rate of 5°C min^{-1} . The synthesis was continued for 48h at the final temperature, followed by free cooling to room temperature. The sample was kept continuously under the flow of nitrogen until reaching thermal equilibrium within the freely cooled furnace. After the synthesis, the nickel crucible with the synthesised PC was transferred to the glove bag and extracted from the crucible with the use of awl and hammer. This additional synthesis of the peritectic compound allows mixing the different inorganic salts but also allows the formation of the new stoichiometric composition, which is required for testing its effect on the investigated CF. Also, the PC synthesis performed is mandatory because of the relatively delayed melting process of LiBr. Indeed, if a simple physical melting had been performed prior to the chemical reactivity study, possibly different experimental results would be obtained.

As for the chemical reactivity test (seen in Fig. III/2-1), CF with predefined dimensions were primarily placed inside the nickel crucible, then covered with a calculated and fixed ratio of alkali hydroxide (40:1), alkali halide (80:1) or PC mixture (40:1). For ensuring a complete impregnation, an additional smaller nickel crucible (10 mL, VWR) was placed onto the CF, for keeping the lightweight CF always at the bottom and in contact with the molten LiOH, LiBr or $\text{Li}_4(\text{OH})_3\text{Br}$. The prepared test samples were transferred inside the previously mentioned stainless steel horizontal tube reactor, always kept under an inert atmosphere. The reactivity tests involved heating the sample from ambient temperature up to different plateau temperatures (500-750°C) with a heating rate of 5°C min^{-1} , under a constant nitrogen flow of 100 mL min^{-1} . Then, the final temperature was maintained with a holding time of 4 hours, before the temperature decreased freely down to ambient temperature. After cooling to room temperature the nickel crucible, with a solid block of salt and the CF immobilised therein, was recovered and the salt was dissolved in a beaker filled with 2 L deionized water at 80°C overnight. The recovered CF was transferred to a funnel with already installed filter paper (Rotolabo® Type 114A $\varnothing 70\text{mm}$) and washed with 1 mol L^{-1} HCl until neutral pH, then dried at 105°C overnight.

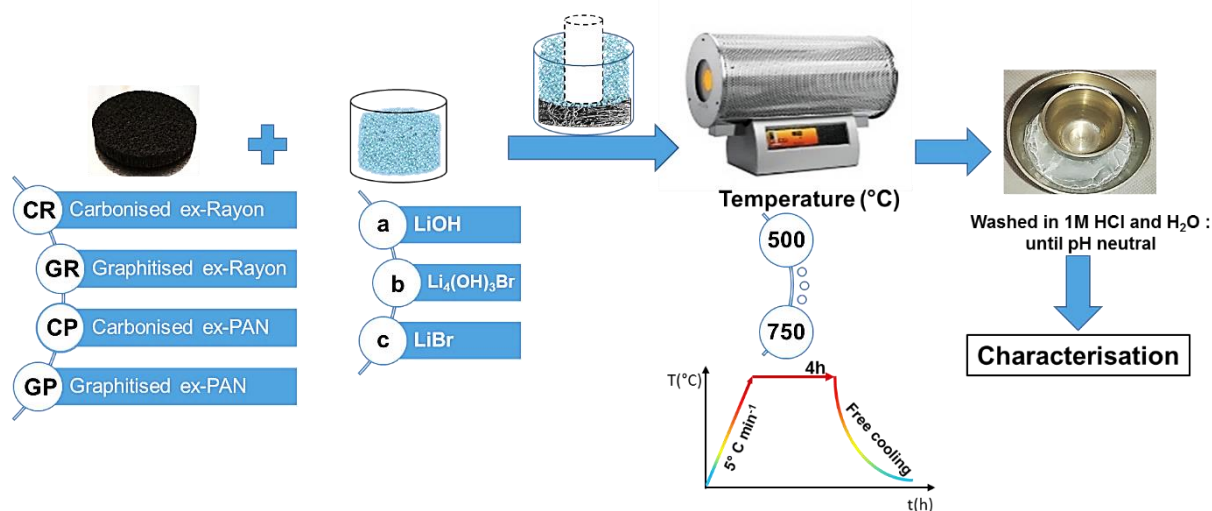


Figure III/2-1 Protocol of CF chemical reactivity test in molten salts.

The weight loss (burn-off (%) = $100 \% - \text{yield} (\%)$), morphology, surface texture, and elemental analysis were performed after each test following the salt removal. It was assumed that the CF weight loss was only associated with the carbons' chemical reactivity in molten LiOH, LiBr or $\text{Li}_4(\text{OH})_3\text{Br}$ (when relevant), by taking into account the performance of the test in constantly flushed inert atmosphere and the use of nickel crucible.

The examined CF were labelled according to this scheme. Whether they were carbonised (i.e., manufactured at a final production temperature of less than 1600°C) or graphitised (i.e., manufactured at a final production temperature of above 2000°C), the first part of CF's name consisted of a capital letter G or C, respectively. The latter was followed by another capital letter, related to the carbon fibre precursor (R for Rayon and P for PAN), and a number referring to the CF commercial supplier code (codes referenced in Table III/2.1). After performing the chemical reactivity test, the presented code labels were followed by a low-case letter related to the chemical reagent (molten salt) used (a for LiOH, b for Li₄(OH)₃Br, or c for LiBr), ending with the test temperature. Thus, for instance, CR1a500 refers to the carbonised CF from Rayon precursor, obtained from CeraMaterials, after a reactivity test with LiOH performed at 500°C. The materials shown in Table III/2-1 represent the same materials reported in subchapter II/2.2, table II/2-1 (with preserved order), yet this new justification is necessary to avoid any confusion. The different coding system was compulsory for emphasising the different affecting parameters in the case of the physical properties study (Chapter II) compared to this study of the CF' chemical stability properties.

Table III/2-1 Sorting of 18 commercial CFs categorised into groups and sub-groups.

Final production heat mode:	Precursor:	Commercial name:	Used sample code:
Needle-punched non-woven soft felts			
Carbonised	Rayon	Carbon (Rayon) felt CeraMaterials	CR1
Graphitised		Graphite (Rayon) felt CeraMaterials	GR1
Carbonised		RSF1 Beijing Great Wall Co.	CR2
Graphitised		RSF2 Beijing Great Wall Co.	GR2
Carbonised		SIGRATHERM® KFA5	CR3
Graphitised		SIGRATHERM® GFA10	GR3
Graphitised		GF2 Schunk	GR4
Carbonised	PAN	ZOLTEK™ PX 35	CP5
Graphitised		GFE-1 CeraMaterials	GP6
Carbonised		BESF Beijing Great Wall Co.	CP7
Carbonised		Carbon (PAN) felt CeraMaterials	CP8
Graphitised		Graphite (PAN) felt CeraMaterials	GP8
Carbonised		PSF1 Beijing Great Wall Co.	CP9
Graphitised		PSF2 Beijing Great Wall Co.	GP9
Chemically rigidized needle-punched non-woven soft felts			
Graphitised	PAN	PRF3 Beijing Great Wall Co.	GP10
Carbonised		Carbon Board (CeraMaterials)	CP11
Chemically bonded rigid boards			
Graphitised	Rayon	SIGRATHERM® MFA	GR12
Graphitised		Graphite Board (CeraMaterials)	GR13

III/2.2 CF impregnation by molten inorganic salts of interest

Up to date, no unified infiltration method of molten salts within fibrous non-wovens has been developed. This can be explained by the fact that each different case study of hybrid material has to be adjusted according to the properties of the PC and its hosting material (Achchaq et al. 2018). In this context and for confirming the infiltration process of CF materials with the molten salts mixture, a simple infiltration apparatus was developed and used, and the corresponding process was thus evaluated as well. The simplified process did not demand the use of additional pressure, nor vacuum assistance, so uniquely a powdered inorganic salt or PC was deposited on the CF host, placed in a transparent infiltration device. After the sample was installed and the system was tightly closed (Fig. III/2-2) to maintain the inner inert atmosphere, the device was placed in a temperature-controlled furnace and the infiltration process was launched at a defined temperature and time program (375°C and 1h, respectively). Then, the process was visually evaluated and next the homogeneity of the composite was characterised.

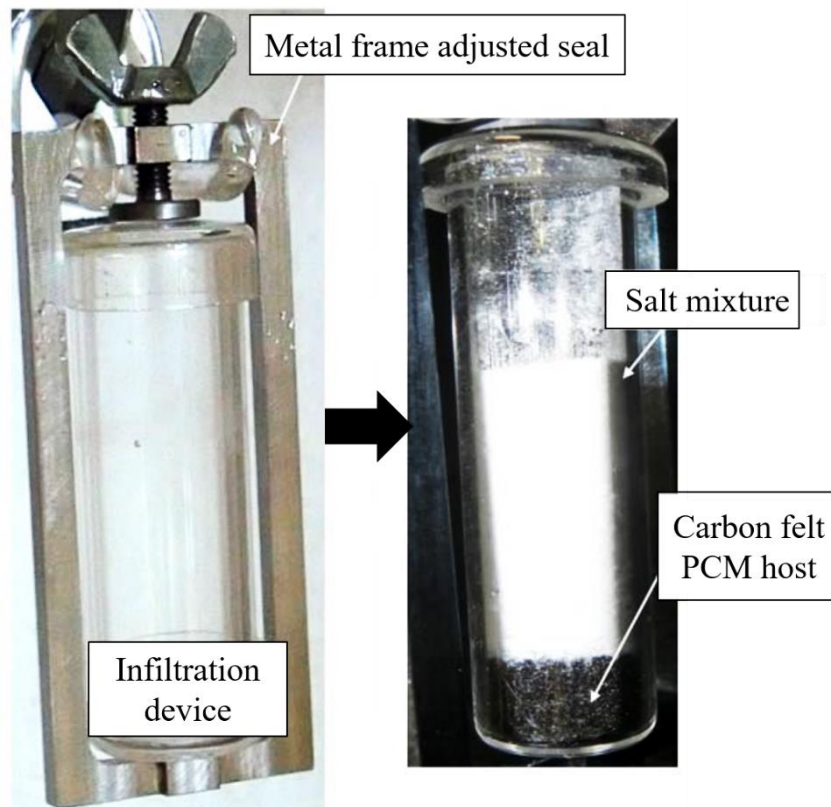


Figure III/2-2 Infiltration device used for CF-PC hybrid composite preparation and process validation.

These infiltration tests were performed at the Institute of Mechanical Engineering - UMR CNRS 5295, followed by SEM analysis at PLACAMAT (Plateforme Aquitaine de Caractérisation des Matériaux) - UMS 5295, as part of a one-month research training in 2017.

Special acknowledgements go to Dr. Fouzia Achchaq for the welcoming collaboration and full access to the laboratories and to Philippe Legros for the performed SEM analysis of the prepared hybrid materials.

III/2.3 Morphological and textural characterisations

III/2.3.a Carbon fibre morphology

The use of SEM technique for microscopic scale observations was already discussed in Chapter II, subsection (II/2.5.a), and further details are given herein in terms of element mapping, performed by energy-dispersive X-ray (EDX) spectroscopy.

EDX analysis can be used to define qualitatively the presence of a chemical element in a sample of interest. This is possible by exciting atoms at the material surface by bombarding them with electrons. As a result, X-rays emitted from the investigated area have energy that depends on the nature of the excited element, which thus gives information on the elements' presence and abundance (Van Grieken and Markowicz 2001; Bergström 2015). The microstructure of the prepared hybrid materials, as presented in subsection III/2.2, was examined by a field-emission scanning electron microscope (FE-SEM, Zeiss Evo 50) equipped with an EDX detector. This analysis led to a mapping of the elements of interest (C, Br, and O) in the prepared CF-PC hybrid materials. For a higher accuracy, the elemental mapping was performed at a long acquisition time of 12 h.

The carbon fibre microstructure was next evaluated by SEM (Philips XL30 SFEG, equipped with field-enhanced thermionic emission gun, performing at 4 kV) to analyse the microstructure of pre-/post-chemical reaction samples. This preliminary characterisation is important to identify any expected alteration of the microstructure, as previously seen on chemical activated carbon fibres (Moon, Kim, and Lim 2006; Maciá-Agulló et al. 2007; G. X. Wang et al. 2011; Zhang et al. 2016). The SEM micrographs of different chemically activated samples were used to determine the carbon fibre alterations compared to the initial corresponding materials by using image analysis software (ImageJ). The mean value of the fibre cross-sectional area was also calculated, assuming circularity.

III/2.3.b Textural properties of CF

The textural material properties and their modifications were measured by gas adsorption analysis. All evaluated samples were first degassed under vacuum for at least 48 h at 110°C. Further, a manometric method was performed by injecting a purified gas into a cell of known volume, already containing a known amount of adsorbent CF material. By observing

a difference between the pressure after expansion in the sample holder, estimated by the gas equation of state, and the measured pressure, one can calculate the adsorbed amount per unit mass of material, represented by the adsorption isotherms.

The porous structures of the pristine and chemically activated CF were derived from nitrogen (N_2) and carbon dioxide (CO_2) adsorption at $-196^\circ C$ and $0^\circ C$, respectively, carried out with automatic adsorption analysers ASAP 2020 (Fig. III/2-3 a) and ASAP 2420 (Micromeritics) (Fig. III/2-3 b), respectively.

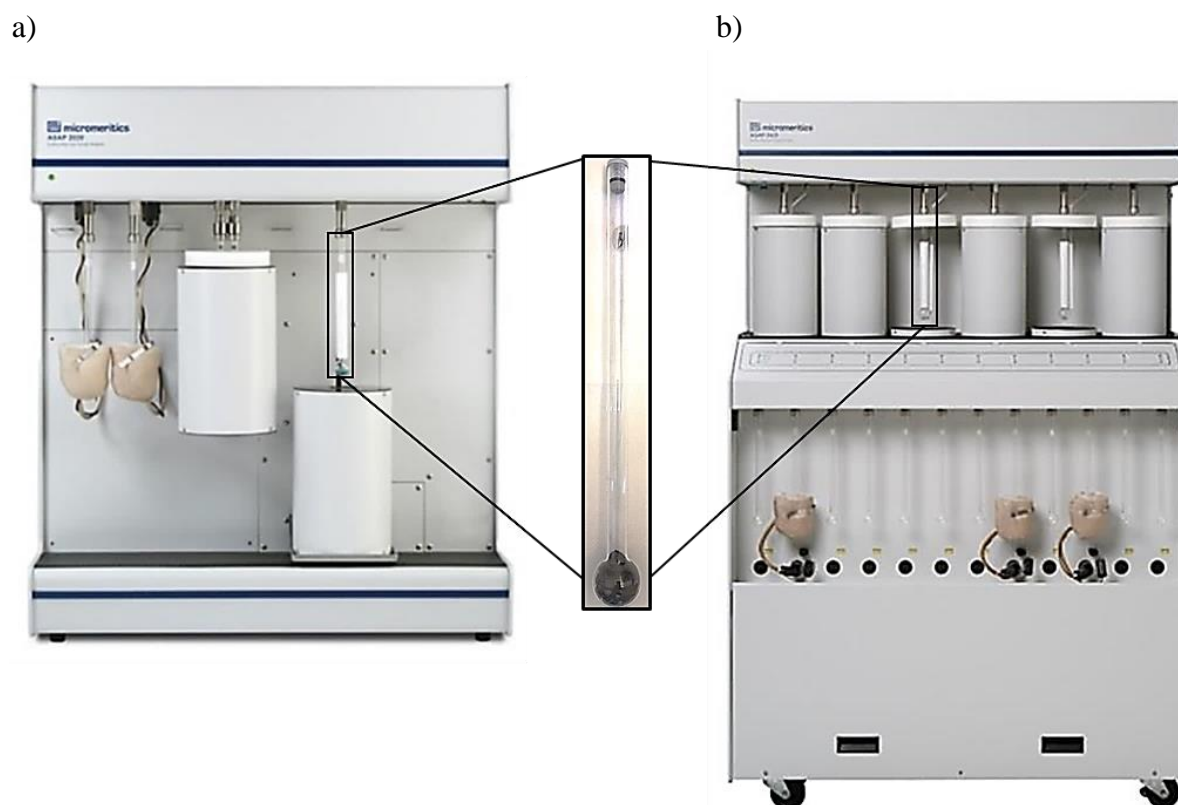


Figure III/2-3 Micromeritics gas adsorption apparatuses: a) ASAP 2020 (here used for N_2), and b) ASAP 2420 (here used for CO_2), with a zoom on the sample holder (in-between the figures).

By using the Microactive[®] and SAIEUS[®] software, the following parameters were calculated:

- specific surface area and total and micropore volumes, by application of the 2D non-local density functional theory for heterogeneous surface of pore walls (2D NLDFT-HS) to N_2 and CO_2 isotherms, S_{NLDFT} ($m^2 g^{-1}$), $V_{tot,2D-NLDFT HS}$ ($cm^3 g^{-1}$) and $V_{\mu,2D NLDFT-HS}$ ($cm^3 g^{-1}$), respectively;

- mesopore volume, V_{meso} ($cm^3 g^{-1}$) = $V_{tot, 2DNLDFT-HS} - V_{\mu, 2D NLDFT-HS}$.

The use of the 2D NLDFT-HS model rather than the traditional BET model, for the performed porous structure studies, is herein considered due to model-combined consideration of nitrogen (N₂) and carbon dioxide (CO₂) adsorption isotherms and the improved modelling of carbon pore walls with heterogeneous surfaces. Additionally, this up-to-date method combines all pore widths to give more accurate porous structure distribution, thus better representing carbon fibre materials having a poorly developed porous structure and a low surface area (Chen 2016).

III/2.4 Structural and elemental characterisation

III/2.4.a X-ray diffraction analysis

Solid carbon materials and their structural properties were among the first to be studied with X-ray diffraction (XRD), as early as 1917 with regards to their disorganised structure (Debye and Scherrer 1917). Desmond and Bragg (1924) gave deeper information on the simplified theory and method regarding the XRD analysis, and further described the tri-periodic layered stacking structure of graphite.

Herein, high-resolution X-ray diffraction was employed to confirm the diffraction patterns of the CF, performed with a D8 Advanced diffractometer, at 50 kV and 45 mA, using a Mo anode ($\lambda=0.7093 \text{ \AA}$) and a Lynxeye detector. The diffraction patterns were recorded in the 2θ range between 8 and 45° (with a scan step of 0.009°) at room temperature.

From the XRD diffraction patterns of the examined CF materials, parameters such as interlayer spacing distance (d_{002}) and crystallite size perpendicular to the carbon layers (L_c) were calculated from the position and the width of the (002) band, respectively. As previously seen, the (002) reflection position θ_{002} has already been defined to agree with the average interlayer graphitic spacing (d_{002}), by using the Bragg equation (Pope 1997):

$$d_{002} = \frac{\lambda}{2 \sin \theta} \quad (\text{III/1})$$

where λ is the wavelength of the used radiation ($\lambda=0.7093 \text{ \AA}$) and θ is the Bragg angle of the (002) reflection.

The crystallite size (L_c) was calculated from the conventional Scherrer's equation:

$$L_c = \frac{K\lambda}{B \cos \theta} \quad (\text{III/2})$$

where K is a constant with a present value of 0.9, and B is the full width at half maximum of the (002) reflection.

III/2.4.b Raman spectroscopy

Since the early seventies, Raman spectroscopy is also used for studying carbon materials and their nanostructures (Tuinstra and Koenig 1970). Unlike the XRD quantitative structure information, averaged from at least 1 mm³ of sample volume, Raman spectra can be accumulated locally and from a surface area range of 1-10 μm² (Pawlyta, Rouzard, and Duber 2015; Vignoles et al. 2015). Raman spectroscopy is seen as an excellent characterisation technique for a fast, simple and non-destructive material analysis. It is already famous for studying carbon materials, because of its sensitivity and reproducibility of any disorder of the graphitic lattice, detected as interrupting the translational symmetry (Pimenta et al. 2007).

This technique is based on the study of molecular vibrations, taking into account the phenomenon of inelastic scattering of light. With the use of monochromatic radiation (from a laser source), the sample surface molecules are excited and form an electromagnetic field, which induces a dipolar moment. From the samples excitement by the induced radiation, other radiations appear (such as transmitted, reflected, and scattered) and their diffusion can be elastic (without change of energy and wavelength - Rayleigh) and inelastic (where the photons interact with molecules by absorbing or giving energy – Stokes or Anti-stokes). The latter inelastic scattering is evaluated as vibrational or rotational energy levels of the excited molecules, detected as a photon frequency shift.

Raman spectra study was performed for chosen carbonised and graphitised CF, produced at different temperatures and derived from Rayon or PAN. This analysis gives important information on the lattice disorder of the examined materials. The structural properties of chosen CF were studied by performing Raman spectra with a Horiba Scientific XploRa Raman spectrometer (seen in Fig. III/2-4), done on samples without additional preparation. The investigation was performed at different magnifications, for both carbon fibre surface and carbon fibre cross-section. The dispersion of the Raman-scattered light was done by a holographic grating at 1200 lines per mm and detected by a CCD camera. A Si sample ($521 \pm 2 \text{ cm}^{-1}$) was used as reference material. Raman spectra were recorded with a laser at a wavelength of 532 nm, circularly polarised and filtered at 10% of its nominal power. Such filtration led to an incident power ($\sim 1.8 \text{ mW}$), too low for overheating and damaging the samples, and thus for influencing the results. Once the measurement conditions were

established, each sample spectrum was obtained by accumulation of two spectra recorded in the range from 800 to 3500 cm^{-1} . Deconvolution of bands was carried out with the Labspec6 software from Horiba.

Typical Raman spectra of partly-graphitising or graphitising carbon materials comprise two main parts. The first-order can comprise the D_1 band (around 1350 cm^{-1}), G band (around 1600 cm^{-1}) and sometime D_2 band (1620 cm^{-1}), and the second-order part mainly have the S_1 (or $2 \cdot D_1$) band (around 2700 cm^{-1}) (Pimenta et al. 2007). Only the G band represents crystallographic perfect graphite, seen unaccompanied in the Raman first-order region and as a result of vibrations from a perfect lattice structure (Sadezky et al. 2005). In contrast, the D_1 and D_2 bands can be observed in the first-order part and only for carbon materials with lattice defects or the presence of heteroatoms. The S_1 (or $2 \cdot D_1$) band can be attributed as an overtone of the D_1 band, whose appearance is related to the graphite nanocrystallite growth. From the D_1 and G bands, their intensity ratio (I_{D_1}/I_G) is calculated, which gives information on the extent of structural defects and on the graphitisation degree in a series of carbon materials. From the Raman spectra deconvolution, the full width at half maximum (FWHM) of the D_1 and G bands is used to estimate the average in-plane size of the graphite nanocrystallite (Pawlyta, Rouzaud, and Duber 2015).

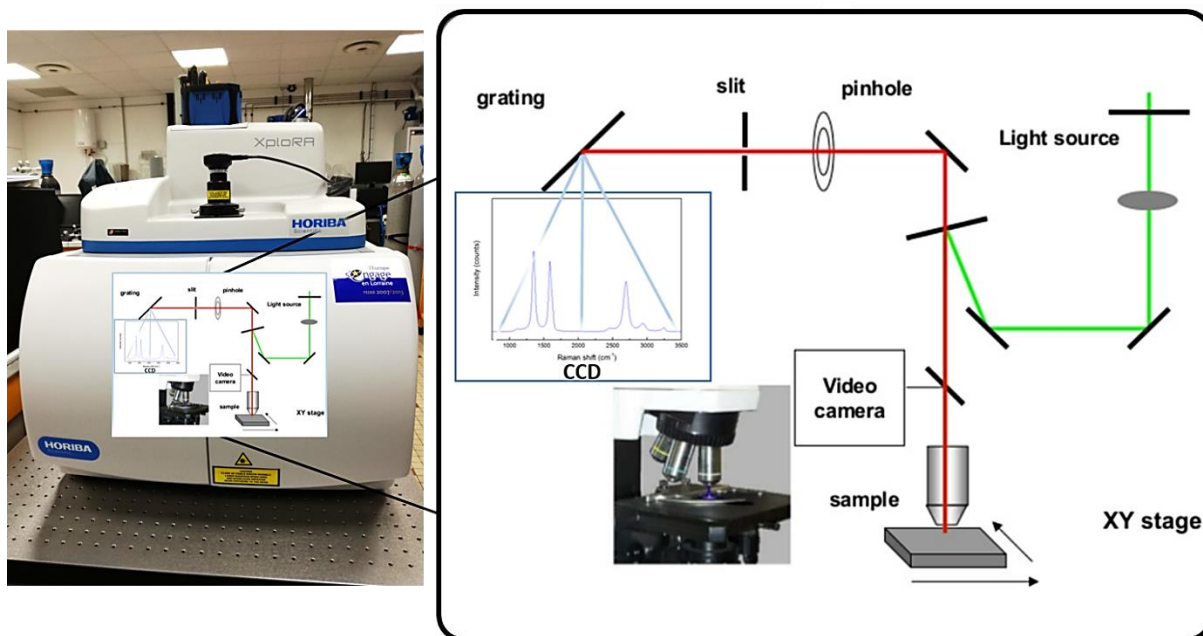


Figure III/2-4 Horiba Scientific XploRa Raman spectrometer with schematic representation of the different parts (modified after Bodycomb 2014).

III/2.4.c Elemental analysis

Previous studies presented correlations between materials' elemental compositions and structural properties, defined by elemental composition and XRD, respectively (Lu et al. 2001; Sonibare, Haeger, and Foley 2010).

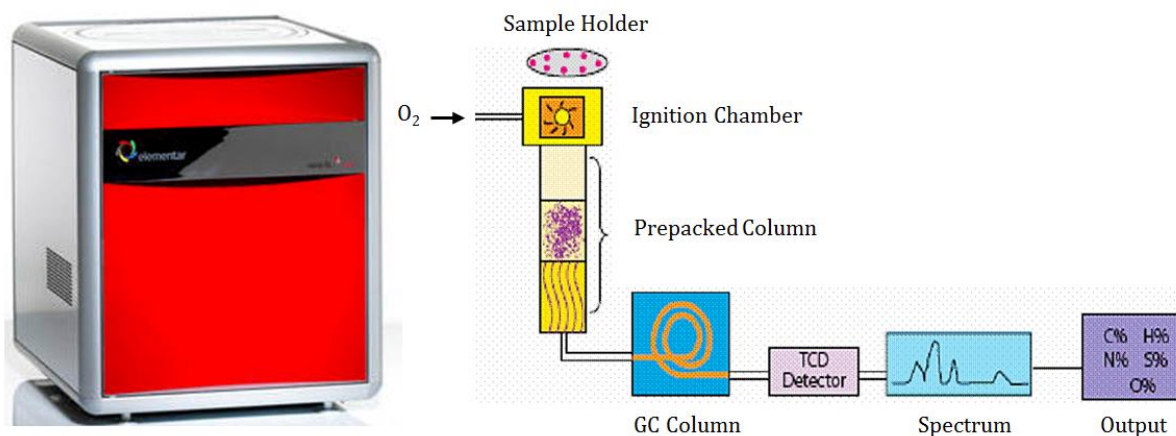


Figure III/2-5 Vario EL Cube elemental analyser and diagram of the measurement process.

For these purposes, the CF materials' elemental composition was investigated and the results were further discussed. The elemental analysis provides total contents of carbon (C), hydrogen (H), oxygen (O), nitrogen (N) and sulphur (S) in the carbonaceous material. Regarding the CF, this analysis was also used to observe changes in the elemental content of as-received fibres vs. de-sized fibres. The step of additional carbonisation (de-sizing) was necessary to ensure the purity (in carbon content) of the commercial CF (important information which was not provided by the producers), thus avoiding the risk of additional chemical contamination and unwanted reactions of the CF with the molten inorganic salts. Therefore, this additional step was always performed after receiving the CF and before doing any further materials' analysis.

The ultimate composition of the CF was determined using a Vario EL Cube (Elementar, Germany) elemental analyser (seen in Fig. III/2-5). The weight fractions of C, H, N, and S were determined from the gases obtained by burning a piece of a sample in an excess of dioxygen at a temperature of approximately 1700°C. Gaseous CO_2 and H_2O were directly obtained, whereas N_2 and SO_2 were produced after the reduction of NO_x and SO_x on hot copper. These four gases were separated and quantified by a chromatographic column. As the oxygen amount present in the sample could not be determined in the same run, additional samples were burnt and the resultant CO_2 and H_2O were reduced into $CO + H_2$, and the quantification of CO lead to the oxygen fraction in the material.

III/3 Results and discussion

III/3.1 Elemental composition of the investigated CF

In addition to the differences of manufacturing process and of precursor, the CF samples also present slight differences in terms of carbon content and presence of foreign atoms. Elemental analysis was carried out to obtain N, C, H, S and O contents in *as-received* and *de-sized* non-woven carbon felts. Because no sulphur was found, this element was omitted from the following result's presentation and discussions. The results are given in Table III/3-1 in units of weight %. From these values, the atomic % values were further calculated and used for CF comparison, by plotting Van Krevelen diagrams. This elemental composition diagram is commonly used to study the hydrogen/carbon (hydrogen index) as a function of the oxygen/carbon (oxygen index) atomic ratios of carbon materials. The resultant diagrams present the influence of the CF manufacturing temperature processes when comparing corresponding materials.

As shown in Table III/3-1, the C element was by far the most abundant in commercially *as-received* CF, with minimal value of 75.95 wt.% and 94.95 wt.% for both ex-Rayon and ex-PAN, respectively. The C amount was further increased, when comparing corresponding CFs (CR1 → GR1; CR2 → GR2; CR3 → GR3; CP8 → GP8; and CP9 → GP9), produced from the same precursor but manufactured at a higher temperature (Ko, Liao, and Liu 2007; Huang 2009). Oxygen was the second most abundant element, with a maximum value of 18.37 wt.% for the ex-Rayon and lower than 1.37 wt.% for the ex-PAN CF. Regarding the latter ex-PAN CFs (CP11), the high O wt.% can be observed due to the chemical origin of the carbon fibre binder (discussed in Subchapter II/3.1.c and seen in Fig. II/3-6). A non-negligible amount of nitrogen was detected (up to 4.1 wt.%) in some carbonised CFs manufactured at lower temperatures. A meaningful reason for the O and N presence is that the regenerated cellulose fibrils are O-rich, and N can be also originally present as an impurity, whereas PAN contains high amounts of C≡N functionalities, respectively (Chiang, Lee, and Lee 2007; Rahaman, Ismail, and Mustafa 2007). Compared to the C content, the amounts of H was found to be low and scattered within all materials, again declining with the increase of the materials' final heat treatment temperature. In general, pyrolysis in inert atmosphere controls the increase of the precursor's carbon content through several complex processes of elimination of CH₄, H₂, N₂, HCN (hydrogen cyanide), H₂O, CO, CO₂, NH₃, tars, and other volatiles (Tang and Bacon 1964; Park and Kim 2015; Al Aiti et al. 2018).

Table III/3-1 Elemental analysis results (in wt.%) of as-received and de-sized CF.

CODE NAME	<i>As-received</i>				<i>De-sized</i>			
	C (%)	N (%)	O (%)	H (%)	C (%)	N (%)	O (%)	H (%)
Rayon soft Felts								
CR1	75.95	3.46	18.37	2.14	77.66	3.18	16.63	2.45
CR2	77.55	3.17	17.15	2.07	78.45	2.77	16.40	2.33
CR3	90.94	0.50	7.64	0.92	89.16	0.12	9.27	1.46
GR1	91.27	0.35	7.46	0.92	97.83	0.13	1.92	0.12
GR2	98.70	0.43	0.78	0.09	99.01	0.10	0.81	0.08
GR4	99.53	0.01	0.39	0.07	99.66	0.03	0.25	0.05
GR3	99.66	0.04	0.24	0.07	99.72	0.01	0.22	0.05
PAN (thin fibre) soft felts								
CP5	96.82	2.82	0.31	0.05	97.01	2.52	0.41	0.06
CP7	97.89	1.59	0.46	0.06	97.85	1.71	0.35	0.09
GP6	99.46	0.03	0.44	0.06	99.58	0.02	0.32	0.08
PAN (thick fibre) soft felts								
CP8	95.07	4.09	0.65	0.19	95.19	3.91	0.60	0.23
GP8	99.44	0.04	0.46	0.06	99.68	0.04	0.22	0.06
CP9	99.50	0.04	0.39	0.04	99.70	0.01	0.23	0.06
GP9	99.61	0.06	0.28	0.05	99.60	0.04	0.30	0.06
Rayon RIGID BOARDS								
GR13	99.40	0.04	0.45	0.07	99.68	0.02	0.25	0.05
GR12	99.59	0.02	0.34	0.05	99.76	0.02	0.18	0.04
Rigidized PAN (thick fibre) felts								
CP11	94.95	2.61	1.37	1.07	93.52	2.77	3.48	0.23
GP10	99.74	0.03	0.20	0.04	99.47	0.01	0.35	0.13

The complementary elemental analysis allowed the comparison of *as-received* with *de-sized* CF. In the case of all ex-PAN and most ex-Rayon CF, no significant changes were observed in terms of elemental composition. The de-sizing heat-treatment (at 900°C) thus did not considerably affect the examined materials, since they were industrially heat-treated at higher temperatures (1200-2400°C). Yet, in separated cases of the carbonised CR1 and CR2, a weight loss (averaged on a dry basis of 7% and 8%, respectively) was observed after the de-sizing treatment. This might produce slight O wt. % decrease and increase of C content from 75.95 to 77.66 wt.% or from 77.55 to 78.45 wt.%, respectively. However, a clear change was not observed regarding the other analysed elements. Another exception was the graphitised ex-Rayon GR1, for which an increase in the C content (from 91.27 to 97.83 wt.%) and a decrease of the O content (from 7.46 to 1.92 wt.%) were seen. However, no clear weight loss was observed. These observations of shifts of elemental composition and weight losses evidence the

existence of some CF sizing (or any other post-production CF alteration) and supports the need of performing an additional de-sizing step before use.

Van Krevelen diagrams of ex-PAN and ex-Rayon CF confirm that both O/C ratio and H/C ratio decrease and that the degree of CF carbonisation increases with the final temperature of treatment (as shown in Fig. III/3-1 a) and b), respectively). In general, most of the ex-PAN CF present low O/C and H/C ratios. Some carbonised materials show similar or even higher purity than the graphitised CFs, as sample CP9, which is not observed when comparing the ex-Rayon materials. Note that the y-axis is used to represent H/C ratios, whereas the x-axis describes O/C ratio variation, with significant scale differences. This indicates that elimination of O is favoured, and that a higher number of H atoms is evident in the final structure of the analysed materials. This is clearly seen from the graphitised CFs. Thus, CFs thermal annealing is clearly seen from the sharp ratio drop for most corresponding materials (such as CP8 → GP8; CR1 → GR1; CR2 → GR2; and CR3 → GR3), also suggesting carbon structural improvement and better chemical stability by the decrease of heteroatom content. Noticeably, it is evident that different precursors or fabrication processes yield CF with different elemental compositions, produced in an inert atmosphere and similar final production temperature. In addition, evident is that the used carbon binder for the rigid ex-Rayon CFs manufacturing did not influence the final elemental composition of these materials (GR12 and GR13). Yet if we compare the rigidized ex-PAN (CP11 and GP 10) with the other soft CF, a higher presence of O and H is observed, regardless of being carbonised or graphitised.

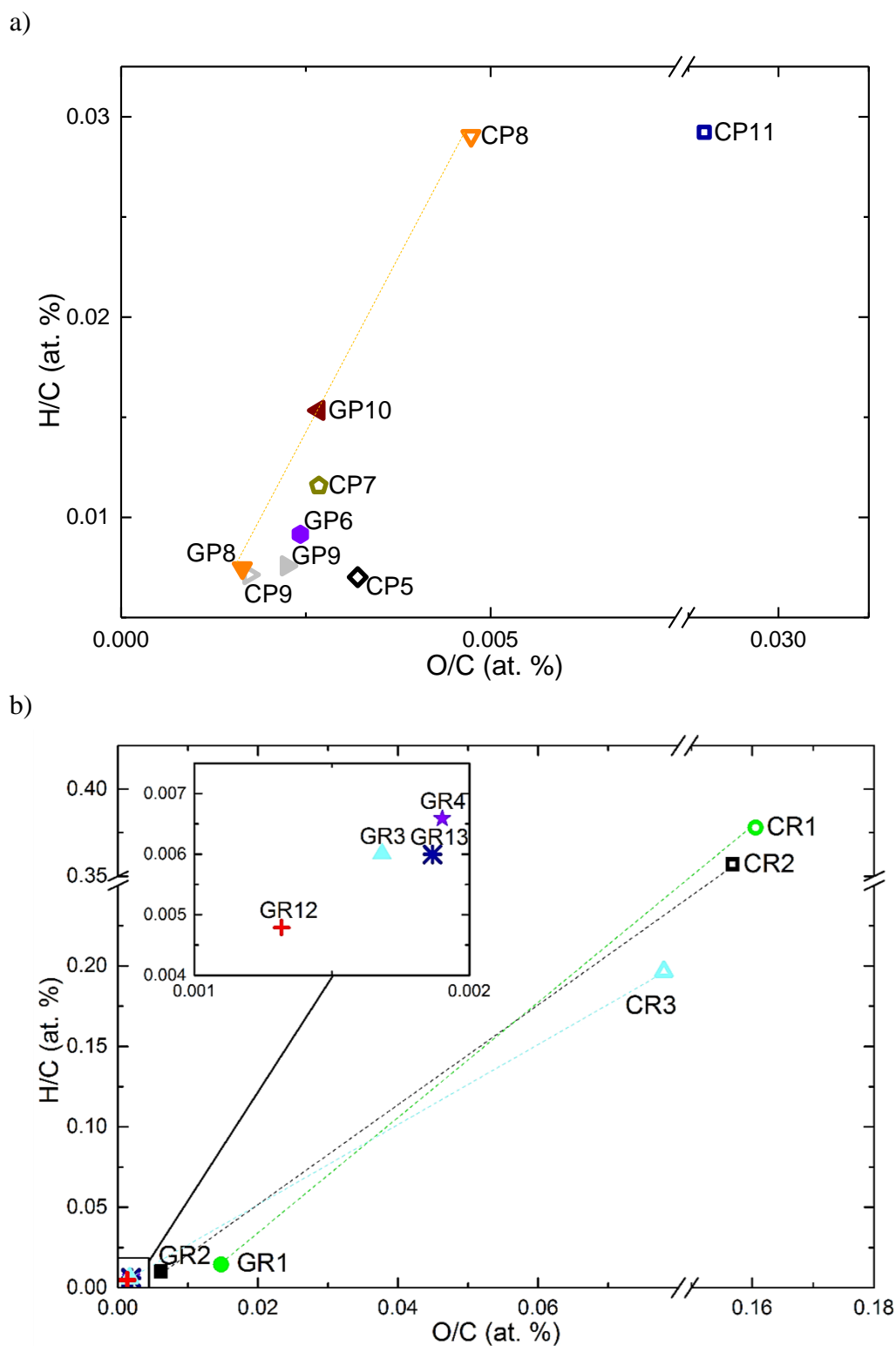


Figure III/3-1 Van Krevelen diagrams of a) ex-PAN and b) ex-Rayon CFs; the dashed lines connect CFs before and after graphitisation (empty symbols for carbonised and full symbols (including cross-like ones) for graphitised CFs).

III/3.2 Structural properties and carbon nanotexture of CF

The XRD and Raman spectroscopy results reveal the presence of poorly or more ordered CF from both Rayon and PAN precursors. As further shown through the results, these structural differences aside of or in combination with other affecting materials properties, play a considerable role in the chemical reactivity of the CF with the investigated molten salts. In general, for all examined CFs, the precursors' nature, fibre formation technique and final manufacturing heat treatment play a major role on the materials structural order, and hence on the graphitic nanocrystallite parameters (Dobiášová et al. 1999; Huang 2009; Al Aiti et al. 2018). This structural order decreased from the graphitised CFs (final heat treatment over 2000°C) to the carbonised CFs (final heat treatment under 1600°C), yet with observed exceptions.

X-ray diffraction (XRD) analysis has been used to obtain global structural information of CFs, even for poorly graphitised materials. The XRD patterns of all 18 commercial CFs are given in Fig. III/3-2 a) for ex-PAN and b) for ex-Rayon), and are presented as a function of their progressive increase of structural order. The characteristics of the (002) reflection are related to the extent of the stacking of graphitic layers and of the interlayer spacing. Its position, width, and intensity changes are indeed associated with different graphitic nanocrystallite properties (Maciá-Agulló et al. 2007; Wang et al. 2014).

The (002) reflections of the ex-Rayon carbonised CFs appear very broad and not completely defined, especially for the CR1, CR2, and CR3 materials. These CFs possess a significant amount of highly disordered and amorphous carbon regions, with minimal structural ordering, thus producing a significant background overlapping the (002) reflection. This can be partly explained as a result of the precursor (Rayon) polymer conformations enabling rearrangement during pyrolysis, of various origins and intra- or inter-molecular hydrogen unit bonds (Wada, Okano, and Sugiyama 2001). In addition and on a larger scale, the Rayon precursor is found to be initially semi-crystalline and has amorphous defects as transitions regions between the crystalline units of a single elementary fibril and between adjacent fibrils (Fink, Hofmann, and Philipp 1995). Therefore, these precursor properties are assumed to lead to the very low structural order of the carbonised CR1, CR2, and CR3. Their XRD patterns also suggest the absence of carbon fibre hot stretching manufacturing step, at the late carbonisation stage, crucial for development or improvement of the carbon structural order (Tang and Bacon 1964; Dumanli and Windle 2012). As for the corresponding GR1, GR2 and GR3, absence or partial improvement of the structural order was observed after the graphitisation step (above

2000°C). The higher temperature of heat treatment clearly defined these materials as non-graphitising (GR1) or partly-graphitising (GR2, GR3, GR13). The split of (002) reflection suggests structural heterogeneity of partly-graphitising material (clearly seen for GR2), due to the presence of graphitic nanocrystallites with different sizes and interlayer spacings between the graphitic layers, also seen by (Kim et al. 2001). The other GF4 and GR13 graphitised CFs coming from Rayon precursors of unknown properties led to narrower reflections, which were also slightly shifted to a higher Bragg angle. The performance of pyrolysis under low heating rate and the use of impregnants or organosilicon compounds (stabilisation agents) can be the reasons for the structural improvements of the ex-Rayon CF with the highest evaluated structural order (Dumanli and Windle 2012; Byrne, Chen, and Fox 2014). The role of these modified or additional manufacturing processes can yield graphitising carbon fibres with reduced voids, stacking faults, residual heteroatoms and/or graphitic lattice defects.

The diffraction patterns obtained from ex-PAN CF fabricated at temperatures below 1200°C presented much better-ordered carbon structure compared to the carbonised ex-Rayon ones, remarkably observed from the CP9 sample. In order to achieve an improved structural order of the carbonised ex-PAN CFs, the precursor grade (pristine/modified PAN homo-/co-polymer) and an optimal stabilisation process (in oxygen) must be ensured to avoid the fibres overheating and heterogeneous shrinking effect (Ko 1991; Gupta and Harrison 1996). The graphitised CFs are materials with improved turbostratic structure, which results in sharper and narrower (002) reflection compared to the carbonised ones. Yet a graphite-like structure is not observed in any of the ex-PAN or ex-Rayon CF.

In general, the additional detected (100) and (110) reflections are related to the stacking arrangements of two-dimensional ($hk0$) graphitic layers, which arise from aromatic hexagonal ring formations and induce turbostratic structure formation (Warren 1941; Dobiášová et al. 1999). The knee that appears next to the (100) reflection, in the case of all graphitised CFs, was previously defined as (004) reflection (Dobiášová et al. 1999). The pair of (100) + (004) reflection should be correlated to the decrease of the interlayer graphitic spacing (d_{002}), with an improved correlation between the graphitic layers and lateral growth of the graphitic nanocrystallites. However, due to their poor appearance and the possibility of significant estimation errors (Carrott et al. 2001; Maciá-Agulló et al. 2007), the discussion of results is omitted with regard to the two-dimensional ($hk0$) lattice (100 and 110) reflections. Very low or no (hkl) reflections were observed confirming the absence of the tri-periodic stacking formation of graphitic structure in all examined CFs.

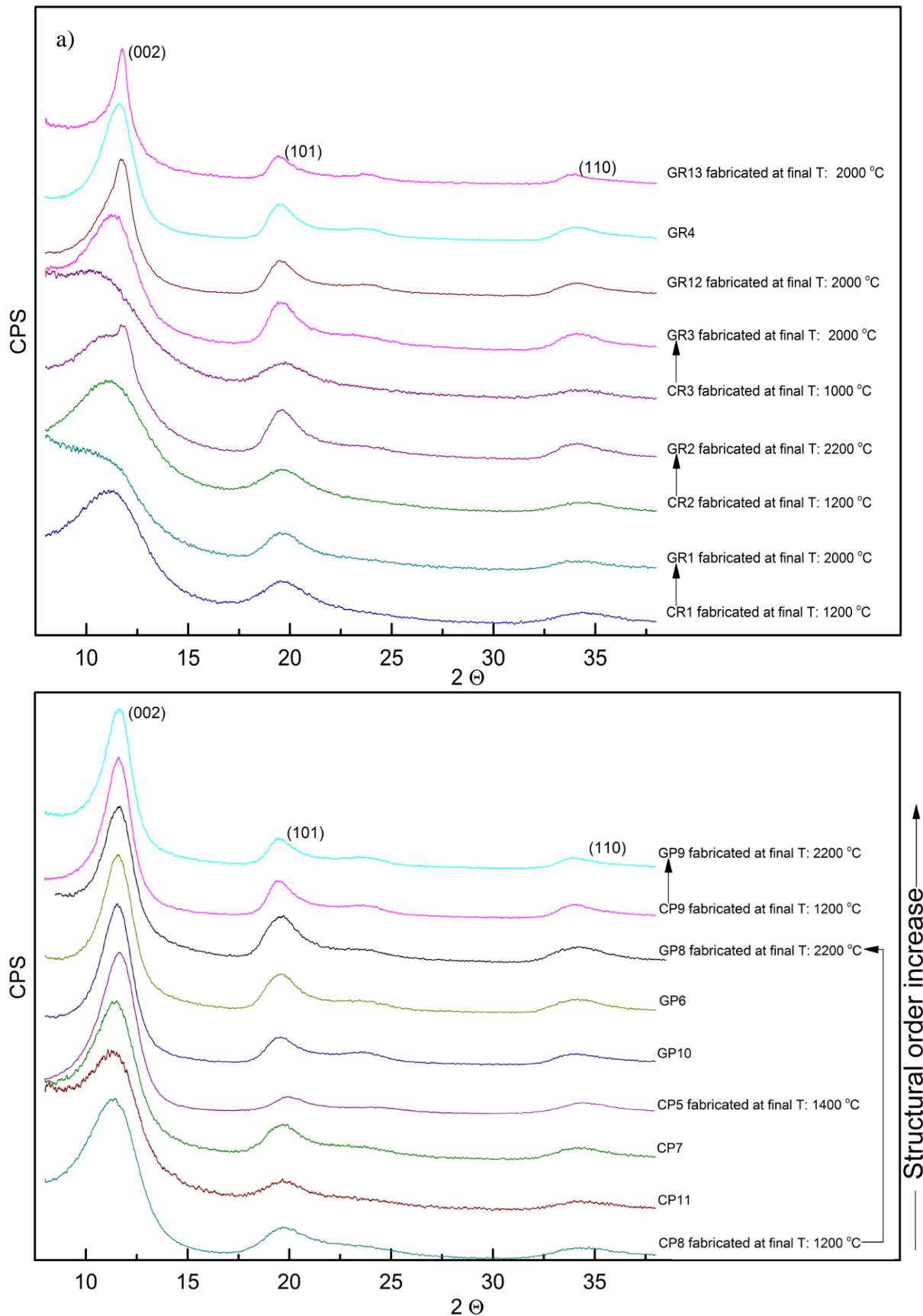


Figure III/3-2 X-ray diffraction patterns of as-received a) ex-Rayon, and b) ex-PAN CFs, presented as a function of their progressive structural order increase and with identical shift of counts per second (CPS) with regard to each other, for easier viewing.

Samples with very poor structural arrangement produce broad diffraction (002) reflections, whose deconvolution did not result in accurate fittings, also seen by (Drits and Tchoubar 1990). As previously observed elsewhere (Sonibare, Haeger, and Foley 2010), the asymmetric appearance (broadening in its lower 2θ values) of (002) reflection suggests the existence of lower intensity reflection attributed to the presence of aliphatic chains attached to the graphitic nanocrystallites' edges. When clearly deconvoluted, the (002) reflection of graphite materials is positioned in the 2θ range from 10.9° to 11.8° . As explained before, its position shift and width correspond to the variation of the interlayer graphitic spacing (d_{002}) and the size of the graphitic crystals (L_c) of carbon materials. The values of structural parameters (d_{002} and L_c) of the graphitic nanocrystallite are calculated from the (002) reflection, using Bragg (III/1) and Scherrer (III/2) equations and were plotted against the CF structural order increase (seen in Fig. III/3-3 a) for ex-Rayon and b) for ex-PAN).

From the corresponding carbonised to graphitised CFs, with the difference in the final temperature treatment, a change in the (002) reflection is generally evident regardless of the Rayon and PAN origin, indicating a decreased interlayer spacing (d_{002}). Therefore, the maximal intensity of the (002) reflections of samples CR2, CP8, and CP9 from 10.9° , 11.4° , and 11.5° shifted to higher 2θ values for samples GF2, GP8 and GP9 at 11.6° , 11.6° , and 11.7° , respectively. The shift of the peak position results in lower interlayer spacing (d_{002}) (seen in Fig. III/3-3). The increase of the final production temperature, in both ex-Rayon and ex-PAN CF, promotes a greater transformation and alignments of the graphite nanocrystallite layers, which indicates an improvement in the structural order degree. In general, the d_{002} values are observed in the range from 3.68 to 3.46 Å and 3.6 to 3.5 Å for the ex-Rayon and ex-PAN CF, respectively. In all the cases, even though a clear decrease was observed with the graphitisation stage, the d_{002} values were much higher than that of graphite, at around 3.35 Å.

Generally, the values of d_{002} and L_c decrease and increase, respectively, for materials having a higher structural organisation (seen in Fig. III/3-3). When compared with the literature, these structural parameters are in good agreement, considering ex-Rayon (Kim et al. 2001; H. Wang et al. 2014) and ex-PAN (Dobiášová et al. 1999; Li, Wang, and Wang 2007; Xiao et al. 2014) carbon fibres, with a clear effect of the thermal treatment history. Our results are additionally confirmed from previous XRD studies of commercially available carbon fibres (Dresselhaus 1988; Anderson 1989, 1991). Therefore, once again the low structural properties and the absence of tri-periodic graphitic stacking were observed assuming the use of general-purpose carbon fibres without additional hot stretching or other structural improvement methods.

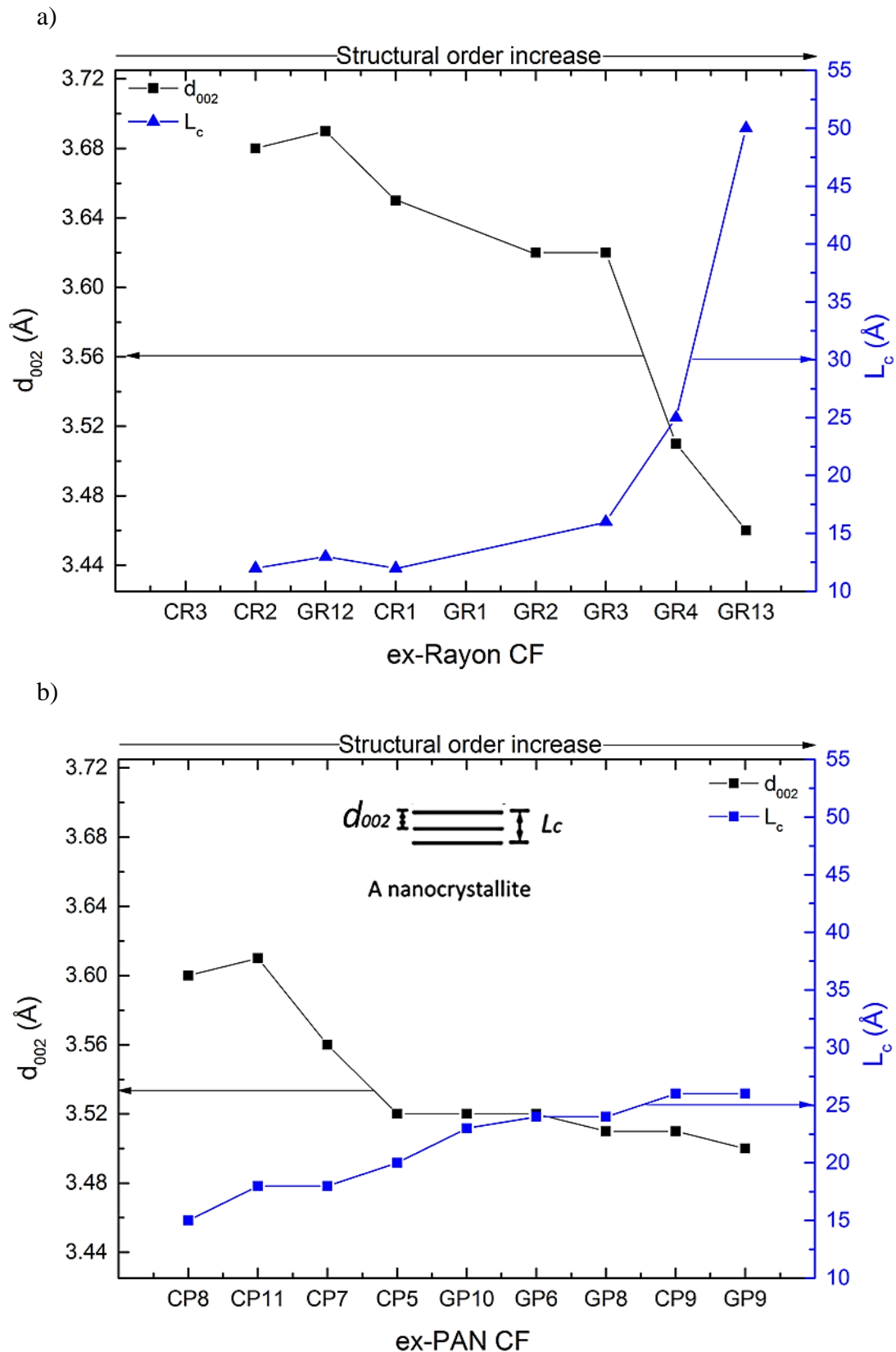


Figure III/3-3 X-ray diffraction analysis of interlayer graphitic spacing (d_{002}) and graphitic nanocrystallite thickness (L_c) (graphically presented) of as-received a) ex-Rayon and b) ex-PAN CFs, plotted as a function of structural order increase.

After investigating the structural order (by XRD) of the tested CF, the next step is to compare their elemental composition and structural properties, in order to obtain additional properties correlations. For this purpose, the O/C and H/C atomic ratios, calculated from the CF elemental analysis, are plotted as a function of the interlayer graphitic spacing (d_{002}) (seen in Fig. III/3-4 for a) ex-Rayon and b) ex-PAN).

There is a reasonable correlation between the decrease of the H and O with respect to C contents, compared to the increase of structural order. In general, the d_{002} decreases when reducing the heteroatom amount in the graphitic lattice, allowing further arrangement in-between the graphitic layers. In addition, the graphitic nanocrystallite growth (L_c) (seen in Fig. III-3-3), in good correlation with the d_{002} , must be influenced by the decrease in the presence of non-carbon atoms and greater sp^2 -hybridisation. These observations suggest that the CF structural information derived from the (002) reflection also reflects the degree of carbon purity in the studied CF, as shown for other carbons (Lu et al. 2001; Sonibare, Haeger, and Foley 2010). The corresponding pairs of CFs (from both groups) show a very good correlation between the analysed elemental composition and graphitic nanocrystallite properties, comparing CR2 and CP8 with GR2 and GR8, respectively. In general, for the ex-PAN samples, the impact of the precursor's homogeneity and crystallinity and the preheating treatment steps can be clearly observed from the carbonised CP5 and CP9. These CFs present high carbon purity and advanced structural properties, comparable to or even better than for some of the graphitised CFs. The ex-Rayon CFs present significantly scattered material relationship, but follow the same trend as of ex-PAN CF. The initial properties of the fibres' precursor or variations in their preparation once again influence high structural differences between CF fabricated at similar final heat treatments. Graphitised GR12 and GR3, having a high purity but a disordered or partially graphitic structure, make it possible to better understand the properties of the precursors and / or the influence of the stabilisation stage. The dissociation of these properties is often observed for materials of biosourced origin. This is supported by studies that show that Rayon fibres can result in carbon fibres with local graphitising structure (up to 2200°C) or completely non-graphitising, even at higher temperature treatments (Fink, Hofmann, and Philipp 1995; Kim et al. 2001; Dumanli and Windle 2012; Kong et al. 2012). In addition, when analysing graphitised CF with an identical carbon purity and a different structural organisation, a clear influence of these CF properties must be observed when carrying out chemical reactivity tests in molten inorganic salts.

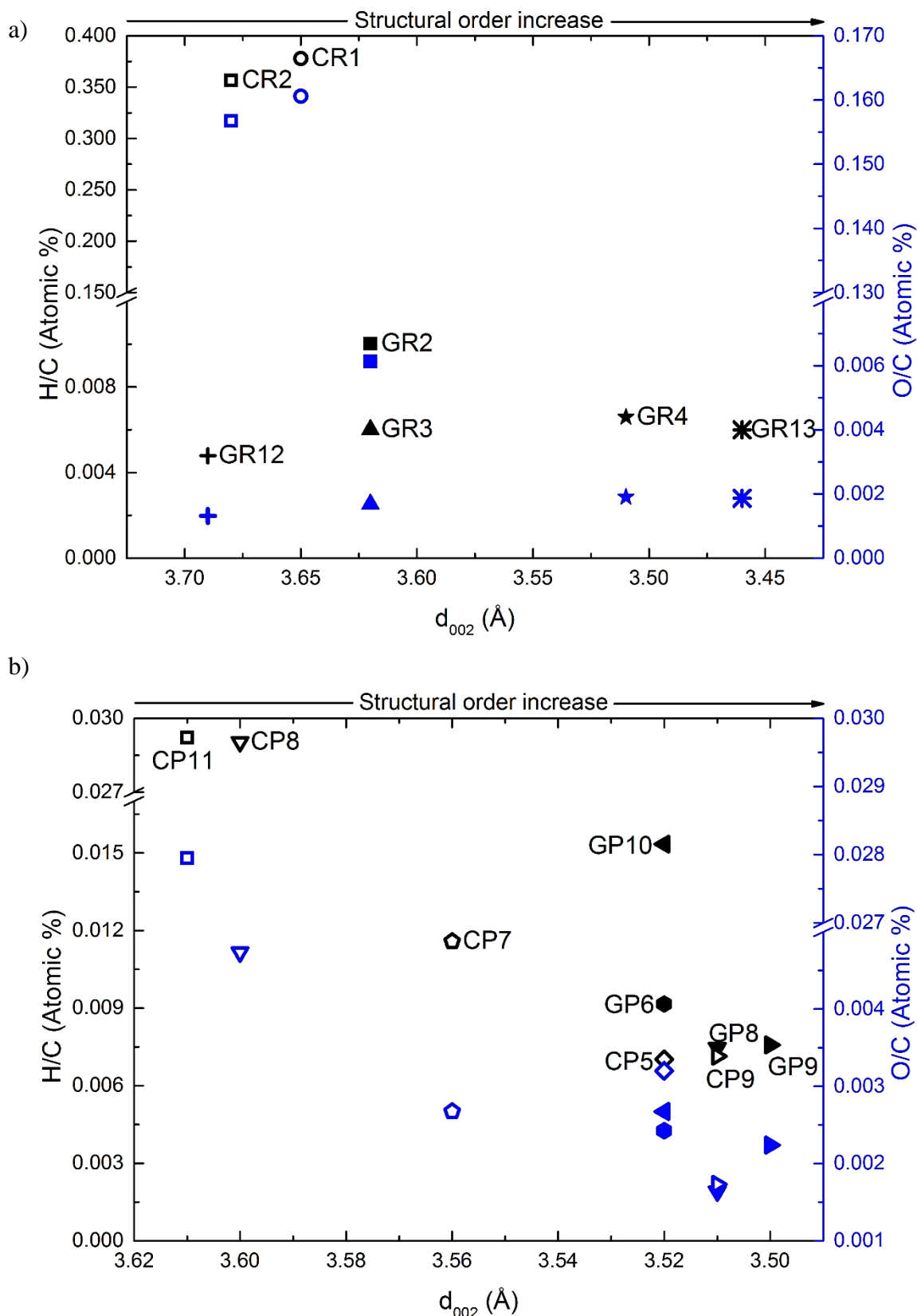


Figure III/3-4 Relationship between the elemental composition as a function of interlayer graphitic spacing (d_{002}) of a) ex-PAN and b) ex-Rayon CFs; empty symbols represent carbonised and full symbols (including cross-like ones) represent graphitised CFs; the difference of colour corresponds to O/C (blue) and H/C (black) atomic ratios.

After carrying out the global structural XRD analysis, Raman spectroscopy was performed for local structural studies of chosen CF. Random zones on different carbon fibres were examined from the outer fibre surface or cross-sections (presented in Fig. III/3-5).

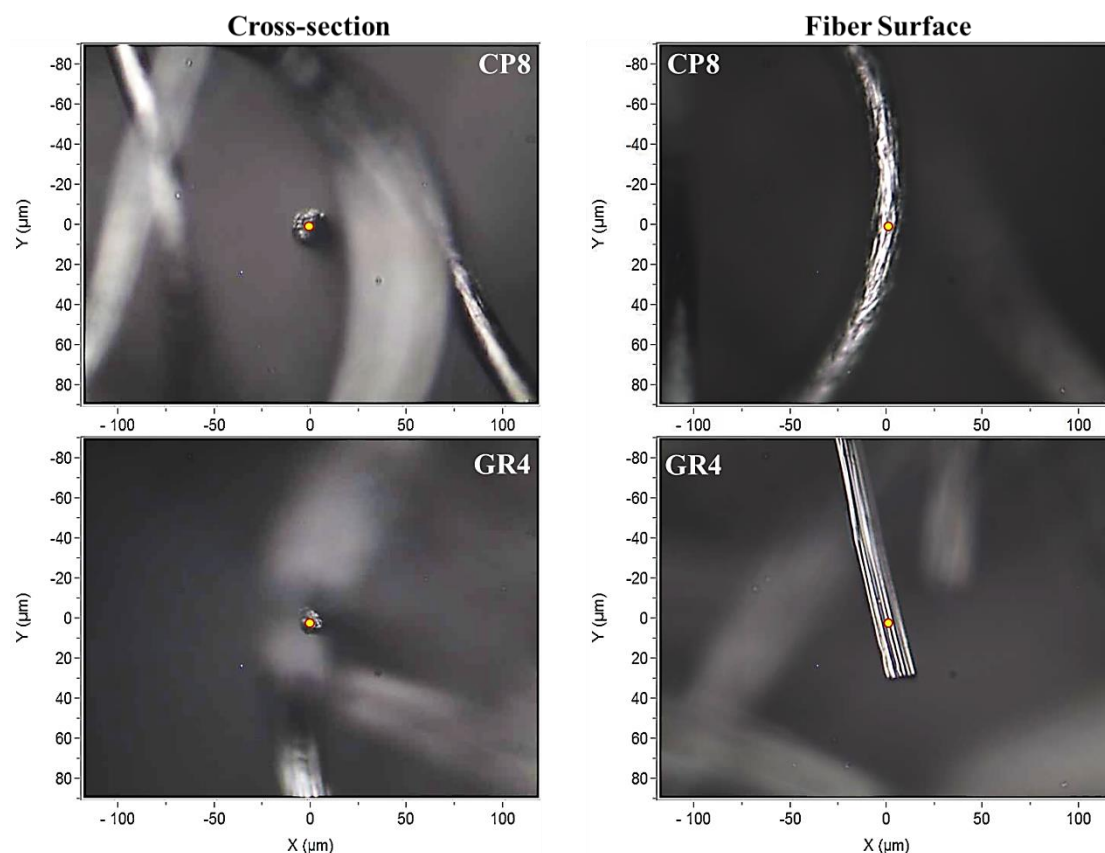


Figure III/3-5 Raman laser spot position (yellow midpoint), for achieving Raman spectra from both ex-PAN (CP8) and ex-Rayon (GR4), cross-section (left) and carbon fibre surface (right micrographs).

Figure III/3-6 presents the Raman spectra of the investigated ex-Rayon and ex-PAN CF, in which the spectra are shifted with respect to each other for easier visualisation of the analysed similarities or differences. The Raman spectra obtained from the same CF at the cross-section and the fibre surface are completely superimposed. This suggests a high homogeneity, observed either on the carbon fibre surface or cross-section (without modifying its surface) for each of the investigated CF, and hence the absence of shell-core structural order. The latter heterogeneous structural properties were previously observed elsewhere (Jones and Duncan 1971; Kong et al. 2012; Newcomb 2016). When performing a micro-Raman analysis, these authors found that the shell of the examined carbon fibres was highly ordered compared to the core, suggesting fast stabilisation (uneven oxygen diffusion from the fibre surface or core) and carbonisation production processes (graphitic nanocrystallites of different sizes and arrangement).

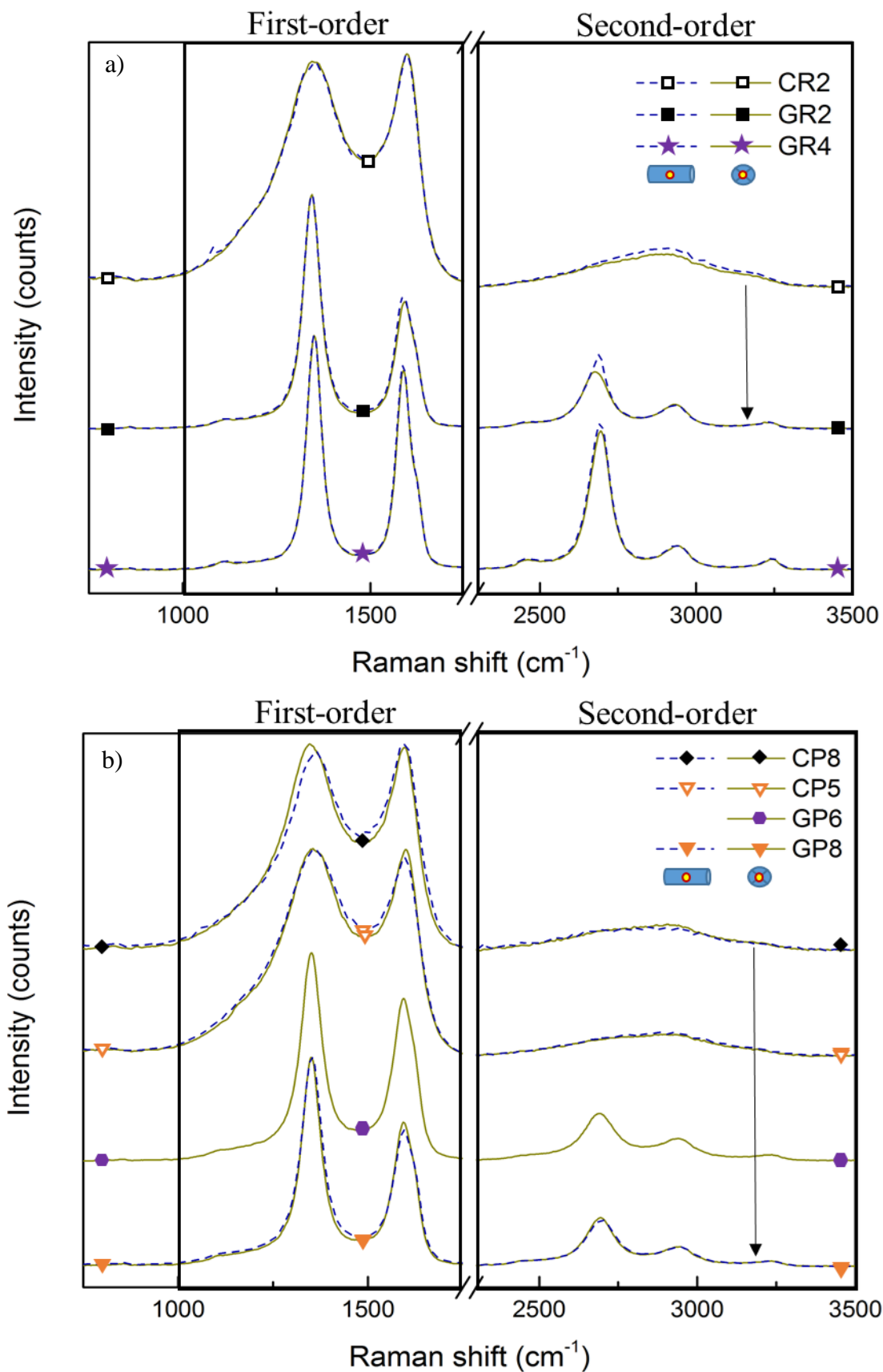


Figure III/3-6 Raman spectra of: a) ex-Rayon and b) ex-PAN CFs, where arrows connect corresponding CFs, thus the dashed or solid line represents spectra derived from carbon fibre surface or cross-section, respectively. For easier viewing, an identical intensity shift was applied.

A first-order part is seen (in the range from 1000 to 1800 cm^{-1}) presenting an intense and broad D_1 band (around 1350 cm^{-1}) and a slightly narrower G band (around 1590 cm^{-1}). A second-order part (in the range from 2200 to 3400 cm^{-1}) is also observed. The latter is poorly structured or well organised, depending on the investigated CF. Therefore, clear differences of spectra are observed when comparing the corresponding CFs, with the only difference in the final manufacturing temperature treatment, as seen from CR2 to GR2 and CP8 to GP8 (linked by the connection arrows in Fig III/3-6).

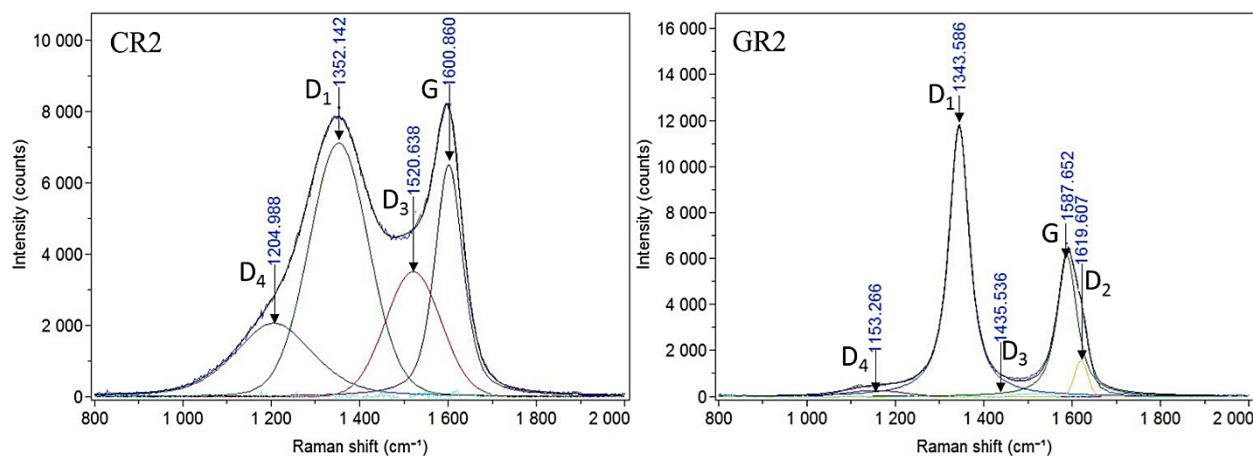


Figure III/3-7 Deconvoluted Raman spectra of CR2 and corresponding GR2 CFs, where the scatter curves indicate the measured intensities and the solid smooth lines represent the fits.

With the deconvolution performed of the Raman spectra (as in Fig. III/3-7), the features of carbonised CR2 (considering also CP5 and CP8) are considered very typical of highly disordered carbon fibres (A. Cuesta et al. 1994; Zickler et al. 2006; Kong et al. 2012). Fabricated by applying additional heat treatment, the graphitised GR2 (as for GR4, GP6, and GP8) present narrower first-order bands, with a difference in band intensity and a much deeper valley between the D_1 and G bands. These band modifications result from the materials' structural order improvement, accompanied by the withdrawal of the D_4 and D_3 and the appearance of the D_2 band. The presence of D_1 , in all CF samples, indicates sp^3 -hybridised carbon atoms, either as such or more probably related to the presence of oxygen, hydrogen and/or nitrogen in the CF, in good correlation with the carried out elemental analysis. In addition to the structural disorder origin, the D_1 band also arises from the presence of small size graphitic nanocrystallites with a low number of graphitic layers, confirmed by the performed XRD analysis and previous Raman and XRD research studies (Pimenta et al. 2007). The D bands (D_1 , D_3 , and D_4) reflect the breathing, edges, and faults in the graphitic lattice symmetry (as A_{1g} symmetry vibrations), expected in disordered carbon rings (Sadezky et al. 2005). Whereas the G band solely represents

the stretching vibration (as E_{2g} symmetry vibrations) in aromatic layers of graphite-like carbons (Sonibare, Haeger, and Foley 2010). The constant presence of the G band in the examined CF, explains the clear existence of sp^2 -hybridised carbon, whose intensity and width of the band is influenced by the 3D evolution of the graphitic nanocrystallite. It is also found that the occurring D_2 is independent of the graphitic lattice edge or fault vibrations, unlike the other D bands. Like the G band, it corresponds to a graphitic lattice (E_{2g} symmetry) vibration of perfect graphene surface layer (1-dimensional) on the graphitic nanocrystallite surface (Pimenta et al. 2007), observed only for the graphitised CF.

The same kind of conclusion is obtained from the estimated full width at half maximum values (FWHM) of the deconvoluted D_1 and G bands, ranging from 169 to 48 and 79 to 45 cm^{-1} , respectively (seen in Fig. III/3-8). The corresponding pairs of CFs (from both groups) show very good correlation of the FWHM of D_1 and G bands, with the structural order increase, comparing CR2, CP8 with GR2 and GR8, respectively. However, the lowest one (FWHM of GR4), 45 cm^{-1} , is much higher than that of highly oriented graphite at about 15 – 16 cm^{-1} (Sadezky et al. 2005). Therefore, the analysis indicates a low degree of improvements in the local graphitic order in the examined CF, which confirms the validity of the d_{002} and L_c values of the carried out XRD analysis.

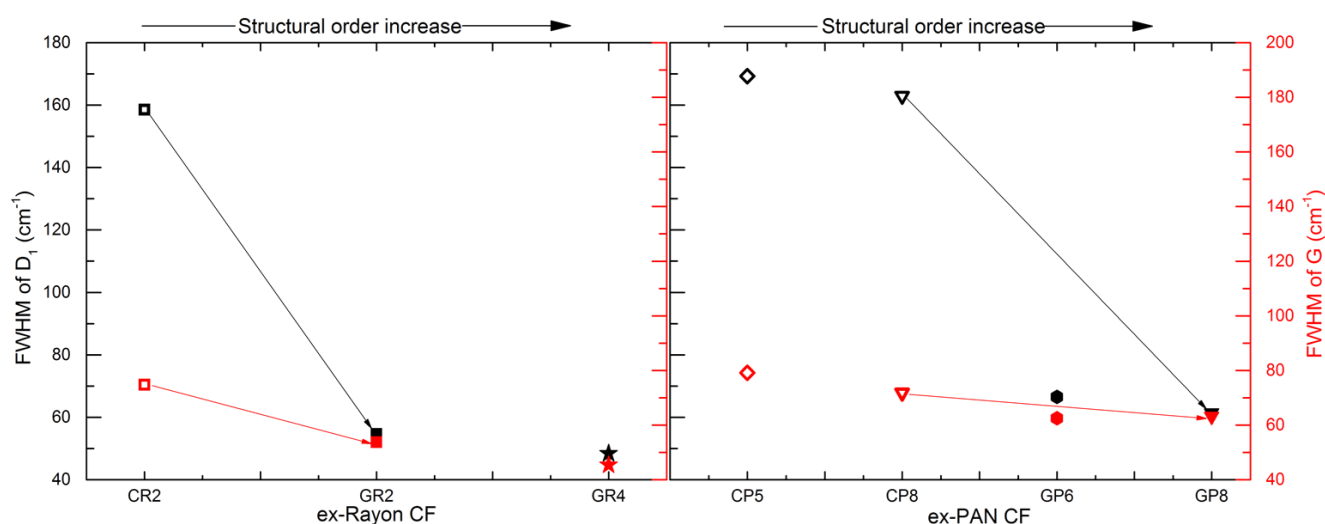


Figure III/3-8 FWHM of deconvoluted D_1 and G bands of: a) ex-Rayon and b) ex-PAN CFs, where arrow connects corresponding CF, empty symbols represent carbonised and full symbols represent graphitised CF, with differences of colour corresponding to D_1 (black) and G (red).

When the band deconvolution is performed for the second-order of the Raman spectra, a clear appearance of the intense S_1 band (attributed to the first overtone of D_1 at around 2700 cm^{-1}) was found only for both ex-Rayon and ex-PAN, graphitised CFs. The observed intensity increase of the S_1 band should correspond to the lateral growth of the graphitic nanocrystallites and to the improvement of the stacking order of the graphitic layers (Kong et al. 2012). Yet, it is known that the S_1 band splits into two bands when the carbon structure acquires a tri-periodic carbon layer stacking (Dresselhaus 1988; Pimenta et al. 2007), which obviously is not the case for any of the investigated materials, in agreement with the performed XRD analysis.

The I_{D_1} (band intensity) is found to be greater than I_G , for the examined CF, including the ones (GR2, GR4, GP6, and GP8) manufactured at higher final heat treatment, above 2000°C . For the corresponding CF pairs (Fig. III/3-9), this I_{D_1}/I_G ratio increases progressively, which is an additional indication that these CF are in the carbonisation regime, whereas in the graphitisation regime, one should expect the opposite (Celzard et al. 2019). Once again, it is likely that only a lateral graphite nanocrystallite growth appears (graphically presented in Fig. III/3-9) with a supposed absence of tri-periodic carbon layers stacking, in good correlation with the information of the S_1 band.

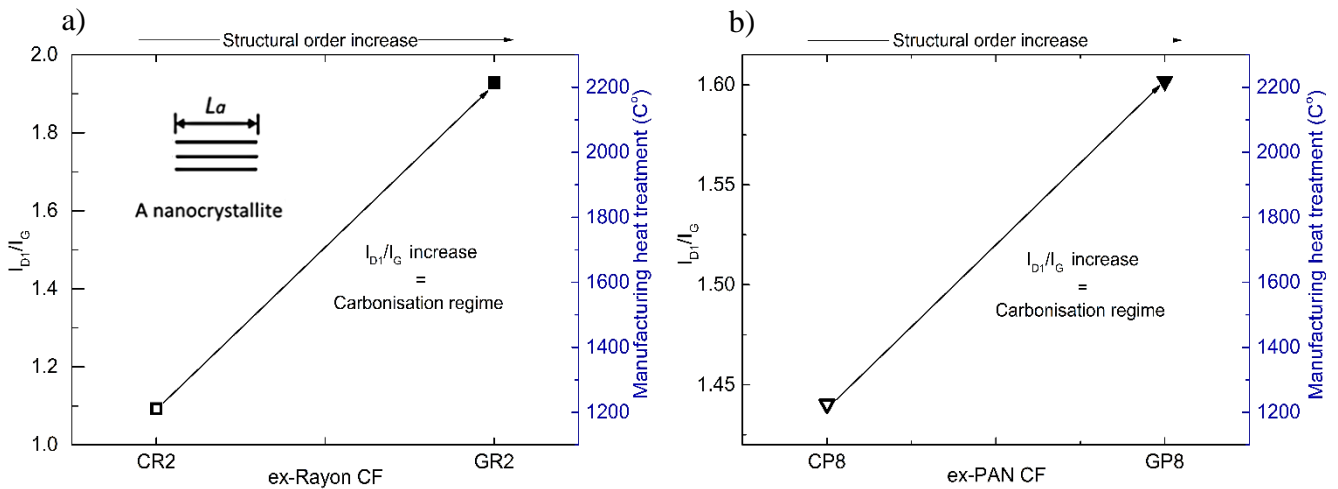


Figure III/3-9 Intensity ratio between deconvoluted D_1 and G bands of corresponding: a) ex-Rayon and b) ex-PAN CFs, with increase-indicating arrow and empty or full symbols for carbonised and graphitised CFs, respectively; graphical presentation of the lateral growth of the graphite nanocrystallite is given in the left upper corner of figure a).

III/3.3 CF complete impregnation in the investigated molten salts - process validation

The different results of the elemental composition and the structural properties were presented for the different CFs, whose chemical stability has yet to be demonstrated. In this logic, the infiltration method presented in Subsection III/2.2 was carried out to ensure complete CF impregnation with the molten inorganic salts of interest. When performed, the tests of different CF samples with porosity as low as $\sim 93\%$ were driven only by gravitation. The results suggest that most CF under investigation can be considered as hybrid material candidates and can be fully infiltrated in a similar manner.

The visual observations were further validated by performing SEM of the prepared CF-PC hybrid material (seen in Fig. III/3-10). From these microscale analyses, performed over a half-cut sample, we observed homogeneous and complete infiltration of the CF, only by a simple infiltration protocol, without the use of additional pressure and with only gravity forces in action (Achchaq et al. 2018).

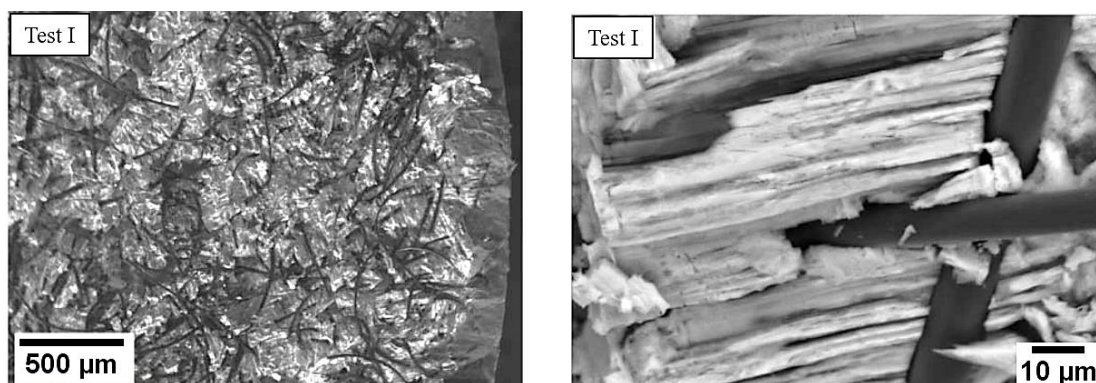


Figure III/3-10 SEM visualisation of the cooled hybrid materials after complete CF infiltration with the PC ($\text{Li}_4(\text{OH})_3\text{Br}$).

The additional EDX mapping (Fig. III/3-11) clearly shows the homogeneous dispersion and the presence of C, Br, and O atoms in the produced CF-PC hybrid material.

In addition, the observed complete impregnation opens the possibility of performing valid chemical reactivity tests. Simply taking into account the required inert atmosphere, further chemical reactivity tests are feasible, for fixed time duration and range of temperatures above that of the impregnation process.

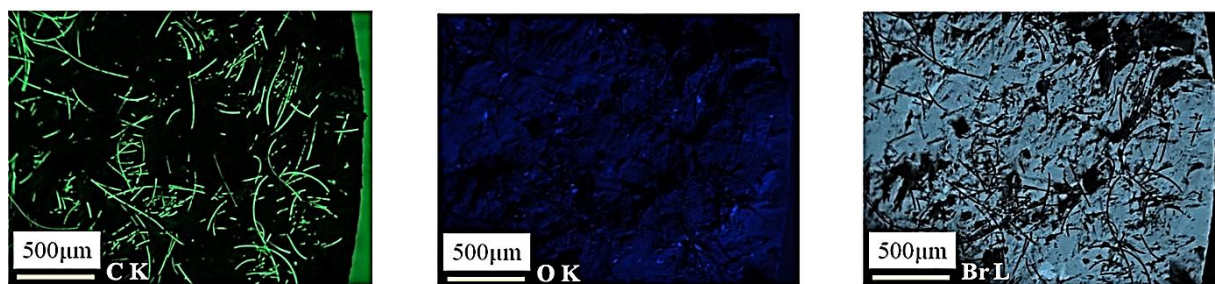


Figure III/3-11 EDX elemental mapping of: left (carbon), middle (oxygen) and right (bromide) of the same material presented in the previous figure.

For the samples representing the groups of rigidized soft and rigid CFs (seen in table III/2-1) and porosity less than 93%, the analysis of their chemical stability with inorganic salts/PC was performed with greater caution. However, high CF wetting affinities with inorganic salts are observed once they reach their melting point, suggesting complete material impregnation. Additional verification of infiltration has always been taken into account by the visual confirmation of a half-cut sample after completion of the chemical reactivity tests.

III/3.4 Carbon chemical reactivity in molten LiOH

Once good CF infiltration has been confirmed, it is necessary to discuss further the possible chemical reactions between the CF and the storage material of interest. From the wetting of CF with the investigated PC, carbon chemical reactions are expected with the LiOH component and its hydroxide group. Therefore, the temperature boundaries of the chemical reactivity study will be based only on its carbon activation properties (as presented in Fig. III/3-12).

In general, testing chemical reactivity of carbon in molten LiOH involves a thermochemical reaction between the carbon and the hydroxide, with final products of CO, H₂ and the alkali metal Li, as seen from Fig. III/3-12 and the following general reaction:



The complete redox reaction (1) is highly endothermic, with a reaction enthalpy estimated at -523 kJ mol^{-1} , and is only accomplished at a very high temperature, above 1600°C . Thus, more than one reaction steps and intermediate species are necessary to reach the final reaction products (Epstein et al. 2001). Therefore, this reaction is carried out in more than two successive steps, initially involving the release of hydrogen and the conversion of LiOH to Li₂CO₃ at a much lower enthalpy, with the reaction:



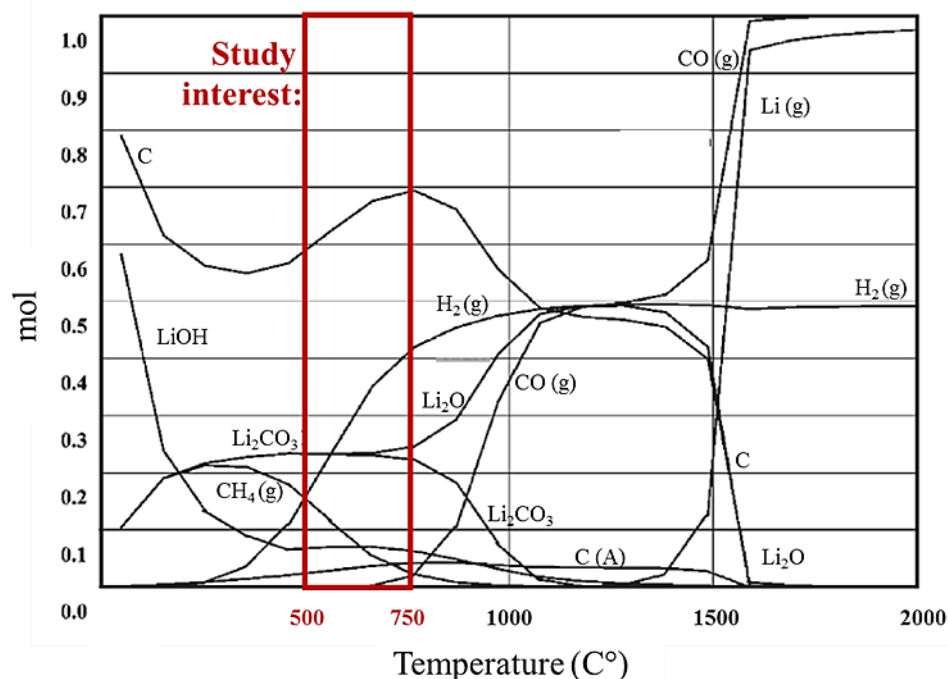


Figure III/3-12 Thermodynamic equilibrium of LiOH and carbon as a function of temperature, with the temperature range of study interest (modified after Epstein et al. 2001).

Here we must consider that the rate of reaction (2) and its activation energy can be modified when testing the reaction of LiOH with a carbonaceous material at different graphitisation stage. This means that less ordered CFs, with a higher amount of heteroatoms and active surface groups, should be much more reactive with LiOH than those with an improved structural order.

Although Li₂CO₃ has a high melting temperature of about 730°C (Wietelmann and Bauer 2000; Schiemann et al. 2016), earlier decomposition can be observed at lower temperatures, even under a constant flow of inert N₂. This further facilitates the beginning of its chemical reaction with carbon as follows:



However, even if it occurs at around 730°C or lower temperature, the rate of reaction (3) should initially be low and quite negligible below 800°C, while considering a less reactive carbon material containing less than 10% of foreign elements (McKee and Chatterji 1975). This also agrees with the study of Sutcu and Dural (2006), which evaluated the LiOH chemical activation with bituminous coal of lower rank (carbon content ~ 73 wt. %). From the performed thermogravimetric analysis, they showed that complete calcination (reaction (3)) of the Li₂CO₃

was accomplished even before 800°C due to the presence of foreign elements, whose functional groups (active reaction sites) increased the reaction rate.

With respect to the investigated information from previous studies (Sadoway 1998; Epstein et al. 2001; Schiemann et al. 2016), the final step to complete the global carbothermic redox reaction (1) is the complete oxidation of the carbon as follows:



However, as confirmed above, the latter reaction is thermodynamically unviable and is outside the study scope, in relation to the lower investigation temperature and in good correlation with the positive Gibbs free energy of reaction (4) at 900°C (Zhou et al. 2016).

This general knowledge of the main chemical reactions that possibly occur when testing the CF chemical stability in molten LiOH is used to complete the general objective of this study. Thus, good control of the experimental variables allows a better understanding of the tested CFs and their validity for later use in the foreseen application. As it is known, the CF materials were tested completely impregnated (at a defined ratio) in the molten inorganic salts or PC system, all variables except one being fixed. Therefore, the only important experimental variable is the heat-treatment temperature range. The information presented in the literature is therefore used to establish the limits of the test and further limits the occurrence of multiple chemical reactions, significantly controlled by the temperature (Linares-Solano et al. 2007). Therefore, the temperature limits in the chemical reactivity study, in the range between 500 and 750°C, should allow a clear distinction between different CFs, and estimate the carbon modification that might occur at the lower application temperature.

By the use of fixed and high LiOH/CF ratio (molar ratio of about 20/1), it is expected that the chemical reaction depends mainly on the CF properties, and not on the alkali/carbon ratio, as was previously seen elsewhere (Yu. V. Tamarkina et al. 2008). In addition, when raising the final reaction temperature (within the defined limits), the phenomena of an increased reaction rate is expected, with respect to the increase of carbon atoms that react with molten LiOH during a fixed time. Additional catalytic or secondary carbon reactions are only expected with respect to the CF properties and the presence of foreign elements since higher test temperatures (above 800°C) would be required to increase significantly the reaction rate of Li₂CO₃ in-high purity materials.

Under the fixed experimental conditions, the magnitude of reaction (2) and the occurrence of reaction (3) are controlled by the carbon activity, which is further observed as a limiting reactant from the experimental results. In this way, it is assumed that a clear separation of the CF candidates is expected with respect to their chemical stability, depending on their elemental composition and structural properties. Therefore, the threefold objectives of these defined CF chemical reactivity tests are to obtain information, previously not reported in the bibliography, such as:

- effect of the CF elemental purity and structural characteristics on their chemical reactivity in molten LiOH;
- compared carbon felt's chemical reactivity after infiltration by molten LiOH, LiBr or their peritectic composition ($\text{Li}_4(\text{OH})_3\text{Br}$);
- CF chemical reactivity under the temperature conditions of the foreseen application.

III/3.5 CF chemical stability with respect to their structural properties

Many materials' or experimental variables, such as precursor, manufacturing technique or temperature, can influence the reaction between carbon and alkali hydroxides. Awareness of their importance will enable us to understand and therefore choose the best CF candidate in terms of high chemical stability, important for the foreseen TES application. All these influencing variables are summarised in the tested properties of the commercial CF, from different starting materials and with different manufacturing histories. Therefore, the results from chemical reaction tests, initially carried out in molten LiOH, highlight the importance of the CF elemental composition, as well as their structural and textural properties.

For both ex-PAN and ex-Rayon materials, as carbon purity increases, the reactivity of the LiOH is reduced and the CF become very stable even at the highest temperature tested (seen in Fig. III/3-13 a) and b), respectively). As expected, the chemical reactivity tests (reported in subsection III/2.1) revealed carbon burn-offs (burn-off = $100 - \text{yield}$ calculated as a % of carbon disappeared per initial CF weight) always increased with temperature. This was evident due to the considerable increase in the reaction rate (consequently more carbon atoms react with the alkali hydroxide) and the existence of surface functional groups, considered as catalysts for the occurring reactions (Linares-Solano et al. 2007). In general, by comparing only carbonised CF from different precursors, ex-Rayon show a higher burn-off (B-O) than ex-PAN CFs, in good agreement with their higher amount of heteroatoms. Moreover, the differences in reactivity are observed between the examined corresponding CFs (CR1a→GR1a, CR2a→GR2a,

CR3a→GR3a or CP8a→GP8a), presented with identical empty or solid symbols for carbonised or graphitised CF in Fig. III/3-13 a) and b), respectively. Most of the carbonised CFs were almost completely consumed by the strong reaction between the carbon surface functional groups and the LiOH at 650 or 750°C for the ex-Rayon or ex-PAN materials, respectively. As explained in subsection III/3.1, the presence of O, N and H in the carbonised ex-Rayon and ex-PAN CFs is associated with the existence of surface functional groups (-C-H; -C-OH; -C-O-C; -C=O; C=N; -COOH; etc.), whose presence decreases with subsequent CF graphitisation at a higher temperature (Pastor et al. 1999; Zhong et al. 1993; Chiang, Lee, and Lee 2007; Ko, Liao, and Liu 2007; Shen, Li, and Liu 2008; Dai et al. 2011; He et al. 2015; Qian et al. 2016). This is in good correlation with Raman analysis performed, where the carbonised CF spectra showed wide and intense D₁, D₄ and D₃, indicating a significant presence of heteroatoms and aliphatic side chains. In addition, the presented chemical reactivity results are in good agreement with other authors who observed similar reactivity trends between low-purity carbons and LiOH, always resulting in high weight loss (Mora et al. 2006; Sutcu and Dural 2006; Leimkuehler 2010; Chowdhury et al. 2013).

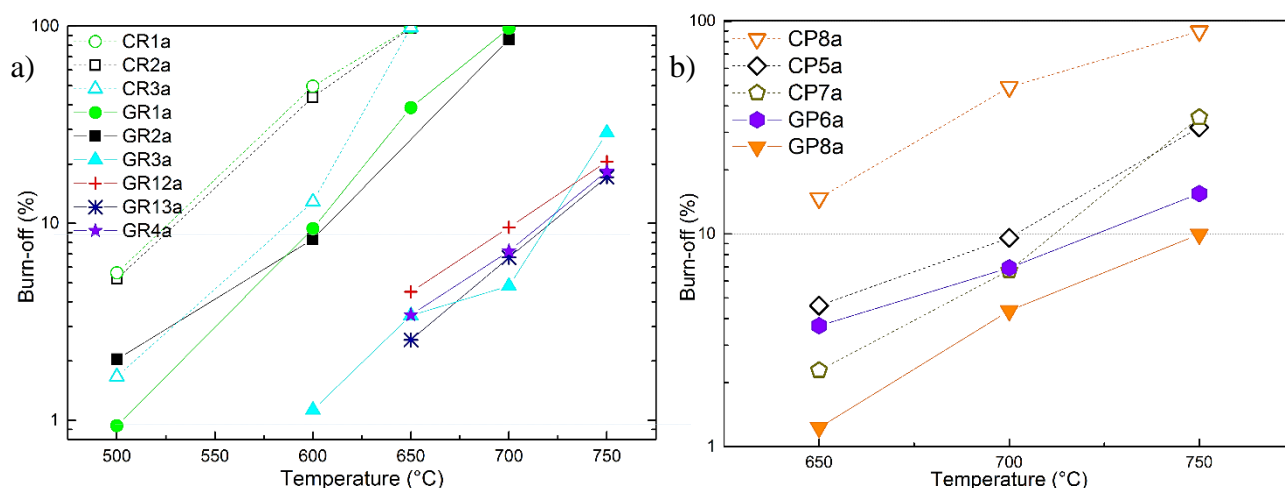


Figure III/3-13 Burn-off (%) vs. reaction temperature of a) ex-Rayon and b) ex-PAN CFs; empty and full symbols (also cross-like ones) represent carbonised and graphitised CFs, respectively; the dashed or solid lines are only guides for the eye.

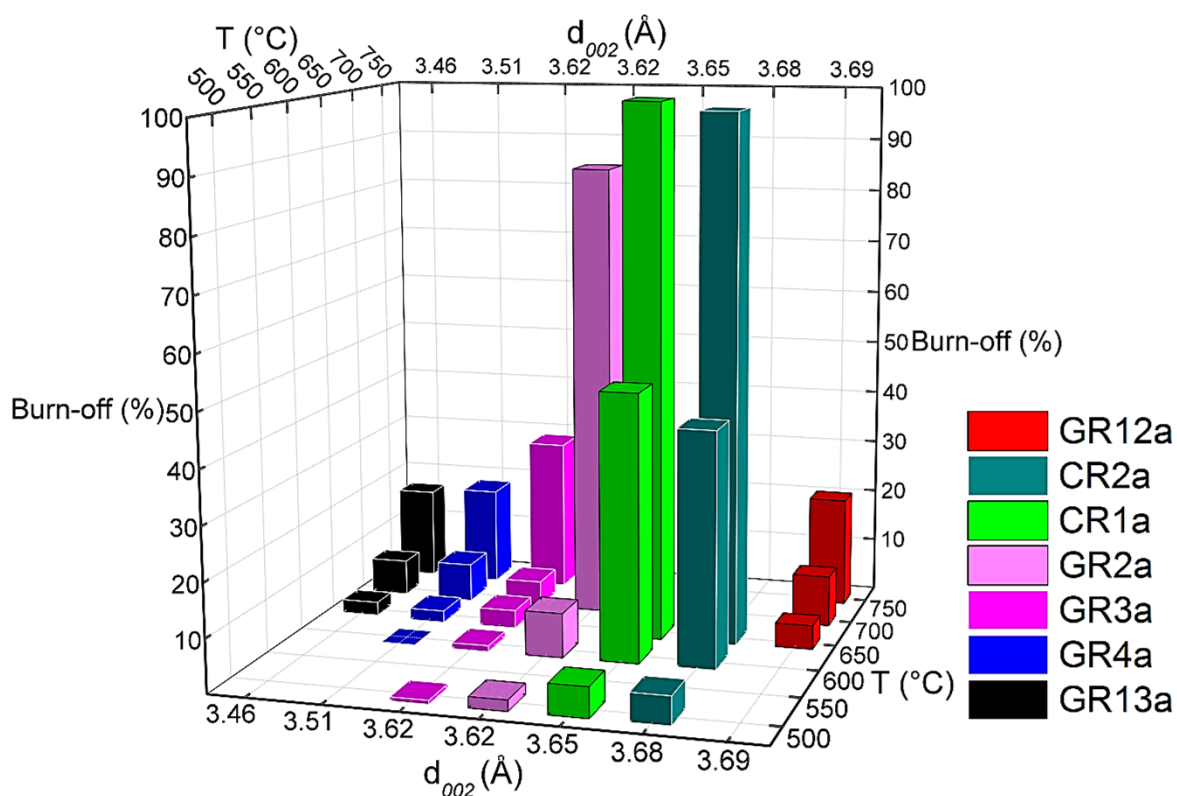
In addition to the current correlation with the studied CF elemental composition, the graphitic improvement of the materials is also compared to the results of the chemical stability tests. As seen in Fig. III/3-14, the B-O results are in correlation with the interlayer graphitic spacing (d_{002}). The plotted results clearly show that LiOH is reactive with carbonised CF and less efficient in the corresponding graphitised materials. However, even if correlations are observed, the decreasing trend of the CF chemical reactivity with respect to the improvement of the structural order should be considered with caution. This is evident for some CFs with

similar interlayer graphitic spacing (d_{002}), as in GR3a \leftrightarrow GR2a and GP8a \leftrightarrow GP6a, but with different B-O results. Coming back to Fig III/3-4, a clear indication of this behaviour can be inferred from the different presence of the O and H in the mentioned CFs. Thus, even if similar structural development is observed, particularly seen for GP8a \leftrightarrow GP6a (from both XRD and Raman analysis), the higher amount of heteroatoms in the latter clearly distinguished this material as being more reactive with LiOH. A consistent discrepancy between B-O results and the interlayer graphitic spacing (d_{002}) is also observed from B-O results demonstrated for CR2a and CR1a, but again in good correlation with the elemental composition.

As proof of the above explanations, the discussed deviations were further confirmed by carrying out an additional chemical reactivity test with a material of low structural order, yet of high carbon purity. Therefore, after testing the chemical reactivity of sample GR12a (seen in Fig. III/3-14 a)) we became aware of the increased importance of the CF elemental composition and its chemical stability effect compared to the materials' structural order. Thus, the obtained B-O results of GR12a are comparable to those of the ex-Rayon CF, for example, GR4, and GR3a, with much higher structural order.

Current correlations show that LiOH is more reactive (higher B-O at a lower test temperature) in the presence of low-purity CF. In most cases, this was independent of the graphitic order reached during the last manufacturing process (carbonisation or graphitisation), taking into account CF from different suppliers. However, the graphitised CF with improved order and size of the graphitic nanocrystallites are clearly seen as better candidates in the intended application. Graphitised CF with high structural order show improved thermal management properties (see again the results in Chapter II) (Pradere et al. 2009; Qiu et al. 2013). In addition, a greater structural order hinders the nanoporosity of carbon fibres, as presented by the Franklin carbon models in Fig III/1-1. The imperfections of the graphitic network are reduced by the evolution of the graphitic nanocrystallites, thus inhibit the development of carbon microporosity, which also influence the lower chemical reaction with molten LiOH.

a)



b)

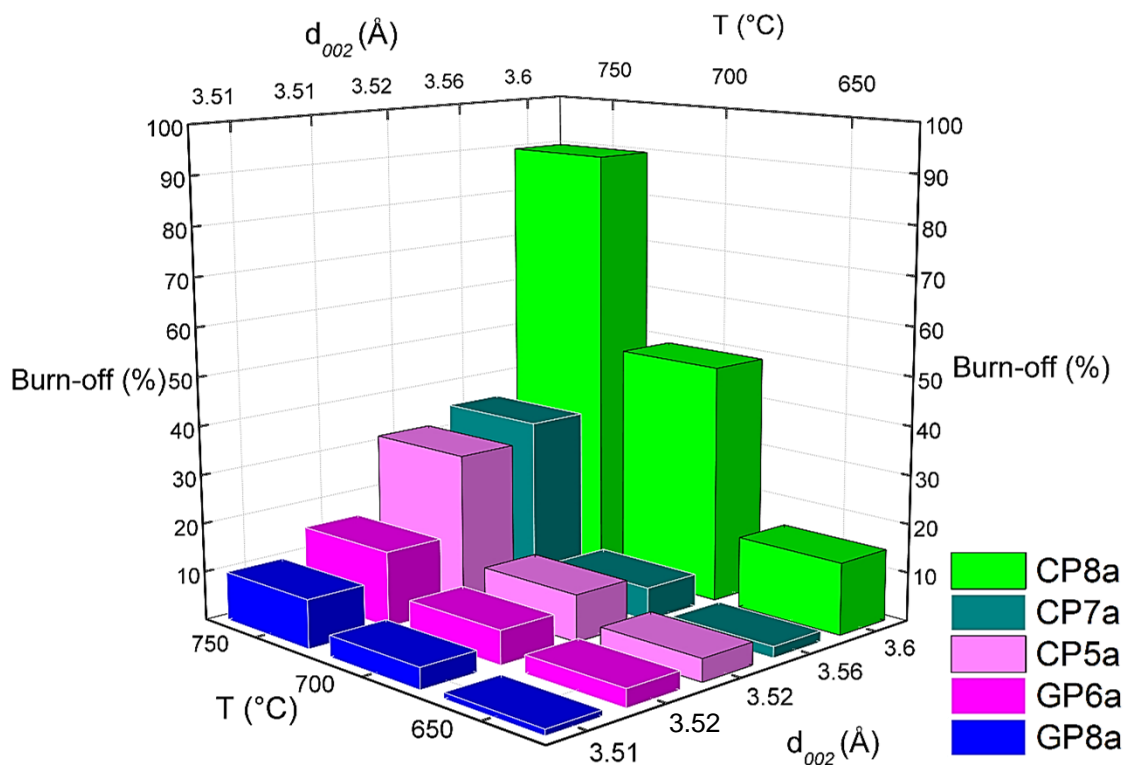


Figure III/3-14 3D bar representation of the B-O (%) variations with respect to the test temperature and to the interlayer graphitic spacing (d_{002}) for a) ex-Rayon and b) ex-PAN CF, tested for their chemical reactivity in molten LiOH.

As the chemical stability of the CF was discussed with respect to their elemental and structural properties, the same correlations were searched with their nanotexture properties. Therefore, the textural analysis was performed as explained in subsection III/2.3.b, by achieving both N₂ and CO₂ adsorption isotherms of *de-sized* (initial) and reacted CFs in molten LiOH (detailed results of the textural analysis are available in Table III/6-1 and Table III/6-2). The application of the 2D NLDFT-HS model to N₂ and CO₂ adsorption was chosen as quite advantageous in terms of improved accuracy. This is very important when adsorption equilibrium is difficult to achieve during the nanotexture analysis of microporous and heterogeneous surface carbon materials (Jagiello and Olivier 2013).

De-sized CF exhibited both type I and type II N₂ adsorption isotherms according to the IUPAC classification (Sing 1994). Thus, the adsorption isotherms of CR1, CR2, GR1, GR2, and GR3 are all type I, suggestive of microporous carbons (seen in Fig. III/3-15 a) and b)). However, the smoothed "knee" formation of the graphitised GR1 N₂ adsorption isotherms and higher adsorbed amounts, as explained by (Lu and Zheng 2001, Maciá-Agulló et al., 2004) indicate the existence of wider micropores and appearance of mesopores, as compared to the other micropore type I isotherms. Graphitised GR3 and GR4 with improved structural order, on the contrary, exhibited N₂ isotherms (seen in Fig. III/3-15 c)), that have a sigmoidal shape with a sharp increase in the region of higher relative pressures, which correspond to type II of IUPAC classification (Jagannathan et al. 2008). These adsorption results are in good line with the structural properties of the investigated CFs. Thus, the improvement of the CF structural order induced a decrease of microporosity, in good agreement with previous carbon fibres studies (Babel and Jurewicz 2004; Maciá-Agulló et al. 2007).

CO₂ adsorption isotherms were performed in addition to the N₂ ones (seen in figure III/3-15 c) and d). They present a great advantage to study microporous CF materials and to avoid well-known issues of restricted gaseous molecules diffusion at low pressures (Landers, Gor, and Neimark 2013). The achieved CO₂ adsorption isotherms agree with the N₂ adsorption isotherms so that the CF order and the general differences of the amounts adsorbed are consistent in both analyses. Therefore, when using the 2D NLDFT-HS model we combined the results of the CF adsorption analysis, which is considered an effective characterisation tool for detailed and reliable textural analysis.

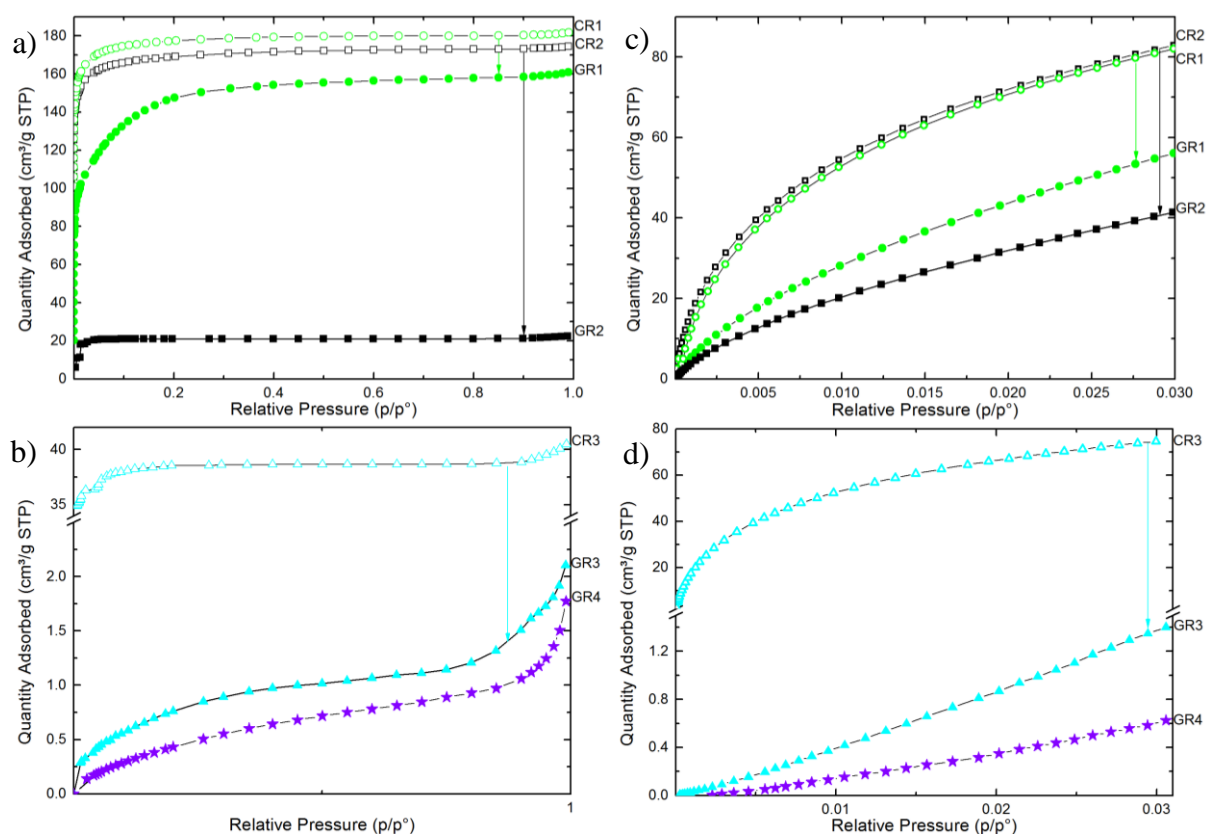


Figure III/3-15 a) and b) N₂ adsorption isotherms at -196 °C and c) and d) CO₂ adsorption isotherms at 0 °C for *de-sized* CFs before reaction in molten salts.

The 2D NLDFT-HS specific surface areas obtained from the CF chemically reacted in molten LiOH were found to vary between 9.6 and 1034 m² g⁻¹, depending on the conditions. A large variety of nanotextures was indeed observed for the *de-sized* CFs with different structural properties, as shown by the adsorption isotherms in Fig. III/3-15. Therefore, the different chemical reactivities in molten LiOH deserve a more detailed discussion.

Although LiOH showed a greater reactivity (seen from the high B-O values) with carbonised CFs with respect to graphitised ones (Fig. III/3-13), the same increasing trend was not observed from the results of the 2D NLDFT-HS surface area. As seen in Fig. III/3-16 and III/3-17, the studied CR1a, GR1a, and GR2a show a monotonous increase of the surface area, at a test temperature of 500 or 600°C. However, one exception of this trend is CR2a with an initial increase (from 907.4 to 985.7 m² g⁻¹ at 500°C) followed by a decrease of surface area at 600°C (814.3 m² g⁻¹). By further increasing the test temperature, the carbonised CR1a and CR2a were completely consumed and textural analysis was not doable. Whereas their corresponding graphitised GR1a and GR2a again showed a slight surface area increase when tested at higher temperatures of 650 or 700°C, respectively. These results of low porosity development or even loss, together with the high B-O results, are observed due to the high LiOH/CF ratio (molar ratio of about 20/1). The high amount of activating agent leads to an intense chemical reaction with the carbon, which reaction rate increases with the temperature. Similar high carbon reactivity in molten LiOH was reported by (Lillo-Ródenas et al. 2007; Girón et al. 2015), even when utilising much lower LiOH/CF molar ratio of 1.5/1. Another important feature is the presence and role of amorphous carbon and heteroatoms (as presented from different functional groups), which crosslink the graphitic nanocrystallites in the carbon fibre structure. When carbonised CFs are compared with graphitised ones, the fraction of amorphous structures is greater and the highly accessible atoms are more likely to perform chemical reactions than the carbon atoms within the graphite nanocrystallites. This is evident when analysing GR3a and GR4a CFs, as these materials have significantly improved structural organisation and carbon purity. Even at higher temperatures of 700 and 750°C, LiOH reacts to a much lesser extent with these CFs, resulting in negligibly low surface area (seen in Fig. III/3-18). These results confirm the information of high structural order, deduced by the performed Raman spectroscopy (as for GR4). Also, the results are in good correlation with the lower oxygen content, previously reported to enhance the fixation of alkaline ions, thus catalysing the carbon gasification reactions (Mikova, Chesnokov, and Kuznetsov 2009).

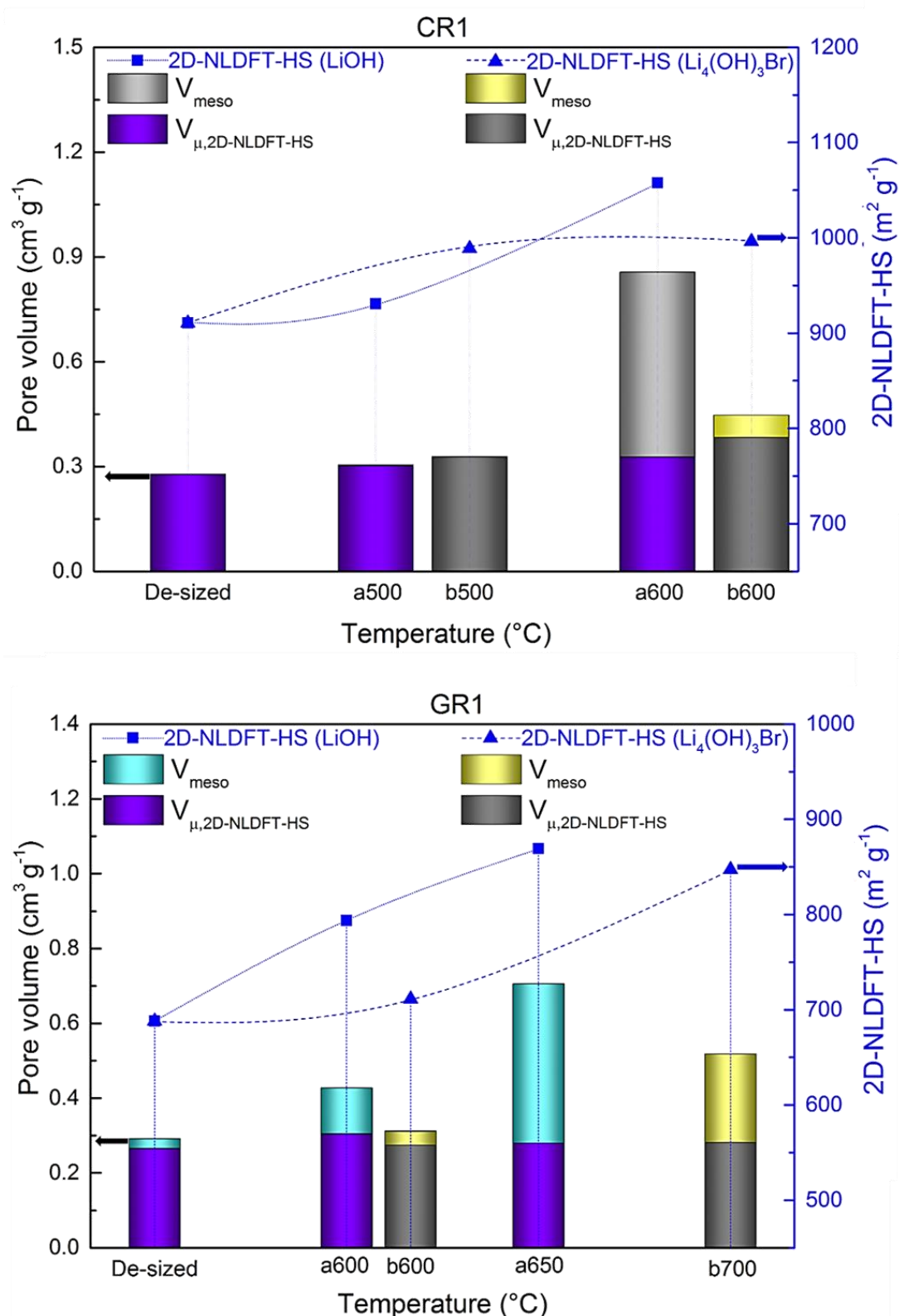


Figure III/3-16 2-D NLDFT-HS specific surface area (scatter symbols) and micro and mesopore volumes (stacked columns) of corresponding a) CR1 and b) GR1 CFs as a function of the reaction temperature in molten LiOH or $\text{Li}_4(\text{OH})_3\text{Br}$; the dotted or dashed lines are only guides for the eye.

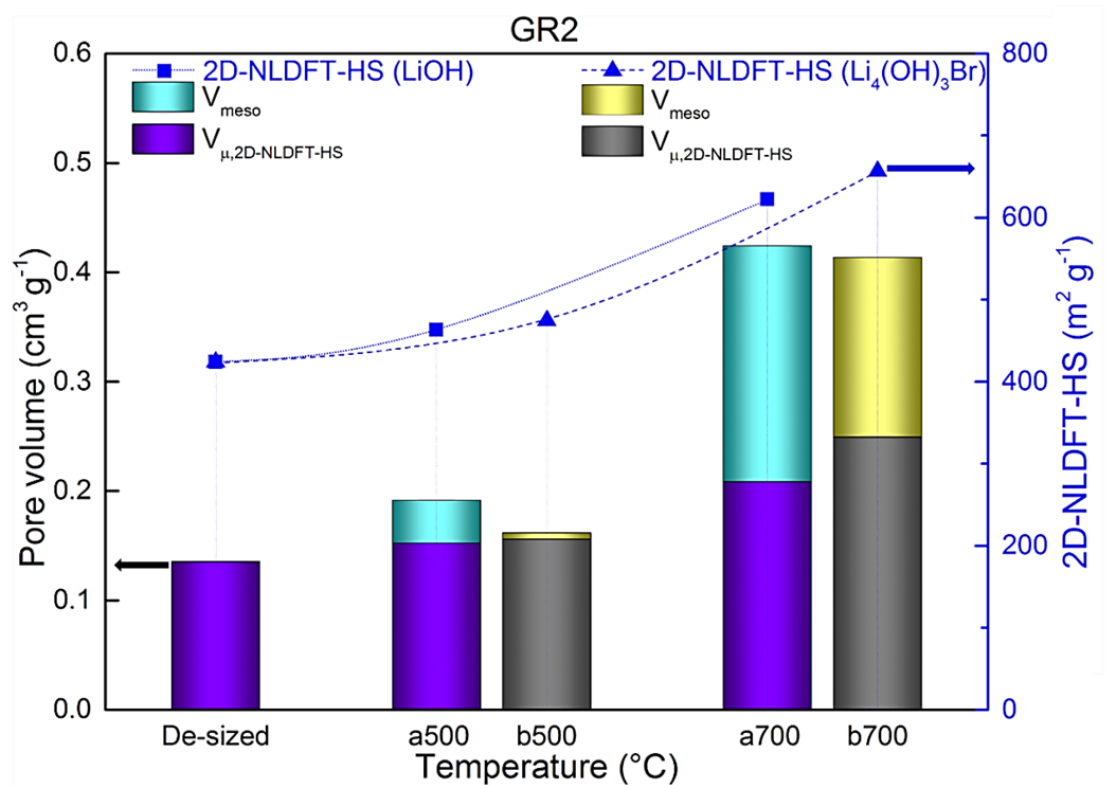
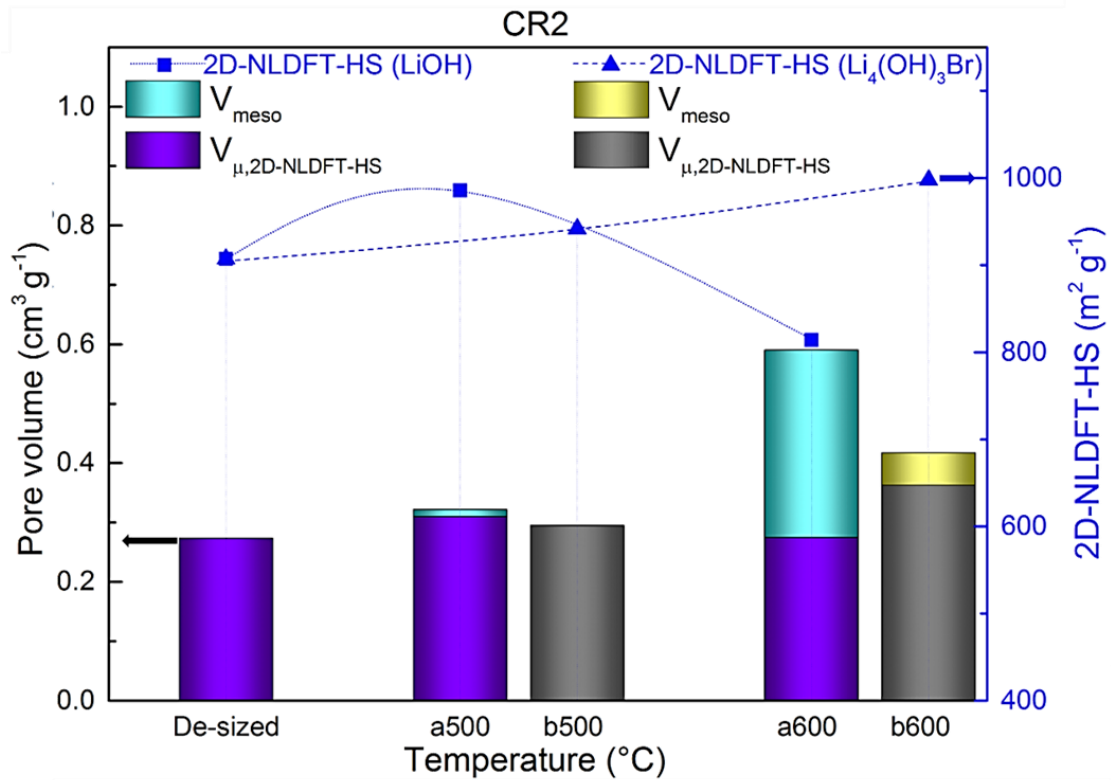


Figure III/3-17 Same as in Fig. III/3-16 but for corresponding a) CR2 and b) GR2.

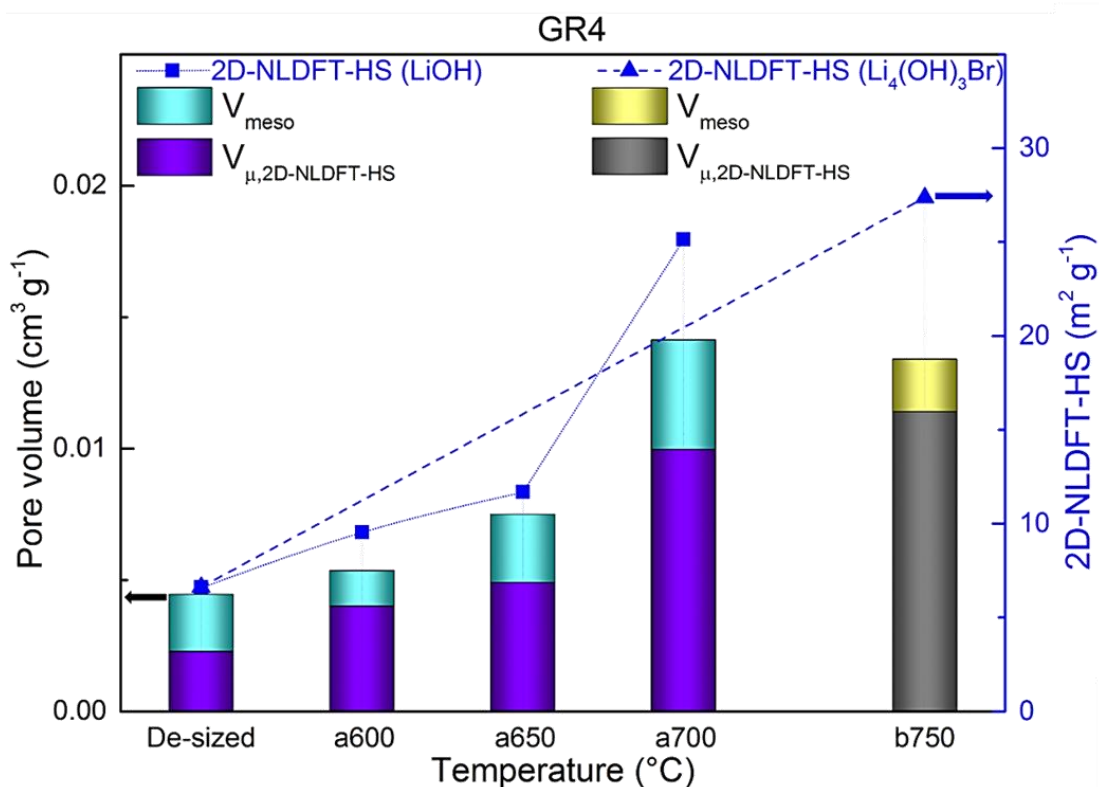
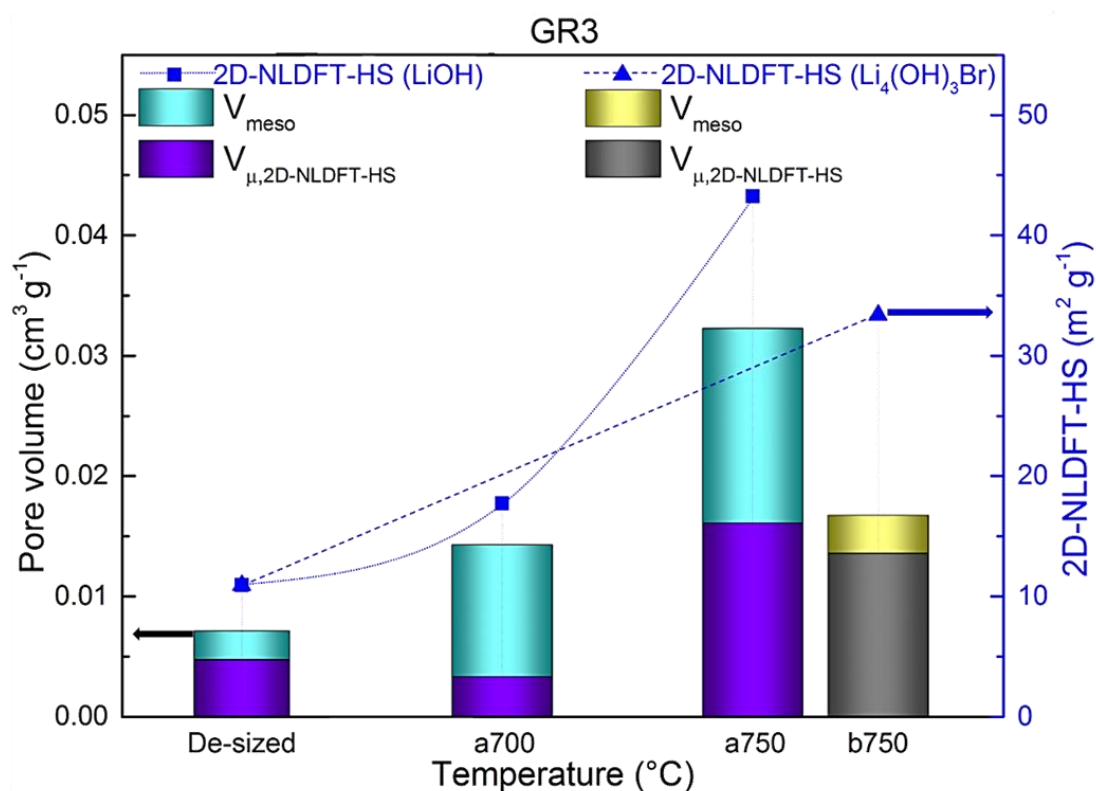


Figure III/3-18 Same as in Fig. III/3-16 but for graphitised a) GR3 and b) GR4 CFs with higher structural order and carbon purity.

The same trends of surface area were observed when analysing the textural properties of the ex-PAN CF, presented in Table III/6-2. Again, the carbonised CFs (presented by CP8a) showed a higher surface area than the corresponding graphitised GP8a, after having been thermally treated in molten LiOH at identical test temperature. Yet due to the poorly developed porosity and the possibly high experimental error, the textural analysis was carried out on a few chemically reacted ex-PAN CF, and the obtained results are presented in Table III/6-2.

In addition, the total pore volume and pore size distributions obtained with the 2D NLDFT-HS model further confirm the trends observed for the specific surface areas. Figures III/3-16 to III/3-18 show that very different porosities are obtained, in terms of micro-/mesoporous volume, depending on the initial CF properties and their reactivity in molten LiOH at tested temperatures. In general, for all examined CF, the increase in micropore volume occurred only by widening the medium-sized micropores (0.7-2.0 nm). Under the same test conditions and temperature of 500°C, the initial microporous volume of the carbonised CR1a500 and CR2a500 was slightly widened, which influenced the appearance of mesopores. This was observed due to the slow chemical reaction, slightly widening the CF microporosity (also seen from the pores size distribution in Fig. III/3-19 a) and III/3-20 a)). From the corresponding graphitised CFs, the pore size distribution was obviously different due to differences of structural order, dividing and/or shifting the micropores to lower pore size. Thus, GR1 had both ultramicropore (<0.7 nm) and medium-sized micropores, the latter extending their range to mesopores, whereas the GR2 was purely microporous (seen in Fig. III/3-19 b) and III/3-20 b)), in good agreement with the structural information from XRD. When testing the latter two CFs at 500°C, it was observed that the chemical reaction in LiOH results in widening the medium-sized micropores in GR1a500, whereas GR2a500 exhibited the formation of medium-sized micropores and mesopores. In both CFs, this clearly influenced the increase of mesopore volume (from 8.99 to 20.56 and from 0.14 to 20.4 %, respectively).

Increasing the test temperatures led to an increase in total pore volume, regardless of the investigated CFs. For the poorly ordered carbonised CFs (CR1 and CR2), this was mainly due to the significant opening of the initially observed microporosity and increase of the mesoporosity (e.g. from 0.30 to 0.86 cm³ g⁻¹ for CR1a600, and from 0.23 to 0.59 cm³ g⁻¹ for CR2a600 at 600°C). The pore size distribution of the aforementioned CFs showed fused micro- and mesopore regions (seen in Fig. III/3-19 a) and III/3-20 a)), which even causes the decrease of the specific surface area of CR2a600 (seen in III/3-17 a)). A high LiOH / CF ratio, stimulated with the unordered structure and the presence of heteroatoms in the carbon, resulted in the

almost complete destruction of the microporosity, probably due to the duration of the accelerated chemical reaction. With respect to graphitised CFs, with an improved structural order (such as GR1 and GR2 compared to CR1 and CR2, respectively), only the medium-sized microporosity was involved in the development of higher micro-/mesopore volume without clear evolution of the initial ultramicropores (seen in Fig. III/3-19 b) and III/3-20 b)). Finally, the examined textural results of CFs with higher carbon purity and improved structural order (presented by GR3 and GR4, respectively) confirm the effect of the initial materials' properties on the significant reduction of reactivity in molten LiOH. As a result, only a slight increase of the initial micro- and mesopore volume was observed, even at the highest examined temperature (seen in Fig. III/3-18 and Fig. III/3-21, for the total pore volume and pore size distribution, respectively). Comparing these latter materials, the higher increase of the mesopore volume of GR3 should also be influenced by the smaller graphite nanocrystallite size and interlayer spacing (d_{002}), not clearly observed for the GR4 materials reacted in molten LiOH.

Generally, higher mesopore volumes and wider pore size distributions are observed in those CFs that suffered a higher B-O. Thus, the textural analysis results of the evaluated CFs once again show the effect of the initial materials' properties on their reactivity in molten LiOH, in accordance with their different commercial preparation procedures and thermal treatment history. Thus, a high carbon purity, followed by an improved graphitic organisation should be preferred for greater chemical stability of the CF in contact with molten LiOH.

It is difficult to make an in-depth comparison between the results presented and those obtained by different authors, because of the different variables used, such as carbon precursor and experimental conditions. But in general, when we compare our results with those reported in the literature, the chemical reactivity of various carbon-based materials with LiOH always give significant carbon loss, but with a low gain in carbon surface area and pore volume (Mora et al. 2006; Sutcu and Dural 2006; Aweed 2008; Tamarkina et al. 2008; Mikova, Chesnokov, and Kuznetsov 2009; Leimkuehler 2010; Tamarkina et al. 2012; Chowdhury et al. 2013; Cabasso and Yuan 2013; Чесноков et al. 2014; Girón et al. 2015; Kucherenko et al. 2017; Krstić 2018; Erdogan 2019). Most of the results of the referenced studies also confirm the strong chemical reactivity of LiOH with the examined carbons, relative to KOH and NaOH, although the latter two hydroxides were far more efficient for developing porosity and surface area. Hence, performing chemical reactions at equal conditions and elevated temperatures, LiOH is found to react with a significantly larger fraction of C, more than 50% higher with respect to both KOH and NaOH (at identical alkali hydroxide to carbon ratio) (Mora et al. 2006; Hung, Anoshkin, and

Rakov 2007; Girón et al. 2015). Also in the bibliography, identical reaction mechanisms (as reaction (2) described in subsection III/3.4) were estimated between the carbon functional groups and MOH (where M stands for Li, Na, or K). The main chemical reaction consists of initial oxidation of easily accessible carbon atoms, by the metals in MOH, and their removal from the carbon matrix as an inorganic compound (e.g. carbonate). Under specific experimental conditions, the formed alkali metal cation resulting from the hydroxide reduction is intercalated between the carbon layers. This process may play some role in the overall reactivity process, influencing the increase of the carbon microporosity by destroying its graphitic organisation (Linares-Solano et al. 2007). Therefore, it was found that the specific surface area and the pore volume strongly depended on the subsequent reaction between the alkali metal cation and the graphitic structure of the carbons (Maciá-Agulló et al. 2007). This has already been confirmed by performing reactions of identical carbon materials with KOH, NaOH and LiOH, where the development of the specific surface area was found in the order of 16: 10: 1, respectively (Tamarkina et al. 2008). These intercalation process differences were related to the difference in the boiling point of the alkali metals (758°C, 883°C, and 1347°C for K, Na, and Li, respectively), delaying or preventing the intercalation of the latter cations depending on the experimental conditions (Mora et al. 2006; Schiemann et al. 2016). In addition, in several other studies, it was confirmed that the microporosity development ability decreased in order of Li < Na < K, with the decrease of the size of the alkali cation and the intercalation activity (Celzard et al. 2007; Mikova, Chesnokov, and Kuznetsov 2009; Zhou et al. 2016).

All this bibliography information agrees with our results of the CF chemical reactivity in molten LiOH and observed carbon weight loss, but with poor development of the surface area and microporosity. The main reason is always indicated as being the strong reaction of the LiOH under the used experimental conditions and the high LiOH/CF ratio. The small size of the alkaline atom should also have promoted high reactivity, allowing easier access to the initial material porosity and further pore widening. This resulted in higher carbon mass loss in the carbonised CFs compared with the graphitised materials. No metallic Li intercalation was observed in any of the examined CF materials, as witnessed from the textural analysis always showing low porosity development. Thus, this can be explained by the fact that Li cannot be converted into metallic vapour (at the investigated temperature range, up to 750°C), then easily diffused, and intercalated between the carbon layers. This is in a good agreement with the similar chemical stability of CFs with different structural order but with high C purity (seen in Fig. III/3-14 a)).

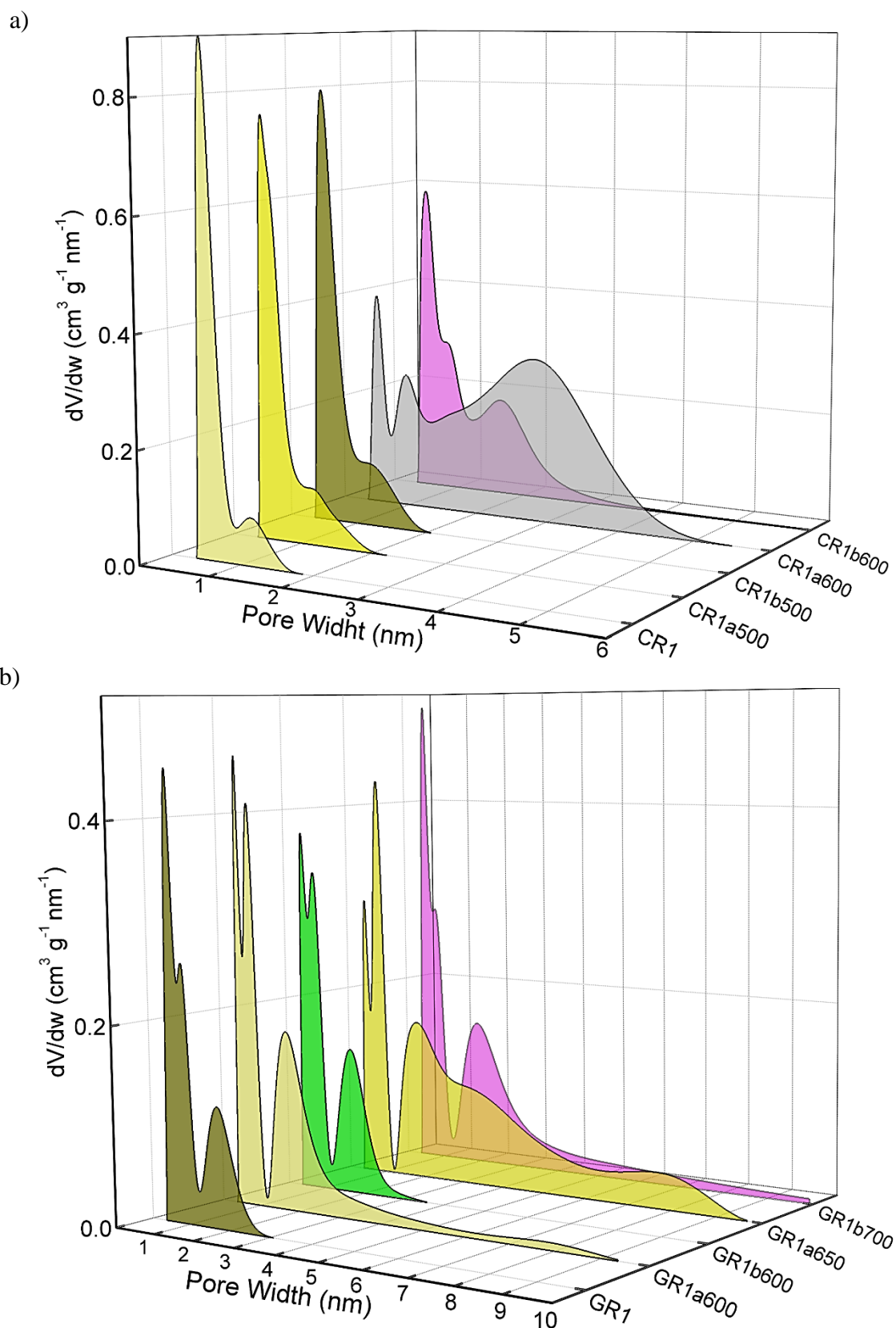


Figure III/3-19 Pore size distribution, based on 2D NLDFT-HS fitting of both N_2 and CO_2 isotherms measured for the carbonised a) CR1 and graphitised b) GR1 corresponding CFs and their chemically reacted derivatives in the presence of LiOH or $\text{Li}_4(\text{OH})_3\text{Br}$ at different final temperatures.

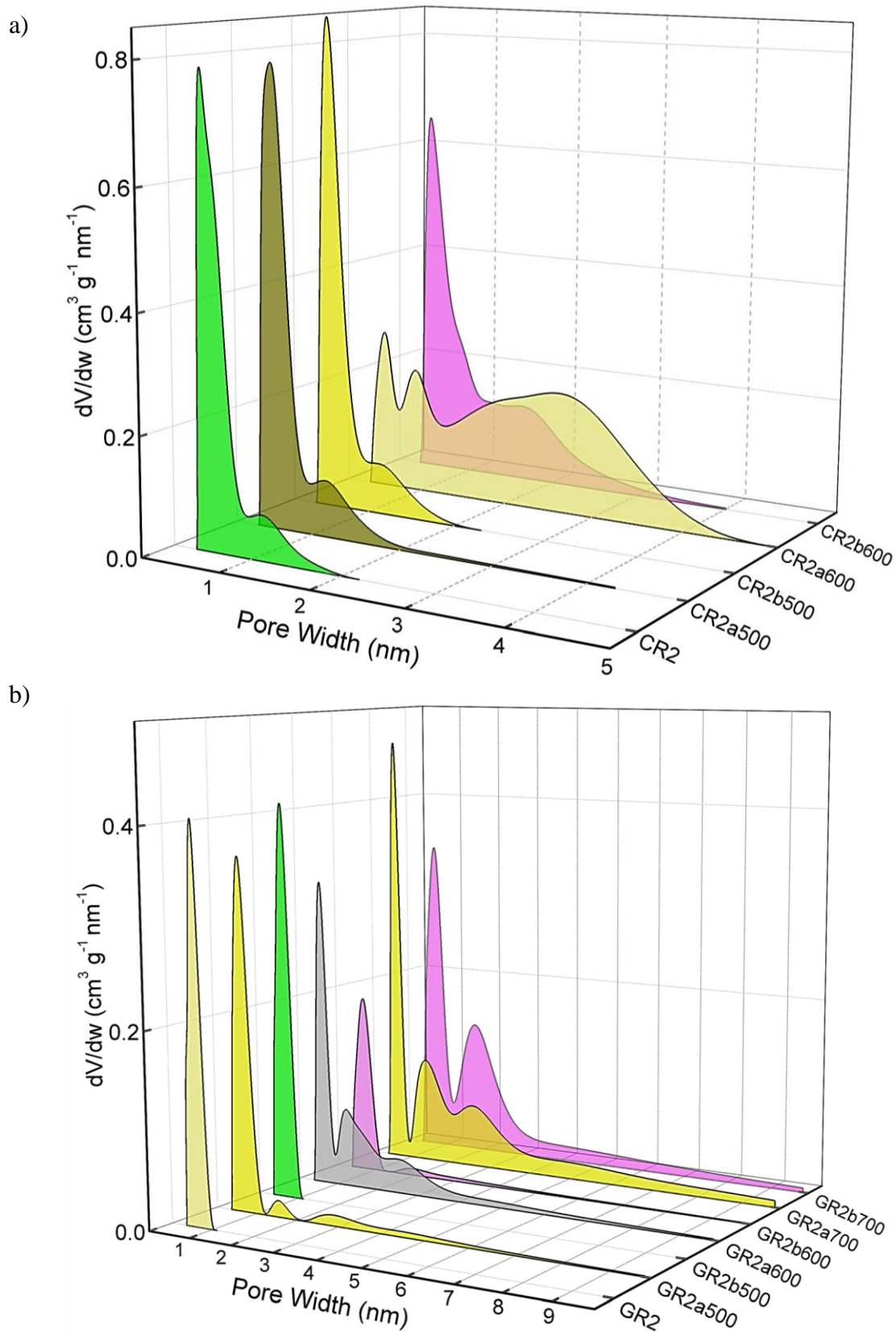


Figure III/3-20 Same as Figure III/3-19 but for a) CR2) and graphitised b) GR2 corresponding CFs.

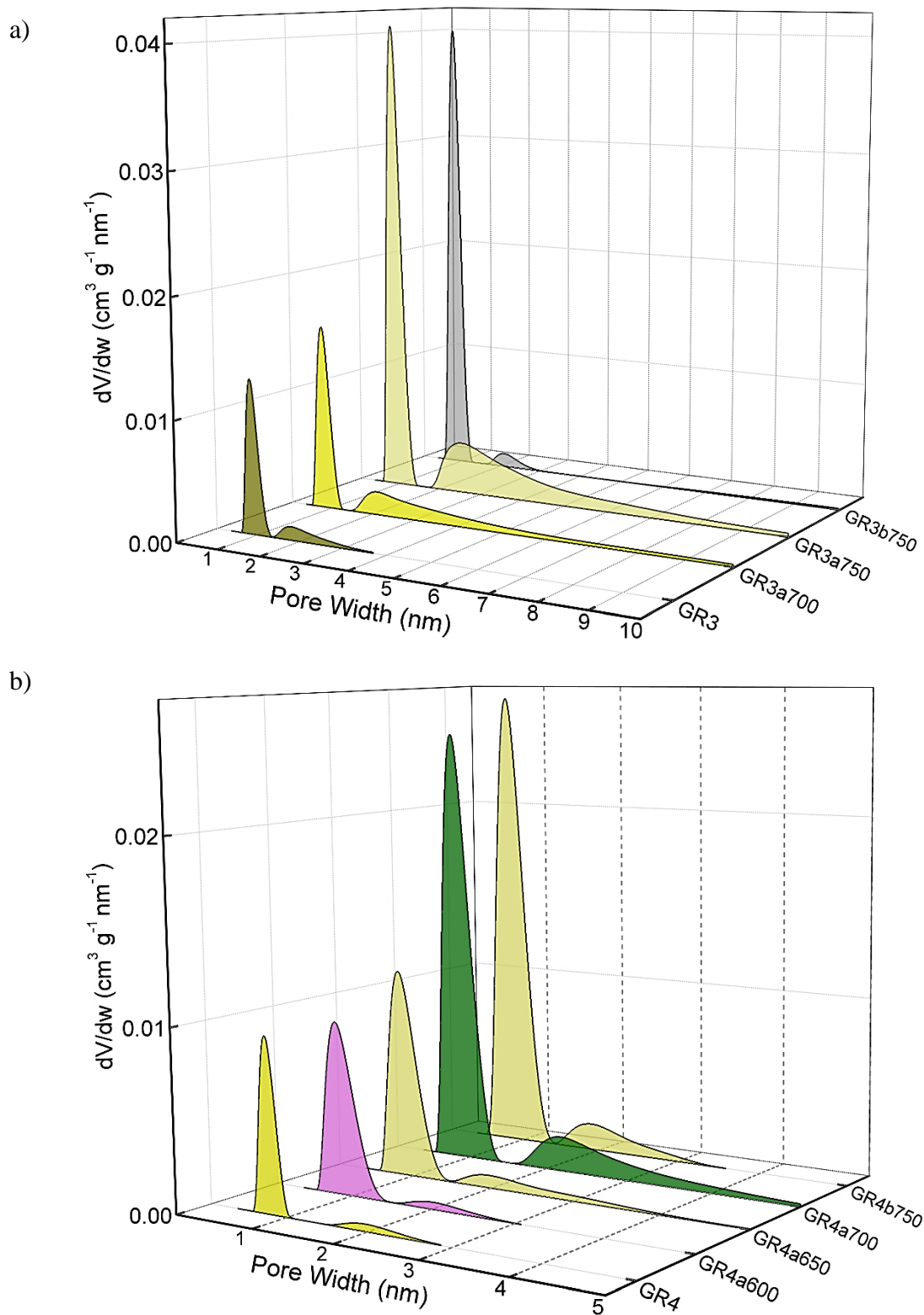


Figure III/3-21 Same as Figure III/3-19 but for the graphitised a) GR3 and b) GR4 CFs.

SEM micrographs of carbon fibre morphology of the *de-sized* CF before and after reaction in molten LiOH (middle column micrographs) are shown in Figure III/3-22 for ex-Rayon and Figure III/3-23 for ex-PAN materials. The surface and cross-section morphology of the *de-sized* carbon fibres before reaction varies depending on precursor and manufacturing technology, as the commercial materials are coming from different suppliers. This was discussed in detail and presented in Chapter II (subsection II/2.3.a) where we defined CF materials of different diameters, cross-sections and carbon fibre surfaces. Therefore, further investigations were conducted to determine whether the carbon fibre structure was uniformly activated during surface contact with LiOH or in a defined pattern, due to the various characteristics of the different CFs.

The only constant observations of the carbon fibres were seen in the form of grooves and striations parallel to the ex-Rayon or ex-PAN fibre axis, observed as results of the manufacturing process of the fibres' precursor. The microscopic impurities visible on most of the carbon fibre surfaces are probably sub-products of de-sizing, as discussed in Chapter II. The ex-Rayon CF presented some pores between the constituting fibrils (as seen for GR1 in Fig. III/3-22), clearly observed from the cross-section of the carbon fibres. Whereas the ex-PAN CF presented evident absence of these pores in both the surface of the fibres or in the cross-section.

Most of the carbon fibres constituting the CFs retain their original overall structure. However, some of them have been destroyed due to a severe chemical reaction with LiOH (as GR1a700 in Fig. III/3-22), in good agreement with the B-O results at high temperatures. From the carbonised ex-Rayon CFs we clearly observed that the prolonged chemical reaction with LiOH deepened the initial grooves and created new cracks, clearly initiating the longitudinal division of the carbon fibres (as seen from the carbonised CR1a600 in Fig. III/3-22). The same is not clearly observed in the other carbonised CR2a600 and CR3a600, when they were reacted at the same temperature but fibres' destruction occurred after the increase in the test temperature (as seen from CR3a650 in Fig. III/6-3). This confirms the use of different materials and methods of fabricating the ex-Rayon carbon fibres and their influence on the structure of the final material, even when produced with similar final heat treatment temperatures (Dumanli and Windle 2012). The influence of the materials' manufacturing history was further seen when comparing the graphitised ex-Rayon CFs. While GR1a700 was almost completely oxidised in the reaction with LiOH and only particles of undefined shape were observed as carbon fibres remnants, GR2a700 maintained the morphology of the initial carbon fibres. However, the chemical activation of the latter in molten LiOH resulted in a skin-core morphology of carbon

fibres, suggesting a core made of significantly less graphitised material. This SEM microscopy information confirms the XRD results suggesting the partly-graphitised fibre structure, splitting the (002) reflection (seen in Fig. III/3-2 a)). However, the results of the Raman spectroscopy did not confirm the "sheath" and "core" effect in *de-sized* GR2 because the local analysis of carbon fibres cross-section gave rise to the same spectrum as that of the skin. As suggested by (Kong et al. 2012; Al Aiti et al. 2018), this partly-graphitised structure is observed from the use of non-stabilised or low-quality stabilised precursor fibres that influence different diffusion rate of the oxygen from the shell or the core in the subsequent thermal treatment processes. If this applies, it follows that the low chemical stability in LiOH of commercial GR1 and GR2 CFs is the result of their manufacturing differences originating from non- or partially-stabilised Rayon fibres, respectively. By further analysing CFs with improved structural properties, even after activation at the highest tested temperature, only pores emerge on the initial surface and apparent cross-section of the tested GR3a750 and GR4a750, caused by etching of amorphous carbon sections. The inner core segment remains unaffected in the reacted carbon fibres, confirming once again the higher carbon purity and structural order of the fibres, greatly improved in the GR4a750 (see in Fig. III/3-22). The larger pits observed in the GR3a750 relative to GR4a750 can be attributed to more amorphous domains, perceived as a memory effect influenced by less homogeneous cellulosic fibres. Therefore, ex-Rayon carbon fibres with less amorphous domains should always be preferred when high CF chemical stability is required in molten LiOH.

Regarding ex-PAN CFs, no swelling and longitudinal peeling of the carbon fibres was observed, as previously seen for stabilised PAN fibres when chemically activated with KOH at a much lower ratio and reaction time (Lee et al. 2004). When similar stabilised carbon fibres were chemically reacted in NaOH the bloating effect was not observed due to the absence of Na gasification and further reaction with the carbon fibre structure. Thus, only surface etching and smoothening were evidenced (Moon et al. 2006). This clearly indicates that by using different alkali hydroxides, different changes in fibre morphology are observed due to the dissimilarities in chemical reactivity, in good correlation with the variations presented in the adsorption analysis. As presented by (Maciá-Agulló et al. 2007), it was also observed that subsequent carbonisation and graphitisation treatments had an influence on the structural improvement of the ex-PAN carbon fibres, which controlled the morphological deformations during chemical activated in KOH or NaOH. Again, a clear effect of the chemical reactivity in molten LiOH was observed at the highest investigated temperature, since the investigated

carbonised ex-PAN CFs (CP5a750 and CP7a750) experienced surface smoothing and shrinkage of the carbon fibre diameter on an average of 2 μm (seen in Fig. III/3-23). The external carbon fibre surface of the graphitised ex-PAN carbon fibres showed modified grooves and striations, elongated parallel to the fibre axis direction following that observed in the initial materials. Thus, submicron pits were uniformly distributed during the chemical activation of the investigated materials (seen in Fig. III/6-4). Again, an overall decrease in the fibre diameter of 0.5 μm was observed, yet much lower in comparison with the carbonised CFs (as comparing the corresponding CP8a650 and GP8a650). The additional increase of test temperature produced larger surface pits and a greater decrease in fibre diameter, observed due to the increased chemical reaction kinetics.

The chemical stability of the investigated CF, regardless of their originating precursor (ex-Rayon or ex-PAN), is directly related to the stability and persistence of the achieved graphitic structure. Again, from the SEM analysis, this is clearly seen when comparing CFs of similar graphitic nanocrystallites size (L_c) and interlayer spacing distance (d_{002}), thus similar carbon purity. Both GR4a750 and GF8a750 show only slight surface modifications after the chemical reaction in molten LiOH, without damaging the overall structure of the constituent carbon fibres.

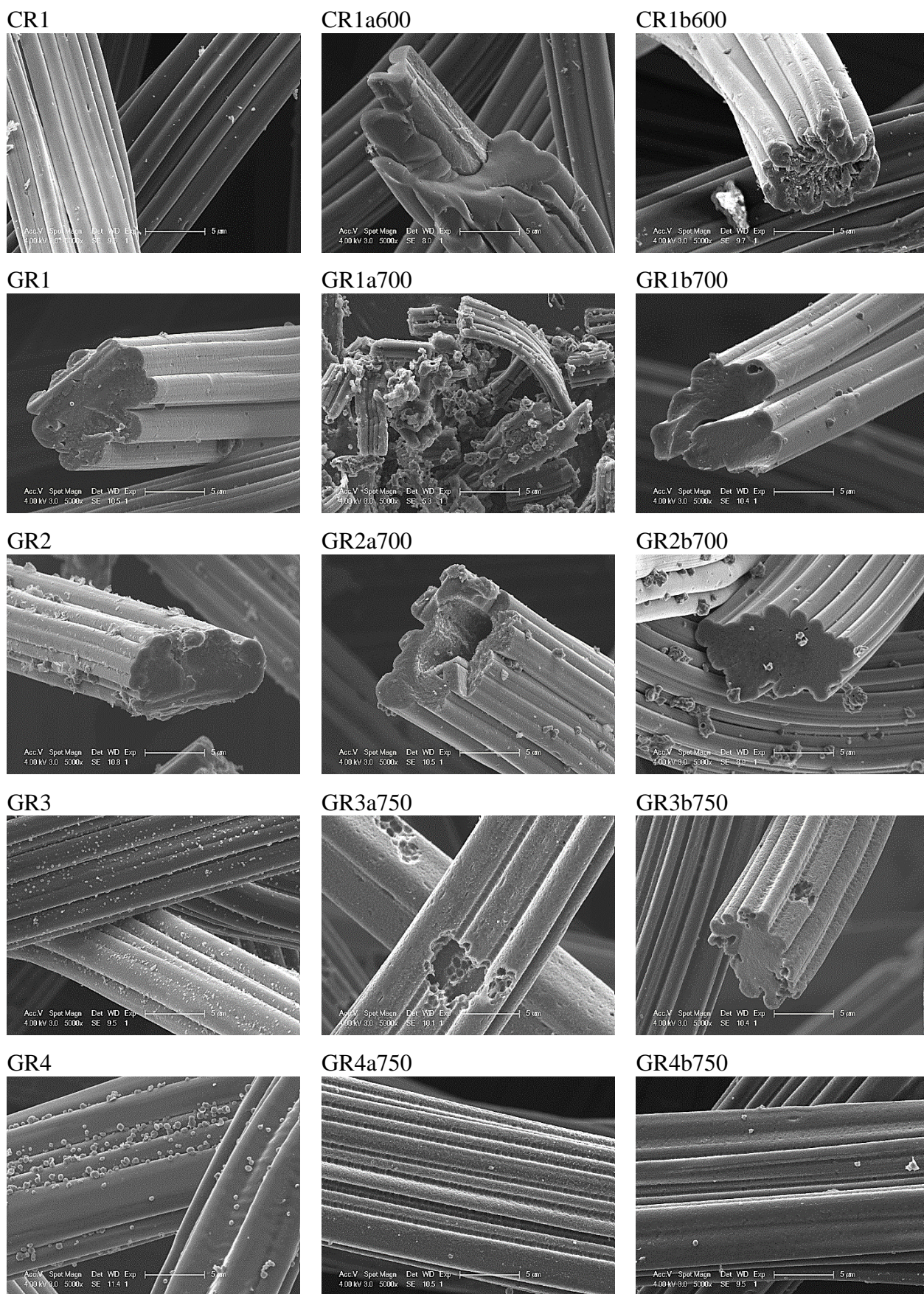


Figure III/3-22 SEM micrograph of *de-sized* ex-Rayon CFs before (left) and after reaction with LiOH (middle) and $\text{Li}_4(\text{OH})_3\text{Br}$ (right) at the highest performed temperature.

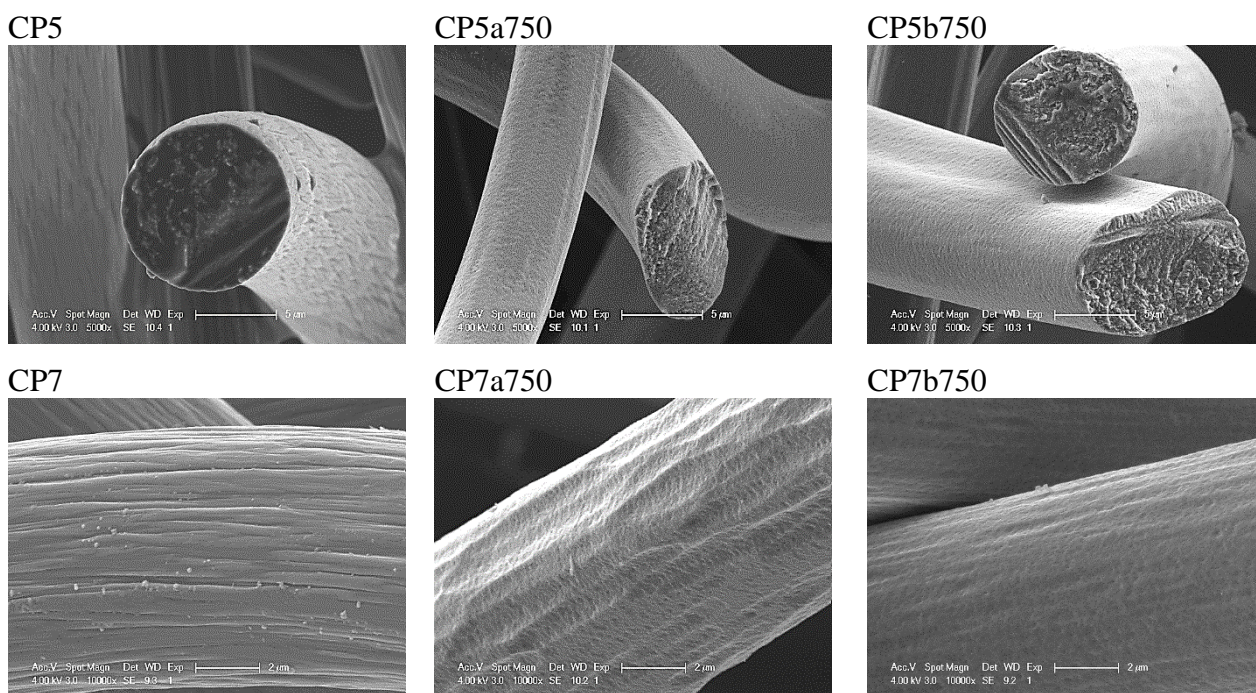


Figure III/3-23 Same as Figure III/3-21 but for ex-PAN CFs.

III/3.6 CF chemical stability in LiBr or $\text{Li}_4(\text{OH})_3\text{Br}$

The study of the CF chemical stability in molten LiBr or $\text{Li}_4(\text{OH})_3\text{Br}$ was next carried out in the same manner as for LiOH (by means of the same experimental method, explained in Subsection III/2.1). It should be emphasised that the experimental reactivity and porosity results are highly reproducible, which makes it possible to compare the samples of CF tested in molten LiOH and $\text{Li}_4(\text{OH})_3\text{Br}$.

This section reveals that the nature of the inorganic LiOH and LiBr, or their peritectic compound, plays an important role on the chemical reactivity of CF. Thus, in all examined samples, a higher chemical reactivity was observed in molten LiOH with respect to $\text{Li}_4(\text{OH})_3\text{Br}$ (seen from the corresponding carbonised and graphitised CF in Fig. III/3-24). Chemical reactivity in molten $\text{Li}_4(\text{OH})_3\text{Br}$ produced B-O values 50% lower, or even less, than those obtained with LiOH in all tested CFs. As previously observed for LiOH, it is again found that the chemical reactivity in molten $\text{Li}_4(\text{OH})_3\text{Br}$ is higher for ex-Rayon than for ex-PAN CFs at similar thermal manufacturing history. Once more, the major properties that regulate the CF chemical stability in molten PC ($\text{Li}_4(\text{OH})_3\text{Br}$) are shown to be the carbon purity and structural (graphitic) order, in the same manner as for LiOH.

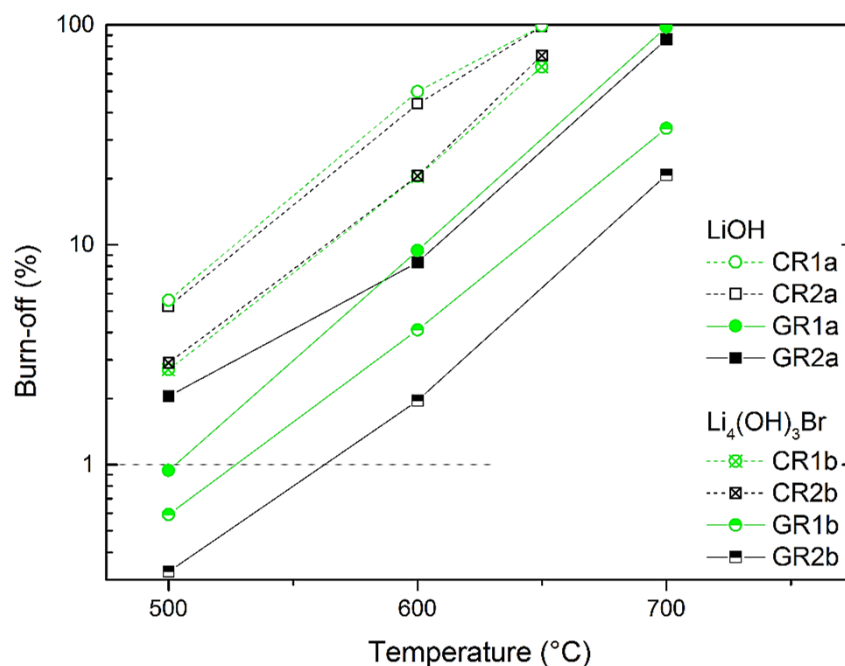


Figure III/3-24 Burn-off (%) vs. reaction temperature of ex-Rayon CF; empty and full symbols present CFs reacted in LiOH and crossed or half-full symbols present CFs reacted in $\text{Li}_4(\text{OH})_3\text{Br}$; the dashed or solid lines are only guides for the eye.

In addition, to study the chemical reactivity role of the second PC component, tests were performed in molten LiBr only for the two CFs (carbonised CR1 and CR2) found to be the most reactive with LiOH. The chemical reactivity tests were performed at the highest tested temperature (750°C), all other conditions remaining the same. By repeating the same experiment twice, no significant difference in weight before and after the performed treatment was observed. Thus, LiBr alone did not affect the structure of the materials and its chemical reactivity with the CF can thus be considered as negligible. The CF chemical inertness in molten LiBr can be explained by the very high melting temperature of LiBr (about 552°C). The poor reactivity of LiBr-KBr eutectic salts with carbons (or their initial precursors) was previously utilised for producing 3D carbon frameworks from biosourced materials under similar thermal treatment conditions as those described herein (Vilian et al. 2018). These results indicate that undesirable chemical reactivity could only occur due to reactions between the carbon fibres and the metal hydroxides. The chemical reaction should start even at a lower temperature, compared to the LiOH alone, since the melting of $\text{Li}_4(\text{OH})_3\text{Br}$ begins with the formation of the peritectic phase (EC) (at around 304°C). The reaction should be further enhanced when the residual solid LiOH is molten at a higher temperature (at around 380°C) in the stoichiometric ratio with LiBr, as shown in the theoretical phase diagram in Figure III/3-26 a).

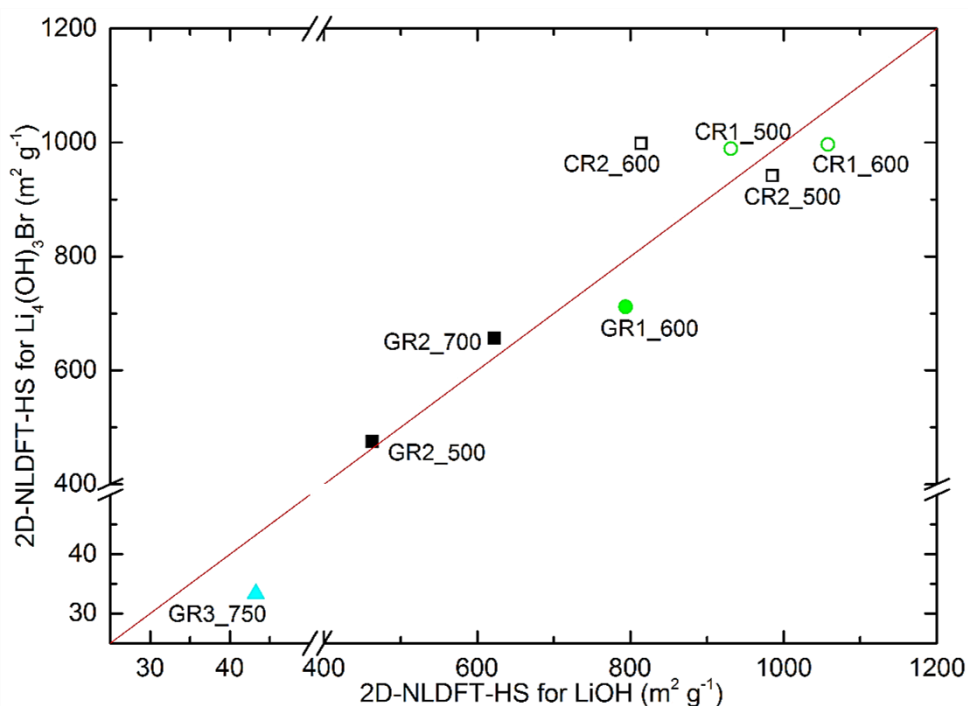


Figure III/3-25 Relationship between the 2D NLDFT-HS surface area of CFs reacted in molten LiOH and in molten Li₄(OH)₃Br; the low dash (“_”) indicates empty space which should be replaced by a for LiOH and b for Li₄(OH)₃Br chemical reaction test.

The textural properties of the CFs also show lower structural modifications with Li₄(OH)₃Br, compared to LiOH. The results presented in figure III/3-25 highlight the reactivity of the CFs with either LiOH or Li₄(OH)₃Br that develop a similar or different surface area when tested at an identical temperature. The symbols on the straight line, added as a guide for the eye, correspond to identical specific surface area results whereas the symbols placed above indicate a higher surface area development from Li₄(OH)₃Br. Symbols below the line mean the same but for LiOH. The results suggest higher surface area development with LiOH. Exceptions are observed for the materials whose microporosity decreased so much during LiOH activation (CR1_500, CR2_600, GR2_500, and GR2_700) that Li₄(OH)₃Br produced higher surface areas. In addition, as in the tests with LiOH, the surface area of CFs tested in molten Li₄(OH)₃Br tends to increase with the final test temperature and is again highly dependent on the CF structural properties. Although the surface area of the examined CF increased, it usually derives from different micro/meso pore volume distribution (seen from Fig. III/3-16 to III/3-18). Therefore, when CFs are activated with Li₄(OH)₃Br, the texture remains essentially microporous, while those of materials activated with LiOH are much more mesoporous. This is clearly seen from samples CR1 and CR2 tested at 600°C. Thus, the strong reaction in molten LiOH destroys most micropores, fusing them with the developed high mesoporosity, which is

observed in molten $\text{Li}_4(\text{OH})_3\text{Br}$ to a much lower extent (seen in Fig. III/3-17 a)). When tests are carried out on CFs with higher carbon purity and structural order (GR3 and GR4), the porosity is less modified in $\text{Li}_4(\text{OH})_3\text{Br}$ with respect to LiOH (seen in Fig. III/3-18 a) and b)). The pore size distribution is more modified for materials tested in molten LiOH compared to that in $\text{Li}_4(\text{OH})_3\text{Br}$ (summarised from Fig. III/3-19 to III/3-21). The results with $\text{Li}_4(\text{OH})_3\text{Br}$ also suggest that only widening the initial micropores seems to occur at lower test temperatures, but the development of larger mesopores is moderate. The development of mesopores from the chemical reaction in molten $\text{Li}_4(\text{OH})_3\text{Br}$ is clearly observed at 600°C , for carbonised CFs, or at a higher temperature for graphitised CFs.

The SEM micrographs of the tested CFs reveal that the carbon fibre modifications strongly depend largely on the presence and nature of the inorganic salt. Thus, all ex-Rayon CFs tested in molten $\text{Li}_4(\text{OH})_3\text{Br}$ retain the initial fibre structure and only surface etching and pitting are observed, compared to the severe destruction of the fibres during reaction with LiOH (seen in Fig. III/3-22). Uniform, smooth and flat surface carbon fibres without the initial surface striations were observed after reaction of the carbonised ex-PAN CFs in molten $\text{Li}_4(\text{OH})_3\text{Br}$ (seen in Fig. III/3-23). Again, the observed lower B-O values suggest a lower decrease of the fibre diameter, $1\ \mu\text{m}$ on average, compared to the decrease seen in LiOH .

In general, the chemical reactions of CFs in the investigated binary PC should be considered similar to those in LiOH , but the presence of the LiBr phase only inhibits the severity of the redox reactions with the hydroxide. The reaction of the hydroxide with the active carbon sites should be inhibited only due to the physical presence of LiBr since no chemical reaction is observed between the latter and the carbon. The present LiBr phase does not completely prevent the reactions but delays them differently depending on the tested CF structural properties. This is clearly evident when comparing identical pore size distribution modification of a CF tested in LiOH , at a lower temperature, and that tested in $\text{Li}_4(\text{OH})_3\text{Br}$, at a temperature 50 to 100°C higher (seen from Fig. III/3-19 to III/3-21). LiOH consumption during the reaction with the CF shifts the molar ratio of lithium salts in the binary system from the stoichiometric composition (pure $\text{Li}_4(\text{OH})_3\text{Br}$ phase, presented by the blue dashed line in Fig. III/3-26 a)) to a higher concentration of LiBr phase. The continuous change of ratio should introduce variations of the viscosity of the binary system and enrichment in the LiBr phase, eventually leading to its separation at the nanoscale. The LiBr phase might, therefore, be trapped in the microporosity after the complete consumption of the LiOH phase, and subsequent reactions cause only widening of the mesoporosity in the materials tested in $\text{Li}_4(\text{OH})_3\text{Br}$.

Depending on the chemical stability of the CF in the LiOH phase within the PC, the relevant stoichiometric ratio for the TES application (i.e., $\text{Li}_4(\text{OH})_3\text{Br}$) can be modified to a different degree, thus threatening the high initial energy density (seen in Fig. III/3-26 b)). Therefore, the choice of the most inert CF should inhibit the chemical reaction in molten LiOH at the application temperature, thus ensuring one of the major advantages of using unaltered $\text{Li}_4(\text{OH})_3\text{Br}$ in its composition: its high energy storage potential.

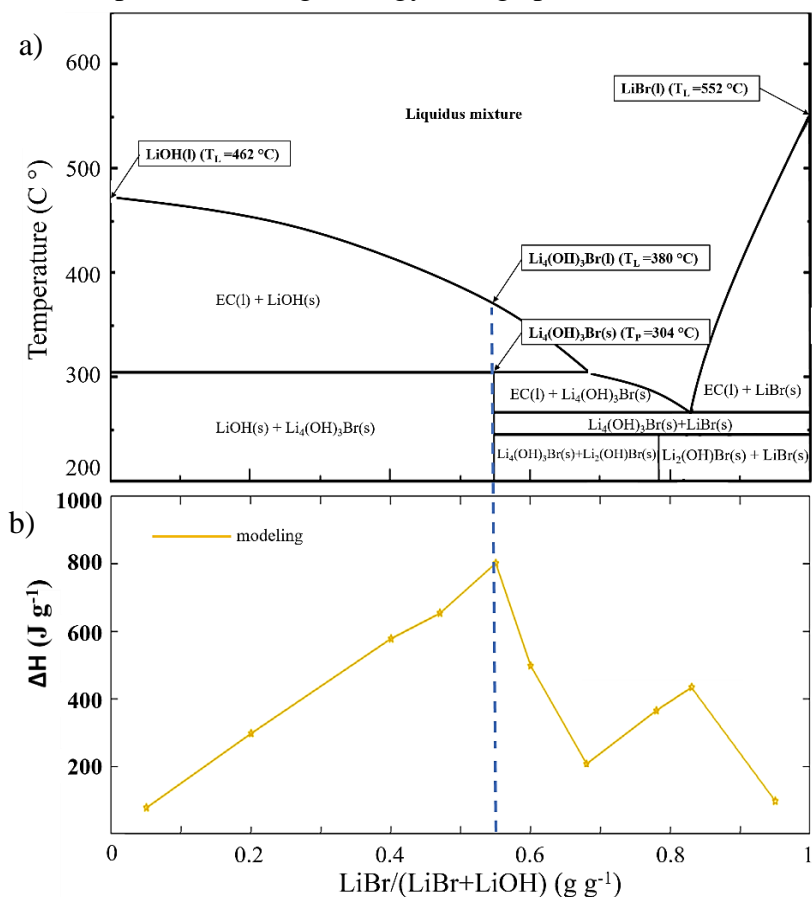


Figure III/3-26 a) Theoretical phase diagram of a PC ($\text{Li}_4(\text{OH})_3\text{Br}$) binary system, with the corresponding peritectic transition (T_P) and liquid temperatures (T_L); b) Gravimetric energy density dependence of the $\text{LiBr}/(\text{LiBr} + \text{LiOH})$ ratio as seen from the calculated (yellow) line (after Achchaq et al. 2019).

Our study of chemically stable CFs shows the beneficial reduction of the chemical reactivity of the LiOH phase in the PC when compared to the LiOH alone. The reduction of the chemical reactivity results in decreased modification of the initial CF pore texture. On the contrary, other authors present the use of various binary systems of different inorganic salts, due to their pore-forming abilities in what they called “salt-templated” carbonisation. Some of the authors suggest the use of reactive/inert phase binary systems that play a dual role: pore-formation (through carbon activation) and pore-template (physical presence), producing well-developed micro/mesoporous carbons (Silvestre-Albero et al. 2015; Pampel and Fellingner

2016). Other binary systems have been only used because of their complete inertness and homogeneous distribution in the organic precursors and resulting in porous carbons (Liu and Antonietti 2014; Vilian et al. 2018). Thus, the only reason for using a binary system, instead of a single salt, is the lower melting temperature of the binary system compared to the higher melting temperatures of the separate phases, found critical for the development of highly porous carbons.

III/3.7 Estimation of CF chemical stability at the application temperature

A detailed study was performed for estimating the activation energy of the reactions occurring with CFs in molten LiOH. The main idea of this part is to obtain more information about the recovered B-O results and use them for estimating materials' B-O at the application temperature (between 300 and 400°C). Therefore, it is expected that the apparent activation energy changes depending on the materials' properties and chemical reaction/reactions that occur in the fixed experimental tests. As discussed in subsection III/3.4, a dominant chemical reaction (2) was expected within the limits of the performed experiments. However, it was evident that for some CFs of low structural order and carbon purity, the carbon/metal hydroxide reaction should be followed by consecutive carbon oxidation reactions in the defined experimental limits. This is recognised by the apparent higher B-O and the dramatic change in the CF textural properties, with clear destruction of the microporosity (clearly seen for CR1 in Fig. III/3-19 a) and CR2 in Fig. III/3-20 a)), both generally seen above 600°C. The occurrence of additional reactions is observed because of the decrease of activation energy of the produced Li_2CO_3 and its further reaction with the unreacted carbon (Sutcu and Dural 2006). However, for all studied CFs (under fixed test parameters and only change of the investigated material), an exponential rise of the B-O is evident by performing the experiment at a higher final temperature. These results clearly show that the kinetics of the occurring chemical reactions depend on the temperature, which makes it possible for the use of Arrhenius' law for estimating the apparent activation energy. The Arrhenius equation reads:

$$k = Ae^{-E_a/RT} \quad (\text{III/3})$$

where k is the reaction rate, T is the absolute temperature, A is a preexponential factor, E_a is the apparent activation energy of the reaction, and R is the universal gas constant ($8.314 \text{ J mol}^{-1} \text{ K}^{-1}$). As in other carbons' oxidation reaction studies (Kissinger 1957), in which the reaction rate constant was simply calculated as the inverse of the test temperature, we implicitly assume that

first-order kinetics applies for most of the chemical reactivity process. Although it is expected that the present oxidation-reduction reactions take place through an elementary mechanism, yet from the obtained results, a combination of several cannot be discarded. But from previous studies of carbon reactions with oxygen or other catalytic agents (McKee and Chatterji 1975; Ana Cuesta, Martinez-Alonso, and Tascon 1993), it has been shown that the preexponential factor and the apparent activation energy change in the same way, even when more than one reaction is occurring. This gives the possibility of using the Arrhenius law to obtain a consistent set of comparative values when considering different carbon materials. Therefore, the Arrhenius law is used to calculate the corresponding activation energy, thus determining the B-O of the CF adjusted to a different temperature, by perfectly applying the linearised form of equation (III/3), as follows:

$$\ln(k) = \frac{-Ea}{R} \left(\frac{1}{T} \right) + \ln(A) \quad (\text{III/4})$$

Applying equation (III/4) led to different expressions with a high coefficient (R^2) higher than 0.919 (seen in Fig. III/3-27). It is found that the apparent activation energy is in the range from 116 to 165 kJ mol^{-1} , from carbonised (empty symbols) to graphitised (solid symbols) CFs, respectively.

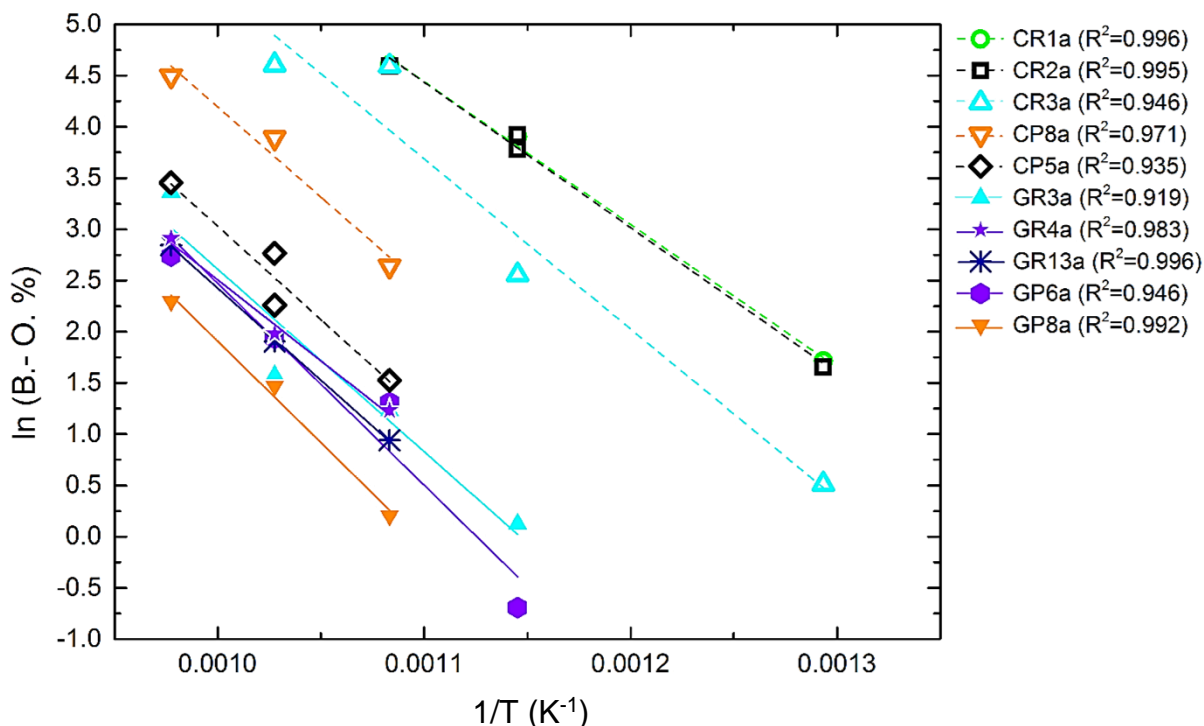


Figure III/3-27 Application of equation (III/4) to the experimentally derived B-O data of most CFs presented in Fig. III/3-13; carbonised or graphitised CFs are presented with empty/solid symbols and dashed/solid linear fits, respectively.

The carbonised CFs, manufactured at temperatures below 1200°C, with a highly disordered structure, high porosity (surface area) and active surface (such as surface heteroatom groups), were more reactive and more prone to oxidation even at lower temperatures. For thermodynamic reasons, the existence of active carbon surface induces a higher number of reaction centres, which decreases the activation energy of the chemical reaction (Cuesta, Martinez-Alonso, and Tascon 1993). The relationship between all the CF characteristics that control the chemical reaction justifies why different slopes were found from the experimental results' fittings. Therefore, the apparent activation energy is lower for the carbonised CFs than for the graphitised CFs, with an improved structure and a lower amount of superficial defects and heteroatom content. Thus, separately for each of the investigated materials, it is found that the estimation of single activation energy values corresponds to the differences of CF structure. This is observed when the activation energy values are plotted as a function of the interlayer spacing distance (d_{002}) or the materials elemental composition (seen in Fig. III/3-28 a) and b), respectively). The results follow a consistent order, with a minor scattering of the observed trends due to possible experimental or following calculation deviations.

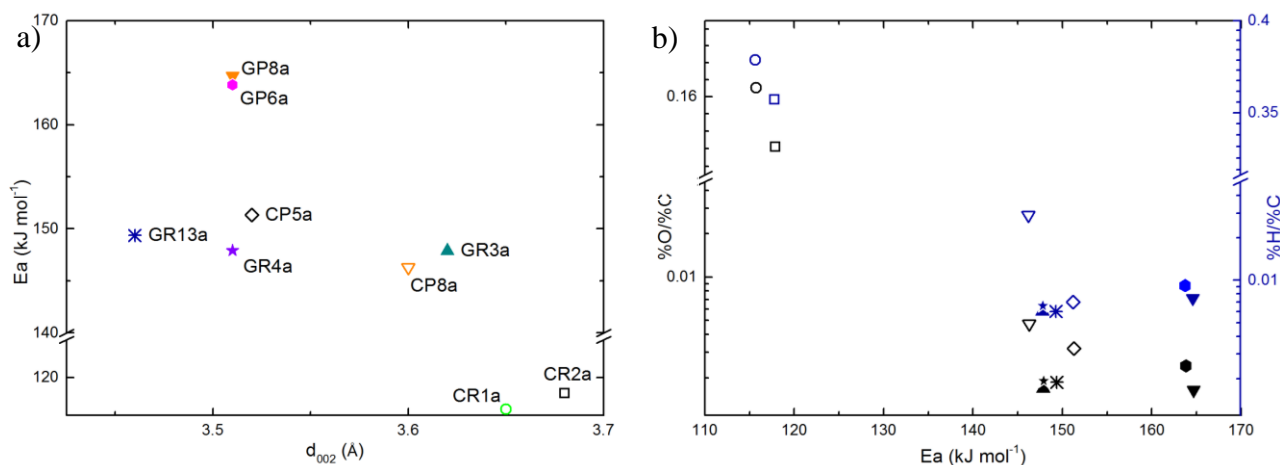


Figure III/3-28 Correlation trends between the estimated apparent activation energy and CF structural properties, as a function of a) interlayer spacing distance (d_{002}) or b) materials elemental composition.

Furthermore, based on the performed bibliographic research, no activation energy values are reported for similar carbon materials tested under the current test conditions and in molten LiOH. However, the estimated apparent activation energy values are in good agreement with others for carbon gasification in the presence of Li salts (such as Li_2CO_3 and LiOH) under inert atmosphere or in the presence of oxygen, carbon monoxide/dioxide, or in steam (McKee and Chatterji 1975, 1978; Kapteijn, Abbel, and Moulijn 1984; Sheth, Agrawal, and Yeboah

1998). In addition, Cuesta et al. (1993) observed that ex-PAN high-purity carbon fibres thermochemically react with oxygen at similar apparent activation energy values, in the range of 117 to 134 kJ mol⁻¹. The slightly inferior activation energy of the high-purity carbon fibres, compared to the current results, was evident since it is known that the reaction of oxygen with carbon is quite exothermic, decreasing the activation energy, in comparison with CO₂, steam or other chemical activation agents (Sevilla and Mokaya 2014). Once again, in all the investigated studies, it was considered that the structural characteristics of the investigated carbons play an important role in the chemical reactivity tendencies. Therefore, the calculated parameters related to the chemical reactions that occur in the CF stability tests seem to correlate well with the bibliography. Hence, the subsequent use of the derived experimental results is considered valid for estimating the rate of B-O, due to undesirable chemical reaction between the CF host and the LiOH at the application temperature.

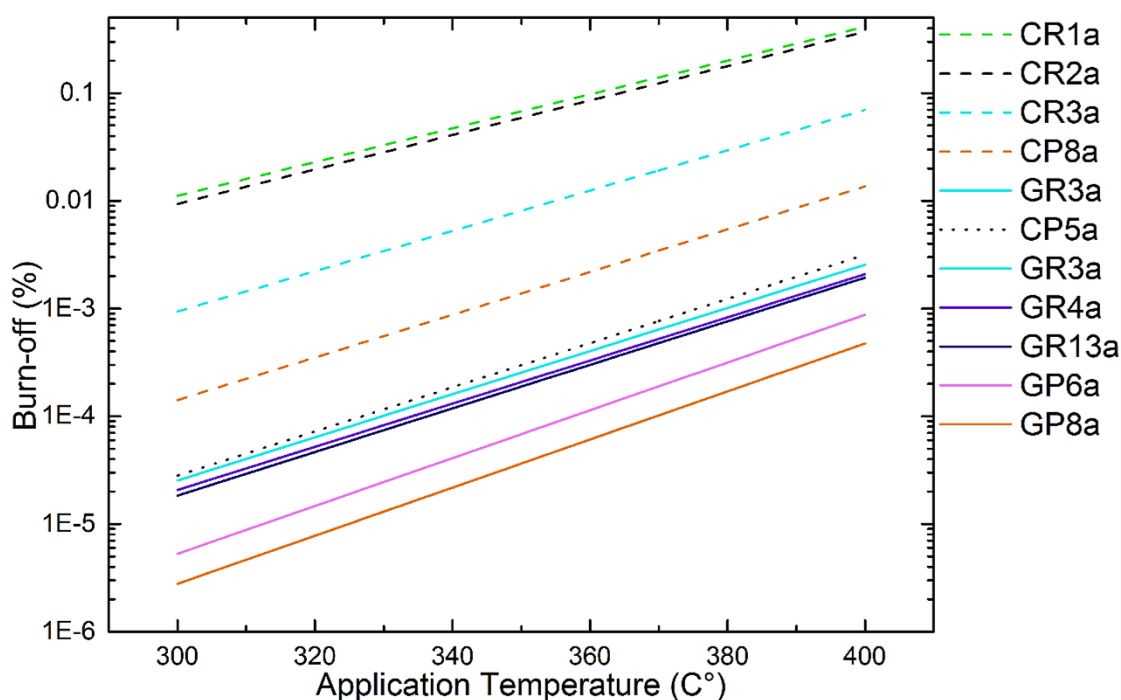


Figure III/3-29 Estimated B-O values from the derived Arrhenius law expressions, for different CFs, in the application temperatures of interest; carbonised or graphitised CFs are presented with dashed (ex-Rayon) / dotted (ex-PAN) or solid trend lines, respectively.

The set of analysed CFs is significantly diversified so that materials of different structures can allow meaningful reactivity estimates at the application temperature (seen in Fig. III/3-29). The estimated B-O values are in agreement with the experimental results, distinguishing the graphitised CFs, with improved purity and structure, from the rest. In addition, we must consider that these estimates are made on the basis of the results of B-O only

with LiOH and that a larger decrease is expected with the PC ($\text{Li}_4(\text{OH})_3\text{Br}$), as discussed in subsection III/3.6 and seen from the estimated B-O of the corresponding carbonised and graphitised ex-Rayon CFs (presented in Fig. III/3-30). Therefore, for the thermal cycling tests on the CF-PC hybrid materials, only the most chemically stable candidates should be considered.

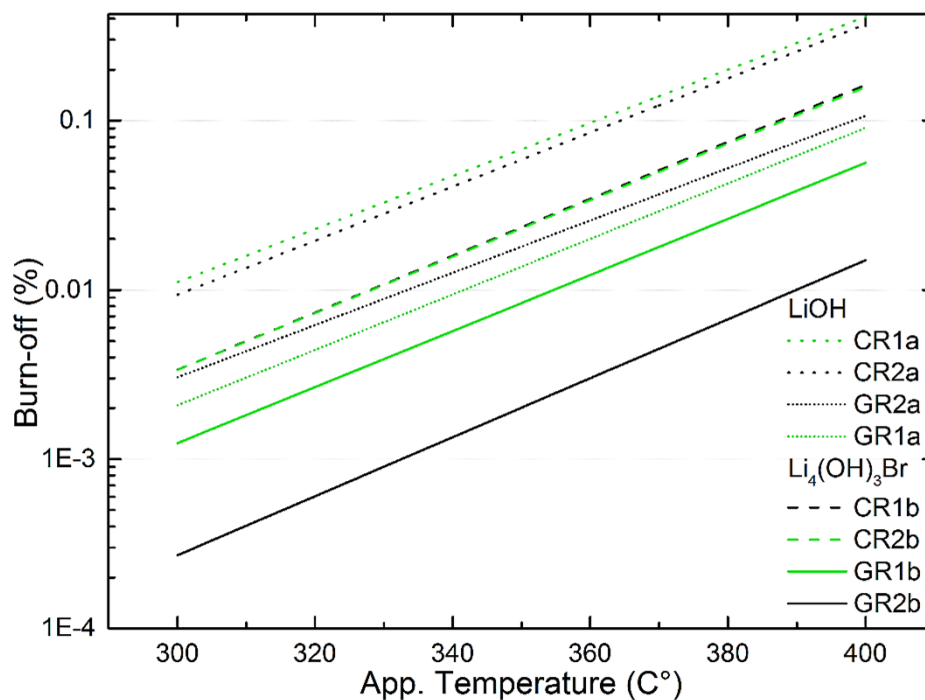


Figure III/3-30 Estimated B-O values from the derived Arrhenius law expressions at the application temperatures of interest, for carbonised or graphitised CFs, presented with dotted/short dotted trend lines; tests in LiOH, and dashed/solid trend lines in $\text{Li}_4(\text{OH})_3\text{Br}$, respectively.

III/4 Conclusion

In the present work, structural, morphological, and textural properties of CFs were characterised by different techniques. The use of different characterisation techniques provides information to better understand the commercial CF properties and compare the observed differences as a function of the performed chemical stability test in molten LiOH, LiBr, and $\text{Li}_4(\text{OH})_3\text{Br}$.

The results of elemental analysis present the influence of CF manufacturing history and various organic origins on their final carbon purity. Overall, the C content is high compared to the amounts of O, H, and N, which decreases with the increase of the final heat treatment

temperature of the commercial CF. The XRD results reveal the presence of disordered or partly-graphitising CF from both Rayon and PAN precursors. Generally, the absence of tri-periodic stacking reflections identifies the graphitic nanocrystallites as turbostratic structures. For all examined CFs, the precursors' nature and final manufacturing heat treatment again play a major role on the materials' structural order, and hence on the graphitic nanocrystallite parameters. The structural order increase from the carbonised CFs (final heat treatment under 1600°C) to the graphitised CFs (final heat treatment over 2000°C), yet with discussed exceptions. Raman spectroscopy is also presented as a powerful analysis tool for understanding the structural properties of carbon fibre materials. The present combination of elemental, XRD and Raman spectroscopy analyses is found to be very effective in obtaining accurate elemental/structural information of CF materials.

Further, the experimental results show that the structural differences in combination with the elemental composition variations play a major role in the CF chemical stability in molten LiOH. For both ex-PAN and ex-Rayon materials, as carbon purity and structural order increase, the reactivity of the LiOH is reduced and the CFs become very stable even at the highest temperature tested. The textural analysis results follow a similar trend with the chemical reactivity decrease, going from severely to slightly modified textural properties. The same is confirmed by the SEM analysis which shows that the carbon fibres' morphology is severely destroyed or fully retained for the carbonised or graphitised CFs, respectively.

The tests in molten LiOH confirm the effect of the temperature by increasing the burn-off due to the increase of the chemical reaction rate. Our results are also in good agreement with those reported in the literature, concluding that the chemical reactivity of various carbons with LiOH always give significant carbon loss, but with a low gain in pore structure development. Thus, the main reasons for the significant carbon loss are indicated as being the high LiOH/CF ratio and the strong reaction of the LiOH under the used experimental conditions. The absence of metallic Li intercalation in any of the examined CF materials is witnessed from the textural analysis always showing low porosity development.

The effect of the salts' nature is evaluated with the performance of additional CF chemical stability tests in inorganic LiBr, or the PC ($\text{Li}_4(\text{OH})_3\text{Br}$). The results show the complete CF inertness in molten LiBr and increased stability in molten PC, compared to the higher chemical reactivity in molten LiOH alone. The textural properties of the CF also confirm lower structural modifications with $\text{Li}_4(\text{OH})_3\text{Br}$, compared to LiOH, and the same conclusion is observed from the SEM morphology analysis. Generally, the chemical reactions of CFs in

the PC are considered similar to those in LiOH alone, but the presence of the inert LiBr phase plays a beneficial role in inhibiting the severity of the redox reactions with the hydroxide. Therefore, the choice of the most chemically stable CF should limit the occurrence of chemical reactions with the PC at the application temperature, thus ensuring one of the major advantages of using unaltered $\text{Li}_4(\text{OH})_3\text{Br}$: its high energy storage potential.

In addition, the experimental results of the chemical stability tests are in excellent agreement with the values estimated by the use of Arrhenius law, again distinguishing particular graphitised CFs, with improved purity and structure, from the rest. Finally, the choice of CFs with the desired high chemical stability can be based on the derived study information revealing the range of potential applicants for further thermal cycling tests of the CF-PC hybrid materials.

III/5 Bibliography

- Achchaq, F., Elena Risueño, Imane Mahroug, Philippe Legros, Blagoj Karakashov, E. Palomo del Barrio, A. Celzard, Vanessa Fierro, and Jean Toutain. 2018. "Development of a Carbon Felt/Salt-Based Hybrid Material for Thermal Energy Storage Applications." <https://doi.org/10.17265/1934-8975/2018.07.004>.
- Achchaq, Fouzia, Elena Palomo del Barrio, Eric Lebraud, Stanislav Péchev, and Jean Toutain. 2019. "Development of a New LiBr/LiOH-Based Alloy for Thermal Energy Storage." *Journal of Physics and Chemistry of Solids* 131 (August): 173–79. <https://doi.org/10.1016/j.jpccs.2019.04.001>.
- Al Aiti, Muhannad, Dieter Jehnichen, Dieter Fischer, Harald Brüning, and Gert Heinrich. 2018. "On the Morphology and Structure Formation of Carbon Fibers from Polymer Precursor Systems." *Progress in Materials Science*, July. <https://doi.org/10.1016/j.pmatsci.2018.07.004>.
- Anderson, David P. 1989. "Carbon Fiber Morphology: Wide-Angle X-Ray Studies of Pitch- and Pan-Based Carbon Fibers." UDR-TR-89-61. Dayton UNIV OH RESEARCH INST.
- Anderson, David P. 1989. "Carbon Fiber Morphology. 2. Expanded Wide-Angle X-Ray Diffraction Studies of Carbon Fibers." DAYTON UNIV OH RESEARCH INST.
- Aweed, Khalid A. 2008. "Preparation of Activated Carbon from Wastes Tires by Minerals Hydroxide (LiOH, NaOH and KOH)." *Tikrit Journal of Pure Science* 13 (3): 71–74.
- Babel, K, and K Jurewicz. 2004. "KOH Activated Carbon Fabrics as Supercapacitor Material." *Journal of Physics and Chemistry of Solids* 65 (2): 275–80. <https://doi.org/10.1016/j.jpccs.2003.08.023>.
- Bergström, Jörgen. 2015. "2 - Experimental Characterization Techniques." In *Mechanics of Solid Polymers*, edited by Jörgen Bergström, 19–114. William Andrew Publishing. <https://doi.org/10.1016/B978-0-323-31150-2.00002-9>.
- Byrne, Nolene, Jingyu Chen, and Bronwyn Fox. 2014. "Enhancing the Carbon Yield of Cellulose Based Carbon Fibres with Ionic Liquid Impregnates." *Journal of Materials Chemistry A* 2 (38): 15758–62. <https://doi.org/10.1039/C4TA04059G>.
- Cabasso, Israel, and Youxin Yuan. 2013. "Nano Structured Activated Carbon for Hydrogen Storage. Project Final Technical Report (May 2, 2005-Dec. 31, 2012)." DE-FG36-05GO15009. Research Foundation of State University of New York, Polymer Research Institute, State University of New York-esf. <https://doi.org/10.2172/1063989>.
- Carrott, P. J. M, J. M. V Nabais, M. M. L Ribeiro Carrott, and J. A Pajares. 2001. "Preparation of Activated Carbon Fibres from Acrylic Textile Fibres." *Carbon* 39 (10): 1543–55. [https://doi.org/10.1016/S0008-6223\(00\)00271-2](https://doi.org/10.1016/S0008-6223(00)00271-2).
- Celzard, A., V. Fierro, J.F. Marêché, and G. Furdin. 2007. "Advanced Preparative Strategies for Activated Carbons Designed for the Adsorptive Storage of Hydrogen." *Adsorption Science & Technology* 25 (3–4): 129–42. <https://doi.org/10.1260/026361707782398254>.
- Celzard, A., A. Pasc, S. Schaefer, K. Mandel, T. Ballweg, S. Li, G. Medjahdi, V. Nicolas, and V. Fierro. 2019. "Floating Hollow Carbon Spheres for Improved Solar Evaporation." *Carbon* 146 (May): 232–47. <https://doi.org/10.1016/j.carbon.2019.01.101>.
- Chen, Jonathan. 2016. "Activated Carbon Fiber and Textiles - 1st Edition." 2016.
- Chiang, Yu-Chun, Chen-Yueh Lee, and Hung-Chih Lee. 2007. "Surface Chemistry of Polyacrylonitrile- and Rayon-Based Activated Carbon Fibers after Post-Heat Treatment." *Materials Chemistry and Physics* 101 (1): 199–210. <https://doi.org/10.1016/j.matchemphys.2006.03.007>.
- Chowdhury, Zaira Zaman, Sharifah Bee Abd Hamid, Rasel Das, Md Rakibul Hasan, Sharifuddin Mohd Zain, Khalisanni Khalid, and Md Nasir Uddin. 2013. "Preparation of

- Carbonaceous Adsorbents from Lignocellulosic Biomass and Their Use in Removal of Contaminants from Aqueous Solution.” *BioResources* 8 (4): 6523–55. <https://doi.org/10.15376/biores.8.4.6523-6555>.
- Cuesta, A., P. Dhamelincourt, J. Laureyns, A. Martínez-Alonso, and J. M. D. Tascón. 1994. “Raman Microprobe Studies on Carbon Materials.” *Carbon* 32 (8): 1523–32. [https://doi.org/10.1016/0008-6223\(94\)90148-1](https://doi.org/10.1016/0008-6223(94)90148-1).
- Cuesta, Ana, Amelia Martínez-Alonso, and Juan M. D. Tascón. 1993. “Correlation between Arrhenius Kinetic Parameters in the Reaction of Different Carbon Materials with Oxygen.” *Energy & Fuels* 7 (6): 1141–45. <https://doi.org/10.1021/ef00042a064>.
- Dai, Zhishuang, Fenghui Shi, Baoyan Zhang, Min Li, and Zuoguang Zhang. 2011. “Effect of Sizing on Carbon Fiber Surface Properties and Fibers/Epoxy Interfacial Adhesion.” *Applied Surface Science* 257 (15): 6980–85. <https://doi.org/10.1016/j.apsusc.2011.03.047>.
- Debye, P., and P. Scherrer. 1917. “Ueber Die Konstitution von Graphit Und Amorpher Kohle” 180–88.
- Desmond, B. J., and Bragg W. L. 1924. “The Structure of Graphite.” *Proceedings of the Royal Society of London. Series A, Containing Papers of a Mathematical and Physical Character* 106 (740): 749–73. <https://doi.org/10.1098/rspa.1924.0101>.
- Dobiášová, L., V. Starý, P. Glogar, and V. Valvoda. 1999. “Analysis of Carbon Fibers and Carbon Composites by Asymmetric X-Ray Diffraction Technique.” *Carbon* 37 (3): 421–25. [https://doi.org/10.1016/S0008-6223\(98\)00207-3](https://doi.org/10.1016/S0008-6223(98)00207-3).
- Dresselhaus, Mildred S. 1988. *Graphite fibers and filaments*. Berlin, Allemagne, France.
- Drits, Victor A., and Cyril Tchoubar. 1990. “Overall Description of Imperfect Lamellar Crystals.” In *X-Ray Diffraction by Disordered Lamellar Structures: Theory and Applications to Microdivided Silicates and Carbons*, edited by Victor A. Drits and Cyril Tchoubar, 1–32. Berlin, Heidelberg: Springer Berlin Heidelberg. https://doi.org/10.1007/978-3-642-74802-8_1.
- Dumanli, Ahu Gümrah, and Alan H. Windle. 2012. “Carbon Fibres from Cellulosic Precursors: A Review.” *Journal of Materials Science* 47 (10): 4236–50. <https://doi.org/10.1007/s10853-011-6081-8>.
- Epstein, Michael, Amnon Yogeve, Chengcai Yao, and Alexander Berman. 2001. “Carbothermal Reduction of Alkali Hydroxides Using Concentrated Solar Energy.” *Energy* 26 (5): 441–55. [https://doi.org/10.1016/S0360-5442\(01\)00010-X](https://doi.org/10.1016/S0360-5442(01)00010-X).
- Fink, H. -P., D. Hofmann, and B. Philipp. 1995. “Some Aspects of Lateral Chain Order in Cellulosics from X-Ray Scattering.” *Cellulose* 2 (1): 51–70. <https://doi.org/10.1007/BF00812772>.
- Franklin Rosalind E. 1951. “Crystallite Growth in Graphitizing and Non-Graphitizing Carbons.” *Proceedings of the Royal Society of London. Series A. Mathematical and Physical Sciences* 209 (1097): 196–218. <https://doi.org/10.1098/rspa.1951.0197>.
- Girón, R. P., R. R. Gil, I. Suárez-Ruiz, E. Fuente, and B. Ruiz. 2015. “Adsorbents/Catalysts from Forest Biomass Fly Ash. Influence of Alkaline Activating Agent.” *Microporous and Mesoporous Materials, SI: Characterization of Porous Solids X*, 209 (June): 45–53. <https://doi.org/10.1016/j.micromeso.2015.01.051>.
- Gupta, A., and I. R. Harrison. 1996. “New Aspects in the Oxidative Stabilization of PAN-Based Carbon Fibers.” *Carbon* 34 (11): 1427–45. [https://doi.org/10.1016/S0008-6223\(96\)00094-2](https://doi.org/10.1016/S0008-6223(96)00094-2).
- Harris, P. J. F. 2001. “Rosalind Franklin’s Work on Coal, Carbon, and Graphite.” *Interdisciplinary Science Reviews* 26 (3): 204–10. <https://doi.org/10.1179/030801801679467>.

- He, Zhangxing, Lang Shi, Junxi Shen, Zhen He, and Suqin Liu. 2015. "Effects of Nitrogen Doping on the Electrochemical Performance of Graphite Felts for Vanadium Redox Flow Batteries." *International Journal of Energy Research* 39 (5): 709–16. <https://doi.org/10.1002/er.3291>.
- Huang, Xiaosong. 2009. "Fabrication and Properties of Carbon Fibers." *Materials* 2 (4): 2369–2403. <https://doi.org/10.3390/ma2042369>.
- Huidobro, A., A. C. Pastor, and F. Rodríguez-Reinoso. 2001. "Preparation of Activated Carbon Cloth from Viscous Rayon: Part IV. Chemical Activation." *Carbon* 39 (3): 389–98. [https://doi.org/10.1016/S0008-6223\(00\)00131-7](https://doi.org/10.1016/S0008-6223(00)00131-7).
- Hung, Nguyen Chan, I. V. Anoshkin, and E. G. Rakov. 2007. "Chemical Activation of Carbon Nanofibers and Nanotubes." *Russian Journal of Applied Chemistry* 80 (3): 443–47. <https://doi.org/10.1134/S1070427207030184>.
- Jagannathan, Sudhakar, Han Gi Chae, Rahul Jain, and Satish Kumar. 2008. "Structure and Electrochemical Properties of Activated Polyacrylonitrile Based Carbon Fibers Containing Carbon Nanotubes." *Journal of Power Sources* 185 (2): 676–84. <https://doi.org/10.1016/j.jpowsour.2008.08.093>.
- Jagiello, Jacek, and James P. Olivier. 2013. "2D-NLDFT Adsorption Models for Carbon Slit-Shaped Pores with Surface Energetical Heterogeneity and Geometrical Corrugation." *Carbon* 55 (April): 70–80. <https://doi.org/10.1016/j.carbon.2012.12.011>.
- Jones, B. F., and R. G. Duncan. 1971. "The Effect of Fibre Diameter on the Mechanical Properties of Graphite Fibres Manufactured from Polyacrylonitrile and Rayon." *Journal of Materials Science* 6 (4): 289–93. <https://doi.org/10.1007/BF02403094>.
- Kapteijn, Freek, Gert Abbel, and Jacob A. Moulijn. 1984. "CO₂ Gasification of Carbon Catalysed by Alkali Metals: Reactivity and Mechanism." *Fuel* 63 (8): 1036–42. [https://doi.org/10.1016/0016-2361\(84\)90184-4](https://doi.org/10.1016/0016-2361(84)90184-4).
- Kim, Dae-Young, Yoshiharu Nishiyama, Masahisa Wada, and Shigenori Kuga. 2001. "Graphitization of Highly Crystalline Cellulose." *Carbon* 39 (7): 1051–56. [https://doi.org/10.1016/S0008-6223\(00\)00221-9](https://doi.org/10.1016/S0008-6223(00)00221-9).
- Kissinger, H. E. 1957. "Reaction Kinetics in Differential Thermal Analysis." *Analytical Chemistry* 29 (11): 1702–6. <https://doi.org/10.1021/ac60131a045>.
- Ko, Tse-Hao. 1991. "The Influence of Pyrolysis on Physical Properties and Microstructure of Modified PAN Fibers during Carbonization." *Journal of Applied Polymer Science* 43 (3): 589–600. <https://doi.org/10.1002/app.1991.070430321>.
- Ko, Tse-Hao, Yuan-Kai Liao, and Ching-Han Liu. 2007. "Effects of Graphitization of PAN-Based Carbon Fiber Cloth on Its Use as Gas Diffusion Layers in Proton Exchange Membrane Fuel Cells." *New Carbon Materials* 22 (2): 97–101. [https://doi.org/10.1016/S1872-5805\(07\)60010-9](https://doi.org/10.1016/S1872-5805(07)60010-9).
- Kong, Kenny, Libo Deng, Ian A. Kinloch, Robert J. Young, and Stephen J. Eichhorn. 2012. "Production of Carbon Fibres from a Pyrolysed and Graphitised Liquid Crystalline Cellulose Fibre Precursor." *Journal of Materials Science* 47 (14): 5402–10. <https://doi.org/10.1007/s10853-012-6426-y>.
- Krstić, Sanja. 2018. "Sinteza, funkcionalizacija i primena aktivnih ugljeničnih mikro i nano materijala." *Универзитет у Београду*, September.
- Krstić, Sanja S., Milan M. Kragović, Vladimir M. Dodevski, Aleksandar D. Marinković, Branka V. Kaluđerović, Gregor Žerjav, Albin Pintar, Maja C. Pagnacco, and Marija D. Stojmenović. 2018. "Influence of Temperature and Different Hydroxides on Properties of Activated Carbon Prepared from Saccharose. Characterization, Thermal Degradation Kinetic and Dyes Removal from Water Solutions." *Science of Sintering* 50 (2).

- Kucherenko, V. A., Yu. V. Tamarkina, G. F. Raenko, and M. I. Chernyshova. 2017. "Thermolysis of Brown Coal in the Presence of Alkali Metal Hydroxides." *Solid Fuel Chemistry* 51 (3): 147–54. <https://doi.org/10.3103/S0361521917030065>.
- Landers, John, Gennady Yu. Gor, and Alexander V. Neimark. 2013. "Density Functional Theory Methods for Characterization of Porous Materials." *Colloids and Surfaces A: Physicochemical and Engineering Aspects*, Characterization of Porous Materials: From Angstroms to Millimeters A Collection of Selected Papers Presented at the 6th International Workshop, CPM-6 April 30 – May 2nd, 2012, Delray Beach, FL, USA Co-sponsored by Quantachrome Instruments, 437 (November): 3–32. <https://doi.org/10.1016/j.colsurfa.2013.01.007>.
- Lee, Young Jae, Jae Hyung Kim, Jang Soon Kim, Dong Bok Lee, Jae Chun Lee, Yun Jung Chung, and Yun Soo Lim. 2004. "Fabrication of Activated Carbon Fibers from Stabilized PAN-Based Fibers by KOH." *Materials Science Forum*. 2004. <https://doi.org/10.4028/www.scientific.net/MSF.449-452.217>.
- Leimkuehler, Eric Paul. 2010. "Production, Characterization, and Applications of Activated Carbon." Thesis, University of Missouri--Columbia.
- Li, Dongfeng, Haojing Wang, and Xinkui Wang. 2007. "Effect of Microstructure on the Modulus of PAN-Based Carbon Fibers during High Temperature Treatment and Hot Stretching Graphitization." *Journal of Materials Science* 42 (12): 4642–49. <https://doi.org/10.1007/s10853-006-0519-4>.
- Lillo-Ródenas, M.a., J.p. Marco-Lozar, D. Cazorla-Amorós, and A. Linares-Solano. 2007. "Activated Carbons Prepared by Pyrolysis of Mixtures of Carbon Precursor/Alkaline Hydroxide." *Journal of Analytical & Applied Pyrolysis* 80 (1): 166–74. <https://doi.org/10.1016/j.jaap.2007.01.014>.
- Linares-Solano, A., D. Lozano-Castell, M. Lillo-Ródenas, and D. Cazorla-Amorós. 2007. "Carbon Activation by Alkaline Hydroxides." In *Chemistry & Physics of Carbon. Series: Chemistry and Physics of Carbon, ISBN: 978-1-4200-4298-6. CRC Press, Edited by Ljubisa Radovic, Pp. 1-62, 1–62*. <https://doi.org/10.1201/9781420042993.ch1>.
- Liu, Xiaofeng, and Markus Antonietti. 2014. "Molten Salt Activation for Synthesis of Porous Carbon Nanostructures and Carbon Sheets." *Carbon* 69 (April): 460–66. <https://doi.org/10.1016/j.carbon.2013.12.049>.
- Lu, L, V Sahajwalla, C Kong, and D Harris. 2001. "Quantitative X-Ray Diffraction Analysis and Its Application to Various Coals." *Carbon* 39 (12): 1821–33. [https://doi.org/10.1016/S0008-6223\(00\)00318-3](https://doi.org/10.1016/S0008-6223(00)00318-3).
- Maciá-Agulló, J. A., B. C. Moore, D. Cazorla-Amorós, and A. Linares-Solano. 2007. "Influence of Carbon Fibres Crystallinities on Their Chemical Activation by KOH and NaOH." *Microporous and Mesoporous Materials* 101 (3): 397–405. <https://doi.org/10.1016/j.micromeso.2006.12.002>.
- McKee, D. W., and D. Chatterji. 1975. "The Catalytic Behavior of Alkali Metal Carbonates and Oxides in Graphite Oxidation Reactions." *Carbon* 13 (5): 381–90. [https://doi.org/10.1016/0008-6223\(75\)90006-8](https://doi.org/10.1016/0008-6223(75)90006-8).
- McKee, D. W., and D. Chatterji. 1978. "The Catalyzed Reaction of Graphite with Water Vapor." *Carbon* 16 (1): 53–57. [https://doi.org/10.1016/0008-6223\(78\)90116-1](https://doi.org/10.1016/0008-6223(78)90116-1).
- Mikova, Nadezhda M., Nikolai V. Chesnokov, and Boris N. Kuznetsov. 2009. "Study of High Porous Carbons Prepared by the Alkaline Activation of Anthracites," March.
- Minke, Christine, Ulrich Kunz, and Thomas Turek. 2017. "Carbon Felt and Carbon Fiber - A Techno-Economic Assessment of Felt Electrodes for Redox Flow Battery Applications." *Journal of Power Sources* 342 (February): 116–24. <https://doi.org/10.1016/j.jpowsour.2016.12.039>.

- Moon, S. Y., Myung S. K., Hyun S. H., and Yun S. L. 2006. "Preparation of Activated Carbon Fibers by Chemical Activation Method with Hydroxides." *Materials Science Forum*. 2006. <https://doi.org/10.4028/www.scientific.net/MSF.510-511.750>.
- Moon, Sook Young, Myung Soo Kim, and Yun Soo Lim. 2006. "Preparation and Characterization of Chemical Activated Fibers on Various Carbon Fibers." *Materials Science Forum*. 2006. <https://doi.org/10.4028/www.scientific.net/MSF.510-511.314>.
- Mora, E., C. Blanco, J. A. Pajares, R. Santamaría, and R. Menéndez. 2006. "Chemical Activation of Carbon Mesophase Pitches." *Journal of Colloid and Interface Science* 298 (1): 341–47. <https://doi.org/10.1016/j.jcis.2005.11.051>.
- Newcomb, Bradley A. 2016. "Processing, Structure, and Properties of Carbon Fibers." *Composites Part A: Applied Science and Manufacturing* 91 (December): 262–82. <https://doi.org/10.1016/j.compositesa.2016.10.018>.
- Oberlin, A., Bonnamy, S., Oshida, K., 2006. Landmarks for graphitization. *TANSO* 2006, 281–298. <https://doi.org/10.7209/tanso.2006.281>
- Oguz Erdogan, F. 2019. "Comparative Study of Sunset Yellow Dye Adsorption onto Cornelian Cherry Stones-Based Activated Carbon and Carbon Nanotubes." *Bulgarian Chemical Communications* 50 (4).
- Pampel, J., and T.-P. Feller. 2016. "Opening of Bottleneck Pores for the Improvement of Nitrogen Doped Carbon Electrocatalysts." *Advanced Energy Materials* 6 (8). <https://doi.org/10.1002/aenm.201502389>.
- Park, Soo-Jin, and Byung-Joo Kim. 2015. "Carbon Fibers and Their Composites." In *Carbon Fibers*, 275–317. Springer Series in Materials Science. Springer, Dordrecht. https://doi.org/10.1007/978-94-017-9478-7_8.
- Pastor, A. C., F. Rodríguez-Reinoso, H. Marsh, and M. A. Martínez. 1999. "Preparation of Activated Carbon Cloths from Viscous Rayon. Part I. Carbonization Procedures." *Carbon* 37 (8): 1275–83. [https://doi.org/10.1016/S0008-6223\(98\)00324-8](https://doi.org/10.1016/S0008-6223(98)00324-8).
- Pawlyta, M., J.-N. Rouzaud, and S. Duber. 2015. "Raman Microspectroscopy Characterization of Carbon Blacks: Spectral Analysis and Structural Information." *Carbon* 84 (April): 479–90. <https://doi.org/10.1016/j.carbon.2014.12.030>.
- Pimenta, M. A., G. Dresselhaus, M. S. Dresselhaus, L. G. Cançado, A. Jorio, and R. Saito. 2007. "Studying Disorder in Graphite-Based Systems by Raman Spectroscopy." *Physical Chemistry Chemical Physics* 9 (11): 1276–90. <https://doi.org/10.1039/B613962K>.
- Pope, Christopher G. 1997. "X-Ray Diffraction and the Bragg Equation." *Journal of Chemical Education* 74 (1): 129. <https://doi.org/10.1021/ed074p129>.
- Pradere, C., J. C. Batsale, J. M. Goyhénèche, R. Pailler, and S. Dilhaire. 2009. "Thermal Properties of Carbon Fibers at Very High Temperature." *Carbon* 47 (3): 737–43. <https://doi.org/10.1016/j.carbon.2008.11.015>.
- Qian, X., Y. G. Zhang, X. F. Wang, Y. J. Heng, and J. H. Zhi. 2016. "Effect of Carbon Fiber Surface Functionality on the Moisture Absorption Behavior of Carbon Fiber/Epoxy Resin Composites." *Surface and Interface Analysis* 48 (12): 1271–77. <https://doi.org/10.1002/sia.6031>.
- Qiu, L., X. H. Zheng, J. Zhu, G. P. Su, and D. W. Tang. 2013. "The Effect of Grain Size on the Lattice Thermal Conductivity of an Individual Polyacrylonitrile-Based Carbon Fiber." *Carbon* 51 (January): 265–73. <https://doi.org/10.1016/j.carbon.2012.08.052>.
- Rahaman, M. S. A., A. F. Ismail, and A. Mustafa. 2007. "A Review of Heat Treatment on Polyacrylonitrile Fiber." *Polymer Degradation and Stability* 92 (8): 1421–32. <https://doi.org/10.1016/j.polymdegradstab.2007.03.023>.
- Sadezky, A., H. Muckenhuber, H. Grothe, R. Niessner, and U. Pöschl. 2005. "Raman Microspectroscopy of Soot and Related Carbonaceous Materials: Spectral Analysis and

- Structural Information.” *Carbon* 43 (8): 1731–42. <https://doi.org/10.1016/j.carbon.2005.02.018>.
- Sadoway, Donald R. 1998. “Toward New Technologies for the Production of Lithium.” *JOM* 50 (5): 24–26. <https://doi.org/10.1007/s11837-998-0027-x>.
- Schiemann, M., Je. Bergthorson, P. Fischer, V. Scherer, D. Taroata, and G. Schmid. 2016. “A Review on Lithium Combustion.” *Applied Energy* 162 (January): 948–65. <https://doi.org/10.1016/j.apenergy.2015.10.172>.
- Sevilla, Marta, and Robert Mokaya. 2014. “Energy Storage Applications of Activated Carbons: Supercapacitors and Hydrogen Storage.” *Energy & Environmental Science* 7 (4): 1250–80. <https://doi.org/10.1039/C3EE43525C>.
- Shen, Wenzhong, Zhijie Li, and Yihong Liu. 2008. Surface Chemical Functional Groups Modification of Porous Carbon. *Recent Patents on Chemical Engineering* 1 (1): 27–40.
- Sheth, Atul, Pradeep Agrawal, and Yaw D. Yeboah. 1998. “Catalytic Gasification of Coal Using Eutectic Salt Mixtures.” DE-FG26-97FT97263-01. Federal Energy Technology Center, Morgantown, WV, and Pittsburgh, PA. <https://doi.org/10.2172/2122>.
- Silvestre-Albero, A., J. Silvestre-Albero, M. Martinez-Escandell, M. Molina-Sabio, A. Kovacs, and F. Rodriguez-Reinoso. 2015. “Novel Synthesis of a Micro-Mesoporous Nitrogen-Doped Nanostructured Carbon from Polyaniline.” *Microporous and Mesoporous Materials* 218 (December): 199–205. <https://doi.org/10.1016/j.micromeso.2015.07.023>.
- Sing, Kenneth S. W. 1994. “Physisorption of Gases by Carbon Blacks.” *Carbon* 32 (7): 1311–17. [https://doi.org/10.1016/0008-6223\(94\)90117-1](https://doi.org/10.1016/0008-6223(94)90117-1).
- Sonibare, Oluwadayo O., Tobias Haeger, and Stephen F. Foley. 2010. “Structural Characterization of Nigerian Coals by X-Ray Diffraction, Raman and FTIR Spectroscopy.” *Energy, The 3rd International Conference on Sustainable Energy and Environmental Protection, SEEP 2009*, 35 (12): 5347–53. <https://doi.org/10.1016/j.energy.2010.07.025>.
- Sutcu, Hale, and Adil Dural. 2006. “Effect of Hydroxides on Carbonization of Bituminous Coal.” *Coal Preparation* 26 (4): 201–8. <https://doi.org/10.1080/07349340601104255>.
- Suzuki, Motoyuki. 1994. “Activated Carbon Fiber: Fundamentals and Applications.” *Carbon* 32 (4): 577–86. [https://doi.org/10.1016/0008-6223\(94\)90075-2](https://doi.org/10.1016/0008-6223(94)90075-2).
- Tamarkina, Yu. V., L. A. Maslova, T. V. Khabarova, and V. A. Kucherenko. 2008. “Adsorption Properties of Carbon Materials Produced by Thermolysis of Brown Coal in the Presence of Alkali Metal Hydroxides.” *Russian Journal of Applied Chemistry* 81 (7): 1167–70. <https://doi.org/10.1134/S1070427208070070>.
- Tamarkina, Yu. V., T. G. Shendrik, V. A. Kucherenko, and T. V. Khabarova. 2012. “Conversion of Alexandriya Brown Coal into Microporous Carbons under Alkali Activation.” *Chemistry* 5 (1): 24–36.
- Tang, M. M., and Roger Bacon. 1964. “Carbonization of Cellulose fibers—I. Low Temperature Pyrolysis.” *Carbon* 2 (3): 211–20. [https://doi.org/10.1016/0008-6223\(64\)90035-1](https://doi.org/10.1016/0008-6223(64)90035-1).
- Tuinstra, F., and J. L. Koenig. 1970. “Raman Spectrum of Graphite.” *The Journal of Chemical Physics* 53 (3): 1126–30. <https://doi.org/10.1063/1.1674108>.
- Van Grieken, Rene, and A. Markowicz. 2001. *Handbook of X-Ray Spectrometry*.
- Vignoles, Gerard L., Patrick Weisbecker, Jean-Marc Leyssale, Stephane Jouannigot, and Georges Chollon. 2015. “Carbones Pyrolytiques Ou Pyrocarbones: Des Matériaux Multiéchelles et Multiperformances.” *Techniques de L'ingénieur NM 3 150*, 1–22.
- Vilian, A. T. Ezhil, Ji Yoon Song, Yun Sung Lee, Seung-Kyu Hwang, Hae Jin Kim, Young-Si Jun, Yun Suk Huh, and Young-Kyu Han. 2018. “Salt-Templated Three-Dimensional Porous Carbon for Electrochemical Determination of Gallic Acid.” *Biosensors and Bioelectronics* 117 (October): 597–604. <https://doi.org/10.1016/j.bios.2018.06.064>.

- Wada, Masahisa, Takeshi Okano, and Junji Sugiyama. 2001. "Allomorphs of Native Crystalline Cellulose I Evaluated by Two Equatorial Spacings." *Journal of Wood Science* 47 (2): 124–28. <https://doi.org/10.1007/BF00780560>.
- Wang, Guang Xue, Hao Han, Li Wei Li, Hai Yu Quan, Yan Ping Shi, Wen Zhen Qin, Ping Lu, and Qi Lin Wu. 2011. "SEM and AFM Studies on the Surface and Cross Section Morphology of Rayon-Based Activated Carbon Fibers." *Materials Science Forum*. 2011. <https://doi.org/10.4028/www.scientific.net/MSF.689.413>.
- Wang, Huiqi, Tao Han, Jinhua Yang, Zechao Tao, Quanguo Guo, Zhanjun Liu, Zhihai Feng, and Lang Liu. 2014. "Structural Evolution of Rayon-Based Carbon Fibers Induced by Doping Boron." *RSC Advances* 4 (103): 59150–56. <https://doi.org/10.1039/C4RA07892F>.
- Warren, B. E. 1941. "X-Ray Diffraction in Random Layer Lattices." *Physical Review* 59 (9): 693–98. <https://doi.org/10.1103/PhysRev.59.693>.
- Wietelmann, Ulrich, and Richard J. Bauer. 2000. "Lithium and Lithium Compounds." In *Ullmann's Encyclopedia of Industrial Chemistry*. American Cancer Society. https://doi.org/10.1002/14356007.a15_393.
- Xiao, Hao, Yonggen Lu, Weizhe Zhao, and Xianying Qin. 2014. "The Effect of Heat Treatment Temperature and Time on the Microstructure and Mechanical Properties of PAN-Based Carbon Fibers." *Journal of Materials Science* 49 (2): 794–804. <https://doi.org/10.1007/s10853-013-7762-2>.
- Yusof, N., and A. F. Ismail. 2012. "Post Spinning and Pyrolysis Processes of Polyacrylonitrile (PAN)-Based Carbon Fiber and Activated Carbon Fiber: A Review." *Journal of Analytical and Applied Pyrolysis* 93 (January): 1–13. <https://doi.org/10.1016/j.jaap.2011.10.001>.
- Zhang, Zhengyang, Jingyu Xi, Haipeng Zhou, and Xinping Qiu. 2016. "KOH Etched Graphite Felt with Improved Wettability and Activity for Vanadium Flow Batteries." *Electrochimica Acta* 218 (November): 15–23. <https://doi.org/10.1016/j.electacta.2016.09.099>.
- Zhong, S., C. Padeste, M. Kazacos, and M. Skyllas-Kazacos. 1993. "Comparison of the Physical, Chemical and Electrochemical Properties of Rayon- and Polyacrylonitrile-Based Graphite Felt Electrodes." *Journal of Power Sources* 45 (1): 29–41. [https://doi.org/10.1016/0378-7753\(93\)80006-B](https://doi.org/10.1016/0378-7753(93)80006-B).
- Zhou, Jin, Zhaohui Li, Wei Xing, Honglong Shen, Xu Bi, Tingting Zhu, Zhipeng Qiu, and Shuping Zhuo. 2016. "A New Approach to Tuning Carbon Ultramicropore Size at Sub-Angstrom Level for Maximizing Specific Capacitance and CO₂ Uptake." *Advanced Functional Materials* 26 (44): 7955–64. <https://doi.org/10.1002/adfm.201601904>.
- Zickler, Gerald A., Bernd Smarsly, Notburga Gierlinger, Herwig Peterlik, and Oskar Paris. 2006. "A Reconsideration of the Relationship between the Crystallite Size L_a of Carbons Determined by X-Ray Diffraction and Raman Spectroscopy." *Carbon* 44 (15): 3239–46. <https://doi.org/10.1016/j.carbon.2006.06.029>.
- Чесноков, Н. В., Н. М. Микова, И. П. Иванов, Б. Н. Кузнецов, Nicolay V. Chesnokov, Nadezhda M. Mikova, Ivan P. Ivanov, and Boris N. Kuznetsov. 2014. "Получение углеродных сорбентов химической модификацией ископаемых углей и растительной биомассы," March.

III/6 Annex

Table III/6-1 Textural parameters from both N₂ and CO₂ isotherms calculated by 2D NLDFT-HS model of *de-sized* CF before and after chemical reaction in molten LiOH (normal style) or Li₄(OH)₃Br (**bold style**), with additional XRD structural data of the initial ones; white cells are for carbonised and grey cells are for graphitised CFs.

Carbon felt (CODE)	B-O (%)	d ₀₀₂ (Å)	L _c (Å)	S _{NLDFT} (m ² g ⁻²)	L _μ (dV) (nm)	L _{tot} (dV) (nm)	V _μ NLDFT (cm ³ g ⁻¹)	V _{tot} NLDFT (cm ³ g ⁻¹)	V _{meso} (cm ³ g ⁻¹)	V _{meso} (%)
CR1	-	3.65	12	910.71	0.68	0.68	0.28	0.28	0.00	0.00
CR1a500	5.6			930.99	0.75	0.80	0.30	0.30	0.00	0.61
CR1a600	49.7			1057.69	1.16	2.39	0.33	0.86	0.53	61.79
CR1b500	2.7			988.98	0.77	0.77	0.33	0.33	0.00	0.04
CR1b600	20.4			996.27	1.01	1.40	0.38	0.45	0.06	14.33
CR1b650	64.5			1011.14	1.15	3.11	0.26	1.04	0.79	75.38
GR1	-	-	-	688.19	0.98	1.12	0.27	0.29	0.03	8.99
GR1a500	0.9			787.86	1.04	1.54	0.30	0.38	0.08	20.56
GR1a600	9.4			793.81	1.06	1.83	0.30	0.43	0.12	28.74
GR1a650	38.7			869.19	1.08	3.14	0.28	0.71	0.43	60.35
GR1b600	4.1			711.52	1.03	1.54	0.27	0.31	0.04	12.10
GR1b700	33.8			847.35	1.01	3.03	0.28	0.52	0.24	45.62
CR2	-	3.68	12	907.39	0.68	0.68	0.27	0.27	0.00	0.04
CR2a500	5.2			985.71	0.73	0.88	0.31	0.32	0.01	3.73
CR2a600	43.7			814.31	1.17	2.07	0.27	0.59	0.32	53.48
CR2b500	2.9			941.69	0.72	0.75	0.29	0.29	0.00	0.23
CR2b600	20.6			998.04	0.95	1.28	0.36	0.42	0.05	13.06
CR2b650	72.6			1033.65	1.17	3.09	0.27	1.10	0.83	75.76
GR2	-	3.62	-	424.11	0.67	0.68	0.14	0.14	0.00	0.14
GR2a500	2.0			463.14	0.75	2.21	0.15	0.19	0.04	20.40
GR2a700	85.9			622.23	1.00	4.01	0.21	0.42	0.22	50.84
GR2b500	0.3			474.65	0.70	0.88	0.16	0.16	0.01	3.62
GR2b700	20.8			656.69	1.09	2.82	0.25	0.41	0.16	39.76

Table III/6-2 Continuation of Table III/6-1.

Carbon felt (CODE)	B-O ₁ (%)	d ₀₀₂ ² (Å)	L _c ³ (Å)	S _{NLDFT} ⁴ (m ² g ⁻²)	L _μ (dV) ⁵ (nm)	L _{tot} (dV) ⁶ (nm)	V _μ NLDFT ⁷ (cm ³ g ⁻¹)	V _{tot} NLDFT ⁸ (cm ³ g ⁻¹)	V _{mes} ⁹ (cm ³ g ⁻¹)	V _{mes} (%)
CR3	-	-	-	769.69	0.56	0.56	0.2029	0.2031	0.0002	0.10
CR3a500	1.7			754.85	0.65	0.65	0.2268	0.2268	0.0000	0.00
CR3a600	12.9			808.65	0.88	0.98	0.2835	0.2991	0.0156	5.22
GR3	-	3.62	16	10.92	1.07	5.02	0.0047	0.0071	0.0024	33.55
GR3a600	1.1			14.72	0.93	9.73	0.0063	0.0104	0.0041	39.36
GR3a650	3.4			17.28	0.89	7.55	0.0058	0.0140	0.0082	58.51
GR3a700	4.8			17.74	0.91	7.28	0.0033	0.0143	0.0110	76.72
GR3a750	28.8			43.24	0.93	4.83	0.0161	0.0323	0.0162	50.11
GR3b750	18.7			33.39	0.87	4.00	0.0136	0.0167	0.0032	18.91
GR4	-	3.51	25	6.62	0.82	6.20	0.0023	0.0045	0.0022	48.70
GR4a600	0.1			9.56	0.92	4.78	0.0040	0.0054	0.0013	25.19
GR4a650	3.4			11.68	0.96	5.63	0.0049	0.0075	0.0026	34.61
GR4a700	7.2			25.15	0.91	3.21	0.0100	0.0141	0.0042	29.53
GR4a750	18.4			13.85	0.95	4.09	0.0061	0.0077	0.0017	21.63
GR4b750	15.9			27.36	0.92	2.91	0.0114	0.0134	0.0020	14.95
CP8	-	3.60	15	-	-	-	-	-	-	-
CP8a650	14.7			33.75	0.90	3.94	0.0100	0.0257	0.0157	61.14
CP8a700	49.0			29.30	0.91	3.77	0.0104	0.0194	0.0091	46.68
GP8	-	3.51	24	-	-	-	-	-	-	-
GP8a650	1.2			10.29	0.86	2.11	0.0041	0.0046	0.0005	10.80
GP8a750	10.0			13.65	0.91	1.95	0.0057	0.0067	0.0010	14.58
CP5	-	3.52	20	-	-	-	-	-	-	-
CP5a500	0.9			15.29	0.91	3.00	0.0061	0.0082	0.0021	25.08
CP5a750	31.7			18.04	0.94	3.26	0.0073	0.0103	0.0030	28.90
GP6	-	3.51	24	-	-	-	-	-	-	-
GP6a750	15.5			24.54	0.95	2.69	0.0104	0.0131	0.0027	20.84

¹ Burn-off = 100 - yield calculated as a % of carbon disappeared per initial CF weight

² Interlayer graphitic spacing (XRD analysis)

³ Graphitic nanocrystallite thickness (XRD analysis)

⁴ Surface areas determined by 2D NLDFT-HS

⁵ Average micropore size

⁶ Average pore size

⁷ Micropore volume (0.36 - 2 nm) determined by 2D NLDFT-HS

⁸ Total pore volume (0.36 - 10 nm) determined by 2D NLDFT-HS

⁹ Mesopore volume (2-10 nm) = V_{tot} 2D NLDFT-HS - V_μ 2D NLDFT-HS

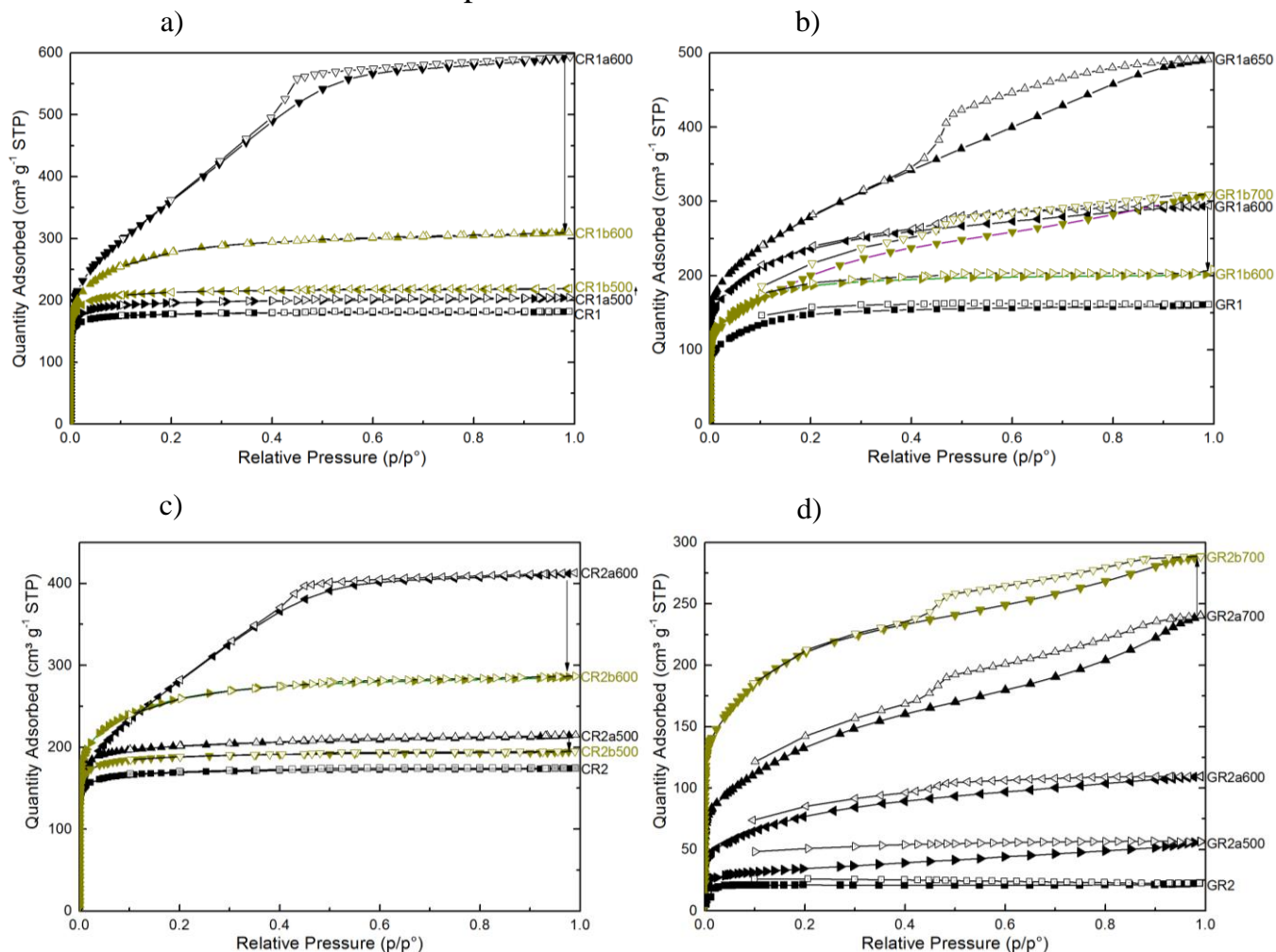
III/6.1 N₂ adsorption isotherms

Figure III/6-1 Nitrogen adsorption isotherms of corresponding carbonised and graphitised CFs before and after the chemical reaction with LiOH (black symbols) and with Li₄(OH)₃Br (green symbols). The arrow is shown for CFs reacted at a same temperature but in different molten salts.

Due to the low amount of material recovered after some chemical reactivity tests, and because of the sometimes very narrow microporous texture, it is hard to achieve closed loop adsorption-desorption isotherms in a few cases. As previously seen elsewhere (Huidobro, Pastor, and Rodríguez-Reinoso 2001), for many CFs, adsorption equilibrium problems are observed due to the slow nitrogen diffusion kinetics in very narrow microporosity, at analysis temperature of -196 °C. In Figure III/6-1, the initial materials are seen as typical microporous carbons, thus type I isotherms are obtained. Therefore, comparing isotherms from reacted CFs in molten LiOH or Li₄(OH)₃Br at the lowest reaction temperature (as of CR1, GR1, CR2, and

GR2), no hysteresis loop and narrower isotherm knees are observed. Performing tests at higher reaction temperature results in most cases in a change of the isotherm shape (to type I-IV) with the appearance of hysteresis loops (of H2 type) and steeper isotherm slope, attributed to the development of mesopores of ill-defined size and shape. Hence, by performing the chemical reaction at 600°C, a hysteresis loop and a wider isotherm knee are observed with LiOH but not with $\text{Li}_4(\text{OH})_3\text{Br}$. An important slope of the isotherm, as seen for CR1a600 and CR2a600, indicates a widespread microporosity (based on adsorbed amounts up to a relative pressure of 0.2), followed by significant contribution of the mesoporosity (also seen from the widest pore size distribution shown in Fig. III/3-19 a) and III/3-20 a)).

The graphitised CFs of higher structural order show type II adsorption isotherms typical of non-porous or macroporous absorbent with negligible hysteresis at relatively high pressure (seen in Fig. III/6-2). After reaction in molten LiOH or $\text{Li}_4(\text{OH})_3\text{Br}$ at the highest investigated temperature, the type of the isotherms remains unchanged, with only a change of the adsorbed quantities depending on the materials' characteristics.

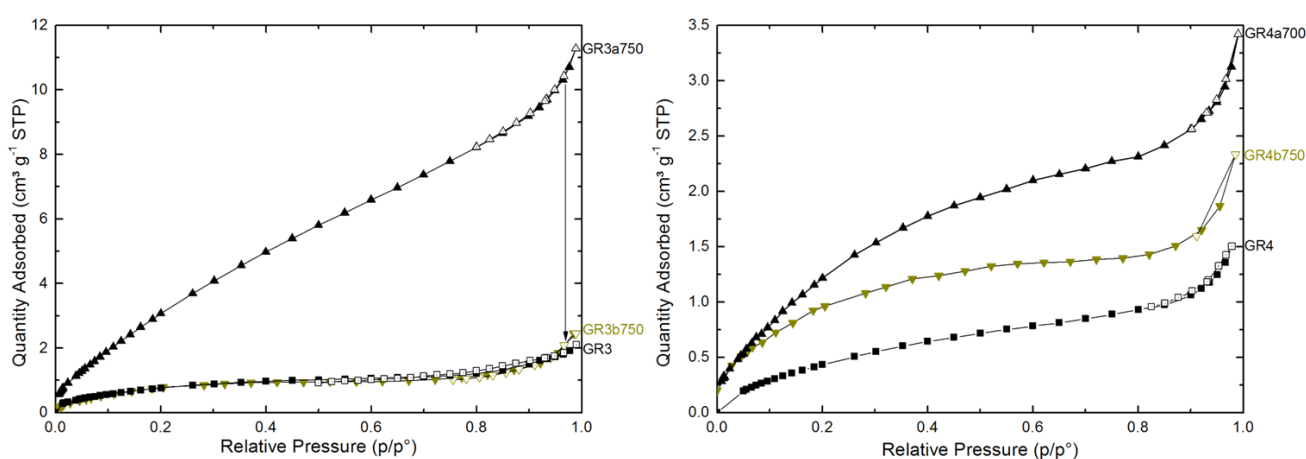


Figure III/6-2 Nitrogen adsorption isotherms of graphitised CFs (of higher structural order) before and after the chemical reaction with LiOH (black symbols) and $\text{Li}_4(\text{OH})_3\text{Br}$ (green symbols) at the highest tested temperature, the latter being emphasised by an arrow.

Clearly, the effect of the chemical reactivity temperature increases as the temperature increases. In parallel, the adsorption isotherms also have a drastically different shape due to the initial material nanotexture. The N_2 adsorption isotherms finally confirm that LiOH reacts more severely with any of the tested CFs than $\text{Li}_4(\text{OH})_3\text{Br}$ under the same experimental conditions.

III/6.2 Additional SEM micrographs of chemically reactivated CFs in molten LiOH

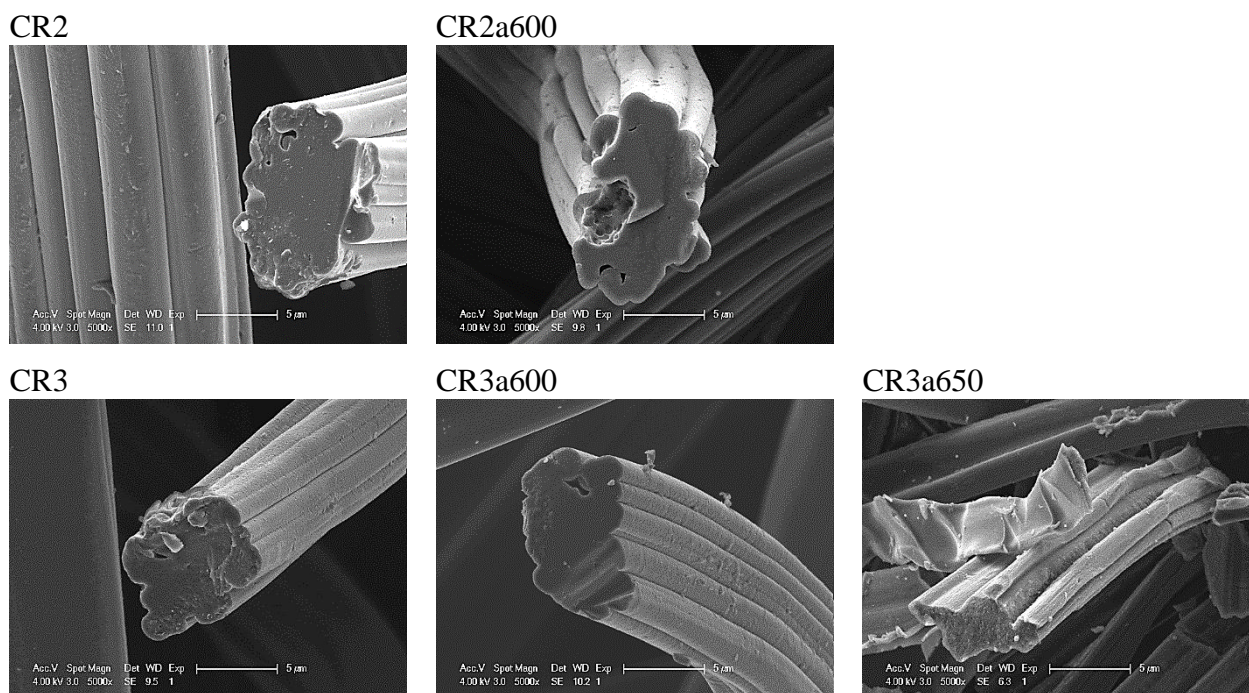


Figure III/6-3 SEM micrographs of *de-sized* ex-Rayon CFs before (left) and after reaction with LiOH (middle and right) at different temperatures.

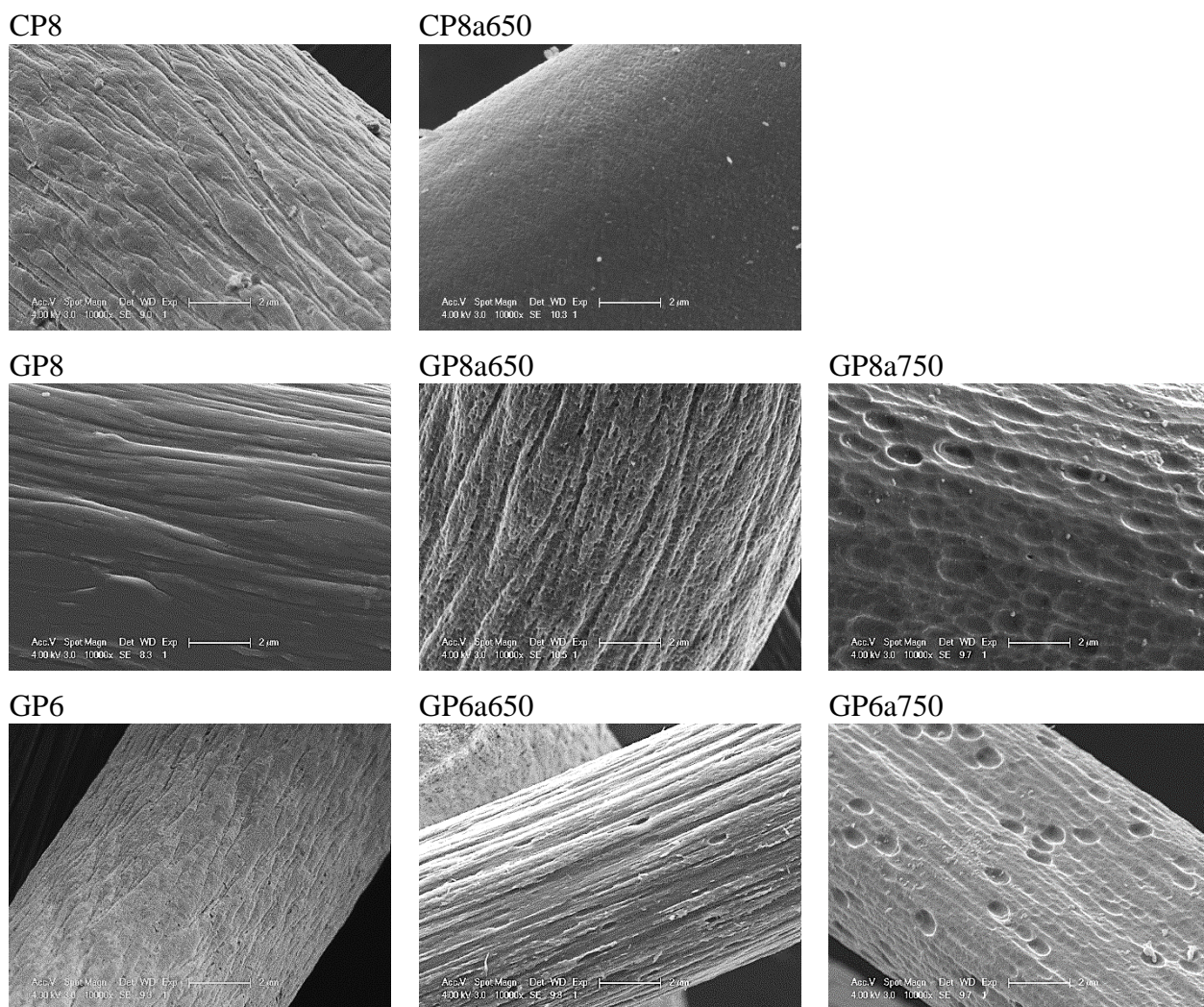


Figure III/6-4 SEM micrographs of *de-sized* ex-PAN CFs before (left) and after reaction with LiOH (middle and right) at different temperatures.

CHAPTER IV:
ADVANCED CARBON FELTS'
MODIFICATIONS AND
APPLICATION TESTS

IV/1 Introduction

As presented in the previous two chapters, a detailed investigation was performed on the morphology, physical/structural properties, and chemical stability of CFs, targeting valuable material information for the production/performance of highly energetic CF-PC hybrid materials. The incorporation of PCM materials into CF hosts should improve the stability and the efficiency of the former. The examined carbons are indeed seen as potential solutions for the disadvantages associated with thermal energy storage (discussed in chapter I). The identification of the crucial material parameters, not previously studied, should also provide a useful guide for future CF improvement and their favourable use in other applications. Nevertheless, during the investigation of the studied CFs, it was clearly observed that some material properties could still be improved, compared to the as-received commercial CFs, thus allowing better performance in their intended end-use. Needle-punched soft CFs are found to be highly porous materials with features able to solve many of the application questions, yet their flexible nature and lack of strong inter-fibre connections limit some of the demanded host properties. In consequence, fabrics' mechanical and heat transfer performances are lower than those of their constituent individual carbon fibres or of the investigated rigid/rigidized CFs.

Broadening this way the scope of this thesis, an advanced morphological modification of a chosen CF was performed to additionally improve materials' properties and compare the newly achieved characteristics with the original ones and/or those of other comparable carbon materials. Thus, the modification of the CF is expected to bring improvement, both in terms of final composite performance and total investment cost.

Composites are usually prepared to improve properties that none of the separate phases alone could provide. A composite material can be prepared from at least two compounds, either completely different materials or phases of the same material. Examples of the latter are carbon/carbon (C/C) composites, produced by deposition of pyrocarbon on a heated carbon fibre preform by dehydrogenation of a hydrocarbon precursor gas (Oberlin 2002). As previously investigated by (Vignoles 2015), one of the most economically viable fibre-based composites are the C/C composites, as prepared by chemical vapour deposition (CVD). CVD is defined as an infiltration process of diluted hydrocarbons, which involves chemical reactions with the carbon fibre preform and leading to a pyrocarbon coating (Zhang et al. 2018). Another advantage of this modification technique is its level of technical and know-how readiness,

which, combined with the use of commercial CFs (the most economically efficient carbon preforms) can be rapidly used for mass industrial production.

Much work has been done for producing a variety of C/C composites in the form of solid materials with high bulk density (Li et al. 2013; Hou et al. 2015; Sharma et al. 2017). On the contrary, the focus here is on highly porous C/C composites where the CF provides the skeleton over which the pyrocarbon phase is deposited, thereby modifying the surface of its carbon fibres. The additional pyrocarbon layer is expected to form a layer on the carbon fibres, generating fixed connections at the contacts between fibres that will improve the overall heat and mechanical transfer, without drastically modifying the overall porosity of the material.

In this chapter, the main focus has been on the preparation of C/C composites and the study of their morphologies, their physical performances, as well as elemental/structural features and finally their chemical stability in molten LiOH, LiBr, and $\text{Li}_4(\text{OH})_3\text{Br}$ (as PCM of interest for the application). The variation in composite density was measured directly from the prepared samples. Imaging analyses were then performed to observe the morphology of the C/C composites and the microstructure of the deposited pyrocarbon. The physical properties and chemical stability of the C/C composites were analysed in the same way as for the commercial CFs in the previous two chapters. The resulting properties of the prepared C/C composites were plotted side by side and compared to the properties of other carbon materials, studied here or found in the literature.

Due to the novelty of the application of carbon fibre materials in high-temperature TES, there is no pilot or industrial installation incorporating this kind of composites. Apart from studies on low-temperature TES favoured by carbon fibres (presented in subchapter I/1.3.b2), only a few other authors have performed studies on the use of graphite fins/flakes/foams or carbon nanotubes as PCM promoters, tested at high temperatures (Ge et al. 2014; Ye et al. 2014; Singh et al. 2016; C. Li et al. 2019). Even though the evaluated PCM properties have been improved, problems remain such as the lack of composite stability, phase separation, and efficiency variations, still appearing as obstacles to the sustainable use of the hybrid materials presented. Given the general problems of the carbon-based promoters mentioned above, we have made preliminary tests of one commercial CF as an effective host for thermal energy storage through peritectic reactions. Thus, the morphological, structural and thermodynamic properties of the synthesised novel PCM and its precursors were analysed, as well as those of the prepared hybrid CF-PCM material. The results presented were used to identify the key design/work parameters for the preparation and performance of CF-PCM hybrid materials, thus

providing answers to the postulated objectives of the final materials' application and useful guidance for future improvements.

IV/2 Experimental

IV/2.1 CF preform and CVD of C/C composites

A single soft CF material was chosen for performing the CVD modification, due to timeframe limitations and the objective of clearly investigating the modification of materials' properties after the deposition of pyrocarbon. Thus, the sample GR4 (SFG1aSC) was considered as a suitable candidate for the preparation of C/C composites, due to morphological and other characteristics detailed through the discussion of the results in this chapter.

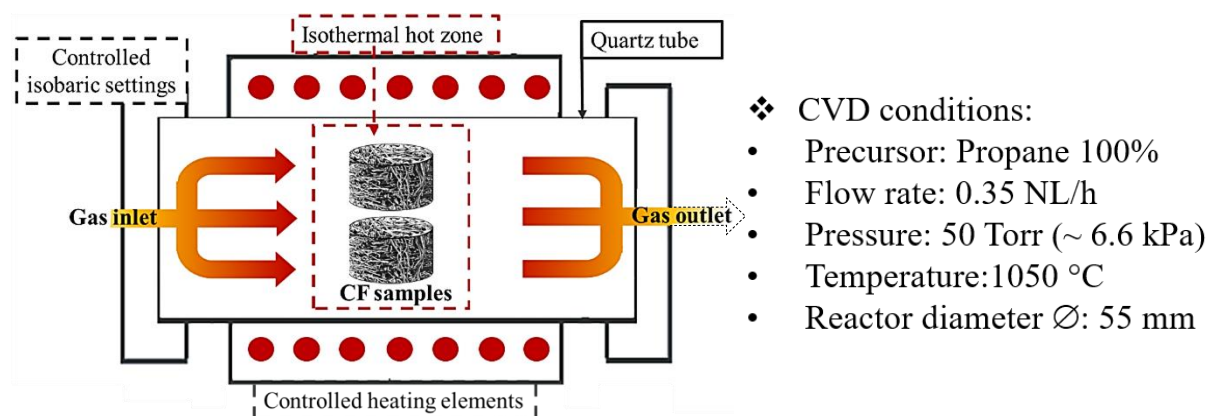


Figure IV/2-1 Schematic presentation of the CVD reactor and synthesis protocol for preparing C/C composites.

The microstructure and properties of the C/C composites are easily tailored and highly dependent on the deposition conditions and the used carbon precursors (Oberlin 2002). Here, commercially viable isobaric-isothermal CVD was performed using a reactor and synthesis conditions detailed in Figure IV/2-1. In short, the process was performed at 1050°C, using propane as a gaseous carbon precursor, without carrier gas and under reduced pressure of 50 Torr. As described elsewhere (Zhang et al. 2018), the pyrocarbon deposition process is initiated once the gaseous precursor is introduced in the porosity of the CF, mainly by diffusion. Hence, the gases are adsorbed and condensed into solid through homo-/hetero-geneous chemical reactions near or on the carbon fibre surface. Simultaneously, gaseous by-products of the chemical reactions are desorbed and diffused out of the CF porosity. Low temperature and reduced gas pressure in combination with the high porosity and permeability of the CF were expected to result in a slow deposition rate, thus leading to a homogeneous distribution of pyrocarbon. Also, a high concentration of propane at reduced gas pressure is reported to favour

anisotropic pyrocarbon nanotexture due to the improved maturation of the hydrocarbon gaseous molecules and the alignment of carbon layers deposited at the surface of the preform (Davies 1992). In addition, the IP direction of the CF was positioned parallel to the gas inlet to ensure that the diffusion of the precursor gases and of the by-products will occur easily along the main direction of the carbon fibres. Different C/C composites were obtained only by varying the time of deposition, thus pyrocarbon layers with different thicknesses were obtained.

Since a single CF preform was used for the modification process, the produced C/C composites were simply labelled by the weight increase calculated after the pyrocarbon deposition. Thus, for instance, %35 refers to the graphitised GR4 (SFG1aSC) (both codes used in the previous chapters) after CVD such that the initial weight increased by 35%. After performing the chemical reactivity tests, the presented code labels were followed by a low-case letter related to the chemical reagent (molten salt) used (a for LiOH or b for $\text{Li}_4(\text{OH})_3\text{Br}$), ending with the test temperature. Thus, for instance, %35a650 refers to a C/C composite after a reactivity test with LiOH performed at 650°C. This different coding system was introduced to emphasise the differences between the pristine CF, examined in the previous two chapters, and the modified C/C composites. The used CF preform, GR4 (SFG1aSC), and all other CFs thus kept the same codes as explained in Chapter II when compared with the results of the modified C/C composites.

IV/2.2 Morphological characterisation of prepared C/C composites

IV/2.2.a Porosity and density

The measurement of the bulk density, ρ_b (g cm^{-3}), was performed in the same conditions as for the rigid board CF, described in Chapter II/2.3. Shortly, the bulk density of the C/C composites was calculated as an average from the measured mass divided by the total volume of not less than three cylindrical samples. The skeletal density, ρ_s (g cm^{-3}), of the prepared C/C composites was considered identical as the one of the used CF preform. From both bulk and skeletal densities, the porosity ε (dimensionless), was calculated using equation (II/1).

IV/2.2.b Pyrocarbon microstructure and textural analysis

The morphological characterisation of the C/C composites also included the estimation of deposited pyrocarbon anisotropy. As observed from the results in Chapter III, the complex structure of carbon materials usually differs from pure graphite due to microstructural and textural defects, contributing to the disorientation of the aromatic layers in graphitic materials. Since the 1970s, different levels of anisotropy of various carbon materials have been identified and categorised through the determination of their optical properties and extinction angle (A_e),

by the use of polarised light optical microscopy and the implementation of semi-quantitative analysis (Oberlin 2002; Charron 2017).

Herein, the properties of the deposited pyrocarbon were investigated following a method applied to estimate the pyrocarbon orientation and anisotropy, described and applied by (Gillard et al. 2015). Before the microscopy analysis, the C/C composite samples were included in epoxy resin, which was next cured and mechanically polished. The latter process revealed regions with well-defined pyrocarbon and carbon fibre zones. The observation of the optical behaviour of deposited pyrocarbon was performed under a Nikon ME500L optical microscope, equipped with an HD Nikon Digital Camera DMX 1200, graduated polariser and analyser. At least 16 micrographs were taken at four different angles of the microscope polariser and analyser, at appropriate magnification and for each analysed regions of different samples. Finally, a digital image alignment was performed to neutralise any effect of sample displacement during the analysis of a single region. Once having well-aligned images, the analyst can estimate the orientation and anisotropy of pyrocarbon through the use of defined orientation (coloured) and anisotropy (grayscale) maps, respectively. This type of representation, as seen in Figure IV/2-2, is therefore used to quantify the orientation of the pyrocarbon microstructure, in agreement with its extinction angle (A_e), thus providing the identification of the pyrocarbon species.

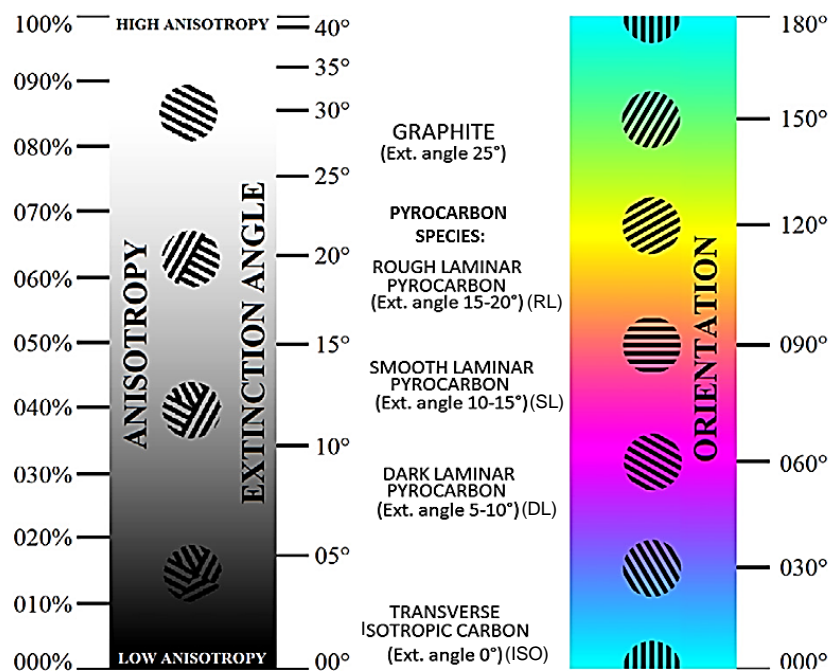


Figure IV/2-2 Scaled anisotropy (grayscale) and orientation (colored) map, with presented extinction angle (A_e) of pyrocarbon microstructure and definition of different pyrocarbon species (after Gillard et al. 2015).

The sample preparation and polarised optical microscopy observations were performed in collaboration with the Laboratory of ThermoStructural Composites (LCTS) - University of Bordeaux. Special acknowledgements go to Prof. Dr. Gerard L. Vignoles and his team for the welcoming participation, help for the performed textural analysis, and acquired results.

IV/2.2.c Imaging of C/C composite microstructure

The SEM technique was used for microscopic scale observations of the prepared C/C composites. The examination of the pyrocarbon thickness, seen from the cross-section fracture of modified carbon fibres, was performed in a similar way and by using image analysis as explained in Chapter II, subsection (II/2.5.a). The analyses were made on randomly picked zones on outer and central regions of cylindrical shape samples, regardless of samples' orientation during the CVD process. This examination is important to identify the expected modification of the fibre-to-fibre contacts compared to the initial CF.

IV/2.3 Physical properties of C/C composites

Physical properties (out-of-plane air permeability, compression properties, and thermal conductivity) were examined at stabilised room temperature (20°C) and relative humidity (50% RH). Thus, analyses of the C/C composites' physical properties were performed using the examination procedures and methods/techniques already described in Chapter II/2.7. Short descriptions and required additional explanations were only introduced in the experimental part in the present chapter.

The fluid flow through the prepared C/C composites was measured following Darcy's law with a Sigma airflow resistance meter (Mecanum, Canada) (Fig. II/2-5), complying with two international standards: ISO 9053:1991 and ASTM C522-03(2016). The investigated airflow permeability k (m^2) of all samples was again derived from the software of the device, as an outcome of equation (II/4).

The thermal conductivity was measured by placing a flat circular nickel probe between two identical C/C composite samples. After the stabilisation time, a low constant current was applied, and then the temperature was deduced from the recorded electrical resistance of the probe to compute materials' thermal conductivity. ASTM D7984¹ and ISO 22007-2²

¹ ASTM D7984 – 16(2018): Standard Test Method for Measurement of Thermal Effusivity of Fabrics Using a Modified Transient Plane Source (MTPS) Instrument

²ISO 22007-2:2015(en): Determination of thermal conductivity and thermal diffusivity — Part 2: Transient plane heat source (hot disc) method

international standards, as well as described transient plane source method, were followed for performing the thermal conductivity tests. More detailed information on the theory behind the thermal conductivity measurement with the transient plane source method is given elsewhere (Palacios et al. 2019).

IV/2.3.a Mechanical characterisation

In the load transfer method, explained in subchapter II/2.7.b for the conventional mechanical compression method, the sample is in direct contact with the compression platens. Herein the compression tests were performed on samples sandwiched between two stiff plates glued to their opposite faces in the OP direction (seen in Fig. IV/2-3). Thus, C/C composite samples were glued with a high-resistance epoxy adhesive (Araldite®) in-between two PMMA (polymethyl methacrylate) plates prior to performing the tests.

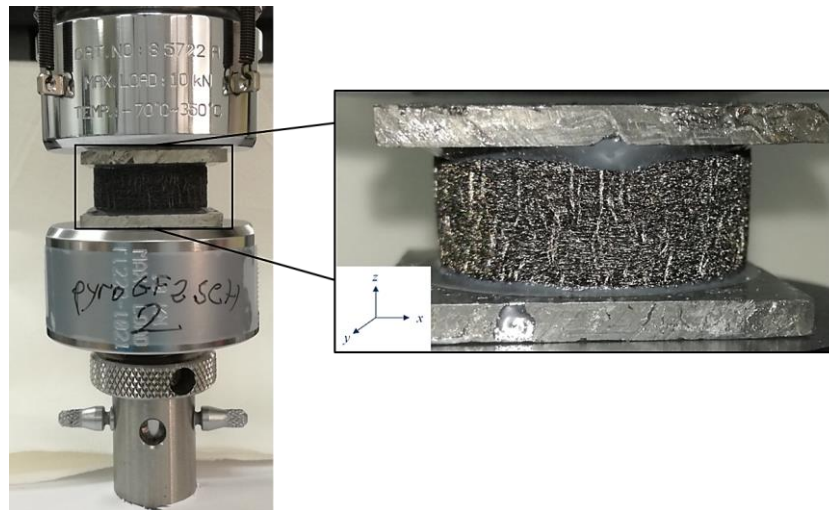


Figure IV/2-3 Compression of a C/C composite by use of an Instron 5944 universal testing machine. The zoom presents the prepared C/C composite, with glued PMMA plates.

Compression with plates has been performed because a brittle mechanical behaviour of the prepared C/C composites was expected. In former studies (Szcurek et al. 2015; Letellier et al. 2017), it was found that the mechanical properties of brittle materials could be strongly affected by the bonding – or not – of the sample ends to the loading plates. As a result of the additional bonding of the sample ends to the stiff loading plates, a homogeneous distribution of the load through the section occurs. Consequently, higher – more representative – values of elastic modulus and compression strength are observed (Delgado-Sánchez et al. 2018).

In the present study, only samples with bonded plates were systematically tested and compared with other soft, rigidized and rigid board CFs, under identical conditions. To avoid any difference due to size, and to improve the reproducibility and robustness of the received

data, all C/C composite samples were prepared and analysed with identical dimensions (diameter of 26 mm and thickness of 10 mm), found to be a good compromise in terms of diameter/compression area ratio. Another important requirement was to test all samples along the same OP (z-axis) direction, deduced from the CF manufacturing orientations (also seen in Fig. IV/2-3).

IV/2.4 Structural and elemental characterisation

Raman spectroscopy was performed only for the selected sample for chemical stability tests, seen as suitable carbon host candidates for application tests. The structural properties of the studied samples were performed following the analysis procedure and using the same analyser as described in Chapter III/2.4.b. Raman spectra, before and after the CVD process, were compared and the results from bands' deconvolution were discussed.

Elemental analysis (i.e., C, H, N, S and O wt.%) of the C/C composites was carried out following the method explained in Chapter III/2.4.c, using a Vario EL Cube (Elementar, Germany) elemental analyser (seen in Fig. III/2-5).

IV/2.5 Chemical stability of C/C composites in molten lithium salts

For testing the CF chemical stability in molten LiOH and in the Li-based PC, identical steps of PC synthesis and chemical reactivity tests were performed as in Chapter III/2.3.a. Hence, C/C composites with identical dimensions as for the previously tested CFs were chemically reacted at a fixed ratio of alkali hydroxide (40:1) or PC mixture (40:1) (after the PC were synthesised).

The weight loss (evidenced in terms of burn-off, B-O), morphology, and surface texture analyses were performed after the reactivity test followed by salt removal. Obtained results were compared to the results derived from the used soft CF and the rest of the investigated CFs. Again, the reaction rate of the C/C composites was associated only with the carbons' chemical reactivity in molten LiOH or $\text{Li}_4(\text{OH})_3\text{Br}$, by taking into account the performance of the test in an inert atmosphere, using nickel crucibles and under defined temperature conditions (650-750°C).

IV/2.6 Preliminary analysis of stoichiometric Li-based PC, alone or in contact with CF host

IV/2.6.a In-situ studies

The Li-based PC, alone or in contact with the CF, was studied in-situ by the use of a hot stage placed inside the chamber of the SEM, the latter being described in subchapter II/2.5.a. As seen in figure IV/2-4, the hot stage allows the control of the temperature in the sample chamber, and the presence of a transparent cover makes it possible to observe and record any change in the material morphology. In addition, the use of this specialised sample holder allows the morphological investigation of the energy storage material under an inert atmosphere during the heating or cooling step. Indeed, the hot stage was chosen for the possibility of controlling the heating rate from 0.01 up to 2°C s^{-1} while having a free cooling afterwards and simultaneously investigating the PC structure in real-time.

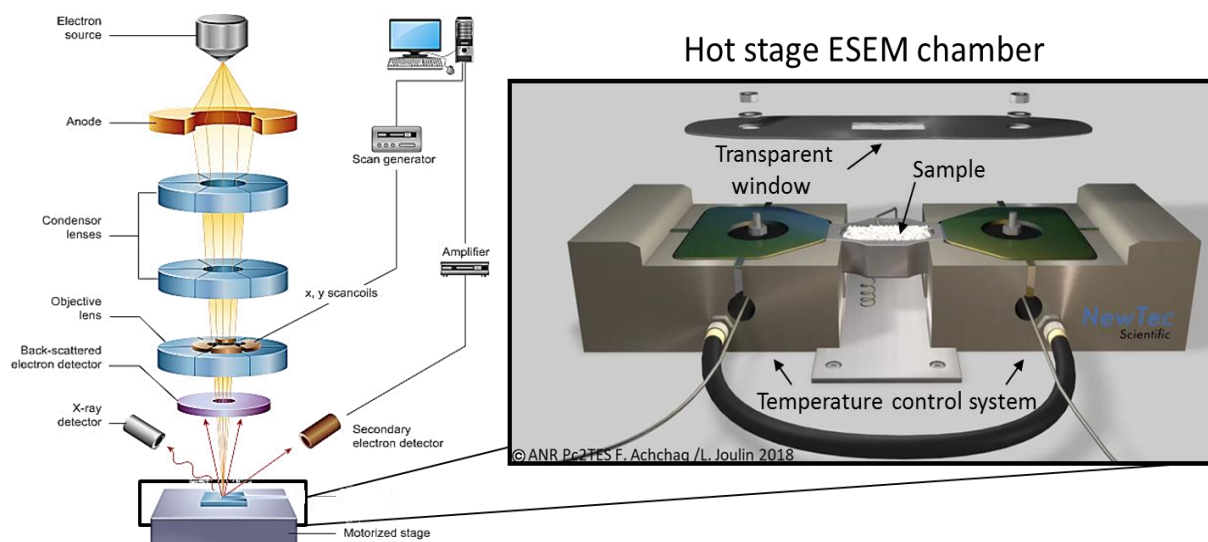


Figure IV/2-4 Schematic representation of the hot stage sample-holder placed inside a SEM chamber (modified after the ANR Pc2TES video presentation).

The in-situ morphology studies of stoichiometric Li-based PC, alone or in the presence of CF hosts, were performed and analysed by our project partners at PLACAMAT (Plateforme Aquitaine de Caractérisation des Matériaux) - UMS 5295 and at the Institute of Mechanical Engineering - UMR CNRS 5295, as part of the joint collaboration within the Pc2TES project.

IV/2.6.b Structural properties analysis

High-resolution X-ray diffraction was employed to observe XRD patterns for confirming the structure of the PC, synthesised according to the stoichiometric LiOH/LiBr ratio, before or after infiltration into a CF host. In addition, the stoichiometric PC was identified by structural analysis of different Li-based compositions produced by varying the synthesis protocol and the LiBr/LiOH ratio according to the LiOH/LiBr binary phase diagram (seen in Fig. III/3 29). The diffraction patterns were recorded in the 2θ range between 8 and 80° (with a scan step of 0.017°) at room temperature with a PANALYTICAL X'PERT 3 Powder diffractometer using a Mo anode ($\lambda = 0.71073 \text{ \AA}$).

These tests were performed and analysed from our project partners at the Institut de Chimie de la Matière Condensée de Bordeaux (ICMCB) - UMR CNRS 5026), as part of the Pc2TES project collaboration.

IV/2.6.c Thermal properties analysis

A preliminary thermal analysis was carried out on separate LiOH and on cylindrical samples (height 5 mm, diameter 1mm) of the synthesised PC, alone or in contact with the CF host, in order to evaluate their thermal properties and their potential for storing thermal energy. Prior to the analysis of the materials of interest, the DSC was calibrated using standard materials of high purity, according to a specific protocol over a chosen temperature range. The temperature charge/discharge program was defined as follows: (i) from room temperature to 450 or 410°C for LiOH or Li₄(OH)₃Br, respectively, at a heating rate of 20°C min⁻¹; (ii) dwell time of 5 min at the maximum temperature; and (iii) cooling rate of 6°C min⁻¹ to the initial temperature.

Lab-made Inconel crucibles were loaded with a sample of LiOH or PC, the latter alone or as a hybrid material with one CF host, and were analysed by DSC one after the other under a continuous flow of dry argon (30 mL min⁻¹). Each of the different samples was tested in DSC by performing at least seven successive charge/discharge sequences to obtain their preliminary thermal analysis. The low number of charge/discharge sequences is due to the highly time-consuming process of establishing the enthalpy-temperature function for a higher number of sequences. Thus, future tests are planned to observe the behaviour of the PC and of the hybrid CF-PC material up to 100 successive cycles of charge/discharge. The identified heat flow and temperature-time signals of the cycles performed for the examined samples were recovered and analysed further.

The presented DSC results will be shown below, but new tests are already being carried out in the laboratories of our project partner at the Institute of Mechanical Engineering - UMR CNRS 5295, as part of the Pc2TES project tasks.

IV/3 Results and discussion

IV/3.1 Morphological characterisations of C/C composites

IV/3.1.a Porosity and density

As expected, the deposition of pyrocarbon on CF preforms resulted in an increase in the final mass of the produced C/C composites, without any observed change in their total volume. Table IV/6-1 presents porosity and density results, with additional information on the C/C composite properties. The change in mass led to a linear increase of bulk density with deposition time, as seen in Fig. IV/3-1 a). This finding can be attributed to the very low density of the soft CF preforms and to their high average pore size. The bulk density ranged from 0.142 to 0.363 $\text{g}\cdot\text{cm}^{-3}$, whereas the produced C/C composited maintained their porosity in the range from 91 to 78 %, respectively. As noticed from other studies, longer CVD time and enhanced pore size reduction should result in a gradual increase of materials density (Shao et al. 2019).

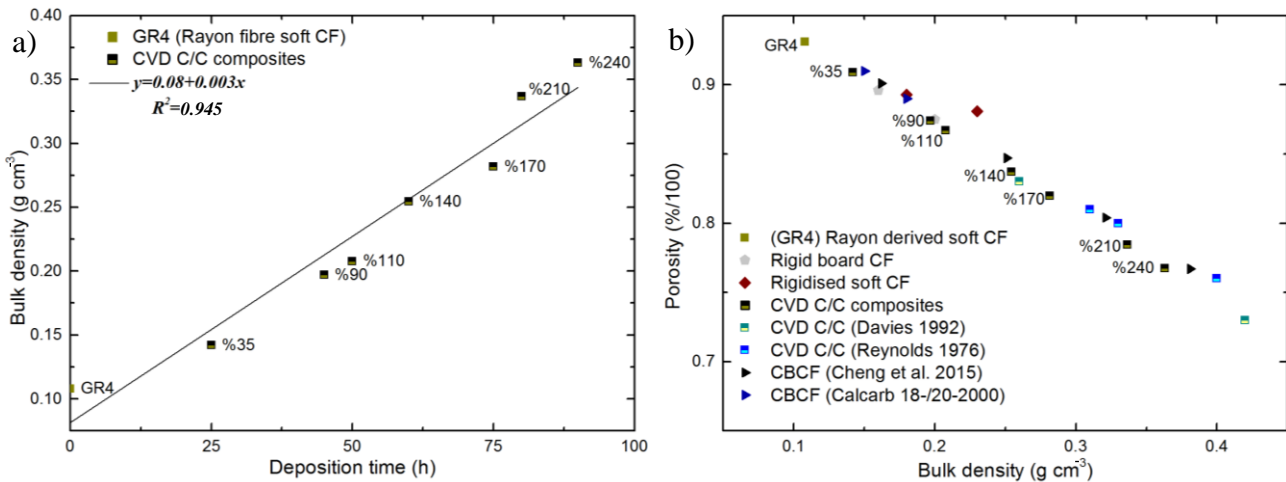


Figure IV/3-1 a) Bulk density ($\text{g}\cdot\text{cm}^{-3}$) as a function of CVD deposition time and b) Porosity of prisitne CF preform, produced C/C composites as well as a few other carbon fibre composites, as a function of their bulk density.

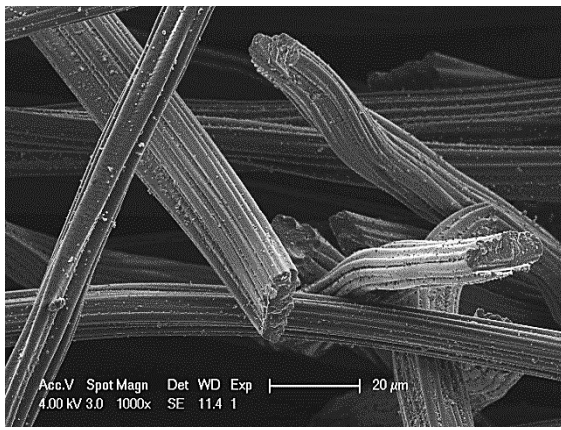
Given the importance of high porosity of the carbon host, it is a good point that the prepared C/C composites (at low weight increase) have a porosity similar to - or only slightly lower than - that of the examined rigid board CFs, at identical material density. The higher porosity of the rigidized soft CF is evident due to the partial and peripheral presence of carbon binder, not affecting the high initial porosity of the original soft CF. As expected, by increasing the pyrocarbon deposition time, the void fraction is decreased accordingly. Thus, the effect of

materials' bulk density on their porosity appears similar to that of other low-density CVD C/C and CBCF (carbon – bonded carbon fibre composites, i.e., compressed chopped carbon fibres and phenolic resin, subsequently carbonised) composites found in the literature and/or commercially available (Reynolds and Ardary 1976; Davies 1992; Cheng et al. 2015; Borner, Panerai, and Mansour 2017). Nevertheless, the porosity of some CBCF is slightly higher than the one of the produced C/C composites due to the intrinsic porosity of the resin binder, present on the fibre-to-fibre contacts/junctions, and to the effect of the final heat-treatment temperature. In the case of CVD, the pyrocarbon was deposited homogeneously on the fibre surface, which lowers the porosity of the materials, yet with expected enhanced properties compared to CBCF materials at similar final heat treatment and bulk densities.

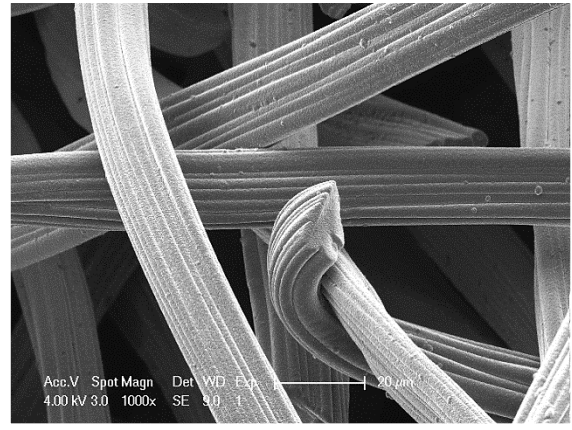
Even though a decrease of porosity was observed when compared to the pristine soft CF, better performance of the final CF-PC hybrid composite is expected from the reported improvements of the carbon host properties. Thus, future tests should investigate whether the studied improvement of the carbon host performances is reasonable and cost-effective when compared to the decrease of both porosity and energy density of the CF-PC hybrid composite.

IV/3.1.b Morphology investigated by SEM

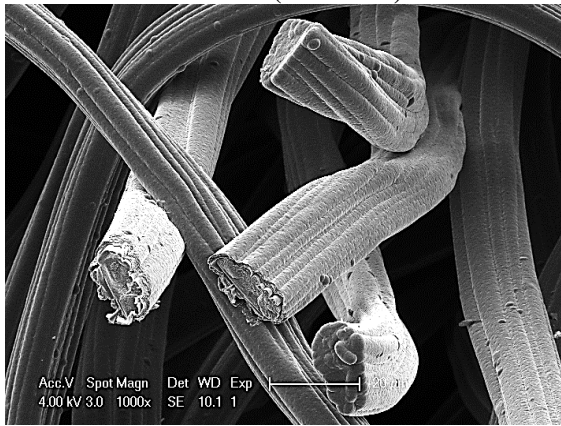
The random orientation of carbon fibres in the IP direction and the existence of additional OP needle-punch fibrous channels result in highly voluminous and permeable CFs, allowing homogeneous chemical reaction/deposition of the precursor gas during the CVD process. The deposition of pyrocarbon on the CF was indeed found to be uniform and without preferential direction within the CF preform, unlike what has sometimes been reported elsewhere (Hou et al. 2015; Xuefeng, Jie, and Kun 2019). From the performed SEM imaging analysis, it is clear that the bulk of all produced C/C composites still consists of interconnected open porosity (with porosity above 78%), even after the longest tested deposition time of 90 hours (seen in Fig. IV/3-2). Nevertheless, fibre-to-fibre discrete contacts and the area in-between carbon fibres, seen in the GR4 (SFG1aSC) carbon preform, was transformed into “fused” junctions in the produced C/C composites. The size and area of the freshly formed, rigid, connections increased with the deposition time. Generally, different types of junctions were formed within the C/C composites, such as X-type junctions linking two or more carbon fibres. Neighbouring fibres within the same fibre orientation also merged, producing a unique virtual fibre of different shapes. Others are mixtures of the aforementioned situations, in various arrangements, all of which being expected to be beneficial regarding composite thermal and mechanical performances.



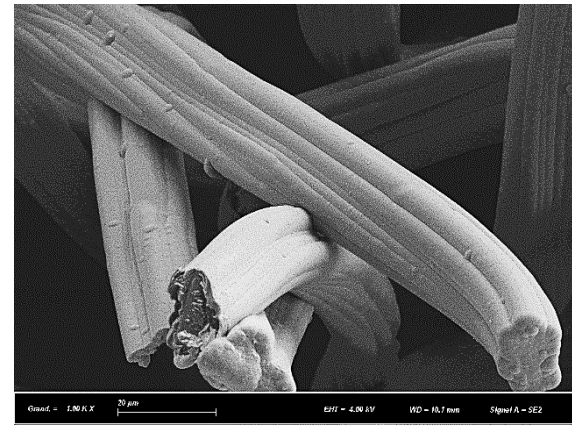
GR4 (SFG1aSC)



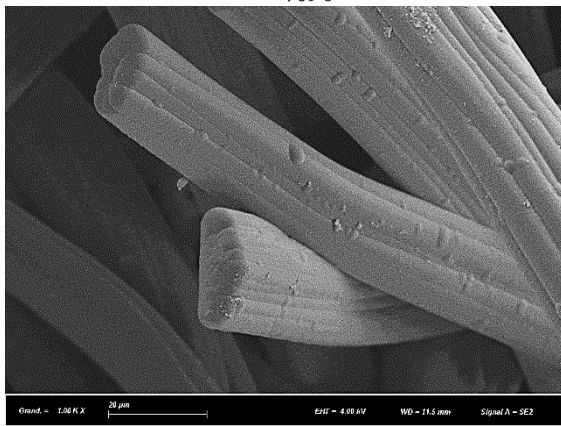
%35



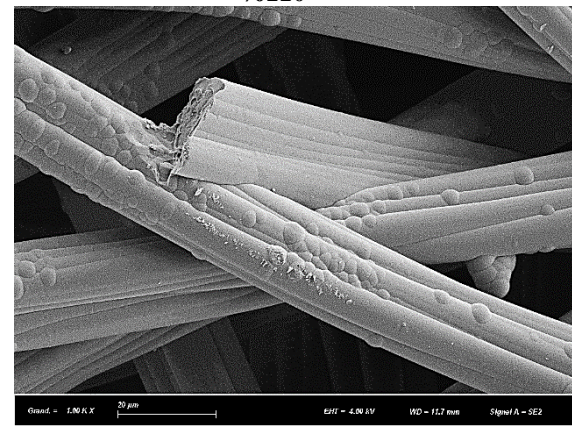
%90



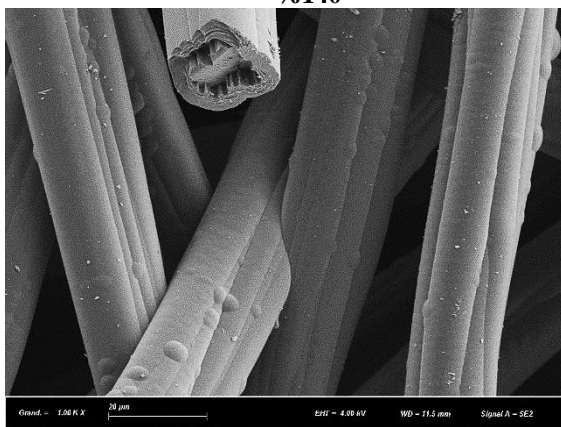
%110



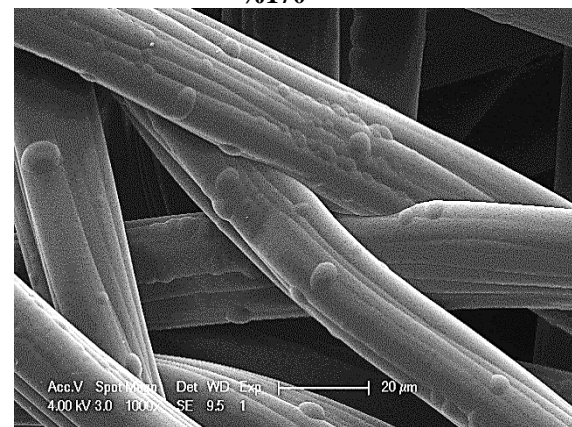
%140



%170



%210



%240

Figure IV/3-2 SEM micrographs of CF preform and produced C/C composites, for different weight increases with respect to the pristine preform.

From Fig. IV/3-2, it is evident that the pyrocarbon is homogeneously deposited, thus fresh fractures were therefore performed to study the pyrocarbon-carbon fibre interface and thickness of the pyrocarbon deposits on the cross-sections of the fibres. The prolonged duration of the CVD caused an obvious increase in pyrocarbon thickness as measured from the SEM micrographs, presented in Figure IV/3-4, and plotted as a function of deposition time in Figure IV/3-3. The deposited pyrocarbon stuck on - and enclosed - the uneven surface of the carbon fibres (already seen from samples %35 in Fig. IV/3-4), mechanically interlocking them. The increase in thickness of the deposit thus resulted in the formation of a smoother outer surface due to the improved alignment of the pyrocarbon (as seen from samples at high weight increase). Moreover, if the pyrocarbon-carbon fibre interface is well-formed, by means of mechanical interlocking and chemical bonding, the pyrocarbon deposition could be essentially considered as a part of the new composite fibre, with a larger diameter (values presented in Table IV/6-1) and modified properties.

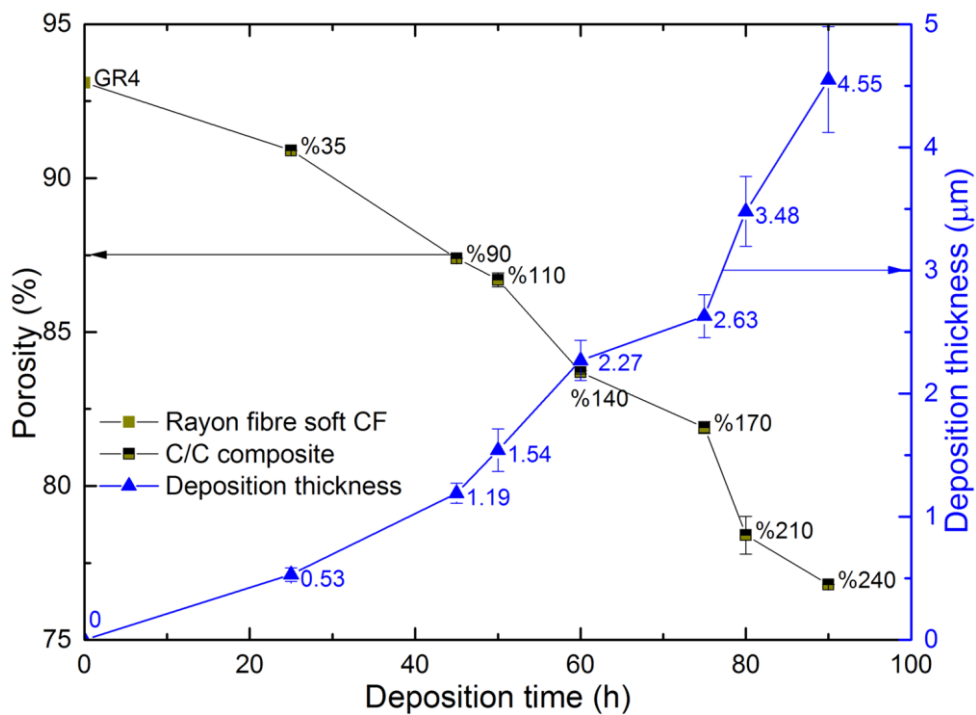


Figure IV/3-3 Effect of CVD deposition time on deposition thickness of the pyrocarbon layer and on C/C composite porosity.

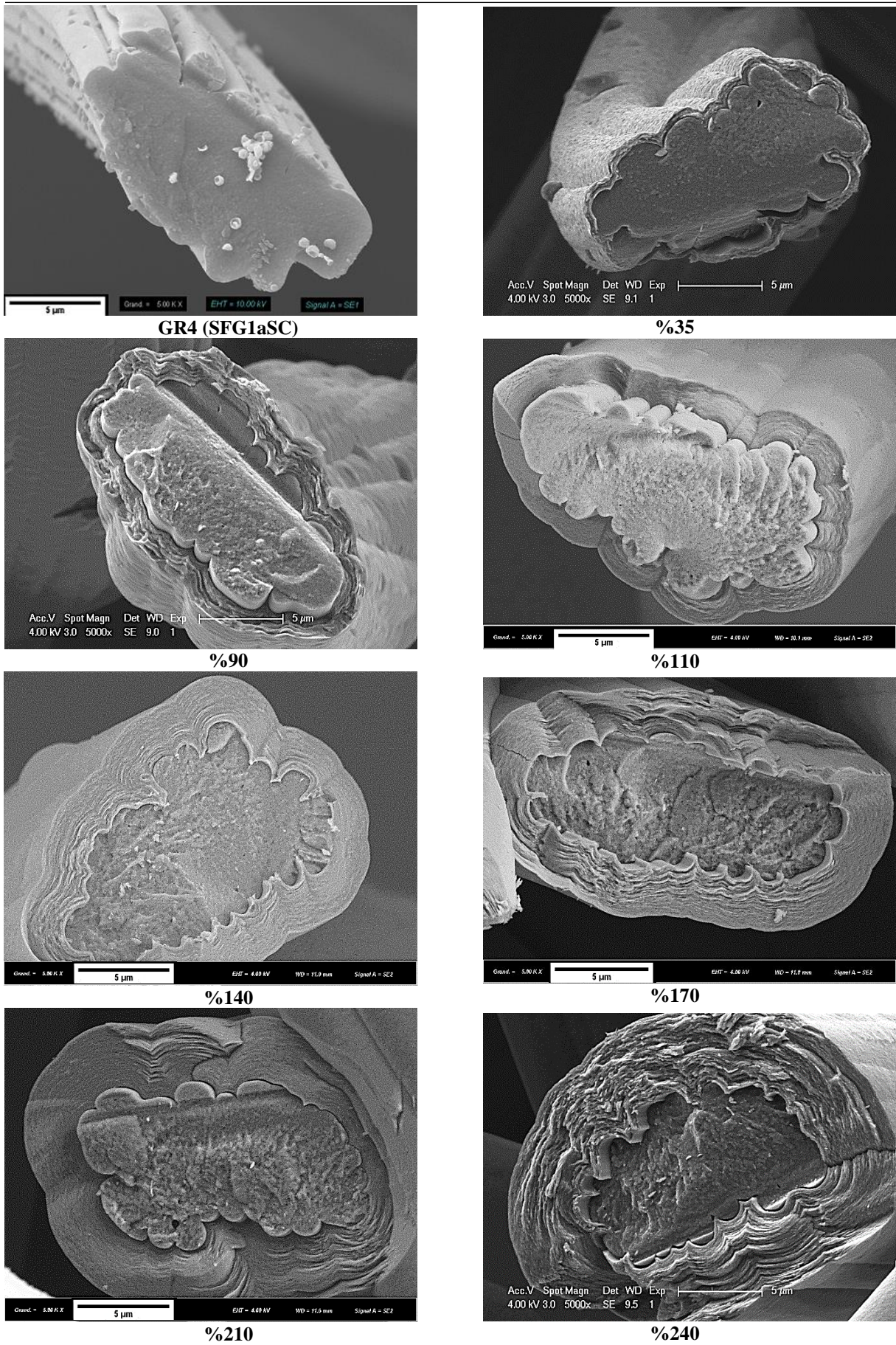


Figure IV/3-4 SEM images of freshly fractured fibre cross-sections, before/after CVD, for different weight increases with respect to the pristine preform.

IV/3.1.c Textural analysis with polarised optical microscopy

The polarised optical microscopy, introduced in subchapter IV/1.2.b and Figure IV/2-2, makes it possible to analyse different types of pyrocarbon due to differences in preferential orientation and textural irregularity, quantified by measuring the extinction angle (A_e). The measurement of the latter is linked with the use of the A_e scale, correlating the observed pyrocarbon texture to a scale-defined angle. Broadening this way the characterisation of the pyrocarbon morphology, we can determine if the pyrocarbon deposits are reproducible during the preparation of C/C composites at different deposition times, at constant CVD protocol and starting CF preform. Nonetheless, the information of this analysis can be also correlated to the mechanical, heat transfer and oxidation stability properties of the produced C/C composites, directly influenced by the pyrocarbon nanotexture (Vignoles 2015).

Optical microscopy analyses were performed on the pristine CF preform, on three C/C composites at different final weight increases (very low, medium and high), and on one additional C/C composite (%650) performed within two separate CVD cycles. The latter C/C composite was exceptionally prepared for comparison purposes with the other samples derived from a single CVD process. Seen in Figure IV/3-5, each resin-impregnated investigated material is presented by its natural light optical micrographs, followed by software-treated micrographs with anisotropy and orientation maps.

The natural light optical micrographs (left column in Fig. IV/3-5) already presents the different grayscale dissimilarities of samples' elements (resin, pyrocarbon, and carbon fibre), due to their intrinsically different reflection coefficients. The micrographs in the middle column present quantified information, i.e., the basis on which pyrocarbons' extinction angle (A_e) is defined. The observed edge orientation on the reference soft CF sample, GR4 (SFG1aSC), is affected by the fibre orientation and the depth of the image, or by a slight texturizing effect of the nearby isotropic resin, rather than by the presence of textured graphene layers. This and the following results confirm that the carbon fibres of the CF preform are poorly textured. Generally speaking, the nanotexture of the pyrocarbon deposits, for all prepared C/C composites, was optically anisotropic, yet to different extents and slightly dissimilar for each sample. Since the deposit thickness was lower than 1 μm , the pyrocarbon texture of sample %35 was difficult to analyse in polarised light. Nonetheless, the extinction angle varied between 6° and 10° , suggesting a weakly anisotropic deposit – dark laminar (DL, codes of pyrocarbon species given in Fig. IV/2-2). In the case of samples %90 or %240, the A_e progressed from the inner to the outer zone of the deposited pyrocarbon, from 10° (SL) or 5° (DL) to 20° (RL) or

13° (SL), respectively. In both cases, the pyrocarbon nanotexture evolved progressively through heterogeneous transition zones (also seen in Fig. IV/5-1). Thus, when a single-stage CVD process was performed, it was observed that the obvious changes in nanotexture anisotropy were continuous, with no clear transition zones. In contrast, the additional sample (%650) presented two distinct deposition layers, the inner one being highly ordered, 21° (RL), and the outer one being poorly ordered, 6° (DL), with clear boundaries between the adjacent domains. The final column of Figure IV/2-5 presents the micrographs showing that the anisotropic pyrocarbon is always layered around the carbon fibres, with the plane layers almost perpendicular to the cross-section of the fibre.

Moreover, the pyrolytic carbon nanotexture is well-known to depend on the CVD processing parameters and on the used gaseous precursor (Ehrburger, Lahaye, and Bourgeois 1981). Being aware of the complex mechanisms involved during the CVD process, even at a fixed CVD process as performed here, the morphology of the deposits was found to be slightly different from one to another deposition experiment. Thus, the observed textural and orientation variations and the progressive evolution of pyrocarbon nanotexture could be a result of the nucleation process, a classical effect in columnar grain growth. Thus, the initial randomly oriented columnar grains grow larger, forming a deposit of preferred orientation. Pyrocarbon nanotexture, at the interface with the carbon fibre, can be also influenced by the presence of carbon active sites (e.g. heteroatom groups and graphitic lattice vacancies), considered as catalysts for enhanced columnar grain nucleation (Besmann, Stinton, and Lowden 1988). Also, some abrupt nanotexture differences might originate from slight alterations of the gas-phase decomposition of the precursor gas (maturation of hydrocarbons) as a result of the occurring homo-/hetero-gaseous reactions and thermal cracking (Feron et al. 1999; Lavenac et al. 2001; Vignoles 2015). Finally, the presented results from the optical microscopy measurements also depend on sample preparation, polishing method, equipment and, to a less extent, on the operator. Accordingly, the results presented in this thesis are found to be consistent with each other, but comparisons with other similar works must be performed with great care.

Given that the results discussed from Figure IV/3-5 slightly deviate from one to another CVD experiment, the control of the pyrocarbon microstructure should be improved. Thus, future steps should be overtaken to ideally achieve stable RL pyrocarbon nanotexture depositions, seen to be graphitisable, additionally improving the final carbon properties towards their heat energy storage application.

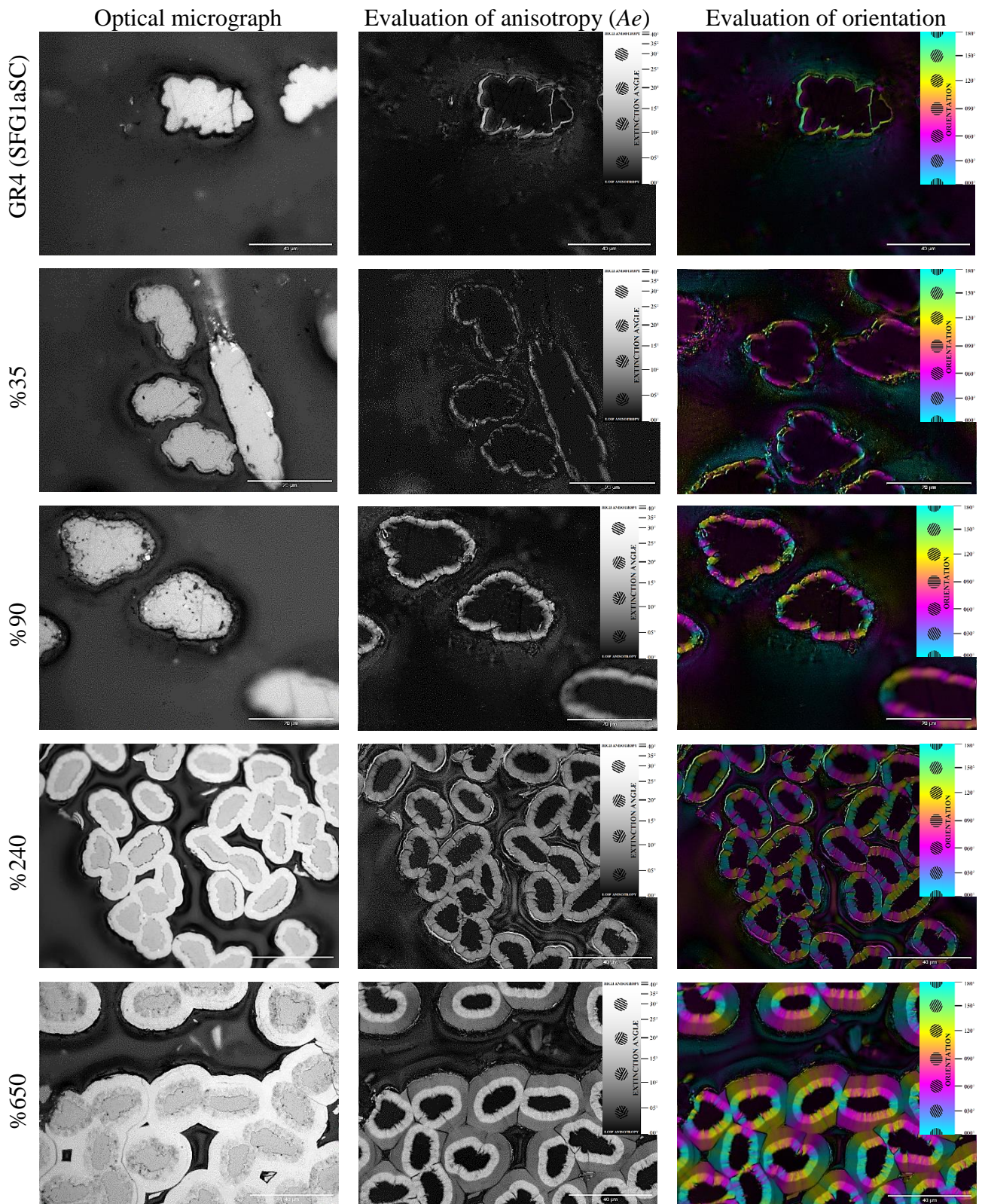


Figure IV/3-5 Textural analysis of pyrocarbon deposit by optical microscopy images: (left row) carbon fibres with pyrocarbon deposition; (middle row) pyrocarbon anisotropy determined through extinction angle (A_e); (right row) preferential orientation of pyrocarbon deposits.

IV/3.2 Physical properties of C/C composites

The presented morphological properties were correlated to the physical properties of the C/C composites, before being used in preparation and testing of the CF-PC hybrid composites. The production of C/C composites has been shown to provide improved and matrix-controlled physical properties with respect to the pristine soft CF. Thus, morphological changes and the formation for fibre junctions have improved heat transfer and mechanical loading, even at the lowest weight increase and hence the preservation of high porosity.

IV/3.2.a Out-of-plane air permeability

From the characterisation in Chapter II/3.3.a1, carbon fibre/felt morphology and tortuosity were considered highly important when CFs are evaluated for fluid flow and as carbon host materials for infiltration with molten salts. The same kind of investigation was also applied for the prepared C/C composites, expected to evidence differences in the permeability properties with regard to the previously evaluated CFs.

As the deposition of the pyrocarbon on the carbon fibres was found to be homogeneous all through the inner and outer zones of the produced C/C composites, the densification process should have little effect on the overall CF anisotropy, discussed in II/3.1c. Therefore, the C/C composite permeability should be solely affected by the evidenced modification of the original fibre morphology, since the final anisotropy of the C/C composite is considered similar to the one of the pristine soft CF. The corresponding values of out-of-plane (OP) permeability are given in Table IV/6-4 with additional information on the results' differences, compared to the permeability of sample GR4 (SFG1aSC).

Figure IV/3-6 presents the permeability results as a function of either porosity a), or fibre diameter b), respectively. In contrast to the commercial CFs, usually lacking a universal trend, the tuned morphological changes of the produced C/C composites resulted in controlled morphology-dependent permeability. The permeability decreased with the increase of the thickness of the pyrocarbon deposit, due to the increase of CVD time. Therefore, the highly permeable sample GR4 (SFG1aSC) was seen as a suitable candidate for the preparation of the C/C composites. It thus appears that the increase of the pyrocarbon deposit fraction resulted in the linear decrease of the OP permeability of the produced C/C composites as a function of both decrease in porosity and increase in fibre diameter, seen as the parameters having the highest effect on the fluid transport through fibrous carbons.

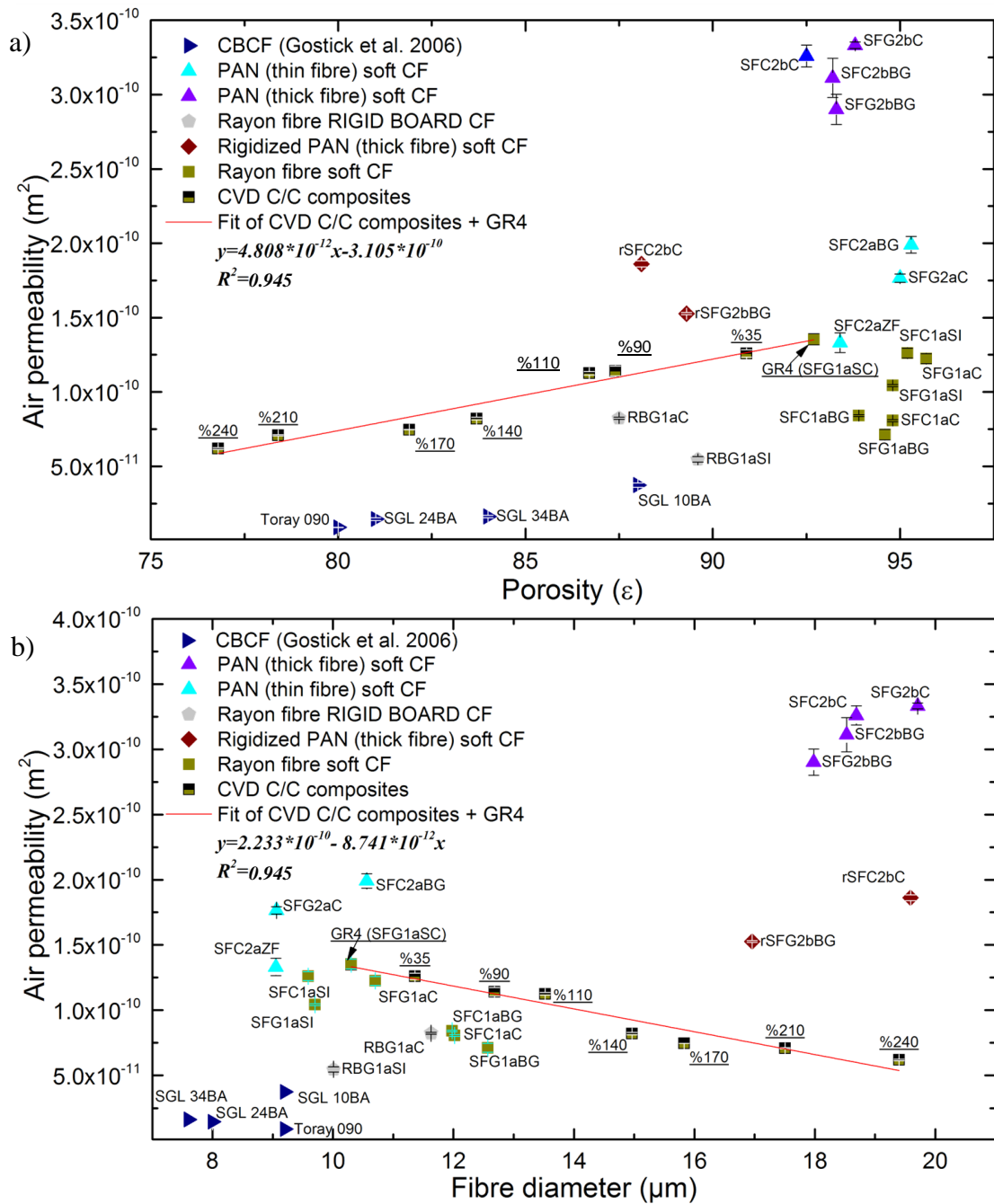


Figure IV/3-6 Out-of-plane permeability of all as-received CFs and modified C/C composites, as a function of: a) overall porosity, and b) average fibre diameter. The CF symbols and codes have the same meaning as in Chapter II, with the addition of the C/C composites (with underlined labels) and other materials, referenced in the legend of the figure.

Even at similar porosity, because of the carbonised resin binder on fibres' intersections, all CBCFs, including the investigated rigid board CF, presented lower permeability than that of the produced C/C composites. The C/C composites' fibres enlarged in diameter but overlapped at their contacts with each other with the increase of the pyrocarbon thickness. This morphological characteristic of the C/C composites presented a lower contact area and less tortuous flow (seen in Fig. IV/6-2) of the fluid when compared to the investigated rigid board CF. It would thus appear that the present C/C composites are produced with a smaller degree of pore-filling and pore-blocking mechanisms as compared to the big resin accumulations on the fibre junctions in rigid board CF. It can be also seen that the C/C composites present higher or similar permeability when compared to the Rayon-derived soft CFs. Added to the observed fibres' diameter overlapping, seen from the SEM analysis, it is also clear that the fibre surface becomes smoother and more regular with the evolution of the pyrocarbon thickness. As a result, the modified surface of the C/C composites' fibres present lower drag to the fluid flow when compared to carbon fibres of the pristine CF having an irregular surface and non-circular cross-sections.

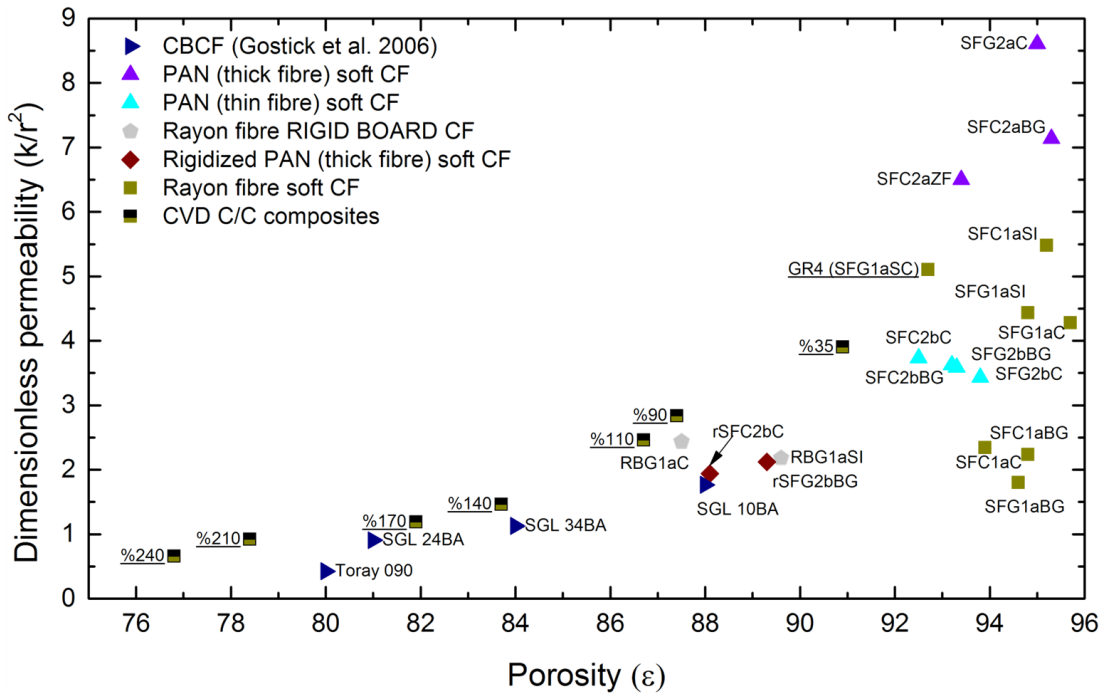


Figure IV/3-7 Out-of-plane reduced permeability of all CF materials as well as prepared C/C composites and a few other ones from the literature, as a function of overall porosity. The symbols have the same meaning as in Fig. IV/3-6.

To improve the evaluation of the new C/C composites further, Figure IV/3-7 presents the dimensionless reduced permeability, k/r^2 , as a function of materials' porosity. The corresponding graph clearly distinguishes %35, %90, and %110 as C/C composites with morphology and permeability properties suitable for impregnation with molten salts, at similar or slightly decreased porous volume compared to the examined commercial CF. Thus, the expected decrease of the final energy density of the CF-PC composites should be well compensated by the improved mechanical, heat transfer and chemical stability performances of the carbon host as a result of the CFs' modifications.

As previously performed for the commercial CFs in Chapter II/3.3.a3, the Kozeny constant (K_c) and hence the viscous tortuosity factor (η_v) of the produced C/C composites were calculated by using equation (II/21). Again and for the first time for low-density C/C composites, we demonstrate the validity of the identified master curve, equation (II/23), and its use for the experimental determination of Archie's coefficient, α (seen in Figure IV/6-2). The experimentally defined Archie's coefficient is therefore considered as an intrinsic material property relating the tortuosity factor (η_b) to the porosity of the low-density C/C composites, important for optimising the porous material behaviour in the present and other potential applications.

IV/3.2.b Mechanical properties

CFs alone or as parts of many different composites are widely used as structural reinforcements in various applications (Xuefeng, Jie, and Kun 2019). Herein, the final use of interest requires that the ultimate CF-PC composite possess sufficient mechanical properties to avoid irreversible deformation under compression stress, and maintain the valuable intrinsic material properties and predicted efficiency. From the obtained results in this thesis, we showed that commercial soft CFs are highly elastic structures with flexible fibre interlocking rather than rigid fibre connections, even after an intensive needle-punching process (as presented in subchapter II/3.3.b1). Thus soft CFs, including sample GR4 (SFG1aSC), presented viscoelastic-plastic non-linear deformation, which was reversible up to almost 50 % strain, yet under very low values of applied stress (seen in Fig. II/3-27). In former studies, the transfer of mechanical load through fibrous materials was improved by introducing a carbon matrix, chemically and/or mechanically interlocked to the carbon fibre surfaces and cross-sections, during the production of different C/C composites (Sharma et al. 2017). Hence, the CVD modification was seen as a reasonable way to introduce discrete but fixed connections between carbon fibres to increase the compression strength and rigidity of the commercial soft CFs.

Generally speaking, the compression properties of C/C composites are related to the mechanical properties of the carbon fibres, pyrocarbon matrix and the fibre-matrix interface, along with the morphological structure of the studied CFs (Reznik et al. 2002). The latter is also one of the reasons why the CVD modification was performed on the same CF, fabricated by a unique manufacturing process and carbon fibres. Therefore, the variation of the CVD time allowed us to attribute the observed compression behaviour only to the resulting change in composites' density and morphologies.

To investigate the effect of the final modification on the compression properties, stress-strain curves of C/C composites are shown in Figure IV/3-8, together with the curves of the unmodified soft GR4 (SFG1aSC) as well as the hyperelasticity model used to calculate its elastic modulus. At least two regimes of deformation are usually observed in the stress-strain curves of the prepared C/C composites (seen in Fig. IV/3-8). Initially, regime I presents a linear increase of stress with compression strain, defining an elastic deformation. In this region, a clear transformation from elastic-plastic to brittle materials is observed due to the change from moderate to sharp slope of the linear deformation, respectively. The use of plates glued on top and bottom sample surfaces (in the OP direction) resulted in a clear change of slope in the linear part and the transition zone between the linear elastic and plateau (plastic) regimes. Thus, the observed compression behaviour was in good correlation with studies of porous foam materials (Chollon, Delettrez, and Langlais 2014; Letellier et al. 2017; Delgado-Sánchez et al. 2018), where gluing the OP opposite surfaces of porous foams to rigid plates improved the transfer of the applied load in the OP direction, thus leading to realistic elastic properties. Consequently, the shift between regime I to regime II, the latter corresponding to pure elastic-plastic materials, is always continuous and non-linear (as in samples %35), whereas for brittle materials (%90 - %240), a sudden drop of stress is observed before the beginning of regime II. The instant drop of stress is mainly due to the sudden matrix failure at the weakest inter-fibre connections, perpendicular to the compression direction, thus completely disconnecting/fragmenting the pyrocarbon deposit in the OP direction. As a result, the bare carbon fibres rearrange until a new contact is re-detected between the detached matrix parts. The regime II of stress vs. strain curve in C/C composites again differs from elastic-plastic to a brittle material. The micro-cracking and gradual collapse of the IP fibre layers, connected with a thin layer of pyrocarbon, lead to a smooth plateau without abrupt changes in the stress-strain curve. Whereas for composites at a higher weight increase the simultaneous collapse of several consecutive IP fibre layers leads to a sudden drop of stress, resulting in a serrated plateau region.

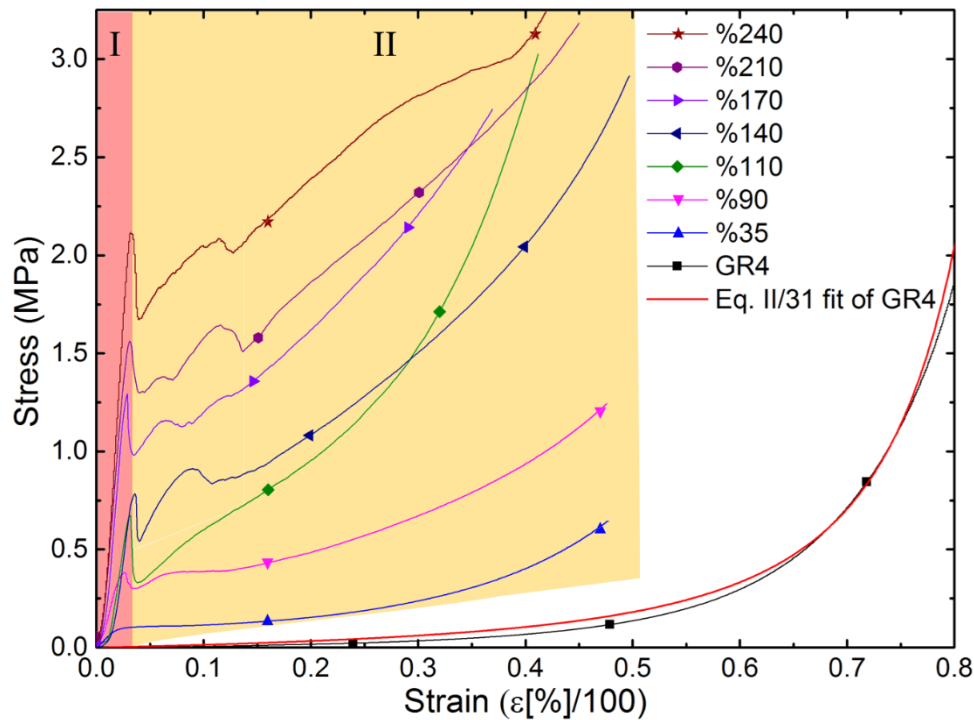


Figure IV/3-8 Stress-strain characteristics of C/C composites and pristine CF preform with its fit to equation (II/31) used for the calculation of the elastic modulus. Coloured zones present different deformation regimes of the C/C composites.

The pyrocarbon matrix deposited over the surface of carbon fibres led to a linear elastic behaviour and to the effective transfer of a much higher compression load absent in the viscoelastic and non-linear deformation of the pristine CF preform. Thus, it was observed that even at the lowest weight increase, the sample %35 presented sufficient fibres integration to assure efficient load transfer through the entire composite, by presenting a clear linear elastic behaviour. It is also observed that the mechanical properties of the C/C composites made with higher weight increases were improved due to the formation of new and additional reinforcement of the existing interfibrous connections. The transfer of the compression load should also be influenced by the mechanical interlocking and/or chemical bonding within the fibre-matrix interface, depending on morphological defects or irregularity of the ex-Rayon fibre surface and the presence of carbon active sites (S. Wu et al. 2016; Frueh et al. 2018). Therefore, improved mechanical interlocking and/or chemical bonding within the fibre-matrix interface was the main reason for choosing an ex-Rayon prior to an ex-PAN soft CF, as the latter is based on carbon fibres of circular cross-sections and improved carbon purity. Nonetheless, the nanotexture of the deposited pyrocarbon can also affect the crack propagation, thus present a dominant effect on the compression properties of C/C composites (Weisshaus, Kenig, and Sivegmann 1991; Savage 1993). Yet, pyrocarbon nanotexture differences, discussed in

subchapter IV/2.1.b, did not induce significant differences in terms of observed failure strains and proved to have modest or no influence on the mechanical behaviour of low-density C/C composites.

The present C/C composites are definitively different in terms of compression modulus and strength, being defined from the initial linear elastic deformation part and from the highest stress seen as the endpoint of the same linear part (yield strength), respectively. As expected, the values of compression strength and elastic modulus of the prepared C/C composites (presented in Table IV/6-4) both significantly increased with density (shown in Fig. IV/3-9 a) and b), respectively. The yield strength was detected (not observed for the soft CF), and the elastic modulus was increased even after the shortest CVD and the lowest weight increase (sample %35). Thus, materials' compression strength and modulus were clearly related to their bulk density.

Benefiting from the “fused” carbon network, the produced low-density C/C composites outperform than - or present similar compression strength and elastic modulus as - commercially available (including the one presented in this thesis) or lab-made CBCF and other CVD C/C composites found in the literature (seen in Fig. IV/3-9).

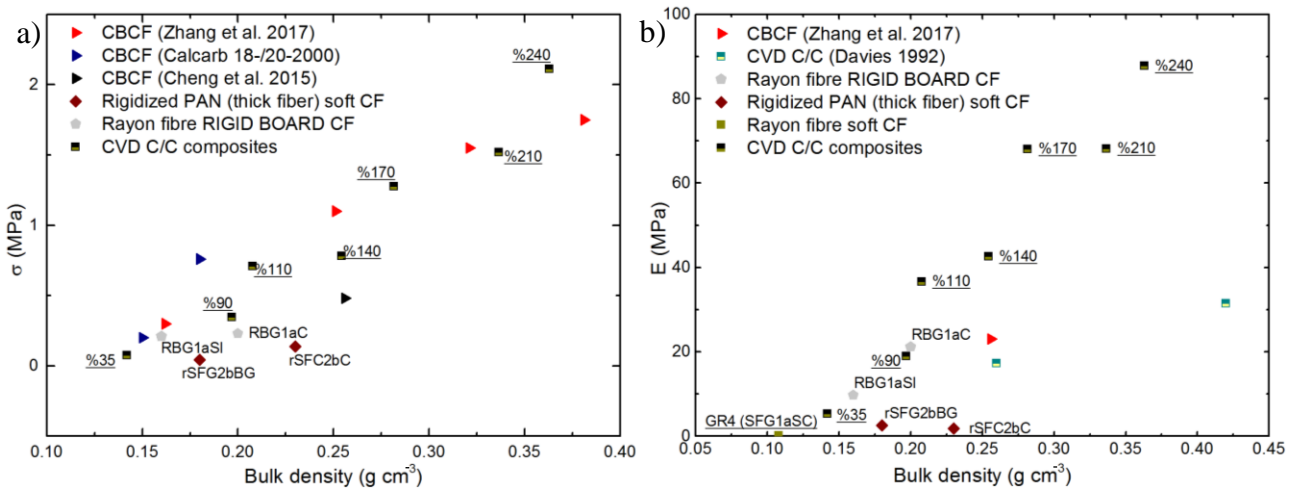


Figure IV/3-9 a) Yield strength and b) elastic modulus measured by compression. The CF symbols and codes have the same meaning as in Chapter II, with the addition of the C/C composites (with underlined labels) and other materials, referenced in the legend of the figure.

The compression strength and the elastic modulus were then plotted on a double-logarithmic scale as a function of bulk density, resulting in a linear ascending trend. This correlation is regularly, analytically and experimentally evidenced to give an accurate description of materials' structure, and the resulting compressive response of different carbon

foams and rigid board CF (CBCF) (Marinković and Dimitrijević 1985; Celzard et al. 2010; Chollon, Delettrez, and Langlais 2014; Zhang et al. 2017). The dependence of the yield strength and elastic modulus on materials' density follows a power law, which can be expressed as:

$$\text{Compression strength, } \sigma \propto \sigma_0 \times \rho_b^n \quad (\text{IV/1})$$

$$\text{Elastic modulus, } E \propto E_0 \times \rho_b^m \quad (\text{IV/2})$$

where σ_0 and E_0 are the yield strength and elastic modulus of the solid constituting the porous material, and the exponents n or m are related to the morphology and deformation mechanics or to the failure mode of the porous C/C composites, respectively.

As evidenced from Figure IV/3-10 a), the exponent n describing the behaviour of the yield strength of C/C composites along the OP directions has a value of 2.42. This value is consistent with previous uniaxial compression studies of carbon-bonded carbon fibre materials (Zhang et al. 2017). Comparable results were observed due to similarity in anisotropic fibre distribution, where again bonding points divided the fibres into random fibre segments. The values of the yield strength, σ_0 , of non-porous solid C/C composite were observed to be the lower boundary of yield strength values previously observed for high-density (low void-containing) C/C composites (Weisshaus, Kenig, and Sivegmann 1991). Yet as previously observed for other C/C composites and fibrous materials (Sahimi 1998; Zhang et al. 2017), the length and the orientation of the fibres can influence the variation of the stress transfer in the matrix, thus have a critical effect on the deformation mechanism and the yield strength of the final porous or solid material.

Figure IV/3-10 b) presents the use of equation (IV/2) to fit the elastic modulus data, leading to an exponent m of value 1.93. According to the percolation theory, found suitable to explain the used power law (Sahimi 1998; Celzard et al. 2010), the value of m (referred to as a "critical exponent") is closely related to the intrinsic characteristic of the structural bonds, i.e., to the pyrocarbon matrix in the evaluated materials. In 2D, 3D systems or intermediate systems of "intermediate dimensionality" due to their marked anisotropy such as the present C/C composites, the obtained value of the exponent m refers to purely central elastic forces, where each inter-bond fibre fragment acts as spring with the absence of angle-changing forces.

The lowest density sample, %35, was observed to slightly deviate from the trends in Figure IV/3-10, supposedly due to incompletely formed junctions, providing much fewer links for the stress transfer in the network and resulting in failure via independent micro-fragmentation and elastic-plastic deformation.

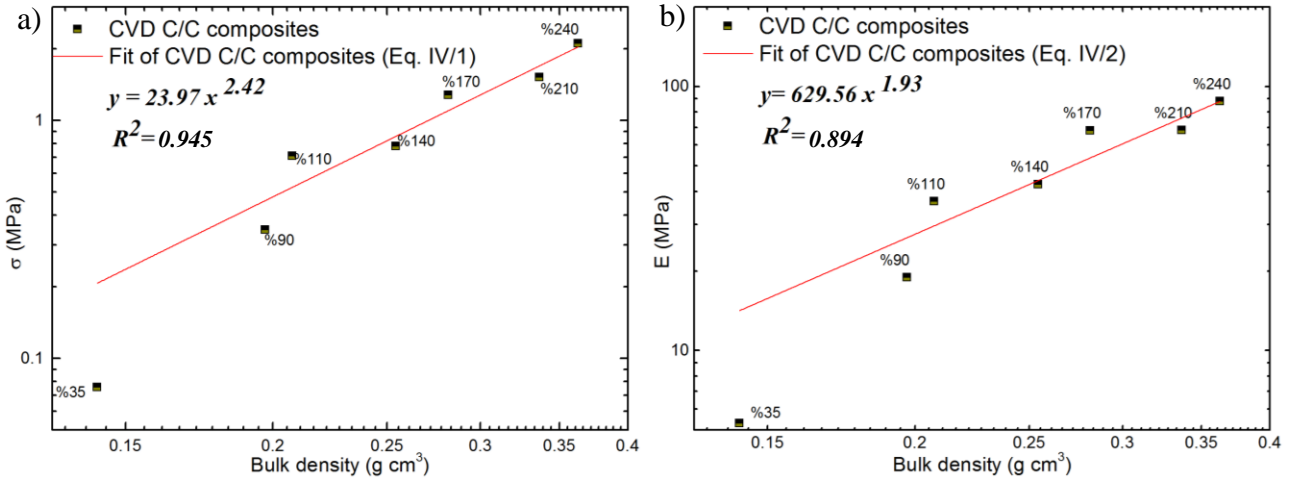


Figure IV/3-10 a) Compression strength and b) elastic modulus in double-logarithmic scale as a function of bulk density of CVD-prepared C/C composites. The solid lines correspond to application of: a) eq. (IV-1) and b) eq. (IV-2).

IV/3.2.c Thermal conductivity

Chapter II/3.3.c has shown that the main parameters influencing the thermal conductivity of the investigated carbon materials were CFs' morphology, structural properties of the carbon fibre, and the different characters of fibre connections. The lack of fixed links and the occurrence of thermal contact resistance between the carbon fibres in the soft CFs was observed to be the main materials' drawback regarding heat transfer performances. Accordingly, the production of C/C composites is a good way to improve the heat transfer between neighbouring carbon fibres and hence to increase the overall thermal conductivity of commercial soft CFs. Previous studies have shown that the pyrocarbon matrix can lead to improved thermal and electrical conductivities along with high chemical resistance of the resultant C/C composites based on CF preforms (Manocha 2003). Thus, CVD C/C composites are referred to as remarkable materials with highly stable thermal and mechanical properties and suitable for applications in which chemical, thermal and mechanical shock resistances must be very good (Sharma et al. 2017).

Herein, the improvement of the thermal conductivity of C/C composites with respect to soft CFs' was examined as a function of CVD deposition time and resulting differences in

composite morphology and bulk density. Figure IV/3-11 a) and b) presents the effects of structure and density modification on the thermal conductivities of the evaluated C/C composites, in both IP and OP directions, respectively. The deposition of pyrocarbon layers onto the existing carbon fibre network effectively supports novel solid transmission routes for heat conduction, thus leading to increased thermal conductivities, evident in the IP direction. The thermal conductivity in the OP direction was observed to be similar to the one found for the soft CF (GR4). The reason for the directional improvement of the thermal conductivity is seen as a consequence of the parallel alignment (deposition) of the pyrocarbon layers on the surface of already aligned carbon fibres, mostly in the IP direction. The second reason for the directional improvement of the thermal conductivity is the enhanced conduction of phonons and electrons along the basal planes (*a* direction) than through the plane (*c* direction) of the anisotropic pyrocarbon layers (described in subchapter IV/2.1.b), aligned along the fibre length. Therefore, as also shown in Table IV/6-2, the thermal conductivity in the IP is higher than in the OP direction and the anisotropy ratio, defined as $\kappa_{x,y}/\kappa_z$, thus increases with the bulk density. Thus, the increase of the anisotropy ratio is correlated to the amount of pyrocarbon connections on mostly IP-oriented carbon fibres, seen through the SEM analysis.

Benefiting from the reduced contact thermal resistance or the absence of less conductive ex-resin/fibre cluster connections, the produced C/C composites outperform the thermal conductivity of almost all carbonised and most of the graphitised commercial CFs (ex-PAN or ex-Rayon) and other CBCFs found in the literature. In some cases, the thermal conductivity is still lower due to differences in carbon structural anisotropy and graphitisation extent, which should lead to different thermal conductivity behaviours of the compared materials. Yet, the examined thermal conductivity values of the prepared C/C composites could be further improved if only rough laminar nanotexture was produced, the graphitisation of which might boost the thermal transport properties. Nevertheless, even if matrix-dominated, the thermal conductivity of low-density C/C composite should be seen as the result of phonons' solid conduction through the carbon fibres and the surrounding pyrocarbon deposit. Therefore, improved fibre-pyrocarbon interface connections could be considered beneficial for an additional increase of the C/C composites' thermal conductivity. Finally, the thermal conductivity of the C/C composites is also expected to increase with the temperature (Luo et al. 2004), and additionally improve the heat transfer in the CF-PC material, as the energy storage temperature should be in the range between 300 and 400°C.

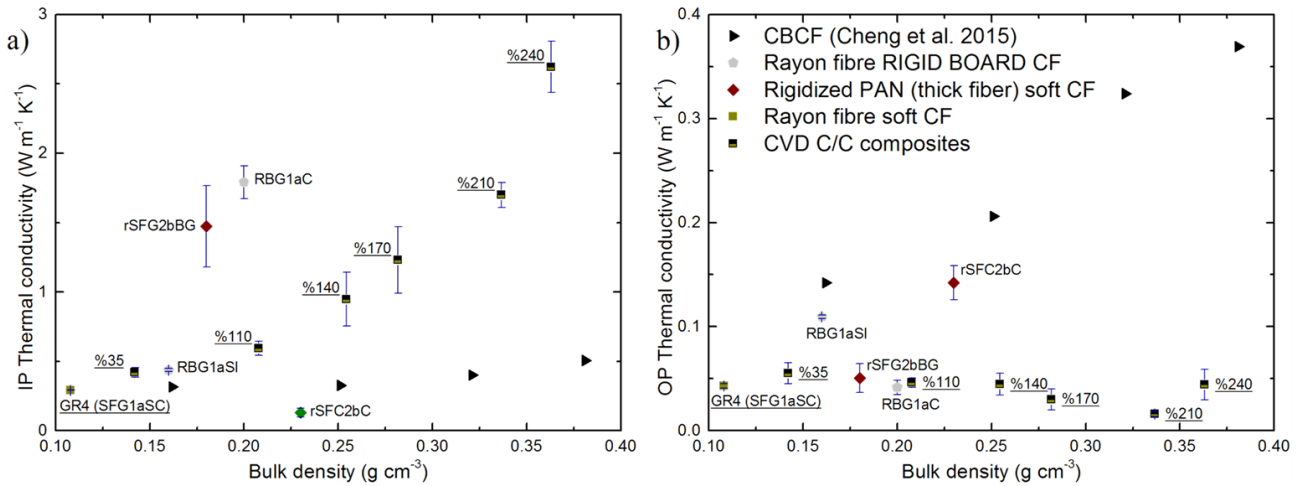


Figure IV/3-11 Thermal conductivity results in: a) IP direction, and b) OP direction, as a function of bulk density. The CF symbols and codes have the same meaning as in Chapter II, with the addition of the C/C composites (with underlined labels) and other materials, referenced in the legend of the figure.

IV/3.3 Chemical stability of C/C composites in LiOH or Li₄(OH)₃Br

In addition to their attractive mechanical and thermal properties, C/C composites are expected to present improved chemical stability when in contact with the concerned molten lithium salts. "Long-life" carbon hosts have to be essentially resistant to environmental conditions without being modified and, more importantly, without modifying the surrounding PC material either. In chapter III, the chemical reactivity of CF materials in contact with Li-based salts was studied to distinguish important material characteristics, revealing their chemical stability in the different phases or the lithium binary PC. It was observed that the rate of chemical reactions was mainly controlled by temperature and that the oxidation of carbon occurred due to the presence of oxygen contained in LiOH and to active carbon sites at the surface of the fibrous carbon materials.

As previously confirmed, the deposition of pyrocarbon can provide good protection for carbon fibre materials against chemical reactions in oxidative environments (Sharma et al. 2017; Zhang et al. 2018). The chemical stability of the C/C composites is promoted by the structural/textural characteristics of the pyrocarbon matrix, but also by the ability of materials to be stabilised (through heat treatment and/or use of oxidation inhibitors) (Fitzer and Manocha 1998). Thus, several studies highlight the high oxidation resistance of pyrocarbon coatings, due to the very low total/active surface area and the preferable orientation of the deposited aromatic layers forming an anisotropic lamellar structure (the basal plane much more stable toward

oxidation compared to its perpendicular direction – edge plane (c axis)) (Davies 1992; Ehrburger and Vix-Guterl 2001).

The aim of the advanced CFs' modification in this subchapter is to improve the chemical stability of commercial CF materials in contact with molten lithium salts by simple pyrocarbon deposition. Nonetheless, the obtained results should also evaluate the role of pyrocarbon morphology/properties in enhancing the chemical stability of the C/C composites and indicate significant ways to optimise the performances of the carbon host in CF-PC hybrid materials.

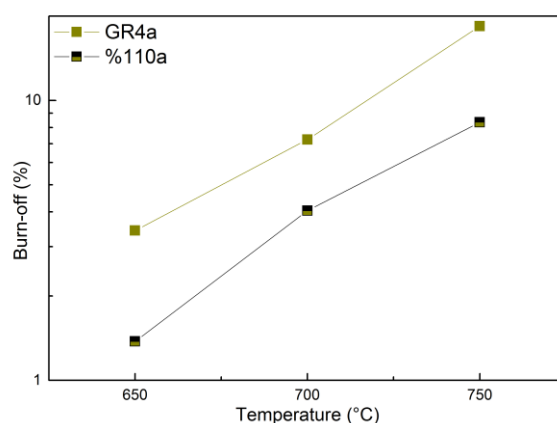


Figure IV/3-12 Burn-off (%) vs. reaction temperature results presenting the chemical reactivity of prepared C/C composites and that of the pristine soft CF in molten LiOH. The solid lines are only guides for the eye.

The principal objective is to investigate how the produced C/C composites resist oxidation when exposed to the chosen lithium salts under an inert atmosphere and at high temperatures (higher than the application temperature). A number of C/C composite samples were prepared at a similar final weight increase of ~110%, and their stability was evaluated in molten LiOH or $\text{Li}_4(\text{OH})_3\text{Br}$, at different final reaction temperatures and reaction times. Figure IV/3-12 shows the burn-off (B-O) results of C/C composites after chemical reaction in molten LiOH as a function of the final reaction temperature, as well as the results from the pristine soft CF used for the preparation of the C/C composites. Table IV/6-6 presents also the B-O results after chemical reaction in molten $\text{Li}_4(\text{OH})_3\text{Br}$, only at the highest final reaction temperature. Nonetheless, all B-O results show chemical stability of the C/C composites higher by more than 50% than that of the pristine soft CF, the latter being the most chemically stable ex-Rayon soft CF.

In order to find the reasons for the improved chemical stability of the produced C/C composites, the pre-/post-reacted samples were investigated with respect to their structural and textural characteristics.

The performed elemental analysis evidenced a higher carbon content of the prepared C/C composites with respect to the pristine soft CF (seen in Fig IV/3-13 and detailed in Table IV/6-5), mainly as a result of the applied CVD and the weight increase in carbon. The reduced presence of heteroatoms should also occur from the desorption of gaseous by-products resulting from the pyrocarbon nucleation reactions with functional groups on the surface of the carbon fibres. Thus, the higher C purity of the pyrocarbon deposit should be one of the reasons for the improved stability of the C/C composite in contact with LiOH, behaving as an oxidiser at high temperature.

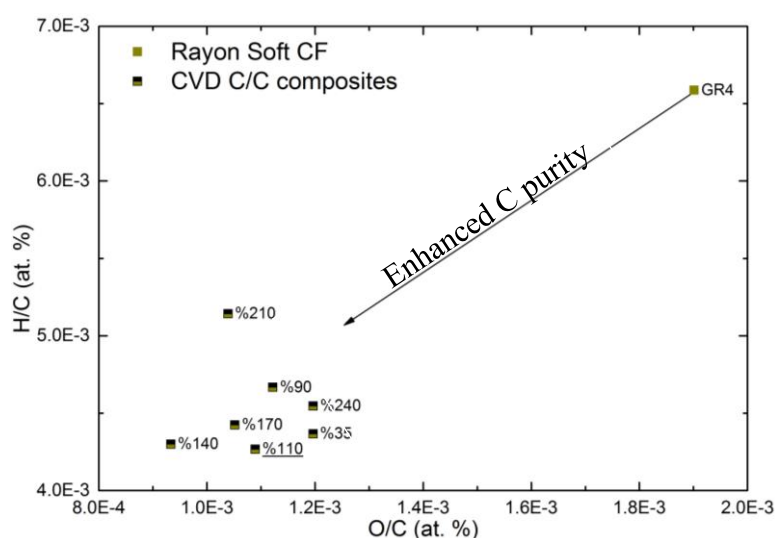


Figure IV/3-13 Van Krevelen diagram presenting the improved carbon content of the prepared C/C composites compared to the pristine soft CF. Sample %110, with underlined label, presents the C purity of materials used for the chemical stability tests.

While elemental analysis show improved C purity, suggesting a decrease in the content of surface heteroatom groups, Raman analysis presents a highly disordered graphitic structure. The Raman spectra of the investigated outer layer of the pyrocarbon deposit (presented in Fig. IV/3-14) were found to be strictly superimposed, as recorded from the top, middle and bottom zones of the examined C/C composite sample (%110). Such identical Raman features suggest high structural homogeneity of the outer surface of pyrocarbon deposits. Both first- and second-order Raman spectra parts are found to be poorly structured, suggesting the poor structural order along the carbon layers and their poor stacking order along the c-axis, respectively (described in Fig. I/2-3).

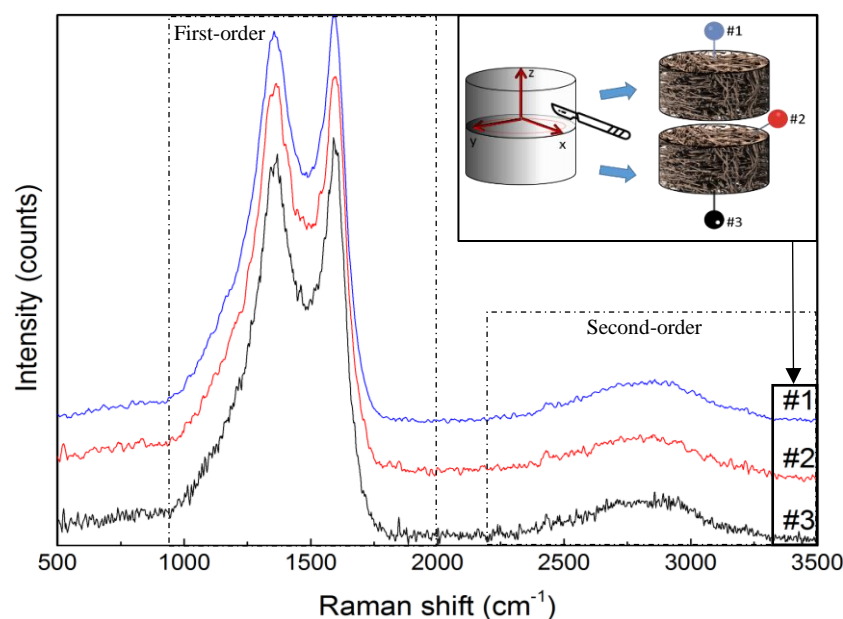


Figure IV/3-14 Raman spectra of C/C composite, %110, recovered from three different regions of the investigated sample, schematically presented in the right top corner. Dashed zones present first- and second-order of the Raman spectra shifted with respect to each other for easier viewing.

The deconvoluted first-order Raman spectra of sample %110 present broader and less resolved D_1 and G bands compared to the one of the pristine soft CF (seen in Fig. IV/3-15). The estimated full width at half maximum values (FWHM) of the deconvoluted D_1 band, 150 cm^{-1} , suggests the high amount of structural disorder of the deposited pyrocarbon layers. Thus, according to the classification of Bourrat et al. (2006), the evidenced high FWHM of the D_1 band can be classified as a regenerative rough laminar pyrocarbon microstructure. The proposed classification is in good agreement with our polarised light optical microscopy analysis and the high extinction angle (A_e) (usually higher than 15°) of the outer zone of the pyrocarbon deposits, confirming the presence of regenerative rough laminar pyrocarbon texture. Although the Raman features indicate a heavily faulted turbostratic pyrocarbon surface, the highly anisotropic (regenerative rough laminar) texture is advantageously graphitisable and can lead to improved graphitic properties when heat-treated at a higher temperature (above 1500°C) (Farbos et al. 2014). Thus, a highly ordered graphitic structure can be realised if seen beneficial for the improvement of the chemical stability of the C/C composites in molten Li-based salts.

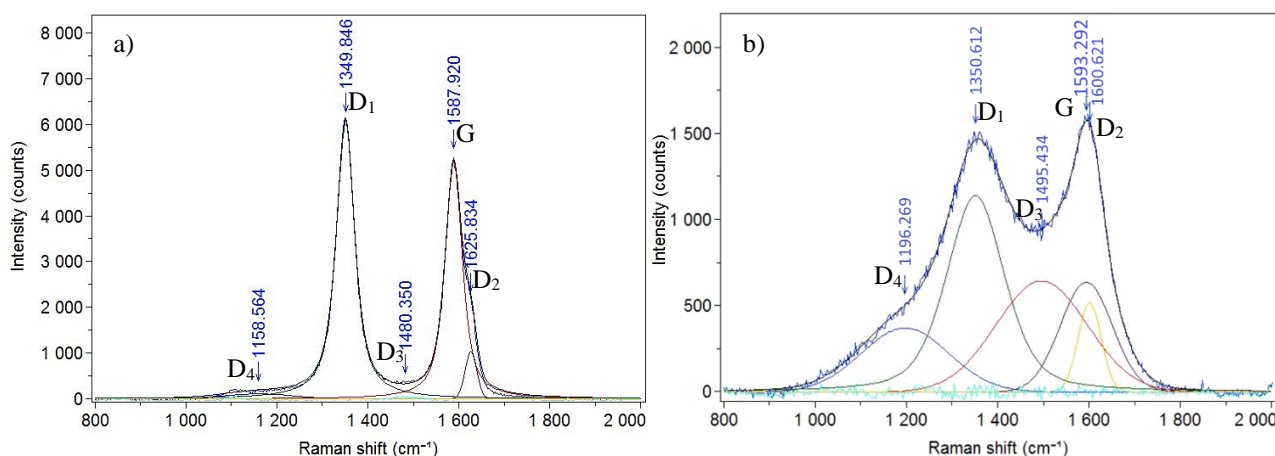


Figure IV/3-15 Deconvoluted Raman spectra of: a) GR4 and b) %110. The scatter curves indicate the measured intensities and the solid smooth lines represent the fits, with presented Raman shift (cm^{-1}) at full maximum and band code.

Evident from the chemical stability tests in Chapter III, high elemental purity and absence of surface functional groups had paramount importance over the chemical stability of the examined commercial CF, when in contact with molten LiOH or $\text{Li}_4(\text{OH})_3\text{Br}$. In agreement with the results from Chapter III, an improved C/C composite chemical stability should be evidenced from the increased carbon content and the reduced level of surface heteroatom groups, simultaneously not influenced by the disordered pyrocarbon structure. In a good correlation with our results, the presence of oxidising metallic salts was previously observed to have a catalytic effect on the oxidation rate of C/C composites. Once more, redox reactions occurred through similar mechanisms, by interactions between the catalyst and the oxygen groups present on the carbon surface (Wu and Radovic 2005; Bevilacqua, Babutskyi, and Chrysanthou 2015).

To better understand the mechanisms of chemical reactivity of the C/C composites tested and to improve information on the chemical stability of the disordered pyrocarbon structure, materials' investigation was continued with SEM analysis. Initially, the outer layer of the pyrocarbon deposits was observed and compared to the morphological modification pattern of the soft CF preform. Figure IV/6-4 presents the micrographs of the C/C composite surface morphology before and after reaction in molten LiOH or $\text{Li}_4(\text{OH})_3\text{Br}$, along with the same for the pristine soft CF. In Chapter III, the carbon fibre surface of the used CF preform was observed to be uniformly etched, creating submicron pits during the surface contact with LiOH or $\text{Li}_4(\text{OH})_3\text{Br}$ and the chemical reactions with the carbon surface functional groups. Contrary to the latter observations, the outer pyrocarbon surface was seen unmodified, retaining

its original morphology, even after chemical reaction with the highly reactive LiOH at the highest tested temperature and the consistently expected increased chemical reaction kinetics. Nonetheless, SEM analysis of the pyrocarbon surface also revealed the existence of cracks and openings randomly occurring on the outer layers, the latter enveloping the carbon fibre frame (seen in Fig. IV/3-16). As observed by Zhang et al. (2012), micro-cavities can occur on the pyrocarbon deposit due to the mismatch of the coefficients of thermal expansion between the pyrocarbon deposits and ex-Rayon carbon fibres, resulting in internal tensile stress during the cooling process after CVD. Thus, the formed micro-voids do not fully seal at the chemical reactivity temperatures (lower than the CVD temperature) and act as the entrance for the molten lithium salts in the composite interface. In addition, sample handling and unforeseen mechanical loads on the structure of the porous C/C composites might have resulted in the occurrence of additional cracks and fractures on the pyrocarbon matrix (of brittle nature), revealing the surface of the carbon fibres. As a result, the latter revelation caught our attention and led us to reasonable evidence for the measured carbon mass loss in the examined C/C composites. The confirmed and other existing submicron cracks/openings of the pyrocarbon matrix, as well as strong interfacial forces, should result in the rapid infiltration of the molten lithium salts into the composite interiors and their spreading over the carbon fibre surface. Thus, chemical reactivity takes place at the interface between the carbon fibre and the pyrocarbon layer and evolves towards the interior of the carbon fibre structure (deepening the initially present grooves), due to the higher amount of oxygen groups, attributed to the ex-Rayon origin (presented in Fig. IV/3-16 by yellow or red arrow, respectively). The micrographs in Figure IV/3-16 b) and c) once more reveals that the oxidative nature of the tested LiOH, and its lower level in the binary peritectic compound with LiBr, plays an important role even in the chemical reactivity with the C/C composite. Thus, the observed samples' morphology shows higher modifications in molten LiOH relative to $\text{Li}_4(\text{OH})_3\text{Br}$, corresponding with the calculated B-O results. Finally, the morphology of the examined C/C composite morphology clearly shows that the chemical reactivity of the outer pyrocarbon surface is negligible compared to that of the exposed carbon fibre surface. Also, the SEM observations are in good agreement with previously reported studies of the catalytic effect of metal salts on the air oxidative reactions occurring in C/C composites (Fitzer and Manocha 1998; Carabineiro et al. 1999; Bevilacqua, Babutskyi, and Chrysanthou 2015).

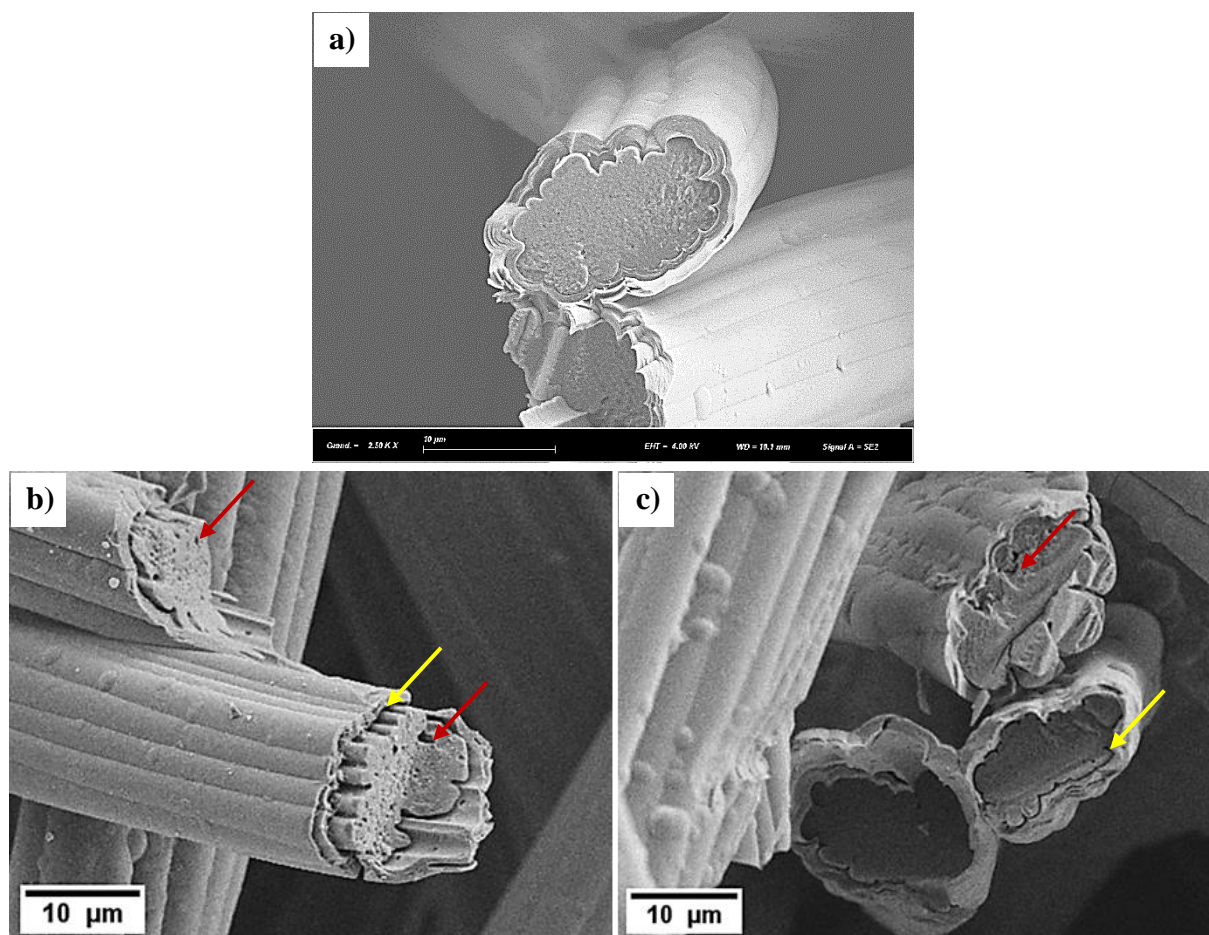


Figure IV/3-16 SEM images of microstructures of C/C composite: a) before chemical reaction, b) after testing in molten LiOH, and c) after testing in molten Li₄(OH)₃Br. The yellow arrows indicate the pyrocarbon/fibre disjoint interfaces and the red ones show the formation of pits on the carbon fibre surface.

Simultaneously to SEM, gas adsorption analyses were performed to examine the nanotexture properties, again for correlating the evaluated B-O results with the structural properties. N₂ and CO₂ adsorption analyses were used to study the nanotexture modification of the C/C composites before and after reaction in molten Li-based salts. As presented by the adsorption isotherms in Fig. IV/5-3, the adsorbed volume decreased because of the deposition of pyrocarbon with poorly or non-developed nanoporosity. Indeed the observed presence of regenerative rough laminar pyrocarbon structure, even if highly microscopically disordered and without a high level of parallelism, lacks developed nanoporosity due to the anisotropic arrangement of highly cross-linked graphene layers (Farbos et al. 2014). Thus, the subsequent calculated surface area/total pore volume and pore size distribution results (seen in Fig. IV/3-17) should only be due to the existence of pyrocarbon cracks and micro-voids allowing gas adsorption on the pyrocarbon/carbon fibre interface and in the surface nanotexture of the fibre.

The presence of nanotexture and surface-active sites in such regions of the C/C is therefore in good agreement with the morphological modification observed by SEM, resulting from the chemical reactivity in the molten Li-based salts.

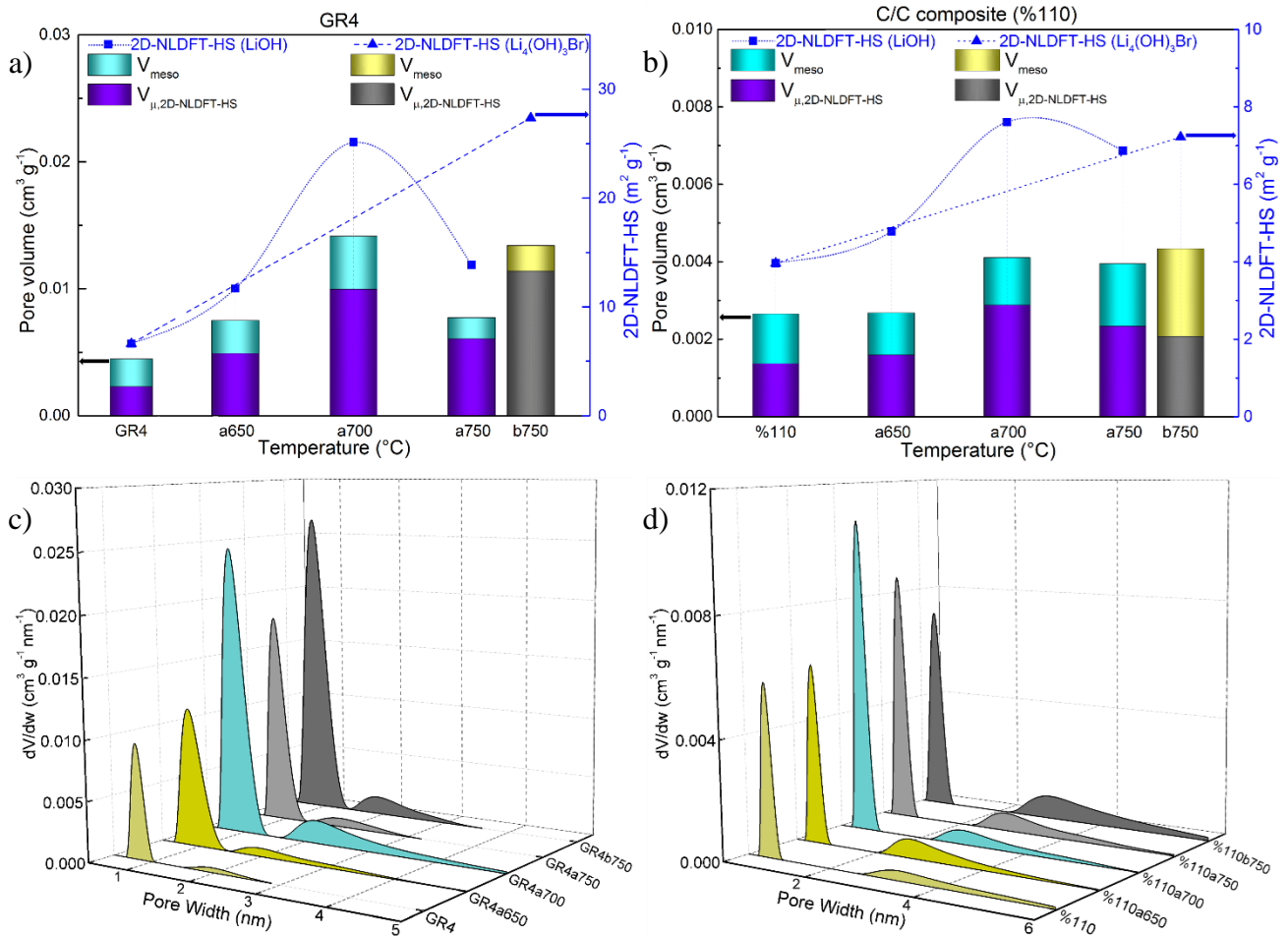


Figure IV/3-17 2D NLDFT-HS fit results for: a) or b) specific surface area (scatter symbols, where the dotted or dashed lines are only guides for the eye) and micro or mesopore volumes (stacked columns), and c) or d) pore size distribution for GR4 (left column) or %110 (right column) and their chemically reacted derivatives in the presence of LiOH or $\text{Li}_4(\text{OH})_3\text{Br}$ at different final temperatures.

Figure IV/3-17 presents the correlation between the results for the pristine soft CF and the C/C composites, thermally treated in LiOH, both showing a monotonous increase of the surface area/total pore volume with the temperature, up to a decrease at the highest tested temperature. As discussed in chapter III, the latter decrease should result from the intense chemical reaction of LiOH with the active carbon fibre surface, which would have the effect of destroying the existent instead of developing a new micro or mesoporosity. Once again, the presence of the chemically inert LiBr phase in the Li-based PC inhibits the chemical reaction

initiated between the LiOH phase and the carbon nanotexture, which only results in nanotexture development.

Clearly, the occurring redox reactions were controlled by the presence of nanoporous surface area, decreased in the C/C composite when compared to the pristine CF preform. Thus, the pyrocarbon deposits should be considered as highly pure carbon materials with negligible surface area when compared to the carbon fibres. Moreover, the decrease in the total surface area, seen in Fig. IV/3-17 b) and Table IV/6-6 should be proportional to the decrease in active sites, thus resulting in a decrease of the B-O results. Jiqiao et al. (2002) identified similar correlations of the decrease of active surface area with the micro-pores surface area for porous C/C composites subjected to an oxidation process. Finally, the increased chemical stability of the C/C composites was evident due to the decreased contact area between the molten LiOH and the active heteroatom surface present on the nanoporosity of the unprotected carbon fibres.

Additional confirmation of the descending trend of both total surface area and available reactive surface after pyrocarbon deposition can be derived from the estimates of the activation energy of chemical reactions occurring with C/C composites in molten LiOH. Again as in subchapter III/3.7, the chemical reactivity of the C/C composites yielded a linear correlation for the log of the examined B-O vs. $1/T$, following the linearised form of Arrhenius law - equation (III/4) (seen in Fig. IV/3-18). The observed B-O values of the C/C composite led to the estimation of activation energy ($141.8 \text{ kJ mol}^{-1}$) similar to that of GR4 ($147.9 \text{ kJ mol}^{-1}$). These values are well correlated to those of other C/C composites oxidised in the presence of catalytic metal salts (Wu and Radovic 2005). In addition, the use of Arrhenius law allows estimating the B-O values at the application temperature. However, lower values are expected with the PC ($\text{Li}_4(\text{OH})_3\text{Br}$), as observed from the measured B-O value (seen in Table IV/6-6) and discussed through the presented results in this subchapter.

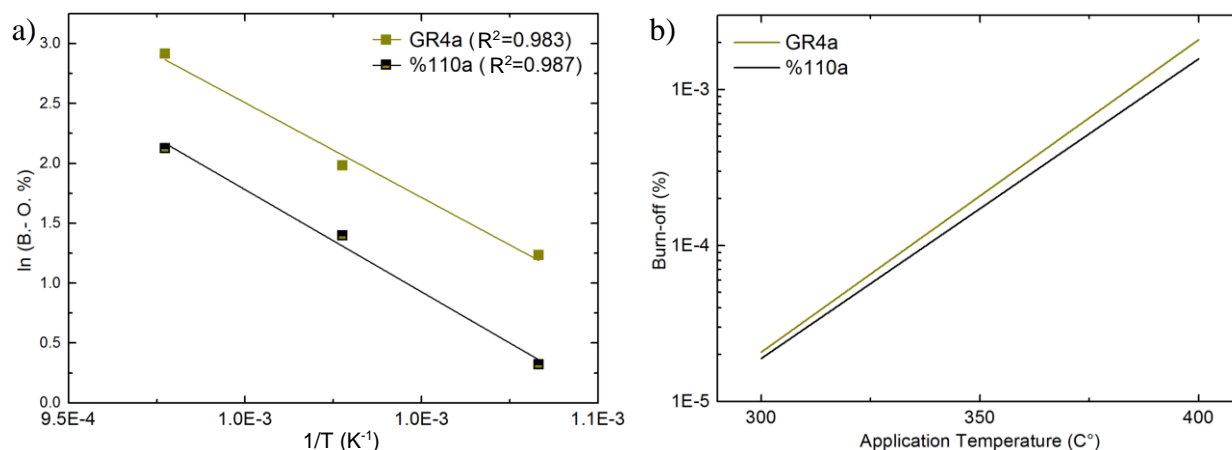


Figure IV/3-18 a) Application of equation (III/4) to the experimentally derived B-O data of C/C composites presented in Fig. IV/3-12 and b) estimated B-O values from the derived Arrhenius law expressions in the application temperatures of interest. The same for the pristine soft CF is introduced for comparison reasons.

IV/3.4 Preliminary results of morphological, structural and thermal analysis of PC, alone or in CF-PC hybrid material

The results of this part correspond to the early stage of the analysis of the foreseen application of the PC, alone or in the hybrid CF-PC material. Due to multiple technical issues and delays, the present data were received from partners of the Pc2TES project as late as one week before the submission deadline of this PhD manuscript. Therefore, this preliminary work could only lead to a first knowledge of the thermal and structural properties of the synthesised PC, the level of compatibility of the phases in the CF-PC hybrid, and the effect of only one single CF (when so many others have been studied here) on the performance of the hybrid material.

At the time of submitting this manuscript, a preliminary analysis of the synthesised Li-based PC in contact with CF host was performed only with sample CP5 (SFC2aZF). This material was initially chosen and investigated due to the evaluated morphological uniqueness of the CF subgroup based on PAN-derived thin fibres, such as high porosity, permeability, mechanical resistance, and in-plane thermal conductivity. Moreover, the material exhibited the highest chemical stability among all other carbonised CF materials, derived from Rayon or PAN, in the tested Li-based salts, with chemical stability results similar to those of graphitised CFs. Therefore, the characteristics of CF materials underlined their promising use as a cost-effective and efficient carbon host solution for the foreseen hybrid CF-PC material.

Figure IV/3-19 shows SEM micrographs illustrating the changes of PC morphology during heating and melting, analysed alone or in the presence of the chosen CF. In both cases the studied PC presented good thermal stability and no phase change until the melting point, followed by materials' melting. Indeed, this in-situ morphology study of the PC in the presence of the CF can be well correlated with the ex-situ observations presented in subchapter III/3.3. In both cases, a homogeneously wetted CF structure is observed, confirming the high affinity of the PC for the present carbon fibres.

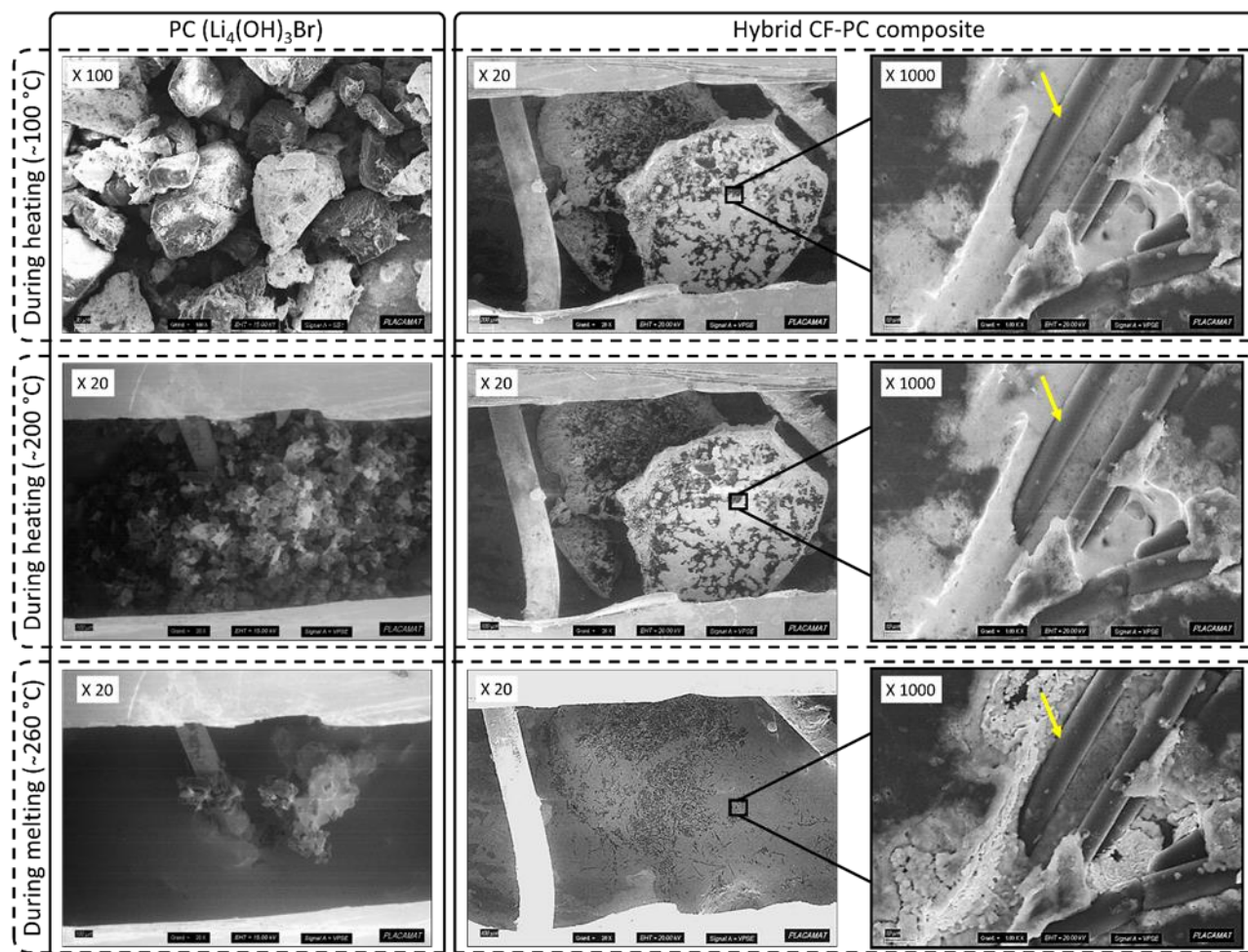


Figure IV/3-19 SEM visualisation of the PC, alone (left column) or in the CF-PC hybrid material (middle and right column, at low and high magnification, respectively) during heating (top and middle row, at different temperatures) and during melting (bottom row). The yellow arrow highlights the carbon fibres in the hybrid CF-PC composite.

In addition to the observation of the melting process, figure IV/3-20 shows the presence of a lamellar crystalline morphology at the end of the cooling process, which strongly supports that the expected PC structure has been formed. Such feature was suggested by the clear morphological differences between LiOH, LiBr and the PC (see Fig. IV/6-5) after cooling, and in parallel was confirmed by XRD analysis. In particular, no negative influence of the presence of the CF on the expected PC behaviour could be noticed during the in-situ investigation. Indeed, the observed lamellar PC morphology was found to agree very well with the results shown in figure III/3-10, from the SEM studies of the same material synthesised ex-situ. Therefore, the synthesis and morphological features of the PC are both confirmed to be unaffected by the presence of the carbon host, which meets one of the initial objectives of the project.

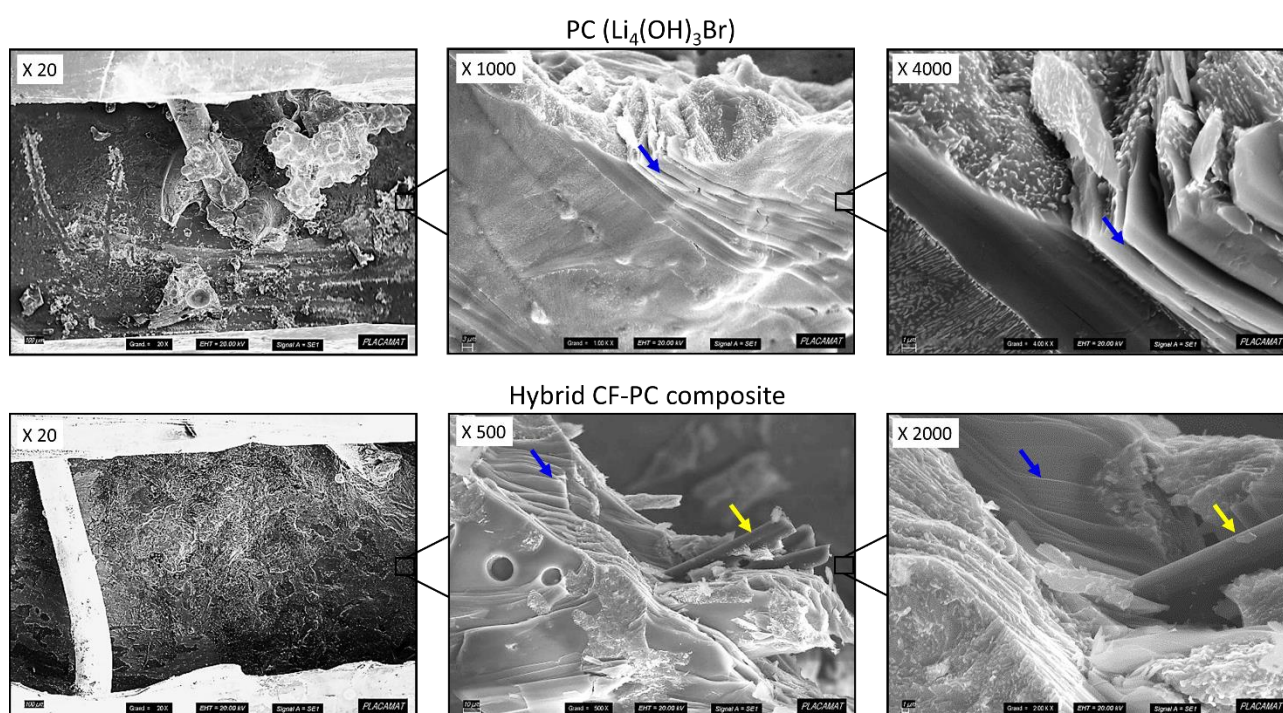


Figure IV/3-20 SEM visualisation of the PC, alone (top row) or in the CF-PC hybrid material (bottom row), at different magnifications and after cooling and complete solidification of the investigated materials. The blue or yellow arrows show the lamellar crystalline morphology typical of the PC structure, without or with carbon fibres in the CF-PC hybrid, respectively.

In parallel, an XRD characterisation was performed to confirm the absence of reaction between the CF and the PC, already suggested by the hot stage SEM analysis. As presented experimentally in subchapter IV/2.6, the results exhibiting the structural characteristics of the stoichiometric PC, synthesised in the hot stage chamber, were compared to those after the infiltration of the CF host by the PC. Figure IV/3.21 shows the corresponding XRD patterns, very well superimposed, thus evidencing the absence of change possibly induced by the contact between the molten PC and the carbon host. Moreover, the presented results are in good correlation with previous XRD results of PC synthesised ex-situ (furnace), then infiltrated in the same CF via a specially designed infiltration device (Achchaq et al. 2018).

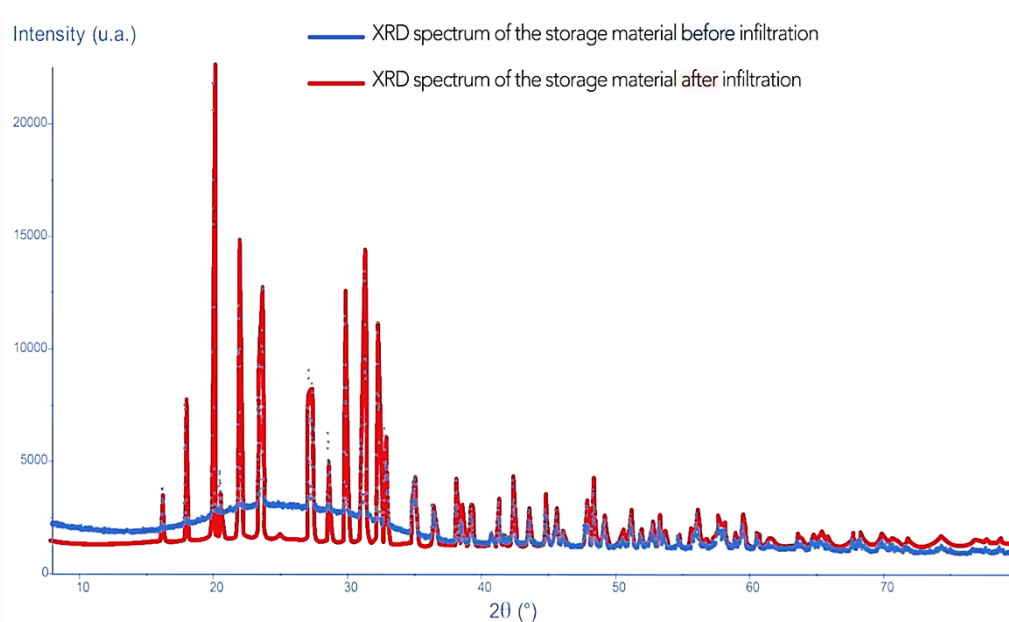


Figure IV/3-21 Superimposed X-ray diffraction patterns of as-synthesised PC (blue pattern) and the same produced by crystallisation inside the CF host (red pattern).

As reported by Achchaq et al. 2019, the performed XRD analysis also provided very important information regarding the structure of the synthesised PC. On the basis of the numeric analysis of the derived XRD results, the synthesised PC compound has a monoclinic crystal symmetry (of $P 1 2_1/m$ type), very similar to the previously proposed $\text{Li}_4(\text{OH})_3\text{Br}$ crystal structure (Hönnerscheid et al. 2003). However, further analysis of the PC, with a purity higher than 98%, confirmed that it strongly depends on the initial LiOH/LiBr mixture and on the thermal history, and can lead to different polymorph crystal structures. In addition, slight deviations from materials' purity and expected crystallographic structure could affect the expected thermodynamic properties of the stoichiometric PC, as introduced in subchapter I/1.3. Therefore, future research is underway to optimise the synthesis process for producing a purer

and larger amount of PC at its stoichiometric composition and to test its potential heat energy density.

Finally, a DSC thermal analysis was carried out in order to determine the thermal energy density, but also the stability and potential performance improvement of the PC in the presence of the CF host. In parallel, a preliminary DSC screening was also performed to investigate and compare the thermodynamic properties of LiOH and compare it with the PC.

Unfortunately, before having any DSC result, the very first tests failed and destroyed the former DSC analyser, delaying dramatically any further research on the thermal properties of the LiOH, LiBr, and PC, alone or as hybrid materials with CF hosts. The reasons for this early-unexpected problem are due to leakage and evaporation of the sample from the used commercial Incoloy³ alloy crucibles, and subsequent chemical attack of the DSC sensor by the molten sample, causing dramatic corrosion (seen in Fig. IV/3-22). In addition, all scheduled tests were postponed until new lab-made Inconel³ alloy crucibles were specially prepared and a new DSC was purchased. It took many months before the required budget could be obtained and the device could be ordered, delivered (whereas the lab was moving at the same time), and people could be trained on it.



Figure IV/3-22 Failure to use Incoloy alloy crucibles to perform DSC tests, and identified problems and solutions considered for future examinations (modified after project Pc2TES ANR -16-CE06-0012-0 meeting presentation by F. Achchaq)

Once the observed problems were solved, the initial DSC tests and the recovered data made it possible to obtain the thermographs of LiOH and of the synthesised PC. Figure IV/6-6 shows the endothermic (melting) and exothermic (solidification) peaks of the different samples

³ Incoloy and Inconel are both alloys mostly based on nickel with excellent, however, slightly different corrosion resistance to particular chemical attacks at high temperatures.

at different temperatures of 450 and 304°C for LiOH and the PC, respectively. Moreover, the shift of the maximum of the endo-/exo-thermic peaks of LiOH, along with the missing results of LiBr, compared to the synthesised PC, should confirm the change in thermodynamic properties and the presence of a single crystallographic phase of the PC.

Figure IV/3-23 a) shows an additional DSC test obtained for the synthesised PC sample in which the melting temperature is well-reproduced and the gravimetric enthalpy change (calculated by mathematical integration of the total peak area) of the endothermic peak is around 270 J g⁻¹. Indeed, the experimental information obtained is well correlated with the melting temperature of the PC compared to the estimated values from the FactSage 6.4[®] databases, presented in Table IV/31-1 and published by Achchaq and Barrio 2017. However, the experimental values of the gravimetric enthalpy change of the exothermic peak were slightly or much lower than the endothermic peak at about 235 J g⁻¹ or identical to the one estimated by the FactSage 6.4[®] database at about 803 J g⁻¹, respectively. At this early stage, the observed deviations could be explained by the presence of impurities and crystallographic differences observed by the XRD analysis when comparing the diffraction patterns of the synthesised and a pure reference PC. In other words, a mismatch in the crystallographic structure and the expected thermodynamic equilibrium at the peritectic transition should be the main reason for the lower heat storage capacity of the presently synthesised PC. Finally, the preliminary XRD and DSC results suggest that more work should be done for future improvement of the synthesis protocol to a purer PC with the correct crystallographic structure, thereby achieving the expected large heat storage capacity.

Figure IV/3-23 b) presents the thermodynamic properties of a PC synthesised in the form of hybrid material with the CF host. The endo-/exo-thermic peaks of the CF-PC sample are identical to those observed in figure IV/3-23 a) for the synthesised PC alone. Therefore, the results once again confirm the chemical inertness between the individual components of the hybrid material and the absence of interference from the CF on melting /recrystallisation of the PC. Figure IV/3-23 c) shows the results of seven consecutive DSC charge/discharge cycles that further confirm the latter observation over a longer time. However, no improvement / stabilisation of the peritectic transition steps and/or enhancement of the thermal properties of the PC in the hybrid material was observed during the seven DSC thermal charge/discharge cycles. Therefore, as presented by Achchaq et al. (2015), the performance of future DSC analyses on a larger sample and on a higher number of charge/discharge cycles is expected to provide more insights into the long-term behaviour of these materials.

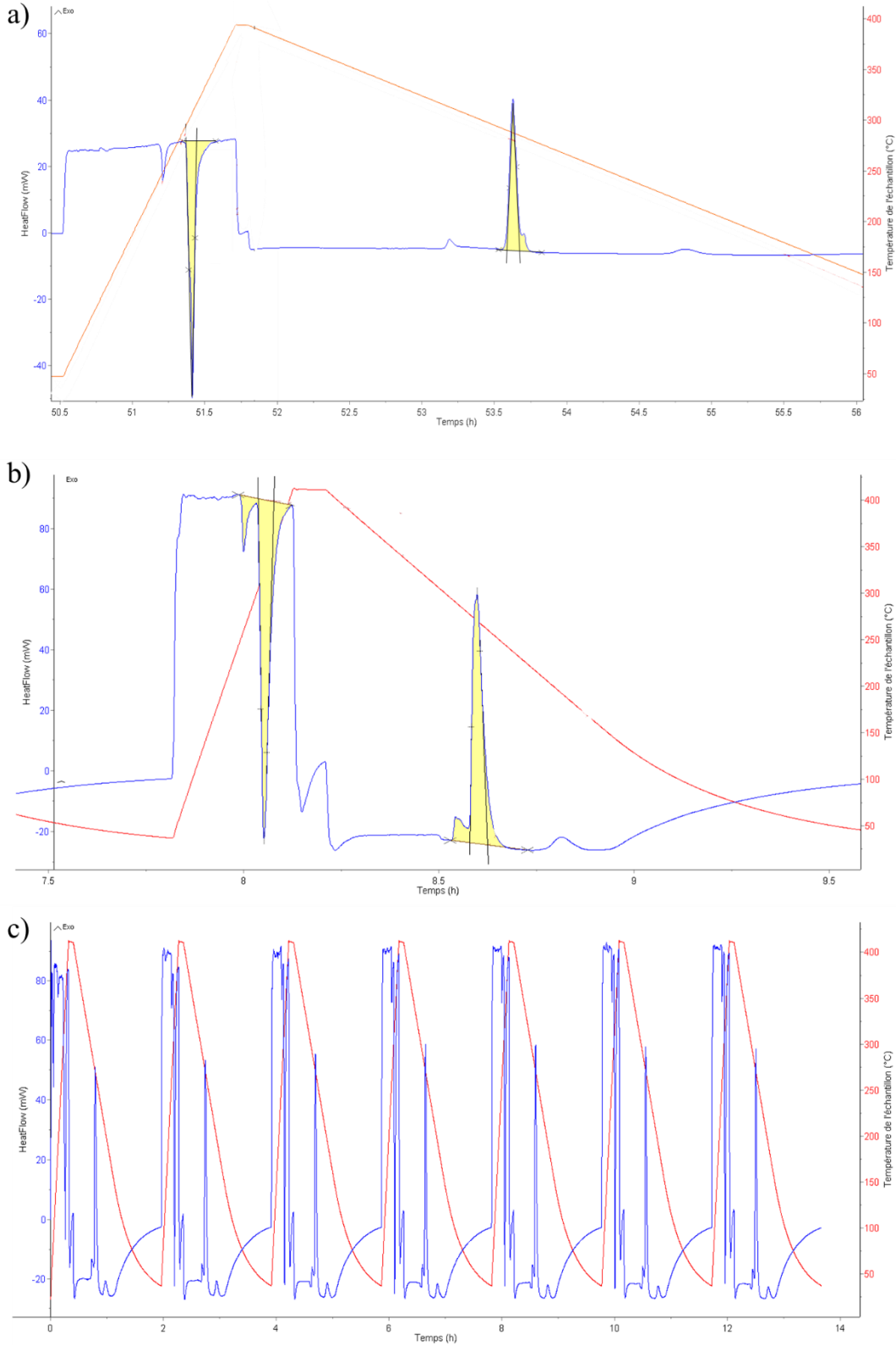


Figure IV/3-23 DSC thermographs of: a) synthesised PC, b) CF-PC hybrid material, and c) seven consecutive charge/discharge cycles of the latter material, where the left blue y-axis and the recovered signal represent the heat flux and its change (in mW), and the right red y-axis and the signal line represent the temperature of the sample and its change (in °C), respectively, as a function of time.

In summary, the performance results of both the PC and the CF in the final CF-PC hybrid material are worth investigating further and should be improved before we can reach the ultimate goal of the Pc2TES research project. It is important to note that future research can undoubtedly be supported by all the information on CF characteristics presented in this thesis, which is necessary to understand the impact of the carbon host on the performance of CF-PC hybrid materials. There is no doubt that PC-based TES is still in its early stage of development and that this work will contribute to an emerging generation of cost-effective and efficient energy storage solutions that remain to be discovered and used in a profitable way.

IV/4 Conclusion

Commercially available CFs were thoroughly characterised as promising carbon supports for innovative peritectic thermal energy storage. Nevertheless, the time and technical limitations of the project imposed the choice of a single CF for testing an appropriate modification solution in order to improve the properties of the carbonaceous fibrous materials. Thus, one of the evaluated soft CFs was chosen for being modified, and the resultant properties were mainly compared with those of the pristine material. The effects of morphology, physical and structural properties and chemical stability of C/C composites prepared by isothermal CVD process have been investigated, and the following conclusions could be derived.

After CVD treatment, the porous C/C composites were slightly less porous and permeable, but also improved their compression stiffness, thermal conductivity, and chemical stability, compared to the CF preform. In addition, the ultimate physical properties of the C/C composites were found to depend significantly on the introduced pyrocarbon matrix properties and the increase in bulk density. Equations linking morphology to permeability on the one hand, and bulk density to deposition time or mechanical properties on the other hand, have been presented, and confirm the existence of meaningful correlations.

It was observed that the use of needle-punched soft CFs with their unique porous design can produce low-density C/C composites with uniform deposition of pyrocarbon, both on the outer surface and on internal parts of the CF preform. With the use of polarised light optical microscopy, we also defined the laminar nature of the anisotropic pyrocarbon presenting carbon layers deposited almost perpendicular to the cross-section of the fibre. The pyrolytic carbon nanotexture was also found to depend strongly on the CVD processing parameters. Carbon fibre, deposited pyrocarbon matrix and the overall C/C composites are altogether found to be

anisotropic in terms of both nanotexture and overall materials' structure, additionally influencing the examined physical and structural properties.

At a low weight increase, the C/C composites retained most of the high permeability of the pristine soft CF, due to the formation of fibre-to-fibre discrete contacts and smooth fibre surface. Thus, the resultant morphological characteristic of the C/C composites presented lower contact area and less tortuous flow of the fluid compared to the investigated Rayon-derived soft CFs and rigid board. The pyrocarbon deposit on the fibre-to-fibre contacts fused the formerly weak contacts between neighbouring carbon fibres, significantly influencing the mechanical and thermal properties of the produced C/C composites. Thus, pyrocarbon deposition, even at the smallest weight increase, resulted in the formation of fibre junctions, ensuring efficient load transfer across the composite and exhibiting linear elastic behaviour. Indeed, the prepared C/C composites demonstrated great improvement in both elastic modulus and compression strength, transforming the hyperelastic soft CF preform into elastic-plastic, at low weight increase, or tough brittle materials at higher weight increase. The formed pyrocarbon junctions also present conductive paths for phonons reducing the thermal contact resistance and improving the thermal conductivity of the C/C composites, mostly in the IP direction and in good correlation with the C/C composite anisotropy. Nevertheless, the low density of the soft CF and initial limited felt/fibre connectivity can lead to the assumption that the mechanical and heat transfer properties of the C/C composites were mainly dominated by the pyrocarbon matrix and its properties.

The results of the elemental analysis showed that the produced C/C composites had a higher carbon content than the pristine soft CF due to pyrocarbon deposition from a pure hydrocarbon precursor. Raman analysis presented the features of a regenerative rough laminar structure of the pyrocarbon deposits, characterised by short-range graphitic layers, anisotropic morphology, and absence of tri-periodic stacking order. Even though highly disordered, the pyrocarbon deposit presented improved chemical stability in contact with molten LiOH, due to the absence of developed nanotexture and surface chemically active sites. Thus, the C/C composites presented improved chemical stability towards LiOH and $\text{Li}_4(\text{OH})_3\text{Br}$, by more than 50% compared to the original CF preform. However, thermal expansion differences between the pyrocarbon and the carbon fibre resulted in interfacial tension stress and the formation of micro-voids on the pyrocarbon surface. Therefore, it is observed that the presence of micro-voids act as gateways for the molten lithium salts in the composite interface and the occurrence of chemical reaction of the latter with the active nanotexture of the exposed carbon fibres.

Reinforcing the ability of the C/C composite to produce matrix defects and fibre-pyrocarbon interface detachment should improve the protection of the carbon fibres, avoiding the chemical reactivity of the latter with the molten LiOH during high-temperature exposure.

As a general conclusion, one of the main objectives of the present thesis was to present the role of the characterised carbon host in the performance of CF-PC hybrid materials with enhanced storage and stability properties, wherein a massive amount of heat energy could be rapidly charged or discharged. Hence, the preparation and performances of the envisaged CF-PC hybrids have been preliminary investigated. However, many technical problems and time constraints limited the choice of CFs for the characterisation of CF-PC materials, compared to PC alone. Thus, the last part of this chapter presented the results of new and well-known strategies for real-time analysis of the morphological, structural and thermodynamic properties of the synthesised PC and one CF-PC hybrid. The morphological analysis showed that the molten PC wets the surrounding carbon fibres, confirming the use of the CF host as a suitable material for accommodating the storage material. In addition, the CF exhibited chemical inertness relative to the synthesised PC and showed no negative influence on the observed lamellar morphology and on the structural properties of the latter. The DSC analysis also confirmed the absence of reaction between the components of the hybrid, and therefore the safe use of the CF requested to prevent the lack of PC stability during peritectic phase changes under thermal charge/discharge cycling. Moreover, the stabilisation and heat transfer effect of the CF hosts in the hybrid CF-PC material has yet to be identified by performing DSC analysis on larger samples and over more than 100 thermal cycles. Nevertheless, the latter study should be carried out once the synthesis of the PC has been improved and the theoretical heat storage capacity has been reached.

In summary, the preliminary results of materials' application tests highlight the need to improve the performance of the PC and the methods of analysing the CF effect in the hybrid material. In addition, the early DSC results of PC thermal performance in the CF-PC hybrids provided few answers to the main objectives of this thesis, thus leaving room for future analyses and verifications of the intended use of commercial/modified CFs. Anyway, the presented study of porous and fibrous carbons in relation to their properties and stability in contact with the concerned molten lithium salts constitutes a good basis for the missing research concerning their foreseen use. The results of this work might be easily implemented once the synthesis of the PC has been improved and future application tests have been carried out, thus making it possible to classify the relevant CF candidates based on the information presented. If necessary,

the present extensive study of carbon materials could also provide useful information on future materials improvement, similar to the modification presented in this chapter. Nevertheless, the current large study of CF materials constitutes the beginning of a new chapter in their use in future TES systems aiming at developing clean and renewable energy solutions.

IV/5 Bibliography

- Achchaq, F., Elena Risueño, Imane Mahroug, Philippe Legros, Blagoj Karakashov, E. Palomo del Barrio, A. Celzard, Vanessa Fierro, and Jean Toutain. 2018. "Development of a Carbon Felt/Salt-Based Hybrid Material for Thermal Energy Storage Applications." <https://doi.org/10.17265/1934-8975/2018.07.004>.
- Achchaq, Fouzia, and Elena Palomo Del Barrio. 2017. "A Proposition of Peritectic Structures as Candidates for Thermal Energy Storage." *Energy Procedia, Materials & Energy I* (2015), 139 (December): 346–51. <https://doi.org/10.1016/j.egypro.2017.11.219>.
- Achchaq, Fouzia, Elena Palomo del Barrio, Eric Lebraud, Stanislav Péchev, and Jean Toutain. 2019. "Development of a New LiBr/LiOH-Based Alloy for Thermal Energy Storage." *Journal of Physics and Chemistry of Solids* 131 (August): 173–79. <https://doi.org/10.1016/j.jpcs.2019.04.001>.
- Achchaq, Fouzia, Elena Palomo del Barrio, Alexandre Renauld, and Sabri Ben-Khemis. 2015. "Characterization of Li₂K(OH)₃ as Material for Thermal Energy Storage at High Temperature."
- Besmann, T. M., D. P. Stinton, and R. A. Lowden. 1988. "Chemical Vapor Deposition Techniques." *MRS Bulletin* 13 (11): 45–51. <https://doi.org/10.1557/S0883769400063910>.
- Bevilacqua, M., A. Babutskyi, and A. Chrysanthou. 2015. "A Review of the Catalytic Oxidation of Carbon-carbon Composite Aircraft Brakes." *Carbon* 95 (December): 861–69. <https://doi.org/10.1016/j.carbon.2015.08.100>.
- Borner, Arnaud, Francesco Panerai, and Nagi N. Mansour. 2017. "High Temperature Permeability of Fibrous Materials Using Direct Simulation Monte Carlo." *International Journal of Heat and Mass Transfer* 106 (March): 1318–26. <https://doi.org/10.1016/j.ijheatmasstransfer.2016.10.113>.
- Bourrat, Xavier, Francis Langlais, Georges Chollon, and Gérard Louis Vignoles. 2006. "Low Temperature Pyrocarbons: A Review." *Journal of the Brazilian Chemical Society* 17 (6): 1090–95. <https://doi.org/10.1590/S0103-50532006000600005>.
- Carabineiro, S. A., I. F. Silva, M. Klimkiewicz, and S. Eser. 1999. "In-Situ Techniques for Studying Deterioration of C/C Composite Aircraft Brakes by Catalytic Oxidation." *Materials and Corrosion* 50 (12): 689–95. [https://doi.org/10.1002/\(SICI\)1521-4176\(199912\)50:12<689::AID-MACO689>3.0.CO;2-A](https://doi.org/10.1002/(SICI)1521-4176(199912)50:12<689::AID-MACO689>3.0.CO;2-A).
- Celzard, A., W. Zhao, A. Pizzi, and V. Fierro. 2010. "Mechanical Properties of Tannin-Based Rigid Foams Undergoing Compression." *Materials Science and Engineering: A* 527 (16): 4438–46. <https://doi.org/10.1016/j.msea.2010.03.091>.
- Charron, Morgan. 2017. "Modélisation basée images du comportement thermomécanique de composite C/C," September. <https://tel.archives-ouvertes.fr/tel-01626860>.
- Cheng, Haiming, Changqing Hong, Xinghong Zhang, and Huafei Xue. 2015. "Lightweight Carbon-Bonded Carbon Fiber Composites with Quasi-Layered and Network Structure." *Materials & Design* 86 (December): 156–59. <https://doi.org/10.1016/j.matdes.2015.07.091>.
- Chollon, Georges, Sophie Delettrez, and Francis Langlais. 2014. "Chemical Vapour Infiltration and Mechanical Properties of Carbon Open-Cell Foams." *Carbon* 66 (January): 18–30. <https://doi.org/10.1016/j.carbon.2013.08.021>.
- Davies, Ian J. 1992. "Mechanical and Physical Properties of Low Density Carbon-Carbon Composites."
- Delgado-Sánchez, C., F. J. Santiago-Medina, V. Fierro, A. Pizzi, and A. Celzard. 2018. "Destructive vs. Non-Destructive Methods for the Mechanical Characterisation of

- Tannin-Based Thermoset Foams.” *Polymer Testing* 69 (August): 332–39. <https://doi.org/10.1016/j.polymertesting.2018.05.046>.
- Ehrburger, P., J. Lahaye, and C. Bourgeois. 1981. “Characterization of Carbon-Carbon composites—I: Textural and Microstructural Properties.” *Carbon* 19 (1): 1–5. [https://doi.org/10.1016/0008-6223\(81\)90097-X](https://doi.org/10.1016/0008-6223(81)90097-X).
- Farbos, B., P. Weisbecker, H. E. Fischer, J. -P. Da Costa, M. Lalanne, G. Chollon, C. Germain, G. L. Vignoles, and J. -M. Leyssale. 2014. “Nanoscale Structure and Texture of Highly Anisotropic Pyrocarbons Revisited with Transmission Electron Microscopy, Image Processing, Neutron Diffraction and Atomistic Modeling.” *Carbon* 80 (December): 472–89. <https://doi.org/10.1016/j.carbon.2014.08.087>.
- Feron, O., F. Langlais, R. Naslain, and J. Thebault. 1999. “On Kinetic and Microstructural Transitions in the CVD of Pyrocarbon from Propane.” *Carbon* 37 (9): 1343–53. [https://doi.org/10.1016/S0008-6223\(98\)00329-7](https://doi.org/10.1016/S0008-6223(98)00329-7).
- Fitzer, E., and Lalit M. Manocha. 1998. “Oxidation and Oxidation Protection of Carbon/Carbon Composites.” In *Carbon Reinforcements and Carbon/Carbon Composites*, edited by E. Fitzer and Lalit M. Manocha, 281–309. Berlin, Heidelberg: Springer Berlin Heidelberg. https://doi.org/10.1007/978-3-642-58745-0_9.
- Frueh, Samuel J., Timothy P. Coons, Justin W. Reutenauer, Rebecca Gottlieb, Michael A. Kmetz, and Steven L. Suib. 2018. “Carbon Fiber Reinforced Ceramic Matrix Composites with an Oxidation Resistant Boron Nitride Interface Coating.” *Ceramics International* 44 (13): 15310–16. <https://doi.org/10.1016/j.ceramint.2018.05.177>.
- Ge, Zhiwei, Feng Ye, Hui Cao, Guanghui Leng, Yue Qin, and Yulong Ding. 2014. “Carbonate-Salt-Based Composite Materials for Medium- and High-Temperature Thermal Energy Storage.” *Particuology*, Energy storage: Materials and processes, 15 (August): 77–81. <https://doi.org/10.1016/j.partic.2013.09.002>.
- Gillard, Adrien P., Guillaume Couégnat, Olivier Caty, Alexandre Allemand, Patrick Weisbecker, and Gerard L. Vignoles. 2015. “A Quantitative, Space-Resolved Method for Optical Anisotropy Estimation in Bulk Carbons.” *Carbon* 91 (September): 423–35. <https://doi.org/10.1016/j.carbon.2015.05.005>.
- Hönnerscheid, Andreas, Jürgen Nuss, Claus Mühle, and Martin Jansen. 2003. “Die Kristallstrukturen der Hydroxyhalogenide $\text{Li}_4(\text{OH})_3\text{Br}$ und $\text{Li}_4(\text{OH})_3\text{I}$.” *Zeitschrift für anorganische und allgemeine Chemie* 629 (2): 317–20. <https://doi.org/10.1002/zaac.200390050>.
- Hou, Zhen-hua, Ming-yang Hao, Rui-ying Luo, Qiao Xiang, Wei Yang, Hai-dong Shang, and Huai-zhe Xu. 2015. “Effects of Fiber-Type on the Microstructure and Mechanical Properties of Carbon/Carbon Composites.” *New Carbon Materials* 30 (4): 364–71. [https://doi.org/10.1016/S1872-5805\(15\)60196-2](https://doi.org/10.1016/S1872-5805(15)60196-2).
- Jiqiao, Liao, Huang Baiyun, Shi Gang, Chen Tengfei, and Xiong Xiang. 2002. “Influence of Porosity and Total Surface Area on the Oxidation Resistance of C/C Composites.” *Carbon* 40 (13): 2483–88. [https://doi.org/10.1016/S0008-6223\(02\)00163-X](https://doi.org/10.1016/S0008-6223(02)00163-X).
- Lavenac, J., F. Langlais, O. Féron, and R. Naslain. 2001. “Microstructure of the Pyrocarbon Matrix in Carbon/Carbon Composites.” *Composites Science and Technology* 61 (3): 339–45. [https://doi.org/10.1016/S0266-3538\(00\)00125-1](https://doi.org/10.1016/S0266-3538(00)00125-1).
- Letellier, M., C. Delgado-Sanchez, M. Khelifa, V. Fierro, and A. Celzard. 2017. “Mechanical Properties of Model Vitreous Carbon Foams.” *Carbon* 116 (Supplement C): 562–71. <https://doi.org/10.1016/j.carbon.2017.02.020>.
- Li, Chuan, Qi Li, Yongliang Li, Xiaohui She, Hui Cao, Peikun Zhang, Li Wang, and Yulong Ding. 2019. “Heat Transfer of Composite Phase Change Material Modules Containing a Eutectic Carbonate Salt for Medium and High Temperature Thermal Energy Storage

- Applications.” *Applied Energy* 238 (March): 1074–83. <https://doi.org/10.1016/j.apenergy.2019.01.184>.
- Li, Wei, He-jun Li, Jie Wang, Shou-yang Zhang, Xi Yang, and Jian-feng Wei. 2013. “Preparation and Mechanical Properties of Carbon/Carbon Composites with High Textured Pyrolytic Carbon Matrix.” *Transactions of Nonferrous Metals Society of China* 23 (7): 2129–34. [https://doi.org/10.1016/S1003-6326\(13\)62707-7](https://doi.org/10.1016/S1003-6326(13)62707-7).
- Luo, Ruiying, Tao Liu, Jinsong Li, Hongbo Zhang, Zhijun Chen, and Guanglai Tian. 2004. “Thermophysical Properties of Carbon/Carbon Composites and Physical Mechanism of Thermal Expansion and Thermal Conductivity.” *Carbon* 42 (14): 2887–95. <https://doi.org/10.1016/j.carbon.2004.06.024>.
- Manocha, Lalit M. 2003. “High Performance Carbon-Carbon Composites.” *Sadhana* 28 (1): 349–58. <https://doi.org/10.1007/BF02717143>.
- Marinković, S., and S. Dimitruević. 1985. “Carbon/Carbon Composites Prepared by Chemical Vapour Deposition.” *Carbon* 23 (6): 691–99. [https://doi.org/10.1016/0008-6223\(85\)90230-1](https://doi.org/10.1016/0008-6223(85)90230-1).
- Oberlin, Agnès. 2002. “Pyrocarbons.” *Carbon* 40 (1): 7–24. [https://doi.org/10.1016/S0008-6223\(01\)00138-5](https://doi.org/10.1016/S0008-6223(01)00138-5).
- Palacios, Anabel, Lin Cong, M. E. Navarro, Yulong Ding, and Camila Barreneche. 2019. “Thermal Conductivity Measurement Techniques for Characterizing Thermal Energy Storage Materials – A Review.” *Renewable and Sustainable Energy Reviews* 108 (July): 32–52. <https://doi.org/10.1016/j.rser.2019.03.020>.
- Reynolds, C. D., and Z. L. Ardary. 1976. “Raport No. Y/DA-6925.” Y/DA-6925. Union Carbide Corporation, Oak Ridge Y-12 Plant, Oak Ridge, Tennessee.
- Reznik, B, M Guellali, D Gerthsen, R Oberacker, and M. J Hoffmann. 2002. “Microstructure and Mechanical Properties of Carbon-carbon Composites with Multilayered Pyrocarbon Matrix.” *Materials Letters* 52 (1): 14–19. [https://doi.org/10.1016/S0167-577X\(01\)00357-3](https://doi.org/10.1016/S0167-577X(01)00357-3).
- Sahimi, Muhammad. 1998. “Non-Linear and Non-Local Transport Processes in Heterogeneous Media: From Long-Range Correlated Percolation to Fracture and Materials Breakdown.” *Physics Reports* 306 (4): 213–395. [https://doi.org/10.1016/S0370-1573\(98\)00024-6](https://doi.org/10.1016/S0370-1573(98)00024-6).
- Savage, G. 1993. “Applications of Carbon-Carbon Composites.” In *Carbon-Carbon Composites*, edited by G. Savage, 323–59. Dordrecht: Springer Netherlands. https://doi.org/10.1007/978-94-011-1586-5_9.
- Shao, Hai-Cheng, Ying-Yi Zhang, Shahid Hussain, Xin-Cheng Liu, Li-Jun Zhao, Xiang-Zhao Zhang, Gui-Wu Liu, and Guan-Jun Qiao. 2019. “Effects of Preform Structures on the Performance of Carbon and Carbon Composites.” *Science of Advanced Materials* 11: 1–9. <https://doi.org/10.1166/sam.2019.3511>.
- Sharma, Raghunandan, N. L. Ravikumar, Kinshuk Dasgupta, J. K. Chakravartty, and Kamal K. Kar. 2017. “Advanced Carbon-Carbon Composites: Processing Properties and Applications.” In *Composite Materials: Processing, Applications, Characterizations*, edited by Kamal K. Kar, 315–67. Berlin, Heidelberg: Springer Berlin Heidelberg. https://doi.org/10.1007/978-3-662-49514-8_10.
- Singh, Dileep, Taeil Kim, Weihuan Zhao, Wenhua Yu, and David M. France. 2016. “Development of Graphite Foam Infiltrated with MgCl₂ for a Latent Heat Based Thermal Energy Storage (LHTES) System.” *Renewable Energy* 94 (August): 660–67. <https://doi.org/10.1016/j.renene.2016.03.090>.
- Szczurek, A., A. Ortona, L. Ferrari, E. Rezaei, G. Medjahdi, V. Fierro, D. Bychanok, P. Kuzhir, and A. Celzard. 2015. “Carbon Periodic Cellular Architectures.” *Carbon* 88 (July): 70–85. <https://doi.org/10.1016/j.carbon.2015.02.069>.

- Vignoles, G. L. 2015. "17 - Modeling of Chemical Vapor Infiltration Processes." In *Advances in Composites Manufacturing and Process Design*, edited by Philippe Boisse, 415–58. Woodhead Publishing. <https://doi.org/10.1016/B978-1-78242-307-2.00017-8>.
- Weisshaus, H., S. Kenig, and A. Sivegmann. 1991. "Effect of Materials and Processing on the Mechanical Properties of C/C Composites." *Carbon* 29 (8): 1203–20. [https://doi.org/10.1016/0008-6223\(91\)90038-K](https://doi.org/10.1016/0008-6223(91)90038-K).
- Wu, Shuai, Yunqi Liu, Yicheng Ge, Liping Ran, Ke Peng, and Maozhong Yi. 2016. "Surface Structures of PAN-Based Carbon Fibers and Their Influences on the Interface Formation and Mechanical Properties of Carbon-Carbon Composites." *Composites Part A: Applied Science and Manufacturing* 90 (November): 480–88. <https://doi.org/10.1016/j.compositesa.2016.08.023>.
- Wu, Xianxian, and Ljubisa R. Radovic. 2005. "Catalytic Oxidation of Carbon/Carbon Composite Materials in the Presence of Potassium and Calcium Acetates." *Carbon* 43 (2): 333–44. <https://doi.org/10.1016/j.carbon.2004.09.025>.
- Xuefeng, Lu, Zhang Jie, and Qian Kun. 2019. "Densification Rate and Mechanical Properties of Carbon/Carbon Composites with Layer-Designed Preform." *Ceramics International* 45 (4): 4167–75. <https://doi.org/10.1016/j.ceramint.2018.11.085>.
- Ye, Feng, Zhiwei Ge, Yulong Ding, and Jun Yang. 2014. "Multi-Walled Carbon Nanotubes Added to Na₂CO₃/MgO Composites for Thermal Energy Storage." *Particuology, Energy storage: Materials and processes*, 15 (August): 56–60. <https://doi.org/10.1016/j.partic.2013.05.001>.
- Zhang, Chengyu, Kefei Yan, Shengru Qiao, Mei Li, Dong Han, and Yong Guo. 2012. "Effect of Oxidation on Fracture Toughness of a Carbon/Carbon Composite." *Journal of Wuhan University of Technology-Mater. Sci. Ed.* 27 (5): 944–47. <https://doi.org/10.1007/s11595-012-0578-0>.
- Zhang, Shouyang, Yulei Zhang, Aijun Li, Qiang Chen, Xiaohong Shi, Jianfeng Huang, and Zhibiao Hu. 2018. "Carbon Composites." In *Composite Materials Engineering, Volume 2: Different Types of Composite Materials*, edited by Xiao-Su Yi, Shanyi Du, and Litong Zhang, 531–617. Singapore: Springer Singapore. https://doi.org/10.1007/978-981-10-5690-1_5.
- Zhang, Yao, Zixing Lu, Zhenyu Yang, Dahai Zhang, Jianjun Shi, Zeshuai Yuan, and Qiang Liu. 2017. "Compression Behaviors of Carbon-Bonded Carbon Fiber Composites: Experimental and Numerical Investigations." *Carbon* 116 (May): 398–408. <https://doi.org/10.1016/j.carbon.2017.02.012>.

IV/6 Annex

IV/6.1 Results of C/C composite analysis

Table IV/6-1 CVD deposition time and morphological properties of evaluated CVD C/C composites and the pristine CF preform.

Sample code:	Deposition time	Bulk density	Weight % of CF preform	Weight % of pyrocarbon deposition	Overall Porosity	Pyrocarbon deposition thickness	Thickness of pyrocarbon-coated fibre	
	(hour)	(g cm ⁻³)	(%)	(%)	(%)	(μm)	(μm) Stdv.	
Rayon Soft CF								
GR4	/	0.108	100	/	93.1	/	/	10.30
CVD C/C composites								
%35	25	0.142	74.6	25.4	90.9	0.53	0.05	11.36
%90	45	0.197	54.8	45.2	87.4	1.19	0.07	12.68
%110	50	0.208	51.9	48.1	86.7	1.54	0.17	13.52
%140	60	0.254	42.6	57.4	83.7	2.27	0.16	14.96
%170	75	0.282	38.3	61.7	81.9	2.63	0.17	15.83
%210	80	0.337	32.1	67.9	78.4	3.48	0.27	17.51
%240	90	0.363	29.7	70.3	76.8	4.55	0.51	19.40

Table IV/6-2 Obtained values of thermal conductivity in anisotropic analysis mode, with additional information on materials' bulk density.

Sample code:	Bulk density	Thermal conductivity (κ_z) (OP-direction)			Thermal conductivity (κ_{xy}) (IP-direction)			Thermal conductivity (κ_{xy}/κ_z) (Anisotropy ratio)
		(g cm ⁻³)	(W m ⁻¹ K ⁻¹)	(W m ⁻¹ K ⁻¹) Stdv.	Variation (%)	(W m ⁻¹ K ⁻¹)	(W m ⁻¹ K ⁻¹) Stdv.	Variation (%)
Rayon Soft CF								
GR4	0.108	0.043	0.002	/	0.292	0.003	/	6.81
CVD C/C composites								
%35	0.142	0.055	0.010	28.7	0.421	0.034	43.9	7.62
%110	0.208	0.046	0.005	7.6	0.594	0.051	103.1	12.85
%140	0.254	0.045	0.010	3.9	0.947	0.194	224.1	21.23
%170	0.282	0.030	0.010	-30.1	1.230	0.240	320.8	41.00
%210	0.337	0.036	0.003	-16.3	1.700	0.090	481.7	47.33
%240	0.363	0.044	0.015	2.8	2.622	0.185	797.4	59.50

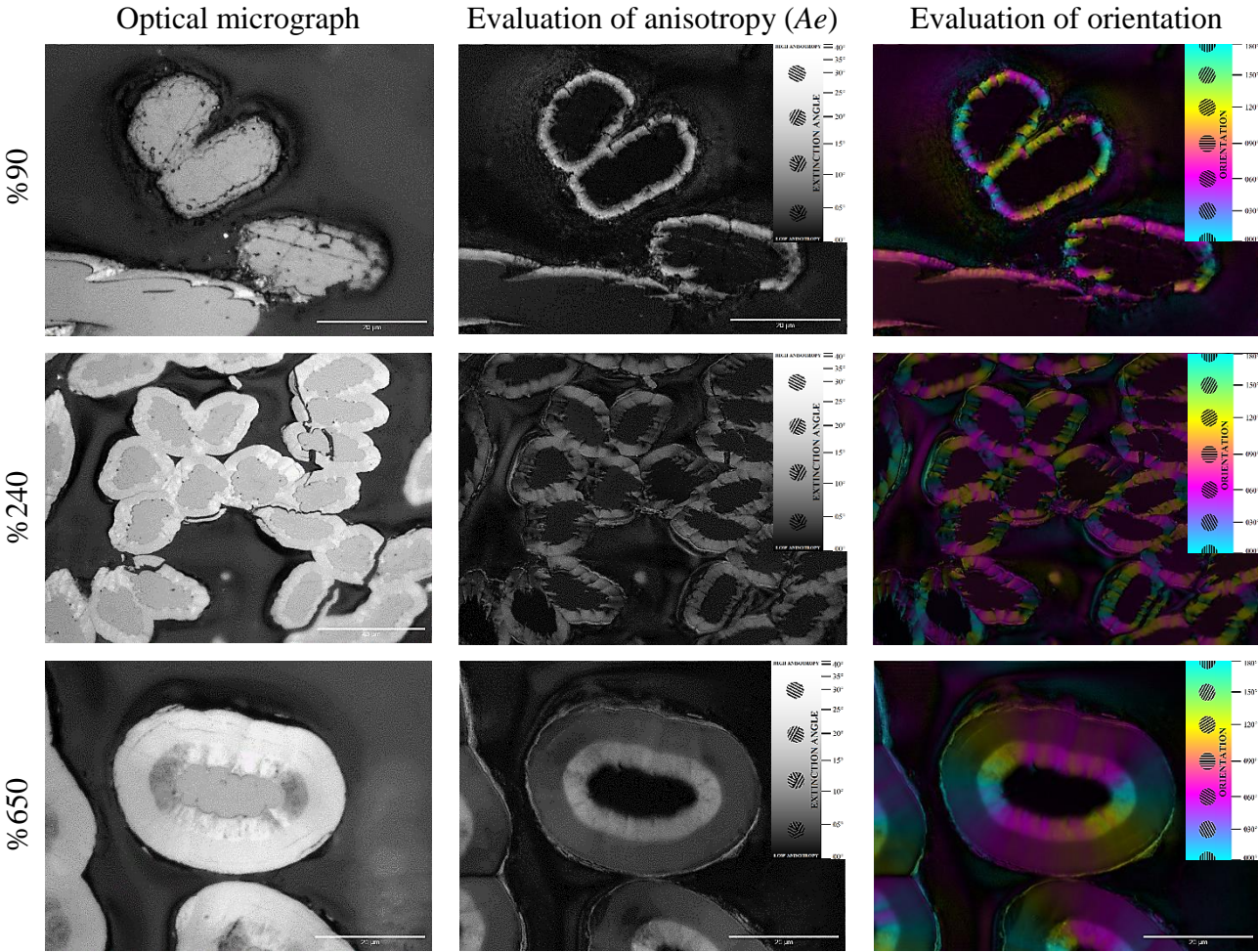


Figure IV/6-1 Additional textural analysis of pyrocarbon deposits at different sample zones by optical microscopy: (left row) carbon fibres with pyrocarbon deposition; (middle row) pyrocarbon anisotropy determined through extinction angle (A_e); (right row) preferential orientation of pyrocarbon deposits.

Table IV/6-3 Averaged air permeability values of evaluated CVD C/C composites and permeability decrease compared to the permeability of the pristine CF preform; Structural characteristics are inserted for comparison.

Sample code:	Bulk density (g cm ⁻³)	Overall Porosity (%)	Air permeability (OP-direction)		
			(m ²)	Stdv.(m ²)	Variation (%)
Rayon Soft CF					
GR4	0.108	93.1	1.35E-10	3.68E-12	/
CVD C/C composites					
%35	0.142	90.9	1.26E-10	2.43E-12	-6.9
%90	0.197	87.4	1.14E-10	3.31E-12	-15.8
%110	0.208	86.7	1.13E-10	1.08E-12	-16.9
%140	0.254	83.7	8.21E-11	8.68E-13	-39.3
%170	0.282	81.9	7.47E-11	6.35E-14	-44.8
%210	0.337	78.4	7.08E-11	4.44E-13	-47.7
%240	0.363	76.8	6.18E-11	6.27E-13	-54.3

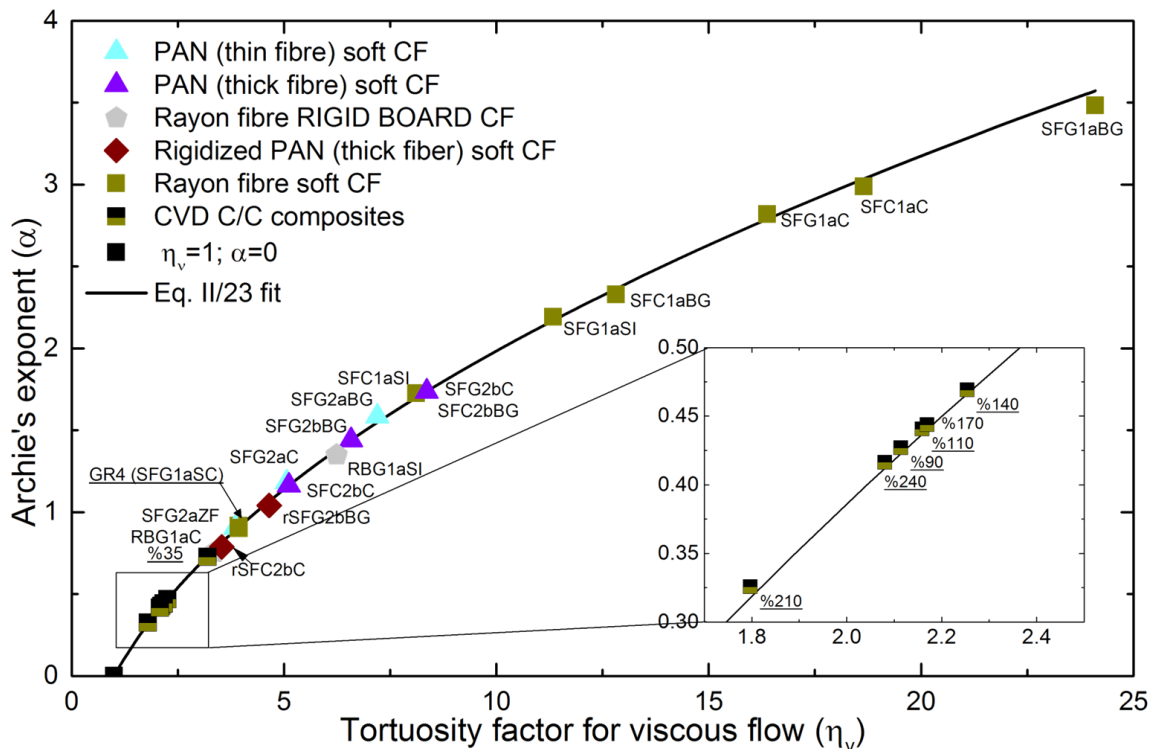


Figure IV/6-2 Archie's coefficient, α , vs. viscous tortuosity factor, η_v , for all fibrous carbon materials investigated in Chapter II, calculated from equation (II/21). The solid line is the identified master curve, equation (II/23), from which the values of the Archie's coefficient were calculated for the C/C composites examined here.

Table IV/6-4 Averaged elastic modulus, modulus increase and yield strength of evaluated CVD C/C composites and the pristine CF preform; Structural characteristics are inserted for comparison.

Sample code:	Bulk density (g cm ⁻³)	Overall Porosity (%)	Elastic Modulus (<i>E</i>)		Yield strength (MPa)
			(MPa)	Variation (%)	
Rayon Soft CF					
GR4	0.108	93.1	0.08	/	/
CVD C/C composites					
%35	0.142	90.9	5.29	6279.52	0.07
%90	0.197	87.4	18.90	22671.07	0.35
%110	0.208	86.7	36.65	44056.63	0.71
%140	0.254	83.7	42.55	51165.05	0.77
%170	0.282	81.9	68.05	81887.94	1.28
%210	0.337	78.4	68.15	82008.42	1.52
%240	0.363	76.8	87.75	105622.88	2.11

Table IV/6-5 Elemental analysis results (in wt.% or at.%, respectively) of pristine soft CF and produced C/C composites at different weight increases.

CODE NAME	Weight%				Atomic%			
	C (%)	N (%)	O (%)	H (%)	C (%)	N (%)	O (%)	H (%)
Rayon Soft CF								
GR4	99.53	0.01	0.39	0.07	99.13	0.03	0.19	0.65
CVD C/C composites								
%35	99.77	0.03	0.16	0.04	99.42	0.03	0.12	0.43
%90	99.79	0.02	0.15	0.04	99.40	0.02	0.11	0.46
%110	99.80	0.02	0.14	0.04	99.45	0.02	0.11	0.42
%140	99.83	0.01	0.12	0.04	99.47	0.01	0.09	0.43
%170	99.81	0.02	0.14	0.04	99.44	0.01	0.10	0.44
%210	99.79	0.02	0.14	0.04	99.36	0.02	0.10	0.51
%240	99.77	0.03	0.16	0.04	99.40	0.03	0.12	0.45

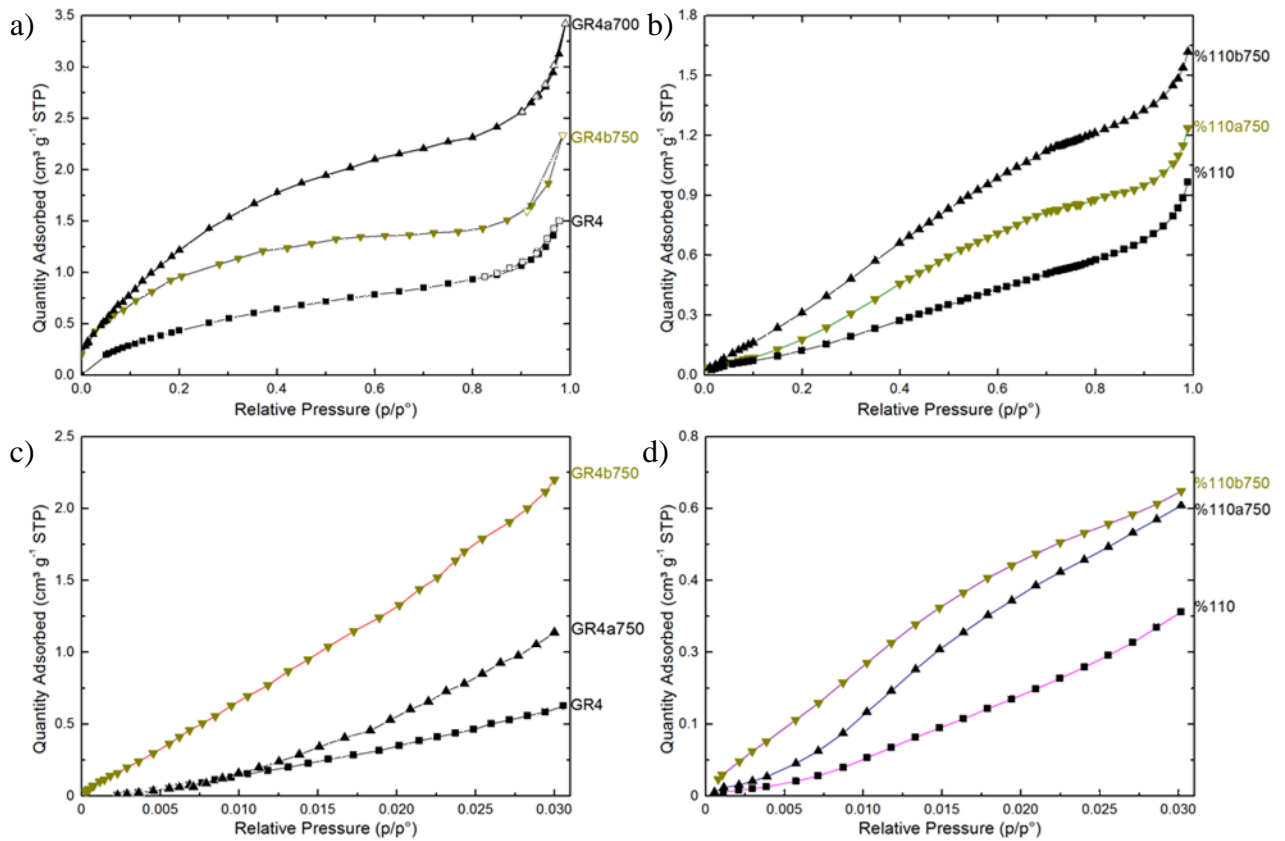


Figure IV/6-3 a) and b) N₂ adsorption isotherms at -196 °C and c) and d) CO₂ adsorption isotherms at 0 °C for pristine CFs and C/C composites, before and after the chemical reaction with LiOH (black symbols) and Li₄(OH)₃Br (green symbols) at the highest tested temperature.

Table IV/6-6 Textural parameters from both N₂ and CO₂ isotherms calculated by 2D NLDFT-HS model of the pristine soft CF (for comparison reasons) and prepared C/C composite at 110% weight increase, before and after chemical reaction in molten LiOH (normal style) or Li₄(OH)₃Br (bold style). The decrease of B-O and S_{NLDFT} (in %) is presented compared to the same for the pristine soft CF, before and after chemical reaction at different final temperatures, respectively.

Carbon felt (CODE)	B-O ₄ (%)	B-O decrease (%)	S _{NLDFT} ⁵ (m ² g ⁻²)	S _{NLDFT} decrease (%)	L _μ (dV) ⁶ (nm)	L _{tot} (dV) ⁷ (nm)	V _μ NLDFT ⁸ (cm ³ g ⁻¹)	V _{tot} NLDFT ⁹ (cm ³ g ⁻¹)	V _{mes} ¹⁰ (cm ³ g ⁻¹)	V _{mes} (%)
GR4	-	-	6.62	-	0.82	6.20	0.002	0.004	0.002	48.70
GR4a650	3.4	-	11.68	-	0.96	5.63	0.005	0.007	0.003	34.61
GR4a700	7.2	-	25.15	-	0.91	3.21	0.010	0.014	0.004	29.53
GR4a750	18.4	-	13.85	-	0.95	4.09	0.006	0.008	0.002	21.63
GR4b750	15.9	-	27.36	-	0.92	2.91	0.005	0.007	0.003	14.95
% 110	-	-	3.96	40.20	0.79	5.37	0.001	0.003	0.001	48.22
% 110a650	1.38	59.84	4.78	59.04	0.84	3.11	0.002	0.003	0.001	40.55
% 110a700	4.04	44.31	7.61	69.76	0.77	3.91	0.003	0.004	0.001	29.76
% 110a750	8.36	54.59	6.87	50.44	0.77	3.91	0.002	0.004	0.002	40.78
% 110b750	5.02	68.32	7.22	73.62	0.69	4.20	0.002	0.004	0.002	52.16

4 Burn-off = 100 - yield calculated as a % of carbon disappeared per initial CF weight

5 Surface areas determined by 2D NLDFT-HS

6 Average micropore size

7 Average pore size

8 Micropore volume (0.36 - 2 nm) determined by 2D NLDFT-HS

9 Total pore volume (0.36 - 10 nm) determined by 2D NLDFT-HS

10 Mesopore volume (2-10 nm) = V_{tot 2D NLDFT-HS} - V_{μ 2D NLDFT-HS}

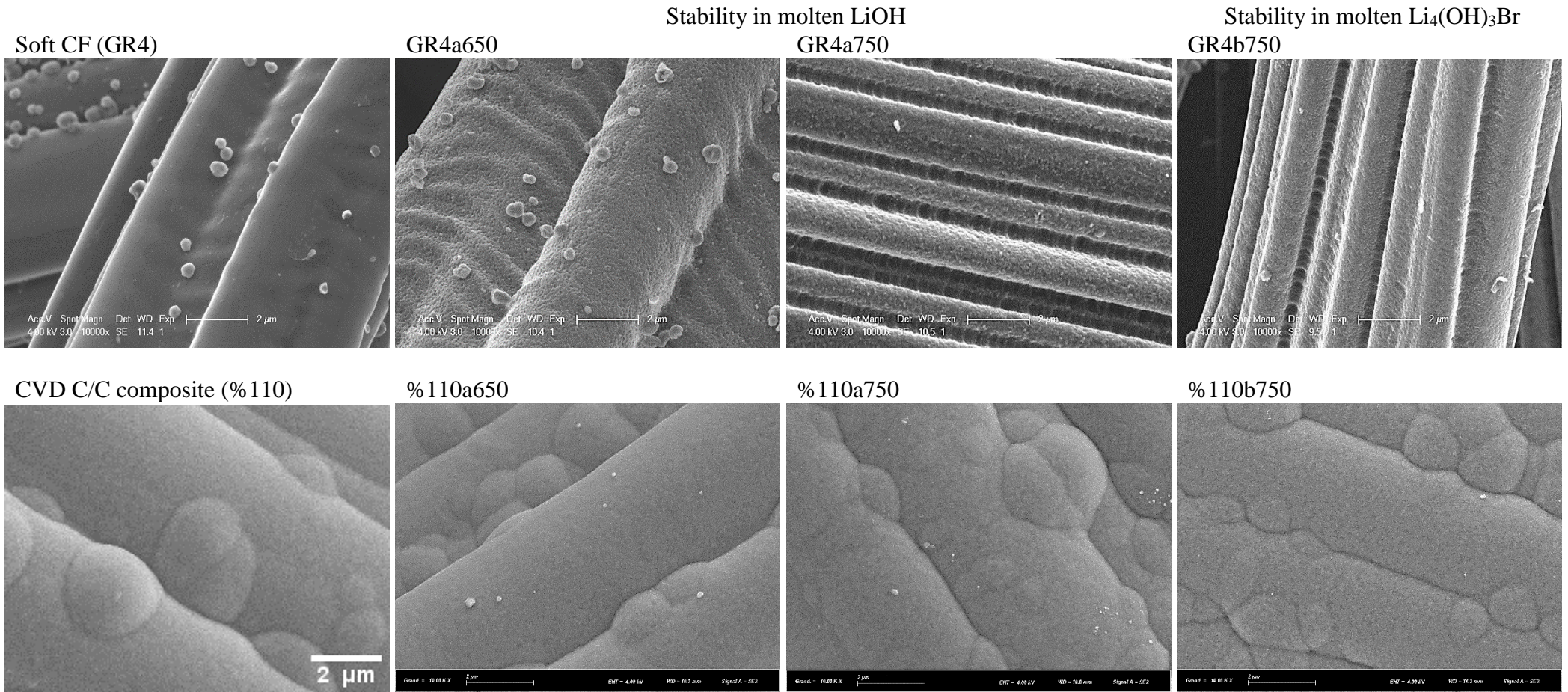


Figure IV/6-4 SEM micrograph of fibre surface of pristine ex-Rayon soft CFs before (top row) and after CVD preparation of C/C composite (down row), before (left column) and after chemical reaction in LiOH (two middle columns) at different performed temperature and $\text{Li}_4(\text{OH})_3\text{Br}$ (right column) at the highest performed temperature.

IV/6.2 Preliminary results of morphological, structural and thermal analysis of PC, alone or in CF-PC hybrid material

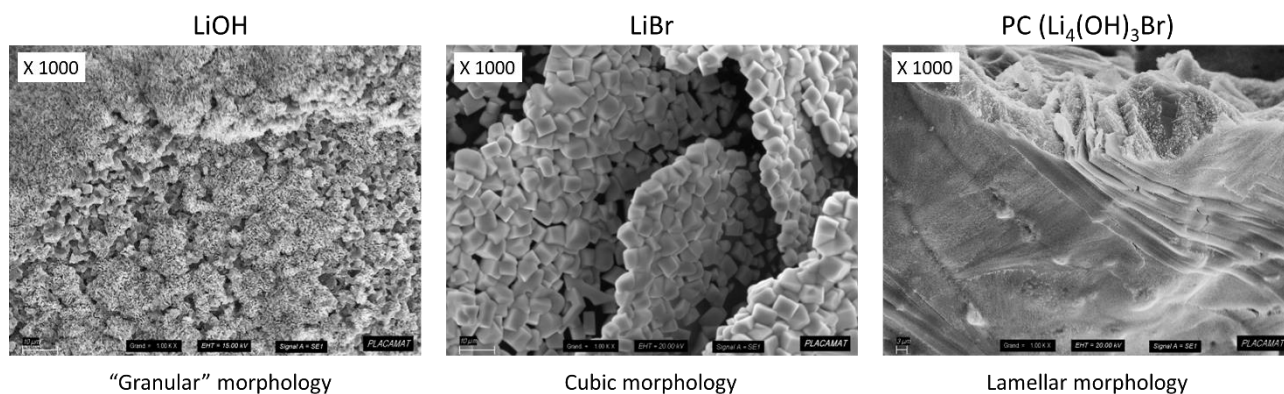


Figure IV/6-5 Morphological differences between LiOH (left), LiBr (middle), and their peritectic mixture at the stoichiometric ratio, i.e., Li₄(OH)₃Br (right)

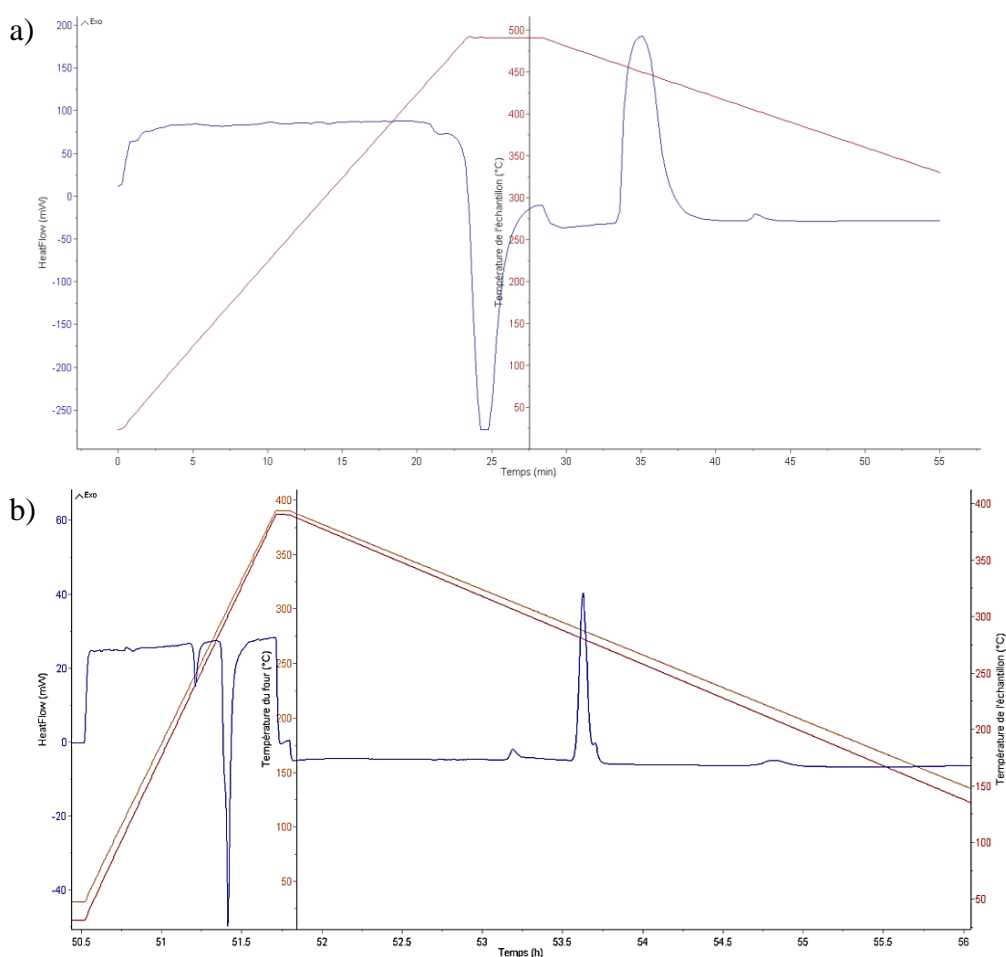


Figure IV/6-6 DSC thermographs of: a) LiOH and b) the synthesised PC, where the left blue y-axis and the recovered signal represent the heat flow and its change (in mW), and the orange/red y-axis and the signal line represent the temperature of the oven/sample and its change (in °C), respectively, as a function of time.

Conclusions et perspectives

Dans cette thèse, différents feutres de carbone (FCs) commerciaux ont été classés par familles, leur morphologie et leurs propriétés physiques et structurales ont été caractérisées de manière détaillée, ils ont été testés pour leur stabilité dans des sels de lithium fondus, et l'un d'eux a été modifié pour améliorer ses performances initiales. L'objectif de cette étude a été d'explorer les différentes propriétés originales ou modifiées des FCs, et d'étudier l'utilisation de ces matériaux en tant que structures hôtes carbonées pour des systèmes de stockage d'énergie thermique. À notre connaissance, aucune autre étude n'avait mis en œuvre ce type d'analyse approfondie en examinant 18 échantillons commerciaux de FCs, reçus de 5 fournisseurs différents. En conséquence, les différents travaux réalisés dans cette thèse ont donné lieu à de nombreuses observations avec des résultats intéressants et originaux.

La première partie de l'étude a concerné la caractérisation d'une très large gamme de carbones fibreux, depuis les FCs souples aux panneaux rigides en passant par les FCs rigidifiés, en termes de structures de non-tissés et de fibres, de densité, de porosité totale, de mouillabilité, de perméabilité à l'air, de propriétés mécaniques en compression, et de conductivité thermique. Tous ces matériaux ont ainsi couvert une grande plage de densités squelettiques et de densités apparentes, ces dernières ayant un effet majeur sur la porosité totale. Les FCs anisotropes étaient consolidées soit mécaniquement, par aiguilletage assisté ou non par une consolidation chimique supplémentaire, soit chimiquement avec une résine carbonisée ultérieurement. Il a été constaté que les FCs étaient fabriqués à partir de fibres ex-Rayonne ou ex-PAN de diamètres différents et de sections transversales circulaires ou non. En conséquence, un ensemble complet de matériaux avec des structures poreuses assez différentes, et donc des propriétés physiques différentes, indépendamment de leur porosité, a été étudié.

L'étude des propriétés physiques des FCs devient impérative dès que leur infiltration est considérée pour produire les matériaux hybrides FC-matériau à changement de phase (MCP) prévus. Les FCs à base de Rayonne présentent ainsi des angles de contact avec l'eau légèrement inférieurs à ceux des matériaux à base de PAN, plus hydrophobes. Les valeurs d'angle de contact mesurées placent les échantillons dans la gamme des matériaux hydrophobes à super-hydrophobes.

L'accroissement de la porosité des matériaux ou la diminution du diamètre des fibres de carbone sont considérées comme les principaux paramètres faisant augmenter la perméabilité des

FCs. Cependant, des différences observées par rapport à ce comportement logique s'expliquent par différentes propriétés morphologiques de la fibre/du feutre obtenues lors de la fabrication des matériaux commerciaux dérivées de précurseurs polymères synthétiques ou naturels. Puisque les matériaux d'intérêt sont généralement extrêmement complexes et difficiles à caractériser, nous avons modélisé ce comportement et trouvé une relation universelle englobant toutes les valeurs mesurées. En effet, l'application des équations de perméabilité pertinentes aux FCs étudiés a permis de calculer le coefficient d'Archie et le facteur de tortuosité visqueuse à partir des valeurs mesurées de porosité, de diamètre de fibre et de perméabilité. Par conséquent, une courbe universelle reliant la tortuosité globale à l'exposant d'Archie et une équation adéquate ont donc été proposées pour ajuster tous les FCs sur une très large gamme de porosités et de structures.

Les propriétés mécaniques des FCs lors de leur compression axiale (hors du plan) sont manifestement complexes et fortement dépendantes de leurs caractéristiques microstructurales et de la technique de formation de ces non-tissés. Les divers FCs présentent d'importantes différences de comportement mécanique, montrant une déformation allant de viscoélastique non-linéaire à élastique-plastique linéaire. En conséquence, différentes approches directes ou de modélisation ont été considérées pour estimer le comportement élastique globaux des différents FCs. De plus, les propriétés mécaniques des FCs souples ont été étudiées selon deux méthodes, une dynamique et destructive d'une part, et une quasi-statique (QMA) et non destructive d'autre part. Enfin, la comparaison entre les modules d'élasticité calculés a mis en évidence l'incapacité de la méthode QMA à déterminer le module d'élasticité global des FCs souples, nécessitant pour cela l'application d'un modèle d'hyperélasticité. Néanmoins, un bon accord a été trouvé avec les modules de la méthode dynamique pour chaque valeur donnée de déformation, et la méthode QMA a également pu être utilisée pour calculer le facteur de perte, qui n'avait encore jamais été mesuré pour les FCs. Cela peut se révéler être très intéressant dans le cas d'études d'autres applications, telles que l'isolation acoustique.

Dans le but de préparer un matériau hybride à base de CF, la conductivité thermique a également été étudiée. Les variations de propriétés texturales des fibres de carbone et de disposition des fibres ont pour conséquence des différences de comportement mécanique et de contact thermique entre fibres, ce qui a un effet important sur la conductivité thermique effective des FCs. Les résultats expérimentaux ont montré également une conductivité thermique fortement anisotrope, avec des valeurs plus élevées dans le plan par rapport à la

direction orthogonale, en raison de l'orientation anisotrope et préférentielle des fibres dans le plan des FCs.

La recherche de critères de sélection de carbones fibreux chimiquement stables était le deuxième objectif de cette thèse, ainsi que la recherche des raisons probables de l'apparition de réactions non désirées entre les constituants des matériaux hybrides FC-MCP. La composition élémentaire et l'organisation texturale des fibres de carbone ont été examinées, avant d'étudier leurs effets sur la stabilité chimique des FCs dans des sels de lithium fondus. Les résultats d'analyse élémentaire, de diffractométrie des rayons X et de spectroscopie Raman, montrent l'influence de l'histoire thermique et des précurseurs sur la pureté finale du carbone et sur son ordre structural, tous deux augmentant avec la température de traitement thermique final, c'est-à-dire des FCs carbonisés jusqu'aux FCs graphitisés.

Tant pour les matériaux ex-PAN qu'ex-Rayonne, la réactivité avec LiOH diminue à mesure que la pureté du carbone et l'ordre structural augmente. Le FC devient alors très stable, même à la température testée la plus élevée. Cependant, à propriétés texturales similaires, la présence d'hétéroatomes a un effet très significatif sur la réactivité des FCs. Les résultats d'analyse de nanotexture et de microscopie électronique à balayage des FCs post-réaction montrent ainsi que, des FCs carbonisés aux FCs graphitisés, la texture de surface passe de significativement à légèrement modifiée. De plus, la réaction des FCs avec le MCP ($\text{Li}_4(\text{OH})_3\text{Br}$) donne des valeurs de burn-off inférieures de 50% à celles obtenues avec LiOH seul, en raison de la présence de la phase de LiBr inerte. La présence de ce dernier composé modère donc les réactions d'oxydo-réduction avec l'hydroxyde. Les résultats expérimentaux des tests de stabilité chimique sont en excellent accord avec les valeurs estimées par application de la loi d'Arrhenius, distinguant encore une fois les FCs graphitisés, à la pureté et à la structure améliorées.

En conclusion, une pureté en carbone élevée et une meilleure organisation texturale doivent être préférées pour une plus grande stabilité chimique des FCs en contact avec du MCP fondu, et pour une gestion thermique améliorée dans le matériau hybride FC-MCP final.

La dernière partie de la thèse est centrée sur l'amélioration supplémentaire d'un FC souple, pour aller au-delà de certaines des limitations observées. Par conséquent, l'objectif de cette partie a été d'identifier l'effet de cette modification en vue d'obtenir des indications utiles pour l'amélioration des matériaux hybrides FC-MCP dans leur utilisation finale.

L'utilisation de la méthode de dépôt chimique en phase vapeur (CVD) résulte en la formation d'un dépôt uniforme de pyrocarbone sans zone préférentielle dans la préforme de FC, en raison de la porosité et de la perméabilité élevées de celle-ci. La présence d'une couche de pyrocarbone sur les fibres génère des jonctions fixes entre elles, dont l'épaisseur et l'étendue augmentent avec le temps de dépôt. Cependant, les composites C/C ainsi produits présentent toujours une porosité ouverte interconnectée, même après la plus longue durée de dépôt testée.

La nature laminaire du pyrocarbone anisotrope, étudiée en microscopie optique en lumière polarisée, se manifeste par des couches de carbone déposées presque perpendiculairement à la section transversale de la fibre. La fibre de carbone, la matrice de pyrocarbone déposée et l'ensemble des composites C/C se révèlent tout-à-fait anisotropes à la fois en termes de nanotexture et de structure globale des matériaux, ce qui influence également leurs propriétés physiques.

L'augmentation de la fraction de pyrocarbone déposé a entraîné une diminution linéaire de la perméabilité des composites C/C, hors du plan, en fonction à la fois de la (faible) baisse de la porosité et de l'augmentation du diamètre des fibres. Cependant, la production de tels composites C/C a donné des propriétés thermiques et mécaniques contrôlées et améliorées par rapport aux FCs souples initiaux, sans modifier radicalement la porosité globale du matériau. Les jonctions en pyrocarbone formées se traduisent par un module élastique plus important et une plus grande résistance à la compression, et produisent également des chemins conducteurs pour les phonons, réduisant les résistances thermiques de contact, et améliorant la conductivité thermique globale par rapport au FC souple de départ. Enfin, un optimum doit toujours être identifié car les propriétés physiques mesurées sont antagonistes, et une augmentation de la densité entraînera toujours une perméabilité plus faible tandis que les propriétés mécaniques et de transfert de chaleur seront meilleures.

Enfin, la couche de pyrocarbone déposée donne une stabilité chimique améliorée aux composites C/C dans l'environnement oxydant testé. Tous les résultats de burn-off ont montré une perte de masse réduite de plus de 50% par rapport au FC souple de départ. La stabilité chimique améliorée du composite C/C ainsi mise en évidence a pu être corrélée à l'augmentation de la teneur en carbone et au niveau réduit en hétéroatomes, compatible avec la présence d'une surface de pyrocarbone laminaire régénéré rugueuse chimiquement stable.

D'autre part, l'étude de la morphologie des matériaux et de la nanotexture a permis de mieux comprendre les mécanismes d'oxydation des composites C/C dans les sels de lithium

fondus. La présence observée de microcavités sur le dépôt de pyrocarbone a entraîné des réactions chimiques à l'interface du composite, et progressant vers l'intérieur de la structure de la fibre de carbone en raison d'une quantité plus élevée de groupes oxygénés attribués à son origine ex-Rayonne. La présence de porosité de surface est supposée uniquement due à l'existence de fissures et de microcavités dans le pyrocarbone. Par conséquent, on a pu conclure que la baisse de la surface spécifique mesurée est proportionnelle à celle des sites réactifs de surface, entraînant ainsi une diminution du burn-off. De plus, les valeurs de burn-off du composite C/C ont conduit à l'estimation d'une énergie d'activation similaire à celle de la préforme FC d'origine.

La fin du dernier chapitre de ce manuscrit a présenté les résultats préliminaires d'analyse in-situ d'une part, et DSC d'autre part, des propriétés morphologiques, structurales et thermodynamiques du MCP et de l'hybride FC-MCP. Ils confirment la bonne mouillabilité du FC et l'inertie chimique entre les constituants de l'hybride, ainsi que la possibilité d'utiliser des FCs en tant que structures hôtes carbonées pour améliorer la stabilité du MCP pendant les changements de phase péritectiques dans les conditions d'application. En fin, les résultats thermodynamiques préliminaires soulignent la nécessité d'améliorer les synthèses du MCP et les méthodes d'analyse de l'effet du FC dans l'hybride FC/MCP.

En conclusion, les études menées dans cette thèse ont apporté des progrès majeurs dans la description - et une meilleure compréhension - des feutres de carbone. Les études expérimentales et analytiques ont permis d'identifier des propriétés clés des matériaux et constitue un guide utile pour leur utilisation dans cette application spécifique. Les résultats de cette thèse ont déjà été mis en perspective lors des discussions et dans les conclusions de chaque chapitre, et plusieurs méthodes d'analyse ou d'amélioration ont été proposées. Les résultats de cette thèse pourraient aussi être facilement mis en œuvre une fois que la synthèse du MCP aura été optimisée et que de futurs tests applicatifs auront été effectués, permettant de classer les candidats FCs les plus appropriés sur la base des informations présentées. Néanmoins, il y a certains points qui à notre avis revêtent un plus grand intérêt encore.

Tout d'abord, cette thèse a été réalisée dans le cadre d'un projet associant différents instituts de recherche. Par conséquent, davantage de résultats sont encore attendus des tests de performances en application réelle des hybrides FC-MCP pour le stockage thermique, actuellement en cours dans un autre laboratoire dans le cadre du projet ANR Pc2TES, qui a été prolongé jusqu'en avril 2021. La poursuite de ce projet décrira plus précisément l'effet des carbones fibreux et de leurs propriétés sur le processus de charge-décharge d'énergie thermique,

et sur la stabilité et l'efficacité du MCP dans le matériau hybride par rapport au MCP seul. Ainsi, les résultats de cette thèse fourniront des indications supplémentaires et utiles pour améliorer les matériaux ou leur utilisation.

Enfin, il est important d'élaborer une stratégie de recherche et développement intégrée et une analyse du cycle de vie, en particulier en termes d'optimisation et de tests préliminaires des hybrides FC-MCP, d'analyse de leur stabilité à long terme, d'évaluation de leurs performances techniques et du coût de ces matériaux, et d'identification et d'estimation de l'impact environnemental associé.

En ce qui concerne la caractérisation des FCs, les éléments suivants sont suggérés pour des travaux futurs et pour l'utilisation de ces matériaux dans différentes applications:

La meilleure mouillabilité de ces structures carbonées hautement poreuses et perméables en présence de liquides peu polaires limite l'estimation précise des angles de contact correspondants, et donc de l'énergie de surface de ces solides par les techniques d'études traditionnelles. Par conséquent, une étude future de l'énergie de surface de ces solides devrait également être menée, notamment par analyse gravimétrique de sorption de vapeurs de différentes polarités. Cette étude devrait fournir une valeur générale de l'énergie de surface des matériaux d'intérêt et donner de meilleures estimations du mouillage des FCs par le MCP fondu. Il était prévu que cette étude soit menée, mais des problèmes techniques sur l'appareil, toujours non résolus, ne l'ont finalement pas permis.

Différentes simulations peuvent aussi être couplées avec de la microtomographie à rayons X pour étudier l'effet de la microstructure sur la perméabilité, la compressibilité et la conductivité thermique de carbones fibreux. Considérées comme une perspective, des études similaires devraient améliorer et faciliter l'intégration des FCs dans l'application TES.

De plus, les informations obtenues sur la morphologie et les propriétés thermiques des FC devraient permettre de progresser dans le développement et l'optimisation d'un modèle analytique pour l'estimation de la conductivité thermique de carbones fibreux.

Ainsi, de futurs tests devraient idéalement étudier la production de dépôts de pyrocarbone dépourvus de micro-vides et moins enclins à la fissuration. De plus, des tests de performances des hybrides FC-MCP devraient démontrer si les modifications apportées et l'amélioration attendue des performances de la structure carbonée hôte sont effectives à l'usage,

et justifient le surcoût correspondant par rapport à la légère diminution de la porosité et donc de la densité d'énergie finale.

Parallèlement à l'application présentée, dans le cadre d'une collaboration avec le Département de Physique de l'Université de Vilnius, les propriétés conductrices électriques des FCs dans une large gamme de températures et de fréquences ont été étudiées. L'origine des fluctuations de voltage et du bruit dans ces structures hautement poreuses a ainsi pu être déterminé, et des applications dans des senseurs ont pu être suggérées.

List of works

Publications in scientific journals

F. Achchaq, E. Risueño, I. Mahroug, P. Legros, E. Lebraud, **B. Karakashov**, E. Palomo del Barrio, V. Fierro, A. Celzard, J. Toutain (2018) Development of a Carbon Felt/Salt-Based Hybrid Material for Thermal Energy Storage Applications, *Journal of Energy and Power Engineering* 12 356-364

B. Karakashov, J. Toutain, F. Achchaq, P. Legros, V. Fierro, A. Celzard (2019) Permeability of fibrous carbon materials, *J Mater Sci* (2019) 54:13537–13556

B. Karakashov, V. Fierro, S. Mathieu, P. Gadonneix, G. Medjahdi, A. Celzard (2019) Structural characterisation and chemical stability of commercial fibrous carbons in molten lithium salts, *Materials* (2019) 12:4232–4262

Publications in preparation for publishing in scientific journals

B. Karakashov, J. Dentzer, D. Julien, F. Achchaq, R. Gadiou, G. Vignoles, V. Fierro, A. Celzard. An investigation into chemical vapour deposition method to enhance the properties of fibrous carbons for high temperature thermal energy storage application

B. Karakashov, V. Fierro, A. Celzard. Mechanical load and heat transfer in fibrous carbons

Publication in conference journal

M. Tretjak, S. Pralgauskaitė, J. Matukas, I. Kranauskaitė, J. Macutkevič, J. Banys, V. Fierro, A. Celzard, **B. Karakashov** (2019) Resistivity Characteristics and Noise Spectroscopy of Composites with Carbon Fiber Felts ICNF 2019: 25TH INTERNATIONAL CONFERENCE ON NOISE AND FLUCTUATIONS (1-4)

Oral communications

B. Karakashov, J. Dentzer, R. Gadiou, V. Fierro, A. Celzard (2019) Characterization and modification of carbon felts for enhanced Thermal Energy Storage (TES) application, *Journées de la Société Francophone d'Étude des Carbones*, 23 – 26 April 2019, Samatan-Gers

B. Karakashov, V. Fierro, A. Celzard (2018) Characterization of commercial non-woven carbon mats for Thermal Energy Storage (TES) application, *Journées de la Société Francophone d'Étude des Carbones*, 15 – 18 May 2018, Obernai

Poster communications

I. Mahroug, E. Risueño, **B. Karakashov**, F. Achchaq, P. Legros, E. Palomo del Barrio, A. Godin, J. Toutain, M. Duquesne, V. Fierro, A. Celzard (2018) Infiltration of a carbon felt with a non-eutectic mixture for thermal energy storage, ICOMÉ, 30 April – 04 May 2018, San Sebastian, Spain

J. F. Vivo-Vilches, M. Etienne, **B. Karakashov**, A. Celzard, V. Fierro, N. Brosse, A. Dufour (2018) Carbon monoliths with hierarchical porous structure for all-vanadium redox flow batteries, CARBON 2018, Madrid, Spain

B. Karakashov, J. Toutain, F. Achchaq, P. Legros, V. Fierro, A. Celzard (2019) Highlighting a universal behavior in the permeability of fibrous carbons, CARBON 2019, Lexington, USA

Abstract

In this thesis, fibrous carbons of renewable or synthetic origin in the form of flexible or rigid porous structures were investigated in-depth in order to evaluate their future use as hosts of phase change materials for thermal energy storage applications. Various commercial fibrous carbons were sorted, their morphological, physical and structural properties were thoroughly characterised, and their chemical stability was tested in molten lithium salts, before and after chemical vapour deposition of pyrocarbon. Either traditional or novel methodologies were proposed to characterise the fibrous carbons properties with respect to their effect on the preparation and performances of a hybrid material: carbon / phase change material. The use of different empirical and analytical models was also presented in order to determine characteristic quantities that are not directly measurable, such as elastic modulus of soft felts and tortuosity, and to validate the accuracy of the experimental results, all having an excellent predictive character. The materials' attractiveness is due to the examined: (i) lightweight and highly porous structure with remarkable physical properties; (ii) resistance to oxidation; (iii) ability of being modified. Indeed, it appears that fibrous carbons with improved characteristics in terms of heat transfer, mechanical strength and chemical stability can be obtained and should produce, without significant loss of porosity and thus of stored thermal energy density, better hybrid materials. Finally, while the work presented here has a direct impact on the future implementation of fibrous carbons in thermal energy storage applications, the results obtained might also be used for many other end-uses.

Résumé

Dans cette thèse, des carbones fibreux d'origine renouvelable ou synthétique sous forme de structures poreuses souples ou rigides ont été étudiés en détail afin d'évaluer leur utilisation future comme matrices hôtes de matériaux à changement de phase pour des applications de stockage d'énergie thermique. Différents carbones fibreux commerciaux ont été classés par familles, leurs morphologies et leurs propriétés physiques et structurales ont été entièrement caractérisées, et leur stabilité chimique a été testée dans des sels de lithium fondus, avant et après dépôt chimique en phase vapeur de pyrocarbone. Des méthodologies classiques ou nouvelles ont été proposées pour caractériser les propriétés des carbones fibreux en ce qui concerne leur effet sur la préparation et les performances d'un matériau hybride: carbone / matériau à changement de phase. L'utilisation de différents modèles empiriques et analytiques a également été présentée afin de déterminer les grandeurs caractéristiques non directement mesurables de ces matériaux, telles que le module élastique des feutres souples et la tortuosité, et de valider la précision des résultats expérimentaux, tous avec un très bon caractère prédictif. L'attractivité des matériaux est due à leur: (i) légèreté et structure hautement poreuse, avec des propriétés physiques remarquables; (ii) résistance à l'oxydation; (iii) aptitude à être modifiés. En effet, il apparaît que des carbones fibreux avec des caractéristiques améliorées en termes de transfert thermique, résistance mécanique et stabilité chimique peuvent être obtenus et pourraient produire, sans perte sensible de porosité et donc de densité d'énergie thermique stockée, de meilleurs matériaux hybrides. Enfin, si les travaux présentés ici ont un impact direct sur la mise en œuvre future de carbones fibreux dans les applications de stockage d'énergie thermique, les résultats obtenus pourraient aussi être utilisés dans de nombreux autres domaines.